Can tailored T cells kill solid tumors? *p. 983*

Paradoxical refugee politics *p. 994*

How dogs process human language *p. 1030*

Science

$15
2 SEPTEMBER 2016
sciencemag.org

AAAS

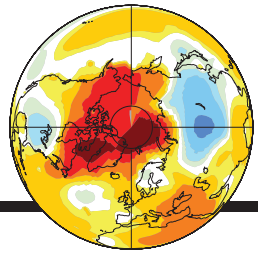


DAWN EXPLORES CERES

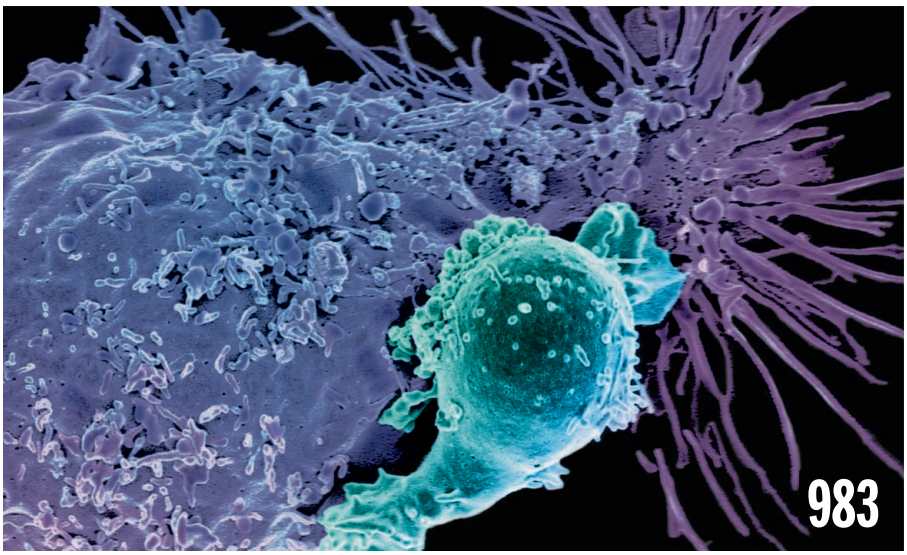
A dwarf planet made of rock and ice *pp. 1003–1010*

CONTENTS

2 SEPTEMBER 2016 • VOLUME 353 • ISSUE 6303



989 Arctic connections?



NEWS

IN BRIEF

970 News at a glance

IN DEPTH

974 **NASA TO LAUNCH ASTEROID-SAMPLING MISSION**
OSIRIS-REx plans to return more than 60 grams of dust from carbon-rich Bennu *By P. Voosen*

975 **LONDON'S BIOMEDICAL BEHEMOTH OPENS ITS DOORS**
The £650 million Francis Crick Institute aims to foster collaboration—but Brexit casts a shadow *By E. Stokstad*

976 **A PAINSTAKING OVERHAUL FOR CARDIAC SAFETY TESTING**
New methods may better predict arrhythmia risk in vitro *By K. Servick*

977 **DUKE FRAUD CASE HIGHLIGHTS FINANCIAL RISKS FOR UNIVERSITIES**
Whistleblower alleges doctored data were used to secure $200 million in grants from NIH and other federal agencies *By A. McCook*

978 **CONGRESS FACES A LENGTHY SCIENCE TO-DO LIST**
2017 spending to be delayed
By Science*'s News Staff*

FEATURES

980 **MENTORING'S MOMENT**
NIH's new mentoring network aims to improve success rates for minority grant applicants. But it faces long odds
By J. Mervis

983 **SECOND CHAPTER**
T cell therapy has successfully targeted blood cancers. A bigger challenge is to make it work on solid tumors
By J. Couzin-Frankel

INSIGHTS

PERSPECTIVES

986 **NANOPOROUS FABRICS COULD KEEP YOU COOL**
Engineered polyethylene materials are opaque but allow heat to radiate
By S. V. Boriskina
▸ REPORT P. 1019

987 **TUMORS SET TIME**
Lung tumors in mice distally alter circadian cycling of transcripts and metabolites in the liver
By I. Shakhmantsir and A. Sehgal

989 **EFFECTS OF A WARMING ARCTIC**
It remains unclear to what extent the warming Arctic affects climate and weather extremes at lower latitudes
By T. G. Shepherd

991 **INDUCED PLURIPOTENT STEM CELLS, PAST AND FUTURE**
Ten years ago, a method to reprogram cells to a pluripotent state changed biomedical research *By E. P. Papapetrou*

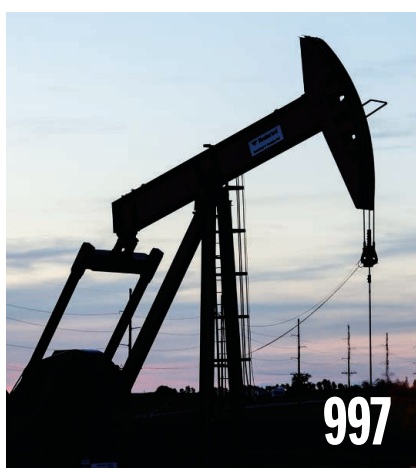
POLICY FORUM

994 **TENSIONS OF REFUGEE POLITICS IN EUROPE**
Electoral, welfare-state, and demographic politics are obstacles to refugees *By R. Hansen and S. Randeria*

BOOKS *ET AL.*

996 **REMEMBERING 9/11**
A historian probes the bitter conflicts that accompanied America's most costly forensic investigation *By S. Black*

997 **THE GREAT DEBATE**
Competing perspectives face off in a quest to find common ground on controversial energy issues
By G. Wong-Parodi



DEPARTMENTS

969 **EDITORIAL**
The science–policy interface
By Peter Gluckman

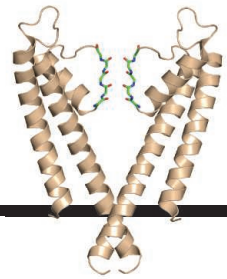
1062 **WORKING LIFE**
Thanks to the glass ceiling breakers
By Yarrow Axford

Science Staff 966
New Products 1050
Science Careers 1052

Downloaded from http://science.sciencemag.org/ on September 2, 2016

Published by AAAS

CONTENTS



1040 How potassium ions move through a channel

2 SEPTEMBER 2016 • VOLUME 353 • ISSUE 6303



998

LETTERS

998 COORDINATE EFFORTS ON EU INVASIVE SPECIES
By P. E. Hulme

998 USGS SCIENTISTS OPEN TO CHANGE
By G. C. Beroza et al.

999 RESCUED WILDLIFE IN CHINA REMAINS AT RISK
By Z.-M. Zhou et al.

RESEARCH

IN BRIEF

1000 From *Science* and other journals

RESEARCH ARTICLES

PLANETARY SCIENCE

1003 Cratering on Ceres: Implications for its crust and evolution
H. Hiesinger et al.
RESEARCH ARTICLE SUMMARY; FOR FULL TEXT:dx.doi.org/10.1126/science.aaf4759

1004 The geomorphology of Ceres
D. L. Buczkowski et al.
RESEARCH ARTICLE SUMMARY; FOR FULL TEXT: dx.doi.org/10.1126/science.aaf4332
▸ PODCAST

1005 Cryovolcanism on Ceres
O. Ruesch et al.
RESEARCH ARTICLE SUMMARY; FOR FULL TEXT: dx.doi.org/10.1126/science.aaf4286

1006 Distribution of phyllosilicates on the surface of Ceres
E. Ammannito et al.
RESEARCH ARTICLE SUMMARY; FOR FULL TEXT: dx.doi.org/10.1126/science.aaf4279

1007 Detection of local H_2O exposed at the surface of Ceres *J.-P. Combe* et al.
RESEARCH ARTICLE SUMMARY; FOR FULL TEXT: dx.doi.org/10.1126/science.aaf3010
▸ REPORT P. 1008

REPORTS

PLANETARY SCIENCE

1008 Dawn arrives at Ceres: Exploration of a small, volatile-rich world
C. T. Russell et al.
▸ RESEARCH ARTICLES PP. 1003, 1004, 1005, 1006, & 1007

WATER SPLITTING

1011 A highly active and stable $IrO_x/SrIrO_3$ catalyst for the oxygen evolution reaction
L. C. Seitz et al.

ORGANIC CHEMISTRY

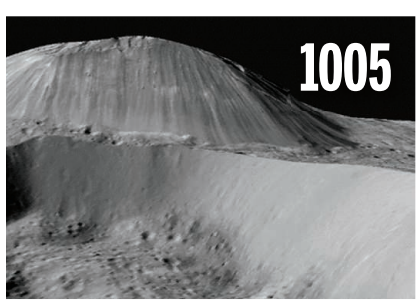
1014 Enantioselective cyanation of benzylic C–H bonds via copper-catalyzed radical relay *W. Zhang* et al.

TEXTILES

1019 Radiative human body cooling by nanoporous polyethylene textile
P.-C. Hsu et al.
▸ PERSPECTIVE P. 986; VIDEO

ASYMMETRIC CATALYSIS

1023 Ligand-accelerated enantioselective methylene C(sp^3)–H bond activation
G. Chen et al.



1005

PLANT SCIENCE

1027 Plant development regulated by cytokinin sinks *E. Zürcher* et al.

SPEECH PROCESSING

1030 Neural mechanisms for lexical processing in dogs
A. Andics et al.
▸ VIDEO

DENGUE VACCINE

1033 Benefits and risks of the Sanofi-Pasteur dengue vaccine: Modeling optimal deployment
N. M. Ferguson et al.

NEURODEVELOPMENT

1037 De novo synaptogenesis induced by GABA in the developing mouse cortex
W. C. Oh et al.

ION CHANNELS

1040 Instantaneous ion configurations in the K^+ ion channel selectivity filter revealed by 2D IR spectroscopy
H. T. Kratochvil et al.

HIV-1 ANTIBODIES

1045 Antibody-mediated protection against SHIV challenge includes systemic clearance of distal virus *J. Liu* et al.

ON THE COVER



The surface of the dwarf planet Ceres, as seen by NASA's Dawn spacecraft. On the left is the pale mountain Ahuna Mons, a 4-kilometer-high cryovolcano formed by an eruption of ice from beneath the surface. On the right is an unnamed 17-kilometer-diameter crater. Orbital imagery was combined with a digital terrain model to create this perspective view. See pages 1003–1010. *Image: NASA/JPL-Caltech/UCLA/MPS/DLR/IDA; Image rendering: C. Bickel/* Science, *K. Hughson/UCLA, and O. Ruesch/USRA-GSFC*

Downloaded from http://science.sciencemag.org/ on September 2, 2016

SCIENCE (ISSN 0036-8075) is published weekly on Friday, except the last week in December, by the American Association for the Advancement of Science, 1200 New York Avenue, NW, Washington, DC 20005. Periodicals mail postage (publication No. 484460) paid at Washington, DC, and additional mailing offices. Copyright © 2016 by the American Association for the Advancement of Science. The title SCIENCE is a registered trademark of the AAAS. Domestic individual membership and subscription (51 issues): $165 ($74 allocated to subscription). Domestic institutional subscription (51 issues): $1522; Foreign postage extra: Mexico, Caribbean (surface mail) $55; other countries (air assist delivery) $89. First class, airmail, student, and emeritus rates on request. Canadian rates with GST available upon request, GST #1254 88122. Publications Mail Agreement Number 1069624. **Printed in the U.S.A.**
Change of address: Allow 4 weeks, giving old and new addresses and 8-digit account number. **Postmaster:** Send change of address to AAAS, P.O. Box 96178, Washington, DC 20090–6178. **Single-copy sales:** $15.00 current issue, $20.00 back issue prepaid includes surface postage; bulk rates on request. **Authorization to photocopy** material for internal or personal use under circumstances not falling within the fair use provisions of the Copyright Act is granted by AAAS to libraries and other users registered with the Copyright Clearance Center (CCC) Transactional Reporting Service, provided that $35.00 per article is paid directly to CCC, 222 Rosewood Drive, Danvers, MA 01923. The identification code for *Science* is 0036-8075. *Science* is indexed in the *Reader's Guide to Periodical Literature* and in several specialized indexes.

Published by AAAS

Science
AAAS
1200 New York Avenue, NW, Washington, DC 20005
Clarendon House, Clarendon Road, Cambridge, UK CB2 8FH

Editor-in-Chief Jeremy Berg
Executive Editor Monica M. Bradford **News Editor** Tim Appenzeller
Deputy Editors Lisa D. Chong, Andrew M. Sugden(UK), Valda J. Vinson, Jake S. Yeston

Research and Insights

DEPUTY EDITOR, EMERITUS Barbara R. Jasny **SR. EDITORS** Caroline Ash(UK), Gilbert J. Chin, Julia Fahrenkamp-Uppenbrink(UK), Pamela J. Hines, Stella M. Hurtley(UK), Paula A. Kiberstis, Marc S. Lavine(Canada), Kristen L. Mueller, Ian S. Osborne(UK), Beverly A. Purnell, L. Bryan Ray, Guy Riddihough, H. Jesse Smith, Jelena Stajic, Peter Stern(UK), Phillip D. Szuromi, Sacha Vignieri, Brad Wible, Nicholas S. Wigginton, Laura M. Zahn **ASSOCIATE EDITORS** Brent Grocholski, Keith T. Smith **ASSOCIATE BOOK REVIEW EDITOR** Valerie B. Thompson **LETTERS EDITOR** Jennifer Sills **LEAD CONTENT PRODUCTION EDITORS** Harry Jach, Lauren Kmec **CONTENT PRODUCTION EDITORS** Jeffrey E. Cook, Chris Filiatreau, Cynthia Howe, Barbara P. Ordway, Catherine Wolner **SR. EDITORIAL COORDINATORS** Carolyn Kyle, Beverly Shields **EDITORIAL COORDINATORS** Aneera Dobbins, Joi S. Granger, Jeffrey Hearn, Lisa Johnson, Maryrose Madrid, Anita Wynn **PUBLICATIONS ASSISTANTS** Nida Masiulis, Dona Mathieu, Le-Toya Mayne Flood, Shannon McMahon, Scott Miller, Jerry Richardson, Alice Whaley(UK), Brian White **EXECUTIVE ASSISTANT** Anna Bashkirova **ADMINISTRATIVE SUPPORT** Janet Clements(UK), Lizanne Newton(UK)

News

NEWS MANAGING EDITOR John Travis **INTERNATIONAL EDITOR** Richard Stone **DEPUTY NEWS EDITORS** Elizabeth Culotta, David Grimm, Eric Hand David Malakoff, Leslie Roberts **CONTRIBUING EDITOR** Martin Enserink(Europe) **SR. CORRESPONDENTS** Daniel Clery(UK), Jeffrey Mervis, Elizabeth Pennisi **NEWS WRITERS** Adrian Cho, Jon Cohen, Jennifer Couzin-Frankel, Carolyn Gramling, Jocelyn Kaiser, Catherine Matacic, Kelly Servick, Robert F. Service, Erik Stokstad(Cambridge, UK) **INTERNS** Jessica Boddy, Ben Panko **CONTRIBUTING CORRESPONDENTS** John Bohannon, Warren Cornwall, Ann Gibbons, Mara Hvistendahl, Sam Kean, Eli Kintisch, Kai Kupferschmidt(Berlin), Andrew Lawler, Mitch Leslie, Charles C. Mann, Eliot Marshall, Virginia Morell, Dennis Normile(Shanghai), Heather Pringle, Tania Rabesandratana(London), Emily Underwood, Gretchen Vogel(Berlin), Lizzie Wade(Mexico City) **CAREERS** Donisha Adams, Rachel Bernstein(Editor), Maggie Kuo **COPY EDITORS** Julia Cole, Dorie Chevlen, Jennifer Levin (Chief) **ADMINISTRATIVE SUPPORT** Jessica Adams

Executive Publisher Rush D. Holt
Publisher Bill Moran **Chief Digital Media Officer** Rob Covey

BUSINESS OPERATIONS AND PORTFOLIO MANAGEMENT DIRECTOR Sarah Whalen **PRODUCT DEVELOPMENT DIRECTOR** Will Schweitzer **PRODUCT DEVELOPMENT ASSOCIATE** Hannah Heckner **BUSINESS SYSTEMS AND FINANCIAL ANALYSIS DIRECTOR** Randy Yi **SENIOR SYSTEMS ANALYST** Nicole Mehmedovich **DIRECTOR, BUSINESS OPERATIONS & ANALYSIS** Eric Knott **MANAGER, BUSINESS OPERATIONS** Jessica Tierney **SENIOR BUSINESS ANALYST** Cory Lipman **BUSINESS ANALYSTS** David Garrison, Michael Hardesty Meron Kebede, Sandy Kim **FINANCIAL ANALYST** Drew Sher **DIRECTOR, COPYRIGHTS LICENSING SPECIAL PROJECTS** Emilie David **PERMISSIONS ASSOCIATE** Elizabeth Sandler **RIGHTS, CONTRACTS, AND LICENSING ASSOCIATE** Lili Kiser **RIGHTS & PERMISSIONS ASSISTANT** Alexander Lee

MARKETING DIRECTOR Elise Swinehart **ASSOCIATE MARKETING DIRECTOR** Stacey Burke Bowers **MARKETING ASSOCIATE** Steven Goodman **CREATIVE DIRECTOR** Scott Rodgerson **SENIOR ART ASSOCIATES** Paula Fry **ART ASSOCIATE** Kim Huynh

FULFILLMENT SYSTEMS AND OPERATIONS membership@aaas.org **MANAGER, MEMBER SERVICES** Pat Butler **SPECIALISTS** Terrance Morrison, Latasha Russell **MANAGER, DATA ENTRY** Mickie Napoleoni **DATA ENTRY SPECIALISTS** Brenden Aquilino, Fiona Giblin **MARKETING ASSOCIATE** Isa Sesay-Bah

PUBLISHER RELATIONS, EASTERN REGION Keith Layson **PUBLISHER RELATIONS, WESTERN REGION** Ryan Rexroth **SALES RESEARCH COORDINATOR** Aiesha Marshall **ASSOCIATE DIRECTOR, INSTITUTIONAL LICENSING OPERATIONS** Iquo Edim **SENIOR OPERATIONS ANALYST** Lana Guz **MANAGER, AGENT RELATIONS & CUSTOMER SUCCESS** Judy Lillibridge

WEB TECHNOLOGIES PORTFOLIO MANAGER Trista Smith **TECHNICAL MANAGER** Chris Coleman **PROJECT MANAGER** Nick Fletcher **DEVELOPERS** Ryan Jensen, Jimmy Marks, Brandon Morrison **BUSINESS ANALYST** Christina Wofford

DIGITAL MEDIA DIRECTOR OF ANALYTICS Enrique Gonzales **DIGITAL REPORTING ANALYST** Eric Hossinger **SR. MULTIMEDIA PRODUCER** Sarah Crespi **MANAGING DIGITAL PRODUCER** Alison Crawford **PRODUCER** Liana Birke **VIDEO PRODUCER** Chris Burns, Nguyên Khôi Nguyễn **DIGITAL SOCIAL MEDIA PRODUCER** Brice Russ

DIRECTOR OF OPERATIONS PRINT AND ONLINE Lizabeth Harman **DIGITAL/PRINT STRATEGY MANAGER** Jason Hillman **QUALITY TECHNICAL MANAGER** Marcus Spiegler **PROJECT ACCOUNT MANAGER** Tara Kelly **DIGITAL PRODUCTION MANAGER** Lisa Stanford **ASSISTANT MANAGER DIGITAL/PRINT** Rebecca Doshi **SENIOR CONTENT SPECIALISTS** Steve Forrester, Antoinette Hodal, Lori Murphy, Anthony Rosen **CONTENT SPECIALISTS** Jacob Hedrick, Kimberley Oster **ADVERTISING OPERATIONS SPECIALIST** Ashley Jeter

DESIGN DIRECTOR Beth Rakouskas **DESIGN EDITOR** Marcy Atarod **SENIOR DESIGNERS** Garvin Grullón, Chrystal Smith **GRAPHICS MANAGING EDITOR** Alberto Cuadra **SENIOR SCIENTIFIC ILLUSTRATORS** Chris Bickel, Katharine Sutliff **SCIENTIFIC ILLUSTRATOR** Valerie Altounian **INTERACTIVE GRAPHICS EDITOR** Jia You **SENIOR GRAPHICS SPECIALISTS** Holly Bishop, Nathalie Cary **PHOTOGRAPHY MANAGING EDITOR** William Douthitt **SENIOR PHOTO EDITOR** Christy Steele **PHOTO EDITOR** Emily Petersen

DIRECTOR, GLOBAL COLLABORATION, CUSTOM PUBLICATIONS, ADVERTISING Bill Moran **EDITOR, CUSTOM PUBLISHING** Sean Sanders: 202-326-6430 **ADVERTISING MARKETING MANAGER** Justin Sawyers: 202-326-7061 science_advertising@aaas.org **ADVERTISING SUPPORT MANAGER** Karen Foote: 202-326-6740 **ADVERTISING PRODUCTION OPERATIONS MANAGER** Deborah Tompkins **SR. PRODUCTION SPECIALIST/GRAPHIC DESIGNER** Amy Hardcastle **SR. TRAFFIC ASSOCIATE** Christine Hall **SALES COORDINATOR** Shirley Young **ASSOCIATE DIRECTOR, COLLABORATION, CUSTOM PUBLICATIONS/CHINA/TAIWAN/KOREA/SINGAPORE** Ruolei Wu: +86-186 0082 9345, rwu@aaas.org **COLLABORATION/CUSTOM PUBLICATIONS/JAPAN** Adarsh Sandhu + 81532-81-5142 asandhu@aaas.org **EAST COAST/E. CANADA** Laurie Faraday: 508-747-9395, FAX 617-507-8189 **WEST COAST/W. CANADA** Lynne Stickrod: 415-931-9782, FAX 415-520-6940 **MIDWEST** Jeffrey Dembksi: 847-498-4520 x3005, Steven Loerch: 847-498-4520 x3006 **UK EUROPE/ASIA** Roger Goncalves: TEL/FAX +41 43 243 1358 **JAPAN** Katsuyoshi Fukamizu(Tokyo): +81-3-3219-5777 kfukamizu@aaas.org **CHINA/TAIWAN** Ruolei Wu: +86-186 0082 9345, rwu@aaas.org

WORLDWIDE ASSOCIATE DIRECTOR OF SCIENCE CAREERS Tracy Holmes: +44 (0) 1223 326525, FAX +44 (0) 1223 326532 tholmes@science-int.co.uk **CLASSIFIED** advertise@sciencecareers.org **U.S. SALES** Tina Burks: 202-326-6577, Nancy Toema: 202-326-6578 **EUROPE/ROW SALES** Sarah Lelarge **SALES ASSISTANT** Kelly Grace **JAPAN** Hiroyuki Mashiki(Kyoto): +81-75-823-1109 hmashiki@aaas.org **CHINA/TAIWAN** Ruolei Wu: +86-186 0082 9345 rwu@aaas.org **MARKETING MANAGER** Allison Pritchard **MARKETING ASSOCIATE** Aimee Aponte

AAAS BOARD OF DIRECTORS, CHAIR Geraldine L. Richmond **PRESIDENT** Barbara A. Schaal **PRESIDENT-ELECT** Susan Hockfield **TREASURER** David Evans Shaw **CHIEF EXECUTIVE OFFICER** Rush D. Holt **BOARD** Cynthia M. Beall, May R. Berenbaum, Carlos J. Bustamante, Stephen P.A. Fodor, Claire M. Fraser, Michael S. Gazzaniga, Laura H. Greene, Elizabeth Loftus, Mercedes Pascual

SUBSCRIPTION SERVICES For change of address, missing issues, new orders and renewals, and payment questions: 866-434-AAAS (2227) or 202-326-6417, FAX 202-842-1065. Mailing addresses: AAAS, P.O. Box 96178, Washington, DC 20090-6178 or AAAS Member Services, 1200 New York Avenue, NW, Washington, DC 20005

INSTITUTIONAL SITE LICENSES 202-326-6730 **REPRINTS:** Author Inquiries 800-635-7181 **COMMERCIAL INQUIRIES** 803-359-4578 **PERMISSIONS** 202-326-6765, permissions@aaas.org **AAAS Member Services** 202-326-6417 or http://membercentral.aaas.org/discounts

Science serves as a forum for discussion of important issues related to the advancement of science by publishing material on which a consensus has been reached as well as including the presentation of minority of conflicting points of view. Accordingly, all articles published in *Science*—including editorials, news and comment, and book reviews—are signed and reflect the individual views of the authors and not official points of view adopted by AAAS or the institutions with which the authors are affiliated.

INFORMATION FOR AUTHORS See pages 624 and 625 of the 5 February 2016 issue or access www.sciencemag.org/authors/science-information-authors

SENIOR EDITORIAL BOARD
Gary King, *Harvard University,* **Susan M. Rosenberg,** *Baylor College of Medicine,*
Ali Shilatifard, *Northwestern University Feinberg School of Medicine*

BOARD OF REVIEWING EDITORS (Statistics board members indicated with **(S)**)

Adriano Aguzzi, *U. Hospital Zürich*
Takuzo Aida, *U. of Tokyo*
Leslie Aiello, *Wenner-Gren Foundation*
Judith Allen, *U. of Edinburgh*
Sonia Altizer, *U. of Georgia*
Sebastian Amigorena, *Institut Curie*
Kathryn Anderson, *Memorial Sloan-Kettering Cancer Center*
Meinrat O. Andreae, *Max-Planck Inst. Mainz*
Paola Arlotta, *Harvard U.*
Johan Auwerx, *EPFL*
David Awschalom, *U. of Chicago*
Clare Baker, *University of Cambridge*
Nenad Ban, *ETH Zurich*
Jordi Bascompte, *University of Zurich*
Franz Bauer, *Pontificia Universidad Católica de Chile*
Ray H. Baughman, *U. of Texas, Dallas*
David Baum, *U. of Wisconsin*
Carlo Beenakker, *Leiden U.*
Kamran Behnia, *ESPCI-ParisTech*
Yasmine Belkaid, *NIAID, NIH*
Philip Benfey, *Duke U.*
May Berenbaum, *U. of Illinois*
Gabriele Bergers, *U. of California, San Francisco*
Bradley Bernstein, *Massachusettes General Hospital*
Peer Bork, *EMBL*
Bernard Bourdon, *Ecole Normale Supérieure de Lyon*
Chris Bowler, *École Normale Supérieure*
Ian Boyd, *U. of St. Andrews*
Emily Brodsky, *U. of California, Santa Cruz*
Ron Brookmeyer, *U. of California Los Angeles* **(S)**
Christian Büchel, *U. Hamburg-Eppendorf*
Joseph A. Burns, *Cornell U.*
Carter Tribley Butts, *U. of California, Irvine*
Gyorgy Buzsaki, *New York U. School of Medicine*
Blanche Capel, *Duke U.*
Mats Carlsson, *U. of Oslo*
Ib Chorkendorff, *U. of Denmark*
David Clapham, *Children's Hospital Boston*
Joel Cohen, *Rockefeller U., Columbia U.*
James J. Collins, *MIT*
Robert Cook-Deegan, *Duke U.*
Lisa Coussens, *Oregon Health & Science U.*
Alan Cowman, *Walter & Eliza Hall Inst.*
Robert H. Crabtree, *Yale U.*
Roberta Croce, *Vrije Universiteit*
Janet Currie, *Princeton U.*
Jeff L. Dangl, *U. of North Carolina*
Tom Daniel, *U. of Washington*
Frans de Waal, *Emory U.*
Stanislas Dehaene, *Collège de France*
Robert Desimone, *MIT*
Claude Desplan, *New York U.*
Dennis Discher, *U. of Pennsylvania*
Gerald W. Dorn II, *Washington U. School of Medicine*
Jennifer A. Doudna, *U. of California, Berkeley*
Bruce Dunn, *U. of California, Los Angeles*
William Dunphy, *Caltech*
Christopher Dye, *WHO*
Todd Ehlers, *U. of Tuebingen*
David Ehrhardt, *Carnegie Inst. of Washington*
Tim Elston, *U. of North Carolina at Chapel Hill*
Jennifer Elisseeff, *U. of N*
Gerhard Ertl, *Fritz-Haber-Institut, Berlin*
Barry Everitt, *U. of Cambridge*
Ernst Fehr, *Johns Hopkins U.*
Anne C. Ferguson-Smith, *U. of Cambridge*
Michael Feuer, *The George Washington U.*
Toren Finkel, *NHLBI, NIH*
Kate Fitzgerald, *U. of Massachusetts*
Peter Fratzl, *Max-Planck Inst.*
Elaine Fuchs, *Rockefeller U.*
Daniel Geschwind, *UCLA*
Karl-Heinz Glassmeier, *TU Braunschweig*
Ramon Gonzalez, *Rice U.*
Julia R. Greer, *Caltech*
Elizabeth Grove, *U. of Chicago*
Nicolas Gruber, *ETH Zurich*
Kip Guy, *St. Jude's Children's Research Hospital*
Taekjip Ha, *U. of Illinois at Urbana-Champaign*
Wolf-Dietrich Hardt, *ETH Zurich*
Christian Haass, *Ludwig Maximilians U.*
Sharon Hammes-Schiffer, *U. of Illinois at Urbana–Champaign*
Michael Hasselmo, *Boston U.*
Martin Heimann, *Max-Planck Inst. Jena*
Yka Helariutta, *U. of Cambridge*
James A. Hendler, *Rensselaer Polytechnic Inst.*
Janet G. Hering, *Swiss Fed. Inst. of Aquatic Science & Technology*
Kai-Uwe Hinrichs, *U. of Bremen*
David Hodell, *U. of Cambridge*
Lora Hooper, *UT Southwestern Medical Ctr. at Dallas*
Tamas Horvath, *Yale University*
Raymond Huey, *U. of Washington*
Fred Hughson, *Princeton U.*
Auke Ijspeert, *EPFL Lausanne*
Stephen Jackson, *USGS and U. of Arizona*
Steven Jacobsen, *U. of California, Los Angeles*
Kai Johnsson, *EPFL Lausanne*
Peter Jonas, *Inst. of Science & Technology (IST) Austria*
Matt Kaeberlein, *U. of Washington*
William Kaelin Jr., *Dana-Farber Cancer Inst.*
Daniel Kahne, *Harvard U.*
Daniel Kammen, *U. of California, Berkeley*
Abby Kavner, *U. of California, Los Angeles*
Hitoshi Kawakatsu, *U. of Tokyo*
Masashi Kawasaki, *U. of Tokyo*
V. Narry Kim, *Seoul National U.*
Robert Kingston, *Harvard Medical School*
Etienne Koechlin, *Ecole Normale Suprieure*
Alexander Kolodkin, *Johns Hopkins U.*
Thomas Langer, *U. of Cologne*
Mitchell A. Lazar, *U. of Pennsylvania*
David Lazer, *Harvard U.*
Thomas Lecuit, *IBDM*
Virginia Lee, *U. of Pennsylvania*
Stanley Lemon, *U. of North Carolina at Chapel Hill*
Ottoline Leyser, *Cambridge U.*
Wendell Lim, *U.C. San Francisco*
Marcia C. Linn, *U. of California, Berkeley*
Jianguo Liu, *Michigan State U.*
Luis Liz-Marzan, *CIC biomaGUNE*
Jonathan Losos, *Harvard U.*
Ke Lu, *Chinese Acad. of Sciences*
Christian Lüscher, *U. of Geneva*
Laura Machesky, *CRUK Beatson Inst. for Cancer Research*
Anne Magurran, *U. of St. Andrews*
Oscar Marin, *CSIC & U. Miguel Hernández*
Charles Marshall, *U. of California, Berkeley*
C. Robertson McClung, *Dartmouth College*
Rodrigo Medellin, *U. of Mexico*
Graham Medley, *U. of Warwick*
Tom Misteli, *NCI*
Yasushi Miyashita, *U. of Tokyo*
Mary Ann Moran, *U. of Georgia*
Richard Morris, *U. of Edinburgh*
Alison Motsinger-Reif, *NC State U.* **(S)**
Thomas Murray, *The Hastings Center*
Daniel Neumark, *U. of California, Berkeley*
Kitty Nijmeijer, *U. of Twente*
Helga Nowotny, *European Research Advisory Board*
Ben Olken, *MIT*
Rachel O'Reilly, *Warwick U.*
Joe Orenstein, *U. of California Berkeley & Lawrence Berkeley National Lab*
Harry Orr, *U. of Minnesota*
Pilar Ossorio, *U. of Wisconsin*
Andrew Oswald, *U. of Warwick*
Isabella Pagano, *Istituto Nazionale di Astrofisica*
Margaret Palmer, *U. of Maryland*
Steve Palumbi, *Stanford U.*
Jane Parker, *Max-Planck Inst. of Plant Breeding Research*
Giovanni Parmigiani, *Dana-Farber Cancer Inst.* **(S)**
John H. J. Petrini, *Memorial Sloan-Kettering Cancer Center*
Samuel Pfaff, *Salk Institute for Biological Studies*
Joshua Plotkin, *U. of Pennsylvania*
Albert Polman, *FOM Institute AMOLF*
Philippe Poulin, *CNRS*
Jonathan Pritchard, *Stanford U.*
Wim van der Putten, *Netherlands Institute of Ecology*
David Randall, *Colorado State U.*
Felix Rey, *Institut Pasteur*
Trevor Robbins, *U. of Cambridge*
Jim Roberts, *Fred Hutchinson Cancer Research Ctr.*
Amy Rosenzweig, *Northwestern University*
Mike Ryan, *U. of Texas, Austin*
Mitinori Saitou, *Kyoto U.*
Shimon Sakaguchi, *Kyoto U.*
Miquel Salmeron, *Lawrence Berkeley National Lab*
Jürgen Sandkühler, *Medical U. of Vienna*
Alexander Schier, *Harvard U.*
Vladimir Shalaev, *Purdue U.*
Robert Siliciano, *Johns Hopkins School of Medicine*
Denis Simon, *Arizona State U.*
Uri Simonsohn, *U. of Pennsylvania*
Alison Smith, *John Innes Centre*
Richard Smith, *U. of North Carolina* **(S)**
John Speakman, *U. of Aberdeen*
Allan C. Spradling, *Carnegie Institution of Washington*
Jonathan Sprent, *Garvan Inst. of Medical Research*
Eric Steig, *U. of Washington*
Paula Stephan, *Georgia State U. and National Bureau of Economic Research*
Molly Stevens, *Imperial College London*
V. S. Subrahmanian, *U. of Maryland*
Ira Tabas, *Columbia U.*
Sarah Teichmann, *Cambridge U.*
John Thomas, *North Carolina State U.*
Shubha Tole, *Tata Institute of Fundamental Research*
Christopher Tyler-Smith, *The Wellcome Trust Sanger Inst.*
Herbert Virgin, *Washington U.*
Bert Vogelstein, *Johns Hopkins U.*
Cynthia Volkert, *U. of Göttingen*
David Wallach, *Weizmann Inst. of Science*
Ian Walmsley, *U. of Oxford*
Jane-Ling Wang, *U. of California, Davis* **(S)**
David Waxman, *Fudan U.*
Jonathan Weissman, *U. of California, San Francisco*
Chris Wikle, *U. of Missouri* **(S)**
Ian A. Wilson, *The Scripps Res. Inst.* **(S)**
Timothy D. Wilson, *U. of Virginia*
Rosemary Wyse, *Johns Hopkins U.*
Jan Zaanen, *Leiden U.*
Kenneth Zaret, *U. of Pennsylvania School of Medicine*
Jonathan Zehr, *U. of California, Santa Cruz*
Len Zon, *Children's Hospital Boston*
Maria Zuber, *MIT*

BOOK REVIEW BOARD
David Bloom, *Harvard U.,* **Samuel Bowring,** *MIT,* **Angela Creager,** *Princeton U.,*
Richard Shweder, *U. of Chicago,* **Ed Wasserman,** *DuPont*

EDITORIAL

The science–policy interface



Sir Peter Gluckman is the Chief Science Adviser to the Prime Minister of New Zealand and is Chair of the International Network for Government Science Advice. Email: peter.gluckman@pmcsa.org.nz

How do we ensure the effective role of science in public policy-making? This well-worn, long-standing question reflects the fact that the answer is not simple. Later this month in Brussels, scientists and policy-makers will convene at the International Network for Government Science Advice (INGSA) Forum to consider the most promising ways forward.

Scientists are often perplexed by the apparent failure of their evidence to affect policy. Despite years of accumulated evidence for anthropogenic climate change, policy-makers have been slow to react. The public health community is frustrated that few countries have adopted effective measures to address obesity. In these and other cases, evidence is often contested, and the policy responses are incremental at best. But policy-makers, too, are vexed by scientists' ability to identify problems, yet frequent inability to place their work in the context of timely and feasible policy solutions.



"...the place of scientific evidence in policy-making is neither straightforward nor guaranteed..."

Often forgotten is that policy-making is messy. Although a tidy, analytically driven cycle of policy-making might seem logical to scientists trained in the tradition of hypothesis generation and testing, policy-making is instead a networked process in which scientific evidence is only one of many inputs. The notion of "evidence" comes in multiple forms. Public opinion polls and anecdotes are often considered "evidence" for a certain course of action. Policy decisions involve balancing empirical data with other arguments.

The place of science is distinguished from other policy inputs by its relative objectivity obtained through formal processes designed to limit bias in data collection and analysis. Much scientific and societal debate emerges because of different views on evaluating the sufficiency of evidence on which to draw conclusions. Moreover, the issues for which scientific input is most needed by policy-makers are the very ones for which the science is often the most complex, multidisciplinary, and incomplete. In the absence of easily digestible scientific evidence, Wikipedia can become a policy analyst's best friend. And with the new lure of big data promising policy-relevant revelations, the need to ensure that policy-makers avoid analytical pitfalls is pressing.

Providing scientific advice to government takes place within an ecosystem. It is a combination of actors who are both internal and external to government, with advice that is formal and informal. All of this comes in many guises and is conditioned by context. For instance, there will be different mechanisms for regulatory advice, program development, and cabinet-level decision-making. The latter often occur as informal conversations and brainstorming at opportune moments. National emergencies, by contrast, require instant scientific input through formal channels linked closely to crisis management and risk communication. For more slow-burning policy questions, internal advisors can ensure the integrity of science while those from outside government—such as academies—are a critical source of analysis and commentary.

But does such an ecosystem not risk becoming a cacophony of complicated claims for the policy-maker? One way forward is to establish principles that underpin effective science advisory mechanisms across all these dimensions and to build capacity on both the supply and demand sides of advisory processes. INGSA is dedicated to doing exactly this. The network brings together advisers, policy-makers, and scholars from more than 70 countries, with the goal of improving knowledge and practice at the interface of science and public policy. With the science-intensive United Nations Sustainable Development Goals, climate change, and other global challenges now part of many countries' policy discourse, the INGSA Forum will facilitate much-needed dialogue. Although the place of scientific evidence in policy-making is neither straightforward nor guaranteed, our commitment to it has never been more important.

–Peter Gluckman

10.1126/science.aai8837

PHOTOS: (INSET) THEMACX/ISTOCKPHOTO.COM; (TOP RIGHT) SYD MANNION

Downloaded from http://science.sciencemag.org/ on September 2, 2016

Published by AAAS

NEWS

> "One of your biggest enemies is boredom. The other big enemies, of course, are the rest of the crew."

German physicist Christiane Heinicke, one of six people who lived for a year in a solar-powered dome in Hawaii, simulating close living quarters on Mars. Heinicke's advice to future participants: Bring something "meaningful" to work on.

IN BRIEF



A deadly earthquake last week devastated the town of Amatrice, Italy, and surrounding villages, toppling centuries-old buildings.

Italy's scientists wrestle with earthquake risk

A magnitude-6.0 earthquake killed at least 290 people in a mountainous area about 100 kilometers northeast of Rome on 24 August—and there's a nonnegligible risk that it will be followed by a major aftershock, a panel of experts has concluded. Several historical earthquakes in central Italy produced powerful aftershocks, Italy's National Commission for the Forecast and Prevention of Major Risks (CGR) said in a press release issued 26 August by the country's Civil Protection Department (DPC). The panel noted examples of similar repeat quakes in 1639 and 1703. The group weighed its words carefully, cognizant of the controversy that followed a 2009 earthquake in L'Aquila, 40 kilometers to the south. Italian prosecutors charged six scientists—some of them CGR members—and a DPC official with falsely assuring residents of L'Aquila that their city was unlikely to be hit days before the earthquake struck and killed 309 people. The six were later acquitted, but the official was convicted (*Science*, 6 November 2015, p. 612). The affair has made scientists gun-shy about communicating seismic risks.

http://scim.ag/ItalyEQrisk

AROUND THE WORLD

Grad students can unionize

WASHINGTON, D.C. | In the culmination of a decadelong battle, the U.S. National Labor Relations Board (NLRB) ruled 23 August that graduate students at private universities are employees and have the right to collective bargaining. NLRB's decision is a reversal of a 2004 ruling, in which the board found that graduate student teaching assistants and research assistants at Brown University were "primarily students, and not workers," and that teaching and conducting research is part of their education. Two years ago, a group of graduate students at Columbia University began the debate anew, filing a petition with the board to join the United Auto Workers. Before the ruling, several private institutions, including Stanford University, the Massachusetts Institute of Technology, and the Ivy League, submitted a brief arguing that defining the student-faculty relationship as an employee-employer relationship would interfere with graduate training and academic freedom. Although

PHOTO: GREGORIO BORGIA/ASSOCIATED PRESS

Downloaded from http://science.sciencemag.org/ on September 1, 2016

Published by AAAS

labor issues at private institutions are governed by NLRB, graduate student unions have existed at public universities, which are governed by state laws.

Rapid glacier fall a deadly mystery

TIBET AUTONOMOUS REGION, IN CHINA | On the night of 17 July, a 5.7-kilometer-long section of Dongru Glacier in western Tibet suddenly collapsed, sweeping down a mountain and killing nine people living below in their summer pasture near Aruco Lake. In all, about 70 million cubic meters of ice fell, according to glaciologists at the Chinese Academy of Sciences in Beijing and The Ohio State University, Columbus. The scientists don't yet know what triggered the sudden collapse: Although glaciers are known to be retreating at a rapid rate on the southeastern side of the Tibetan Plateau, those in western Tibet have tended to be stable, or even advancing. However, the region has experienced rapid warming in recent years; increased precipitation in 2016 combined with warming ice could have led to the glacier's instability, the scientists say—suggesting that other glaciers in the region may present a looming geo-hazard.

California boosts climate bill

SACRAMENTO | California's legislature is keeping the Golden State at the forefront of government efforts to rein in climate change. On 25 August, it sent a bill to Governor Jerry Brown requiring that by 2030, statewide greenhouse gas emissions must be 40% below 1990 levels. The new measure, which Brown says he will sign, goes beyond the current goal of returning emissions to 1990 levels by 2020; the state is on track for that target. The bill puts the state, which by one measure has the world's sixth largest economy, on par with European climate change efforts. The legislature didn't tackle California's troubled cap-and-trade program, however, which puts a price on carbon pollution and is a key part of the state's climate policy. The system expires in 2020, faces a legal challenge, and has experienced a major drop in demand for tradeable pollution permits.

Resistant gonorrhea on the rise

GENEVA, SWITZERLAND | In a sign that antibiotic-resistant strains of gonorrhea have become a global problem, the World Health Organization (WHO) issued new guidelines on 30 August for treating the sexually transmitted disease, which infects an estimated 78 million people per year. Existing guidelines, isssued in 2003, recommended quinolones, a class of antibiotics derived from natural sources such as plants and bacteria, as the first-line treatment, but quinolones have become all but useless against *Neisseria gonorrhoeae*, the bacterium that causes gonorrhea. The new guidelines, already in use in most Western countries, recommend starting with cephalosporins, which are derived from the mold *Cephalosporium*. Many countries have reported strains resistant to cephalosporins as well; when these drugs fail, all that doctors have left are older antibiotics that have been studied less and to which resistance evolves very quickly, says Teodora Wi of WHO's Department of Reproductive Health and Research in Geneva, Switzerland. "We will be running out of alternatives soon," Wi says. WHO also updated guidelines for treatment of syphilis and chlamydia, two diseases for which resistance is less of a problem.

PHOTO: MARK SULLIVAN NMFS PERMIT 10137-07/NOAA



About half the world's Hawaiian monk seals live along the northwestern Hawaiian islands.

New protections for U.S. lands and waters

Hawaii's Papahānaumokuākea Marine National Monument is now the largest protected area on the planet, thanks to an order signed 26 August by U.S. President Barack Obama. The park, one of the most biologically diverse places in the world, more than quadruples the size of the existing monument, to 1.5 million square kilometers. (That's twice the size of Texas.) Resources can still be removed for Hawaiian traditions or scientific research with a permit, but commercial resource extraction—including most fishing—is now prohibited. Hawaiian state officials say Obama's move will preserve a cultural seascape and provide critical protection for more than 7000 marine species. Across the country, last week Maine's Mount Katahdin became the centerpiece of a new 35,000-hectare national park site, days after the 100th anniversary of the creation of the National Park Service.

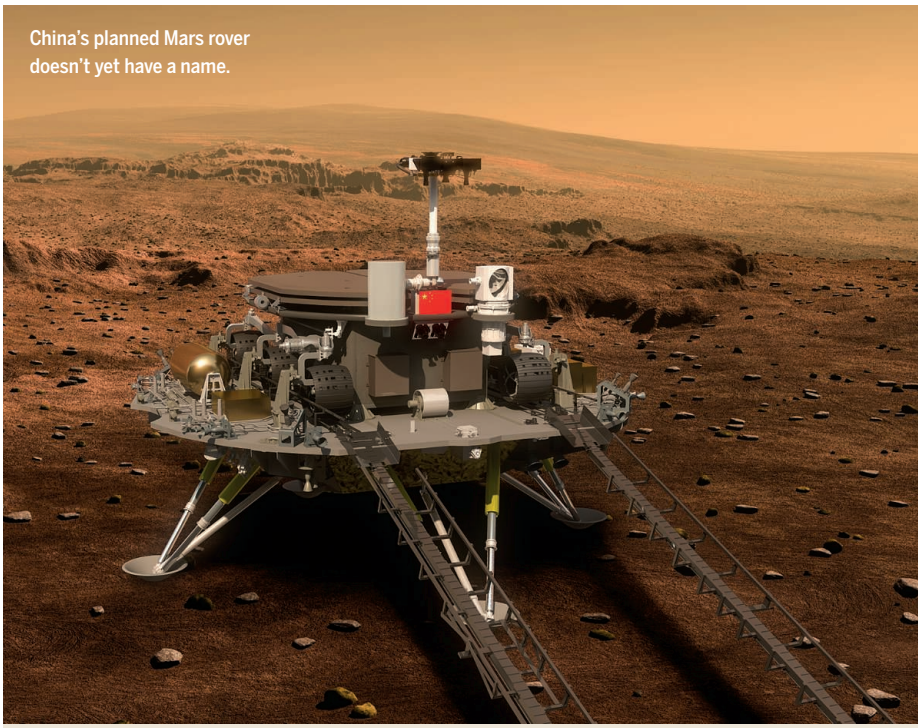
NEWSMAKERS

New child health chief

Prenatal geneticist **Diana Bianchi** will become director of the Eunice Kennedy Shriver National Institute of Child Health and Human Development (NICHD) in Bethesda, Maryland, on 31 October. Now at Tufts University School of Medicine in Boston, Bianchi, 61, has studied ways to isolate and analyze fetal cells or DNA in a mother's blood to detect fetal disorders, in the process discovering that fetal cells can remain in the mother's blood for decades after pregnancy. She is also exploring drugs that could be given in the womb to prevent abnormal brain development due to Down syndrome. Bianchi's multidisciplinary background should serve her well as head of the $1.3 billion NICHD, which funds research ranging from basic developmental biology to adolescent health. She says her priorities will include funding more high-quality grants, innovation, supporting young clinician-scientists, and involving patients and families in study design. She expects to bring her lab with her and to commute from Boston, where her family will remain. "I have advocated for the crucial importance of research to improve the health of mothers and babies and people with disabilities," she says. "So to be able to do this on a national level is incredibly special."

Downloaded from http://science.sciencemag.org/ on September 1, 2016

Published by AAAS



China's planned Mars rover doesn't yet have a name.

China unveils new Mars rover

China gave the first glimpse of its planned solar-powered Mars rover, intended to head to the Red Planet in 2020. Last week, the Chinese State Administration of Science, Technology, and Industry for National Defense released computer-generated images of the six-wheeled rover, which will weigh about 200 kilograms and will be powered by four solar panels. It incorporates technology already tested on the Jade Rabbit rover, which landed on the moon in 2013 and ended its mission in early August. The new rover will explore the Mars surface for 3 months, studying its soil, atmosphere, and physical fields, and hunting for water and ice. It doesn't yet have a name—China has launched a public competition to determine both its name and a logo for the mission.

Jailed physicist 'spy' paroled

Iran-born laser physicist **Omid Kokabee**, who was convicted of espionage by an Iranian court 4 years ago, won parole on 29 August. Kokabee, 34, was arrested at Tehran Imam Khomeini International Airport at the end of a family visit on 30 January 2011 while attempting to return to his Ph.D. studies at the University of Texas, Austin. Prosecutors charged him with "communicating with a hostile government" and labeled his graduate stipend "illegal earnings." In May 2012, he was sentenced to 10 years in prison. In letters to friends, Kokabee claimed he had turned down several offers to work in Iranian military and intelligence organizations. Amnesty International in 2013 declared him a prisoner of conscience, and the American Physical Society and AAAS (publisher of *Science*), among others, gave him scientific freedom awards. Kokabee continued his research in prison, uploading a paper on ultrafast ytterbium lasers to arXiv.org in 2014 in which he listed his affiliation as Evin Prison in Tehran. In April, he was diagnosed with advanced kidney cancer and his right kidney was removed, and he left prison on medical furlough in May. Sources told *Nature* that now that parole has been granted, Kokabee is free to leave Iran.

FINDINGS

New hope for genetic medicines

Psoriasis sufferers may have new hope: The first-ever clinical trial in humans of drugs called spherical nucleic acids (SNAs) hints that they may be effective in fighting the debilitating skin disease. The trial's findings may also reinvigorate a downtrodden therapy called antisense RNA, designed to prevent the production of disease-related proteins. Strands of RNA convey genetic information from DNA to protein factories called ribosomes. Antisense RNA therapies can bind to certain messenger RNA strands related to the disease, preventing them from being read by ribosomes. But RNA snippets tend to get chopped up by enzymes before they reach their target. However, SNAs, which can have 100 RNA snippets attached to a central particle, can withstand the enzymes. Earlier this year, Skokie, Illinois–based Exicure launched an SNA trial in Germany that targeted a protein called tumor necrosis factor-α (TNF-α), which is overexpressed in psoriasis patients. At the American Chemical Society meeting last week in Philadelphia, Pennsylvania, SNA pioneer Chad Mirkin of Northwestern University, Evanston, in Illinois, said that the initial trial results suggest the therapy is safe and can knock down TNF-α. If other proteins can be targeted by changing the RNA code on the SNA particles, it could open a new pathway for antisense RNA therapies.

BY THE NUMBERS

20%

Fraction of genetics papers in top scientific journals that contain errors in gene names due to autoformatting in Microsoft Excel. For example: *Septin-2*, often called *SEPT2*, is "corrected" to the date 2 September (*Genome Biology*).

17%

Fraction of 3000 Australian teenagers who became pregnant by age 20 after enrolling in a pregnancy prevention program in which they cared for a lifelike baby doll. Only 11% of a control group of peers became pregnant by age 20 (*The Lancet*).

22%

Portion of tenured research scientists at the U.S. National Institutes of Health who are women, according to a gender bias complaint. The rate is the same at medical schools.

PHOTO: XINHUA NEWS AGENCY/NEWSCOM

Downloaded from http://science.sciencemag.org/ on September 1, 2016

Published by AAAS



OSIRIS-REx will gather dust from Bennu in a 3- to 5-second "touch and go" encounter.

PLANETARY SCIENCE

NASA to launch asteroid-sampling mission

OSIRIS-REx plans to return more than 60 grams of dust from carbon-rich Bennu

By **Paul Voosen**

Twelve years ago, Dante Lauretta, a budding meteorite scientist at the University of Arizona in Tucson, was close to a breakthrough. His team was examining carbon-rich meteorites and had detected whiffs of triphosphate—the "TP" in adenosine triphosphate, or ATP, the molecule that powers life. But they couldn't nail it because of terrestrial contamination. One sample, for instance, came from a meteorite that had crashed into an Australian manure ditch. Lauretta needed something pristine.

Soon after, his mentor, Michael Drake, called. Lockheed Martin wanted to build a spacecraft for NASA that would go to an asteroid and return a fresh sample to Earth, he said. Could Lauretta craft a science case for it? Could he ever. "I'd been doing that for the past year," he recalls.

On 8 September, Lauretta will be a space flight away from getting his wish, with the launch of the $1 billion Origins-Spectral Interpretation-Resource Identification-Security-Regolith Explorer (OSIRIS-REx). Although it won't be the first spacecraft to bring asteroid dust back to Earth—Japan's Hayabusa 1 returned several thousand grains of dust in 2010—the scoop of grit it delivers in 2023 could reveal new insights into the unaltered building blocks of the solar system and the types of amino acids and other organic molecules that asteroid impacts delivered to an early Earth. "We are bringing back scientific treasure," says Lauretta, who took over as principal investigator following Drake's death in 2011.

The samples will come from Bennu, a half-kilometer-wide asteroid that's as black and dense as coal. It's a "B-type" asteroid, one of the parent bodies suspected to be responsible for the carbon-rich meteorites that Lauretta studied. Its orbit at times brings it nearly as close to Earth as the moon, so astronomers have studied it well. Nevertheless, mystery remains. There's a small chance, for instance, that a hint of blue in its reflection could point to a past episode of heating that might have destroyed the anticipated organic molecules, says Mike Zolensky, a space dust scientist at NASA's Johnson Space Center in Houston, Texas.

> ***"We are bringing back scientific treasure."***
>
> **Dante Lauretta**, OSIRIS-REx principal investigator

Upon arrival in August 2018, the spacecraft will survey Bennu from 240 meters above the surface. It will study the Yarkovsky effect, in which photons emitted from the sun-heated surface of a small, rotating asteroid generate a minuscule force that can alter its orbit. Because the effect varies greatly depending on subtle differences in shape and reflectivity, scientists want an opportunity to study it up close. The effect can also be used to trace asteroid orbits back in time, in order to identify the events that created them. Team scientists hope to confirm suspicions that Bennu was born hundreds of millions of years ago in collisions within the asteroid belt.

As it traces out the lumpy contours below, the spacecraft will also identify up to 12 sites for potential sampling. Lauretta and his team will then narrow these candidates based on accessibility and safety: The spacecraft can't reach Bennu's poles, for example, and it will avoid slopes, boulders, and pebbles. After that, the science comes in, along with debates. Some, interested in the early solar system, will favor pristine samples recently exhumed from the asteroid's interior; others will want surface dust that has been blasted by radiation and endured "space weathering." Ideally, investigators will find a shallow crater where both types of material coexist. It will ultimately be NASA and Lauretta's call. "It's the billion-dollar decision," Lauretta says.

OSIRIS-REx won't land on Bennu. It will pogo off it. Extending an arm with a vacuum chamber at its end—a scheme that engineers first demonstrated with a Solo plastic cup and an air compressor—the spacecraft will make contact with the surface for 3 to 5 seconds, blasting it with nitrogen to kick dust into the chamber, before rebounding off. Ideally, it will be a "safe, smooth, slow high-five of that surface," says Christina Richey, a deputy

PHOTO: NASA'S GODDARD SPACE FLIGHT CENTER CONCEPTUAL IMAGE LAB

Downloaded from http://science.sciencemag.org/ on September 1, 2016

Published by AAAS

program scientist at NASA headquarters in Washington, D.C.

The dust harvest—anywhere from 60 to 300 grams—"won't be much, but NASA scientists have become masters at working with practically nothing," says Hap McSween, a planetary scientist at the University of Tennessee, Knoxville. McSween leads the curation of the Bennu samples, which will be kept at the Johnson Space Center. The majority will be reserved for future scientists, following the model set by Apollo's moon rocks.

Will these pricey and precious samples be worth it? Alan Rubin, a meteorite scientist at the University of California, Los Angeles, says that meteorites offer something better—clean samples of an asteroid's interior—and they're cheap. "Go some millimeters below the fusion crust" of a meteorite, he says, "and that stuff is still pristine."

But team members say that although carbon-rich meteorites probably come from asteroids like Bennu, they don't know for sure. And they believe the dust sample will tell stories about Bennu's past—biographical information that could not be gleaned from a meteorite. Mark Sykes, director of the Planetary Science Institute in Tucson, is curious to see whether the dust samples show that Bennu has a wide mix of materials—say, rocks formed at both high and low temperatures. That would indicate that, early on, the asteroid's orbit migrated toward or away from the sun, which could support the notion that the solar system "was a pretty rough and tumble environment," Sykes says.

The greatest challenge for the mission will be keeping its samples safe and unsullied—the very thing Lauretta was after in the first place. When the mission's capsule falls onto Utah's West Desert in 2023, it will be protected by a heat shield and slowed by a parachute. But Hayabusa 1's similar return capsule, carrying samples from a silicate asteroid, suffered an O-ring leak, contaminating its contents with earthly organics. NASA's Stardust mission, which raced through a comet's tail, catching dust as it went, was also plagued by contamination, and its samples were deeply modified by their high-speed collection. OSIRIS-REx, designed for a gentle encounter, aims to do better.

Even if OSIRIS-REx succeeds, its cargo will not be the first carbon-rich asteroid dust in human hands. Hayabusa 2, launched in 2014 and set to return at least 100 micrograms of dust in 2020, ought to hold that distinction. But the U.S. and Japanese teams see their mirrored purposes as a strength, offering a chance to check each other's results. Nor can any one asteroid tell a universal story. "You don't go to one of them and say, 'I understand how all these things work,'" Sykes says. ■

PHOTO: COURTESY OF THE FRANCIS CRICK INSTITUTE

U.K. SCIENCE

London's biomedical behemoth opens its doors

The £650 million Francis Crick Institute aims to foster collaboration—but Brexit casts a shadow

By **Erik Stokstad**

The largest biomedical research building in Europe—the £650 million Francis Crick Institute in London—is finally complete, and jaws are dropping. "It's very, very big," says science policy expert Paul Nightingale of the University of Sussex in the United Kingdom. With gleaming metal roofs that curve over four wings of laboratories, the Crick has nearly 93,000 square meters of floor space—the equivalent of 13 soccer fields—and "more rooms than Buckingham Palace," a press release trumpeted in April. A basement twice the size of the Royal Albert Hall is packed with top-flight instruments, a special lab for dangerous pathogens, and animal facilities with 35,000 cages.

This week, the first of 1500 researchers and support staff will move into four floors of laboratories designed to facilitate collaboration. "It's going to be a showcase for British science," says Bruce Stillman, president of Cold Spring Harbor Laboratory in New York. But the United Kingdom's vote in June to leave the European Union has dampened some of the elation, as the Crick relies on overseas talent. More than 60% of the first wave of scientists to move in are foreigners, nearly one-third of those from within the European Union. And its startuplike culture, with minimal management and plans for a workforce of mostly young scientists who can stay no longer than 12 years, means the Crick will require a stream of talent from around the world.

The Crick's allure for U.K. scientists also raises concerns. Although supporters say the behemoth will strengthen science nationwide, others fret that it will suck up so much talent and funding that universities outside London will suffer. "It's a massive gamble," says Kieron Flanagan, a science policy expert at the University of Manchester in the United Kingdom.

A decade ago, two major biomedical institutes in London—the Medical Research Council's (MRC's) National Institute for Medical Research and the London Research Institute, operated by the charity Cancer Research UK—were outgrowing their aging facilities. In 2007, the two purchased a plot of land near St. Pancras station in downtown London, and not long after they agreed to merge. U.K. geneticist and Nobel



More than 60% of the first wave of scientists to move into the Francis Crick Institute in London are foreigners.

Downloaded from http://science.sciencemag.org/ on September 1, 2016

Published by AAAS

laureate Paul Nurse, then-president of The Rockefeller University in New York City, became CEO of the joint venture. To help build the structure, the government contributed £220 million; the Wellcome Trust also gave a significant amount.

Construction went relatively smoothly for such a complicated project, observers say. Objections from worried neighbors did not prevent completion of a biosafety level 3 lab for studying diseases such as tuberculosis and influenza. Researchers have their own construction worries, however: The planned route of a new underground railway line was shifted closer to the Crick in 2013. Its vibrations and magnetic interference could affect sensitive devices such as those in MRC's facility for biomolecular liquid-state nuclear magnetic resonance.

The two founding institutes will shift about 900 scientists—including 180 Ph.D. students—and 250 support staff to the new institute by early 2017. As tenured researchers retire, they will be replaced with early career investigators who have a 6-year contract that can be renewed only once. "There will be continual renewal through new people coming in," says Richard Treisman, a scientific director at the Crick. "It's an effective way of keeping a research system lively and vibrant," says Iain Mattaj, director general of the European Molecular Biology Laboratory in Heidelberg, Germany.

Another 200 scientists from University College London, Imperial College London, and King's College London—which each gave £40 million toward construction—will bring in additional expertise during visits lasting from a few months to 6 years. Pharmaceutical giant GlaxoSmithKline will dispatch 20 researchers to work on joint projects with Crick scientists. The proximity to many London hospitals will make translational and clinical research easier.

Some worried that the high cost of living in London might discourage candidates. Mattaj doubts that. "I think the Crick will be a superattractive place." The appeal for Ph.D. students is already clear: Thirteen hundred applied for 44 positions this year.

The United Kingdom's future relationship with the European Union casts a bigger shadow (*Science*, 29 July, p. 437). "It is a blight that is hanging over the whole of British science, but especially the Crick, because it's big and new," says University of London neuroscientist and former MRC chief executive Colin Blakemore. Restrictions on migration could make it more difficult to recruit, Treisman says, and limited access to EU research funds could squeeze the £130 million operating budget, about 5% of which comes from EU grants. "We just don't know what's going to happen." ■

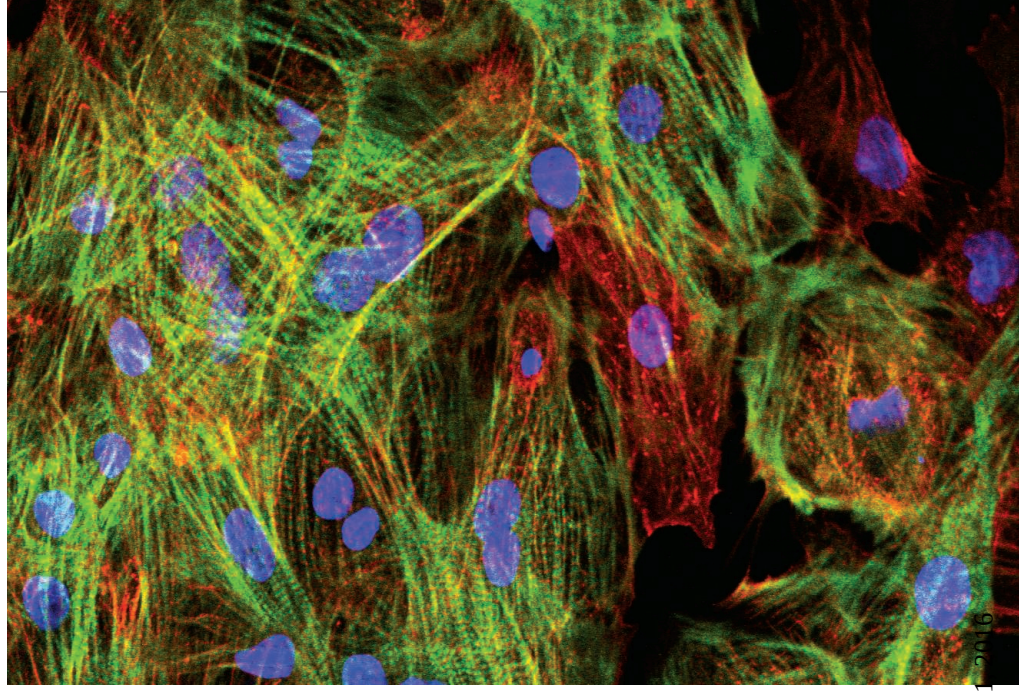


PHOTO: JOSEPH WU LAB/STANFORD CARDIOVASCULAR INSTITUTE

DRUG DEVELOPMENT

A painstaking overhaul for cardiac safety testing

New methods may better predict arrhythmia risk in vitro

By **Kelly Servick**

If any safety test should err on the side of caution, it's one for whether a new medicine might accidentally stop your heart. But for years, researchers have worried that preclinical tests for cardiac risk are so simplistic and conservative that they might lead drugmakers to abandon promising and safe treatments early in development.

Now, an international team of regulators, academic researchers, and drug companies is nearing completion of a project to validate a new—and hopefully more accurate—set of cardiac safety tests, known as the Comprehensive in vitro Proarrhythmia Assay (CiPA). In the coming weeks, a key component of that assay, based on stem cell–derived heart cells, will undergo blind testing on drugs with known risks at various academic and industry labs.

Regulators in the United States, Europe, and Japan rely on standards for arrhythmia risk testing set in 2005 by a body called the International Council for Harmonisation of Technical Requirements for Pharmaceuticals for Human Use (ICH). Those standards were born from a series of grim surprises. In the 1990s, several drugs were yanked from the market for dramatic cardiac side effects. One prominent example, an antihistamine called terfenadine, was reported to cause cardiac arrest in more than 100 patients before the U.S. Food and Drug Administration (FDA) withdrew its approval in 1997.

It turned out that terfenadine blocked a key ion channel on the membrane of cardiac muscle cells. Electrical signals from the flow of ions across these membranes rhythmically contract the heart, and this particular channel—encoded by a gene known as *hERG*—helps restore equilibrium after a contraction by letting potassium ions out. If it is blocked, heart cells are slower to "recharge" after a beat, which can lead to an irregular rhythm and sometimes death.

ICH standards require that drug developers test candidates for *hERG*-blocking activity in cultured cells. Not all compounds with *hERG* activity turn out to be dangerous; more than a dozen ion channels interact to affect the rhythm of heart contractions. But researchers spooked by an ominous *hERG* assay sometimes "end up throwing drugs away that most likely would be good drugs," says Gary Gintant, a research fellow at drugmaker AbbVie Inc. in Chicago, Illinois, who leads one of the teams within CiPA. In phase II trials, most drugs get another safety test: Patients' electrocardiograms (ECGs) can reveal potentially dangerous lengthening of the heart's electrical cycle. That process costs millions of dollars, can throw up a red flag after a company is heavily invested in a drug, and sometimes generates both false

Downloaded from http://science.sciencemag.org/ on September 1, 2016

Published by AAAS

Clusters of stem cell–derived cardiac muscle cells model how the heart may respond to a new drug.

positives and false negatives, Gintant notes.

Better ways to predict how heart muscle will behave would allow drug developers to advance more candidates into trials and maybe avoid large-scale, late-phase ECG studies. Some drug companies and academic labs are already exploring whether channels other than *hERG* are good predictors of arrhythmia risk. They have also begun developing more realistic models of the human heart in a dish, using induced pluripotent stem (IPS) cells—reprogrammed adult cells capable of differentiating into many types of cells. The challenge now is to turn that new science into a well-validated, standard set of tests.

The CiPA initiative, a partnership between FDA and several agencies and consortia, including Health Canada, the European Medicines Agency, and Japan's National Institute of Health Sciences, is an attempt to do just that. One group within CiPA is investigating seven channels (including *hERG*) known to regulate heart rhythm to find which combination of channel-blocking tests might best predict safety. A second team is refining a computer model of the human ventricle's electrical behavior; it will turn ion channel data into estimates of arrhythmia risk. A third is testing how well clusters of IPS-derived heart muscle cells mimic the behavior of the adult heart when exposed to various drugs. Some predict that this stem cell approach, after much refining, could even eliminate the need to test individual ion channels.

In a first round of validation last year, academic and industry labs blindly exposed IPS-derived cells to eight different compounds. Data across study sites "looked surprisingly similar," says Joseph Wu, a cardiologist and stem cell biologist at Stanford University in Palo Alto, California, who led one of the testing efforts.

A second round of FDA-funded tests for a set of 28 compounds began this month. By the end of next year, CiPA collaborators intend to propose the complete assay—a three-part process combining ion-channel assays, computer simulation, and IPS-derived cells—to a group within ICH that could choose to revise the 2005 standard.

Even with this new set of tools, companies may still decide that a compound that acts on multiple cardiac ion channels is too risky to pursue, says Icilio Cavero, a retired cardiovascular pharmacologist and safety consultant to drug companies who is based in Paris. And it will take more than these initial 28 compounds to prove that IPS-derived cells can be reliable safety predictors. "The idea [of CiPA] is beautiful," Cavero says, but "new things scare everybody." ■

DATA: RETRACTION WATCH

RESEARCH MISCONDUCT

Duke fraud case highlights financial risks for universities

Whistleblower alleges doctored data were used to secure $200 million in grants from NIH and other federal agencies

By **Alison McCook**, *Retraction Watch*

On a Friday in March 2013, a researcher working in the lab of a prominent pulmonary scientist at Duke University in Durham, North Carolina, was arrested on charges of embezzlement. The researcher, biologist Erin Potts-Kant, later pled guilty to siphoning more than $25,000 from the Duke University Health System, buying merchandise from Amazon, Walmart, and Target—even faking receipts to legitimize her purchases. A state judge ultimately levied a fine, and sentenced her to probation and community service.

Then Potts-Kant's troubles got worse. Duke officials took a closer look at her work and didn't like what they saw. Fifteen of her papers, mostly dealing with pulmonary biology, have now been retracted, with many notices citing "unreliable" data. Several others have been modified with either partial retractions, expressions of concern, or corrections. And last month, a U.S. district court unsealed a whistleblower lawsuit filed by a former colleague of Potts-Kant. It accuses the researcher, her former supervisor, and the university of including fraudulent data in applications and reports involving more than 60 grants worth some $200 million. If successful, the suit—brought under the federal False Claims Act (FCA)—could force Duke to return to the government up to three times the amount of any ill-gotten funds, and produce a multimillion-dollar payout to the whistleblower.

The Duke case "should scare all [academic] institutions around the country," says attorney Joel Androphy of Berg & Androphy in Houston, Texas, who specializes in false claims litigation. It appears to be one of the largest FCA suits ever to focus on research misconduct in academia, he says, and, if successful, could "open the floodgates" to other whistleblowing cases.

False claims lawsuits, also known as qui tam suits, are a growing part of the U.S. legal landscape. Under an 1863 law, citizen whistleblowers can go to court on behalf of the government to try to recoup federal funds that were fraudulently obtained.

Holding universities liable for research fraud

Whistleblowers have a mixed record of success in False Claims Act (FCA) lawsuits against research universities that involve allegations of scientific misconduct. Highlights from selected cases:

YEAR	WHISTLEBLOWER	DEFENDANT	ALLEGATIONS	OUTCOME
2009	Taryn Resnick, former employee	Weill Medical College of Cornell University	In grants totaling $14 million, researcher Lorraine J. Gudas falsified data, failed to disclose other funding, and misapplied funding.	College settled for $2.6 million, plus attorneys' fees and expenses.
2012	Daniel Feldman, fellowship program participant	Weill Medical College of Cornell University and psychiatrist Wilfred van Gorp	Misuse of research training grant; deviated from submitted plan.	Defendants paid $887,714, plus $602,898.63 in attorneys' fees and expenses.
2012	Kenneth Jones, researcher	Brigham and Women's Hospital, Massachusetts General Hospital, and researchers Marilyn Albert and Ronald Killiany	Including falsified data in application for Alzheimer's disease research grant.	Failed; whistleblower ultimately lost at trial.
2014	Terri King, former associate professor	University of Texas Health Science Center	Falsifying research data.	Failed. U.S. Supreme Court upheld lower court ruling that the public university was exempt from FCA liability.

Downloaded from http://science.sciencemag.org/ on September 1, 2016

Published by AAAS

Winners can earn big payoffs, getting up to 30% of any award, with the rest going to the government. Whistleblowers filed a record 754 FCA cases in 2013, and last year alone won nearly $600 million. The U.S. government, meanwhile, has recouped more than $3.5 billion annually from FCA cases in recent years.

Relatively few of these cases have targeted research universities (see box, p. 977); many allege fraud in health care or military programs. But that's changing. The FCA "is increasingly being used to target alleged fraud in a diverse array of industries, including research and academia," says attorney Suzanne Jaffe Bloom of Winston & Strawn LLP in New York City. Although recent court rulings suggest public universities may have some protection from qui tam suits because they are government entities, private institutions do not. Eleven private universities, including Duke, are among the top 25 recipients of federal funding for academic science over the past decade.

The Duke case centers on allegations made by biologist Joseph Thomas, who, according to court documents, joined Duke's cell biology department in 2008. In 2012 Thomas moved to the pulmonary division, where Potts-Kant worked under William Michael Foster investigating how pollutants affect the body's airways. After Potts-Kant was placed on leave in 2013, the pulmonary division conducted an investigation of the data produced by Foster's lab, according to the lawsuit. (Duke has not released the results of the investigation.) Investigators analyzed raw data, recalculated results, and reran experiments, according to the suit. Thomas, who says he participated in the review, claims that other reviewers and pulmonary division staff told him that Potts-Kant doctored nearly every experiment or project in which she participated. Sometimes, the suit alleges, she hadn't exposed mice to the right experimental conditions or run the experiments at all. Other times, Thomas alleges, Potts-Kant had run the experiments but altered the data, tweaking them to match the hypothesis or boost their statistical significance.

Thomas, who no longer works at Duke, alleges that Foster and others at Duke were aware of concerns raised about Potts-Kant's work even before the investigation began. There were obvious red flags, he contends. For example, she spent far less time completing a research task than required by an equally experienced researcher. And at least one outsider had raised questions about her data at a scientific meeting. But the university withheld the scope of what it knew from federal funding agencies as it filed reports on existing grants and applied for new ones, the lawsuit alleges.

Specifically, Thomas alleges that since 2006 Duke received at least 49 grants worth $82.8 million from the National Institutes of Health (NIH), the Environmental Protection Agency, and other agencies "that were directly premised on and/or arose from the research misconduct and fraud of Potts-Kant and/or the Foster lab." And he alleges that the doctored data helped other institutions win 15 additional grants, worth $120.9 million, from NIH. (Those grants involved using the Duke lab for some research tasks.)

Foster did not respond to requests for comment on the case. Thomas—who is represented by his brother John Thomas of Gentry Locke LLP in Roanoke, Virginia—would not comment, and Potts-Kant could not be reached. In a statement, Duke spokesperson Michael Schoenfeld says that officials learned of the "discrepancies" in Potts-Kant's data only after her embezzlement was discovered in 2013. "Even though the full scope of Ms. Potts-Kant's actions were not known at the time, Duke notified several government agencies in June 2013 about the matter and immediately launched a formal scientific misconduct investigation, as required by federal law," he stated. "Since then, Duke has provided extensive information to the government regarding the grants in question, and we will continue to cooperate with their investigation." (The government has not joined the case, but could later.)

> ***"You can have research misconduct without having a false claim."***
> **Torrey Young**, Foley & Lardner LLP

An attorney not associated with the case says it may face obstacles. Although the high number of retractions suggests that Thomas can meet the FCA's requirement that "falsity" exists, it may be more difficult to show that the inclusion of fraudulent data was key to winning the grants, another essential aspect of an FCA case, says Torrey Young of Foley & Lardner LLP in Boston. "An important concept," she says, is that "you can have research misconduct without having a false claim." ■

Alison McCook is an editor at Retraction Watch based in Philadelphia, Pennsylvania. This story was produced under a collaboration between Science *and Retraction Watch.*

SCIENCE POLICY

Congress faces a lengthy science to-do list

2017 spending to be delayed

By ***Science*****'s News Staff**

Congress returns next week from a 7-week summer break with a lengthy list of unfinished business, some of great interest to the U.S. research community—and just a few weeks to tackle it. Lawmakers aren't likely to pare that list by much before they leave next month to campaign in advance of the 8 November elections. They might give some issues a second look after the election, however, when they return for a lame duck session after the country has picked a successor to President Barack Obama and a new Congress.

The one big responsibility Congress can't shirk is passing some kind of spending bill to keep the government running for the 2017 fiscal year, which begins on 1 October. But Republicans, who control both the House of Representatives and the Senate, don't agree on whether to abide by an existing spending pact made with Obama, or to modify it to increase the defense budget and cut domestic programs. As a result, legislators this month are expected to put off a decision by temporarily extending 2016 spending levels into 2017 with a so-called continuing resolution (CR). The CR likely will fund the government through late December, allowing lawmakers to wait until they know whether they will be dealing with Hillary Clinton or Donald Trump before devising a final 2017 spending plan.

Practically speaking, a CR means the budgets of federal research agencies will be frozen: Administrators won't be able to start new programs or benefit from the spending hikes envisioned in some preliminary appropriations bills awaiting final action. They include a hefty proposed increase for the National Institutes of Health (NIH), another big boost for a NASA mission to a jovian moon, a new Coast Guard icebreaker that would enhance polar research, and a third midsized research vessel for the U.S. academic fleet. A CR also would leave

Downloaded from http://science.sciencemag.org/ on September 1, 2016

Published by AAAS



Lawmakers must decide whether to spend $1 billion to replace the aging heavy icebreaker *Polar Star*.

hanging major disagreements between the House and Senate on whether to continue U.S. participation in ITER, the costly international fusion project, and how much earth science NASA should carry out.

Here's more on a few issues science lobbyists are tracking:

Funding for NIH and the cancer moonshot. Research groups are hoping lawmakers will give NIH its second substantial increase in a row after 12 years of flat budgets. A Senate committee has approved a 6% increase to $34.1 billion, a $2 billion jump, whereas a House panel has approved a 4% boost. Both proposals would boost Alzheimer's disease research, with the Senate calling for a $400 million, 40% increase. They would also add $100 million to the president's Precision Medicine Initiative, bringing the total to $300 million. But neither bill contains the $680 million that the White House requested for Vice President Joe Biden's moonshot to accelerate progress against cancer.

Accelerating medical treatments. Proponents of a sweeping bill that the House passed to speed the discovery and development of new medical treatments hope the Senate will embrace at least some of its key provisions this year. Both the House bill, known as the 21st Century Cures Act, and a set of 19 smaller Senate bills endorse plans to create incentives and scale back regulatory requirements for certain high-priority treatments, such as drugs to treat rare, life-threatening infections. But the Senate has so far balked at a plan in the House Cures bill to boost NIH's budget by $8.75 billion over 5 years through so-called mandatory spending mechanisms, which aren't subject to annual appropriations. Senate leaders hope to win support for a shorter-term mandatory funding "surge" for high-priority research, including Biden's cancer moonshot.

New policy for the National Science Foundation (NSF)? Both the House and the Senate have been working on legislation that would tweak an expired 2010 law, the America Creating Opportunities to Meaningfully Promote Excellence in Technology, Education, and Science Act, which sets funding targets and operational policy for NSF, the National Institute of Standards and Technology, the White House Office of Science and Technology Policy, and government-wide science education programs. Now, science lobbyists face the challenge of trying to generate support for the Senate legislation, which they generally like, while fighting bills they oppose that have cleared the House.

Critics—including Democrats and science groups—say the House bills would undermine peer review at NSF and force scientists to pass political litmus tests, as well as throttle back on curiosity-driven research. House Republicans counter that they just want to ensure that limited dollars are spent wisely and block the Obama administration's politically motivated research agenda. The battle may not end this year.

Easing the "administrative burden" on universities. This bland phrase belies the academic community's sense of urgency about easing regulations that govern federally funded research done on campus. A succession of blue-ribbon panels has implored the government to streamline the process of applying and accounting for federal grants, and several House and Senate bills offer a range of reforms. But finding common ground may be difficult.

A new icebreaker? The United States is down to just one heavy icebreaker, the *Polar Star*, after its twin, the *Polar Sea*, was shut down in 2010. As a result, experts say, the United States is losing the ability to supply Antarctic bases and conduct Arctic science, even as other nations expand their polar fleets. But a new heavy icebreaker is expected to cost $1 billion. The White House wants to start building a replacement by 2020, and a Senate spending panel has put the needed funds into a 2017 defense spending bill. But House appropriators are skeptical.

Energy research funding. Both House and Senate appropriators have given the Department of Energy's (DOE's) basic research wing, the Office of Science, a 1% bump, to $5.4 billion, for 2017. But the chambers disagree on how that money, short of Obama's 4% request, should be spent. For example, the Senate would cut DOE's fusion budget by about one-third and cancel money for ITER; the House would back ITER and boost fusion spending by 3%, to $450 million.

Researchers and advocates are also eyeing House-Senate negotiations over a major energy bill that would set future funding targets for the Office of Science, as well as encourage the development of energy resources—a goal hailed by industry. But Obama has threatened to veto any bill that weakens environmental protections.

Meanwhile, at the White House. … Congress is a bystander on some of the most momentous research issues that are in play. The Obama administration is rushing to complete a host of new regulations, including rules on greenhouse gas emissions and environmental protection. (Which have triggered highly publicized fights with Republicans.) Biomedical scientists are most interested in something not generating major headlines: a potential update of the so-called Common Rule on protecting human research subjects. Critics warn that, by tightening consent requirements, the proposed update could endanger certain types of research. They want regulators to go back to the drawing board. ■

With reporting by Jeffrey Mervis, Jocelyn Kaiser, Adrian Cho, Kelly Servick, Carolyn Gramling, and David Malakoff.

PHOTO: WIKIMEDIA COMMONS/U.S. COAST GUARD

Downloaded from http://science.sciencemag.org/ on September 1, 2016

Published by AAAS



Downloaded from http://science.sciencemag.org/ on September 1, 2016

MENTORING'S MOMENT

NIH's new mentoring network aims to improve success rates for minority grant applicants. But it faces long odds

By **Jeffrey Mervis**

Growing up in a working-class neighborhood of South Los Angeles, California, Blake Riggs was 1 day away from enlisting in the U.S. Navy when the University of California (UC), Santa Cruz, admitted him in 1992. Riggs, who is black, hoped to major in marine biology. And his plans got a big boost when he was chosen for the Minority Access to Research Careers program, a long-running effort funded by the National Institutes of Health (NIH) to help minority students launch their scientific careers.

But Riggs crashed soon after takeoff. Riggs says an instructor in the dolphin lab where he was assigned to work told him that other students were more qualified, and implied that he only got the job because of his race. Over the next several months, Riggs says he was denied access to the physiological data he was supposed to collect. And rather than standing up for his student, Riggs's faculty adviser lectured him on the need to do his own research and ultimately booted him out of his group.

Riggs was determined to remain in science, however, and a cell biologist offered him a lab job—and some crucial mentoring. With that support, Riggs finished his undergraduate degree and later returned to UC Santa Cruz to earn his Ph.D. in cell biology. In 2010, he joined the biology faculty at San Francisco State University (SFSU) in California; this spring, at age 41, he received tenure.

The only minority faculty member in his department, Riggs has paid homage to the importance of mentors in his own career by making mentoring a priority. Students of color comprise the majority in his lab. Last December, the National Science Foundation gave Riggs a prestigious CAREER award to expand to the entire campus a student "near-peer" mentoring program he created as well as to support his own research, on asymmetrical cell division.

Diversity advocates have long believed that mentoring holds the key to increasing

PHOTO: NOAH BERGER

Published by AAAS



Blake Riggs, a biologist at San Francisco State University in California, talks with undergraduate Iris Avellano (right) and lab tech Mark Velasquez (left).

minority participation in U.S. science. NIH acknowledged its importance in October 2014 by launching the 5-year, $22 million National Research Mentoring Network (NRMN) as part of a larger, multipronged, 10-year initiative to enhance the diversity of the biomedical workforce.

NRMN—"Norman" to insiders—is NIH's biggest ever focused investment in mentoring. But it is off to a rocky start. Even before it was publicly announced, divisions within the diversity community prompted NIH officials to take the unusual step of adding to its leadership team a scientist who had been part of a group that lost out in the competition to create the network. And earlier this year, the principal investigator (PI) for the multisite network, which is based at Boston College in Chestnut Hill, Massachusetts, resigned after continuing conflicts with NIH officials over NRMN's direction, leaving it in disarray.

NIH has spent billions of dollars over the past 40 years on programs aimed at removing obstacles to participation by underrepresented groups, a category that also includes Latinos, Native Americans, people with disabilities, and those from disadvantaged backgrounds. But it has little to show for it, officials acknowledge. "We are far short of where we want to be," NIH Director Francis Collins in Bethesda, Maryland, said on the day NRMN was announced.

Some diversity advocates are worried that unfortunate track record may continue despite the new initiative. In particular, they fear that NIH may end support for NRMN after 5 years if the network falls short of some short-term, quantitative goals.

"If you're looking for meaningful outcomes at the end of 5 years, then you might as well pull the plug now, because [NRMN] is going to fail," predicts Donald Wilson, co-founder of the Association for Academic Minority Physicians (AAMP), which since 1968 has pushed for increased minority participation in academic medicine. Wilson, a retired medical school dean in Owings Mills, Maryland, who is a part of NRMN's administrative core, says "many of us are concerned that if NIH officials don't see results immediately, they will say, 'Too bad, we tried. But that's the best we can do.'" (NIH officials say they will assess NRMN in the same way they would judge any large project.)

THE MENTORING NETWORK and NIH's larger diversity initiative are the products of an unusual exercise in bureaucratic self-examination. In 2008, then–acting NIH Director Raynard Kington gave Donna Ginther, an economist at the University of Kansas, Lawrence, and other outside scholars unprecedented access to confidential data on the agency's grants process. The goal was to explore possible racial bias in grant awards.

Their findings were a bombshell: A black applicant's chance of winning an R01 grant—NIH's bread-and-butter research award—was 10 percentage points lower than a white colleague's (*Science*, 19 August 2011, p. 925). Only 185 black applicants were funded between 2000 and 2006, for example; the number would have been 337 if blacks had been funded at rates equal to whites. (Such disparities have persisted, NIH officials reported this summer [*Science*, 17 June, p. 1379]. The comparison was between those with similar credentials. An in-house analysis of a more recent cohort of 1054 matched pairs of applicants found that black grant seekers were 35% less likely to be successful than whites.)

The Ginther report, as it became known, didn't address whether the disparity exists because minority applicants were victims of discrimination or simply because their proposals were less competitive. But it drove home the lack of diversity in NIH's applicant pool. Black people, for instance, made up just 1.4% of the some 83,000 applicants included in the study, although they constitute 13% of the U.S. population.

The 2014 diversity initiative is essentially NIH's response to the Ginther report. Its biggest component is the Building Infrastructure Leading to Diversity (BUILD) program, in which 10 minority-serving institutions expect to receive $20 million to $25 million over 5 years to improve the undergraduate experience for underrepresented students majoring in the life sciences. Many of those universities already run other NIH programs with a similar goal, but NIH officials say that the BUILD initiative is designed to test the efficacy of specific approaches in a much more rigorous way than has been done to date. Those experiments will be monitored by a team at UC Los Angeles, which will also be coordinating links between NRMN and BUILD and evaluating the impact of the entire diversity initiative.

FOR DAVID BURGESS, a cell biologist at Boston College, NIH's 2013 announcement of a competition for a national mentoring network was "the opportunity I'd been waiting for my whole career." A member of the Cherokee tribe and a former president of the Society for Advancement of Chicanos/Hispanics and Native Americans in Science, Burgess has spent 4 decades mentoring students from groups underrepresented in science. He also has served on numerous advisory panels that have urged U.S. government agencies to improve the diversity of the scientific workforce.

After winning one of seven planning grants, Burgess joined forces with three other first-round winners to create what became the winning NRMN proposal. It has several components. Burgess would lead the administrative core. Molecular geneticist Jamboor Vishwanatha, at the University of North Texas Health Science Center in Fort Worth, would create an online mentoring network for budding researchers to connect with senior academic mentors anywhere in the nation. For the first time, students at smaller or less research-intensive institutions would be able to learn from the best in the business, not just from those on their campus. So far, 1146 mentors have signed up to work with 2078 students.

A third element, based at the University of Wisconsin, Madison, and led by cell biologist Christine Pfund, would train faculty to become better mentors. "Just because you had a good mentor doesn't mean that you know how to do it," says Pfund, who has spent more than a decade studying how to improve the training of both new and veteran faculty members.

A fourth component, run by Kola Okuyemi of the University of Minnesota, Twin Cities, would help postdocs and junior faculty better

Downloaded from http://science.sciencemag.org/ on September 1, 2016

Published by AAAS

understand the NIH grantsmaking process. "We're investing in people who are close to applying for an R01," he says. Such training would be especially helpful for scientists at institutions with relatively little NIH funding and, thus, few faculty members who have successfully navigated the system.

From the beginning, however, there were grumblings from the minority research community about the makeup of the NRMN team and its ability to connect with its intended audience. Leaders of minority-serving institutions, some with medical schools, were upset that NIH chose Boston College, a largely white, Jesuit institution without a medical school, to lead the mentoring network.

Some advocates took their complaints directly to senior NIH officials, including Collins. Their intervention ultimately paid off when NIH took what many agency observers say is an unusual action: expanding NRMN by adding a PI from a proposal that had lost to the submission from Burgess's team. The new PI, cardiologist Elizabeth Ofili of the Morehouse School of Medicine in Atlanta, leads an NIH-funded network of research centers at minority-serving institutions focused on translational medicine, and she brought that network into NRMN. NIH also directed NRMN to fund Wilson and AAMP to conduct a training session on mentoring for AAMP members and other national leaders at the group's annual meeting.

Collins has declined to talk with *Science* about how NRMN was assembled. But Lawrence Tabak, principal deputy NIH director, says that the changes were made "to ensure appropriate outreach to all communities. We took a look at the mix of opportunities, and we thought that we could enhance what was already present by expanding it."

It took Burgess and the NRMN team months, however, to integrate the new PI and activities demanded by NIH. Then, just 1 year into the award, NIH officials wrote a sharply critical report of NRMN's management. They were especially unhappy with what they characterized as slow progress in developing the online mentoring component of the network. Feeling that NIH had lost confidence in his leadership, and weighed down by the continuing tensions, Burgess stepped down shortly after the NRMN team received the report last December. Boston College will continue to manage the network.

BURGESS'S DEPARTURE "was a big shock to the system," Pfund says. And some diversity advocates say the program's travails pose a larger question: Will NIH's response to Ginther actually increase the number of underrepresented minorities in the agency's applicant pool anytime soon?

Some of the factors causing the award disparity are beyond NIH's control to fix, they note. The agency is in a poor position to address the lifelong negative effects of poverty, for instance, or the low-quality education many students from underrepresented groups receive before attending college. There's also the sorry legacy of covert and overt discrimination within academia. And NIH can't change the fact that most life science majors don't earn biomedical Ph.D.s, that most Ph.D.s won't enter academia, and that most academics will never apply for an R01 grant, much less obtain one. So even if NRMN is successful at enrolling and mentoring large numbers of minority students and faculty members, its efforts may not translate into higher success rates for minority applicants on R01 grants.

But even actions within NIH's reach, such as funneling resources to programs aimed at underrepresented minorities, carry political and legal peril. The dangers include potential lawsuits from critics claiming that such programs amount to reverse discrimination. NIH's response to that threat has been to insist that NRMN and other programs aimed at fostering diversity be open to all students and faculty members, not just minorities. But that broad scope may dilute their impact on the problem.

Another challenge is the relatively short duration of the NRMN and BUILD programs (a 5-year award with the possibility of a 5-year renewal). It means that few of the students and faculty involved will be ready to apply for an NIH grant before the effort ends.

In the meantime, Riggs represents both the promise of programs like NRMN—and how hard it will be to achieve the changes NIH seeks. He's already signed up for NRMN's fledgling online mentoring network, and is working with a minority student attending graduate school in Arkansas. He's also served as a liaison between NRMN and the BUILD project based at SFSU and UC San Francisco.

Despite all of his efforts, Riggs says his own odds of becoming part of NIH's R01 grant pool remain poor. Although NIH has funded his lab through a program for minority-serving institutions that receive relatively little NIH funding, Riggs has never applied for an R01 grant. "The people in the grants office keep telling me to apply, but I don't think our proposal would be competitive," he says. "[SFSU] doesn't have a Ph.D. program, and NIH doesn't have a history of funding people from master's programs."

Although he'd like NRMN to succeed, Riggs concedes that "they're kinda stalled right now." NRMN's Pfund agrees. "It's been uphill so far," she told *Science* earlier this year. "But the promise remains. The next 3 years offer us a real opportunity to demonstrate not only the value of mentoring, but also to learn how to do it better." ■

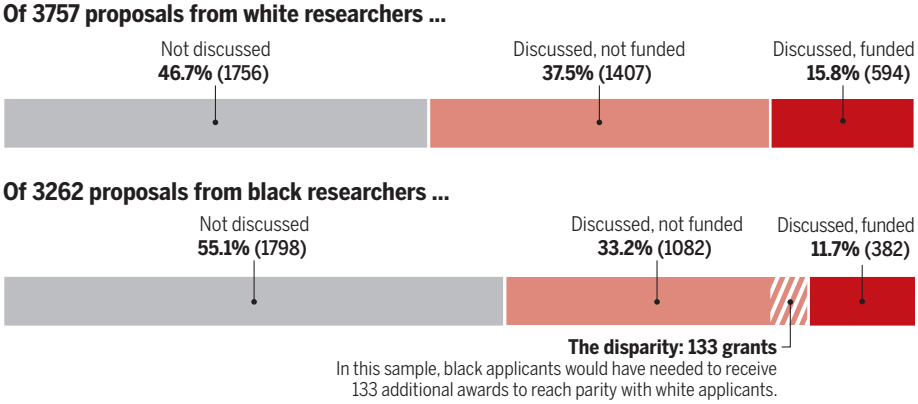
Obstacles to success for black scientists include a shallow pool ...

Black scientists comprised only 1.5% of the applicants for R01 grants between 2000 and 2010.



... and longer odds.

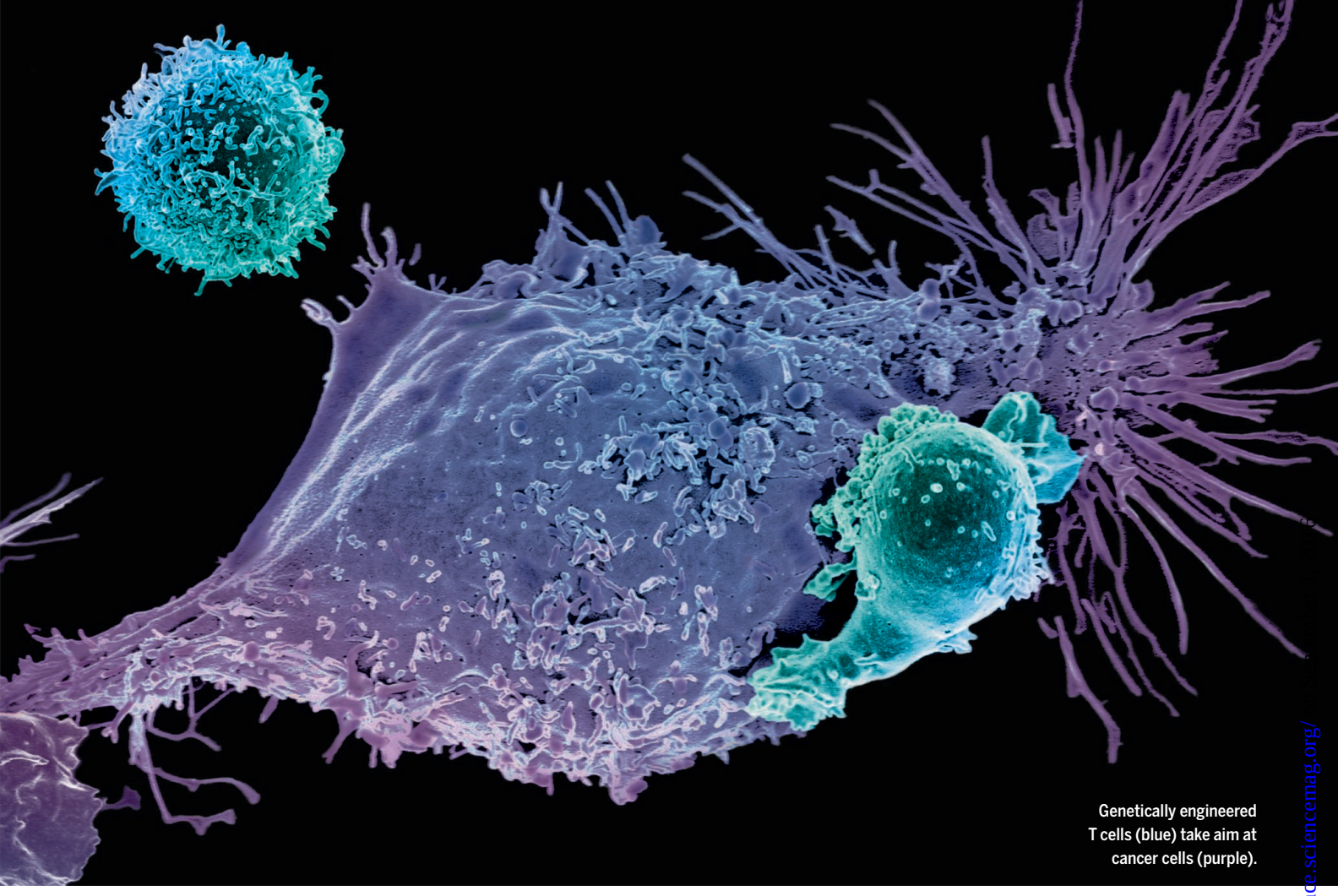
A National Institutes of Health study of 1054 matched pairs of applicants for R01 grants between 2010 and 2015 found a disparity in success rates between white and black scientists.



CREDITS: (GRAPHIC) G. GRULLÓN/*SCIENCE*; (DATA) NATIONAL INSTITUTES OF HEALTH

Downloaded from http://science.sciencemag.org/ on September 1, 2016

Published by AAAS



Genetically engineered T cells (blue) take aim at cancer cells (purple).

IMAGE: LAURENT SCHMITT AND NINA LAMPEN, PRASAD ADUSUMILLI LABORATORY/MEMORIAL SLOAN KETTERING CANCER CENTER

Downloaded from http://sciencemag.org/

SECOND CHAPTER

T cell therapy has successfully targeted blood cancers. A bigger challenge is to make it work on solid tumors

By **Jennifer Couzin-Frankel**

Last month, Roisin O'Cearbhaill, an Irish oncologist who looks younger than her 37 years, slipped on gloves and a protective gown and stepped through the doorway of a room in her hospital's intensive care unit. Patient No. 1 awaited her.

All other treatments had failed this woman, who is in her early 70s and has ovarian cancer. Now, she was about to be infused with her own T cells, the workhorses of the immune system, which had been removed and genetically engineered to fight her disease.

Like all first-in-human trials, O'Cearbhaill's is small and narrowly focused: She hopes to enroll just 15 women at her home base, Memorial Sloan Kettering Cancer Center in New York City, over the next 18 months, and she's testing mainly whether the treatment is safe. But it's hard not to fantasize about something more dramatic. Genetically engineered T cells have proven almost miraculously effective in some patients with blood cancers, including certain leukemias and lymphomas. Dozens of adults and children near death have been helped, and some remain healthy 4 or 5 years after treatment.

As researchers try to take T cell therapy in blood cancers from proof-of-principle to practical treatment, trials like O'Cearbhaill's present another looming test for the approach: Can engineered T cells also save people with solid tumors spreading through the breasts, lungs, brain, and ovaries? Solid tumors are far more common than blood cancers and, if they metastasize, can be very difficult to halt. Immunotherapy drugs called checkpoint inhibitors are approved or in testing for a number of solid tumors—but even there, the fraction that responds is often modest and response doesn't always last. O'Cearbhaill and colleagues at Sloan Kettering, around the country, and beyond hope this first wave of clinical trials will help chart a path toward success for a strategy that could upend cancer treatment as we know it.

Published by AAAS



Pediatric oncologist Nabil Ahmed talks with a young cancer patient who is part of his CAR T cell trial at Texas Children's Hospital in Houston.

But the last few years have been humbling as well as exhilarating. Doctors increasingly recognize that to melt away solid tumors, T cell therapy must clear daunting hurdles it didn't face in blood cancers. Because of the genetic quirks of solid tumors and their skill at manipulating their environment to protect themselves, they are far trickier to treat. Furthermore, the T cell treatments that might be most promising can't be tried in full doses right away because of the risk of severe side effects. Doctors like O'Cearbhaill must walk a tightrope between the most aggressive strategy, with greater odds of success, and the one least likely to harm vulnerable patients and wound a nascent field.

So far there are glimmers of T cells' power, but nothing close to what blood cancer patients have experienced. "We're definitely not selling it as a wonder treatment," O'Cearbhaill says. But eventually, once investigators master the dosing and add other drugs to bolster the T cells' effectiveness, she hopes it will prove to be so for some patients. "We just have to figure out how to make it work."

> ***"We're definitely not selling it as a wonder treatment. We just have to figure out how to make it work."***
>
> **Roisin O'Cearbhaill**, Memorial Sloan Kettering Cancer Center

TO GRASP THE HURDLES, one must first untangle the successes. This treatment goes by the unwieldy name of chimeric antigen receptor (CAR) T cell therapy. That's because the patients' immune cells are genetically modified to target "antigens," substances on the surface of a cancer cell.

In the summer of 2011, physicians at the University of Pennsylvania (UPenn) electrified the world when they described three men with late-stage chronic lymphocytic leukemia whom they treated with genetically engineered T cells. One man died from disease, but the other two remain healthy today. Children and adults with an aggressive leukemia, acute lymphoblastic leukemia (ALL), fared even better. More than 80% have had a complete response to the treatment, which remains in clinical trials. One poster child is 11-year-old Emily Whitehead, who 4 years ago nearly died from side effects of T cell therapy but rallied at the eleventh hour. She's been cancer-free ever since.

For those first patients, there were "many, many stars aligning at the same time," says Nabil Ahmed, a pediatric oncologist at Texas Children's Hospital in Houston. Going in, doctors at UPenn, Sloan Kettering, and elsewhere focused on a subset of blood cancers driven by an overproliferation of B cells, a type of white blood cell that helps fight infections. B cells turned out to be an ideal target.

First, every one of these cancer cells boasted the same antigen, called CD19, on its surface. And second, the only healthy cells in the body with CD19 are B cells, and people can survive without their B cells. That meant that a successful treatment shouldn't severely compromise a patient long-term.

A third advantage was that both blood cancer cells and T cells reside in the bone marrow. So after being removed from a patient's body, genetically engineered in a lab, and reinfused through a vein, the T cells traveled back to where the cancer was thriving. From that locale, they could readily stage an attack.

But clean, clear targets like CD19 are exceedingly rare in cancer. Solid tumors are far more genetically diverse than those that flourish in blood, both among patients and even within the same person's body. In metastatic sarcoma, for instance, distant tumors may be awash in certain genetic markers that are barely present in the primary mass in the leg's soft tissue. A gene might be turned on in one person's breast cancer and switched off in another's. There's no single antigen that shows up on every ovarian cancer cell and that can be targeted.

Another critical difference between many blood cancers and solid tumors is the milieu. "A tumor is more than just tumor cells," says Charles Sentman, an immunologist at Dartmouth College. "Cancer is both a disease of transformed cells and a disease of the environment." In solid tumors, the surrounding tissue is far less hospitable to T cells than bone marrow. It's low in glucose and oxygen. It's very acidic. Nutrients are scarce, gobbled up by the tumor. And sometimes the tumor itself secretes chemicals that suppress the immune system. "All those factors tend to turn T cells off and make them dysfunctional," says UPenn's Steven Albelda, who is involved in CAR T cell trials for various solid tumors.

HE AND OTHERS face a Catch-22: The most prudent course is often unlikely to be the most effective. Earlier trials, although startlingly successful in blood cancers, put the risks of CAR T therapy on vivid display. The cells can send the immune system into overdrive, a phenomenon known as a "cytokine storm," which almost killed young Emily. In 2009, a 39-year-old woman with

PHOTO: NATHAN LINDSTROM

Downloaded from http://science.sciencemag.org/ on September 1, 2016

Published by AAAS

metastatic colon cancer died from respiratory distress after CAR T cell treatment, perhaps because the cells clustered in her lungs and triggered a cytokine storm. Earlier this year, three leukemia patients died in a CAR T cell trial, possibly because they were given a chemotherapy drug on top of the T cells.

Researchers are adopting an ultracautious approach for solid tumors, in part because, unlike in blood cancers, it's not clear how well the treatment will work and what the side effects will be. O'Cearbhaill's trial and many others begin with very low doses of T cells. Even though oncologists recognize that a single antigen target, like CD19, probably won't be sufficient in solid tumors, they're starting there. And although many oncologists think the cells work best after pretreating patients with chemotherapy, to kill off other immune cells and provide extra space for the engineered T cells to flourish, they're often not giving chemo up front because it further compounds risks.

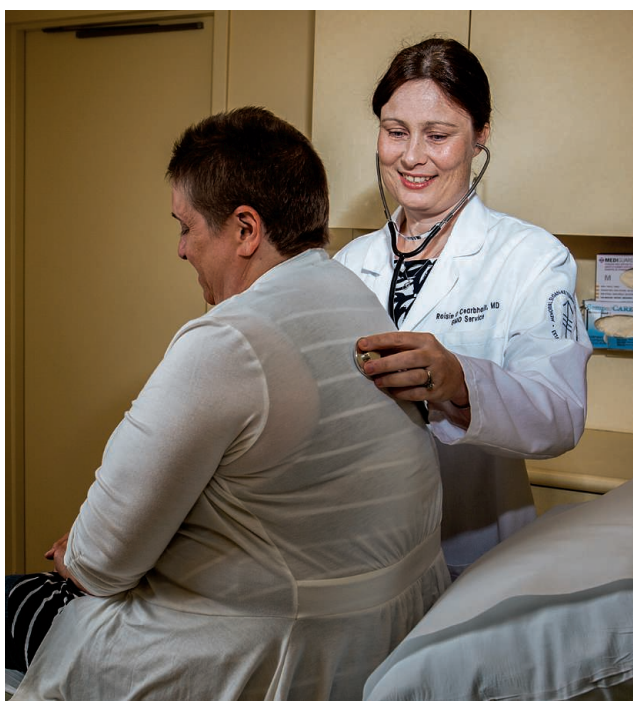
Ahmed is frustrated by the painstaking pace. "Patients are dying every minute," he says, and the treatments he's left with—like removing a teenager's leg—are "medieval medicine." But he knows, too, that "this is how the rules are. You have to test one by one"—one antigen at a time, one variable at a time, to protect patients, protect the field, and be best positioned to decipher what works and what doesn't.

So far, "it hasn't worked very well," Albelda says, sounding gloomy. His team recently finished two trials in patients with mesothelioma, lung cancer, and pancreatic cancer, targeting a protein called mesothelin. The therapy seemed safe but, at best, minimally effective. "I think a lot of people are in that same boat," he says.

But glimmers of effectiveness are occasionally popping up. One patient with glioblastoma, a particularly deadly form of brain cancer, was treated early this year at City of Hope in Duarte, California, with 16 infusions of CAR T cells delivered into the brain tumor cavity and cerebrospinal fluid. Tumors in the brain and spine regressed by more than 75%. The patient remained stable for almost 8 months before relapsing and is now seeking other treatments. That response was "very exciting," says Christine Brown, a brain tumor immunologist at City of Hope who helped design the CAR T cells.

In a sarcoma trial at Texas Children's Hospital, pediatric oncologist Stephen Gottschalk was heartened to see that engineered T cells persisted for up to 6 weeks—considered an achievement in this setting, even though they can hang around for years in people with leukemia. One patient's disease did not advance for more than a year, and three other patients, whose tumors were removed after T cell treatment, have been cancer-free for up to 4 years. And that's with a tiny, "almost homeopathic" T cell dose, Gottschalk says.

For solid tumors that have spread, even incremental advances may warrant cheers because the alternative is so dismal. "The ALL response rates of 90%, those first CAR therapies—I don't care who's doing it, you're not going to get 90% of non–small cell lung cancer," says Richard Morgan, vice president of immunotherapy at bluebird bio, a biotech firm in Cambridge, Massachusetts. "But the fact is, with metastatic lung cancer, if you were able to get a 20% response rate … that is huge."



Oncologist Roisin O'Cearbhaill hopes that T cells modified to target ovarian cancer will help the women she treats, like this one.

PHOTO: DANNY GHITIS

THE NEXT WAVE OF TRIALS may deliver more encouragement. Many studies in the planning stage or just starting, including O'Cearbhaill's, aim to add extra layers to T cell treatment. One strategy is to combine CAR T cell therapy with checkpoint inhibitor drugs, which could recruit more of a patient's immune cells to assist the engineered ones designed to combat cancer. "The merit of that approach is it makes use of things that are available," says Michel Sadelain, a cell therapist also at Sloan Kettering, who treated some of the first blood cancer patients.

A second approach, which Sadelain considers especially hopeful, is to encourage the modified T cells to secrete their own powerful molecules. O'Cearbhaill and her colleagues, for example, are tinkering with the cells so that, in addition to matching up with an antigen on ovarian cancer cells, they also release interleukin-12 (IL-12), which helps T cells survive and may coax a patient's own body to make new ones. When infused through the whole body, IL-12 can have serious side effects. But this trial, like several others, starts by injecting the therapy locally. In this case, it's funneled into a woman's peritoneal cavity.

With life-threatening side effects in mind, O'Cearbhaill's trial, along with some others, includes a way to halt treatment once it has been delivered. The T cells are modified to express a marker that can destroy them if patients receive a particular antibody therapy—which they will if things go awry.

Running in parallel to clinical trials is work in the lab, where oncologists are trying to better understand the T cells they want to harness and the cancers they hope to vanquish. Sadelain combs through protein atlases, tissue sections, and RNA expression data to try to find the very best antigens to target. In another Sloan Kettering lab, thoracic surgeon Prasad Adusumilli is trying to learn what distinguishes the T cells that infiltrate a tumor from those that don't, in hopes of reengineering the laggards or isolating just the cells that excel. In Houston, Ahmed is working to establish a "profile" for different solid tumors—essentially the best combination of tumor antigens for the T cells to target.

For now, doctors are taking it one patient at a time. The woman with ovarian cancer left Sloan Kettering 5 days after an uneventful treatment. She'll be monitored carefully from head to toe, and physicians are keeping an especially close watch on her eyes, which also express the ovarian cancer antigen O'Cearbhaill targeted—and which could in theory be damaged by the genetically engineered cells. Two more women are waiting, their treatment likely to happen this fall. Three others have consented to be screened for the trial.

Whatever one thinks of the therapy's prospects, there's no shortage of patients stepping forward to try it. ■

Downloaded from http://science.sciencemag.org/ on September 1, 2016

Published by AAAS

A circadian dimension of the tumor macroenvironment p. 987 ▸

An era of induced pluripotent stem cells p. 991



PERSPECTIVES

TEXTILES

Nanoporous fabrics could keep you cool

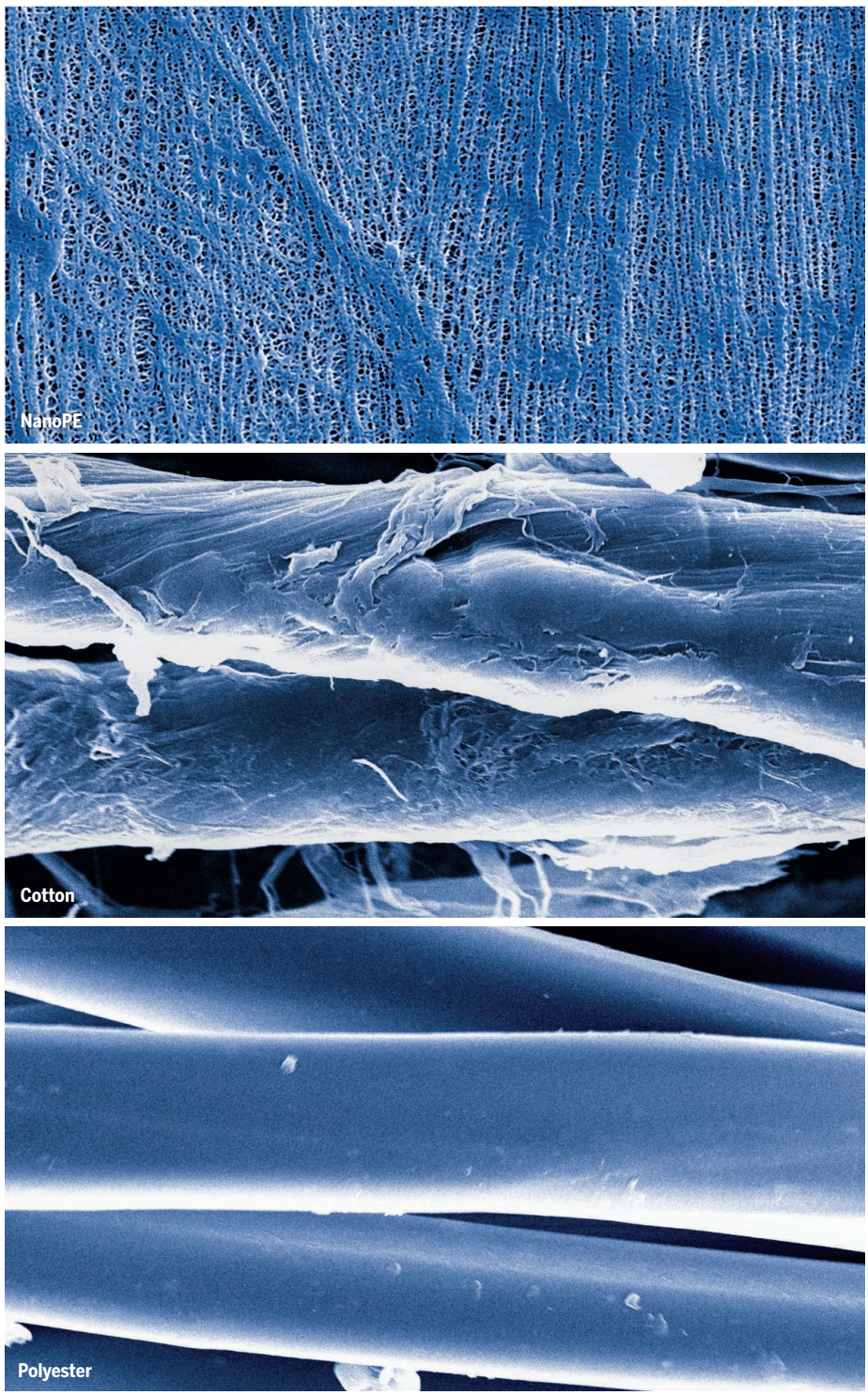
Engineered polyethylene materials are opaque but allow heat to radiate

By **Svetlana V. Boriskina**

From early days when animal skins were the season's fashion until modern times, clothes have been typically engineered for comfort in cold environments by tailoring their thermal conduction. Air pockets in feathers, furs, and woolen fabrics help reduce thermal conduction and keep warmth inside. Cooling, however, is much harder to achieve without the use of external active devices such as fans, air conditioners, or wearable thermoelectric coolers. The wicking technology used in modern athletic apparel to enhance convective cooling is not ideal for everyday clothes because it only works once perspiration begins. On page 1019 of this issue, Hsu *et al.* (*1*) report passive cooling of an object by a few Celsius degrees by simply allowing thermal radiation to pass efficiently through a nanoporous fabric. This demonstration may make possible wearable technologies for personalized cooling and paves the way for energy savings by reduced use of air conditioning.

The human body is an almost perfect emitter of thermal radiation in the mid-infrared (IR) spectral range. However, conventional fabrics block mid-IR waves by partially reflecting them and partially absorbing the thermal energy. The stark variations in the

Department of Mechanical Engineering, Massachusetts Institute of Technology, Cambridge, MA 02139, USA.
Email: sborisk@mit.edu



Oh the difference clothes can make. Scanning electron microscopy images reveal the porosity of nanoPE fiber (**top**), which allows IR light to pass, versus the dense fibers of cotton (**middle**) and polyester (**bottom**).

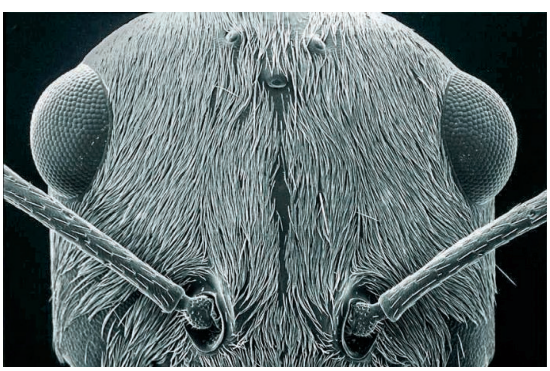
PHOTOS: (TOP TO BOTTOM) YI CUI GROUP/STANFORD UNIVERSITY; JAMES LOOMIS/ UNIVERSITY OF AUCKLAND

Downloaded from http://science.sciencemag.org/ on September 1, 2016

Published by AAAS

intensity of the thermal emission from the bare skin and through clothes can be easily observed in photos taken with an IR camera. Thus, clothes made from fabrics that are transparent to the mid-IR radiation emitted by the skin offer an opportunity to shed energy via thermal emission (*2*–*4*). Transparent clothes might sound like an odd idea because the fabric needs to be opaque in the visible range but transparent for mid-IR radiation.

A simple solution to this dilemma is offered by the Mie theory of resonant scattering from objects with sizes either comparable with or much smaller than the wavelength of the propagating electromagnetic field. This same physical effect causes the blue color of the sky caused by the scattering of the short wavelength part of the solar spectrum by the small molecules of the atmosphere. Likewise, fabrics with pore sizes that are comparable on average with the wavelength of visible light (400 to 700 nm) scatter visible light strongly and make the fabric opaque to human eyes. However, if the pore sizes are much smaller than the body's mid-IR radiation wavelength (7 to 14 μm), such fabrics are still highly transparent to the thermal emission (*2*).



Fine hairs covering the body of the Saharan silver ant reflect sunlight to avoid overheating.

PHOTO: N. N. SHI *ET AL.* (*6*)

Hsu *et al.* used a commercially available polyethylene material—nanoporous polyethylene (nanoPE), which has interconnected pores 50 to 1000 nm in diameter—to experimentally demonstrate radiative cooling (see the photo). Their spectral transmission measurements revealed that the nanoPE exhibits >90% total IR transmittance for wavelengths longer than 2 μm but is completely opaque in the visible spectrum because of the strong scattering off the nanopores. The ideal size distribution of the nanopores sets this material apart from conventional fabrics, such as those woven from cotton or polyester fibers with sizes comparable with the wavelength of the body thermal emission.

Polyethylene is far from being a conventional material for making clothes, but it has another advantage: It is mostly absorption-free in the mid-IR spectral range owing to the absence of C–O, C–N, and S=O vibrational stretching modes that are typical for other textile materials. To increase the fabric comfort, the authors modified the material so as to improve its breathability and to add water-wicking functionality by chemically modifying the fabric to be hydrophilic. Clothes fabricated from such IR-transparent textile could allow for air conditioning setpoints to be set higher than usual while maintaining the same level of personal thermal comfort. Depending on the climate, a 1 to 4 Celsius degree increase in the setpoint temperature could save up to 45% of the energy required for the building's cooling (*5*).

Although Hsu *et al.* provide the experimental demonstration of the artificial cooling fabrics designed for humans, nature already offers analogous solutions for the animal thermal control. One striking example of such natural nanotechnology is the skin hair cover of the Saharan silver ant (see the figure) (*6*). The hairs are fine enough to strongly scatter and reflect sunlight to avoid overheating by absorption. At the same time, they are transparent at IR wavelengths for shedding heat. Removal of the hairs increased the ant temperature by a couple of Celsius degrees.

Much remains to be done to bring the radiative cooling technology to the clothing market. Other materials need to be explored or synthesized that would provide the required level of mid-IR transparency combined with a higher level of personal comfort and durability. Fabrics woven from fine fibers (*2*) rather than those made by introducing nanopores into continuous films can open possibilities for using conventional textile fabrication technologies and equipment to facilitate the technology-to-market transition. IR-transparent dyes and pigments also need to be investigated and synthesized to maintain the cooling functionality of colored fabrics. However, the approach used by Hsu *et al.* could be used to address the thermal management of tents, buildings, and vehicles (*3*, *7*, *8*) with considerable energy savings.

REFERENCES

1. P.-C. Hsu *et al.*, *Science* **353**, 1019 (2016).
2. J. K. Tong *et al.*, *ACS Photonics* **2**, 769 (2015).
3. G. Smith, A. Gentle, M. Arnold, M. Cortie, *Nanophotonics* **5**, 55 (2016).
4. S. V. Boriskina *et al.*, *Nanophotonics* **5**, 134 (2016).
5. T. Hoyt, E. Arens, H. Zhang, *Build. Environ.* **88**, 89 (2015).
6. N. N. Shi *et al.*, *Science* **349**, 298 (2015).
7. T. M. J. Nilsson, G. A. Niklasson, *Sol. Energy Mater. Sol. Cells* **37**, 93 (1995).
8. A. R. Gentle, K. L. Dybdal, G. B. Smith, *Sol. Energy Mater. Sol. Cells* **115**, 79 (2013).

10.1126/science.aah5577

CANCER

Tumors set time

Lung tumors in mice distally alter circadian cycling of transcripts and metabolites in the liver

By **Iryna Shakhmantsir** *and* **Amita Sehgal**

The field of cancer research has expanded from merely observing cancer in isolation to studying it as a systemic phenomenon. Tumors occupy "environments" where they actively interact with multiple cellular processes, signaling pathways, and homeostatic mechanisms, such as, according to a recent study by Masri *et al.* (*1*), circadian rhythms. Tumor-secreted molecular messengers (the secretome) can spread over a range of distances and have both short-range and systemic influences on normal tissues and organs (*2*). To highlight the systemic effects of the cancer secretome, the concept of tumor "macroenvironment" has been coined (*3*). Masri *et al.* took this "macro" approach to inquire how tumors affect circadian cycling in a distal organ not yet infiltrated by metastasis.

In their study, Masri *et al.* used a robust mouse model of non–small cell lung cancer (NSCLC) induced by concomitant activation of a lung-specific Kirsten rat sarcoma (Kras) oncogene and deletion of the gene encoding the classic tumor suppressor p53. Having verified the absence of metastatic lesions in the livers of the tumor-bearing mice, the authors used standard transcriptomic and metabolomic analyses to evaluate hepatic circadian profiles in these mice and compared them to those of healthy mice. They demonstrated that lung adenocarcinomas had a potent distal effect on the profiles of circadian transcripts and metabolites in the liver. Specifically, the presence of lung tumors affected the types of genes oscillating in the liver. And in many of the subsets of genes and metabolites that continued to cycle in both normal and tumor-bearing mice, lung adenocarcinomas altered the phase of peak expression. Notably, the number of oscillating lipids was reduced in the livers of tumor–bearing mice. To further contextualize this

Howard Hughes Medical Institute, Perelman School of Medicine, University of Pennsylvania, Philadelphia, PA 19104, USA. Email: amita@mail.med.upenn.edu

Downloaded from http://science.sciencemag.org/ on September 1, 2016

Published by AAAS

tumor-induced metabolic phenotype, Masri *et al.* demonstrated that mice with lung tumors had overactivated the energy sensor AMP-activated protein kinase (AMPK) and decreased sterol-regulatory element–binding protein 1 (SREBP1) signaling, which is driven by circadian rhythms and regulates lipid metabolism, in their livers. These aberrations could account for the suppression of fatty acid synthesis and induction of cholesterol biosynthesis observed in the livers of mice with lung tumors.

The finding that cancer signals can directly affect transcriptional and metabolic oscillations in a distal organ raises the question about the systemic signals that mediate this coupling. When profiling serum cytokine concentrations to assess tumor-derived inflammatory signals, Masri *et al.* identified a substantial increase in the production of interleukin-6 (IL-6) cytokine, corroborating previous reports that implicated IL-6 signaling in Kras-induced tumorigenesis (*4, 5*). The authors note that elevated amounts of signal transducer and activator of transcription 3 (STAT3), an IL-6–responsive transcription factor, could potentially contribute to the decreased insulin signaling in the liver and elevated fasting serum glucose concentrations seen in the mice with lung tumors. Deleterious health consequences of this metabolic phenotype are suggested by the association of reduced plasma glucose concentrations in tumor-bearing animals with longer survival rates (*6, 7*). In agreement with findings in mice, human studies suggest that NSCLC patients with elevated fasting blood glucose have a higher mortality risk compared to patients with normal glucose concentrations (*8*).

The role of the circadian clock in regulating the hepatic macroenvironment of the tumor-bearing mice is debatable. Evidently, Kras-induced lung cancer can distally reprogram circadian transcription and metabolism in the liver, but the cause-effect relationship is unclear: Does clock disruption cause the reported metabolic phenotypes, or does the deregulated metabolism affect circadian cycling (see the figure)? The latter might be a plausible hypothesis, given that all the core clock components maintained their normal expression and circadian cycling in the livers of mice with lung adenocarcinomas. However, given that their livers display cyclic expression of some genes that do not cycle in wild-type livers, it is likely that output from the clock is affected, perhaps in addition to direct impact on some metabolic genes. Further studies are needed to address how the cycling of the hepatic transcriptome and metabolome gets reprogrammed under the influence of lung adenocarcinoma, given the seemingly flawless ticking of the core circadian clock in the liver.

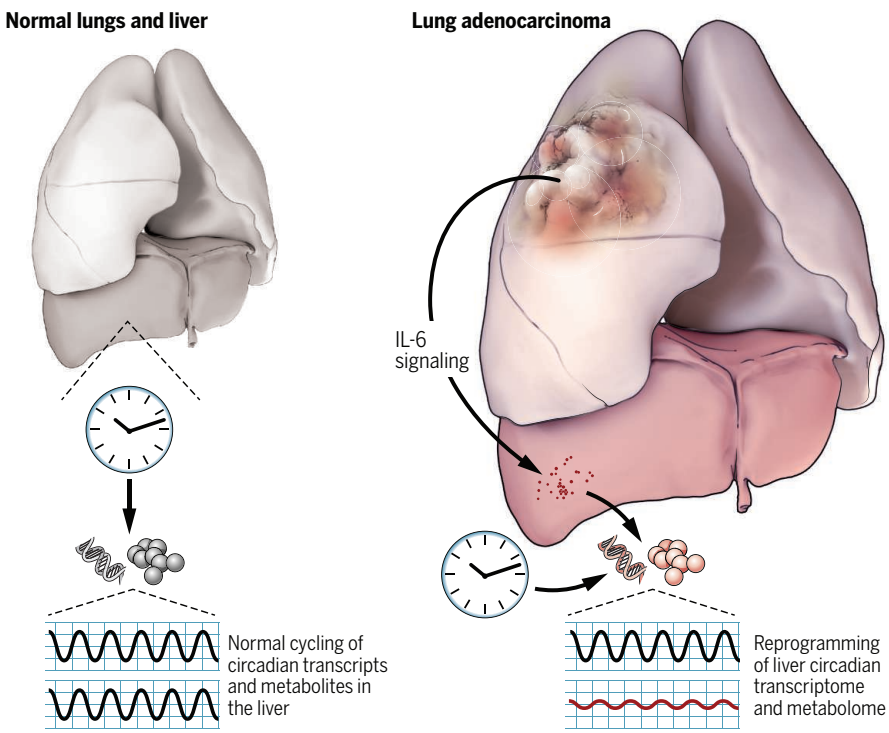
Of note, circadian clock disruptions have been previously associated with an imbalance in metabolic homeostasis, which can contribute to a number of pathologies, particularly cancer (*9*). Cancer progression is an energetically demanding process with unique metabolic requirements. Thus, there might exist a reciprocal relationship between the tumor-induced circadian phenotype and the primary oncogenic lesion. It remains to be determined whether rewiring of hepatic circadian outputs can act as a sensitizing factor to precipitate or exacerbate tumorigenesis. Intriguingly, epidemiological data indicate a correlation between chronic circadian misalignment, particularly that experienced by shift-workers and night nurses, and a higher incidence of cancer (*10*). Mouse models with clock disruptions, by contrast, have yielded mixed results, cautioning against concluding that it is the "broken" clocks as opposed to noncircadian roles of core clock genes that promote tumorigenesis (*11*).

Could a forced circadian synchronization prolong survival and halt metastasis in mice (and humans) with lung tumors? Temporal restricted feeding is a potent circadian organizer for hepatic clocks (*12*). Even mice with disrupted clock genes can synchronize their clocks when subjected to a structured timed-meal regimen. Moreover, temporal restricted feeding in mice can apparently slow tumor growth and improve cancer prognosis (*13*). Considering the therapeutic promise of these observations, it is tempting to hypothesize that feeding-induced clock entrainment in the livers of tumor-bearing mice could slow the progression of their lung adenocarcinomas.

Collectively, a zoomed-out macro view encourages a more integrated notion of cancer. Masri *et al.* add a circadian dimension to the concept of tumor macroenvironment, which could contribute to the development of novel therapeutic strategies to manage cancer systemically. ■

Remote control

Lung adenocarcinoma (right) releases systemic inflammatory cytokines, such as IL-6, that can act distally to reprogram the circadian transcriptome and metabolome in the liver. It remains to be determined how IL-6 can globally rewire hepatic circadian outputs without affecting the ticking of the core circadian clock.



GRAPHIC: V. ALTOUNIAN/*SCIENCE*

REFERENCES

1. S. Masri *et al.*, *Cell* **165**, 896 (2016).
2. S. S. McAllister, R. A. Weinberg, *Nat. Cell Biol.* **16**, 717 (2014).
3. W. Al-Zoughbi *et al.*, *Semin. Oncol.* **44**, 281 (2014).
4. S. P. Gao *et al.*, *J. Clin. Invest.* **117**, 3846 (2007).
5. G. D. Brooks *et al.*, *Cancer Res.* **76**, 866 (2016).
6. G. A. Santisteban *et al.*, *Biochem. Biophys. Res. Commun.* **132**, 1174 (1985).
7. T. N. Seyfried *et al.*, *Br. J. Cancer* **89**, 1375 (2003).
8. J. Luo, Y. J. Chen, L. J. Chang, *Lung Cancer* **76**, 242 (2012).
9. S. Sahar, P. Sassone-Corsi, *Nat. Rev. Cancer* **9**, 886 (2009).
10. S. P. Megdal *et al.*, *Eur. J. Cancer* **41**, 2023 (2005).
11. F. C. Kellerher, A. Rao, A. Maguire, *Cancer Lett.* **342**, 9 (2014).
12. Y. Tahara, S. Shibata, *Nat. Rev. Gastroenterol. Hepatol.* **13**, 217 (2016).
13. E. Filipski *et al.*, *J. Natl. Cancer Inst.* **97**, 507 (2005).

10.1126/science.aai7631

Downloaded from http://science.sciencemag.org/ on September 1, 2016

Published by AAAS



During winter storm Juno, several U.S. states declared snow emergencies. The photo shows South End, Boston, during the storm.

CREDITS: (PHOTO) SUZANNE KREITER/THE BOSTON GLOBE VIA GETTY IMAGES; (GRAPHIC) ADAPTED BY N. CARY/*SCIENCE* FROM A GRAPHIC BY M. HEGGLIN

CLIMATE CHANGE

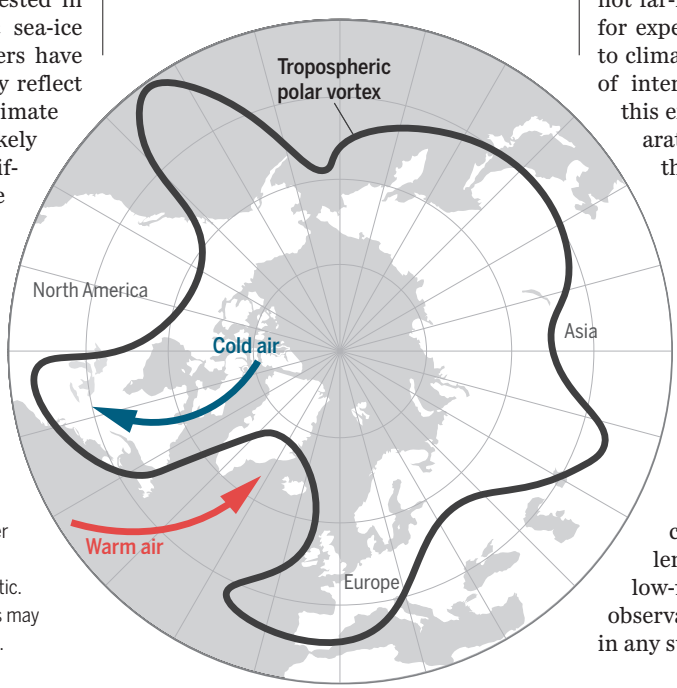
Effects of a warming Arctic

It remains unclear to what extent the warming Arctic affects climate and weather extremes at lower latitudes

By **Theodore G. Shepherd**

Recent years have seen a series of unusually cold winters in northern mid-latitudes, including the eastern United States, where they have been accompanied by extremely heavy snowfalls. Some atmospheric scientists have argued that such cold events may be associated with the rapid warming of the Arctic that has been observed over recent decades and that is manifested in the precipitous decline of Arctic sea-ice extent since the early 1990s. Others have argued that the cold events merely reflect the chaotic variability of the climate system and are becoming less likely under climate change. How can different atmospheric scientists come to such different conclusions from the same data?

On basic thermodynamic grounds, climate change is expected to raise winter surface temperatures over land, with an amplified warming in the Arctic. This is what is seen in observations over sufficiently long periods. All else being equal, this would lead not only to fewer cold events but also to less variability in surface temperature as a result of the reduced latitudinal temperature gradient, although heavy snowfalls could increase due to the moister atmosphere (*1*). Arguments for more frequent cold events thus rely on a change in atmospheric dynamics, and here the scientific understanding is very poor (*2*). Various mechanisms have been proposed, but they represent hypotheses rather than predictive theories (*3*).



Cold snap. Schematic of the weather situation on 26 January 2015, when winter storm Juno hit Boston. The edge of the tropospheric polar vortex separates cold Arctic air and warmer mid-latitude air. A wavier vortex leads to enhanced transport of cold air to lower latitudes and of warm air into the Arctic. It remains unclear whether such wavier states may become more common under climate change.

Weather systems provide most of the heat transport from mid- to high latitudes during winter. In some years, a strong tropospheric polar vortex inhibits the exchange of air masses between the Arctic and mid-latitudes. In other years, a weaker and wavier polar vortex enhances the exchange, leading to mid-latitude cold spells and a warmer Arctic (see the first figure). An increased tendency for the latter state results in a trend toward cold continents and a warm Arctic, although North America and Eurasia can vary independently. Such a trend is seen in recent decades, with a cooling tendency over the eastern United States and, especially, central Asia and an accelerated warming of the Arctic compared with that seen over the past 50 years (see the second figure).

Given the uncertainties surrounding dynamical aspects of climate change, a reasonable null hypothesis would be that climate change is dominated by its thermodynamic aspects. The unusual behavior seen in recent decades would then reflect natural variability. The contrary hypothesis is that the accelerated warming of the Arctic is part of the climate-change signal and has changed the weather patterns in mid-latitudes through changes in the tropospheric polar vortex. Such a hypothesis is not far-fetched: There are general grounds for expecting that the dynamical response to climate change will resemble the modes of internal variability (*4*). Unfortunately, this expectation makes it difficult to separate the signal from the noise, because they have similar spatial patterns.

One aspect of the scientific debate has focused on whether the observed changes associated with particular hypotheses are statistically significant. This is rather beside the point, because the definition of statistical significance is arbitrary (*5*). A lack of statistical significance does not mean that the effect is not there, and a positive finding does not imply any attribution to climate change. It is also extremely challenging to accurately characterize the low-frequency noise from the limited observational record. A deeper difficulty in any such analysis is that correlation does

Downloaded from http://science.sciencemag.org/ on September 1, 2016

Published by AAAS

not imply causality. Kretschmer *et al.* (*6*) recently used the concept of causal effect networks to overcome this limitation. They found that a loss of Barents/Kara sea ice (which induces local warming) can indeed be considered a causal driver of a weakened tropospheric polar vortex.

Another aspect of the debate has focused on what numerical models predict. Many studies have attempted to model the response of the mid-latitude circulation to Arctic warming, usually induced through reduced sea-ice extent. The results have generally been inconclusive, showing only that the answer depends sensitively on the model setup. The only result that seems to consistently emerge is a cooling in central Asia (much as seen in recent decades; see the second figure) resulting from loss of Barents/Kara sea ice (*7*). This result can be understood in terms of the circulation response to a local warming. It matches the observationally determined causal relationship (*6*) and could account for the attribution of the observed increase in cold extremes in central Asia to circulation changes (*8*).

Comprehensive climate models do not provide any indication of increased wintertime cold events in northern mid-latitudes in response to climate change, suggesting that any such tendency arising from Arctic warming (if it exists) is overwhelmed by other factors. However, it remains unclear whether the models represent the relevant physical processes in a sufficiently accurate way for the results to be considered as definitive. Models with stronger Arctic warming have a tendency toward surface pressure increases over northern Eurasia (*9*), broadly consistent with the results reported by Kretschmer *et al.* (*6*) and Mori *et al.* (*7*).

Given the current model projections and the impossibility of ruling out natural variability as the explanation for the observed behavior in recent decades, the null hypothesis is certainly a scientifically defensible position (*10*). However, multiple lines of evidence support the hypothesis of an Arctic–mid-latitude connection in central Asia, although not in the eastern United States. Moreover, the either/or dichotomy between a forced response to climate change and natural variability is overly simplistic. For example, the meanders in the tropospheric polar vortex induced by teleconnections from Pacific sea surface temperature variations can be expected to be larger if the vortex is weaker. Thus, it is possible that variability and the forced response to climate change act together to affect extreme weather.

The question is not whether Arctic changes are affecting mid-latitudes but rather how and by how much. Framing studies in this way will avoid polarization and aid progress. It is encouraging to see recent collaborations between scientists from what might be considered opposing camps (*11*); this sort of productive interaction will move the science, and with it the public discourse, forward. ■

Department of Meteorology, University of Reading, Reading, UK. Email: theodore.shepherd@reading.ac.uk

REFERENCES AND NOTES

1. P. A. O'Gorman, *Nature* **512**, 416 (2014).
2. B. J. Hoskins, T. Woollings, *Curr. Clim. Change Rep.* **1**, 115 (2015).
3. J. Cohen *et al.*, *Nat. Geosci.* **7**, 627 (2014).
4. T. G. Shepherd, *Nat. Geosci.* **7**, 703 (2014).
5. R. Nuzzo, *Nature* **506**, 150 (2014).
6. M. Kretschmer *et al.*, *J. Clim.* **29**, 4069 (2016).
7. M. Mori *et al.*, *Nat. Geosci.* **7**, 869 (2014).
8. D. E. Horton *et al.*, *Nature* **522**, 465 (2015).
9. E. Manzini *et al.*, *J. Geophys. Res. Atmos.* **119**, 7979 (2014).
10. L. Sun, J. Perlwitz, M. Hoerling, *Geophys. Res. Lett.* **43**, 10.1002/2016GL069024 (2016).
11. J. A. Screen, J. A. Francis, *Nat. Clim. Change* **6**, 10.1038/NCLIMATE3011 (2016).
12. GISTEMP Team, 2016: *GISS Surface Temperature Analysis (GISTEMP)*. Data set accessed 2016-07-22; http://data.giss.nasa.gov/gistemp/.
13. J. R. Hansen *et al.*, *Rev. Geophys.* **48**, RG4004, 10.1029/2010RG000345 (2010).

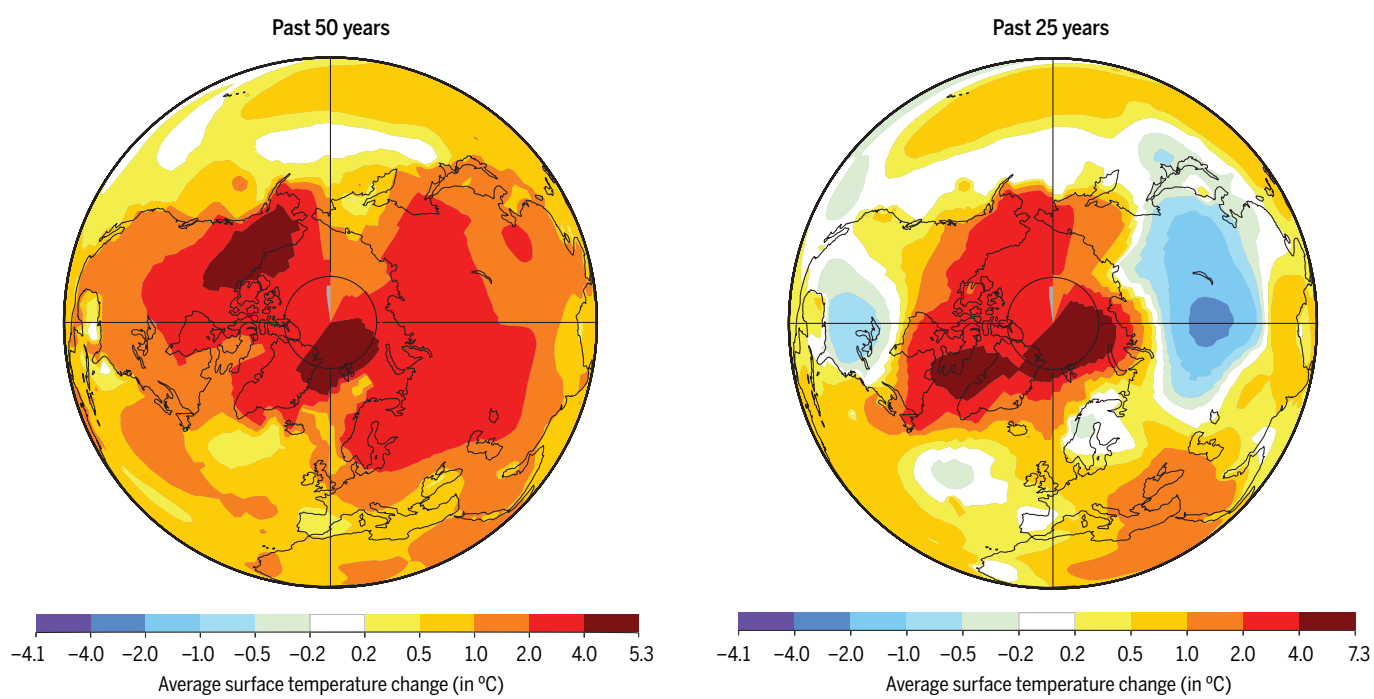
ACKNOWLEDGMENTS

The author is supported by the Royal Society, the European Union, and the European Research Council.

10.1126/science.aag2349

A matter of time

Over the past 50 years, average winter temperatures (December, January, and February) show the warming over land and enhanced warming over the Arctic expected from climate change. Departures from this behavior in the past 25 years may be due to natural variability, an altered climate-change response caused by sea ice declines, or a combination of the two. Data and graphics from (*12*).



GRAPHIC: N. CARY/*SCIENCE*

Downloaded from http://science.sciencemag.org/ on September 1, 2016

Published by AAAS

STEM CELLS

Induced pluripotent stem cells, past and future

Ten years ago, a method to reprogram cells to a pluripotent state changed biomedical research

By **Eirini P. Papapetrou**

Ten years ago, Shinya Yamanaka and his student Kazutoshi Takahashi did an experiment of exquisite simplicity and elegance that changed biomedical research forever (*1*). By showing that a set of transcription factors could reprogram somatic cells to acquire a pluripotent stem cell state, they ushered in the era of induced pluripotent stem cells (iPSCs). The discovery made it crystal clear that cell identity is much more malleable than previously thought, and provided an invaluable tool for disease-oriented and translational researchers, bridging reductionism with patient-derived relevance. Combined with other maturing technologies, most notably genome editing and three-dimensional (3D) cell culture systems, iPSC technology has enabled investigation that was hitherto only possible in model organisms (*2, 3*).

THE PAST

The Takahashi and Yamanaka report took the stem cell community by storm. The first years were marked by studies published at a remarkable pace by researchers primarily from the stem cell, developmental biology, and genetic engineering fields who jointly contributed to milestones and controversies that have ultimately shaped our current—and still very incomplete—understanding of what iPSCs are and how reprogramming works.

Milestones of the first decade

Technical achievements were reached, proofs of principle in disease models were established, and biological insights into reprogramming with transcription factors were gained precipitously over the past decade. The methods of reprogramming cells to pluripotency evolved from using integrating retroviral vectors and excisable lentiviral and transposon-based vehicles, to nonintegrating episomes and RNA-based systems (Sendai virus vectors and messenger RNA transfection). Thus far, methods based solely on protein transduction or chemical compounds have been only partially successful. The stoichiometric and kinetic requirements for expressing the key transcription factors [octamer-binding transcription factor 4 (OCT4), sex determining region Y-box 2 (SOX2), Kruppel-like factor 4 (KLF4), and cellular myelocytomatosis (cMYC)] were determined, as were alternative combinations of these factors and other factors or compounds as reprogramming "enhancers" (*4*). As the cell types that could be reprogrammed quickly expanded, it became clear that transcription factor reprogramming to pluripotency is a robust and universal process that works with nearly any cell type from any species. An array of disease-specific iPSCs were derived from patients, and proof-of-concept for their use in disease modeling, drug testing, and regenerative medicine by means of cell therapy (which can also be combined with gene therapy) was achieved (*5, 6*).

> ***"...iPSCs and the CRISPR-Cas9 system 'democratized' stem cell modeling and genome editing..."***

How reprogramming works at the molecular level has been, not surprisingly, a harder problem to crack. Models of transcription factor reprogramming provided some evidence for both stochastic and deterministic components, potentially occurring at distinct phases of the process. Intermediate steps were described that may involve the "pioneer" binding of transcription factors to closed chromatin, a balancing act between opposing actions of lineage-specifying factors and/or a reversal of normal development, ultimately mediating the silencing of somatic genes and the activation of an endogenous network of pluripotency regulators, thereafter establishing a remarkably stable new cell identity (*4*). However, a clear picture of the critical events and a consensus universal model of transcription factor reprogramming remain largely elusive.

Controversies of the first decade

Along with important milestones came a series of controversial issues that quickly captured the imagination of the scientific and lay communities, as they provided grounds for questioning the value of iPSCs as sources for cell therapies and disease modeling. Fortunately, most of the initial concerns turned out to be based either on artifacts or on much more nuanced phenomena, rather than problems intrinsic to iPSCs (*7*). The idea of epigenetic memory arose from the finding that at an early stage of cell cultivation, iPSCs harbor DNA methylation remnants and exhibit differentiation propensities biased towards their cell of origin. This was later proven to be due mostly to incomplete reprogramming as a result of poor technique or early passage in cell culture. The idea that iPSCs may have more unstable genomes than other cells arose from the discovery of copy-number and single-nucleotide variants in iPSC lines (which are typically clonal) at a higher frequency compared to the donor tissue (which is typically highly polyclonal). These initial observations were later largely attributed to detection limits, as most genetic aberrations found in iPSCs could be shown, with sensitive methods, to preexist in the cell of origin (most human somatic tissues are highly genetically mosaic), and to have been merely captured and clonally amplified. Additional genomic variation was found to occur during cell expansion, as happens with all cultured cells. Concerns that iPSCs have immunogenic properties that could lead to their rejection, even in an autologous setting, turned out to be based on heavily context-dependent observations, while immune tolerance of iPSCs and their derivatives turned out to be, not surprisingly, dependent on multiple parameters related to the quality of the starting cell and the final cell product. Concerns that variability between iPSC lines—epigenetic, transcriptional, or in differentiation potential—could pose a serious impediment to their use were eased by conclusive evidence that most of the variability is neither random nor intractable, but stems from differences in genetic background (as iPSC lines are as genetically diverse as people and certainly much less so than inbred mice). The iPSC line-to-line variability is also not higher than that observed among the gold-standard embryonic stem cell (ESC) lines, derived either from blastocysts or by somatic cell nuclear transfer (SCNT).

THE FUTURE

Whereas iPSCs can contribute to breakthroughs in all fields, some areas in which

Department of Oncological Sciences, Icahn School of Medicine at Mount Sinai, One Gustave L. Levy Place, New York, NY 10029, USA. Email: eirini.papapetrou@mssm.edu

Downloaded from http://science.sciencemag.org/ on September 1, 2016

Published by AAAS

iPSCs can be uniquely useful over other models include disease modeling, drug development, regenerative medicine, and understanding gene regulation (see the figure).

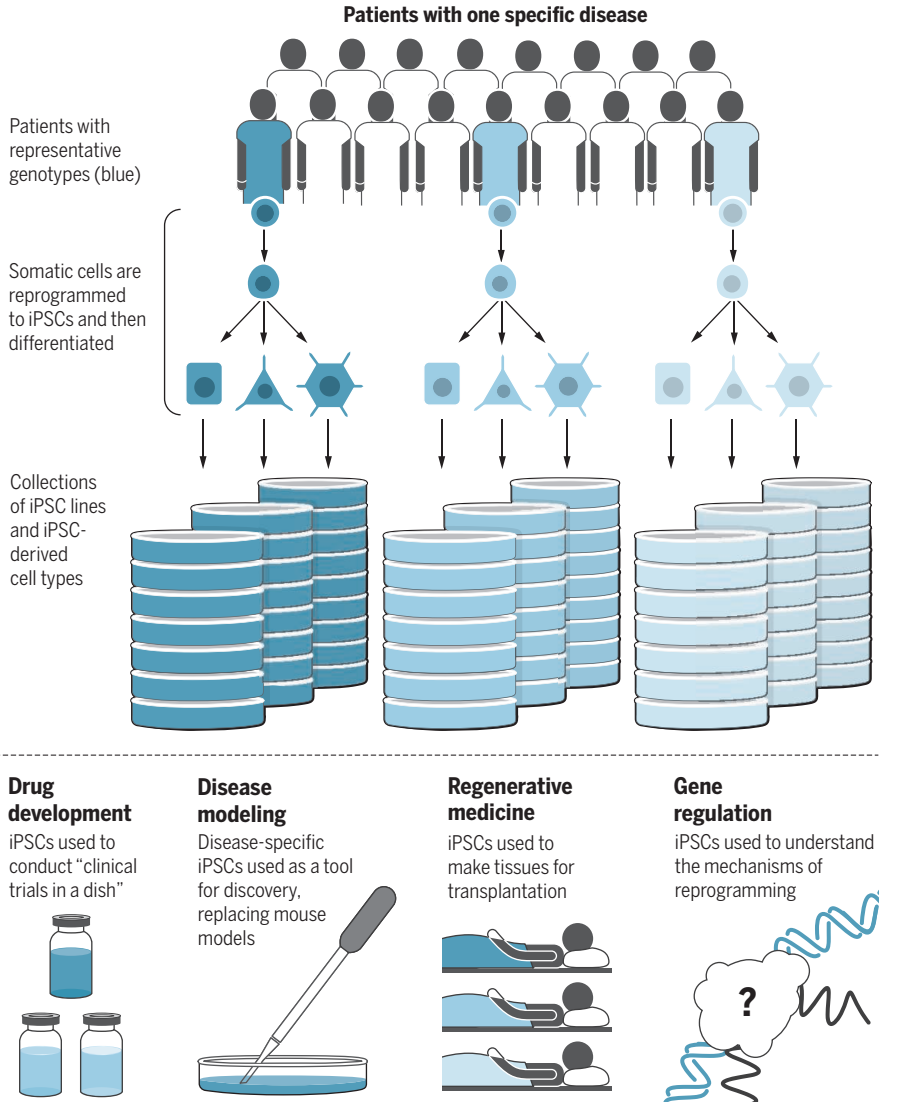
Disease modeling

The first disease modeling studies mostly focused on well-characterized, monogenic diseases and established the principle that iPSCs derived from patients could recapitulate disease manifestations already suspected or known from previous studies using other disease models. A next wave of studies started tackling polygenic and more complex disorders, including psychiatric diseases, infectious diseases, and cancer, and also started to examine the role of human genetic variation (*8*). The next frontier is turning disease-specific iPSCs into a true tool for primary discovery. Because of the compelling strengths and new opportunities they provide, iPSCs are expected to become what mouse models have been in the past two to three decades. A collection of iPSC models for practically any disease and any disease-related gene mutation—also leveraging genome editing technologies, mainly the clustered regularly interspaced short palindromic repeats (CRISPR)–Cas9 system—will be steadily assembled over the next few years. These cell models will also be increasingly used in conjunction with other emerging technologies, including organoids and other 3D culture systems, organs-on-chips, and xenografts. These approaches will also likely leverage advances from fields such as synthetic biology and bioengineering to increasingly afford multicellularity, and more physiological modeling of healthy and diseased human tissue at a higher level of organization.

Building collective experience in the scientific community in the strengths and weaknesses of iPSC disease models, and increasing confidence in their readouts, will benefit from lessons in the mouse modeling field. iPSC disease models will only be as good as the iPSC lines and the differentiated cells made from them, and readouts will only be as relevant and predictive as the surrogate cellular phenotypes. Careful characterization of disease iPSC lines is therefore imperative, as is their maintenance, authentication, and distribution—which would be best handled by dedicated repositories. It will also be important to strike the right balance between studying a few well-validated lines and still capturing enough of the genetic diversity of the disease under study. Although the need for high-quality well-characterized iPSC lines and standardized differentiation procedures is broadly recognized, a less widely discussed issue is what constitutes a disease-relevant phenotype and how one can determine for what organismal phenotype a cellular phenotype observed in an iPSC disease model can serve as a surrogate. This is of utmost importance as human diseases typically manifest with diverse clinical symptoms and signs that are linked to the underlying pathogenic processes with varying degrees of relatedness and causality.

New frontiers in iPSC research

Collections of iPSC lines and diverse differentiated cell types derived from them can be assembled in repositories and used for multiple purposes.



GRAPHIC: K. SUTLIFF/*SCIENCE*

Drug development

Apart from serving as tools to discover new mechanisms of disease and new therapeutic targets, iPSCs will occupy increasingly more central roles in drug development, including candidate drug testing, compound screening, drug repurposing, and toxicity testing. Collections of iPSCs that capture a range of diseases and genotypes can be used to conduct "clinical trials in a dish" to discover biomarkers of response, while phenotype-based screens empowered by isogenic controls can provide a road to drug discovery in diseases with no known molecular targets. Candidate drug testing and high-throughput screening in iPSC-derived cells from patients with neurological disorders, such as amyotrophic lateral sclerosis (ALS) and familial dysautonomia, have already produced promising compounds, which are making their way to clinical trials (*9*, *10*). In parallel, the ability to generate multiple normal tissues from the same initial cells offers well-defined conditions for toxicology studies (*11*).

Downloaded from http://science.sciencemag.org/ on September 1, 2016

Published by AAAS

Regenerative medicine

The idea of regenerating humans by replacing damaged organs and tissues with brand-new ones has fascinated scientists and the public alike for years and is feeding into most of the hype around stem cells. Initial aspirations that stem, progenitor, and precursor cells administered to an animal or human will find the cues needed to home to the right place, integrate harmoniously with the environment, and functionally benefit the host organism have proved to be overly optimistic [with the sole exception of hematopoietic stem cells (HSCs)], and it is now obvious that all of these requirements are major obstacles that stand in the way of translating stem cell research into cell therapies. The diseases that will be in line for clinical trials using cells derived from human pluripotent stem cells (hPSCs, including iPSCs and ESCs) is by and large determined by two questions: (i) What cells can be made from hPSCs in vitro with sufficient yield and functionality; and (ii) is there a disease that can be treated with these hPSC-derived cells with a reasonable chance of success and acceptable risk to patients? By these criteria, eye diseases gained priority and the first clinical trial using iPSC-derived retinal pigment epithelial cells to treat macular degeneration started patient enrollment in 2014 in Japan. The next candidates approaching the clinic include Parkinson's disease, spinal cord trauma, diabetes, and myocardial infarction. Although hPSC-derived HSC therapies are not currently on the horizon because of the inability to generate transplantable HSCs from hPSCs, a single breakthrough may catapult them to the finish line, owing to the ease of administration and the long clinical experience with HSC transplantation.

Apart from scientific advances in cell and tissue engineering, a paramount task for moving the field forward is establishing guidelines on what tests and thresholds should be used to determine quality and safety of iPSC-derived cell products. The first iPSC clinical trial was halted 1 year later, after the safety of a patient-derived iPSC line could not be firmly established because the effects of two mutations found by next-generation sequencing could not be determined.

A major decision is whether to pursue iPSC-derived cell therapies in an autologous or allogeneic setting. As both approaches have obvious pros and cons, it is likely that this decision will be made on a case-by-case basis. Different tissues have less or more stringent requirements for tissue matching, as experience from solid organ transplantation has shown. The acceptable level of immunosuppression and the alignment of cell preparation with treatment timelines depend on the underlying condition. Cell therapies will also be influenced by the present and future status of good manufacturing practice capabilities that will largely determine the financial sustainability, scalability, and time scales of cell manufacturing. For acute life-threatening conditions, an immediately available off-the-shelf treatment may be a more viable option. The development of banks of iPSC lines homozygous for major histocompatibility complex antigens or even universal donor lines that can potentially be engineered through genome editing could provide histocompatible cells that a large number of patients can accept without mounting an immune response. For patients requiring repeated cell administration, such as blood product transfusions or enzyme replacement therapies, and who often become sensitized to major and minor antigens, autologous therapies might be both more efficacious and cost-effective. iPSC products may be transplanted, at increasing levels of complexity, as cells in suspension, 2D sheets, 3D tissues, or even entire organs. The latter could well be generated entirely in vitro or in xenogeneic conditions in large animal chimeras.

"The next frontier is turning disease-specific iPSCs into a true tool for primary discovery."

Gene regulation

The success of transcription factor reprogramming could not have been predicted and cannot be explained with current models of gene regulation, which is why the mere fact that it worked ten years ago was originally met with so much disbelief and awe. The "Yamanaka experiment" required a leap of faith, as the only evidence at the time supporting the rewiring of a somatic cell nucleus to pluripotency were nuclear transplantation and cell fusion experiments and a few transcription factor–mediated cell fate conversions (notably the conversion of fibroblasts to muscle by the transcription factor MyoD). These were viewed as isolated oddities. Although it is now a well-established phenomenon that combinations of only few key transcription factors can induce dramatic cell fate changes (including transitions across somatic cell lineages without going through a pluripotent state), how and why this happens remains as much of a mystery as it was 10 years ago.

It is entirely possible that current models of gene regulation are missing some fundamental functionality of the genome and/or action of transcription factors. Revised models that are built upon new insights into how gene expression programs and cell identity are established may be needed to explain cell fate transitions. New experimental systems that accommodate reprogramming with high efficiency and similar kinetics will be needed to address these questions, preferably in human cells. Interdisciplinary approaches that combine single-cell analysis and systems biology methodologies are also part of this next frontier. Breakthroughs in understanding the molecular mechanisms of transcription factor reprogramming may ultimately lead to processes that generate iPSCs of the highest possible quality.

Two highly synergistic technologies in the past decade, iPSCs and the CRISPR-Cas9 system "democratized" stem cell modeling and genome editing, respectively, by making them widely accessible to the scientific community. Their convergence, together with the recent avalanche of human genome sequencing data, is revolutionizing the study and treatment of human disease. iPSCs are poised to play a central role in a shift that is already underway in the use of primary human patient material from late-stage validation studies to the front line of biomedical discovery. As iPSCs will be put to use in increasingly diverse scientific questions and applications, it will be important for all stakeholders to manage the expectations of scientists, patients, and the public, and to provide safeguards on the one hand without impeding progress on the other. As iPSC-based therapies move to the clinic, lessons from other related fields should be remembered: the boldness of the HSC transplantation field (in severe cases where this is justified) that pushed the boundaries of clinical practice beyond scientific knowledge of the time; the caution of the chimeric antigen receptor (CAR) T cell field that, through engineering of T cells and adoptive cell transfer achieved so much in treating cancers with few fatalities; and the lesson from the gene therapy field that safety cannot be ascertained until therapeutic levels of the administered cell product are reached. ■

REFERENCES

1. K. Takahashi, S. Yamanaka, *Cell* **126**, 663 (2006).
2. D. Hockemeyer, R. Jaenisch, *Cell Stem Cell* **18**, 573 (2016).
3. M. A. Lancaster, J. A. Knoblich, *Science* **345**, 1247125 (2014).
4. K. Takahashi, S. Yamanaka, *Nat. Rev. Mol. Cell Biol.* **17**, 183 (2016).
5. J. Hanna *et al.*, *Science* **318**, 1920 (2007).
6. E. P. Papapetrou *et al.*, *Nat. Biotechnol.* **29**, 73 (2011).
7. N. Tapia, H. R. Schöler, *Cell Stem Cell* 10.1016/j.stem.2016.06.017 (2016).
8. N. Zeltner, L. Studer, *Curr. Opin. Cell Biol.* **37**, 102 (2015).
9. J. McNeish *et al.*, *Cell Stem Cell* **17**, 8 (2015).
10. G. Lee *et al.*, *Nat. Biotechnol.* **30**, 1244 (2012).
11. P. W. Burridge *et al.*, *Nat. Med.* **22**, 547 (2016).

10.1126/science.aai7626

Downloaded from http://science.sciencemag.org/ on September 1, 2016

Published by AAAS



POLICY FORUM

INTERNATIONAL POLITICS

Tensions of refugee politics in Europe

Electoral, welfare-state, and demographic politics are obstacles to refugees

By **Randall Hansen**[1] *and* **Shalini Randeria**[2,3]

Globally, there are at least 65 million displaced persons, made up of 41 million internally displaced persons (those fleeing violence and/or persecution within their state's borders), 21 million refugees (those fleeing persecution beyond those borders), and 3 million asylum seekers (*1*). Europe is not bearing the main brunt of the refugee crisis. Roughly 85% of the world's refugees today are in the global South, and half of them are in countries with a per capita Gross Domestic Product of less than U.S. $5000 (*2*). The continent is nonetheless in the center of a political and social storm from the roughly 1,255,600 people who applied for asylum in the European Union (EU) in 2015 (*3*).

We are now witnessing a battle over the control of European borders, or lack thereof, and the distribution of refugees within the EU member states that is transforming the very political and economic structures of the EU. Divisions have emerged not simply between the former communist Eastern Europe and the liberal democracies of Western Europe or between the indebted southern European countries and the more prosperous northern ones. Rather, there is a divide within every European country, in Poland and Hungary as much as in France, Switzerland, Germany, and the Netherlands. It is an urban-rural divide in every country: a division between liberal, cosmopolitan elites and supporters of nativist right-wing populist ideologies.

An open-door policy for refugees retains support in some quarters, such as universities and businesses, but overall, there is frustration with the EU's approach to refugees (*4*). Large majorities, at times >90% of the national population, are strongly critical of the EU's handling of the crisis [on business support, see (*5*)]. Viktor Orbán, the Hungarian prime minister, has used the refugee crisis to mount what he calls a defense of "Christian civilization," while explicitly repudiating liberal principles (*6*).

In Germany, the new far-right party, the Alternative for Germany, enjoys increasing popularity because of its opposition to refugees and its anti-Islamic stance. In France, the National Front's Marine Le Pen currently has between 26 and 30% support in the opinion polls (*7*). In Italy, Switzerland, Slovakia, Hungary, and Poland, extreme-right parties, claiming to speak on behalf of national majorities ignored by pro-European elites, have gained between 20 and 45% of the popular vote (*8*) (see the figure).

The EU, which has for years had a common asylum policy, proved inadequate to manage the influx of refugees. The Dublin system, under which asylum-seekers' applications must be processed in the first European country of their arrival, broke down not only under Germany's decision to waive the requirement but also under the sheer weight of numbers and Hungary's hostility to refugees, whom it did not permit to cross its borders. The Schengen system of uncontrolled borders allowing free movement through Europe came under severe strain, as one country after another introduced border controls. A cross-EU resettlement scheme for 160,000 refugees failed because of member-state intransigence and refugees' desire to move to northern Europe: As of May, only 1324 refugees living in Greece were processed for resettlement (*9*). In March 2016, Austria, the Czech Republic, Slovakia, Croatia, Serbia, and Macedonia agreed to seal their borders, effectively closing the Balkan route and causing a huge backlog of refugees stranded in Greece. Meanwhile, opposition to refugees and far-right, anti-Islamic advocacy grew

[1]*Centre for European, Russian, and Eurasian Studies, Munk School of Global Affairs; Department of Political Science, University of Toronto, Toronto Ontario M5S 3K7, Canada.*
[2]*Institute for Human Sciences, 1090 Vienna, Austria.*
[3]*Graduate Institute of International and Development Studies, 1202 Geneva, Switzerland. Email: r.hansen@utoronto.ca*

PHOTO: EPA EUROPEAN PRESSPHOTO AGENCY B.V./ALAMY STOCK PHOTO

Downloaded from http://science.sciencemag.org/ on September 1, 2016

Published by AAAS

Supporters of anti-immigrant activists and nationalists in Warsaw, Poland, 12 September 2015, march to protest against the Polish government's decision to accept migrants from Syria and North Africa.

(*4*). Far from ameliorating the crisis, the EU's inactivity made it worse.

Following this failure, the EU Commission proposed on 13 July 2016 a "Common European Asylum System" (*10*). The emphasis is on control: speeding up processing by quickly rejecting "manifestly unfounded" cases; limiting secondary movements (applying in, for instance, Poland then moving on to Germany); expanding temporary protection (returning refugees when home country conditions improve); and making social assistance conditional on integration courses. On the refugee rights side, the proposal urges common standards (free legal assistance and a right to an interview and legal representation), an obligation to take home country information into account when processing refugee applications, and quicker access to the labor market. These are only proposals: The Council (the EU's executive) would have to adopt them. However, member states will continue to guard their sovereignty and will remain the key players.

POLITICS AND PARADOX

The story of Europe is partly one of populists offering simple solutions to complex problems. But there is more to it than this: A liberal, humanitarian approach to the crisis would have Europe accept at least its fair share of refugees. Given its wealth and size this would be between 5 and 10 million, or 25 to 50% of the world's refugees. However, in all democracies the world over—with the notable exception of Canada—a majority of voters want fewer foreigners and/or immigrants. Most politicians fearful of their jobs opt to go with the democratic will that stands in opposition to liberal principles. International treaties that have been signed, such as the Human Rights Convention, are being pushed aside in attempting to placate democratic majorities.

With their coordinated and training-based economies and robust welfare states, Scandinavia, Switzerland, Germany, and Austria face particular challenges in accepting refugees. Most professions in these countries require extensive training in the form of a 3-year apprenticeship. Individuals with inadequate language skills face enormous challenges in securing apprenticeships and thus qualifying for even low-skilled jobs, such as in sales, which are defined as professions. At the same time, relatively generous income support levels in northern Europe—plus free health care and subsidized accommodation—can discourage low-wage employment when that employment pays less than social support (*11*). By contrast, the United States and Canada have dynamic labor markets, less demand for apprenticeship, and very low income support in times of unemployment (*12*–*14*). As a result, migrants to Europe integrate too often into welfare, whereas those in North America integrate into work (*15*).

An obvious means to tackling the welfare challenge is reducing income support for refugees while allowing the market to determine their wages. However, social democrats, who support immigration and are more welcoming toward refugees are resolutely opposed to lower income-support levels on grounds of equality and social justice. The economic consequences are obvious: Low-skilled immigrants with poor language skills will not secure scarce apprenticeships, whereas benefits act as a disincentive to securing low-wage employment. Paradoxically, low wages and good welfare are acting as stumbling blocks to assimilating refugees. Mainstream conservative politicians are much more willing to countenance the labor market and welfare reforms that would accommodate unskilled immigration. But unlike social democrats, conservatives have been opposed to easy or early naturalization, and they reject dual citizenship.

All things being equal, aging and shrinking populations should lead Europeans to welcome young foreigners, be they refugees or migrants, who could relieve shortages in the labor market and shore up depleted state pension funds through their tax contributions. Rather than elation at a possible demographic dividend, conservative European politicians and the popular press have generated a demographic panic, a "fear of small numbers" (*16*): of being overwhelmed by foreigners and of a loss of national identity (*17*). The resentment felt by those who perceive themselves as "threatened majorities" defines the debate on who belongs to the political community, which is understood in narrow ethnic-religious terms. Hungarian Prime Minister Orbán plays upon these fears, along with a much older anti-Islamic sentiment common in southeastern Europe, when he raises the specter of a Christian Europe overrun by an "invasion" of Muslims (*17*). In 8 of 10 countries recently surveyed (*18*), at least half the people believe that there is a greater likelihood of terrorism because of the incoming refugees (*18*). Public perceptions rather than facts rule the day: Although Hungary has hardly accepted any refugees in the past or present, 82% of Hungarians believe that refugees were taking their jobs and benefits.

Given current demographic trends, we believe Europe needs more migration. The constraints we have described, however, make this seemingly realistic goal elusive. To begin with, the EU and its member states must be seen to be in control of their external borders; when publics believe the state has lost control of its borders, opposition to immigration grows, often sharply. In the EU, the proposal for common standards for granting asylum and speedier labor market access for refugees should be adopted. Moving forward, EU member states should agree to accept a certain number of refugees directly from the Middle East, obviating the need to depend on Turkey to stem the flow of refugees. It should increase development aid and target it at nationals and refugees in the global South, where most of the world's refugees are currently housed. Its new policy (*19*) of making development aid to African countries contingent on their imposition of migration controls at their own borders is not only ethically and politically unacceptable but also unlikely to be effective. ■

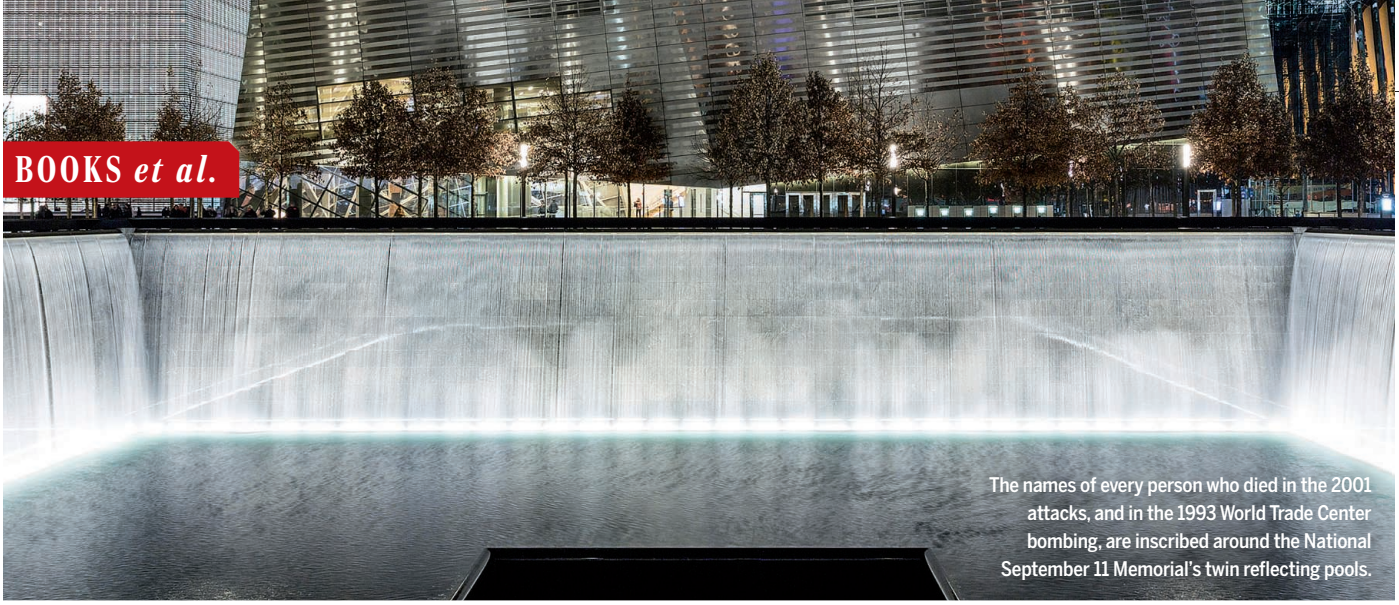
REFERENCES AND NOTES

1. A. Edwards, Global forced displacement hits record high (United Nations High Commissioner for Refugees, Geneva, 2016); http://bit.ly/reGlobalTrendsReport.
2. German Federal Office for Migration and Refugees (BAMF), Asylgeschäftsstatistik für den Monat März 2016 (BAMF, Berlin, 2016), p. 10; http://bit.ly/GermanAsylumStatistics.
3. Eurostat, Record Number of over 1.2 million first time asylum seekers registered in 2015; http://bit.ly/NosAsylumSeekers.
4. B. Stokes, Euroskepticism beyond Brexit (Pew Research Center: Global Attitudes and Trends, Washington, DC, 2016); www.pewglobal.org/2016/06/07/euroskepticism-beyond-brexit/.
5. Business and Human Rights Resource Center, Europe: Businesses take steps to offer support while others are accused of contributing to anti-refugee sentiment (BHRRC, 2016); http://bit.ly/BusinessSupport-or-Lack.
6. R. D. Keleman, *Foreign Affairs*, 20 September 2015;. https://www.foreignaffairs.com/articles/europe/2015-09-20/europes-hungary-problem.
7. Election présidentielle 2017: dates, candidats, sondages, résultat (L'Intern@ute, 2016); http://election-presidentielle.linternaute.com.
8. A. Mucci, *Politico* (Pavia), 29 January 2016; http://politi.co/2bs0zOd.
9. D. Robinson, K. Hope, *Financial Times*, 16 May 2016; https://next.ft.com/content/826f1bf2-1b75-11e6-b286-cddde55ca122.
10. European Commission, Towards a Fair and Sustainable Asylum System; http://europa.eu/rapid/press-release_IP-16-1620_en.htm.
11. Interview with an official from the Austrian Finance Ministry, Vienna, 23 October 2015.
12. T. Jacoby, *The Atlantic*, 16 October 2014; http://bit.ly/GermanyWorkTraining.
13. On differences between North American and German–north European capitalism generally, see (*14*).
14. P. A. Hall, D. Soskice, *Varieties of Capitalism: The Institutional Foundations of Comparative Advantage* (Oxford Univ. Press, Oxford, 2000).
15. P. L. Martin, *Migrat. Lett.* **13**, 307 (2016).
16. A. Appadurai, *Fear of Small Numbers: An Essay on the Geography of Anger* (Duke Univ. Press, Durham, NC, 2006).
17. M. Brinbaum, *Washington Post*, 17 July 2016; http://bit.ly/AfterAttackonNice.
18. WND (WorldNetDaily), Europe facing "invasion" of refugees who are "fit men," 24 September 2015; http://bit.ly/MuslimRefugeesinEurope.
19. R. Wike, B. Stokes, K. Simmons, Europeans fear wave of refugees will mean more terrorism, fewer jobs (Pew Research Center: Global Attitudes and Trends, Washington, DC, 2016); http://bit.ly/FearofTerrorFewerJobs.
20. J. Barigassi, T. Palmeri, *Politico* (Pavia), 7 June 2016; http://politi.co/2aWo9qP.

Published online 25 August 2016
10.1126/science.aag1556

Downloaded from http://science.sciencemag.org/ on September 2, 2016

Published by AAAS



The names of every person who died in the 2001 attacks, and in the 1993 World Trade Center bombing, are inscribed around the National September 11 Memorial's twin reflecting pools.

FORENSIC SCIENCE

Remembering 9/11

A historian probes the bitter conflicts that accompanied America's most costly forensic investigation

By **Sue Black**

There is no dispute that the terrorist events that unfolded in the United States on 11 September 2001 changed western history forever. Governments debated how they would have responded had it happened on their home soil, aviation authorities reconsidered security, emergency services reassessed practices, and parents hugged their children tighter. Those of us in other countries willed Americans to rise above the senseless brutality and steadfastly defy the insult with patriotism, empathy, unity, and resilience.

What we did not expect was the tawdry infighting, discord, and bitter dispute that would come to surround the identification and memorialization of those who lost their lives that day. This text by Jay Aronson is a nonjudgmental chronicle of the monumental conflict between the many passionate stakeholders—from those seeking to rebuild the commercial heart of the city to the grieving families—all of whom were battling with their own demons while trying to reach a resolution in the absence of a common vision.

The location and format of the memorial structure were among the most contentious issues that emerged in the aftermath of 9/11, and they form the core of this text. Aronson recounts the conflicts between the Lower Manhattan Development Corporation, the designers, the funders, the media, the public, the emergency services, and the family support groups, each of whom seemed to have different ideas about every single aspect of the memorial's concept and its build.

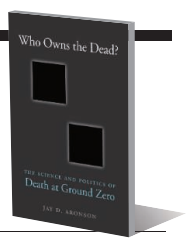
The disputes included where the memorial should be sited, what retail was appropriate, where unidentified remains should be stored, how the names of the deceased should be displayed, how the museum should portray the event, and many, many more. The relationships among these groups were fractious at best and downright hostile at times, culminating in lawsuits in some instances.

The value of this unbiased chronicle is that it allows us to relive the time with the benefit of hindsight and locate moments and flashpoints where an intervention, or a different approach, might have diffused the situation sooner and helped those in great pain and suffering to find a resolution more swiftly. There can be no predetermined course when grief is a critical driving factor. But could the conflict between families and city hall have been avoided or at least managed better?

Aronson shows how a small series of early breakdowns in communication became exaggerated into distrust and activism. The use of dump trucks and the transportation of debris to the unfortunately named Fresh Kills landfill, for example, initiated an understandable animosity between city officials and grieving families. That thousands of remains were found years later in sewers, and on the window ledges and in the ducting of surrounding buildings, left families further questioning the thoroughness of the search process.

The reviewer is at the Leverhulme Research Centre for Forensic Science, University of Dundee, Dundee, Scotland, UK. Email: s.m.black@dundee.ac.uk

Who Owns the Dead? The Science and Politics of Death at Ground Zero
Jay D. Aronson
Harvard University Press, 2016. 326 pp.



The enormity of the logistical issues that arose in the aftermath of 9/11 was enough to overwhelm almost anyone, but strong and compassionate leadership might have done a better job of walking the fine line between pragmatism and respect.

It is extremely challenging to write a text and show no favoritism, but Aronson succeeds incredibly well, encouraging readers to come to their own conclusions. He masterfully chronicles the bitter debate between those who "gave" their lives and those who "lost" their lives, those who lived in Manhattan and those who died in Manhattan, those who lost family members and those who wished to rebuild a city.

That the grief of the day led, for some, to a legacy of continued pain is deeply saddening. "[A]ll we've got is a pile of dirt, a price estimate nearing $1 billion, and a nasty, behind-the-scenes war of wills," read an article in *New York* magazine in 2006, poignantly summarizing the state of the memorial.

Although the core of the text concentrates on ownership of the dead and how they should be memorialized, there is also no doubt that a scientific precedent was set by the Office of the Chief Medical Examiner that day. It vowed to investigate in perpetuity until every piece of the many thousand human remains is identified and repatriated. I fear that most of the rest of us could never afford to commit to such a promise. Thus, for the rest of the world, the legacy of 9/11 may be the challenge of living up to this ambitious expectation.

10.1126/science.aah4476

PHOTO: TIM GRAHAM/ALAMY STOCK PHOTO

Downloaded from http://science.sciencemag.org/ on September 1, 2016

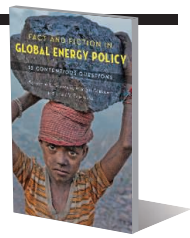
Published by AAAS

ENERGY POLICY

The great debate

Competing perspectives face off in a quest to find common ground on controversial energy issues

By **Gabrielle Wong-Parodi**



Fact and Fiction in Global Energy Policy
15 Contentious Questions
Benjamin K. Sovacool, Marilyn A. Brown, and Scott V. Valentine
Johns Hopkins University Press, 2016. 387 pp.

When I was a young researcher, I naïvely assumed that presenting lay audiences with information about climate change would be enough to change the hearts and minds of science skeptics. My fieldwork interviewing ranchers and coal miners in Wyoming about their perception of technologies designed to mitigate global warming soon disabused me of this. There, I found that more was at stake than simply belief. Not only were people's livelihoods on the line, so too were the way of life they loved and the places that they cherished. I came to appreciate that there are as many "truths" as there are people and began to believe that understanding this in a deeply respectful way is how we can best make progress on the big and seemingly intractable challenges facing our planet.

In *Fact and Fiction in Global Energy Policy*, Sovacool, Brown, and Valentine make clever use of the Hegelian dialectic to take on 15 core energy questions (e.g., "Do conventional energy resources have a meaningful 'peak'?"), showing how each has a mutually exclusive thesis and antithesis. By understanding these differing viewpoints, the idea is that the truth in both can be revealed and perhaps reconciled in a synthesis. The authors take an evidence-based approach when considering differing perspectives, often drawing from primary sources of literature and data sets to build each side's case.

Take, for example, their treatment of the question "Is mitigation or adaptation the best way to address climate change?" Here the authors first present the biologist Garrett Hardin's lifeboat metaphor, originally used to discuss the ethical dilemmas related to overpopulation.

Picture a lifeboat floating in the ocean with 50 people on board and room for only 10 more. There are 100 people swimming in the water who desperately need to get on the boat to survive. Overloading the lifeboat will cause it to sink, spelling doom for all on board.

The authors ask the reader to imagine this metaphor in the context of climate change. Given the limited capacity of our lifeboat, planet Earth, should we help the swimmers in the water through abatement strategies (adaptation measures, such as sea walls) or limit the number of swimmers in the water by reducing the amount of greenhouse gas emissions released to the atmosphere (mitigation measures, such as energy efficiency)?



"[E]nacting a technological transition from one energy technology to another is less about facilitating technological change than about overcoming entrenched interests."

On the one hand, proponents of mitigation argue that "it is better to stop emissions than to deal with their likely effects." For example, advocates often claim that mitigation efforts can be cost-effective and that developed nations should be doing these things anyway. Using the McKinsey & Company cost-abatement curve as an example, the authors present compelling evidence that actions such as energy-efficiency investments in buildings and homes both are profitable and mitigate climate change.

However, proponents of adaptation argue that climate change is already happening and we need to protect people and infrastructure that are already at risk. Furthermore, efforts to mitigate climate change on the national stage have fallen far short of what is needed to avoid the worst climate change. Taking a historical perspective, the authors present evidence that many of the "larger GHG emitters either have backtracked on climate change mitigation commitments or continue to sit on the sidelines."

For each question, the authors then tease out the truths on both sides in an attempt to reach a common ground. In the case of mitigation versus adaptation, they conclude that both are needed and should be cooptimized.

The authors are careful to caution that this analytical exercise is not intended or designed to reveal the "capital-T" Truth but is a way to learn more about how difficult energy problems are conceptualized. A clear "winner" may emerge, but the goal is to have "fewer, better disagreements" (*1*).

I have rarely read a book or policy piece that has so clearly laid out the competing perspectives on contentious energy questions with such sympathy, humility, and rigor. In light of the tremendous energy and environmental challenges facing us today and in the future, this would be an excellent book for classes in environmental policy, political science, and geography. Indeed, this is a must read for researchers and practitioners interested in understanding how to address the most pressing contentious energy questions of our day.

Too much is at stake for us to pretend that other perspectives don't matter. They do, and we ignore them not at our own peril but at the peril of future generations.

The reviewer is at the Department of Engineering and Public Policy, Carnegie Mellon University, Pittsburgh, PA 15213, USA. Email: gwongpar@cmu.edu

REFERENCES
1. B. Fischhoff, *Proc. Natl. Acad. Sci. U.S.A.* **110**, 140333 (2013).

10.1126/science.aah4474

PHOTO: SIPA USA VIA ASSOCIATED PRESS

Downloaded from http://science.sciencemag.org/ on September 1, 2016

Published by AAAS

LETTERS

Edited by **Jennifer Sills**

Coordinate efforts on EU invasive species

AN AMBITIOUS MOVE by the European Union to eradicate, or at least contain, 37 invasive alien species across the region (*1*) may fail if Member States do not coordinate their efforts. Despite calls for the establishment of a coordinating authority (*2*, *3*) and the recognition of the cost-effectiveness of such a body (*4*), the European Parliament had little appetite to fund another centralized regulatory body. It thus elected to establish only a legal framework without a dedicated body or resources to oversee its implementation. As a result, Member States will have to proceed alone or make ad hoc arrangements with their neighbors when implementing the new regulations (*5*). Given that many of the invasive alien species occur in more than one Member State and can easily spread across national borders ("Red squirrels rising," E. Stokstad, News Feature, 10 June, p. 1268), eradication and management plans must be coordinated at a regional scale to ensure that no Member State undermines its neighbors by failing to effectively manage species in its own territory.

The risk of such weak links is high because the burden of invasive alien species is not equally shared across Europe (*6*). Four countries (Belgium, France, Italy, and the United Kingdom) will need to manage as many as half of the species listed by the European Union, whereas none of the listed species occurs in either Cyprus or Malta (*7*). Although the upfront public cost of a coordinating body might be high, it would amount to less than 0.5% of the annual cost of invasive species to the European economy (*8*). In addition to coordinating surveillance, rapid response, and long-term management, a coordinating body would have the resources to support nations that need financial assistance and thus avoid the threat of weak links. Furthermore, without support, Member States may have to redirect conservation efforts away from alien species that are especially problematic at the national scale in order to devote attention to less worrisome species that happen to be of EU concern.

Coordination will also be needed with neighboring countries outside of the European Union because they also host many of the invasive alien species listed as being of EU concern. Adoption of the EU regulation on invasive alien species could be made a condition for accession to the European Union in the case of candidate countries such as Macedonia, Montenegro, and Serbia. Before negotiations begin to bring other nations—such as Russia and Switzerland (and in the future the United Kingdom)—onboard with the new EU regulations, a regionally coordinated management plan with clear goals will have to be established. In the same way that the European Union funds the European Centre for Disease Prevention and Control (*9*), a coordinating body addressing prevention and control of biological invasions will be essential if the region aims to deliver on its ambition to eradicate invasive alien species.



Invasive species, such as the Eastern gray squirrel, pose risks to native species in multiple EU countries.

Philip E. Hulme

The Bio-Protection Research Centre, Lincoln University, 7647 Canterbury, New Zealand. Email: philip.hulme@lincoln.ac.nz

REFERENCES

1. European Commission, Commission Implementing Regulation (EU) 2016/1141 of 13 July 2016 adopting a list of invasive alien species of Union concern pursuant to Regulation (EU) No 1143/2014 of the European Parliament and of the Council (European Commission, Brussels, 2016).
2. P. E. Hulme, P. Pyšek, W. Nentwig, M. Vilà, *Science* **324**, 40 (2009).
3. J. Beninde, M. L. Fischer, A. Hochkirch, A. Zink, *Conserv. Lett.* **8**, 199 (2015).
4. C. Shine *et al.*, "Assessment to support continued development of the EU Strategy to combat invasive alien species" (Institute for European Environmental Policy, Brussels, 2010).
5. European Parliament, "Report on the proposal for a regulation of the European Parliament and of the Council on the prevention and management of the introduction and spread of invasive alien species" (European Parliament, Brussels, 2014).
6. P. Pyšek *et al.*, *Proc. Natl. Acad. Sci. U.S.A.* **107**, 12157 (2010).
7. DAISIE, *Handbook of Alien Species in Europe* (Springer, Dordrecht, 2009).
8. P. E. Hulme, W. Nentwig, P. Pyšek, M. Vilà, *Neobiota* **8**, 3 (2009).
9. European Centre for Disease Prevention and Control (http://ecdc.europa.eu/).

10.1126/science.aah6700

USGS scientists open to change

THE RECENT NEWS Feature "Hurdling obstacles" (E. R. Shell, 8 July, p. 116) provided an insightful summary of Marcia McNutt's career. However, we reject the idea that "USGS [U.S. Geological Survey] scientists… were known for their resistance to change." As interviews with USGS scientists throughout the article demonstrate, scientists in Menlo Park applauded (literally) the changes Director McNutt brought to the USGS when she announced them. The scientists at the USGS continue to do yeoman's work with near level (and due to inflation, effectively declining) budgets. Moreover, their programs are vulnerable to further cuts due to increasing costs of space at the Menlo Park campus. USGS researchers in Menlo Park continue to be world leaders across a broad spectrum of disciplines in the Earth sciences.

Gregory C. Beroza,[1]* William L. Ellsworth,[1] Marcia K. McNutt[2]

[1]Department of Geophysics, Stanford University, Stanford, CA 94305–2215, USA. [2]National Academy of Sciences, Washington, DC 20418, USA.

*Corresponding author. Email: beroza@stanford.edu

10.1126/science.aah5743

PHOTO: DOPEYDEN/ISTOCKPHOTO.COM

Downloaded from http://science.sciencemag.org/ on September 1, 2016

Published by AAAS

Rescued wildlife in China remains at risk

THE THEME OF the United Nations' World Environment Day this year—Go Wild for Life—focuses on efforts to counter illegal wildlife trade, especially through law enforcement. However, the treatment of "rescued" animals is also crucial. Animal suffering, or premature death after rescue, undermines animal welfare goals.

In China, Convention on International Trade in Endangered Species of Wild Fauna and Flora (CITES) guidelines (*1*) on the appropriate treatment of live rescued animals are not well known by government authorities, and the euthanasia of rescued wildlife is not permitted (*2*). Consequently, indigenous and exotic animals are either held in captivity indefinitely at animal rescue centers or released to the wild after discretionary quarantine and rehabilitation (*3*), the standards of which vary substantially.

In Yunnan Province alone, about 18,000 wild animals are seized annually (*4*). Accessing rare Chinese records detailing the rescues of live animals from 2010 to 2015 (*5*), we estimated that fewer than 30% of 12,473 native reptiles (14 species) were released to the wild (*6*). The rest went to poor, crowded sanctuaries and even into the pet or food trade (*7*). Of these native species, 2000 individuals likely originated from neighboring countries, based on the locations of their rescue (*5*). Of 155 native birds (20 species) all were released, but 886 exotic birds (10 species) were kept in sanctuaries until they died. Of 156 native mammals (primarily primates, Asiatic bears, and pangolins) almost all remain in captivity, often in appalling enclosures (*5*, *8*). Even charismatic exotic species tend not to be repatriated; none of five Asiatic elephants rescued in 2005 have been returned to Myanmar. Standards of animal housing and veterinary care are unregulated in China, and discretionary releases often involve unfamiliar release sites without follow-up on survival.

China urgently needs welfare legislation to protect rescued wildlife. Rescued animals should be released responsibly, and standards of care and record-keeping should be improved.

Zhao-Min Zhou,[1]* Chris Newman,[2] Christina D. Buesching,[2] David W. Macdonald,[2] Youbing Zhou[2,3]

[1]Key Laboratory of Southwest China Wildlife Resources Conservation (Ministry of Education), China West Normal University, Nanchong 637002, China. [2]Wildlife Conservation Research Unit, The Recanati-Kaplan Centre, Department of Zoology, University of OxfordOX13 5QL, Oxford, UK. [3]State Key Laboratory of Vegetation and Environmental Change, Institute of Botany, Chinese Academy of Sciences, Beijing 100093, China.

*Corresponding author. Email: zhouzm81@gmail.com

REFERENCES AND NOTES

1. CITES 1997, Resolution Conf. 10.7 (Rev. CoP15): Disposal of confiscated live specimens of species included in the Appendices (https://cites.org/eng/res/10/10-07R15.php).
2. State Forestry Administration, People's Republic of China, 2014, Regulation on rescue and asylum of terrestrial wildlife (www.jsforestry.gov.cn/art/2015/5/5/art_31_80890.html) [in Chinese].
3. Z.-M. Zhou *et al.*, *Front. Ecol. Environ.* **12**, 97 (2014).
4. J. Y. Song, *Spring City Evenings* (4 March 2015); http://ccwb.yunnan.cn/images/2015-03/04/A14/20150304A14_pdf.PDF [in Chinese].
5. Data from the Forensic Department of Yunnan Public Security Bureau for Forests has been reproduced in English at http://dx.doi.org/10.5061/dryad.875kh.
6. H. L. Wu, L. Yang, *Xinhuanet* (2013); http://news.xinhua.net.com/2013-04/11/c_115357947.htm [in Chinese].
7. Z. H. Dai, *Spring City Evenings* (16 December 2014); http://ccwb.yunnan.cn/html/2014-12/16/content_910746.htm?div=-1 [in Chinese]
8. A. F. Carpenter, W. Song, Crit. Asian Stud. 48, 380 (2016).

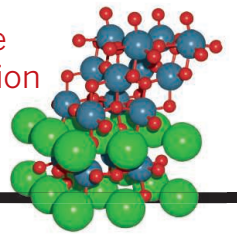
10.1126/science.aah4291

Downloaded from http://science.sciencemag.org/ on September 1, 2016

RESEARCH

Electrocatalysts for the oxygen evolution reaction

Seitz et al., *p. 1011*



IN *SCIENCE* JOURNALS

Edited by **Caroline Ash**



Dogs' brains integrate praise words with their owners' intonation.

SPEECH PROCESSING

Language representation in the dog brain

Dogs have been domesticated for many thousands of years. Humans and dogs have thus had plenty of time to develop close communication bonds for work and play. Using brain-scanning techniques, Andics *et al.* investigated how dogs process human speech. The left brain hemisphere in dogs responds more strongly to praise words, and a right auditory brain region distinguishes intonation. Reward regions only light up if both the word and the intonation are consistent with praise. Hence, the subtlety of dog-human communication has become hardwired in the absence of language. —PRS

Science, this issue p. 1030

DENGUE VACCINE

Discerning dengue vaccine protection

Clinical trials of the Sanofi-Pasteur dengue vaccine have not been an unmixed success because of complex immune interactions between dengue subtypes. Ferguson *et al.* analyzed data from the published phase III clinical trials to work out how best to deploy the vaccine and minimize the risk of enhancing disease. Vaccination has the same immunological effect as a silent natural infection: It boosts protection in people who are seropositive but puts naïve individuals at risk of the potentially severe effects of subsequent natural infection. Thus, routine vaccination success critically depends on the proportion of the target group that has experienced prior dengue infections. —CA

Science, this issue p. 1033

NEURODEVELOPMENT

Signposts for synapses

Brain development entails not only positioning the neurons in the right place but also building the correct connections for functional circuits. In the early postnatal mouse brain, Oh *et al.* discovered how the exact locations for synapse development are specified. The neurotransmitter GABA (γ-aminobutyric acid) induces the formation of dendritic spines, accumulation of anchoring sites, and subsequent recruitment of GABA receptors. Thus, the release of GABA, usually known as an inhibitory neurotransmitter in the adult brain, serves in the developing brain to determine just where synapses are built. —PJH

Science, this issue p. 1037

ION CHANNELS

Snapshots of a potassium channel

Potassium channels help maintain the appropriate charge difference between the inside and the outside of a cell. The channel's selectivity for potassium is imparted by a pore so narrow that potassium ions must pass in single file. How potassium ions move through this pore is much debated. Kratochvil *et al.* obtained instantaneous snapshots of ions in the pore by using ultrafast two-dimensional infrared spectroscopy. It appears that, like beads on a string, potassium ions and water molecules occupy alternating binding sites in the channel. —VV

Science, this issue p. 1040

HIV-1 ANTIBODIES

How antibodies protect against HIV-1

A protective vaccine is a major goal in HIV-1 prevention. Such a vaccine needs to elicit neutralizing antibodies to block infection. To understand mechanisms of protection by neutralizing antibodies, Liu *et al.* first treated rhesus macaques with an antibody known to block infection, then infected them with a monkey-adapted HIV-1. Subsequently, viral DNA and RNA were found in the macaques' gut and lymph nodes a few days after genital tract infection. This suggests that

PHOTO: TIERFOTOAGENTUR/ALAMY STOCK PHOTO

Published by AAAS

antibodies may block the virus in multiple sites throughout the body, rather than just at the site of entry. —KLM

Science, this issue p. 1045

IMMUNOLOGY

Divergent responses, same receptor

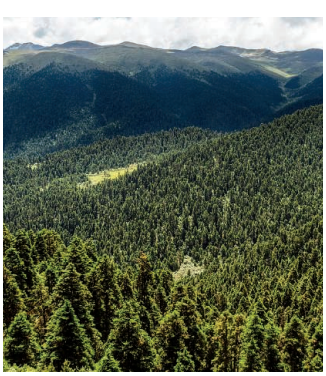
Macrophages detect infection or tissue injury with pattern recognition receptors, including the Toll-like receptors (TLRs). Piccinini *et al*. investigated how macrophages react to the bacterial product lipopolysaccharide (LPS) and the extracellular matrix component tenascin-C, both of which stimulate TLR4. Although both stimuli activated some common signaling pathways, LPS stimulation predisposed macrophages to destroy the extracellular matrix, whereas tenascin-C stimulation induced macrophages to synthesize matrix components. Thus, diverse stimuli can trigger the appropriate inflammatory or tissue-repair response, even though they activate the same receptor. —JFF

Sci. Signal. **9**, ra86 (2016).

GLOBAL CHANGE BIOLOGY

Trees surge on the Tibetan Plateau

So many factors affect tree growth that it is almost impossible to develop a concise idea of how forests will respond to global change. Accelerating tree growth on the Tibetan Plateau provides an opportunity to explore the issue. Silva *et al*. analyzed stable isotopes of carbon, oxygen, and nitrogen in the rings of trees from Tibet to understand why there has been a recent surge in growth during the past ~250 years. Elevated CO_2, changes in water use efficiency, and permafrost thawing may explain the enhanced growth. —SN



Tibet's trees are experiencing a growth spurt.

PHOTOS (FROM LEFT): CHEN PELLED/ALAMY STOCK PHOTO; ANDREY NEKRASOV/ALAMY STOCK PHOTO

Sci. Adv. 10.1126.sciadv.1501302 (2016).

TEXTILES

Keeping cool without losing your shirt

People use clothing to retain warmth in cold weather. But what about clothing to keep us cool when it is hot? The challenge is to find a material that lets radiation from the human body pass through but that is opaque to visible light. Hsu *et al.* have created a nanoporous polyethylene textile that has both of these characteristics (see the Perspective by Boriskina). The key feature of the material is the pore size, which can be tuned to absorb visible light while being almost invisible to mid-infrared radiation. The material is water-wicking and strong and keeps skin much cooler than cotton. —BG

Science, this issue p. 1019; see also p. 986

ORGANIC CHEMISTRY

Copper-catalyzed radical relay

Breaking C-H bonds can produce highly reactive carbon radicals that enzymes can use to form new bonds to such carbon centers. Zhang *et al.* show that when the radicals escape the environs of their formation, a copper catalyst can also finely direct their reactivity. Chiral ligands on copper guide the asymmetric addition of a CN group to form a nitrile product with high enantioselectivity that can be used for pharmaceutical intermediates. —JSY

Science, this issue p. 1014

IN OTHER JOURNALS

Edited by **Kristen Mueller** *and* **Jesse Smith**



Comb jellies have through-guts.

GUT EVOLUTION

Just passing through

Our understanding of how guts evolved has included a long-held misconception. Despite reports dating back to the 1800s of a gut with more than one opening in metazoans (jellies and comb jellies), textbooks often present this group as having a sac-like gut with only one opening. Presnell *et al.* housed two species of comb jellies under laboratory conditions and captured high-resolution images of their feeding and excretion. Their detailed imaging revealed that comb jellies do not excrete through the mouth but rather through multiple anal pores, confirming that they do indeed possess a through-gut. These results suggest that our understanding of gut evolution may require a rethink. —SNV

Curr. Biol. 10.1016/j.cub.2016.08.019 (2016).

CELESTIAL MECHANICS

The closest quasi-satellite to Earth

A quasi-satellite orbits close to a planet, circling the Sun with the same orbital period, but it is not gravitationally bound to the planet. The fifth known quasi-satellite of Earth was discovered earlier this year: an asteroid with the snappy name (469219) 2016 HO_3. In a recent study, de la Fuente Marcos and de la Fuente Marcos investigated its orbit with numerical simulations, showing that it will remain an Earth quasi-satellite for a few centuries. The asteroid, which is a few dozen meters across, stays between 38 and 100 times as far away from Earth as the Moon. This proximity and its low relative velocity make the object a tempting target for a visit by a sample-return mission—or even by astronauts. —KTS

Mon. Not. R. Astron. Soc. 10.1093/mnras/stw1972 (2016).

Published by AAAS

ALSO IN *SCIENCE* JOURNALS

Edited by **Caroline Ash**

PLANETARY SCIENCE

Dawn explores the dwarf planet Ceres

In March 2015, the Dawn spacecraft arrived in orbit around Ceres, a dwarf planet and the largest object in the asteroid belt. Over the following months, the Dawn team extensively mapped the surface of Ceres and investigated its properties. Russell *et al*. give an overview of Ceres' global properties and the discovery of a plasma bow shock, which they interpret as due to a transient atmosphere. Hiesinger *et al.* investigated the surface craters, whose morphology and distribution allow the surface to be dated and indicate that the crust is made from a mixture of rock and ice. Buczkowski *et al*. describe the geological features and topology of the surface, such as domes and linear structures, which suggest cryomagmatism and subsurface ice. Ruesch *et al.* present a detailed study of the mountain Ahuna Mons, concluding that it is a cryovolcano formed by the eruption of a viscous mixture of salt and ice. Ammannito *et al.* mapped the mineral composition of the surface, which is dominated by clay-like phyllosilicates. Combe *et al.* report exposed water ice in Oxo crater, which must have been brought to the surface relatively recently. Together, these papers indicate a complex world of rock and ice, very different from previously investigated asteroids, and will underpin the analysis of Dawn data for years to come. —KTS

Science, this issue pp. 1008, 1003, 1004, 1005, 1006, and 1007

CLIMATE CHANGE

Warm Arctic–cold continents?

In recent decades, temperatures in the Arctic have risen rapidly, causing widespread losses in sea ice. In a Perspective, Shepherd considers whether these rising Arctic temperatures could also play a role in unusually cold winters in northern mid-latitudes. Some scientists have argued that a trend toward a warm Arctic and cold mid-latitudes can be explained by natural climate variability; others contend that it is caused by climate change. Shepherd concludes that this either/or dichotomy is too simplistic: Rather, natural variability and climate change are likely to act together to affect weather patterns in the Arctic and beyond. —JFU

Science, this issue p. 989

WATER SPLITTING

Strontium's loss is iridium's gain

Neither plants nor people split water with the goal of making oxygen. It is simply a by-product of liberating the H in H_2O for downstream use. Nonetheless, the slow kinetics of the so-called oxygen evolution reaction (OER) pose a challenge to improving the efficiency of water-derived hydrogen production. Seitz *et al.* have enhanced iridium oxide catalysts using the strontium-bearing precursor $SrIrO_3$ in acid conditions. Initially, strontium leaches out of the surface layers, leaving behind a highly active, stable OER catalyst. —JSY

Science, this issue p. 1011

PLANT SCIENCE

Hormone clearance and morphogenesis in plants

Cytokinins are a class of plant hormones that help regulate plant morphogenesis. Züercher *et al.* show how cytokinin signaling in plant cells can be regulated. Purine permease 14 (PUP14) is a transporter located in the cell membrane that vacuums up cytokinin from the continuum of the plant's cell walls (the apoplast). PUP14 delivers cytokinin to the intracellular space, where it is degraded. When cytokinin is removed from the apoplast, the cytokinin sensor on the plasma membrane finds no signal. Regulation of this signaling sink fine-tunes morphogenesis. —PJH

Science, this issue p. 1027

CARDIAC ARRHYTHMIA

Genetic underpinnings of atrial fibrillation

The fluttery heartbeat of atrial fibrillation puts people in danger of stroke and heart disease. Genomic studies have identified gene variants that increase the risk for this abnormality. Nadadur *et al*. show how these genes influence the beat of the heart's atrium. In a mouse model of atrial fibrillation, which lacks the gene *Tbx5*, the authors describe a multitiered transcriptional network that links seven of these atrial fibrillation risk loci. Organized as an incoherent feed-forward loop, the network tightly controls expression of atrial rhythm genes, and its perturbation by the risk loci causes susceptibility to atrial fibrillation. —KLK

Sci. Transl. Med. **8**, 354ra115 (2016).

ASYMMETRIC CATALYSIS

Targeting just one of two C-H bonds

Direct replacement of C-H bonds with C-C bonds is an especially efficient way to make complex molecules. Palladium catalysts are effective at asymmetric variants of this reaction and are valuable in pharmaceutical development. However, selecting one of two C-H bonds on the same carbon center is particularly challenging. Chen *et al.* have developed a set of two-coordinate chiral ligands that confer high selectivity in that particular scenario. Palladium complexes of these ligands append a variety of aryl rings to CH_2 groups in amides and several carboxylic acids. —JSY

Science, this issue p. 1023

Published by AAAS

RESEARCH ARTICLE SUMMARY

PLANETARY SCIENCE

Cratering on Ceres: Implications for its crust and evolution

H. Hiesinger,* S. Marchi, N. Schmedemann, P. Schenk, J. H. Pasckert, A. Neesemann, D. P. O'Brien, T. Kneissl, A. I. Ermakov, R. R. Fu, M. T. Bland, A. Nathues, T. Platz, D. A. Williams, R. Jaumann, J. C. Castillo-Rogez, O. Ruesch, B. Schmidt, R. S. Park, F. Preusker, D. L. Buczkowski, C. T. Russell, C. A. Raymond

INTRODUCTION: Thermochemical models have predicted that the dwarf planet Ceres has, to some extent, formed a mantle. Moreover, due to viscous relaxation, these models indicate that Ceres should have an icy crust with few or no impact craters. However, the Dawn spacecraft has shown that Ceres has elevation excursions of ~15 km, cliffs, graben, steep-sided mountains, and a heavily cratered surface.

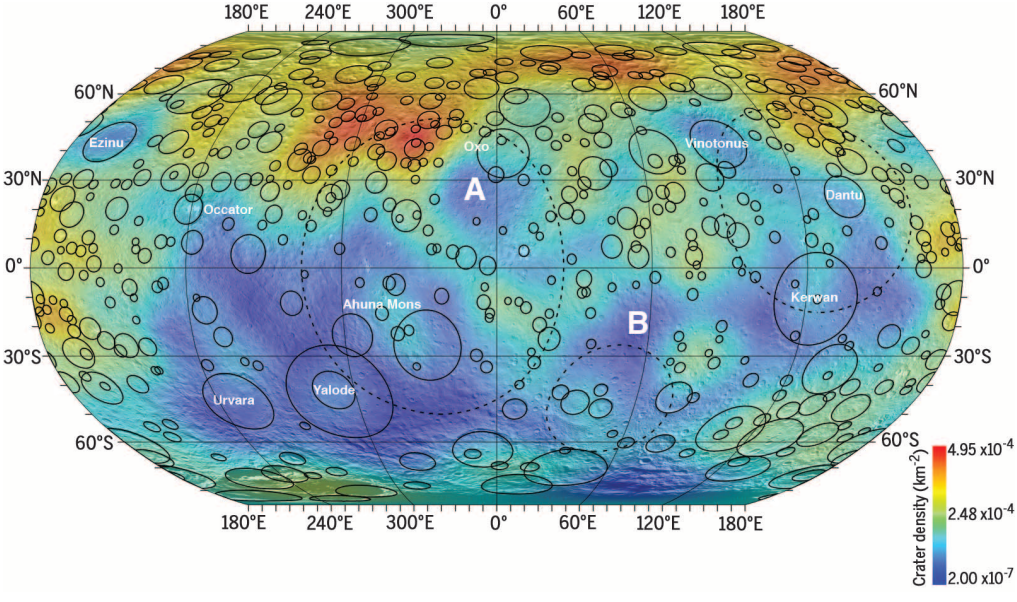
RATIONALE: We used Dawn's Framing Camera to study the morphology, size frequency, and spatial distribution of the craters on Ceres. These data allow us to infer the structure and evolution of Ceres' outer shell.

RESULTS: A large variety of crater morphologies are present on Ceres, including bowl-shaped craters, polygonal craters, floor-fractured craters, terraces, central peaks, smooth floors, flowlike features, bright spots, secondary craters, and crater chains. The morphology of some impact craters is consistent with water ice in the subsurface. Although this might have favored relaxation, there are also large unrelaxed craters. The transition from bowl-shaped simple craters to modified complex craters occurs at diameters of about 7.5 to 12 km. Craters larger than 300 km are absent, but low-pass filtering of the digital elevation model suggests the existence of two quasi-circular depressions with diameters of ~570 km (125.56°E and 19.60°N) and ~830 km (24.76°W and 0.5°N). Craters are heterogeneously distributed across Ceres' surface, with more craters in the northern versus the southern hemisphere. The lowest crater densities are associated with large, well-preserved southern hemisphere impact craters such as Urvara and Yalode. Because the low crater density (LCD) terrain extends across a large latitude range in some cases (e.g., Urvara and Yalode: ~18°N and 75°S; Kerwan: ~30°N and 46°S), its spatial distribution is inconsistent with simple relaxation driven by warmer equatorial temperatures. We instead propose that impact-driven resurfacing is the more likely LCD formation process, although we cannot completely rule out an internal (endogenic) origin. We applied two different methodologies to derive absolute model ages from observed crater size-frequency distributions. The lunar-derived model adapts the lunar production and chronology functions to impact conditions on Ceres, taking into account impact velocities, projectile densities, current collision probabilities, and surface gravity. The asteroid-derived model derives a production function by scaling the directly observed object size-frequency distribution from the main asteroid belt (extended to sizes <5 km by a collisional model) to the resulting size-frequency distribution of cerean craters, using similar cerean target parameters as the lunar-derived model. By dating a smooth region associated with the Kerwan crater, we determined absolute model ages of 550 million and 720 million years, depending on which chronology model is applied.

CONCLUSION: Crater morphology and the simple-to-complex crater transition indicate that Ceres' outer shell is likely neither pure ice nor pure rock but an ice-rock mixture that allows for limited relaxation. The heterogeneous crater distribution across the surface indicates crustal heterogeneities and a complex geologic evolution of Ceres. There is evidence for at least some geologic activity occurring in Ceres' recent history. ■

ON OUR WEBSITE

Read the full article at http://dx.doi.org/10.1126/science.aaf4759



Spatial density of craters larger than 20 km on Ceres. Crater rims are shown as black solid circles. Blue indicates areas with LCDs; yellow and red represent more highly cratered areas. The smallest dashed ellipse denotes the idealized former rim of an extremely degraded impact crater at 48.9°E and 44.9°S, which is barely recognizable in imagery but apparent from the global digital elevation model. Also shown as dashed circles are the outlines of two large putative basins. Unambiguously recognized basins >300 km in diameter are missing, and there are several areas with LCDs associated with large impact craters (e.g., Yalode, Urvara, Kerwan, Ezinu, Vinotonus, Dantu, and two unnamed craters northeast and southeast of Oxo). Areas A and B are topographic rises with central depressions that also show LCDs.

The list of author affiliations is available in the full article online.
*Corresponding author. Email: hiesinger@uni-muenster.de
Cite this article as H. Hiesinger *et al.*, *Science* 353, aaf4759 (2016). DOI: 10.1126/science.aaf4759

Downloaded from http://science.sciencemag.org/ on September 1, 2016

RESEARCH ARTICLE

PLANETARY SCIENCE

Cratering on Ceres: Implications for its crust and evolution

H. Hiesinger,[1]* S. Marchi,[2] N. Schmedemann,[3] P. Schenk,[4] J. H. Pasckert,[1] A. Neesemann,[3] D. P. O'Brien,[5] T. Kneissl,[3] A. I. Ermakov,[6] R. R. Fu,[6] M. T. Bland,[7] A. Nathues,[8] T. Platz,[8] D. A. Williams,[9] R. Jaumann,[10,3] J. C. Castillo-Rogez,[11] O. Ruesch,[12] B. Schmidt,[13] R. S. Park,[11] F. Preusker,[10] D. L. Buczkowski,[14] C. T. Russell,[15] C. A. Raymond[11]

Thermochemical models have predicted that Ceres, is to some extent, differentiated and should have an icy crust with few or no impact craters. We present observations by the Dawn spacecraft that reveal a heavily cratered surface, a heterogeneous crater distribution, and an apparent absence of large craters. The morphology of some impact craters is consistent with ice in the subsurface, which might have favored relaxation, yet large unrelaxed craters are also present. Numerous craters exhibit polygonal shapes, terraces, flowlike features, slumping, smooth deposits, and bright spots. Crater morphology and simple-to-complex crater transition diameters indicate that the crust of Ceres is neither purely icy nor rocky. By dating a smooth region associated with the Kerwan crater, we determined absolute model ages (AMAs) of 550 million and 720 million years, depending on the applied chronology model.

Ceres is the largest (~940-km diameter) and most massive object in the asteroid belt and, as a protoplanet, possibly holds clues to our understanding of the early solar system history (*1*). Pre-Dawn mission studies, mostly based on data acquired by Earth-based telescopes and the Hubble Space Telescope, have revealed several notable results. For example, some pre-Dawn geophysical models have predicted that Ceres is a differentiated body with a silicate-rich core and a water-rich shell (*2*–*5*), resulting in a hydrostatic shape and relatively rapid viscous relaxation (i.e., removal) of topographic features, including impact craters (*4*). In addition, early spectral data of Ceres were interpreted as evidence for water in clay minerals, brucite, carbonates, iron-rich serpentine, and ammoniated phyllosilicates (*6*–*10*). Volatile-rich CI and CM chondrites are probably the best meteoritic analog materials for Ceres (*11*, *12*). Dawn is the first spacecraft to visit Ceres and closely observe its surface from an orbit as low as 850 km in radius (*5*). Although Dawn carries several instruments, including a Visible and Infrared Spectrometer (VIR) (*13*) and a Gamma Ray and Neutron Detector (GRaND) (*14*), in this study we mostly rely on images of the Framing Camera (FC) (*15*), which observes the cerean surface in one broadband clear filter (400 to 1100 nm) and seven narrowband color filters (438, 555, 653, 749, 829, 917, and 965 nm).

[1]Institut für Planetologie, Westfälische Wilhelms-Universität, Münster, Germany. [2]Southwest Research Institute, Boulder, CO 80302, USA. [3]Institute of Geological Sciences, Freie Universität Berlin, Berlin, Germany. [4]Lunar and Planetary Institute, Houston, TX 77058, USA. [5]Planetary Science Institute, Tucson, AZ 85719, USA. [6]Massachusetts Institute of Technology, Cambridge, MA 02139, USA. [7]U.S. Geological Survey, Astrogeology Science Center, Flagstaff, AZ 86001, USA. [8]Max-Planck Institute for Solar System Research, Göttingen, Germany. [9]Arizona State University, Tempe, AZ 85281, USA. [10]German Aerospace Center (DLR), Berlin, Germany. [11]Jet Propulsion Laboratory, California Institute of Technology, Pasadena, CA 91109, USA. [12]NASA Goddard Space Flight Center, Greenbelt, MD 20771, USA. [13]Georgia Institute of Technology, Atlanta, GA 30332, USA. [14]John Hopkins Applied Physics Laboratory, Laurel, MD 20723, USA. [15]Department of Earth and Space Sciences, University of California, Los Angeles, CA 90095, USA.
*Corresponding author. Email: hiesinger@uni-muenster.de

Crater morphology

We studied FC (*15*) images with a spatial resolution of up to 137 m per pixel that reveal a rich inventory of morphologic features, such as cliffs, graben, steep-sided mountains, and craters. In fact, FC images show a large number and variety of crater morphologies, including bowl-shaped craters, polygonal craters, floor-fractured craters, crater terraces, central peaks, smooth crater floors, craters with flowlike features, and secondary craters and crater chains (Fig. 1). The morphologies of <30- to 40-km-diameter craters on Ceres are indistinguishable from craters on mid-sized icy moons of Saturn (e.g., Dione and Tethys) (*16*). At Ceres, floor-filling smooth material is commonly observed in craters >40 km but has not been reported from mid-sized icy moons (*16*). The smooth deposits occur at various elevations, embay other crater material, and might represent mixed mobilized impact melt or debris, impact-triggered volcanism, or postimpact melting. At some crater walls, we observe flowlike deposits with steep lobe fronts and sides, as well as striations in downslope direction that we interpret as evidence for mobilization of crustal material in the presence of ice (*17*). Craters larger than 40 km exhibit additional morphologies not observed at smaller craters—for instance, central pits, possible pit floors, and floor fractures. Central pits similar to pits on Ganymede and Callisto occur preferentially in craters >75 km. These crater morphologies are described in more detail in a companion paper by Buczkowski *et al.* (*17*). On the basis of their morphological characteristics, we propose that craters on Ceres were formed in a relatively weak target (i.e., much weaker than intact or partially fractured crystalline rock) when compared with Vesta or the Moon, consistent with the presence of ice (*2*–*4*, *18*).

Several pre-Dawn thermochemical models have predicted that Ceres is, to some extent, a differentiated body that potentially has a silicate-rich core and a water-rich shell (*2*–*5*, *18*–*20*). The more differentiated structure models would allow for a hydrostatic shape and relatively rapid viscous relaxation of craters (*4*). The predicted paucity of craters resulted from the assumption of a 10- to 100-km-thick surface-ice layer and relatively high surface temperatures, which allow for rapid viscous relaxation. Image-based digital elevation models (DEMs) (*21*–*23*) help determine the degree of differentiation by revealing elevation differences of ~15 km, indicating that Ceres' shell may contain less ice than predicted by the more differentiated models. If Ceres contains an ice-dominated layer, it was predicted that even small craters would relax within 10 million to 100 million years (My) (assuming relatively warm temperatures of 180 K) and that pristine craters could survive only near the poles (*4*). This is not consistent with Dawn observations.

Improved temperature models (*24*) suggest lower equatorial temperatures of 155 K, and <110 K at latitudes higher than ~80°, slowing viscous relaxation and increasing the survival time of craters. An undifferentiated rocklike model, in which water is entirely bound to minerals in the form of hydrated salts and silicates (*25*), predicts that relaxation of craters is not expected (*4*). However, Castillo-Rogez (*19*) argued that the undifferentiated model is not realistic from a thermal evolution standpoint, and it is also inconsistent with Dawn observations of moderately relaxed craters. We find that, unlike in (*4*), viscous relaxation is relevant only at scales of several hundreds of kilometers. Among Ceres' few features of that size is the Kerwan impact crater (284 km), which appears partially relaxed because of the absence of a central peak, the subdued rim, the gently-sloped smooth floor, and the lower crater density compared with the surrounding terrain. Although we cannot completely exclude geologic processes—such as degradation from subsequent impact cratering or cryovolcanism—that might have operated locally or regionally in the Kerwan area, we favor viscous relaxation as the most likely origin of this crater's unusual morphology. This is because of Kerwan's position close to the warm equator, its size and morphology, as well as results of viscoelastic finite element models of Bland *et al.* (*26*). In addition, Kerwan is located in an area with a low crater density (LCD), making degradation by subsequent impact craters less likely. Similarly, we did not find unambiguous

Downloaded from http://science.sciencemag.org/ on September 1, 2016

evidence for cryovolcanic resurfacing of Kerwan. In contrast to Kerwan, Dawn DEMs indicate that the majority of Ceres' craters are deep. For example, Vinotonus (140 km, 94.8°E and 43.1°N), Ezinu (120 km, 195.4°E and 43.2°N), Urvara (170 km, 248.6°E and 46.3°S), Yalode (267 km, 292.5°E and 42.3°S), and several other large craters have depths of >4 km. They are deeper than similar-sized fresh lunar craters (*27*) and modestly shallower than fresh craters on Tethys (*16*). Further, Ceres' craters are much deeper than the completely flattened craters predicted by Bland (*4*) in this size range for a pure ice layer. Thus, Dawn's observations of preserved and relaxed craters, along with Ceres' shape (*5*), are inconsistent with a pure rocky outer shell. Clearly, viscous relaxation has played a limited but important role in subduing some craters. The lack of observed relaxation for craters smaller than Kerwan indicates that any outer shell has a rheology much stronger than that of pure water ice (*4*). Thus, Ceres' outer shell is probably neither pure ice nor pure rock but an ice-rock mixture that allows for limited relaxation at the longest wavelengths. In addition, differences in relaxation across the surface possibly indicate spatial variations in the ice content of the outer layer on Ceres.

Crater morphometry

A second test of the proposed thermochemical models is the transition diameter from simple (bowl-shaped) to complex (e.g., central peaks, terraces, rings) crater morphology. Provided that Ceres is a predominantly icy body with a gravity of 0.28 m/s^2 (*5*), it has been predicted that the transition would occur at a diameter of ~16 km; it would occur at ~50 km for a rocky body (*4*). In particular, Bland (*4*) suggested that a transition diameter of 10 to 20 km would be consistent with a thick icy layer, whereas a diameter of more than 20 km would support the undifferentiated model of Zolotov (*25*). To determine the simple-to-complex transition diameter, we selected ~160 well-preserved craters on the basis of their crisp morphology and the absence of obvious post-impact erosion or modification. Two criteria were used: (i) inflection in the depth-diameter curve

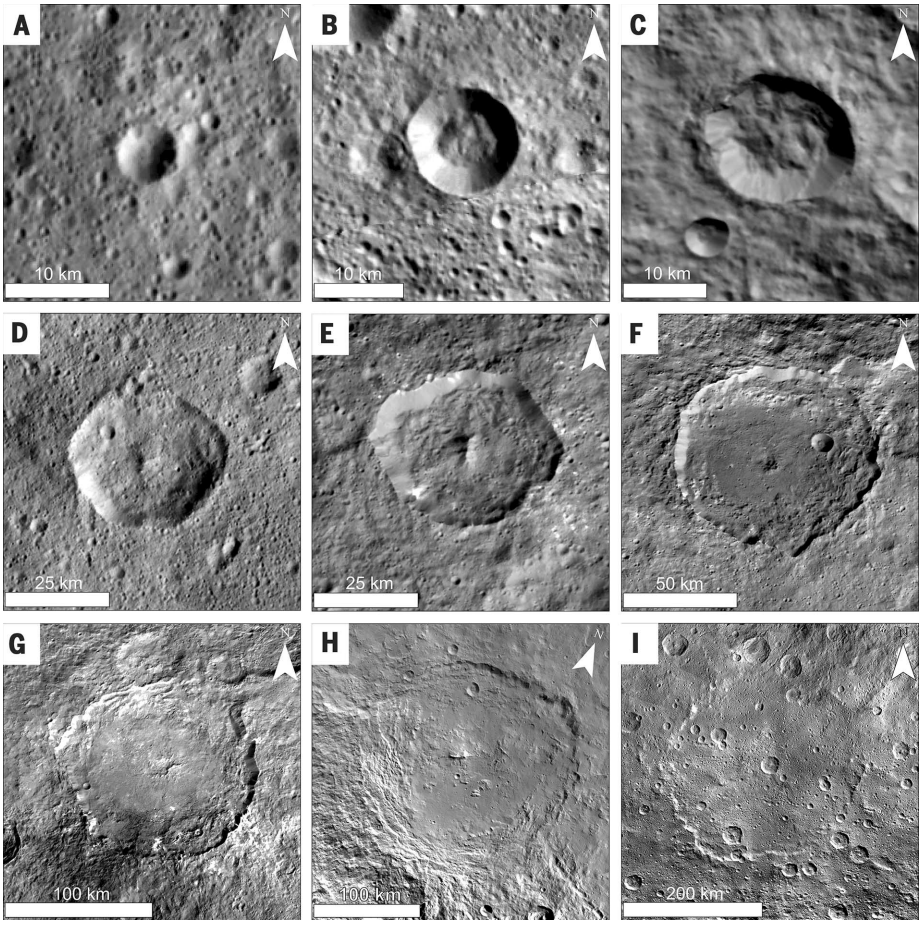


Fig. 1. Morphologies of impact craters on Ceres. (**A**) Unnamed 6-km simple bowl-shaped crater (105°E and 3°N). (**B**) Unnamed 12.5-km modified simple crater (161.7°E and 13°S) with mass-wasting deposits on the floor. (**C**) Unnamed 16- to 18.8-km complex crater (279°E and 23°S) with possible terraces and evidence for mass wasting on the floor and walls. Mass-wasting deposits form ridges on the crater floor. (**D**) Unnamed 34- to 37-km complex crater with central peak (108°E and 10°N). (**E**) Achita, a 41-km polygonal complex crater (65.8°E and 25.8°N) with mass-wasting ridges on the floor. (**F**) Gaue crater (84 km, 85.9°E and 30.9°N) showing multiple terraces, a central pit, a smooth and flat floor, and a small peak close to the central pit. (**G**) Dantu crater (125 km, 137.8°E and 24.4°N), with concentric terraces, a possible peak ring structure or central pit, a smooth and flat floor, and considerable albedo variations at the southwestern rim. (**H**) Urvara crater (170 km, 248.6°E and 46.3°S), with concentric terraces, a small elongated central peak, a smooth and flat floor, and a relaxed morphology. (**I**) Kerwan crater (284 km, 123.6°E and 10.9°S) shows a partially relaxed morphology and does not have a central peak but instead a central depression. This crater's rim is subdued, and the floor is gently sloped and almost completely covered by smooth material with a lower crater density than the surrounding terrain. Arrowheads point north.

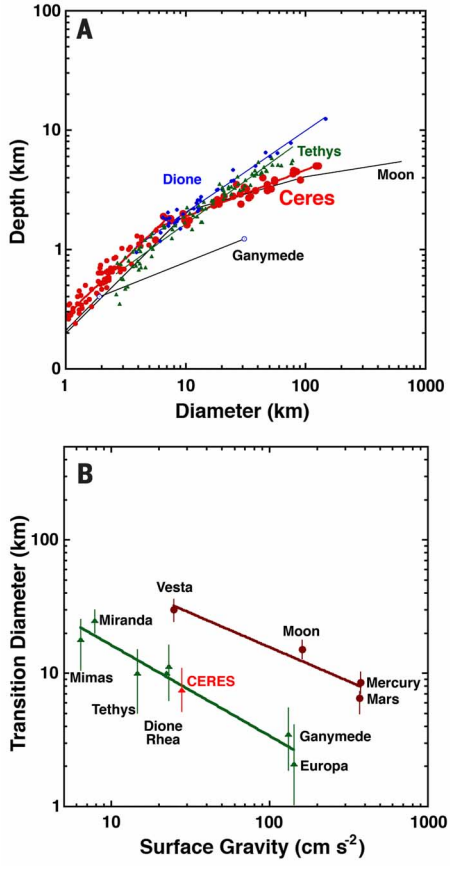


Fig. 2. Simple-to-complex transition diameters of impact craters on Ceres and selected icy moons and rocky bodies. (**A**) Simple-to-complex crater transitions (i.e., those with more than 50% modified floors) on Ceres (small red circles represent simple craters; large red circles represent complex craters) occur at diameters of 7.5 to 12 km. The depth/diameter ratios of the dry Moon (black line) and those of the icy bodies Dione (blue circles), Tethys (green triangles), and Ganymede (blue open circles) are shown for comparison. (**B**) The transition diameters to complex craters scale inversely with surface gravity of the respective body. Taking into account its surface gravity, the depth/diameter ratio of Ceres (red triangle) follows the same trend as other icy bodies (green triangles). The transition diameters to complex craters of rocky bodies (brown circles) are shown for comparison.

Downloaded from http://science.sciencemag.org/ on September 1, 2016

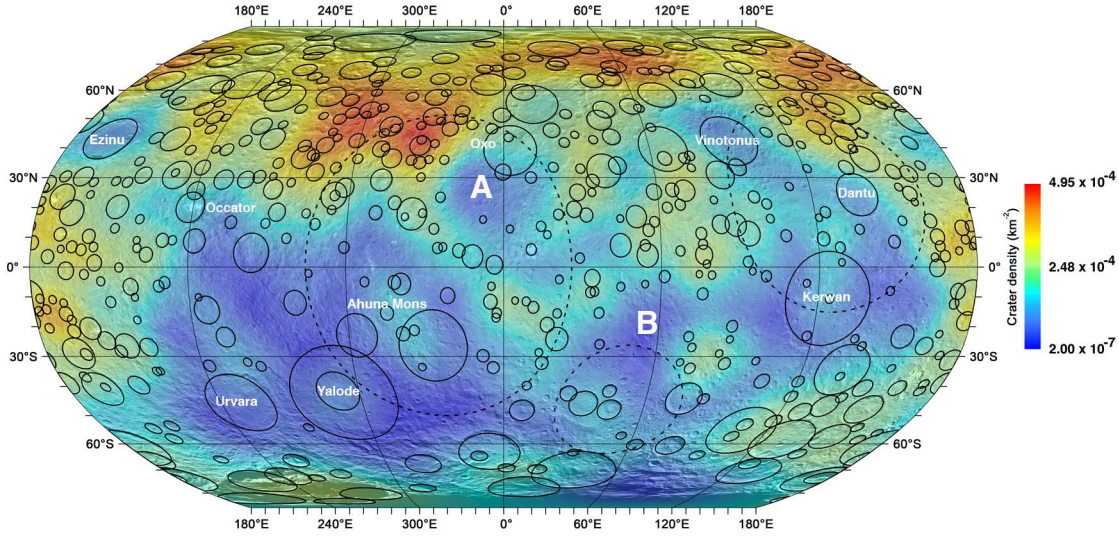


Fig. 3. Spatial density of >20-km craters on Ceres. Crater rims are shown as black solid circles. Blue indicates areas with LCDs; yellow and red represent highly cratered areas. The smallest dashed ellipse marks the idealized former rim of an extremely degraded impact crater at 48.9°E and 44.9°S, which is barely recognizable in the FC clear filter data but visible in the global DEM. Also shown as dashed circles are the outlines of two large putative basins. Unambiguously recognized basins with diameters >300 km are missing, and there are several areas with LCDs associated with large impact craters (e.g., Yalode, Urvara, Kerwan, Ezinu, Vinotonus, Dantu, and two unnamed craters northeast and southeast of Oxo). Areas A and B are topographic rises with central depressions (described in the text) that also show LCDs.

and (ii) the morphologic transition from simple (relatively unmodified) bowl-shaped craters to those with modified floors. Our criteria for the latter was when modified floors exceed 50% of the crater diameter and when the number of craters in a size bin exceeds 50% occurrence of modified complex crater floors. These are the same criteria used for comparison to icy satellites (*28*). We used the current High-Altitude Mapping Orbit (HAMO) topographic map of Ceres, which has an effective horizontal resolution of ~137 m and a vertical sensitivity of 10 m (*23*), to measure crater depths. For craters less than ~8 km in diameter, we determined the crater depths from shadow measurements. We found that the transition from bowl-shaped simple craters to modified simple craters (based on observations of floor-fill material and on the inflection in the depth-diameter curve) occurs at about 7.5 to 12 km. These results are generally similar to those of other icy bodies with similar gravity, such as Tethys (~10 km) and Dione (~10 to 12.5 km), when measured with the same criteria (Fig. 2A). Assuming that simple-to-complex transition diameters scale inversely with gravity (*29*) (Fig. 2B), we can independently calculate the Ceres simple-to-complex transition diameter following the approach used in (*30*) and (*31*), which gives the simple-to-complex transition diameter as $2g_{Ganymede}/g_{Ceres}$ (g, gravity). Assuming a gravity of 1.428 m/s^2 for Ganymede (*32*) and of 0.28 m/s^2 for Ceres (*5*), this yields a simple-to-complex transition on Ceres at ~10.3 km. In contrast, if Ceres is primarily a rocky body, then Ceres' transition diameter could be near 50 km (*4*), as can be obtained by the extrapolation of the values associated with silicate planets from (*29*). Thus, these independent calculations support the fact that Ceres has a crust made of an ice-rock

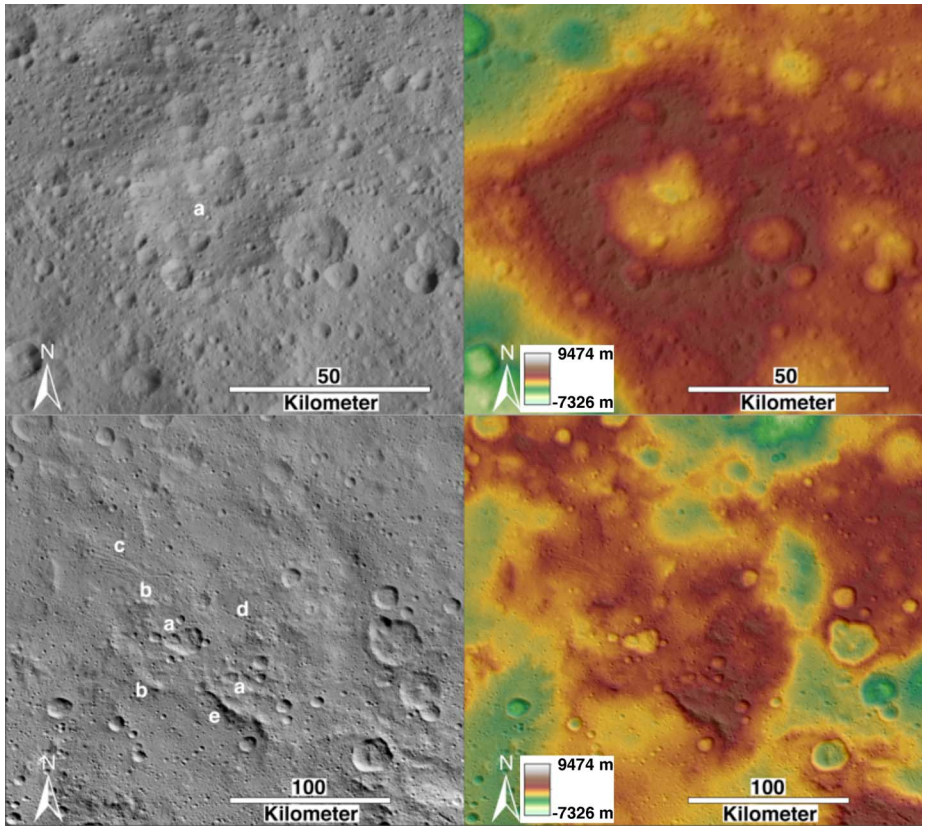


Fig. 4. Detailed views of areas A and B. (**Top**) Area A, as seen from the HAMO (left) and with superposed color-coded topography (right). The area is characterized by a topographic rise with nested, irregularly shaped depressions (a). (**Bottom**) Area B, as seen from the HAMO (left) and with superposed color-coded topography (right). The area is characterized by a topographic rise with nested, irregularly shaped depressions (a); linear settings of domelike structures (b); a graben system (c); a >50-km-long, straight, pitted fracture (d); and the steep cliff of Niman Rupes (e). The topographic range in both DEMs is from –7326 to 9474 m.

Downloaded from http://science.sciencemag.org/ on September 1, 2016

mixture. Hence, the observed simple-to-complex crater transition diameters on Ceres are most consistent with an ice-bearing upper crust or a material mixture of similar viscosity. Together with the apparent absence of widespread viscous relaxation, the relatively small measured transition diameters indicate that, paradoxically, Ceres' crust is weak (icelike) on the time scale of crater formation and modification but relatively strong over longer, geologic time scales. At a temperature of 160 K, it has been estimated that the upper tens of kilometers of a "weak" (icelike) crust have a viscosity of 10^{22} Pa·s. The upper limit is less well constrained and is estimated to be on the order of 10^{25} to 10^{27} Pa·s (*26*). Thus, the crust of Ceres is not as strong as pure rock.

Spatial distribution of craters

On the basis of Survey orbit data (400 m per pixel), we globally (95%) mapped all impact craters down to a few kilometers in size. Several coauthors have independently produced crater catalogs (see supplementary materials) on the basis of images from different mission phases [Approach, pre-Survey, and Survey (*5*)] that all agree well with each other concerning the absolute number of craters in different diameter ranges. Figure 3 and Table 1 show craters larger than 20 km, which are clearly visible at the given FC pixel scale, to avoid effects of incomplete counts, terrain effects, and secondary cratering. All catalogs show an absence of craters larger than 300 km, while low-pass filtering of the DEM suggests the existence of at least two quasi-circular depressions with diameters of ~570 (125.56°E and 19.60°N) and ~830 km (24.76°W and 0.5°N). Given the uncertainties in the earliest impact flux on Ceres, such basins are consistent with the estimates of de Elía and Di Sisto (*33*), who calculated the number of craters produced by main-belt asteroids as a function of crater diameter. From figure 4 of (*33*), the largest crater produced by asteroids on Ceres has a diameter of ~600 km. The survival of such large basins might hint at limited amounts of viscous relaxation in these areas compared with other areas or relatively young ages of these basins.

Craters are heterogeneously distributed across the surface of Ceres, with the northern hemisphere being more heavily cratered than the southern hemisphere. The lowest crater densities—associated with large, well-preserved impact craters (e.g., Urvara and Yalode)—are located in the southern hemisphere. Additional regions with relatively LCDs are associated with craters Kerwan, Ezinu, Vinotonus, and two unnamed craters southeast (155 km, 4.0°E and 38.8°N) and northeast (110 km, 14.0°E and 54.7°N) of Oxo crater (10 km) (Fig. 3). Plausible reasons for the LCD terrains include viscous relaxation (*4*, *34*), ejecta burial (*35*), and seismic shaking (*36*). Because the LCD terrain sometimes extends across a large latitude range (e.g., Kerwan: ~30°N to 46°S; Urvara and Yalode: ~18°N to 75°S), its spatial distribution is inconsistent with simple relaxation driven by warmer equatorial temperatures. Instead, because the LCD terrain is associated with large craters, we propose that impact-driven resurfacing is the more likely process of formation, although we cannot completely rule out an endogenic origin. Such an endogenic origin might be plausible for two LCD terrains [i.e., area A (349.5°E and 22.5°N) and area B (54.2°E and 23.3°S)] (Fig. 3). Both areas appear to be positive topographic structures with central depressions. Area A is a ~100-km-wide, ~6-km-high topographic rise and exhibits heavily eroded nested pits that are up to ~2 km deep (Fig. 4). Area B is a ~130-km-wide topographic rise and is characterized by nested ~7- to 20-km pits with different depths, chains of ~5- to 20-km domelike structures, and a ~15-by-60–km swarm of subparallel ~1- to 2-km-wide east-west oriented graben-like valleys (i.e., rilles) (Fig. 4). If these areas were resurfaced by the deposition of endogenic material, its thickness must be on the order of ~700 to 800 m to obliterate 20-km-large craters (*27*). Ahuna Mons, a possible cryovolcanic construct (*37*), is located in an area that is more heavily cratered than the immediate vicinity, implying that potential cryovolcanism did not substantially resurface that region.

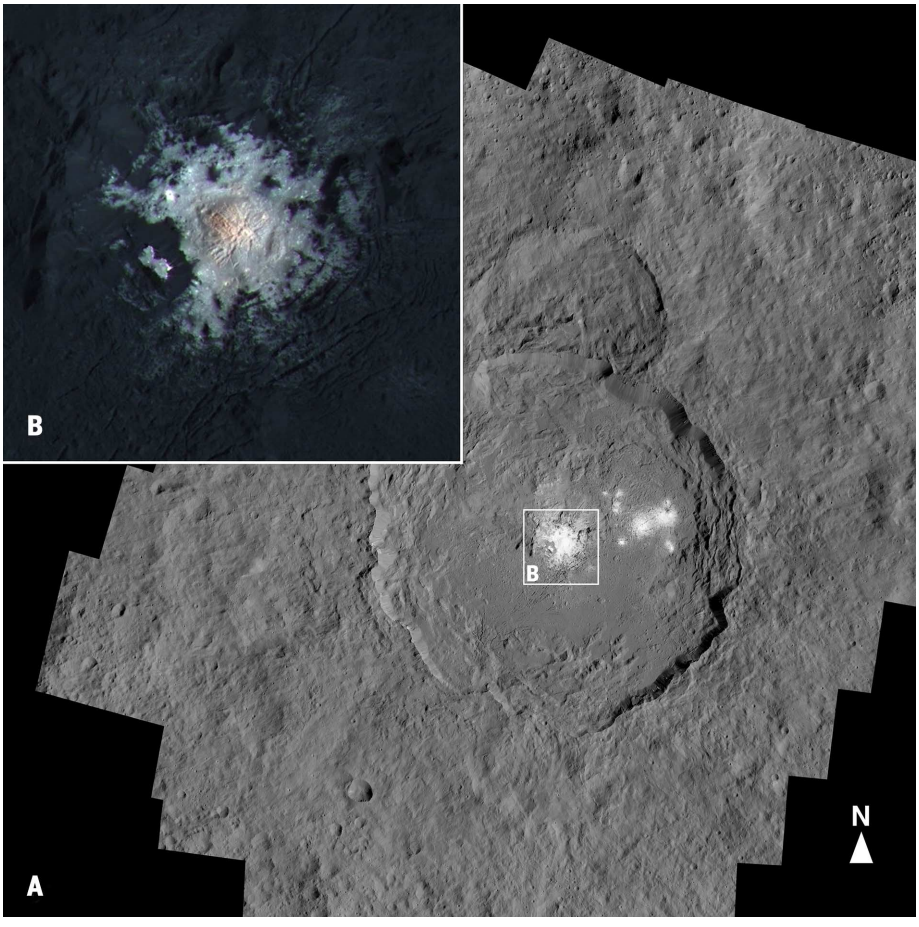


Fig. 5. Occator crater. Occator is a 92-km-diameter, 4-km-deep impact crater that contains the brightest spot on Ceres. Panel (**A**) shows a Low-Altitude Mapping Orbit FC mosaic indicating the location of enhanced-color inset (**B**), which shows the sharply defined bright spot associated with a central dome with a radial fracture pattern surrounded by concentric fractures.

Table 1. Frequency of craters per diameter bin of the crater catalog shown in Fig. 3.

Crater diameter (km)	Number of craters
20–25	137
25–30	98
30–35	67
35–40	52
40–45	27
45–50	34
50–55	24
55–60	18
60–65	10
65–70	17
70–75	9
75–80	6
80–85	6
85–90	1
90–100	6
100–120	10
120–150	5
150–200	1
200–300	3

Downloaded from http://science.sciencemag.org/ on September 1, 2016

FIND
MORE
FREE
MAGAZINES

FREEMAGS.CC

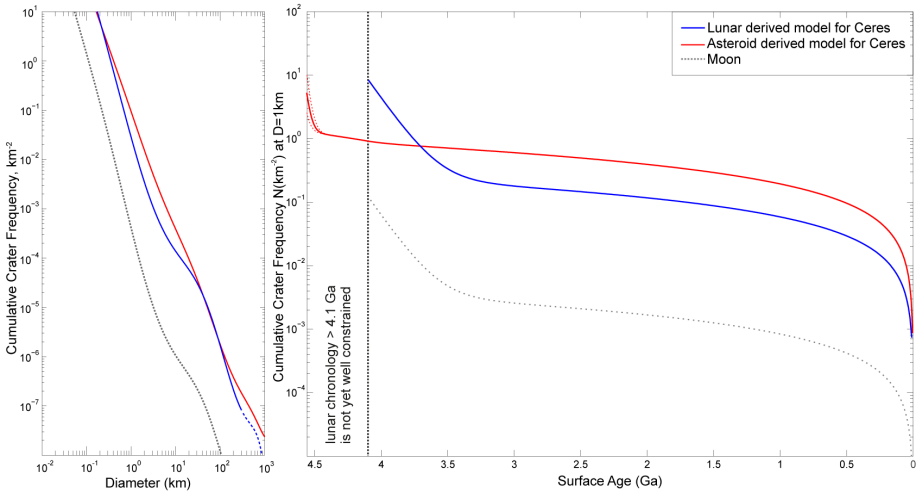


Fig. 6. Production functions and chronology functions for Ceres and the Moon. (**Left**) PFs for the Moon and Ceres, based on the LDM and the ADM. The LDM PF is shown as a dashed line for crater sizes larger than 300 km, which are outside of the valid diameter range of the lunar PF (*44*). (**Right**) CFs for the Moon and Ceres (LDM and ADM). The lunar PF and CF are from (*44*). D, diameter.

A heterogeneous crust is not only indicated by the spatial distribution of impact craters but also by FC and VIR color data (*10*, *38*). In FC images, the surface of Ceres is rather dark, but some craters (such as Occator) exhibit a high albedo and a central pit spectrum that has been interpreted as hydrated magnesium sulfate (*38*) or sodium carbonates mixed with a dark component, small amounts of phyllosilicates, ammonium carbonates, and/or ammonium chloride (Fig. 5) (*39*). False-color composites and VIR spectral data reveal compositional differences on the surface that reflect crustal heterogeneities at all scales (*10*, *38*, *40*). For example, Occator crater shows the largest diversity in colors, ranging from bright spectrally reddish units (central pit) to dark spectrally convex-shaped units (ejecta). Though local deviations from nearly-neutral spectral slopes in the red-visual spectrum to negative slopes are characteristic at many sites, pronounced positive slopes are almost absent and confined to small exposures (*38*).

Absolute model ages (AMAs)

Crater size-frequency distribution (CSFD) measurements are commonly used to derive relative and AMAs of unsampled planetary surfaces (*41*–*44*). To obtain AMAs from observed CSFDs, two main components are needed: a production function (PF) and a chronology function (CF) (Fig. 6). A PF, which describes the time-average idealized shape of the cumulative size-frequency distribution of craters, is needed to extrapolate the measured CSFD to a distinct reference diameter (e.g., 1 or 10 km), whose cumulative crater frequency can then be used to obtain an AMA from the CF (*41*–*44*), which correlates crater densities with absolute ages. Here we describe two approaches to derive such functions. The lunar-derived model (LDM) adapts the lunar PF and CF to impact conditions on Ceres, taking into account a number of parameters [e.g., impact velocities (Fig. 7), projectile densities, current collision probabilities, and surface gravity] in a similar manner as has been done for Mars and Mercury, among others (*41*). The asteroid-derived model (ADM) derives a PF by scaling the directly observed object size-frequency distribution from the main asteroid belt, extended to sizes smaller than 3 to 5 km by a collisional model (*45*), to the resulting size-frequency distribution of craters on Ceres using similar cerean target parameters as the LDM (*46*–*48*). A CF for the ADM is derived independently from lunar observation and is exclusively based on collision rates as they are observed in the current asteroid belt, in combination with dynamical models of the early evolution of the asteroid belt (*49*, *50*). The two approaches are described in detail in the Materials and methods section.

Both approaches have their advantages: For instance, the PF from the ADM is at least partly derived from direct observations of objects in the main asteroid belt, and the CF benefits from the latest dynamical models of the asteroid belt (*49*, *50*). On the other hand, assuming that the asteroid belt shows the same declining flux as the Moon, the functions from the LDM profit from the lunar PF being based on direct crater observations, even down to the smallest crater diameter range, and from the absolute calibration of the lunar CF using radiometric ages from Apollo and Luna samples. However, both approaches also have uncertainties. For example, the LDM assumes that the flux of the impacting projectiles in the asteroid belt exhibits the same characteristics as on the Moon, including an exponential decay of the flux from at least ~4.1 billion to ~3 billion years ago (Ga). This would lead to a massive primordial main belt, resulting in high numbers of expected impact basins on Ceres' ancient surface, which is inconsistent with current observations but might partially be explained by relaxation processes. On the other hand, the PF used in the ADM can only be directly derived from the size-frequency distribution (SFD) of projectiles (>~3 to 5 km) in the asteroid belt, resulting in crater diameters of ~20 to 30 km, whereas the portion of the PF for smaller diameters has to be extrapolated due to incomplete observations of smaller bodies (potential projectiles) in the asteroid belt. Furthermore, the CF from the ADM cannot be properly calibrated using radiometric ages from planetary samples and depends on the assumed parameters of the dynamical models.

We applied both LDM and ADM to CSFDs of the smooth deposits around Kerwan crater because unraveling the geologic history of the Kerwan region is essential for our understanding of past and recent processes on Ceres' surface (Fig. 8). In addition, the region shown at left in Fig. 8, which corresponds to about 9 to 10% of the cerean surface, was selected because it represents a large, first-order homogeneous unit, which is necessary for reliable CSFD-based age determinations. CSFDs were independently determined by four team members and agree well with each other, implying that craters were reliably identified and their numbers and sizes consistently measured. By applying the LDM to these CSFD measurements, we derive an AMA of ~720 My; we obtain a somewhat younger AMA of ~550 My when applying the ADM (Fig. 8).

We also used the LDM and ADM to estimate the potential formation ages of the two ~570- and ~830-km-large depressions detected in the filtered topography data. Assuming that these depressions are impact structures formed by single impacts, their sizes are comparable with those of the Rheasilvia and Veneneia basins on Vesta if scaled to Ceres size. Like Rheasilvia and Veneneia on Vesta, the quasi-circular depressions on Ceres might represent the two youngest, surviving, large basinlike features on Ceres. If correct, based on the LDM we would expect the formation of the smaller feature within the past 3.5 billion years (Gy) and the formation of the larger feature within the past 3.7 Gy, consistent with the formation of the youngest basins on other planetary bodies (Moon, Mars), as well as on Vesta [lunar-like model (*42*)]. In the ADM, the formation of the smaller feature would be expected within the past 2.8 Gy, whereas the larger feature probably formed shortly after the advent of the solar system. The ages of the two depressions are relatively close together in the LDM, as the chronology curve has a steep slope in that age range. In contrast, the chronology curve in the ADM is much flatter until ~4.4 Ga before rising steeply; hence, the ages of the two basins in the ADM are more widely separated (Fig. 6).

Conclusions

Ceres is a heavily cratered object that shows a wide variety of impact sizes and morphologies, although we observe an absence of large (>300 km) craters. The small amount of observed relaxation suggests that the crust contains less ice and/or may be thicker than predicted by some models. Craters are heterogeneously distributed across the surface, indicating crustal heterogeneities and a complex geologic evolution of Ceres' crust and upper mantle, an interpretation supported by FC

Downloaded from http://science.sciencemag.org/ on September 1, 2016

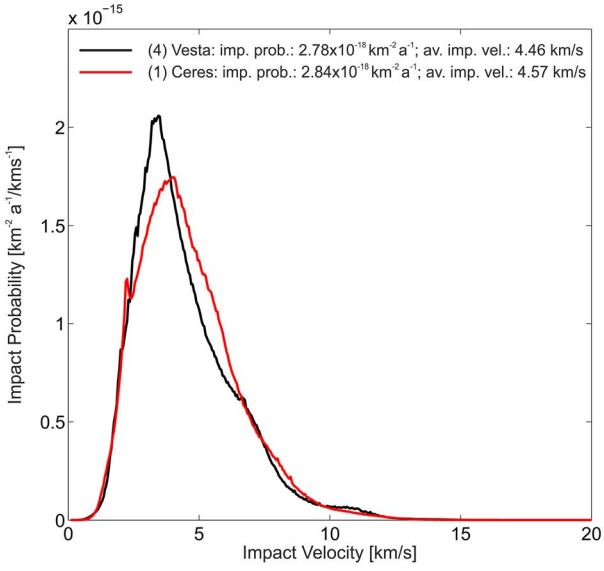


Fig. 7. Intrinsic impact probability with respect to impact velocity for Ceres and Vesta. The calculation is for ≥5-km bodies that cross the orbits of Vesta and Ceres (*62*). Details of the calculation are provided in the Materials and methods section.

and VIR color data. Dating the smooth deposits around Kerwan, one of the largest and most relaxed craters on Ceres, revealed young retention ages of 550 and 720 My, indicating that at least some geologic activity took place in the recent history of Ceres.

Materials and methods

Lunar-derived model (LDM)

The determination of AMAs at Ceres on the basis of the LDM, follows the approach of (*42*, *51*, *52*). The first publication describes in detail the methodology of converting the lunar chronology system (crater PF and CF) to main-belt asteroids of rocky composition. The authors reproduce results of earlier publications (*53*–*55*) and link the AMA related to the formation of the Rheasilvia basin on Vesta to the youngest and most prominent reset event of brecciated HED meteorites about 3.5 Ga (*56*). Here we extend that approach to Ceres, whose surface composition (*8*, *10*, *38*) and related models of thermochemical evolution (*2*, *3*, *18*) are consistent with high abundances of volatile materials. The remarkable similarities in crater morphologies between Ceres and saturnian icy satellites may be a result of similar rheologic characteristics of the target material as well as similar surface gravities.

For converting the lunar cratering record to the impact conditions on Ceres we use the scaling laws by (*57*) (Eqs. 1 to 3) that are designed for scaling between projectile and crater sizes of nonporous, zero-friction rocks.

$$C_D = \left[1.16\left(\frac{\delta}{\rho}\right)^{\frac{1}{3}}(v\sin(\alpha))^{0.44}\right]^{1/0.78} \quad (1)$$

$$\frac{D_t}{D_P} = \frac{C_D}{[g(D_{sg}+D_t)]^{0.282}} \quad (2)$$

$$D_t = D_{SC}^{0.15} D^{0.85} \quad (3)$$

Equations 1 and 2 represent the Ivanov scaling laws (*57*). Equation 3 is only used for converting between sizes of complex and transient craters. Following (*51*), we assume that the sizes of simple bowl shaped craters are similar to transient crater sizes, thus, neglecting potential collapse of such craters, which would result in an enlargement of the final crater when compared to the transient diameter. In these equations, the variables are defined as: D, observed crater diameter; D_t, transient crater diameter; D_P, projectile diameter; g, surface gravity of target body; δ, projectile density; ρ, target density; v, impact velocity; α, impact angle; D_{sg}, strength to gravity transition crater diameter; D_{SC}, simple to complex transition crater diameter.

Key parameters in the used scaling laws are the transition size from simple-to-complex craters and the transition size from the strength to gravity scaling regime. Both parameters scale inversely with surface gravity for icy and rocky bodies but are offset between both body types (*27*, *51*, *58*, *59*). Hence, scaling the lunar cratering record to icy bodies requires correction for the different scaling behavior in rocky and icy target materials. In a previous study (*60*), the cerean crater PF has been predicted before high-resolution imaging data were available. In that approach the strength-to-gravity crater diameter as well as the surface gravity of Ceres were incorrectly adjusted in a way as if Ceres is a rocky body with a simple-to-complex transition crater diameter of ~12 km. High-resolution crater measurements of Ceres acquired subsequently did follow the predicted PF very closely. Although this approach resulted in an agreement between theoretical and observed crater distribution, it severely underestimated crater sizes for a given projectile size, which resulted in a too low estimation for the projectile flux.

Here, we present a more sophisticated approach in which the upper limit for the cerean strength-to-gravity transition can be estimated by the size of the largest stable crater with Eq. 4 (*61*).

$$\rho g D_{sg} \leq 13.5 Y_0 \quad (4)$$

With a simple-to-complex transition of 10 km and Eq. 5 (*61*), we get for Y_0 a value of about 0.15 MPa.

$$\frac{27 Y_0}{\rho g} \leq D_{SC} \quad (5)$$

Thus, for Ceres we find a value of ~5 km as upper limit for D_{sg} using values from table S1.

In order to find the correct value, we reduced D_{sg} in Eq. 2 until we arrived at a solution that best resembled the shape of the crater PF of (*60*). This resulted in a D_{sg} of 1.75 km and also implies a value for Y_0 of about 50 kPa, which is the average material cohesion during the process of crater formation.

The PF is a model of cumulative crater frequencies in dependence of crater diameters. It should resemble the observed crater size-frequency distribution of the body measured on surfaces undisturbed by geological processes or additional secondary craters. Table S2 gives the coefficients of an 11th-degree polynomial equation (Eq. 6) (*44*, *52*) that describes the shape of the LDM crater PFs for the Moon and Ceres.

$$\log N_{cum} = a_0 + a_1\log(D) + a_2(\log(D))^2 + \ldots + a_{11}(\log(D))^{11} \quad (6)$$

The CF relates measured cumulative crater frequencies to AMAs using a crater reference diameter, typically N(1). For estimates of the current intrinsic collision probability of Ceres, we follow the approach of (*62*) and use orbital statistics of Ceres crossing asteroids of ≥5 km diameter. This analysis gives an intrinsic impact probability of 2.84×10^{-18} km^{-2} a^{-1} and an average impact velocity of about 4.57 km/s (Fig. 7). The conversion of collision probabilities into a lunar-like chronology is detailed by (*42*) for the case of Vesta.

Table S3 gives the coefficients of the CF with exponential smooth decay for ages older than about 3.5 Gy (Eq. 7) (*41*) for the Moon, Vesta, and Ceres. For ages older than 4.1 Gy, the cratering history of the Moon is still ambiguous (*63*). Therefore, the given functions may only be used with great caution for older ages.

$$N_{cum}(D \geq 1\text{km}) = C_1(e^{C_2 t} - 1) + C_3 t \quad (7)$$

The presented LDM chronology system for Ceres (Fig. 6) is an estimation of the cratering history averaged over billions of years. A break up event inside the main belt could cause higher impact rates on Ceres as well as on other asteroids for a short period of time. If such an event occurred recently, young areas may appear older than they actually are. Very old areas are less affected, because short fluctuations in impact rate average out over time. In addition to statistical errors that arise from fitting the crater PF to the measured crater size-frequency distribution, there might be systematic errors present as well. Such errors could be related to the shape of the derived crater PF or the estimation of intrinsic collision probabilities.

Asteroid-derived model (ADM)

The ADM uses the chronology curve derived for Vesta by (*43*), adjusted for the different production rates of craters on Ceres (Fig. 6). Briefly, the chronology curve is based on the best current models of main-belt dynamical and collisional history, accounting for two main phases: (i) an initial sharp decline in mass of the belt during the ~100 Ma immediately following the formation of the solar system (*64*–*66*); and (ii) the subsequent depletion of the belt by a factor of ~4

Downloaded from http://science.sciencemag.org/ on September 1, 2016

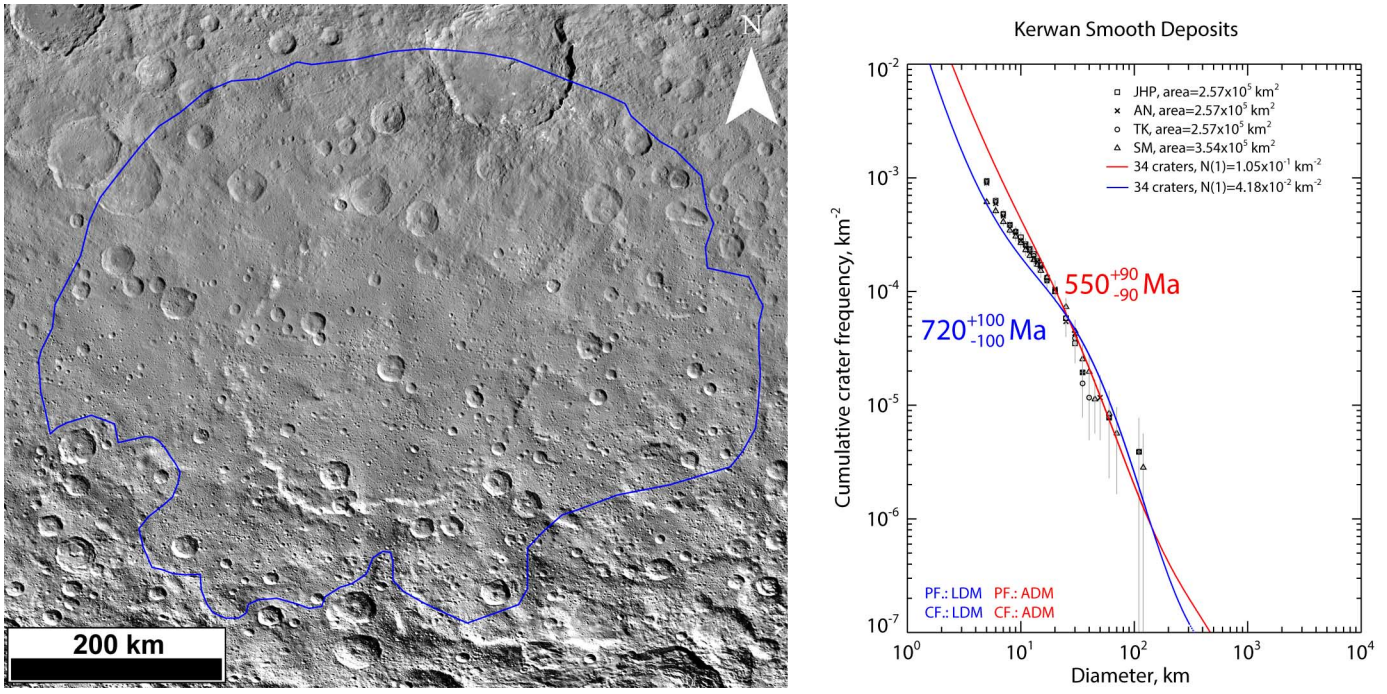


Fig. 8. Age determination for the Kerwan impact crater on Ceres. (**Left**) The HAMO mosaic shows the smooth deposits associated with Kerwan crater. The area for which we (J.H.P., A.N., S.M.) performed CSFD measurements is outlined in blue. The count area of S.M. overlaps this area and extends farther to the west. (**Right**) CSFD plot for the area shown at left. Several coauthors (J.H.P., A.N., T.K., and S.M.) independently performed CSFD measurements. To derive AMAs, we used the PFs and CFs of the LDM (blue) and the ADM (red).

during the time of the Late Heavy Bombardment due to secular resonance sweeping (*49*) and the loss of dynamically unstable asteroids (*50*). It is important to note that while the chronology curve for the asteroid belt derived in this manner differs significantly in shape from the lunar chronology curve (and hence also the LDM curve) (Fig. 6), there is no a priori reason to think that they should be the same (which is a central assumption of the LDM). In fact, Morbidelli *et al.* (*63*) show that the asteroid flux into the terrestrial planet region due to dynamical depletion processes within the asteroid belt results in an impact flux on the Moon consistent with the lunar chronology of (*41*, *52*, *67*).

To apply the ADM chronology curve to Ceres, the current production rate of craters on Ceres must be calculated. The chronology curve allows for the extrapolation of the impact rate back in time. The crater PF is calculated adopting a model main-belt SFD, an asteroid impact velocity distribution based on current asteroids larger than 50 km crossing the orbit of Ceres, and a crater scaling law from (*68*). It should be noted that the main-belt SFD is taken from (*45*), which provides a good fit to the observed main-belt SFD down to the completeness limit of ~3 km. The resulting PF also has produced a reasonable match to crater counts on young surfaces on Vesta (*46*). Further details of the model can be found in (*46*, *48*, *69*).

REFERENCES AND NOTES

1. C. T. Russell, C. A. Raymond, The Dawn mission to Vesta and Ceres. *Space Sci. Rev.* **163**, 3–23 (2011). doi: 10.1007/s11214-011-9836-2
2. J. C. Castillo-Rogez, T. B. McCord, Ceres' evolution and present state constrained by shape data. *Icarus* **205**, 443–459 (2010). doi: 10.1016/j.icarus.2009.04.008
3. T. B. McCord, C. Sotin, Ceres: Evolution and current state. *J. Geophys. Res.* **110**, E05009 (2005). doi: 10.1029/2004JE002244
4. M. T. Bland, Predicted crater morphologies on Ceres: Probing internal structure and evolution. *Icarus* **226**, 510–521 (2013). doi: 10.1016/j.icarus.2013.05.037
5. C. T. Russell *et al.*, Dawn arrives at Ceres: Exploration of a small, volatile-rich world. *Science* **353**, aaf4219 (2016).
6. L. A. Lebofsky, M. A. Feierberg, A. T. Tokunaga, H. P. Larson, J. R. Johnson, The 1.7- to 4.2- μm spectrum of asteroid 1 Ceres: Evidence for structural water in clay minerals. *Icarus* **48**, 453–459 (1981). doi: 10.1016/0019-1035(81)90055-5
7. T. V. V. King, R. N. Clark, W. M. Calvin, D. M. Sherman, R. H. Brown, Evidence for ammonium-bearing minerals on ceres. *Science* **255**, 1551–1553 (1992). doi: 10.1126/science.255.5051.1551; pmid: 17820166
8. A. S. Rivkin, E. L. Volquardsen, B. E. Clark, The surface composition of Ceres: Discovery of carbonates and iron-rich clays. *Icarus* **185**, 563–567 (2006). doi: 10.1016/j.icarus.2006.08.022
9. R. E. Milliken, A. S. Rivkin, Brucite and carbonate assemblages from altered olivine-rich materials on Ceres. *Nat. Geosci.* **2**, 258–261 (2009). doi: 10.1038/ngeo478
10. M. C. De Sanctis *et al.*, Ammoniated phyllosilicates with a likely outer solar system origin on (1) Ceres. *Nature* **528**, 241–244 (2015). doi: 10.1038/nature16172; pmid: 26659184
11. C. R. Chapman, J. W. Salisbury, Comparisonos of meteorite and asteroid spectral reflectivities. *Icarus* **19**, 507–522 (1973). doi: 10.1016/0019-1035(73)90078-X
12. T. B. McCord, M. J. Gaffey, Asteroids: Surface composition from reflection spectroscopy. *Science* **186**, 352–355 (1974). doi: 10.1126/science.186.4161.352; pmid: 17839866
13. M. C. De Sanctis *et al.*, The VIR spectrometer. *Space Sci. Rev.* **163**, 329–369 (2011). doi: 10.1007/s11214-010-9668-5
14. T. H. Prettyman *et al.*, Dawn's Gamma Ray and Neutron Detector. *Space Sci. Rev.* **163**, 371–459 (2011). doi: 10.1007/s11214-011-9862-0
15. H. Sierks *et al.*, The Dawn Framing Camera. *Space Sci. Rev.* **163**, 263–327 (2011). doi: 10.1007/s11214-011-9745-4
16. P. Schenk *et al.*, "An ice-rich mantle on Ceres from Dawn mapping of central pit and peak crater morphologies," abstract P53E-2186, presented at the American Geophysical Union Fall Meeting, San Francisio, CA, 14 to 18 December 2015.
17. D. L. Buczkowski *et al.*, The geomorphology of Ceres. *Science* **353**, aaf4332 (2016).
18. T. McCord, J. Castillo-Rogez, A. Rivkin, Ceres: Its origin, evolution and structure and Dawn's potential contributions. *Space Sci. Rev.* **163**, 63–76 (2011). doi: 10.1007/s11214-010-9729-9
19. J. C. Castillo-Rogez, Ceres – Neither a porous nor a salty ball. *Icarus* **215**, 599–602 (2011). doi: 10.1016/j.icarus.2011.08.007
20. P. C. Thomas *et al.*, Differentiation of the asteroid Ceres as revealed by its shape. *Nature* **437**, 224–226 (2005). doi: 10.1038/nature03938; pmid: 16148926
21. R. Jaumann *et al.*, Vesta's shape and morphology. *Science* **336**, 687–690 (2012). doi: 10.1126/science.1219122; pmid: 22582254
22. F. Preusker *et al.*, Stereo topographic models of Mercury after three MESSENGER flybys. *Planet. Space Sci.* **59**, 1910–1917 (2011). doi: 10.1016/j.pss.2011.07.005
23. F. Preusker *et al.*, Dawn at Ceres – Shape models and rotational state. *Lunar Planet. Sci. Conf.* **47**, abstract 1954 (2016).
24. P. O. Hayne, O. Aharonson, Thermal stability of ice on Ceres with rough topography. *J. Geophys. Res.* **120**, 1567–1584 (2015). doi: 10.1002/2015JE004887
25. M. Y. Zolotov, On the composition and differentiation of Ceres. *Icarus* **204**, 183–193 (2009). doi: 10.1016/j.icarus.2009.06.011
26. M. T. Bland *et al.*, Composition and structure of the shallow subsurface of Ceres as revealed by crater morphology. *Nat. Geosci.* **9**, 538–542 (2016). doi: 10.1038/ngeo2743
27. R. J. Pike, "Geometric interpretation of lunar craters" (U.S. Government Printing Office, 1980).
28. O. L. White, P. M. Schenk, A. J. Dombard, Impact basin relaxation on Rhea and Iapetus and relation to past heat flow. *Icarus* **223**, 699–709 (2013). doi: 10.1016/j.icarus.2013.01.013
29. P. M. Schenk *et al.*, "Ages and interiors: The cratering record of the Galilean satellites," in *Jupiter*, F. Bagenal, T. Dowling, W. McKinnon, Eds., (Cambridge Univ. Press, 2004), pp. 427–456.
30. R. G. Kraus, L. E. Senft, S. T. Stewart, Impacts onto H_2O ice: Scalling laws for melting, vaporization, excavation, and final crater size. *Icarus* **214**, 724–738 (2011). doi: 10.1016/j.icarus.2011.05.016

Downloaded from http://science.sciencemag.org/ on September 1, 2016

31. R. P. Di Sisto, M. Zanardi, The production of craters on the mid-sized Saturnian satellites by Centaur objects. *Astron. Astrophys.* **553**, A79 (2013). doi: 10.1051/0004-6361/201220568
32. G. Steinbrügge, A. Stark, H. Hussmann, F. Sohl, J. Oberst, Measuring tidal deformations by laser altimetry: A performance model for the Ganymede Laser Altimeter. *Planet. Space Sci.* **117**, 184–191 (2015). doi: 10.1016/j.pss.2015.06.013
33. G. C. de Elía, R. P. Di Sisto, Impactor flux and cratering on Ceres and Vesta: Implications for the early solar system. *Astron. Astrophys.* **534**, A129 (2011).
34. E. M. Parmentier, J. W. Head, Viscous relaxation of impact craters on icy planetary surfaces: Detrermination of viscosity variation with depth. *Icarus* **47**, 100–111 (1981). doi: 10.1016/0019-1035(81)90095-6
35. D. E. Wilhelms, "The geologic history of the Moon" (U.S. Geological Survey Professional Paper 1348, 1987).
36. J. E. Richardson Jr., H. Melosh, R. Greenberg, D. Obrien, The global effects of impact-induced seismic activity on fractured asteroid surface morphology. *Icarus* **179**, 325–349 (2005). doi: 10.1016/j.icarus.2005.07.005
37. O. Ruesch *et al*., Cryo-volcanism on Ceres. *Science* **353**, aaf4286 (2016).
38. A. Nathues *et al*., Sublimation in bright spots on (1) Ceres. *Nature* **528**, 237–240 (2015). doi: 10.1038/nature15754; pmid: 26659183
39. M. C. De Sanctis *et al*., Bright carbonate deposits as evidence of aqueous alteration on (1) Ceres. *Nature* **536**, 54–57 (2016). doi: 10.1038/nature18290; pmid: 27362221
40. E. Ammannito *et al*., Distribution of phyllosilicates on the surface of Ceres. *Science* **353**, aaf4279 (2016).
41. G. Neukum, B. A. Ivanov, W. K. Hartmann, Cratering records in the inner solar system in relation to the lunar reference system. *Space Sci. Rev.* **96**, 55–86 (2001). doi: 10.1023/A:1011989004263
42. N. Schmedemann *et al*., The cratering record, chronology and surface ages of (4) Vesta in comparison to smaller asteroids and the ages of HED meteorites. *Planet. Space Sci.* **103**, 104–130 (2014). doi: 10.1016/j.pss.2014.04.004
43. D. P. O'Brien *et al*., Constraining the cratering chronology of Vesta. *Planet. Space Sci.* **103**, 131–142 (2014). doi: 10.1016/j.pss.2014.05.013
44. G. Neukum, "Meteoritenbombardement und Datierung planetarer Oberflächen," thesis, University of Munich (1983).
45. W. F. Bottke Jr. *et al*., Linking the collisional history of the main asteroid belt to its dynamical excitation and depletion. *Icarus* **179**, 63–94 (2005). doi: 10.1016/j.icarus.2005.05.017
46. S. Marchi *et al*., Small crater populations on Vesta. *Planet. Space Sci.* **103**, 96–103 (2014). doi: 10.1016/j.pss.2013.05.005
47. S. Marchi *et al*., High-velocity collisions from the lunar cataclysm recorded in asteroidal meteorites. *Nat. Geosci.* **6**, 303–307 (2013). doi: 10.1038/ngeo1769
48. S. Marchi *et al*., The violent collisional history of asteroid 4 Vesta. *Science* **336**, 690–694 (2012a). doi: 10.1126/science.1218757; pmid: 22582255
49. A. Morbidelli, R. Brasser, R. Gomes, H. F. Levison, K. Tsiganis, Evidence from the asteroid belt for a violent past evolution of Jupiter's orbit. *Astron. J.* **140**, 1391–1401 (2010). doi: 10.1088/0004-6256/140/5/1391
50. D. A. Minton, R. Malhotra, Dynamical erosion of the asteroid belt and implications for large impacts in the inner solar system. *Icarus* **207**, 744–757 (2010). doi: 10.1016/j.icarus.2009.12.008
51. B. A. Ivanov, Mars/Moon cratering rate ratio estimates. *Space Sci. Rev.* **96**, 87–104 (2001). doi: 10.1023/A:1011941121102
52. G. Neukum, B. A. Ivanov, "Crater size distributions and impact probabilities on Earth from lunar, terrestrial-planet, and asteroid cratering data," in *Hazard Due to Comets and Asteroids*, T. Gehrels, Ed. (Univ. of Arizona Press, 1994), pp. 359–416.
53. C. R. Chapman, J. Veverka, M. J. S. Belton, G. Neukum, D. Morrison, Cratering on Gaspra. *Icarus* **120**, 231–245 (1996). doi: 10.1006/icar.1996.0048
54. C. R. Chapman *et al*., Cratering on Ida. *Icarus* **120**, 77–86 (1996). doi: 10.1006/icar.1996.0038
55. S. Marchi *et al*., The cratering history of asteroid (21) Lutetia. *Planet. Space Sci.* **66**, 87–95 (2012). doi: 10.1016/j.pss.2011.10.010
56. D. D. Bogard, K-Ar ages of meteorites: Clues to parent-body thermal histories. *Chemie der Erde – Geochemistry* **71**, 207–226 (2011). doi: 10.1016/j.chemer.2011.03.001
57. S. C. Werner, B. A. Ivanov, "Exogenic dynamics, cratering, and surface ages," in *Treatise on Geophysics* (Elsevier, ed. 2, 2015), vol. 10, pp. 327–365.
58. P. M. Schenk, Ganymede and Callisto: Complex crater formation and planetary crusts. *J. Geophys. Res.* **96**, 15635–15664 (1991). doi: 10.1029/91JE00932
59. J. M. Moore *et al*., Impact features on Europa: Results of the Galileo Europa Mission (GEM). *Icarus* **151**, 93–111 (2001). doi: 10.1006/icar.2000.6558
60. N. Schmedemann *et al*., A preliminary chronology for Ceres. *Lunar Planet. Sci. Conf.* **46**, abstract 1418 (2015).
61. H. J. Melosh, *Impact Cratering – A Geologic Process* (Oxford Univ. Press, 1989).
62. W. F. Bottke Jr., M. C. Nolan, R. Greenberg, R. A. Kolvoord, Velocity distributions among colliding asteroids. *Icarus* **107**, 255–268 (1994). doi: 10.1006/icar.1994.1021
63. A. Morbidelli, S. Marchi, W. F. Bottke, D. A. Kring, A sawtooth-like timeline for the first billion years of lunar bombardment. *Earth Planet. Sci. Lett.* **355–356**, 144–151 (2012). doi: 10.1016/j.epsl.2012.07.037
64. G. W. Wetherill, An alternative model for the formation of the asteroids. *Icarus* **100**, 307–325 (1992). doi: 10.1016/0019-1035(92)90103-E
65. J. Petit *et al*., The primordial excitation and clearing of the asteroid belt. *Icarus* **153**, 338–347 (2001). doi: 10.1006/icar.2001.6702
66. D. P. O'Brien, A. Morbidelli, W. F. Bottke, The primordial excitation and clearing of the asteroid belt—Revisited. *Icarus* **191**, 434–452 (2007). doi: 10.1016/j.icarus.2007.05.005
67. G. Neukum, D. E. Wilhelms, "Ancient lunar impact record," in *Lunar and Planetary Institute Science Conference*, abstracts of Lunar and Planetary Institute (Technical Report 13, 1982), pp. 590–591.
68. K. A. Holsapple, K. R. Housen, A crater and its ejecta: An interpretation of Deep Inpact. *Icarus* **187**, 345–356 (2007). doi: 10.1016/j.icarus.2006.08.029
69. S. Marchi *et al*., The cratering history of asteroid (2867) Steins. *Planet. Space Sci.* **58**, 1116–1123 (2010). doi: 10.1016/j.pss.2010.03.017

ACKNOWLEDGMENTS

We thank the Dawn team for the development, cruise, orbital insertion, and operations of the Dawn spacecraft at Ceres. C.T.R. is supported by the Discovery Program through contract NNM05AA86C to the University of California, Los Angeles. A portion of this work was performed at the Jet Propulsion Laboratory, California Institute of Technology, under contract with NASA. J.H.P. and H.H. are supported by the DLR Space Administration on behalf of the German Federal Ministry for Economic Affairs and Energy, grant 50 OW 1502 (DAWN). M.T.B. was supported by NASA's Dawn at Ceres Guest Investigator Program. Dawn data are archived with the NASA Planetary Data System. FC data may be obtained at http://sbn.psi.edu/pds/resource/dwncfc2.html. VIR spectral data may be obtained at http://sbn.psi.edu/pds/resource/dwncvir.html. GRaND data may be obtained at http://sbn.psi.edu/pds/resource/dwncgrd.html. The Ceres crater catalog described in the text and measurements of the transition diameter from simple to complex craters are available in the supplementary materials. As chair of the Dawn chronology working group, H.H. coordinated the contributions and prepared the manuscript. S.M. provided input on the distribution of craters and the PFs and CFs. N.S., A.Ne., T.K., and D.P.O. also provided input for the PFs and CFs. P.S. and T.P. made contributions to the simple-to-complex transition. J.H.P. performed CSFD measurements and helped with preparing the manuscript. A.Na. provided the description of color properties. A.I.E., R.R.F., R.S.P., F.P., J.C.C.-R., M.T.B., and C.A.R. contributed their expertise in geophysical modeling. D.A.W., R.J., B.S., D.L.B., and O.R. helped with manuscript preparation and provided useful comments and suggestions. C.T.R. is the Dawn principal investigator and guided the research.

SUPPLEMENTARY MATERIALS

www.sciencemag.org/content/353/6303/aaf4759/suppl/DC1
Tables S1 to S3
Reference (*70*)
Data S1

14 February 2016; accepted 29 July 2016
10.1126/science.aaf4759

Downloaded from http://science.sciencemag.org/ on September 1, 2016

RESEARCH ARTICLE SUMMARY

PLANETARY SCIENCE

The geomorphology of Ceres

D. L. Buczkowski,* B. E. Schmidt, D. A. Williams, S. C. Mest, J. E. C. Scully, A. I. Ermakov, F. Preusker, P. Schenk, K. A. Otto, H. Hiesinger, D. O'Brien, S. Marchi, H. Sizemore, K. Hughson, H. Chilton, M. Bland, S. Byrne, N. Schorghofer, T. Platz, R. Jaumann, T. Roatsch, M. V. Sykes, A. Nathues, M. C. De Sanctis, C. A. Raymond, C. T. Russell

INTRODUCTION: Observations of Ceres, the largest object in the asteroid belt, have suggested that the dwarf planet is a geologically differentiated body with a silicate core and an ice-rich mantle. Data acquired by the Dawn spacecraft were used to perform a three-dimensional characterization of the surface to determine if the geomorphology of Ceres is consistent with the models of an icy interior.

RATIONALE: Instruments on Dawn have collected data at a variety of resolutions, including both clear-filter and color images. Digital terrain models have been derived from stereo images. A preliminary 1:10 M scale geologic map of Ceres was constructed using images obtained during the Approach and Survey orbital phases of the mission. We used the map, along with higher-resolution imagery, to assess the geology of Ceres at the global scale, to identify geomorphic and structural features, and to determine the geologic processes that have affected Ceres globally.

RESULTS: Impact craters are the most prevalent geomorphic feature on Ceres, and several of the craters have fractured floors. Geomorphic analysis of the fracture patterns shows that they are similar to lunar Floor-Fractured Craters (FFCs), and an analysis of the depth-to-diameter ratios shows that they are anomalously shallow compared with average Ceres craters. Both of these factors are consistent with FFC floors being uplifted due to an intrusion of cryomagma.

Kilometer-scale linear structures cross much of Ceres. Some of these structures are oriented radially to large craters and most likely formed due to impact processes. However, a set of linear structures present only on a topographically high region do not have any obvious relationship to impact craters. Geomorphic analysis suggests that they represent subsurface faults and might have formed due to crustal uplift by cryomagmatic intrusion.

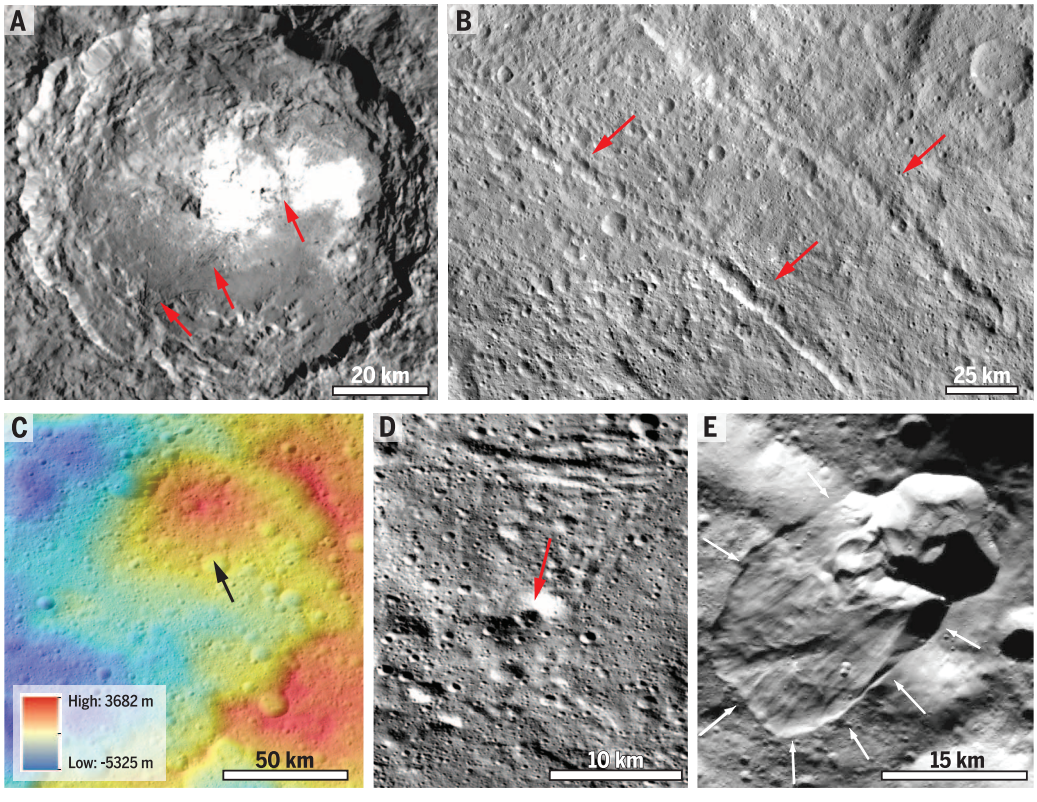
ON OUR WEBSITE

Read the full article at http://dx.doi.org/10.1126/science.aaf4332

Domes identified across the Ceres surface present a wide range of sizes (<10 km to >100 km), basal shapes, and profiles. Whether a single formation mechanism is responsible for their formation is still an open question. Cryovolcanic extrusion is one plausible process for the larger domes, although most small mounds (<10-km diameter) are more likely to be impact debris.

Differences in lobate flow morphology suggest that multiple emplacement processes have operated on Ceres, where three types of flows have been identified. Type 1 flows are morphologically similar to ice-cored flows on Earth and Mars. Type 2 flows are comparable to long-runout landslides. Type 3 flows morphologically resemble the fluidized ejecta blankets of rampart craters, which are hypothesized to form by impact into ice-rich ground.

CONCLUSION: The global trend of lobate flows suggests that differences in their geomorphology could be explained by variations in ice content and temperature at the near surface. Geomorphic and topographic analyses of the FFCs suggest that cryomagmatism is active on Ceres, whereas the large domes are possibly formed by extrusions of cryolava. Although spectroscopic analysis to date has identified water ice in only one location on Ceres, the identification of these potentially ice-related features suggests that there may be more ice within localized regions of Ceres' crust. ■



Dawn High-Altitude Mapping Orbit imagery (140 m per pixel) of example morphologic features. (**A**) Occator crater; arrows point to floor fractures. (**B**) Linear structures, denoted by arrows. (**C**) A large dome at 42° N, 10° E, visible in the elevation map. (**D**) A small mound at 45.5° S, 295.7° E. (**E**) Type 1 lobate flow; arrows point to the flow front.

The list of author affiliations is available in the full article online.
*Corresponding author. Email: debra.buczkowski@jhuapl.edu
Cite this article as D. L. Buczkowski *et al.*, *Science* 353, aaf4332 (2016). DOI: 10.1126/science.aaf4332

Downloaded from http://science.sciencemag.org/ on September 1, 2016

RESEARCH ARTICLE

PLANETARY SCIENCE

The geomorphology of Ceres

D. L. Buczkowski,[1*] B. E. Schmidt,[2] D. A. Williams,[3] S. C. Mest,[4] J. E. C. Scully,[5] A. I. Ermakov,[6] F. Preusker,[7] P. Schenk,[8] K. A. Otto,[7] H. Hiesinger,[9] D. O'Brien,[4] S. Marchi,[10] H. Sizemore,[4] K. Hughson,[11] H. Chilton,[2] M. Bland,[12] S. Byrne,[13] N. Schorghofer,[14] T. Platz,[15] R. Jaumann,[7] T. Roatsch,[7] M. V. Sykes,[4] A. Nathues,[15] M. C. De Sanctis,[16] C. A. Raymond,[5] C. T. Russell[11]

Analysis of Dawn spacecraft Framing Camera image data allows evaluation of the topography and geomorphology of features on the surface of Ceres. The dwarf planet is dominated by numerous craters, but other features are also common. Linear structures include both those associated with impact craters and those that do not appear to have any correlation to an impact event. Abundant lobate flows are identified, and numerous domical features are found at a range of scales. Features suggestive of near-surface ice, cryomagmatism, and cryovolcanism have been identified. Although spectroscopic analysis has currently detected surface water ice at only one location on Ceres, the identification of these potentially ice-related features suggests that there may be at least some ice in localized regions in the crust.

The Dawn spacecraft (*1*) left Vesta in late 2012 and went into orbit around Ceres on 6 March 2015. Framing Camera (*2*) images were taken during the Approach (1.3 km/pixel), Survey (415 m/pixel), High-Altitude Mapping Orbit (HAMO) (140 m/pixel), and Low-Altitude Mapping Orbit (LAMO) (35 m/pixel) phases of the mission (*3*). Clear filter and color images, together with digital terrain models derived from stereo images, have enabled a three-dimensional characterization of the surface, which we have used to determine whether the geomorphology of Ceres is consistent with models of the dwarf planet having an icy interior (*3*).

Geologic mapping

As was done at Vesta (*4*), a geological mapping campaign was conducted at Ceres. A preliminary geologic map at a scale of 1:10 M was constructed using images obtained during the Approach and Survey orbital phases (Fig. 1). Surface features have been organized into discrete map units that are defined and characterized based on physical attributes such as albedo, morphology, structure, color, and topography. These units were then related to the putative geologic processes that produced them, such as volcanism, tectonism, impact cratering, and/or deposition.

Stereophotogrammetric analysis of Ceres was used in the geologic mapping, and it showed that there is ~15 km of relief (Fig. 2A), referenced to the mean radius, considerably less than the ~41 km of total relief that was observed on Vesta (*5*). Although analysis of the topography suggested that there is no obvious elevation that discriminates between highlands and lowlands, one discrete topographically high region centered at 15°N, 230°E (*3*) was identified and named Hanami Planum (Fig. 2A, white dashed circle).

We used the map to assess the geology of Ceres at the global scale, to identify geomorphic and structural features, and to determine the geologic processes that have affected Ceres globally. Geomorphic features identified on Ceres include impact craters, linear structures, domical features, and lobate flows.

Impact craters

Impact craters are the most prevalent geomorphic feature on Ceres (*6*), and resurfacing appears to be primarily driven by impact (*6*). Regions of low crater density are strongly associated with major craters, such as Urvara, Yalode, and Kerwan (*6*) (Fig. 1). Before Dawn's arrival, it was expected that most craters on Ceres would be relaxed (*7*), but instead there is a large inventory of craters with sharp walls and deep floors (*6*).

To study the dynamic range of the topography of Ceres, we created a hypsogram, which displays the elevation of Ceres plotted against the percentage of surface area at that elevation (Fig. 2). Previously published hypsograms for the rocky planets (Mercury, Venus, Earth, and Mars) have a positive skew because mountainous terrain and in-filled depressions lead to a long tail of positive topography (Fig. 2C). However, the hypsogram of Ceres topography shows a unimodal distribution that skews slightly (–0.17) toward the negative (Fig. 2B). This is similar to the hypsogram for the icy moon Titan, which is also slightly negatively skewed. On Titan, this negative skew was determined to represent a significant population of unfilled depressions (*8*). It is likely that the unexpectedly large inventory of nonrelaxed craters on Ceres similarly skews its hypsogram toward a slightly longer tail of negative topography (Fig. 2B).

Occator crater

A number of small anomalously bright features were observed during the Approach to Ceres. The brightest of these occur in the center and northeastern floor of Occator, a 92-km-diameter crater centered at 19.9°N, 239.1°E, (Fig. 3). The Occator bright spots coincide with one of two longitudes where observations by the Herschel space telescope suggested water vapor emission from Ceres (*9*).

Occator's crater rim is scalloped, with multiple straight segments and several 90° bends, and its walls are terraced (Fig. 3A). The crater has ~4 km of relief from floor to rim (Fig. 3B). A smooth to knobby floor material embays the terraced wall material but is overlain by lobate flows whose margins suggest that they emanate from the center of the crater (Fig. 3C). Many of the bright-spot materials in Occator overlie the lobate flows and are strongly associated with fractures on its floor (Fig. 3, A to C). However, the largest bright spot is associated with a 9-km-wide, ~1-km-deep central pit (*6*, *10*) that has a 2-km-wide, ~400-m-high central dome on its floor (*6*). Similar domes have been identified in large (>60-km diameter) central pit craters on Ganymede and Callisto (*11*); it has been hypothesized that these domes form due either to uplift of the surface during the impact event or to postimpact cryomagmatic intrusions in craters that impacted where target materials were ice-rich (*11*, *12*). The similarity of the morphology of the Occator pit and dome to those seen in impact craters on Ganymede and Callisto implies that similar mechanisms may be operating on these three bodies. Therefore, the association of the most prominent bright spot in Occator with the central structure suggests that either uplift or localized extrusion is involved in bright-spot formation.

Floor-Fractured Craters

Several of the impact craters on Ceres have patterns of fractures on their floors (Figs. 3D and 4). These fractures appear similar to those found within a class of lunar craters referred to as Floor-Fractured Craters (FFCs) (*13*). Lunar FFCs are characterized by crater floors cut by radial, concentric, and/or polygonal fractures (*13*). The depth versus diameter (*d*/*D*) relationship of the FFCs is distinctly shallower than the same association for other lunar craters (*14*). FFCs have been classified into crater classes, Types 1 to 6, based on their morphometric properties (*13*–*15*). Models for FFC formation have invoked both floor uplift due to magmatic intrusion beneath the crater (*13*–*15*) or floor shallowing due to

[1]Johns Hopkins University Applied Physics Laboratory, Laurel, MD 20723, USA. [2]Georgia Institute of Technology, Atlanta, GA 30332, USA. [3]Arizona State University, Tempe, AZ 85287, USA. [4]Planetary Science Institute, Tucson, AZ 85719, USA. [5]NASA Jet Propulsion Laboratory, La Cañada Flintridge, CA 91011, USA. [6]Massachusetts Institute of Technology, Cambridge, MA 02139, USA. [7]German Aerospace Center (DLR), Berlin 12489, Germany. [8]Lunar and Planetary Institute, Houston, TX 77058, USA. [9]Westfälische Wilhelms-Universität Münster, Münster 48149, Germany. [10]Southwest Research Institute, Boulder, CO 80302, USA. [11]University of California, Los Angeles, CA 90095, USA. [12]United States Geological Survey, Flagstaff, AZ 86001, USA. [13]Lunar and Planetary Laboratory, Tucson, AZ 85721, USA. [14]University of Hawaii at Manoa, Honolulu, HI 96822, USA. [15]Max Planck Institute for Solar System Research, Göttingen 37077, Germany. [16]Istituto di Astrofisica e Planetologia Spaziale INAF, Rome 00133, Italy.
*Corresponding author. Email: debra.buczkowski@jhuapl.edu

Downloaded from http://science.sciencemag.org/ on September 1, 2016

viscous relaxation [e.g., (*16*)] to explain their anomalously shallow floors.

FFCs have also been identified on Mars (*17*). Martian FFCs exhibit morphological characteristics similar to the lunar FFCs, but many of their rims have been highly dissected. Analyses suggest that the martian FFCs also formed due to volcanic activity but that the final morphologies were heavily influenced by interactions with groundwater and/or ice (*17*).

As on the Moon, the style of fracturing within Ceres FFCs can vary from crater to crater. We have cataloged the Ceres FFCs according to the classification scheme designed by (*13*) and used by (*14*, *15*). Occator crater has several sets of fractures on its floor, including circumferential fractures encircling the central pit, linear fractures crossing its floor, and circumferential fractures close to the crater wall (Fig. 3D). Dantu crater (126-km diameter) similarly has both circumferential and radial fractures on its floor (Fig. 4A), whereas Azacca crater (49.9-km diameter) has only linear fractures (Fig. 4B). These large (>50 km) craters are most consistent with Type 1 lunar FFCs, which are described as generally large craters with deep floors, central peak complexes, extensive wall terraces, and radial and/or concentric fractures (*13*); they were found to be most consistent with formation by magmatic intrusion (*15*, *16*).

Other craters on Ceres are more consistent with Type 4 FFCs (*13*). These lunar craters are defined by the presence of a V-shaped moat separating the wall scarp from the crater interior. However, there are three subclasses (4a, 4b, and 4c) that differ in the depth of the moat, whether there is an inner ridge associated with the moat, and how pronounced the floor fractures are (*15*). Viscous relaxation models were unable to produce moats of any shape in the crater interiors (e.g., *16*, *18*), but in magmatic intrusion models, a V-shaped moat marks the extent of the subsurface intrusion (*15*). Lociyo crater is representative of a Ceres Type 4b crater. It has a hummocky interior, with subdued grooves instead of sharp fractures (Fig. 4C), and its topographic profile shows V-shaped moats and interior ridges (Fig. 4E).

An analysis of the *d*/*D* ratio of the Ceres FFCs shows that they are anomalously shallow compared with average Ceres craters (Fig. 4D). The shallow *d*/*D* of Ceres FFCs is similar to that observed for the lunar FFCs (*15*) and suggests that these craters may also be experiencing an intrusion of a low-density material from below the craters that has uplifted their floors. Although on the Moon and Mars the intrusive material is hypothesized to be silicate magma, this is unlikely for Ceres. However, a cryovolcanic extrusive edifice has been identified on Ceres (*19*), suggesting that cryomagmatic intrusions could be responsible for the formation of the Ceres FFCs.

Polygonal craters

Polygonal craters, a type of crater whose rims are composed of at least two straight segments, are widespread on Ceres (Fig. 5). These angular craters are commonly found on asteroids, such as Mathilde (*20*), Eros (*21*), and Lutetia (*22*), and have also been identified on icy moons such as Iapetus (*23*) and Dione (*24*). Polygonal craters have been hypothesized to form when preexisting subsurface fracturing affects crater formation (*20*), causing crater rims to form parallel to preexisting planes of weakness (*25*, *26*). Their widespread presence on Ceres suggests that the

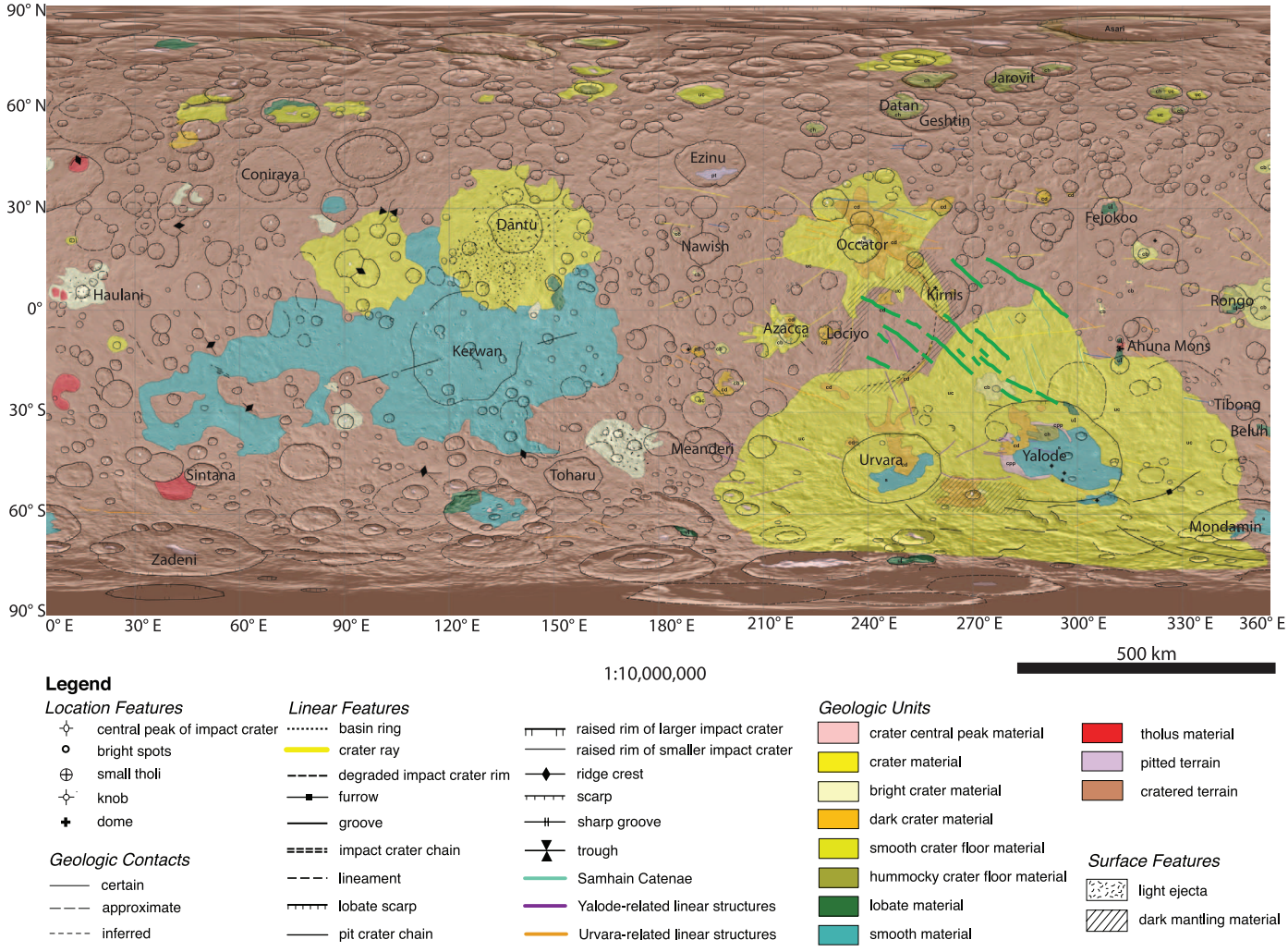


Fig. 1. The geologic map of Ceres based on Survey orbit data. The map, presented at 1:10 M scale, is displayed in simple cylindrical projection, with legend.

Downloaded from http://science.sciencemag.org/ on September 1, 2016

crust is extensively fractured, which in turn suggests that the near-surface crust must be both brittle enough to fracture and strong enough to retain fractures for long periods of time (*3*).

Linear structures

Kilometer-scale linear structures—including grooves, pit crater chains, fractures, and troughs—cross much of Ceres (Figs. 1 and 6). Some of these structures appear to be radial to the large craters Urvara and Yalode (Fig. 6A) and most likely formed due to impact processes. However, a set of regional linear structures named the Samhain Catenae do not have any obvious relationship to impact craters, and a geomorphic analysis suggests that they represent subsurface faults.

The majority of the Samhain Catenae are made up of linear assemblages of small depressions, although there are also some grooves and one large trough identified as belonging to this group of structures. The lack of raised rims on the merged pits of the Samhain Catenae (Fig. 6B) makes it unlikely that these are secondary crater chains (*27*). Instead, the morphology of the Samhain Catenae more closely resembles that of pit crater chains, a type of feature identified on many planetary bodies, including Earth, Mars, Enceladus, Eros, and Vesta (*28*). There is a strong correlation between pit crater chains and fault-bounded graben on Mars (*29*), and they have been hypothesized to represent buried normal faults on a number of small bodies (*28*). The theory suggests that sudden widening (dilation) at steep sections

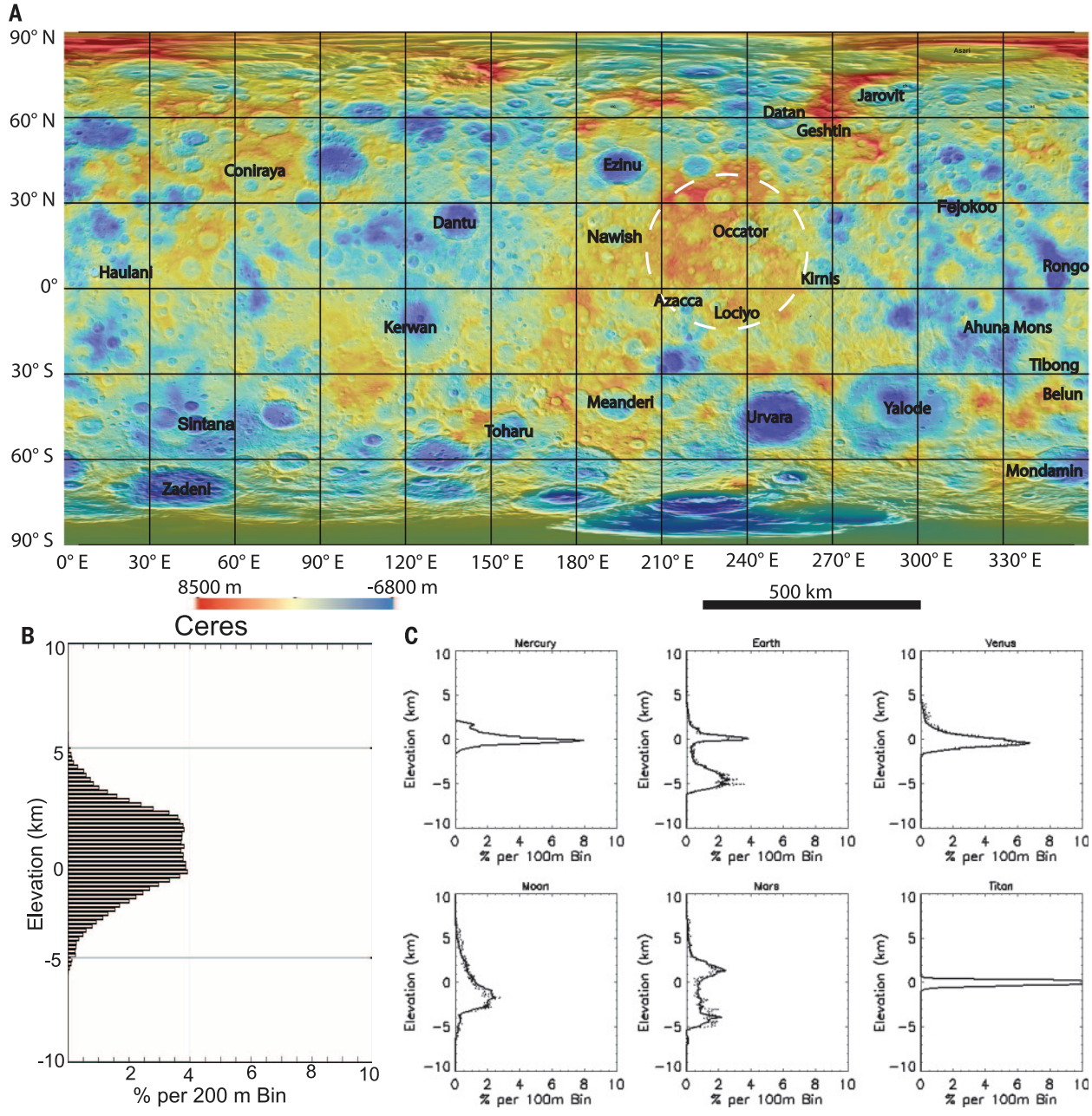


Fig. 2. Ceres topography. (**A**) Stereophotogrammetric digital terrain model of Ceres (displayed in simple cylindrical projection), overlying the Survey global mosaic. Heights are relative to the triaxial ellipsoid dimensions (482 by 482 by 446 km). The white dashed circle outlines Hanami Planum. (**B**) The Ceres hypsogram, which shows elevations as height above the equipotential surface of Ceres as determined by the gravity field (CERES 18b, truncated at degree 11). The standard deviation is 1.842 km, the skewness is −0.17, and the kurtosis is 2.65. The curve has a slightly longer tail in the negative direction. (**C**) Hypsograms of Mercury, Venus, Earth, Mars, the Moon, and Titan from (*8*), for comparison. Only Earth and Mars have bimodal distributions. Most hypsograms have a positive skew, with a long tail in the positive direction. Only Titan shows a negative skew, similar to that found for Ceres.

Downloaded from http://science.sciencemag.org/ on September 1, 2016

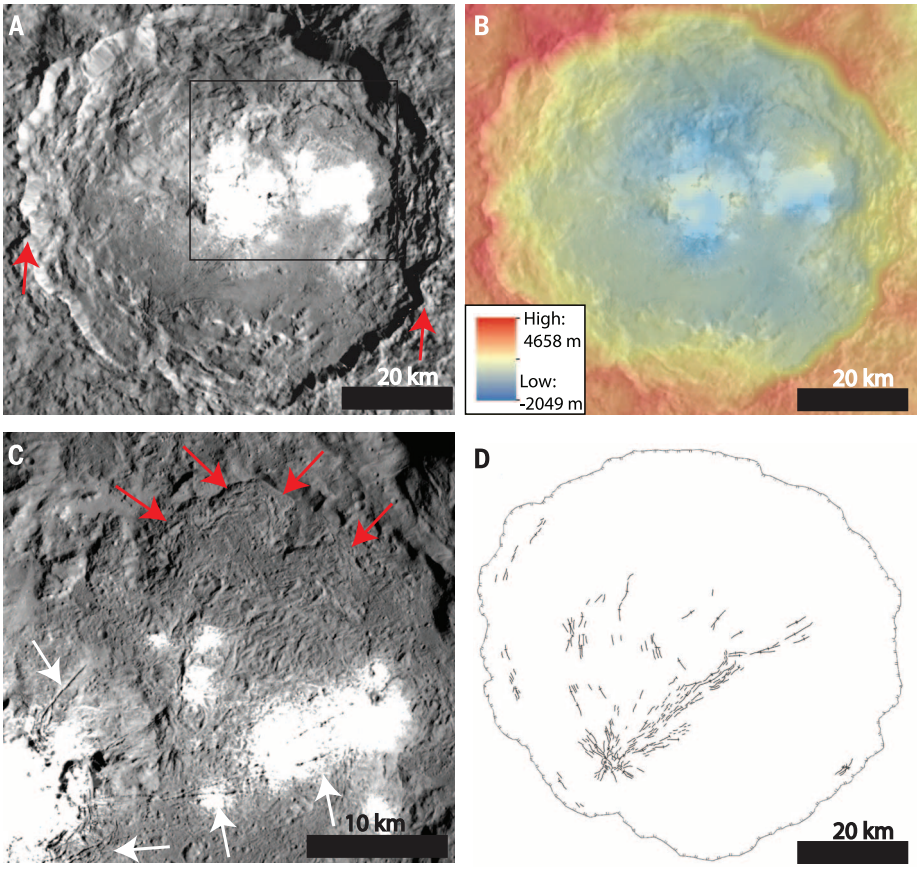


Fig. 3. Occator crater. (**A**) HAMO mosaic of Occator crater (140 m/pixel). North is up. Inset shows location of (C). Red arrows point to 90° bends in the crater rim. (**B**) HAMO topography of Occator overlain on the HAMO mosaic. (**C**) LAMO resolution (35 m/pixel) mosaic of the lobate flows in Occator. Red arrows point to flow margins. White arrows point to fractures on the crater floor. (**D**) Map of the fractures on the floor of Occator. The crater rim is outlined.

of the buried fault causes overlying material to collapse into the openings along its length (*29*). The individual pits can then merge together to form merged pits, and eventually grooves, as the feature matures (*29*). This maturation of pit crater chains is a probable cause for the occasional groove and merged pits found among the Samhain Catenae (Fig. 6B).

Polygonal craters in close proximity to the Samhain Catenae have straight crater rims aligned with the grooves and troughs (Fig. 5). This alignment supports our inference that the Samhain Catenae are in fact fracture systems, not ejecta scour or secondary craters. The orientation of the Samhain Catenae relative to each other is suggestive of en echelon fractures; many of the longer Samhain Catenae are made up of smaller structures that have joined together via S-shaped linkages (Fig. 6B). A cross section of one Samhain Catena structure is displayed in the wall of Occator crater, at the locations where the crater rim suddenly bends 90° in both the western and eastern walls of the crater (Figs. 3A and 6C). Profile views of the Occator wall at these locations suggest that (i) the structure dips ~60° and (ii) there is downward motion on the hanging wall, strongly implying normal faulting. Many of the Samhain Catenae are crosscut by the linear features radial to Urvara and Yalode (Fig. 6A), indicating that they are older than fractures formed during those impact events.

By mapping the Samhain Catenae directly onto the Ceres shape model and modeling them as planes that cut through the dwarf planet, we were able to determine an approximate strike and dip for the underlying faults by plotting the pole directions of the modeled planes on a lower-hemisphere graph (a stereonet) (Fig. 6D). Clustering of the pole directions (Fig. 6D) suggests that the

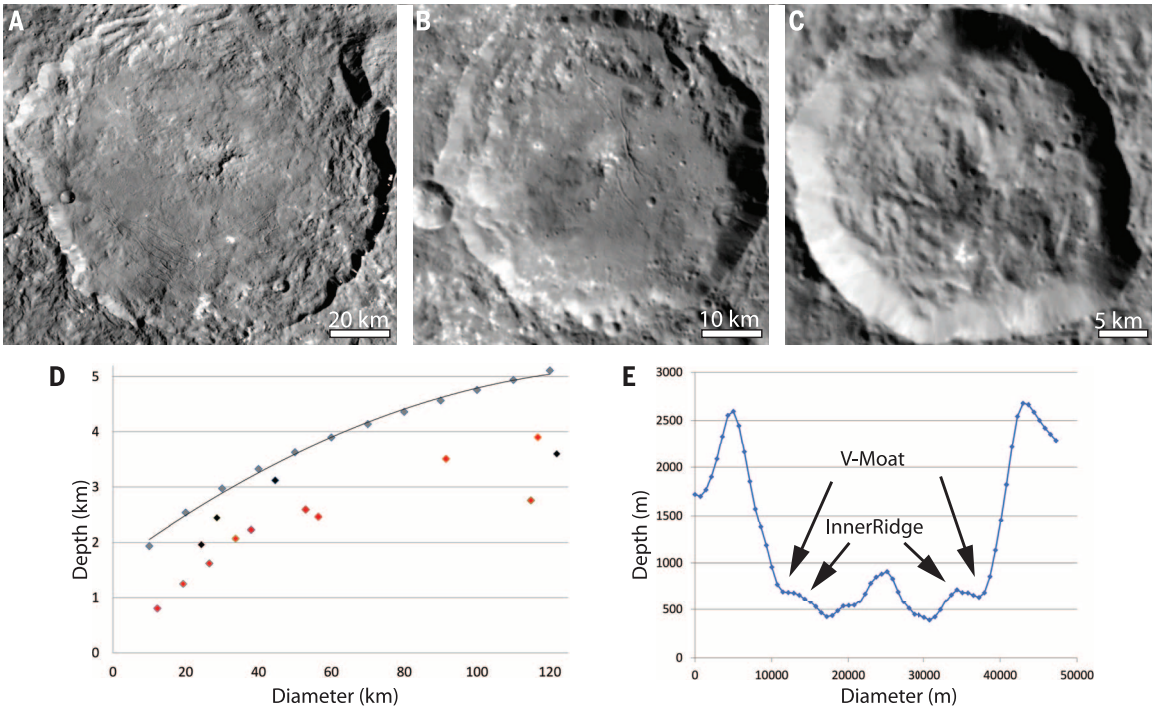


Fig. 4. FFCs. HAMO mosaics (140 m/pixel) of (**A**) Dantu crater, (**B**) Azacca crater, and (**C**) Lociyo crater. (**D**) Depth-to-diameter ratio of the FFCs currently identified on Ceres. Red dots are FFCs on Hanami Planum; black dots represent FFCs located elsewhere on Ceres. The black line is a second-order polynomial fit to the depth-to-diameter ratio for the average Ceres crater, as derived by (*6*). (**E**) The topographic profile of Lociyo crater shows the V-shaped moats and interior ridges characteristic of a Type 4 FFC.

Downloaded from http://science.sciencemag.org/ on September 1, 2016

Samhain Catenae represent similarly oriented planes and implies a common formation mechanism of the corresponding structures. In similar analyses of linear structures on Vesta (*5*) and Eros (*30*), the coordinates of the pole cluster correlated to an impact crater, which was then theorized to have produced the impact stresses that caused the faults to form. However, the poles of the Samhain Catenae do not correspond to any visible impact crater on Ceres, making it unlikely that they formed due to impact stresses.

The extent of the Samhain Catenae is constrained to Hanami Planum (Figs. 1 and 2). This roughly circular, topographically high region, 555 km in diameter, is also the location of many of the currently identified FFCs (Fig. 4, red dots). If we accept that the FFCs have fractured floors due to cryomagmatic intrusion beneath their floors, as is thought for the Moon (*13*–*15*), then it seems reasonable to hypothesize that the high-standing regions that they are predominantly found upon may be elevated due to intrusion of a lower-density material. The uplift of the crust due to this putative intrusion could possibly be responsible for the formation of the Samhain Catenae.

Patterns of smaller-scale linear structures have been identified on the topographic high regions

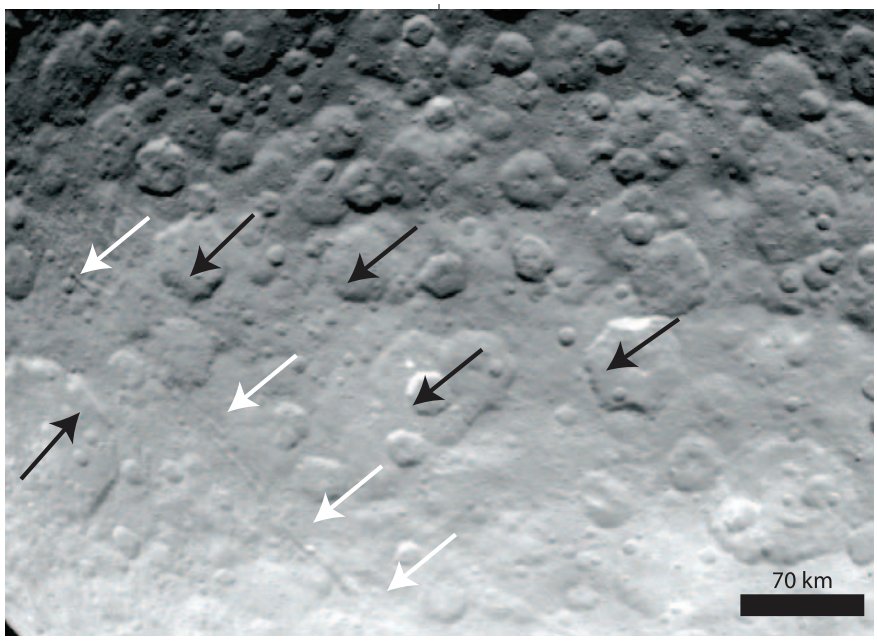


Fig. 5. Polygonal craters. A Survey (415 m/pixel) image of Ceres showing several polygonal craters in the vicinity of kilometer-scale linear structures (white arrows). Black arrows point to the straight rims of polygonal craters that are aligned with the Samhain Catenae.

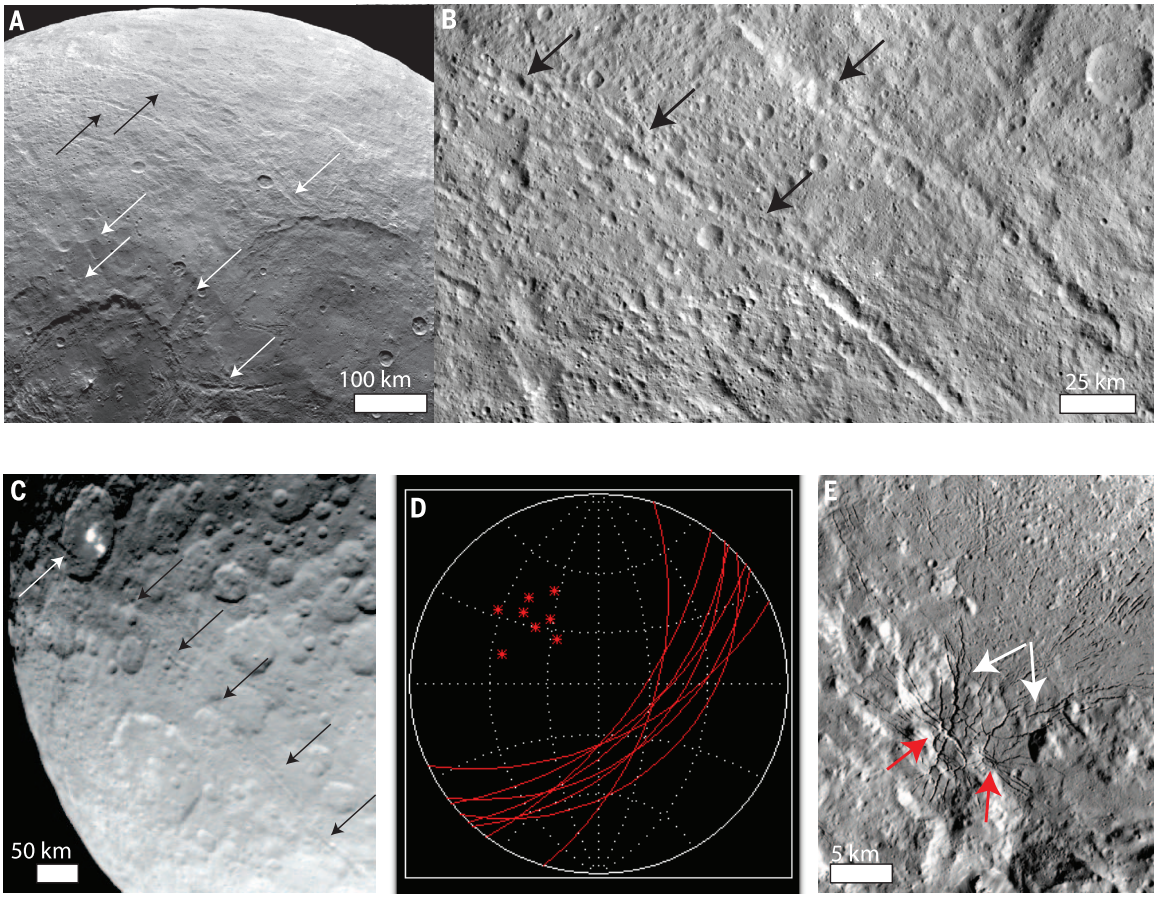


Fig. 6. Regional linear structures. (**A**) Survey image (415 m/pixel) of Urvara (left) and Yalode (right) craters. White arrows point to linear structures radial to the craters. Black arrows point to linear structures in (B). (**B**) HAMO (140 m/pixel) Framing Camera clear-filter image of regional linear structures (north is up). The pits do not have rims, suggesting that these are pit crater chains (PCCs), not impact crater chains. The northernmost PCC deforms the southwestern rim of Kirnis crater. Black arrows point to S-shaped junctions connecting three smaller en echelon structures. (**C**) Survey image (415 m/pixel) of a regional linear structure (black arrows) that cuts the rim of Occator crater (white arrow points to 90° bend in Occator's western rim). (**D**) Stereonet plots of the Samhain Catenae. Pole positions cluster, centered at ~45°N, ~300°E. (**E**) LAMO image (35 m/pixel) of a system of fractures at 16.6°N, 237.1°E that strongly resembles fracturing associated with asymmetric domal uplift.

Downloaded from http://science.sciencemag.org/ on September 1, 2016

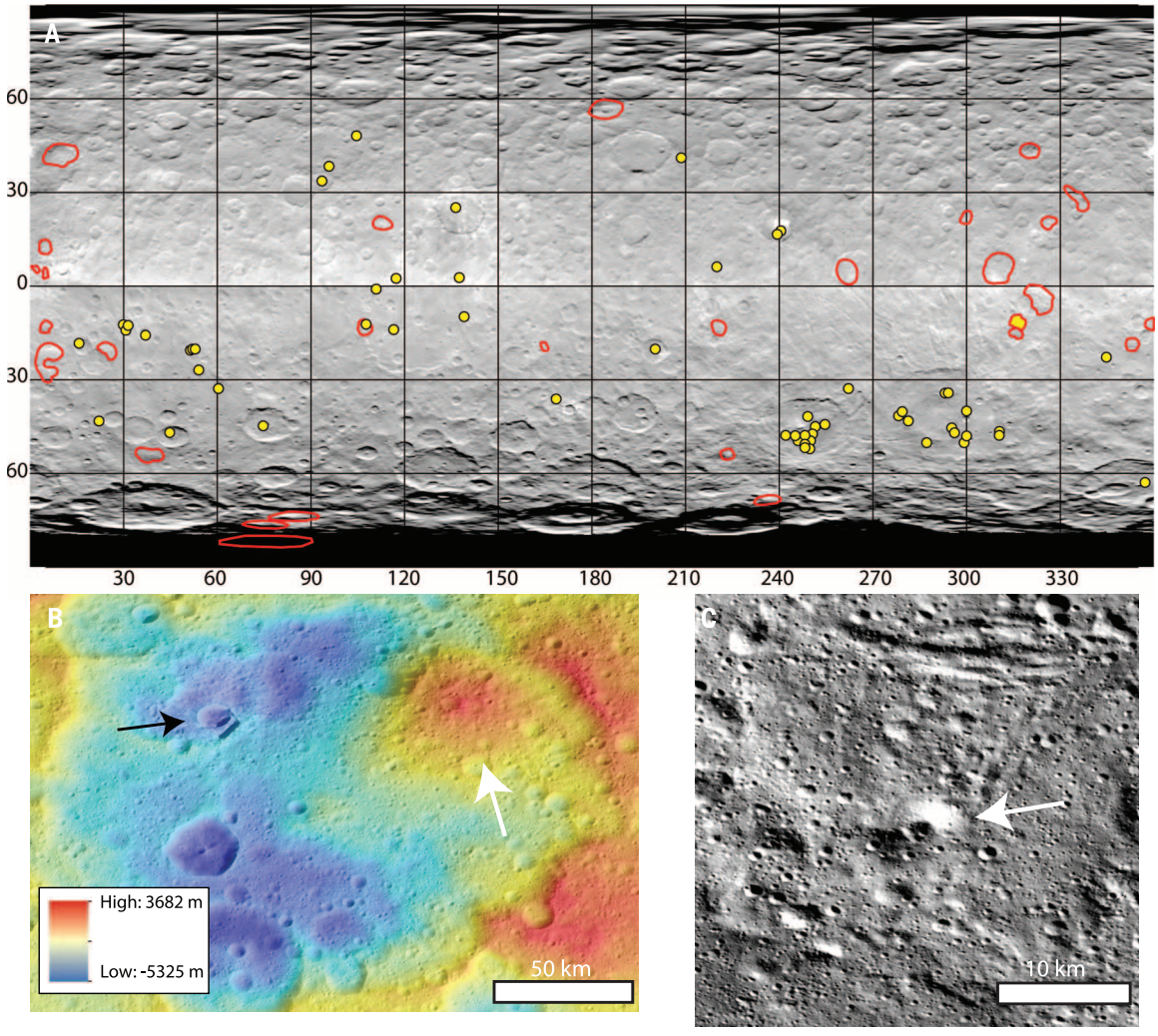


Fig. 7. Domical features on Ceres. (**A**) Global map, based on HAMO (140 m/pixel) grayscale imagery. Large domes are outlined in red; small mounds are marked by yellow dots. Ahuna Mons is the red outline filled in with yellow. (**B**) Color HAMO topography model over HAMO grayscale image of a 53-km dome at 42°N, 10°E, located within an unnamed 135-km crater. The white arrow points to the large dome; the black arrow points to nearby Oxo crater, where surface water ice has been identified (*47*). (**C**) LAMO (35 m/pixel) grayscale image of small mound (white arrow) with a summit pit identified in Yalode crater at 45.5°S, 295.7° E.

near the Samhain Catenae (Fig. 6E), which are consistent with models of asymmetrical domal uplift (*31*). This system shows apparent broad outer arc extension, with at least two central peaks (Fig. 6E, black arrows). Away from these peaks, the fracturing transitions to radial fault patterns, which geological models have shown can occur due to the change in stress orientation that occurs at the edge of a dome (*31*).

Similar structures form on the surface of salt domes on Earth (*31*). Terrestrial salt domes form when layers of evaporite minerals are buried under a denser overburden material; salts are buoyant under these conditions and can intrude into the overlying rock strata (*32*). Differential loading of the overburden material is a driving force in terrestrial salt tectonics, but thick layers of either the cover material or the salt itself are not necessarily required (*33*). Instead, salt flow can occur where there is a laterally varying (*32*), or even a thin (*33*), overburden thickness. The growth of the salt diapirs then creates pressure on the surface materials, deforming the overlying material. Where the salt extrudes onto the surface, lobate flows can form.

Salt tectonics is at least theoretically possible on Ceres. Layers of salt have long been hypothesized to exist deep within the so-called ocean worlds (*34*–*37*), which include Ceres (*34*). Compositional upwelling similar to terrestrial salt dome formation has even been hypothesized to occur (*35*). The interior of Ceres has been determined to contain a silicate core, a water-rich mantle, and a mechanically strong crust (*3*). The main components of the crust were determined to be rock, ice, and salt hydrates (*3*), including carbonates (*38*), ammoniated phyllosilicates (*38*, *39*), and a dark material that is thought to be magnetite (*38*). Although these crustal materials are not particularly dense, the putative subsurface salts would have even lower densities (*28*), and so salt diapirism could potentially occur. The structure patterns identified on the surface of Ceres (Fig. 6E), while not exclusively indicative of salt upwelling, are certainly suggestive of it.

Domes and mounds

Domical features on Ceres fall into two broad classes: large domes that are 10s to 100s of kilometers in diameter, with heights 1 to 5 km, and small mounds <10 km in diameter exhibiting subkilometer relief (Fig. 7). However, whether or not a single formation mechanism is responsible for their formation is still an open question. The 28 large domes identified in HAMO images are circular to ovoid in plan form, are 30 to 100 km in diameter, and typically exhibit 2 to 5 km of relief (Fig. 7B). They are commonly, but not exclusively, located in large impact basins. Detailed geomorphic analysis and physical modeling of the 4-km-high Ahuna Mons suggest that this large dome is most likely a cryovolcanic edifice formed by the extrusion of a viscous water-ice-silicate mixture (*19*). The other large domical features (Fig. 7A, red outlines) are suggested to also be cryovolcanic in nature, although perhaps of a different age and/or rheology (*19*).

Of the ~200 small mounds identified (Fig. 7A, yellow dots), many are located preferentially in smooth regions associated with impact materials. These mounds are thus most likely impact debris, or possibly preexisting topography embayed or draped by smooth material, analogous to mounds observed in lunar-impact melt sheets. Early analysis of these features was motivated by the expectation that localized cryovolcanic activity or frost-heave phenomena might occur in crater interiors soon after impact if Ceres' shallow subsurface were ice-rich. So far there is little morphological evidence that these features are genetically related to ice, although there are individual small

Downloaded from http://science.sciencemag.org/ on September 1, 2016

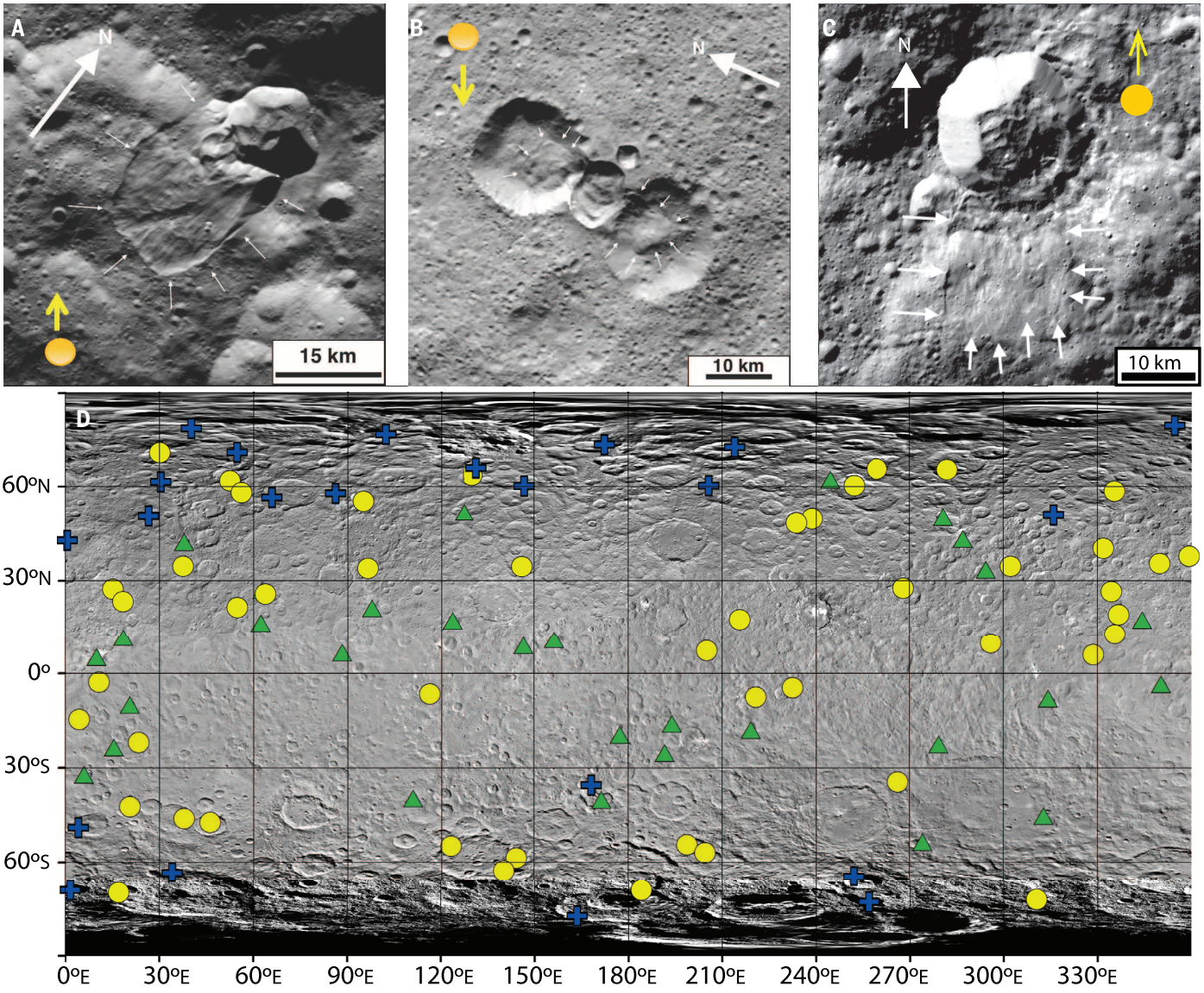


Fig. 8. Lobate flows on Ceres. White arrows point to flow margins. Yellow arrows point away from the Sun (yellow dot) in the direction of illumination. (**A**) Type 1 flow. (**B**) Type 2 flow. (**C**) Type 3 flow. (**D**) Location of lobate flows on Ceres. Blue crosses represent Type 1 flows, green triangles are Type 2 flows, and yellow dots are Type 3 flows.

mounds (e.g., Fig. 7C) for which an ice-rich origin cannot be ruled out.

Lobate flows

A range of mass-wasting flows are observed across the surface of Ceres, and differences in their morphology suggest that multiple emplacement processes might be operative. These features, which are always associated, either internally or externally, with the rims of impact craters, are broadly divided into three types, based on their morphology.

Type 1 flows (Fig. 8A) are lobate, have notably steep frontal toes, and are usually >100 m thick at their termini. They are as wide as their source, possessing nested sets of parallel linear furrows 10s of meters deep along the direction of downslope motion and steep-fronted toes with distal ramparts. These lobate flows occur in high-latitude craters and morphologically are similar to ice-cored and ice-cemented flows on Earth (*40*, *41*) and Mars (*42*). Type 1 flows are found typically above 50° latitude (Fig. 8D).

Type 2 flows (Fig. 8B) have long, fan-shaped thin flows that originate at a crater wall. Thinner than Type 1 flows (generally between 10 and 100 m thick at their termini), they traverse generally longer distances despite their shallow slopes. They range from relatively narrow to broad, having conical to lobate shapes, but are always composed of platy sheets with rounded tapered toes. Morphologically, these flows are similar to long-runout landslides found on icy satellites such as Iapetus (*43*). Type 2 flows are found across Ceres but mainly at mid to high latitudes (Fig. 8D).

In Type 3 flows (Fig. 8C), broad sheets of smooth material, which are thinner than Type 1 flows at 10 to 100 m thick at their termini, extend outward from crater rims, terminating in layered sets of lobes or cusps. Their acute triangular lobes, absence of deep furrows, and textures—relatively smooth surfaces interspersed with hummocky regions—are similar to the morphology of fluidized ejecta blankets of rampart craters on Mars [e.g., (*44*, *45*)] and Ganymede (*46*), features that are commonly thought to form by impact into ice-rich ground. Type 3 flows are found in low to mid latitudes (Fig. 8D) and are wider than Type 2 flows.

Discussion and conclusions

The lack of a large inventory of relaxed craters on Ceres suggests that its crust is too strong to be dominated by ice (*3*, *6*, *7*). Similarly, the presence of ancient surface fractures, and extensive subsurface fracturing (as demonstrated by the widespread distribution of polygonal craters), is more consistent with a mechanically strong crust, not

Downloaded from http://science.sciencemag.org/ on September 1, 2016

an ice-dominated crust (*3*). These observations are consistent with spectroscopic analyses that have currently identified surface water ice at only one location on Ceres (*47*). However, studies have shown that a crust strong enough for both negligible crater relaxation and the preservation of linear structures could be provided by a mixture of ice, rock, and/or salt hydrates (*48*).

The identification of potentially ice-related geomorphic features suggests that there may be some ice in localized regions in the crust on Ceres. Global mapping of the lobate flows shows that there is a latitudinal trend in the distribution of the observed type morphologies (Fig. 8D). This, along with their morphologic similarity to features that form on other planetary bodies by varying ice-related processes, suggests that the differences in lobate flow morphology might be explained by variations in ice content and temperature in the near surface.

Likewise, there is geomorphic evidence that the interior of Ceres is ice-rich, as models (*3*) have suggested. Geomorphic and topographic analyses of the FFCs suggest that cryomagmatism has been active on Ceres. The central dome on the floor of Occator crater also indicates that cryomagmatism may have occurred. In addition, Ahuna Mons and the other large domes appear to be cryovolcanic in nature (*19*).

In conclusion, although the observed geomorphic features are not consistent with an ice-dominated crust, they are consistent with Ceres having an ice-rich upper mantle and a crust that is composed of a rock-ice mixture.

REFERENCES AND NOTES

1. C. T. Russell, C. A. Raymond, The Dawn mission to Vesta and Ceres. *Space Sci. Rev.* **163**, 3–23 (2011). doi: 10.1007/s11214-011-9836-2
2. H. Sierks *et al*., The Dawn Framing Camera. *Space Sci. Rev.* **163**, 263–327 (2011). doi: 10.1007/s11214-011-9745-4
3. C. T. Russell *et al*., Dawn arrives at Ceres: Exploration of a small, volatile-rich world. *Science* **353**, 1008–1010 (2016).
4. R. A. Yingst *et al*., Geologic mapping of Vesta. *Planet. Space Sci.* **103**, 2–23 (2014). doi: 10.1016/j.pss.2013.12.014
5. R. Jaumann *et al*., Vesta's shape and morphology. *Science* **336**, 687–690 (2012). doi: 10.1126/science.1219122; pmid: 22582254
6. H. Hiesinger *et al*., Cratering on Ceres: Implications for its crust and evolution. *Science* **353**, aaf4759 (2016).
7. M. T. Bland, Predicted crater morphologies on Ceres: Probing internal structure and evolution. *Icarus* **226**, 510–521 (2013). doi: 10.1016/j.icarus.2013.05.037
8. R. D. Lorenz *et al*., Hypsometry of Titan. *Icarus* **211**, 699–706 (2011). doi: 10.1016/j.icarus.2010.10.002
9. M. Küppers *et al*., Localized sources of water vapour on the dwarf planet (1) Ceres. *Nature* **505**, 525–527 (2014). doi: 10.1038/nature12918; pmid: 24451541
10. A. Nathues *et al*., Sublimation in bright spots on (1) Ceres. *Nature* **528**, 237–240 (2015). doi: 10.1038/nature15754; pmid: 26659183
11. P. M. Schenk, Central pit and dome craters: Exposing the interiors of Ganymede and Callisto. *J. Geophys. Res.* **98** (E4), 7475–7498 (1993). doi: 10.1029/93JE00176
12. V. J. Bray, P. M. Schenk, H. J. Melosh, J. V. Morgan, G. S. Collins, Ganymede crater dimensions – Implications for central peak and central pit formation and development. *Icarus* **217**, 115–129 (2012). doi: 10.1016/j.icarus.2011.10.004
13. P. H. Schultz, Floor-fractured lunar craters. *Moon* **15**, 241–273 (1976). doi: 10.1007/BF00562240
14. L. M. Jozwiak, J. W. Head, M. T. Zuber, D. E. Smith, G. A. Neumann, Lunar floor-fractured craters: Classification, distribution, origin and implications for magmatism and shallow crustal structure. *J. Geophys. Res.* **117**, 2012JE004134 (2012). doi: 10.1029/2012JE004134
15. L. M. Jozwiak, J. W. Head, L. Wilson, Lunar floor-fractured craters as magmatic intrusions: Geometry, modes of emplacement, associated tectonic and volcanic features, and implications for gravity anomalies. *Icarus* **248**, 424–447 (2015). doi: 10.1016/j.icarus.2014.10.052
16. J. L. Hall, S. C. Solomon, J. W. Head, Lunar floor-fractured craters: Evidence of viscous relaxation of crater topography. *J. Geophys. Res.* **86** (B10), 9537–9552 (1981). doi: 10.1029/JB086iB10p09537
17. M. Bamberg, R. Jaumann, H. Asche, T. Kneissl, G. G. Michael, Floor-fractured craters on Mars – Observation and origin. *Planet. Space Sci.* **98**, 146–162 (2014). doi: 10.1016/j.pss.2013.09.017
18. A. J. Dombard, J. Gillis, Testing the viability of topographic relaxation as a mechanism for the formation of lunar floor-fractured craters. *J. Geophys. Res.* **106** (E11), 27901–27909 (2001). doi: 10.1029/2000JE001388
19. O. Ruesch *et al*., Cryovolcanism on Ceres. *Science* **353**, aaf4286 (2016).
20. P. C. Thomas *et al*., Mathilde: Size, shape and geology. *Icarus* **140**, 17–27 (1999). doi: 10.1006/icar.1999.6121
21. L. Prockter *et al*., Surface expressions of structural features on Eros. *Icarus* **155**, 75–93 (2002). doi: 10.1006/icar.2001.6770
22. M. Massironi *et al*., Geological map and stratigraphy of asteroid 21 Lutetia. *Planet. Space Sci.* **66**, 125–136 (2012). doi: 10.1016/j.pss.2011.12.024
23. C. C. Porco *et al*., Cassini imaging science: Initial results on Phoebe and Iapetus. *Science* **307**, 1237–1242 (2005). doi: 10.1126/science.1107981; pmid: 15731440
24. C. B. Beddingfield, D. M. Burr, L. T. Tran, Polygonal impact craters on Dione: Evidence for tectonic structures outside the wispy terrain. *Icarus* **274**, 163–194 (2016). doi: 10.1016/j.icarus.2016.03.020
25. D. T. Eppler, R. Ehrlich, D. Nummedal, P. H. Schultz, Sources of shape variation in lunar impact craters – Fourier shape analysis. *Geol. Soc. Am. Bull.* **94**, 274–291 (1983). doi: 10.1130/0016-7606(1983)94<274:SOSVIL>2.0.CO;2
26. T. Öhman, M. Aittola, V.-P. Kostama, J. Raitala, J. Korteniemi, Polygonal impact craters in Argyre region Mars: Implications for geology and cratering mechanics. *Meteorit. Planet. Sci.* **43**, 1605–1628 (2008). doi: 10.1111/j.1945-5100.2008.tb00632.x
27. V. R. Oberbeck, R. H. Morrison, Laboratory simulation of the herringbone pattern associated with lunar secondary crater chains. *Moon* **9**, 415–455 (1974). doi: 10.1007/BF00562581
28. D. L. Buczkowski, D. Y. Wyrick, Tectonism and magmatism identified on asteroids. *Geol. Soc. Lond. Spec. Publ.* **401**, 423–441 (2014). doi: 10.1144/SP401.18
29. D. Y. Wyrick, D. A. Ferrill, A. P. Morris, S. L. Colton, D. W. Sims, Distribution, morphology, and origins of martian pit crater chains. *J. Geophys. Res.* **109**, E06005 (2004). doi: 10.1029/2004JE002240
30. D. L. Buczkowski, O. S. Barnouin-Jha, L. M. Prockter, 433 Eros lineaments: Global mapping and analysis. *Icarus* **193**, 39–52 (2008). doi: 10.1016/j.icarus.2007.06.028
31. D. W. Sims *et al*., Analog modeling of normal faulting above Middle East domes during regional extension. *Am. Assoc. Pet. Geol. Bull.* **97**, 877–898 (2013).
32. M. R. Hudec, M. P. A. Jackson, Terra infirma: Understanding salt tectonics. *Earth Sci. Rev.* **82**, 1–28 (2007). doi: 10.1016/j.earscirev.2007.01.001
33. J.-P. Brun, X. Fort, Salt tectonics and passive margins: Geology versus models. *Mar. Pet. Geol.* **28**, 1123–1145 (2011). doi: 10.1016/j.marpetgeo.2011.03.004
34. J. C. Castillo-Rogez, T. B. McCord, Ceres' evolution and present state constrained by shape data. *Icarus* **205**, 443–459 (2010). doi: 10.1016/j.icarus.2009.04.008
35. J. S. Kargel *et al*., Europa's crust and ocean: Origin, composition and the prospects for life. *Icarus* **148**, 226–265 (2000). doi: 10.1006/icar.2000.6471
36. N. A. Spaun, J. W. Head III, A model of Europa's crustal structure: Recent Galileo results and implications for an ocean. *J. Geophys. Res.* **106** (E4), 7567–7576 (2001). doi: 10.1029/2000JE001270
37. M. Y. Zolotov, An oceanic composition on early and today's Enceladus. *Geophys. Res. Lett.* **34**, 2007GL031234 (2007). doi: 10.1029/2007GL031234
38. M. C. De Sanctis *et al*., Ammoniated phyllosilicates with a likely outer solar system origin on (1) Ceres. *Nature* **528**, 241–244 (2015). doi: 10.1038/nature16172; pmid: 26659184
39. E. Ammannito *et al*., Distribution of phyllosilicates on Ceres. *Science* **353**, aaf4279 (2016).
40. S. E. White, Rock glaciers and block fields, review and new data. *Quat. Res.* **6**, 77–97 (1976). doi: 10.1016/0033-5894(76)90041-7
41. O. Humlum, The geomorphic significance of rock glaciers: Estimates of rock glacier debris volumes and headwall recession rates in West Greenland. *Geomorphology* **35**, 41–67 (2000). doi: 10.1016/S0169-555X(00)00022-2
42. J. W. Holt *et al*., Radar sounding evidence for buried glaciers in the southern mid-latitudes of Mars. *Science* **322**, 1235–1238 (2008). doi: 10.1126/science.1164246; pmid: 19023078
43. K. N. Singer, W. B. McKinnon, P. M. Schenk, J. M. Moore, Massive ice avalanches on Iapetus mobilized by friction reduction during flash heating. *Nat. Geosci.* **5**, 574–578 (2012). doi: 10.1038/ngeo1526
44. M. H. Carr *et al*., Martian impact craters and emplacement of ejecta by surface flow. *J. Geophys. Res.* **82**, 4055–4065 (1977). doi: 10.1029/JS082i028p04055
45. L. E. Senft, S. T. Stewart, Impact crater formation into icy layered terrains on Mars. *Met. Planet. Sci.* **43**, 1993–2013 (2008). doi: 10.1111/j.1945-5100.2008.tb00657.x
46. J. Boyce, N. Barlow, P. Mouginis-Mark, S. Stewart, Rampart craters on Ganymede: Their implications for fluidized ejecta emplacement. *Met. Planet. Sci.* **45**, 638–661 (2010). doi: 10.1111/j.1945-5100.2010.01044.x
47. J.-Ph. Combe *et al*., Detection of local H_2O exposed at the surface of Ceres. *Science* **353**, aaf3010 (2016).
48. W. B. Durham, S. H. Kirby, L. A. Stern, Effects of dispersed particulates on the rheology of water ice at planetary conditions. *J. Geophys. Res.* **97**, 20883–20897 (1992). doi: 10.1029/92JE02326

ACKNOWLEDGMENTS

We thank the Dawn Operations team, the Flight team, and the Instrument teams for all their work. M.B. and N.S. thank NASA's Dawn at Ceres Guest Investigator Program for support. Dawn data are archived with the NASA Planetary Data System. (http://pds-smallbodies.astro.umd.edu/data_sb/missions/dawn/index.shtml). D.L.B. wrote the manuscript and coordinated coauthor contributions; performed the analysis of linear structures, Occator structures, and FFCs; and participated in the geologic mapping. B.E.S. led the Ground Ice Working group and the analysis of lobate flows. D.A.W., S.C.M., and J.E.C.S. participated in the Survey global geologic map. A.I.E. evaluated the Ceres hypsogram, and F.P. worked on the Ceres topography. P.S., K.A.O., H.H., D.O., S.M., and T.P. all contributed to the evaluation of Ceres craters. P.S. led the study of Occator's central dome and its similarity to central domes on other icy bodies. H.S. mapped the global extent of domes, and K.H. mapped the global extent of lobate flows. H.C., S.B., M.B., H.S., and T.P. participated in the evaluation of potential ice-cored features. R.J., T.R., M.V.S., A.N., M.C.D.S., and C.A.R. provided useful comments and suggestions during manuscript preparation. C.T.R. is the mission principal investigator and guided the research.

SUPPLEMENTARY MATERIALS

www.sciencemag.org/content/353/6303/aaf4332/suppl/DC1
Figs. S1 to S3

6 February 2016; accepted 22 July 2016
10.1126/science.aaf4332

Downloaded from http://science.sciencemag.org/ on September 1, 2016

RESEARCH ARTICLE SUMMARY

PLANETARY SCIENCE

Cryovolcanism on Ceres

O. Ruesch,* T. Platz, P. Schenk, L. A. McFadden, J. C. Castillo-Rogez, L. C. Quick, S. Byrne, F. Preusker, D. P. O'Brien, N. Schmedemann, D. A. Williams, J.-Y. Li, M. T. Bland, H. Hiesinger, T. Kneissl, A. Neesemann, M. Schaefer, J. H. Pasckert, B. E. Schmidt, D. L. Buczkowski, M. V. Sykes, A. Nathues, T. Roatsch, M. Hoffmann, C. A. Raymond, C. T. Russell

INTRODUCTION: Classic volcanism prevalent on terrestrial planets and volatile-poor protoplanets, such as asteroid Vesta, is based on silicate chemistry and is often expressed by volcanic edifices (unless erased by impact bombardment). In ice-rich bodies with sufficiently warm interiors, cryovolcanism involving liquid brines can occur. Smooth plains on some icy satellites of the outer solar system have been suggested as possibly cryovolcanic in origin. However, evidence for cryovolcanic edifices has proven elusive. Ceres is a volatile-rich dwarf planet with an average equatorial surface temperature of ~160 K. Whether this small (~940 km diameter) body without tidal dissipation could sustain cryovolcanism has been an open question because the surface landforms and relation to internal activity were unknown.

RATIONALE: The Framing Camera onboard the Dawn spacecraft has observed >99% of Ceres' surface at a resolution of 35 m/pixel at visible wavelengths. This wide coverage and resolution were exploited for geologic mapping and age determination. Observations with a resolution of 135 m/pixel were obtained under several different viewing geometries. The stereo-photogrammetric method applied to this data set allowed the calculation of a digital terrain model, from which morphometry was investigated. The observations revealed a 4-km-high topographic relief, named Ahuna Mons, that is consistent with a cryovolcanic dome emplacement.

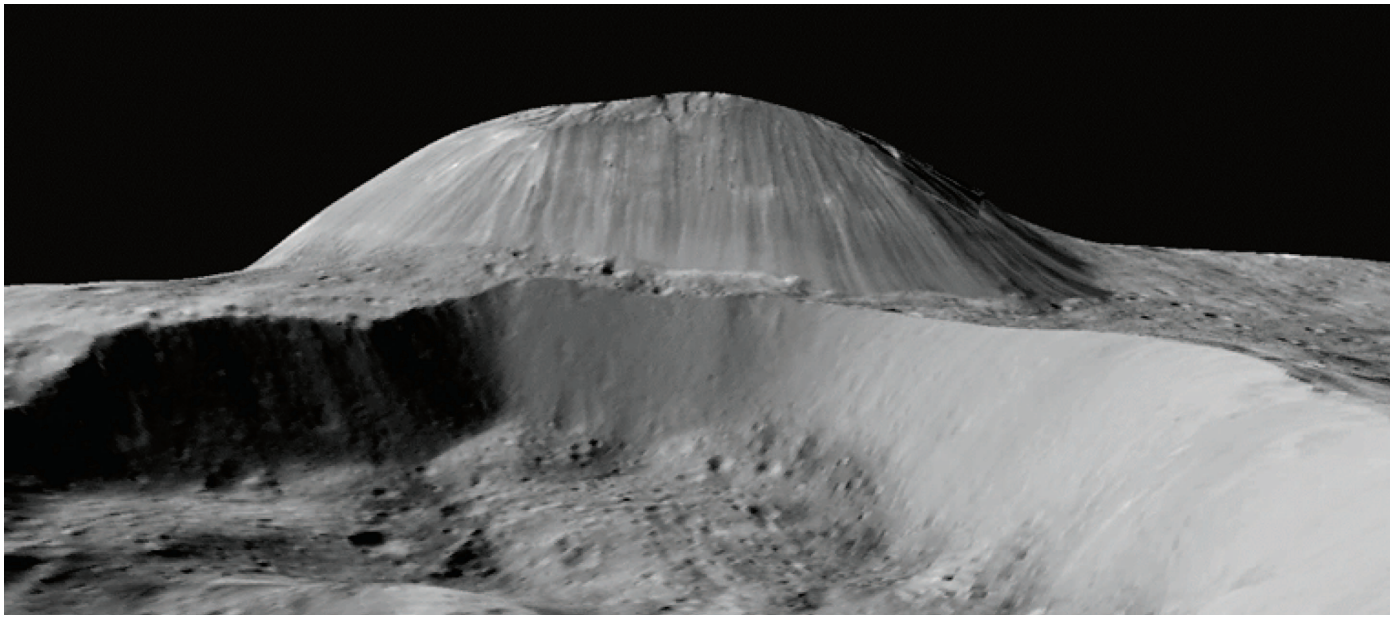
RESULTS: The ~17-km-wide and 4-km-high Ahuna Mons has a distinct size, shape, and morphology. Its summit topography is concave downward, and its flanks are at the angle of repose. The morphology is characterized by (i) troughs, ridges, and hummocky areas at the summit, indicating multiple phases of activity, such as extensional fracturing, and (ii) downslope lineations on the flanks, indicating rockfalls and accumulation of slope debris. These morphometric and morphologic observations are explained by the formation of a cryovolcanic dome, which is analogous to a high-viscosity silicic dome on terrestrial planets. Models indicate that extrusions of a highly viscous melt-bearing material can lead to the buildup of a brittle carapace at the summit, enclosing a ductile core. Partial fracturing and disintegration of the carapace generates slope debris, and relaxation of the dome's ductile core due to gravity shapes the topographic profile of the summit. Modeling of this final phase of dome relaxation and reproduction of the topographic profile requires an extruded material of high viscosity, which is consistent with the mountain's morphology. We constrained the age of the most recent activity on Ahuna Mons to be within the past 210 ± 30 million years.

ON OUR WEBSITE

Read the full article at http://dx.doi.org/10.1126/science.aaf4286

CONCLUSION: Cryovolcanic activity during the geologically recent past of Ceres constrains its thermal and chemical history. We propose that hydrated salts with low eutectic temperatures and low thermal conductivities enabled the presence of cryomagmatic liquids within Ceres. These salts are the product of global aqueous alteration, a key process for Ceres' evolution as recorded by the aqueously altered, secondary minerals observed on the surface. ■

The list of author affiliations is available in the full article online.
*Corresponding author. Email: ottaviano.ruesch@nasa.gov
Cite this article as O. Ruesch *et al.*, *Science* 353, aaf4286 (2016). DOI: 10.1126/science.aaf4286



Perspective view of Ahuna Mons on Ceres from Dawn Framing Camera data (no vertical exaggeration). The mountain is 4 km high and 17 km wide in this south-looking view. Fracturing is observed on the mountain's top, whereas streaks from rockfalls dominate the flanks.

Downloaded from http://science.sciencemag.org/ on September 1, 2016

RESEARCH ARTICLE

PLANETARY SCIENCE

Cryovolcanism on Ceres

O. Ruesch,[1]* T. Platz,[2] P. Schenk,[3] L. A. McFadden,[4] J. C. Castillo-Rogez,[5] L. C. Quick,[6] S. Byrne,[7] F. Preusker,[8] D. P. O'Brien,[6] N. Schmedemann,[9] D. A. Williams,[10] J.-Y. Li,[6] M. T. Bland,[11] H. Hiesinger,[12] T. Kneissl,[9] A. Neesemann,[9] M. Schaefer,[2] J. H. Pasckert,[12] B. E. Schmidt,[13] D. L. Buczkowski,[14] M. V. Sykes,[6] A. Nathues,[2] T. Roatsch,[8] M. Hoffmann,[2] C. A. Raymond,[5] C. T. Russell[15]

Volcanic edifices are abundant on rocky bodies of the inner solar system. In the cold outer solar system, volcanism can occur on solid bodies with a water-ice shell, but derived cryovolcanic constructs have proved elusive. We report the discovery, using Dawn Framing Camera images, of a landform on dwarf planet Ceres that we argue represents a viscous cryovolcanic dome. Parent material of the cryomagma is a mixture of secondary minerals, including salts and water ice. Absolute model ages from impact craters reveal that extrusion of the dome has occurred recently. Ceres' evolution must have been able to sustain recent interior activity and associated surface expressions. We propose salts with low eutectic temperatures and thermal conductivities as key drivers for Ceres' long-term internal evolution.

The nature of Ceres' landforms and their relation to potential interior activity were unknown until the arrival of NASA's Dawn spacecraft in March 2015 (*1*). Ceres has a silicate interior overlain by an outer layer rich in volatiles (*1*, *2*) and a regolith bearing carbonates and phyllosilicates (*3*). Annual average surface temperature at the equator is ~160 K (*4*). Volcanism involving melt composed mostly of brines and other volatiles has been suggested on a theoretical basis for that type of body (*5*), differing from that of silicate volcanism on terrestrial planets. Some icy satellites of the outer solar system have surfaces dominated by plains of probable cryovolcanic origin (*6*–*8*). Evidence for cryovolcanic extrusive edifices such as volcanoes or domes remains elusive, however (*9*–*11*). The Dawn Framing Camera (FC) (*12*) acquired multiband visible images at a resolution of 35 m/pixel, covering >99% of Ceres' surface. A digital terrain model was calculated from stereophotogrammetry at a resolution of 205 m/pixel (Materials and methods). An isolated mountain, named Ahuna Mons [centered at 10.3°S, 316.2°E, (*1*)], has been identified (Fig. 1). Topographic rises broader than Ahuna Mons are common on Ceres (*13*), but the mountain is distinct in its size, shape, and morphology.

[1]NASA Goddard Space Flight Center/Universities Space Research Association (USRA), Greenbelt, MD, USA. [2]Max Planck Institute for Solar System Research, Göttingen, Germany. [3]Lunar and Planetary Science Institute, Houston, TX, USA. [4]NASA Goddard Space Flight Center, Greenbelt, MD, USA. [5]Jet Propulsion Laboratory, California Institute of Technology, Pasadena, CA, USA. [6]Planetary Science Institute, Tucson, AZ, USA. [7]Lunar and Planetary Laboratory, University of Arizona, Tucson, AZ, USA. [8]German Aerospace Center (DLR), Berlin, Germany. [9]Institute of Geosciences, Freie Universität Berlin, Berlin, Germany. [10]School of Earth and Space Exploration, Arizona State University, Tempe, AZ, USA. [11]U.S. Geological Survey, Astrogeology Science Center, Flagstaff, AZ, USA. [12]Institut für Planetologie, Westfälische Wilhelms-Universität, Münster, Germany. [13]Georgia Institute of Technology, Atlanta, GA, USA. [14]Johns Hopkins Applied Physics Laboratory, Laurel, MD, USA. [15]Department of Earth and Space Sciences, University of California, Los Angeles, CA, USA.
*Corresponding author. Email: ottaviano.ruesch@nasa.gov

Regional context

The photogeologic map presented in Fig. 1D represents a discretization of the surface geology into three-dimensional units formed by distinct events and processes. Map units were defined and characterized through visual investigation of surface texture and morphology, quantitative investigation of albedo and topography, and determination of ages on the basis of relative stratigraphy and crater size-frequency distributions (CSFDs). The area close to Ahuna Mons is moderately cratered (*14*) and is dissected by troughs (in the "cratered unit"; Fig. 1D, brown). Topographically, it presents two positive reliefs (a tholus and a mons) and two negative reliefs (crater A and crater B). The tholus is a ~30-km-wide topographic bulge (Fig. 1D), with an irregular base rising ~2 km above the surroundings. A ~40-km-diameter impact crater (Fig. 1D, crater A) cuts the southern part of the tholus and is thus younger. The northern section of this crater floor is filled with material displaying two parallel ridges a few kilometers long. The origin of the fill could be ejecta from adjacent impacts or other material related to the continuing development of the tholus after the formation of crater A. North of the tholus is a 17-km-diameter and moderately degraded impact crater (Fig. 1D, crater B) that may have contributed to the fracturing of the subsurface near the tholus. Ahuna Mons is located southeast of the 17-km-diameter impact crater and dominates the northern flank of the tholus (Fig. 2B). The basal planform of Ahuna Mons is elliptical (21 by 13 km), and its topographic profile is concave downward (Fig. 2C) with an elevation of ~4 km, leading to an aspect ratio (height/basal average diameter) of ~0.24. The mountain is surrounded by a smooth-textured unit (Fig. 1D, "smooth unit," blue), which is less cratered than adjacent material. The smooth unit may represent ejecta material from the 17-km-diameter crater or could be associated with the formation of the mountain.

Morphology of Ahuna Mons

Ahuna Mons consists of steep (30° to 40°) flanks of talus (slope debris) material (Fig. 3C, "talus unit," green) and a slightly (~300 m deep) topographically depressed (Fig. 3B) summit unit (Fig. 3C, "summit unit," pink). Little accumulated debris at the base of the talus unit leaves a dramatically sharp contact between the talus and the surrounding smooth unit (Fig. 3A). The contact to the northwest is characterized by a curvilinear relief of smooth unit material, less than 50 m high, and oriented parallel to the mountain's flank. It could represent uplifted and tilted material due to a subsurface intrusion or a compressional ridge formed by the edifice sagging and spreading (*15*). Downslope lineations are evident on the flanks and are likely caused by gravitationally driven rock falls (Fig. 3A). They are associated with photometrical and spectral variations (Materials and methods) (Fig. 4). The summit of Ahuna Mons is not covered by debris and displays a variety of structures. Troughs and ridges are present, with an average length of 1 km, 1 km maximum width, and variable orientation (Fig. 3C). They are plausibly formed by extensional forces in a brittle layer. Summit areas lacking troughs and ridges appear hummocky, with depressions smaller than 1 km (Fig. 3C, "pit") and hills less than 500 m in diameter (Fig. 3C, "knob"). Depressions can be the product of both exogenic (impacts) and endogenic (explosion or sublimation) events. Small hills could represent tilted blocks of a disrupted brittle layer or extrusion of new material penetrating the layer.

Age of Ahuna Mons

The ages of the smooth unit and the 17-km crater unit (crater B) sets the oldest possible formation age of Ahuna Mons because these units predate or are contemporaneous with the mountain formation. We measured CSFDs on these units and applied two different chronology models to derive absolute model ages (*14*). Measurements of CSFDs were performed within a geographic information system (GIS) environment (Esri's ArcGIS) by using the CraterTools add-in (*16*). The measurements were carried out on the basis of High Altitude Mapping Orbit FC clear-filter image, and the resulting CSFDs were analyzed in their cumulative form with the software CraterStats (*17*). One chronology model scales the lunar crater production and chronology functions to impact conditions on Ceres. This approach assumes for Ceres the same size-distribution of projectiles and the same time-dependence of the projectile flux as observed on the Moon (*14*). The alternative model derives a production function from the observed and extrapolated object size-frequency distribution of the main asteroid belt and a chronology

Downloaded from http://science.sciencemag.org/ on September 1, 2016

function based on simulated collision rates in the main asteroid belt (*14*). We determined that the smooth unit and the 17-km crater unit are of similar age: 210 ± 30 million years and 160 ± 30 million years, respectively, using the Lunar Derived Model or 70 ± 20 million years and 70 ± 20 million years, respectively, using the Asteroid Derived Model (Fig. 5). Both ages indicate that Ahuna Mons formed in the geologically recent past. Downslope lineations occur on young steep slopes of bodies where the regolith is immature (*18*). On asteroid Vesta, where the regolith develops at a lower rate than on Ceres (*19*), downslope lineations are erased on surfaces older than 200 to 400 million years (*18*). Thus, these features on the flanks of Ahuna Mons are consistent with the young age inferred from crater size-frequency distributions. Although the compositional or surface physical variation represented by the lineations is not discernible in the current data set, it is typical of recently exposed surfaces on Ceres, such as morphologically fresh impact craters. Additionally, a recent emplacement explains the sharp contact between the smooth and talus units because with time and impact bombardment on the flank, the contact would become increasingly diffuse and gradated.

Formation mechanisms

The morphological units of the region near Ahuna Mons and their stratigraphic relations (Fig. 1D) are indicative of a geological construct. There is no evidence for compressional tectonism nor erosional features such as mesas. Likewise, surface upwarping by diapirism (buoyantly rising material), without piercing the surface, is excluded as a formation mechanism because it requires a thin elastic crust, for which no evidence has been found on Ceres (Materials and methods). Instead, the aspect ratio of Ahuna Mons points to a dome formed mostly through extrusion (*20*). The variety of morphologies characterizing the summit unit and the nonsystematic orientation of troughs and ridges are presumably manifestations of multiple dome-forming phases. In contrast, solid-state extrusions on Earth, represented by salt plugs, are formed in a single phase of continuous, slow influx of plug material (*21*). The ductile plug material develops characteristic surface structures (such as folds and salt glaciers) (*22*) not observed on the summit unit.

Multiple phases of fracturing and possibly small-scale extrusions (hills) recorded on the summit indicate the composite nature of Ahuna Mons. This characteristic is analogous to high-viscosity volcanic domes on Earth that grow through a sequence of events such as extensional fracturing and extrusion of lobes (*23*–*25*). The summit unit thus represents a brittle dome carapace, formed by cooling of the outermost region of a ductile core. The fracturing of the carapace leads to its partial disintegration and production of boulders and smaller debris (*26*). Through mass wasting, these unconsolidated materials accumulate into talus. Thus, the talus formation is genetically part of the dome emplacement process and is not the result of erosion by impacts.

The aspect ratio, talus collar, and summit morphologies are indicative of an extrusive volcanic dome, similar to those found on Earth and the Moon (Fig. 6) (*20*, *23*, *27*). The aspect ratio and absence of flow morphologies suggest that the ductile core has a relatively high viscosity (*23*), as discussed in detail below. Although the materials compositions are different, the number of geomorphological analogies between Ahuna Mons and edifices on Earth suggests that other key properties (such as viscosity) between different planetary bodies are similar and lead to comparable geomorphologic features.

Modeling of topographic profile

We verify that the observed topographic profile of the Ahuna Mons is similar to that of a viscous volcanic dome, as suggested by its aspect ratio. For this purpose, we assume that the profile of a static dome reflects the mechanical equilibrium between a brittle carapace enclosing a pressurized ductile material (*28*). A carapace thickness of several hundred meters, as inferred from the summit troughs (Materials and methods), reproduce the concave downward profile of the Ahuna Mons summit (Fig. 7A), indicating that high-viscosity dome development is a viable mechanism for the formation of the mountain. The farthest section (lower flank) of the profile is found to be of constant slope (Fig. 7, A and B, black line), as expected for talus (*28*).

For estimates of rheological properties of the material, we turn to a dynamic model that describes the lateral spreading of a dome under the effect of gravity (*29*, *30*). The volume of the dome, calculated from the static model profile, is considered constant, and thus the dynamic model simulates only the final phase of dome evolution. Initial apparent dynamic viscosity of the dome material is set as a free parameter and is allowed to increase with time because of cooling and will halt the spreading. Modeling

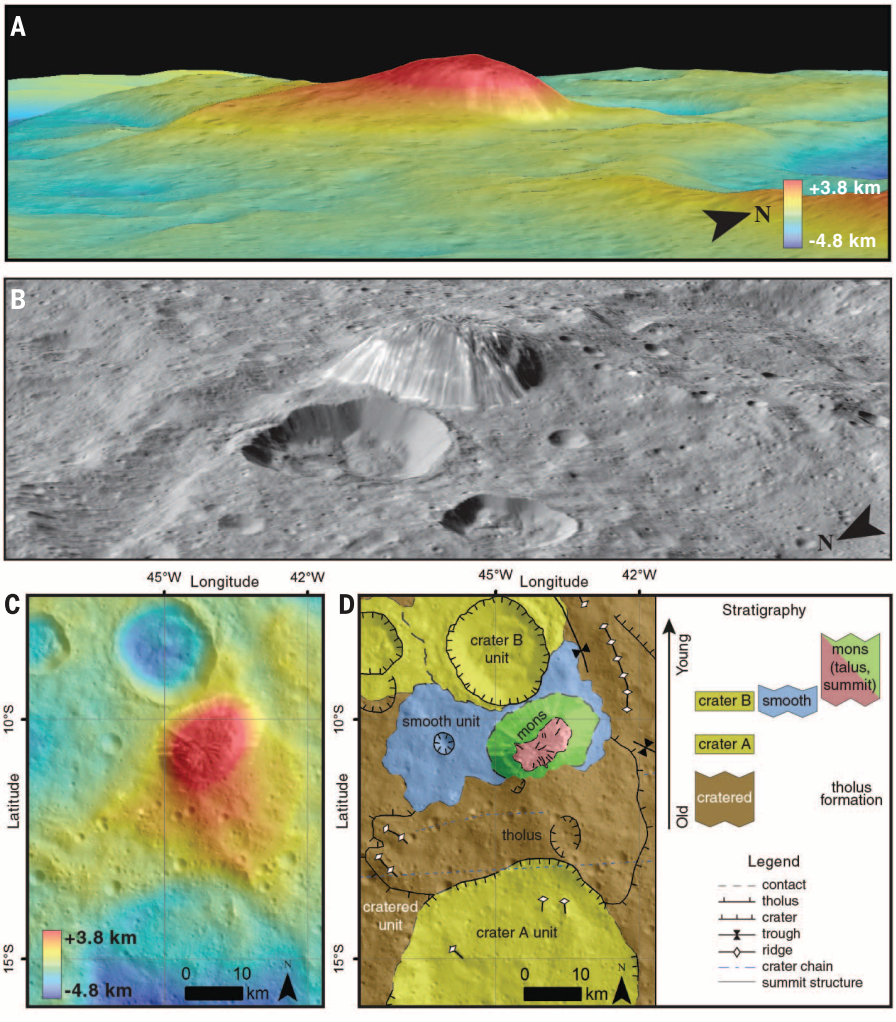


Fig. 1. Geologic context of Ahuna Mons. (**A**) Perspective view of the Ahuna Mons region derived from FC images and digital terrain model (Materials and methods). The view is looking west, and the scene is ~70 km wide in the foreground. (**B**) Perspective view of Ahuna Mons region looking southeast. Scene is ~70 km wide in the foreground. (**C**) Cylindrical projection of the FC image (FC21A0039691) and digital terrain model shown in (A). (**D**) Geologic map of the region shown in (C), with colors corresponding to units shown in the stratigraphic column.

Downloaded from http://science.sciencemag.org/ on September 1, 2016

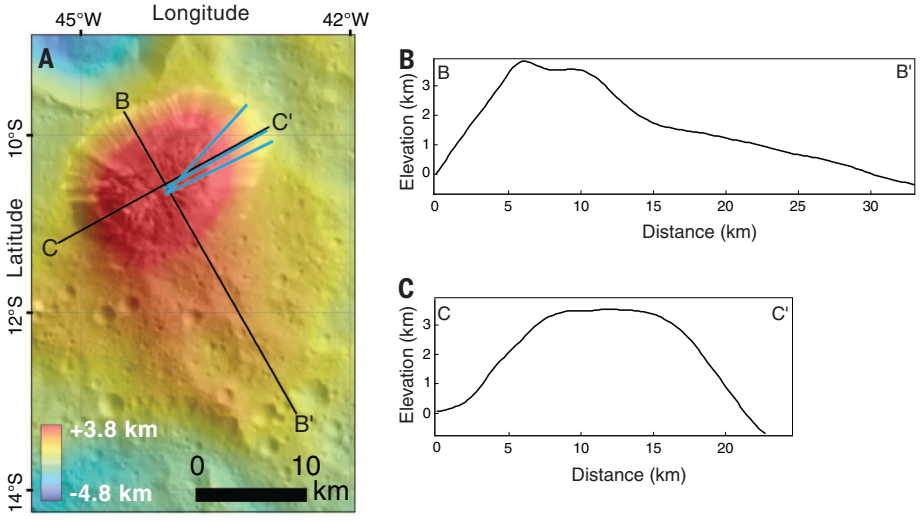


Fig. 2. Topography of Ahuna Mons and adjacent bulge. (**A**) Color-coded digital terrain model. The location of profile B–B' and C–C' are indicated with black lines and are shown in (B) and (C). The half cross sections shown in blue are averaged and shown in Fig. 7B. (**B**) Topographic profile across the tholus and mons. The profile of Ahuna Mons is asymmetrical. (**C**) Topographic profile across the Ahuna Mons. The profile is relatively symmetrical. Elevations are relative to an ellipsoid (482 by 482 by 446 km).

dome topography in this way (Fig. 7B) allows us to explore the range of initial apparent viscosity and the relaxation (spreading) time that reproduce the topography of Ahuna Mons (Materials and methods). The duration of spreading is constrained by a range of cooling time scales of the dome. The time scale based on radiative cooling is 4×10^2 years, whereas conductive cooling requires 3×10^5 years (Materials and methods). The size and shape of the Ahuna Mons profile can be reproduced within the fast cooling time scale with an initial apparent viscosity of 4×10^{15} Pa s, or within the slow cooling time with an initial apparent viscosity of 3×10^{18} Pa s (Fig. 7B). The viscosities are referred to as apparent because they represent the viscosity of the entire dome at the onset of spreading, including the ductile core and brittle carapace, which is known to mechanically limit the spreading of the dome. The effect of the carapace has been characterized as an increase in the apparent viscosity of the entire dome of approximately four orders of magnitude (*31*). This leads to initial actual dynamic viscosities ranging from 4×10^{11} to 3×10^{14} Pa s. The advance of the dome front is further reduced by the talus collar, and therefore, we consider this range as an upper estimate. This rheological evaluation confirms the highly viscous nature of the material inferred from morphology. Viscosities of terrestrial volcanic domes calculated from morphometry and detailed modeling of dome growth and evolution are up to 3×10^{12} Pa s, within the range estimated here (*32*).

Discussion

For the formation of Ahuna Mons, we thus propose a volcanic process involving ascent of cryomagma and extrusion onto the surface followed by dome development and spreading. Pathways for rising material were possibly provided by fractures produced by nearby impacts (Fig. 1D, crater B) and by the regional troughs (Fig. 1D). Second, large impacts on planetary bodies generate shock waves that can cause fracturing of the outermost layers at regions antipodal to impact structures (*33*). Ahuna Mons could be part of a broader, fractured antipodal region of Kerwan (10.9°S, 123.6°E), the largest preserved impact basin on Ceres with a diameter of ~280 km (*14*).

With the plausible initial viscosities presented above and Ceres composition revealed by the Dawn visible and near-infrared imaging spectrometer (*3*, *34*), a few characteristics of the cryomagma can be proposed. Ceres has warmer surface temperatures than those of icy satellites (*4*) but is of relatively small size and lacks tidal dissipation as a heat source. Temperatures were predicted to be as warm as 230 K starting at >50 km depth (*35*), conditions at which the homologous temperature of water ice is low. Our results imply a long-term heat source in the interior as well as the presence of low-eutectic temperature materials for the production of cryomagma (*5*). On the basis of mineralogical observations at the Occator crater (*34*), chloride salts may be present at depths within Ceres. The eutectic temperatures of chlorides are close to or lower than 230 K, hence enabling melt formation at ~50 km depth, or at shallower depths (*35*, *36*). The presence of a few percent of melt lead to a decrease in viscosity by >5 orders of magnitude compared with the solid parent material, and even more if the melt is connected (*37*). We propose that the parent material of the cryomagma may consist of chloride-rich brines, the potential melt phase; secondary minerals, such as carbonates and phyllosilicates (*3*); and water ice. Crucial information on the extruded material at a microscopic scale—compositional and textural characteristics at a sample scale—is missing, and despite chloride brines being frequent in terrestrial environments, relevant rheological data are lacking. As a consequence, we are unable to determine the melting behavior of the proposed parent material (for example, the percentage of melt upon extrusion), nor the proportions of the components in the resulting cryomagma, or the exact mechanism enabling its ascent and eruption. However, our understanding will improve with further determination of local-scale mineralogy and gravity measurements, as well as supporting experimental measurements. The presence of low-eutectic salts is consistent with a past phase of aqueous alteration of the rocky component at a global scale, as indicated by the surface mineralogy (*3*). This process was key for Ceres chemical and thermal evolution because the interaction enabled the leaching of alkali, alkaline-earth, and other soluble materials from the rock into fluids. The aqueous alteration allowed the fluid to become enriched with impurities, such as salts of low thermal conductivity, and radionuclides (^{40}K in particular)—hence, the displacement of the main long-term heat source from the core to the mantle (*38*) where cryomagma production occurred.

Although the broader and more degraded topographic rises on Ceres (*13*) are distinct from Ahuna Mons in several aspects, they might share a common formation process and imply that volcanic activity occurred over an extended period. Their different morphologies might be related to a change in the rheological properties of cryomagmas with time or during ascent, as proposed for lunar analogs (*27*). Ceres cryovolcanic activity and the composition of its cryomagma adds to the geological diversity of the solar system because they differ from volcanism of volatile-poor protoplanets. For example, on Vesta, volcanism based on igneous minerals was active only in the first tens of millions of years (*39*). The evolution of Ceres, dictated by its volatile-rich composition, resulted in the production of cryomagmatic liquids that enabled surface activity in geologically recent times.

Materials and methods

Description of digital terrain model method

The stereo-photogrammetric processing of Ceres Framing Camera images is based on a software suite described in (*40*–*44*). The stereo-photogrammetric processing is segmented into five steps: photogrammetric block adjustment, multi-image matching, surface point triangulation, digital terrain model (DTM) generation, and basemap generation (*42*). The cartography system is the International Astronomical Union system defined by the tiny crater Kait (*1*). The DTM used in this study is calculated with respect to an ellipsoid with a grid space of ~205 m/pixel. The height is given with an uncertainty of 14 m.

Discussion of diapirism as formation mechanism

The surface topography of an elastic layer resulting from an ascending spherical diapir was described by (*45*). With an elastic modulus of 1-10 GPa and Ceres' surface gravity of 0.28 m s^{-2} (*1*),

Downloaded from http://science.sciencemag.org/ on September 1, 2016

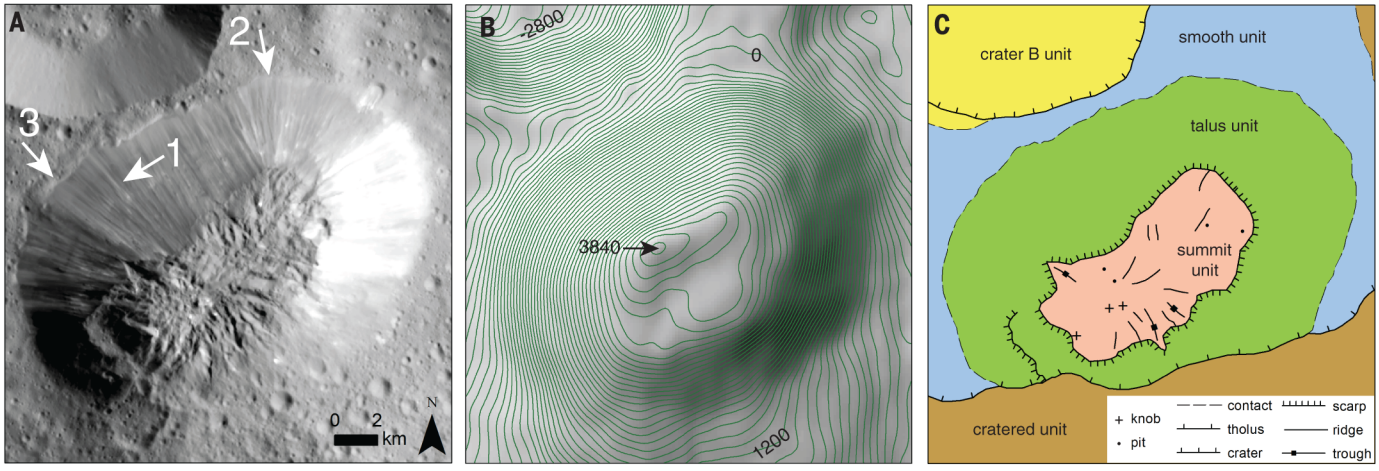


Fig. 3. Morphologies of Ahuna Mons. (**A**) FC image of the Ahuna Mons at a resolution of 35 m/pixel. Arrow 1 points to one of many brighter downslope lineations. Arrow 2 points to the sharp contact between smooth and talus units. Arrow 3 indicates where the smooth unit forms a relief extending along the contact with the talus unit. Cylindrical projection is centered at 10.3°S, 316.2°E. (**B**) Hill-shaded digital terrain model with superimposed 100 m contour lines. Key elevations are marked. Same location and projection as (A). (**C**) Close-up of the geologic map centered on Ahuna Mons. Same location and projection as (A).

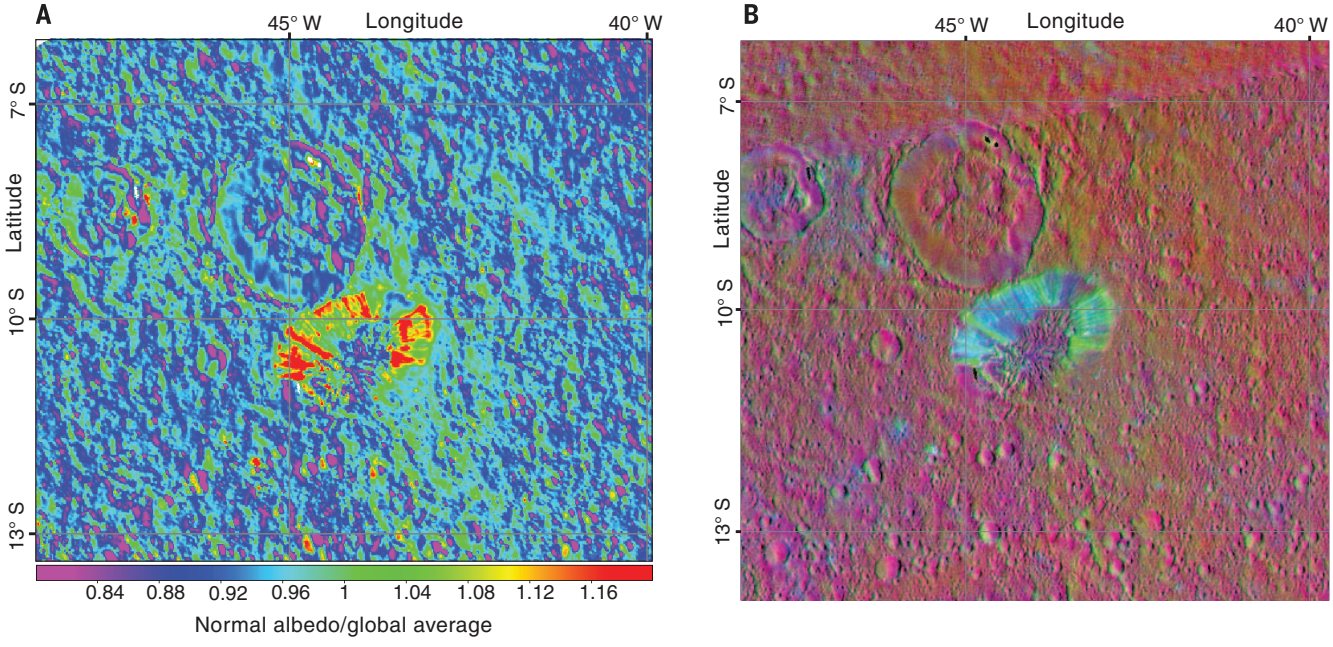


Fig. 4. Albedo map and color composite from FC images. (**A**) Mosaic of ~135 m/pixel, with color code indicating variations relative to the global normal albedo. Ahuna Mons is identified by its high albedo (red color) lineations. Image is ~70 km wide. (**B**) Mosaic of color ratio images [R (red) = 0.97 μm /0.75 μm, G (green) = 0.75 μm, and B (blue) = 0.44 μm /0.75 μm]. Image is ~70 km wide.

the high aspect ratio (edifice height/basal diameter) of Ahuna Mons (~0.24) can be produced by a thin elastic layer (<5 km) and a large density contrast (between diapir and surroundings) of >500 kg m^{-3}. Evidence for a thin elastic crust on Ceres is currently lacking (*1*, *14*), while such a large density contrast would require a high concentration of volatiles within a spatially limited (few tens of km) location. Hence the case for diapiric process and surface upwarping is not supported by existing conditions observed on Ceres.

Description of FC albedo and color mosaic

The Framing Camera is equipped with filters covering the range 0.4 μm to 1.0 μm (*12*) for multi-spectral analyses. We used the global average photometric models of Ceres derived from ~400 m/pixel data (*46*) to correct the local scattering geometry to incidence angle 30°, emission angle 0°, and phase angle 30° and remove the effect of local topography in ~135 m/pixel images (Fig. 4A). The photometrically corrected images from multiple filters were rectified and map projected, and combined to produce false-color mosaic for the Ahuna Mons region. The false-color mosaic was calculated with the following reflectance ratios: red channel shows R(0.97 μm)/R (0.75 μm), green channel shows R(0.75 μm) and blue channel shows R(0.44 μm)/R(0.75 μm), with R the reflectance at the given wavelength (Fig. 4B). These ratios enable the identification of the changes in the visible spectrum of Ceres at global and regional scales. The area surrounding

Downloaded from http://science.sciencemag.org/ on September 1, 2016

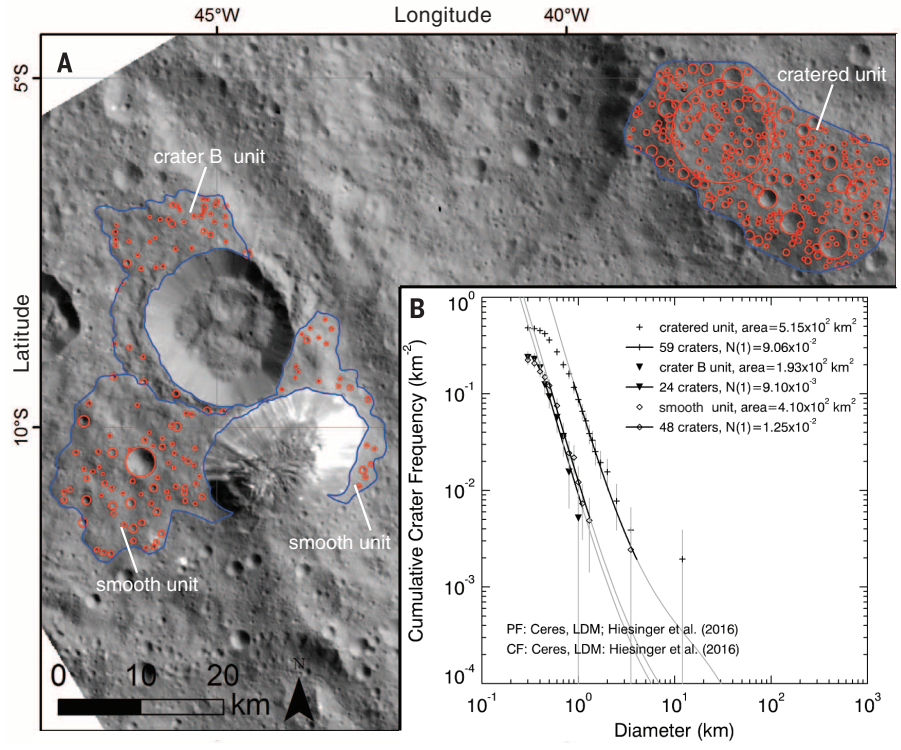


Fig. 5. Crater size-frequency distribution measurements of three areas in the Ahuna Mons region. (**A** and **B**) Two sets of production and chronology functions are applied in order to derive absolute model ages (*14*). (B) The Lunar Derived Model gives the following absolute model ages: cratered unit (crosses), 1.55 ± 0.20 Ga; smooth unit (diamonds), 210 ± 30 Ma; crater B unit (inverted solid triangle), 160 ± 30 Ma. The Asteroid Derived Model gives the following absolute model ages: cratered unit (crosses), ~440 ± 60 million years; smooth unit (diamonds), 70 ± 20 million years; crater B unit (inverted solid triangle), 70 ± 20 million years. The crater size-frequency distribution technique cannot be applied for the talus and summit units because of the slope and overall small surface area. Secondary crater chains (Fig. 1C) heavily affect the surface of the tholus, preventing reliable determination of crater size-frequency distributions for the area.

Ahuna Mons appears reddish punctuated by blue spots, probably small (<1 km) impact craters. The talus unit with downslope lineations has different values, appearing cyan and yellow in Fig. 4B; similar values are found elsewhere on Ceres on morphologically fresh-appearing slopes of impact craters and on bright ejecta rays. Most of the lineations display high albedos, reaching values 15% higher than the global average, and their visible wavelength spectrum possesses a negative (blue) slope relative to surrounding material. The summit unit is distinct from the talus and contains reddish areas similar the surrounding terrain. Aside from the downslope lineations, no other clear correlation is found with the geologic map of Fig. 1D.

Estimation of trough depth and carapace thickness

Accurate estimate of the carapace thickness would require knowledge of the troughs (Fig. 3C) formation mechanism and geometry, which cannot be precisely determined at the resolution of the images and the digital terrain model. As a first order approximation, we consider the troughs as symmetric grabens, and adopt the relationship of (*47*). Symmetric graben formation is a consequence of fracturing and uplifting of a brittle layer by an upward intruding viscous fluid (*47*). The width of the graben has a linear correlation with the thickness of the brittle layer, the thickness to width ratio being 0.89 (*47*). With trough widths in the range ~500 m to ~1 km, the carapace depth is estimated to be in the range 450-890 m. This range represents a lower estimate, however, as other formation scenarios are plausible, such as horst and graben or tilted-blocks systems (*48*). Therefore the carapace can be thicker than the estimated range.

Description of the topographic profiles

The topographic profile used for comparison with the static and dynamic models is calculated as follows. As shown in Fig. 2B, the topographic profile SSE-NNW of the Mons is strongly asymmetric, probably because of the pre-existing tholus topography (*28*). A similar setting is found for the Compton-Belkovich complex on the Moon. The profile shown in Fig. 2C perpendicular to the Fig. 2B profile is oriented along the tholus flank and better represents the unaffected Mons shape. Because the profiles differ, three WSW-ENE profiles are averaged (blue lines in Fig. 2A) and used for model comparison (Fig. 7B). The use of the WSW flank is avoided because it is affected by a terrace.

Description of the static model

The shape of a dome in static equilibrium between the pressurized ductile interior (magma) and the rigid carapace can be described by r, the radial coordinate, z, the vertical coordinate, and ϕ the angular coordinate. These variables are related by the following equations (*28*):

$$\frac{d(\sin\phi)}{dr} + \frac{\sin\phi}{r} = \frac{\rho g}{\sigma t} \quad (1)$$

$$\tan\phi = \frac{dz}{dr} \quad (2)$$

where t and σ are the thickness and tensile strength of the carapace, and ρ is the density of the ductile material. Ceres gravitational acceleration is g (0.28 m s^{-2}, (*1*)). The solution of these equations, i.e., the shape of the dome, is governed by a single dimensionless parameter that incorporates all physical parameters, i.e.,

$$D = 1/h\sqrt{\sigma t/\rho g} \quad (3)$$

with h the pressure head (expressed in m) at the apex of the dome (*28*). For magma density we adopt the outer layer density range of 1680–1950 kg m^{-3}, estimated from Dawn's gravity and shape measurement and considering a two layer model for Ceres' interior (*2*). The carapace thickness is estimated to be in the range of 450-890 m based on the summit troughs width and assuming that they formed as symmetric grabens. Tensile strength is taken between 1×10^6 and 1×10^7 Pa, as of terrestrial high-viscosity magmas such as dacites (*28*). The choice of a different composition, i.e., using tensile strength of water ice, has no effect as this water ice property (*49*) is comparable to that of high-viscosity dacite material.

The model profile is fitted to the measured profile for radial distances from the center up to 6.7 km. The latter value represents the distance beyond which the measured profile is dominated by the constant angle of repose of the talus. The talus angle of repose is calculated in a representative section of the profile between the distances 8-11 km. In this range, the difference between the profile calculated with the angle of repose and the measured profile is less than 100 m. The measured profile deviates from the constant angle of repose profile by more than 100 m at distances less than 6.7 km. A root-mean-square error is calculated between distances 0 and 6.7 km. For matching the model and measured profiles an additional constraint is defined: at distances greater than 6.7 km, the model profile is required to have lower elevations than the measured profile.

The static model with the smallest root mean square (RMS) error (~1.0%) is obtained with D

Downloaded from http://science.sciencemag.org/ on September 1, 2016

values of ~5 (Fig. 7A). These values are achieved with a pressure at the dome apex (in excess of the hydrostatic pressure) between 5×10^4 Pa and 2×10^5 Pa, depending on the tensile strength, density and thickness ranges, an order of magnitude lower than viscous dome magma pressures on Earth (*28*).

Description of dynamic model

The dynamic model is described in (*30*) and is an improvement of the gravity current model of Newtonian fluids applied to volcanic domes of (*29*). Newtonian fluid behavior is used for simplicity to approximate the complex lava material bearing melt, crystals and volatiles, and usually behaving as a viscoplastic material (*23*, *50*). The model applied here takes into account the viscosity increase with time, an important effect not fully considered in previous work (*29*). We assume a homogeneous ductile core with a circular basal planform. These two properties represent a simplification of Ahuna Mons, because the composite nature of the dome suggests variations in rheology within the core and the basal planform is approximately elliptical. The equation governing the profile of the dome, i.e., elevation h and radius r as a function of time t, is (*30*):

$$h(r,t) = \frac{4V}{3\pi r_0^2}\frac{1}{\left(1+\frac{\theta}{\tau}\right)^{1/4}}\left[1-\frac{r^2}{r_0^2}\frac{1}{\left(1+\frac{\theta}{\tau}\right)^{1/4}}\right]^{1/3} \quad (4)$$

The volume is defined by the profile of the static model ($V = 6.14 \times 10^{11}$ m^3). Keeping the volume constant means spreading occurs once all material is extruded. This is a further simplification of the process forming Ahuna Mons: a possible co-occurrence of spreading and ongoing material extrusion. The initial radius r_o is arbitrarily taken between 2–6 km. Using values within this range, the final kinematic viscosity value varies less than 10%. The initial elevation h_o, is defined by the volume and initial radius. τ is a time constant. The transformation variable for the time-dependent viscosity is:

$$\theta(t) = \Gamma\left(1 - e^{-t/\Gamma}\right) \quad (5)$$

and it results from defining the time-dependent viscosity as

$$\nu = \nu_0 e^{t/\Gamma} \quad (6)$$

Γ, the timescale over which the viscosity increases exponentially, is found iteratively with the requirement that the dome front does not advance once the relaxation time is reached. The time constant τ is defined with ν_0, the initial bulk kinematic viscosity, as follows:

$$\tau = \left(\frac{3}{4}\right)^5\left(\frac{\pi}{V}\right)^3\frac{\nu_0\nu_0^8}{g} \quad (7)$$

The relaxation time is estimated by considering that the dome stops spreading after significant cooling. An upper estimate is obtained by considering that cooling is limited by conduction. For a dome of elevation d, the cooling by conduction timescale can be approximated as follows (*51*):

$$t_c \sim \frac{d^2}{\kappa} \quad (8)$$

With k delineating thermal diffusivity. Radiative cooling represents a lower estimate as it assumes that the entire dome remains isothermal (*52*):

$$t_r \sim \frac{\rho c_p d}{\sigma T^3} \quad (9)$$

where ρ and c_p are the density and heat capacity, respectively. T is the temperature during spreading and σ the Stefan-Boltzmann constant. The diffusivity depends on the density, thermal conductivity, heat capacity and temperature of the material (*53*). We consider that the material has a density corresponding to the highest value presented above, i.e., 1950 kg m^{-3} (*2*). Uncertainties due to the choice of this composition are discussed at the end of this section. Because the types, proportions and states of mineral components of the Ahuna Mons material are not known, for this calculation we assume it is composed of silicates (density of 2540 kg m^{-3}) and water ice (920 kg m^{-3}). The following properties are calculated assuming a mixture of silicates and ice of density 1950 kg m^{-3} (*53*). Thermal diffusivity is estimated at ~1.5×10^{-6} m^2 s^{-1} and heat capacity at 1242 J kg^{-1} K^{-1} (*53*). The temperature is set at 230K as it is the highest value found at a depth of >50 km from thermal evolution model of Ceres (*35*). Conductive cooling timescales is 3.1×10^5 years, whereas radiative timescale is 4.2×10^2 years.

The fit between the dynamic model profile and the measured profile is performed as for the static model and is described above. For t = 4.2×10^2 years, the smallest RMS error (1.1%) is obtained with $\Gamma = 1.3 \times 10^2$ years and an initial apparent kinematic viscosity of 2.2×10^{12} m^2 s^{-1}, or an initial apparent dynamic viscosity of 4.3×10^{15} Pa s. For t = 3.1×10^5 years, the smallest RMS error (1.1%) is obtained with $\Gamma = 9.2 \times 10^4$ years and an initial apparent kinematic viscosity of 1.6×10^{15} m^2 s^{-1}, or an initial apparent dynamic viscosity of 3.1×10^{18} Pa s. In summary, initial apparent dynamic viscosity is in the range of 4×10^{15} –3×10^{18} Pa s.

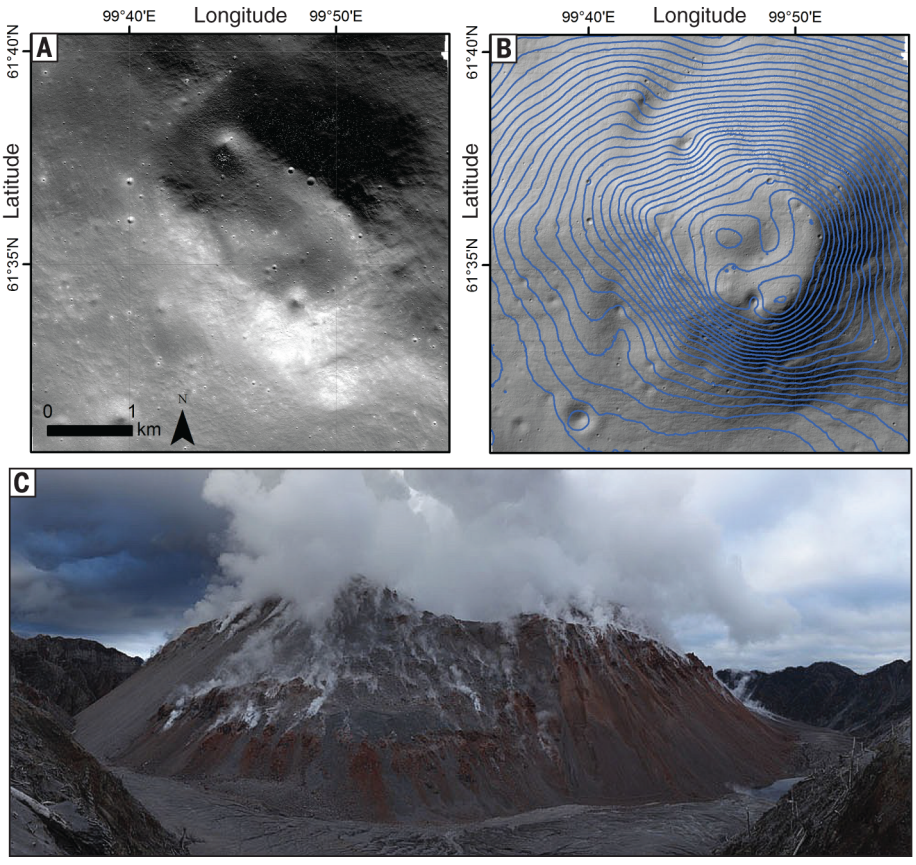


Fig. 6. Lunar and terrestrial analogs. (**A**) Lunar Reconnaissance Orbiter image of the major dome in the Compton-Belkovich volcanic complex on the Moon (*25*). (**B**) Hill-shaded digital terrain model (*27*), with superimposed contour lines in 25-m increments. Same location as (A). The dome has an aspect ratio of ~0.2 (~0.24 for Ahuna Mons) and slopes of ~23° (30° to 40° for Ahuna Mons). An irregular central depression characterizes the summit. (**C**) North view of the Chaitén dome (Chile), where a talus collar with steep slopes is well developed. The dome is 1.7 km in diameter and has an aspect ratio of ~0.2. [Image credit: R. Roscoe]

Downloaded from http://science.sciencemag.org/ on September 1, 2016

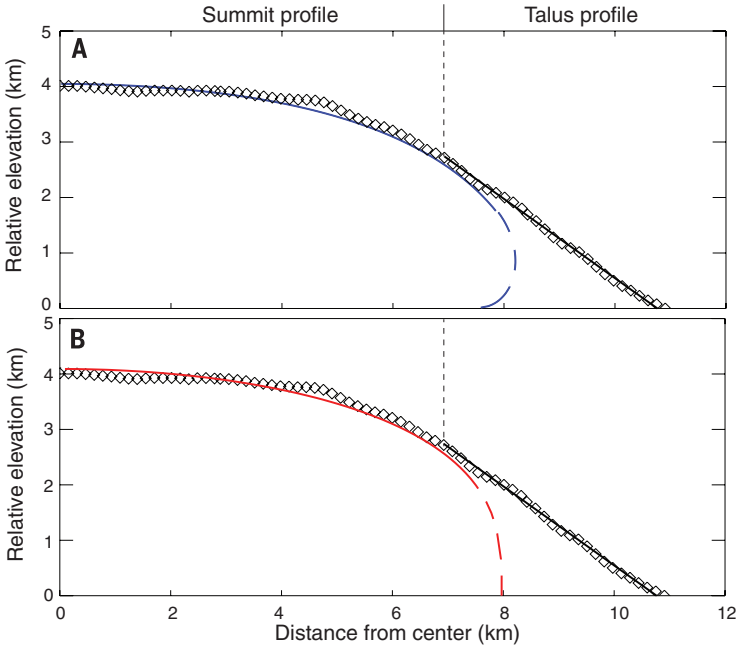


Fig. 7. Topographic profiles of Ahuna Mons and models. (**A**) Average, half topographic profile of Ahuna Mons (from Fig. 2) shown in diamonds, compared with a calculated profile of a static volcanic dome (blue line). The model profile is calculated with carapace tensile strength of 10^7 Pa, thickness of 450 m, and ductile material density of 1680 kg m^{-3}. The blue line is dashed where talus material covers the profile. The constant slope of the talus material is highlighted with a black line (35°). (**B**) Same as (A) but with a calculated profile from a dynamic model of volcanic dome (red line). Key values for the model curve are initial radius of 5.6 km, initial height of 8.2 km, initial actual viscosity of 4×10^{15} Pa s, and a relaxation time of 4×10^2 years. The red line is dashed where talus material covers the profile.

The following timescales and viscosities are obtained if a material of pure water ice at 230 K is considered. Although the material of Ahuna is unlikely to correspond to such composition, the differences from a silicate-dominated material are here considered as an estimate of the uncertainties due to composition. Thermal diffusivity for water ice at 230 K is 1.6×10^{-6} m^2 s^{-1} (*53*), leading to conductive timescale of 2.9×10^5 years. Heat capacity is 1803 J kg^{-1} K^{-1} (*53*), leading to radiative timescale of 2.9×10^2 years. Initial apparent dynamic viscosities are in the range 1.4×10^{15}–1.4×10^{18} Pa s, on the same order of magnitude as for a silicate-dominated mixture of density 1950 kg m^{-3}.

REFERENCES AND NOTES

1. C. T. Russell *et al.*, Dawn arrives at Ceres: Exploration of a small volatile-rich world. *Science* **353**, 1008–1010 (2016).
2. R. S. Park *et al.*, A partially differentiated interior for (1) Ceres deduced from its gravity field and shape. *Nature* 10.1038/nature18955 (2016). doi: 10.1038/nature18955; pmid: 27487219
3. M. C. De Sanctis *et al.*, Ammoniated phyllosilicates with a likely outer Solar System origin on (1) Ceres. *Nature* **528**, 241–244 (2015). doi: 10.1038/nature16172; pmid: 26659184
4. P. O. Hayne, O. Aharonson, Thermal stability of ice on Ceres with rough topography. *J. Geophys. Res.* **120**, E004887 (2015).
5. J. S. Kargel, Brine volcanism and the interior structures of asteroids and icy satellites. *Icarus* **94**, 368–390 (1991). doi: 10.1016/0019-1035(91)90235-L
6. J. S. Kargel, Cryovolcanism on the icy satellites. *Earth Moon Planets* **67**, 101–113 (1994). doi: 10.1007/BF00613296
7. P. M. Schenk, W. B. McKinnon, D. Gwynn, J. M. Moore, Flooding of Ganymede's bright terrains by low-viscosity water-ice lavas. *Nature* **410**, 57–60 (2001). doi: 10.1038/35065027; pmid: 11242037
8. C. C. Porco *et al.*, Cassini observes the active south pole of Enceladus. *Science* **311**, 1393–1401 (2006). doi: 10.1126/science.1123013; pmid: 16527964
9. L. M. Prockter *et al.*, Characteristics of icy surfaces. *Space Sci. Rev.* **153**, 63–111 (2010). doi: 10.1007/s11214-010-9649-8
10. K. Stephan, R. Jaumann, R. Wagner, Geology of icy bodies, in *Science of Solar System ices*, M.S. Gudipati, J. Castillo-Rogez, Eds. (Springer, 2013), pp. 279–370.
11. S. A. Fagents, Considerations for effusive cryovolcanism on Europa: The post-Galileo perspective. *J. Geophys. Res.* **108** (E12), 2139 (2003). doi: 10.1029/2003JE002128
12. H. Sierks *et al.*, The Dawn Framing Camera. *Space Sci. Rev.* **163**, 263–327 (2011). doi: 10.1007/s11214-011-9745-4
13. D. L. Buczkowski *et al.*, The geomorphology of Ceres. *Science* **353**, aaf4332 (2016).
14. H. Hiesinger *et al.*, Cratering on Ceres: Implications for its crust and evolution. *Science* **353**, aaf4759 (2016).
15. O. Merle, A. Borgia, Scaled experiments of volcanic spreading. *J. Geophys. Res.* **101** (B6), 13805–13817 (1996). doi: 10.1029/95JB03736
16. T. Kneissl, S. van Gasselt, G. Neukum, Map-projection-independent crater size-frequency determination in GIS environments—New software tool for ArcGIS. *Planet. Space Sci.* **59**, 1243–1254 (2011). doi: 10.1016/j.pss.2010.03.015
17. G. G. Michael, G. Neukum, Planetary surface dating from crater size-frequency distribution measurements: Partial resurfacing events and statistical age uncertainty. *Earth Planet. Sci. Lett.* **294**, 223–229 (2010). doi: 10.1016/j.epsl.2009.12.041
18. O. Ruesch *et al.*, Geologic map of the northern hemisphere of Vesta based on Dawn Framing Camera (FC) images. *Icarus* **244**, 41–59 (2014). doi: 10.1016/j.icarus.2014.01.035
19. Impact flux on Ceres and Vesta are similar for 1-km craters, but different target properties result in larger crater diameters on Ceres relative to Vesta.
20. J. H. Fink, N. T. Bridges, Effects of eruption history and cooling rate on lava dome growth. *Bull. Volcanol.* **57**, 229–239 (1995). doi: 10.1007/BF00265423
21. M. R. Hudec, M. P. A. Jackson, Terra infirma: Understanding salt tectonics. *Earth Sci. Rev.* **82**, 1–28 (2007). doi: 10.1016/j.earscirev.2007.01.001
22. C. J. Talbot, P. Aftabi, Geology and models of salt extrusion at Qum Kuh, central Iran. *J. Geol. Soc. London* **161**, 321–334 (2004). doi: 10.1144/0016-764903-102
23. S. Blake, Viscoplastic models of lava domes, in *Lava Flows and Domes*, J. H. Fink, Ed. (Springer, 1990), pp. 88–126.
24. S. W. Anderson, J. H. Fink, The development and distribution of surface textures at the Mount St. Helens dome, in *Lava Flows and Domes*, J. H. Fink, Ed. (Springer, 1990), pp. 25–46.
25. A. V. Shevchenko, V. N. Dvigalo, I. Y. Svirid, Airborne photogrammetry and geomorphological analysis of the 2001–2002 exogenous dome growth at Molodoy Shiveluch Volcano, Kamchatka. *J. Volc. Geoth. Res.* **304**, 94–107 (2015). doi: 10.1016/j.jvolgeores.2015.08.013
26. S. W. Anderson, E. R. Stofan, J. J. Plaut, D. A. Crown, Block size distributions on silicic lava flow surfaces: Implications for emplacement conditions. *GSA Bull.* **110**, 1258–1267 (1998). doi: 10.1130/0016-7606(1998)110<1258:BSDOSL>2.3.CO;2
27. B. L. Jolliff *et al.*, Non-mare silicic volcanism on the lunar farside at Compton-Belkovich. *Nat. Geosci.* **4**, 566–571 (2011). doi: 10.1038/ngeo1212
28. R. M. Iverson, Lava domes modeled as brittle shells that enclose pressurized magma, with application to Mount St. Helens, in *Lava Flows and Domes*, J. H. Fink, Ed. (Springer, 1990), pp. 47–69.
29. H. E. Huppert, The propagation of two-dimensional and axisymmetric viscous gravity currents over a rigid horizontal surface. *J. Fluid Mech.* **121**, 43–58 (1982). doi: 10.1017/S0022112082001797
30. L. C. Quick, L. S. Glaze, S. M. Baloga, E. R. Stofan, New approaches to inferences for steep-sided domes on Venus. *J. Volc. Geoth. Res.* **319**, 93–105 (2016). doi: 10.1016/j.jvolgeores.2016.02.028
31. C. R. Manley, Extended cooling and viscous flow of large, hot rhyolite lavas: Implications of numerical modeling results *J. Volc. Geoth. Res.* **53**, 27–46 (1992). doi: 10.1016/0377-0273(92)90072-L
32. A. J. Hale, E. S. Calder, G. Wadge, S. C. Loughlin, G. A. Ryan, Modelling the lava dome extruded at Soufriere Hills Volcano, Montserrat, August 2005-May 2006 part 1: Dome shape and internal structure. *J. Volc. Geoth. Res.* **187**, 53–68 (2009). doi: 10.1016/j.jvolgeores.2009.08.023
33. P. H. Schultz, D. A. Crawford, Origin of nearside structural and geochemical anomalies on the Moon. *GSA Special Papers* **477**, 141–159 (2011).
34. M. C. De Sanctis *et al.*, Bright carbonate deposits as evidence of aqueous alteration on (1) Ceres. *Nature* **536**, 54–57 (2016). doi: 10.1038/nature18290; pmid: 27362221
35. J. C. Castillo-Rogez, T. B. McCord, Ceres' evolution and present state constrained by shape data. *Icarus* **205**, 443–459 (2010). doi: 10.1016/j.icarus.2009.04.008
36. D. W. Davis, T. K. Lowenstein, R. J. Spencer, Melting behavior of fluid inclusions in laboratory-grown halite crystals in the systems NaCl–H_2O, NaCl–KCl–H_2O, NaCl–$MgCl_2$–H_2O, and NaCl–$CaCl_2$–H_2O. *Geo. Cosm. Acta* **54**, 596–601 (1990).
37. M. Arakawa, N. Maeno, Effective viscosity of partially melted ice in the ammonia-water system. *Geophys. Res. Lett.* **21**, 1515–1518 (1994). doi: 10.1029/94GL01041
38. J. C. Castillo-Rogez, J. I. Lunine, Evolution of Titan's rocky core constrained by Cassini observations. *Geophys. Res. Lett.* **37**, L20205 (2010). doi: 10.1029/2010GL044398
39. H. Y. McSween, D. W. Mittlefehldt, A. W. Beck, R. G. Mayne, T. J. McCoy, HED meteorites and their relationship to the geology of Vesta and the Dawn mission. *Space Sci. Rev.* **163**, 141–174 (2011). doi: 10.1007/s11214-010-9637-z
40. R. Jaumann *et al.*, The high-resolution stereo camera (HRSC) experiment on Mars Express: Instrument aspects and experiment conduct from interplanetary cruise through the nominal mission. *Planet. Space Sci.* **55**, 928–952 (2007). doi: 10.1016/j.pss.2006.12.003
41. K. Gwinner *et al.*, Derivation and validation of high-resolution digital terrain models from Mars Express HRSC data. *Photogramm. Eng. Remote Sensing* **75**, 1127–1142 (2009). doi: 10.14358/PERS.75.9.1127
42. F. Preusker *et al.*, Stereo topographic models of Mercury after three MESSENGER flybys. *Planet. Space Sci.* **59**, 1910–1917 (2011). doi: 10.1016/j.pss.2011.07.005
43. R. Jaumann *et al.*, Vesta's shape and morphology. *Science* **336**, 687–690 (2012). doi: 10.1126/science.1219122; pmid: 22582254
44. F. Preusker *et al.*, Shape model, reference system definition, and cartographic mapping standards for comet 67P/Churyumov-Gerasimenko–Stereo-phptogrammetric analysis of

Downloaded from http://science.sciencemag.org/ on September 1, 2016

Rosetta/OSIRIS image data. *Astron. Astrophys.* **583**, A33 (2015). doi: 10.1051/0004-6361/201526349
45. A. B. Watts, *Isostasy and Flexure of the Lithosphere* (Cambridge Univ. Press, 2001).
46. J.-Y. Li *et al.*, Surface albedo and spectral variability on Ceres. *Astrophys. J.* **817**, L22 (2016). doi: 10.3847/2041-8205/817/2/L22
47. E. Brothelande, O. Merle, Estimation of magma depth for resurgent domes: An experimental approach. *Earth Planet. Sci. Lett.* **412**, 143–151 (2015). doi: 10.1016/j.epsl.2014.12.011
48. R. T. Pappalardo, R. Greeley, A review of the origins of subparallel ridges and troughs: Generalized morphological predictions from terrestrial models. *J. Geophys. Res.* **100** (E9), 18985–19007 (1995). doi: 10.1029/94JE02638
49. J. J. Petrovic, Review mechanical properties of ice and snow. *J. Mater. Sci.* **38**, 1–6 (2003). doi: 10.1023/A:1021134128038
50. H. J. Melosh, D. M. Janes, Ice volcanism on ariel. *Science* **245**, 195–196 (1989). doi: 10.1126/science.245.4914.195-a; pmid: 17787879
51. D. L. Turcotte, G. Schubert, *Geodynamics* (Cambridge Univ. Press, ed. 3, 2014).
52. J. Crisp, S. Baloga, A model for lava flows with two thermal components. *J. Geophys. Res.* **95** (B2), 1255–1270 (1990). doi: 10.1029/JB095iB02p01255
53. T. B. McCord, C. Sotin, Ceres: Evolution and current state. *J. Geophys. Res.* **110** (E5), E05009 (2005). doi: 10.1029/2004JE002244

ACKNOWLEDGMENTS

The Framing Camera system on the spacecraft was developed and built under the leadership of the Max Planck Institute for Solar System Research in Göttingen, Germany, in collaboration with the DLR Institute of Planetary Research in Berlin and the Institute of Computer and Communication Network Engineering in Braunschweig. The Framing Camera project is funded by the Max Planck Society, DLR, and NASA/Jet Propulsion Laboratory. The Dawn spacecraft Operations and Flight teams made the observations possible and are acknowledged for their efforts. O.R. is supported by an appointment to the NASA Postdoctoral Program at the NASA Goddard Space Flight Center administered by Universities Space Research Association through a contract with NASA. N.S., A.Ne., and J.H.P. acknowledge partial support by DLR. M.T.B. acknowledges support by the NASA Dawn at Ceres Guest Investigator Program Award NNH15AZ85I. We acknowledge the careful and highly beneficial reviews by anonymous referees. Dawn Framing Camera data are archived with the NASA Planetary Data System at http://sbn.psi.edu/pds/resource/dwncfc2.html. O.R. conceived the study, performed the geologic and modeling analyses, and wrote the manuscript. T.P., L.C.Q., D.P.O., S.B., and M.T.B. contributed to the geologic or modeling analyses. J.-Y.L., M.S., A.Na., T.R., M.H., and T.P. contributed with FC data products, and P.S. and F.P. contributed with digital terrain models. N.S., D.P.O., H.H., T.K., A.Ne., and J.H.P. provided absolute model ages. L.A.M., J.C.C.-R., D.A.W., B.E.S., D.L.B., and M.V.S. contributed to the interpretation of the data and its clear communication. C.A.R. and C.T.R. lead the Dawn mission. All authors contributed to the discussion of the results.

5 February 2016; accepted 20 July 2016
10.1126/science.aaf4286

Downloaded from http://science.sciencemag.org/ on September 1, 2016

RESEARCH ARTICLE SUMMARY

PLANETARY SCIENCE

Distribution of phyllosilicates on the surface of Ceres

E. Ammannito,* M. C. DeSanctis, M. Ciarniello, A. Frigeri, F. G. Carrozzo, J.-Ph. Combe, B. L. Ehlmann, S. Marchi, H. Y. McSween, A. Raponi, M. J. Toplis, F. Tosi, J. C. Castillo-Rogez, F. Capaccioni, M. T. Capria, S. Fonte, M. Giardino, R. Jaumann, A. Longobardo, S. P. Joy, G. Magni, T. B. McCord, L. A. McFadden, E. Palomba, C. M. Pieters, C. A. Polanskey, M. D. Rayman, C. A. Raymond, P. M. Schenk, F. Zambon, C. T. Russell

INTRODUCTION: The surface of the dwarf planet Ceres is known to host phyllosilicate minerals, but their distribution and origin have not previously been determined. Phyllosilicates are hydrated silicates, and their presence on the surface of Ceres is intriguing given that their structure evolves through an aqueous alteration process. In addition, some phyllosilicates are known to bear NH_4, which places a constraint on the pH and redox conditions during the evolution of Ceres. We studied the distribution of phyllosilicates across the planet's surface to better understand the evolutionary pathway of Ceres.

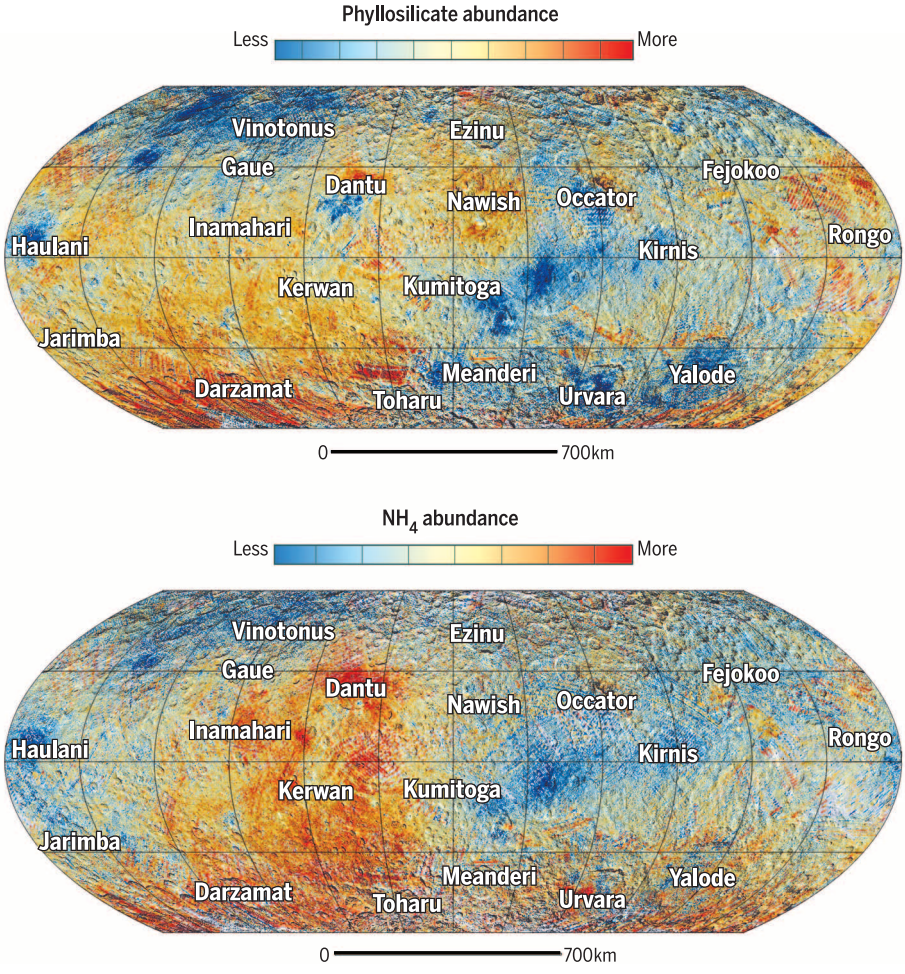
RATIONALE: Using the data acquired by the mapping spectrometer (VIR) onboard the Dawn spacecraft, we mapped the spatial distribution of different minerals on Ceres on the basis of their diagnostic absorption features in visible and infrared spectra. We studied the phyllosilicates through their OH-stretch fundamental absorption at about 2.7 μm and through the NH_4 absorption at about 3.1 μm. From our composition maps, we infer the origin of the materials identified.

ON OUR WEBSITE

Read the full article at http://dx.doi.org/10.1126/science.aaf4279

RESULTS: We found that Mg- and NH_4-bearing phyllosilicates are ubiquitous across the surface of Ceres and that their chemical composition is fairly uniform. The widespread presence of these two types of minerals is a strong indication of a global and extensive aqueous alteration—i.e., the presence of water at some point in Ceres' geological history. Although the detected phyllosilicates are compositionally homogeneous, we found variations in the intensity of their absorption features in the 3-μm region of the reflectance spectrum. Such variations are likely due to spatial variability in relative mineral abundance (see the figure).

CONCLUSION: The large-scale regional variations evident in the figure suggest lateral heterogeneity in surficial phyllosilicate abundance on scales of several hundreds of kilometers. Terrains associated with the Kerwan crater (higher concentration of phyllosilicates) appear smooth, whereas the Yalode crater (lower concentration of phyllosilicates) is characterized by both smooth and rugged terrains. These distinct morphologies and phyllosilicate concentrations observed in two craters that are similar in size may reflect different compositions and/or rheological properties. On top of this large-scale lateral heterogeneity, small-scale variations associated with individual craters could result from different proportions of mixed materials in a stratified upper crustal layer that has been exposed by impacts. Variations associated with fresh craters, such as the 34-km-diameter Haulani, indicate the presence of crustal variations over a vertical scale of a few kilometers, whereas much larger craters, such as the 126-km-diameter Dantu, suggest that such stratification may extend for at least several tens of kilometers. ■



Abundance maps. Qualitative maps of the abundances of (**top**) phyllosilicates and (**bottom**) NH_4, based on the depth of their absorption features. The two maps have a similar global pattern, although they differ in some localized regions such as Urvara. The scale bar is valid at the equator.

The list of author affiliations is available in the full article online.
*Corresponding author. Email: eleonora.ammannito@igpp.ucla.edu
Cite this article as E. Ammannito *et al.*, *Science* **353**, aaf4279 (2016). DOI: 10.1126/science.aaf4279

Downloaded from http://science.sciencemag.org/ on September 1, 2016

RESEARCH ARTICLE

PLANETARY SCIENCE

Distribution of phyllosilicates on the surface of Ceres

E. Ammannito,[1]* M. C. DeSanctis,[2] M. Ciarniello,[2] A. Frigeri,[2] F. G. Carrozzo,[2] J.-Ph. Combe,[3] B. L. Ehlmann,[4,5] S. Marchi,[6] H. Y. McSween,[7] A. Raponi,[2] M. J. Toplis,[8] F. Tosi,[2] J. C. Castillo-Rogez,[5] F. Capaccioni,[2] M. T. Capria,[2] S. Fonte,[2] M. Giardino,[2] R. Jaumann,[9] A. Longobardo,[2] S. P. Joy,[1] G. Magni,[2] T. B. McCord,[3] L. A. McFadden,[10] E. Palomba,[2] C. M. Pieters,[11] C. A. Polanskey,[5] M. D. Rayman,[5] C. A. Raymond,[5] P. M. Schenk,[12] F. Zambon,[2] C. T. Russell[1]

The dwarf planet Ceres is known to host phyllosilicate minerals at its surface, but their distribution and origin have not previously been determined. We used the spectrometer onboard the Dawn spacecraft to map their spatial distribution on the basis of diagnostic absorption features in the visible and near-infrared spectral range (0.25 to 5.0 micrometers). We found that magnesium- and ammonium-bearing minerals are ubiquitous across the surface. Variations in the strength of the absorption features are spatially correlated and indicate considerable variability in the relative abundance of the phyllosilicates, although their composition is fairly uniform. These data, along with the distinctive spectral properties of Ceres relative to other asteroids and carbonaceous meteorites, indicate that the phyllosilicates were formed endogenously by a globally widespread and extensive alteration process.

The surface of the dwarf planet Ceres exhibits low reflectance and a relatively featureless spectrum in the range of 0.5 to 2.6 μm, with the exception of a broad absorption feature centered around 1.2 μm (*1*,*2*). Thermally corrected reflectance data from 2.6 to 4.2 μm, measured from onboard the Dawn spacecraft, reveal a spectrum rich in absorption features at 2.72, 3.05 to 3.1, 3.3 to 3.5, and 3.95 μm, which are diagnostic of the composition of the surface (*3*). The band from 3.05 to 3.1 μm is clearly visible in ground-based spectra and has been attributed to a variety of different phases including water ice (*4*), hydrated or NH_4-bearing clay minerals (*5*, *6*), or brucite (*7*), whereas the 3.95-μm band has been definitively attributed to carbonates (*8*). Initial Dawn observations obtained during the Approach and Survey phases of the mission indicate that Ceres' average surface is a mixture of NH_4-bearing phyllosilicates such as serpentines and smectites, carbonates, and absorbing dark materials such as organic carbon or magnetite (*3*). As Dawn has continued to orbit Ceres (*9*), the visible and infrared mapping spectrometer onboard the spacecraft [VIR (*10*)] has obtained spatially resolved hyperspectral images of Ceres, which have been projected to generate maps of spectral parameters that characterize Ceres' mineralogy. Dawn's orbital characteristics and the orientation of Ceres' spin axis (*11*) have enabled 84% of the surface to be mapped with the VIR's infrared channel. The maps discussed here have roughly 1.1-km spatial resolution, global longitude coverage, and latitude coverage spanning from 60°S to 60°N (see the Materials and methods section for further details). All the maps and coordinates are given using the Kait Prime Meridian Reference System (*12*).

Albedo at 0.55 μm, measured by the VIR

The geometric albedo measured by the VIR instrument is 0.094 ± 0.008 at 0.55 μm (Materials and methods section). Given the low albedo of the surface, single scattering dominates the surface reflectance. Figure 1 is an albedo map, in reflectance at standard geometry, indicating a variable proportion of low- and high-albedo materials on Ceres' surface. Roughly 70% of the mapped surface has a radiance factor (I/F, defined as π × reflectance, where I is the measured radiance and F is solar flux) at 0.55 μm that is within the range 0.032 to 0.036, with a central value of 0.034.

Shown in Fig. 2A is an example of a typical thermally corrected reflectance spectrum of Ceres acquired by VIR. Diagnostic absorptions at 2.7 and 3.05 to 3.1 μm are well defined, and we measured and mapped the strength of these features globally across Ceres (Fig. 3 and Materials and methods section).

Variability of the 2.7- and 3.1-μm absorption bands

The strong and narrow absorption near 2.7 μm is an OH-stretch fundamental, centered at 2.72 to 2.73 μm (*13*). This relatively strong absorption dominates the overall spectral properties and is a distinctive indicator of OH-bearing minerals such as phyllosilicates (*14*). The exact spectral position of the absorption is indicative of Mg-OH phases, such as antigorite (Mg-serpentine) or saponite (Mg-smectite) (*15*). We found that the spectral

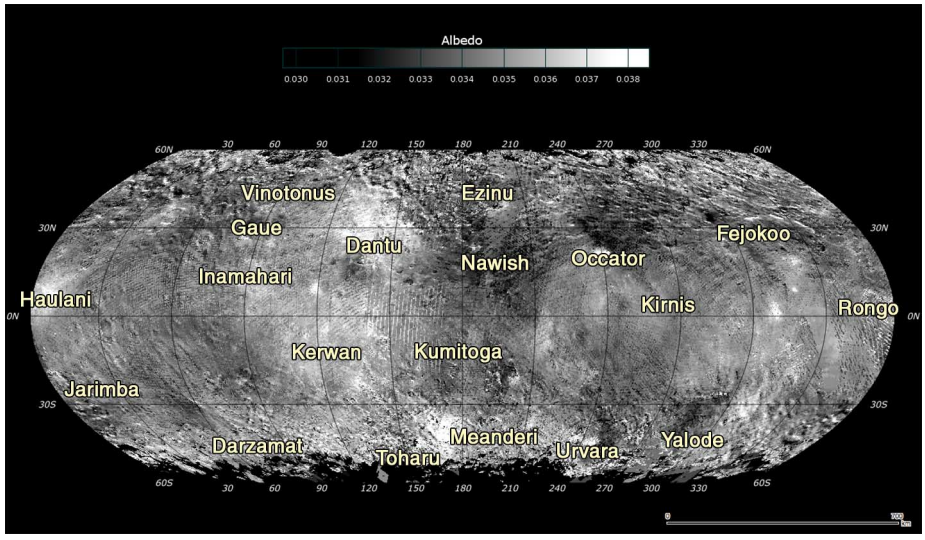


Fig. 1. Albedo map. The map shows the albedo in terms of the radiance factor (I/F) at 0.55 μm, photometrically corrected and converted to standard observation geometry (incidence angle = 30°, emission angle = 0°, phase angle = 30°). Some of the brightest regions are out of scale, namely, Occator, Toharu, and Haulani. The scale bar is true at the equator.

[1]Earth Planetary and Space Sciences, University of California–Los Angeles, 603 Charles Young Drive, Los Angeles, CA 90095-1567, USA. [2]Istituto di Astrofisica e Planetologia Spaziali, Istituto Nazionale di Astrofisica, 00133 Roma, Italy. [3]The Bear Fight Institute, Winthrop, WA 98862, USA. [4]Division of Geological and Planetary Sciences, California Institute of Technology, Pasadena, CA 91125, USA [5]Jet Propulsion Laboratory, California Institute of Technology, Pasadena, CA 91109, USA. [6]Southwest Research Institute, Boulder, CO 80302, USA. [7]Department of Earth and Planetary Sciences, University of Tennessee, Knoxville, TN 37996-1410, USA. [8]Institut de Recherche en Astrophysique et Planétologie (UMR 5277), Université de Toulouse, F-31400 Toulouse, France. [9]Institute of Planetary Research, Deutsches Zentrum für Luft- und Raumfahrt, 12489 Berlin, Germany. [10]NASA Goddard Space Flight Center, Greenbelt, MD 20771, USA. [11]Department of Earth, Environmental, and Planetary Sciences, Brown University, Providence, RI 02912, USA. [12]Lunar and Planetary Institute, Houston, TX 77058, USA.
*Corresponding author. Email: eleonora.ammannito@igpp.ucla.edu

Downloaded from http://science.sciencemag.org/ on September 1, 2016

position of this absorption does not vary significantly across the mapped portion of the surface (2.727 ± 0.003 μm; Materials and methods section), which is an indication that the chemical composition of the phyllosilicates does not change substantially. Within the mapped portion of Ceres, the only locations that shift toward longer wavelengths, and therefore that point to a different chemical composition of the phyllosilicates, are the small bright regions on the floor of Occator crater (*16*). Mg-rich serpentines are commonly present in carbonaceous chondrite meteorites, along with a large number of other distinct phyllosilicates (*14*). Carbonaceous chondrites in the CM group have matrix compositions that systematically vary from the least aqueously altered samples, which have a 2.7-μm absorption consistent with cronstedtite (Fe-serpentine), to the most aqueously altered samples, which have shorter wavelength absorptions characteristic of antigorite (Mg-serpentine) (*17*). The pervasive presence of Mg- rather than Fe-serpentine across Ceres thus indicates that aqueous alteration has been extensive. Although the presence and the position of the 2.7-μm absorption are globally constant, its intensity shows significant variations beyond the 2σ errors associated with the measurements. The computed average value is 0.251 ± 0.006, and the range of variability is between 0.226 and 0.270. The spatial distribution of the 2.7-μm band depth (Fig. 3A) shows two broad regions containing terrains in which the values of the band depths are lower than the average (blue in Fig. 3A). One region is in the northeast quadrant and the other is in the southwest. In contrast, the region around the smooth Kerwan terrains has deeper Mg-OH band depths with respect to the nearby regions; specific regions near the northern Dantu and northeastern Occator craters also have deeper band depths. The lack of geochemical variation inferred from the band center position suggests either that the exposed upper layer has no substantive phyllosilicate compositional gradient or that some homogenization process has been very efficient at the spatial scale sampled by VIR. The latter is unlikely because although the position of the bands do not vary, there are variations in the intensity of the same absorption in some craters (Haulani, Dantu, and Urvara), and a homogenization process would have affected both parameters.

The distinct absorption feature at about 3.1 μm has been attributed to ammoniated phyllosilicates (*3*, *5*). The analysis of this feature shows that its band center position does not vary across the surface, and its value, computed after removal of the local continuum, is 3.061 μm with a standard deviation of 0.011 μm (Materials and methods section). As with the 2.7-μm absorption, the absence of variability in the central wavelength of the 3.1-μm absorption suggests that the ammoniated phyllosilicate phase is compositionally homogeneous over most of Ceres' surface. The average value of the intensity of the 3.1-μm absorption is 0.055 (with a standard deviation of 0.012). The spatial variability in the 3.1-μm band intensity (Fig. 3B) broadly follows that of the 2.7-μm band (Fig. 3A), with the same broad regions described above. However, at smaller spatial scales, there are locations where intensity variations are inversely correlated (e.g., the Urvara crater), whereas elsewhere the intensities of the two absorption features show a weak positive correlation (Fig. 4A). In contrast, neither the 2.7- nor the 3.1-μm band exhibits an intensity that meaningful correlates at the global scale with the I/F ratio (Fig. 4, B and C), although a correlation is sometimes evident locally, as in the Haulani crater.

The Haulani crater (5.7°N, 10.9°E; diameter, 34 km) and its ejecta stand out in the global maps (Figs. 1, 3A, and 3B), showing high albedo but shallower bands with respect to the surroundings (Fig. 5B). The shallowest bands (blue color in Fig. 5A and blue spectrum in Fig. 5B) are found inside the crater and in nearby bright ejecta. In this crater, the shallow bands are associated with bright material that was excavated and deposited by the impact. However, as noted above, the anticorrelation of band depth and albedo is not global. A second example is the Dantu crater (24.35°N, 138.2°E; diameter, 126 km), which is divided into two terrains: the northern area, with higher band depths (yellow spectrum in Fig. 5, C and D), and the southern area, with shallower bands (blue in Fig. 5, C and D). Unlike in Haulani, in Dantu, there is no correlation between band depth and albedo. The area just outside the northern rim of the crater has a similar albedo to that of the floor, whereas the deepest absorptions are found only within the rim.

Implications of variability in the band intensities

Variations in the band depth could be due to a variety of factors, such as (i) relative abundance and grain size of spectrally opaque dark phases, (ii) phase changes caused by impact processes (e.g., dehydration), (iii) variations in the quantity of impact-delivered material, (iv) depth-dependent variation in the abundances of materials exposed by craters, and/or (v) heterogeneity of the external layer of the surface.

The relative abundance and size of opaque phases in a mixture has a major effect on spectral contrast and the strength of absorption bands, as well as on albedo. With increasing abundance of fine-grained opaque content, albedo and band strength decrease nonlinearly (*18*, *19*). Thus, band strength should be correlated with albedo. Given that this is not observed on Ceres, variation in opaque content cannot account for the observed variations in band strength.

Dehydration of phyllosilicates at increased temperatures generated by impacts should reduce the intensity of the OH-stretch band at 2.7 μm (*20*, *21*) and of the NH_4-related band at 3.1 μm (*20*, *22*). However, prominent craters such as Kerwan (diameter, 280 km) are associated with deeper absorption bands, whereas the similar-sized crater Yalode (diameter, 260 km) is associated with much shallower bands. Although it is conceivable that impact heating could have been

Downloaded from http://science.sciencemag.org/ on September 1, 2016

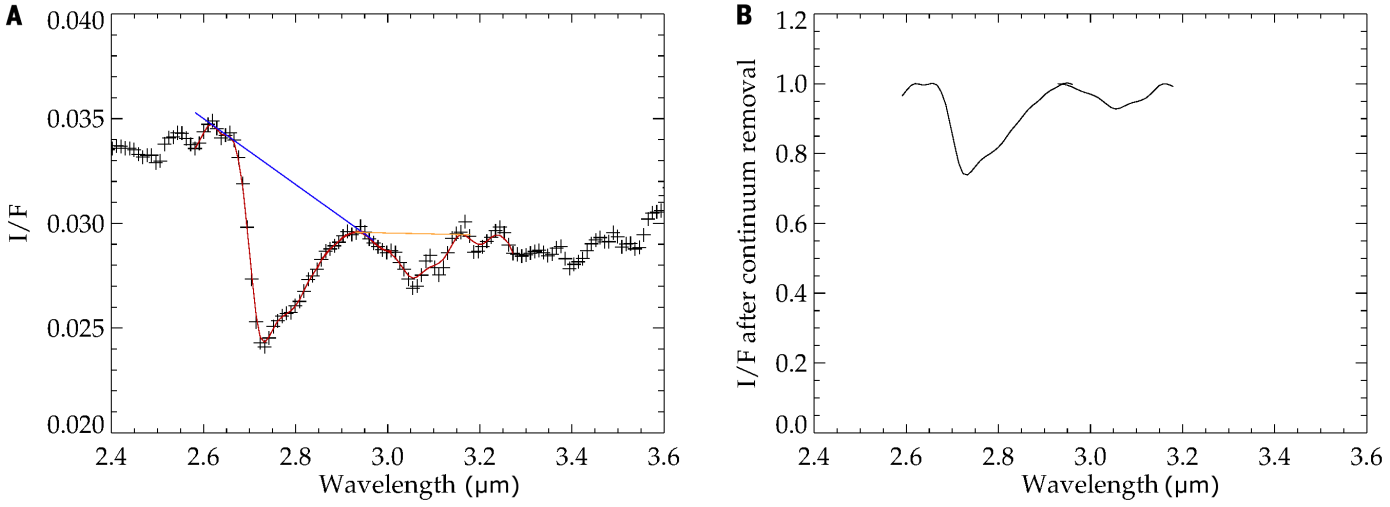


Fig. 2. Computation of band parameters. (**A**) Example Ceres spectrum (black crosses) with the smoothed spectrum superimposed (red line). The blue and yellow lines represent the straight line used to compute the continuum of each band. (**B**) Continuum-removed spectrum (black line).

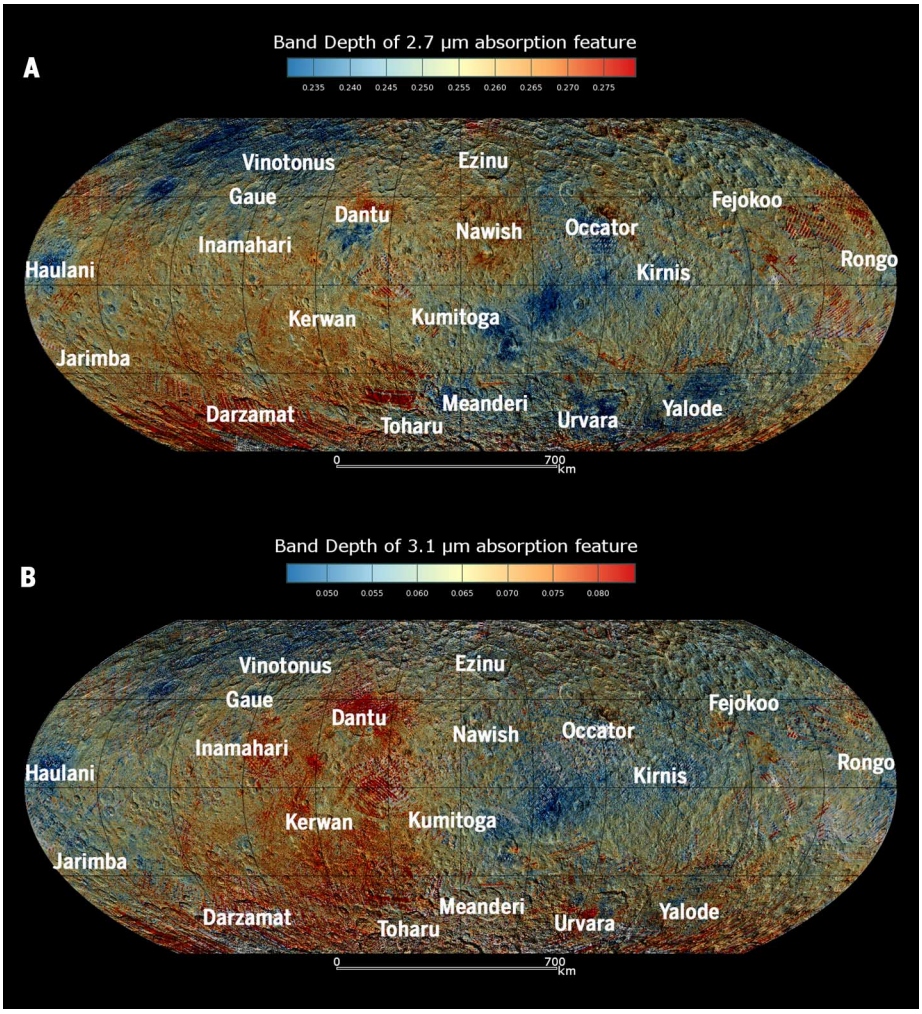


Fig. 3. Band depth maps. Maps of the peak absorption depths of (**A**) the 2.7-μm OH-stretch band and (**B**) the 3.1-μm NH_4 band. The two maps have a similar global pattern, although they differ in some localized regions such as Urvara. The scale bar is true at the equator.

different in these two cratering events, it is unlikely to be the cause of the observed spatial heterogeneity. Furthermore, there are craters, such as Dantu, that expose diverse materials with both deeper and shallower band depths.

The band depth distribution does not correlate with crater size or inferred age. For instance, the pristine morphologies of the Dantu and Haulani craters suggest recent formation [Dantu certainly postdates Kerwan on the basis of superposition (*23*)]. The fact that craters of very different sizes and formation ages show heterogeneities reduces the likelihood that contamination from impactor materials and space weathering is a principal cause of the observed distribution of band depth variations. This conclusion is also reinforced by the constant position of the absorption band centers across the surface, limiting the potential role of contamination from impactor materials (unless they had exactly the same composition as Ceres, which seems unlikely, given the wide range of asteroid spectra and chondrite compositions).

The most likely explanation is that the variability in the strengths of these two diagnostic mineral absorptions is associated with a variation in the abundance of phyllosilicates relative to the other components of the surface. According to the modeling technique used in (*3*), the range of variability observed on Ceres is compatible with abundance variations in the range of 6 to 12% and 3 to 9% for Mg-rich phyllosilicates and NH_4-bearing species, respectively. We stress that the data indicate that the composition of phyllosilicate species is constant, but that it is their relative abundance that varies. Therefore, the correlation expressed in Fig. 4A between the depths of the absorptions at 2.7 and 3.1 μm indicates that the abundances of Mg-phyllosilicates and ammoniated phyllosilicates are generally correlated. In combination with the absence of Fe-phyllosilicates, this suggests that the ammoniated phyllosilicates, as well as the other phyllosilicates, are endogenous, and that the aqueous alteration processes creating such minerals were global and not due to the local environment.

The distribution of measured spectral properties is compatible with the presence on Ceres of a single Mg-phyllosilicate composition, sometimes including embedded ammonium. However, we cannot exclude the possibility of a collection of phyllosilicates defining a spatially homogeneous composition. Current thermal evolution models for Ceres (*24*, *25*) are compatible with an evolutionary pathway that starts from a parent body of primitive carbonaceous chondrite–like material, which undergoes aqueous alteration processes in a hydrothermal environment whose pH and redox conditions favor the stability of ammonium (over ammonia). The substitution of potassium and, to a lesser extent, alkali earth metals by ammonium is a well-understood phenomenon resulting in the production of Mg- and NH_4-bearing clays (e.g., *26* and references therein).

Although the Ceres phyllosilicates are compositionally homogeneous, we interpret the observed variations in the depth of absorptions in the 3-μm region as an indication of variability in their abundance. The large-scale regional variations shown in Fig. 3, A and B, suggest lateral heterogeneity in phyllosilicate abundance over a scale of several hundreds of kilometers. Terrains associated with Kerwan (higher concentration of phyllosilicates) appear smooth in texture, whereas Yalode (lower concentration of phyllosilicates) is characterized by both smooth and rugged terrains (*27*). This pronounced difference in morphology and phyllosilicate concentration between two craters that are similar in size may reflect different compositions and/or rheological properties. On top of this large-scale lateral heterogeneity, we found small-scale variations associated with craters (examples in Fig. 5) that could result from different proportions of mixed materials in a stratified upper layer exposed by impacts. Fresh craters such as Haulani indicate the presence of different materials over a vertical scale of a few kilometers, whereas much larger craters such as Dantu suggest that such stratification may extend for at least several tens of kilometers.

Materials and methods

VIR measurements at Ceres

The Dawn spacecraft has been acquiring data about the dwarf planet Ceres since January 2015 (*11*). During the Approach phase (January to April 2015), there were nine opportunities to point the optical instruments toward Ceres and to acquire spectral information about its surface. In late April/early May 2015, the spacecraft performed an observational campaign while the spacecraft was in orbit around Ceres at an altitude of 13,600 km. In this mission phase, called RC3, the instruments acquired limb and high phase images while the spacecraft was on the night side of the orbit and nadir images while it was on the day side. After this initial part of the exploration, in three consequent orbits Survey (4400-km altitude), High Altitude Mapping Orbit (HAMO, 1470-km altitude) and Low Altitude Mapping Orbit (LAMO, 385-km altitude), the instruments acquired data in the dayside section of the orbit at increasing resolution. The spectrometer VIR (visible channel: 0.25- to 1.0-μm range and 0.002-μm resolution; infrared channel: 1.0- to 5.0-μm range and 0.010-μm resolution) acquired data during all the mapping

Downloaded from http://science.sciencemag.org/ on September 1, 2016

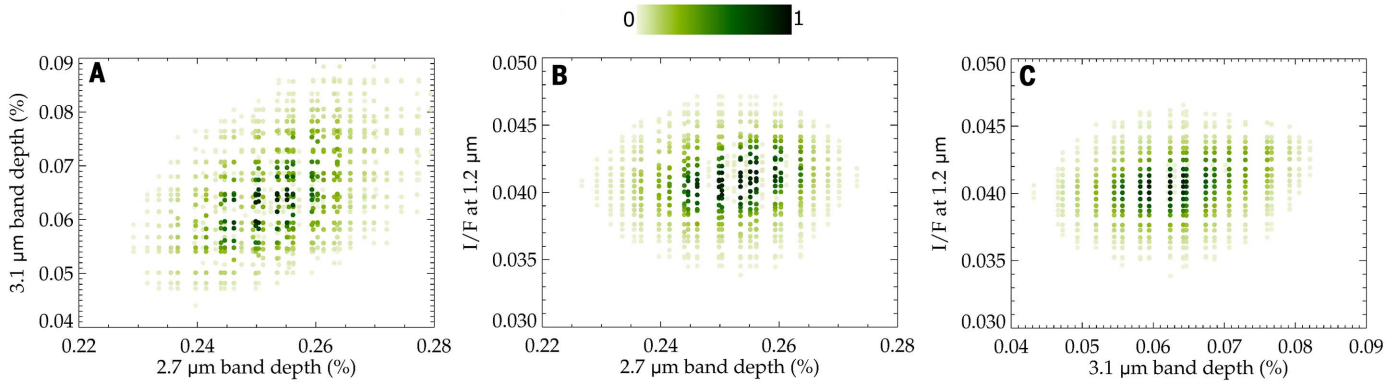


Fig. 4. Scatterplots of Ceres global spectral parameters associated with diagnostic absorptions. (**A**) 3.1-μm band absorption depth versus 2.7-μm band absorption depth. (**B**) *I/F* at 1.2 μm versus 2.7-μm band absorption depth. (**C**) *I/F* at 1.2 μm versus 3.1-μm band absorption depth. The color scale represents the frequency of each data point normalized to the maximum value in each plot.

orbits, although in this paper we used data from RC3 and Survey. In RC3, VIR acquired 1.9 million infrared spectra and 1.9 million visible spectra with an average linear resolution of 3.4 km. In Survey orbit, VIR acquired 2.8 million infrared spectra and 4.3 million visible spectra with an average linear resolution of 1.1 km. Resolutions indicated here do not consider the smearing.

Geometric albedo and albedo maps

Geometric albedo is computed from eq. 12.58 in (*28*)

$$A_p(w,\bar{\theta}) = \frac{w}{8}\{[1+B_0]p(0)-1\} + U(w,\bar{\theta})\frac{r_0}{2}\left(1+\frac{r_0}{3}\right)$$

where w is the single scattering albedo, B_0 is the opposition effect amplitude, $p(0)$ is the single particle phase function at 0° phase angle, and $U(w,\bar{\theta})$ accounts for large scale surface roughness through the slope parameter $\bar{\theta}$. Hapke's model parameters derived in (*29*) from spectrophotometric analysis of VIR observations of Ceres have been assumed.

Albedo map has been produced by reporting VIR measured radiance factor (*I/F*) with generic incidence, emission, and phase angles (i, e, α) to standard observation geometry (i = 30°, e = 0°, α = 30°) by means of the relation

$$I/F(30^\circ,0^\circ,30^\circ) = \frac{I/F(i,e,\alpha)}{I/F_{\mathrm{m}}(i,e,\alpha)} I/F_{\mathrm{m}}(30^\circ,0^\circ,30^\circ)$$

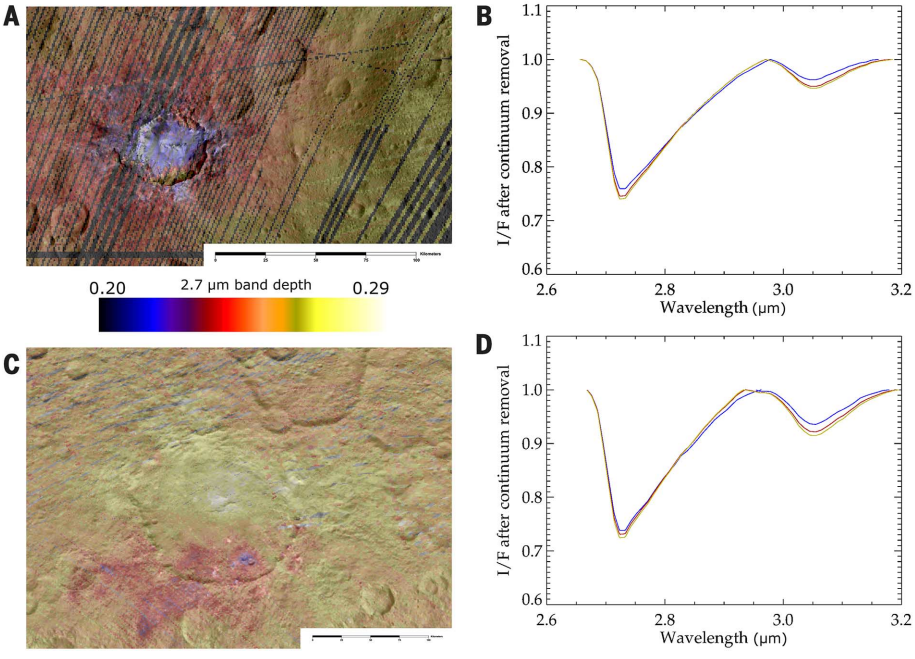


Fig. 5. Haulani and Dantu craters. (**A** and **B**) Haulani. (**C** and **D**) Dantu. For each crater, we show a map of the 2.7-μm band depth [(A) and (C)] and the continuum-removed spectra [(B) and (D)]. Each spectrum shown here is an average of locations in the image that share the same band depth. The color of each spectrum corresponds to the band depth.

where the subscript m indicates that reflectance has been modeled applying Hapke's theory (*28*) as shown in (*29*).

Band parameters

The band parameters have been computed with the following steps: (i) Removal of thermal emission. The thermal emission has been modeled as the Planck function that best fit the measured *I/F*. (ii) Smoothing of the spectra (from black crosses to red line in Fig. 2A). The spectra have been smoothed with a boxcar average of 3 spectral channels. (iii) Evaluation of the continuum and continuum removal. The band continuum of each band has been computed as the straight line between the two local maxima (blue line for 2.7-μm band and orange line for 3.1-μm band in Fig. 2A). The continuum-removed spectrum is the ratio of the smoothed spectrum and the continuum. (iv) Band centers: after the continuum removal, the band center is the wavelength which corresponds to the local minimum after the continuum removal (Fig. 2B). (v) Band depths are defined as $1–R_c/R_b$, where R_b is the reflectance at the band minimum and R_c is the reflectance of the continuum at the same wavelength as R_b.

Photometric correction of band parameters

Band centers have not been corrected. Band depths (*BD*) have been rescaled to a reference condition with emission angle (e) equal to 0°, incidence angle (i) equal to 30°, and phase angle (φ) equal to 30°. The scaling has been done using an empirical approach. According to this approach, the rescaled band depth ($BD_{(0,30,30)}$) can be computed as

$$BD_{(0,30,30)} = BD_{(e,i,\varphi)} \times LS \times f_\lambda(\varphi)$$

where $BD_{(e,i,\varphi)}$ is the band depth computed according to the procedure described in the previous paragraph, *LS* is the Lommel Seeliger factor

$$LS = 0.46 \times \frac{\cos i + \cos e}{\cos i}$$

Downloaded from http://science.sciencemag.org/ on September 1, 2016

and $f_\lambda(\varphi)$ is the phase function of each absorption band that has been modeled with a polynomial of the second order

$$f_{2.7}(\varphi) = \frac{0.26}{0.25 - 8.62{*}10^{-5}{*}\varphi + 1.33{*}10^{-5}{*}\varphi^2}$$

$$f_{3.1}(\varphi) = \frac{0.08}{0.07 - 2.60{*}10^{-4}{*}\varphi + 1.12{*}10^{-5}{*}\varphi^2}$$

Maps of band parameters

The RC3 and Survey data sets have been mapped using a Mollweide projection in the latitude range 60°S to 60°N. Data from both mission phases have been filtered for illumination conditions and level of reflectance. In the maps of the band parameters, only the spectra with incidence and emission angles lower than 70°, phase angle between 15° and 60°, and average I/F brightness higher than 0.004 have been considered. To generate the maps discussed in this work, rather than an average, the RC3 map has been used only to fill the gaps in the Survey-based map.

REFERENCES AND NOTES

1. S. J. Bus, R. P. Binzel, Phase II of the small main-belt asteroid spectroscopic survey: The observations. *Icarus* **158**, 106–145 (2002). doi: 10.1006/icar.2002.6857
2. S. J. Bus, R. P. Binzel, Phase II of the small main-belt asteroid spectroscopic survey: A feature-based taxonomy. *Icarus* **158**, 146–177 (2002). doi: 10.1006/icar.2002.6856
3. M. C. De Sanctis *et al*., Ammoniated phyllosilicates with a likely outer Solar System origin on (1) Ceres. *Nature* **528**, 241–244 (2015). doi: 10.1038/nature16172; pmid: 26659184
4. L. A. Lebofsky, M. A. Feierberg, A. T. Tokunaga, H. P. Larson, J. R. Johnson, The 1.7–4.2 μm spectrum of asteroid 1 Ceres: Evidence for structural water in clay minerals. *Icarus* **48**, 453–459 (1981). doi: 10.1016/0019-1035(81)90055-5
5. T. V. King, R. N. Clark, W. M. Calvin, D. M. Sherman, R. H. Brown, Evidence for ammonium-bearing minerals on Ceres. *Science* **255**, 1551–1553 (1992). doi: 10.1126/science.255.5051.1551; pmid: 17820166
6. P. Vernazza *et al*., Analysis of near-IR spectra of 1 Ceres and 4 Vesta, targets of the Dawn mission. *Astron. Astrophys.* **436**, 1113–1121 (2005). doi: 10.1051/0004-6361:20042506
7. R. E. Milliken, A. S. Rivkin, Brucite and carbonate assemblages from altered olivine-rich materials on Ceres. *Nat. Geosci.* **2**, 258–261 (2009). doi: 10.1038/ngeo478
8. A. S. Rivkin, E. L. Volquardsen, B. E. Clark, The surface composition of Ceres: Discovery of carbonates and iron-rich clays. *Icarus* **185**, 563–567 (2006). doi: 10.1016/j.icarus.2006.08.022
9. C. T. Russell, C. A. Raymond, The Dawn Mission to Vesta and Ceres. *Space Sci. Rev.* **163**, 3–23 (2011). doi: 10.1007/s11214-011-9836-2
10. M. C. De Sanctis *et al*., The VIR spectrometer. *Space Sci. Rev.* **163**, 329–369 (2011). doi: 10.1007/s11214-010-9668-5
11. C. T. Russell *et al*., Dawn arrives at Ceres: Exploration of a small volatile-rich world. *Science* **353**, 1008–1010 (2016).
12. T. Roatsch *et al*., Ceres Survey Atlas derived from Dawn Framing Camera images. *Planet. Space Sci.* **121**, 115–120 (2016). doi: 10.1016/j.pss.2015.12.005
13. V. C. Farmer, "The layer silicates," in *The Infrared Spectra of Minerals* (Monograph 4, The Mineralogical Society of Great Britain and Ireland, 1974), pp. 331–363.
14. A. J. Brearley, Phyllosilicates in the matrix of the unique carbonaceous chondrite Lewis Cliff 85332 and possible implications for the aqueous alteration of CI chondrites. *Meteoritics* **32**, 377–388 (1997). doi: 10.1111/j.1945-5100.1997.tb01281.x
15. J. L. Bishop, M. D. Lane, M. D. Dyar, A. J. Brown, Reflectance and emission spectroscopy study of four groups of phyllosilicates: Smectites, kaolinite-serpentines, chlorites and micas. *Clay Miner.* **43**, 35–54 (2008). doi: 10.1180/claymin.2008.043.1.03
16. M. C. De Sanctis *et al*., Bright carbonate deposits as evidence of aqueous alteration on (1) Ceres. *Nature* **536**, 54–57 (2016). doi: 10.1038/nature18290; pmid: 27362221
17. D. Takir *et al*., Nature and degree of aqueous alteration in CM and CI carbonaceous chondrites. *Meteorit. Planet. Sci.* **48**, 1618–1637 (2013).
18. R. N. Clark, Spectral properties of mixtures of montmorillonite and dark carbon grains: Implications for remote sensing minerals containing chemically and physically adsorbed water. *J. Geophys. Res.* **88**, 10635–10644 (1983). doi: 10.1029/JB088iB12p10635
19. C. M. Pieters, Strength of mineral absorption features in the transmitted component of near-infrared reflected light: First results from RELAB. *J. Geophys. Res.* **88**, 9534–9544 (1983). doi: 10.1029/JB088iB11p09534
20. J. D. Russell, V. C. Farmer, Infra-red spectroscopic study of the dehydration of montmorillonite and saponite. *Clay Miner. Bull.* **5**, 443–464 (1964). doi: 10.1180/claymin.1964.005.32.04
21. R. L. Frost, A. M. Vassallo, The dihydroxylation of the kaolinite clay minerals using infrared emission spectroscopy. *Clays Clay Miner.* **44**, 635–651 (1996). doi: 10.1346/CCMN.1996.0440506
22. B. Chourabi, J. J. Fripiat, Determination of tetrahedral substitutions and interlayer surface heterogeneity from vibrational spectra of ammonium in smectites. *Clays Clay Miner.* **29**, 260–268 (1981). doi: 10.1346/CCMN.1981.0290403
23. H. Hiesinger *et al*., Cratering on Ceres: Implications for its crust and evolution. *Science* **353**, aaf4759 (2016).
24. T. B. McCord, C. Sotin, Ceres: Evolution and current state. *J. Geophys. Res.* **110**, E05009 (2005). doi: 10.1029/2004JE002244
25. J. C. Castillo-Rogez, T. B. McCord, Ceres' evolution and present state constrained by shape data. *Icarus* **205**, 443–459 (2010). doi: 10.1016/j.icarus.2009.04.008
26. S. Engel, J. I. Lunine, D. L. Norton, Silicate interactions with ammonia-water fluids on early Titan. *J. Geophys. Res.* **99**, 3745–3752 (1994). doi: 10.1029/93JE03433
27. D. Buczkowski *et al*., The geomorphology of Ceres. *Science* **353**, aaf4332 (2016).
28. B. Hapke, *Theory of Reflectance and Emittance Spectroscopy* (Cambridge Univ. Press, ed. 2, 2012).
29. M. Ciarniello, M. C. De Sanctis, E. Ammannito, A. Raponi, A. Longobardo, E. Palomba, F. G. Carrozzo, F. Tosi, J.-Y. Li, S. Schröder, F. Zambon, A. Frigeri, S. Fonte, M. Giardino, C. M. Pieters, C. A. Raymond, C. T. Russell, http://arxiv.org/abs/1608.04643 (2016).

ACKNOWLEDGMENTS

We thank the Italian Space Agency (ASI), NASA, and the Deutsches Zentrum für Luft- und Raumfahrt for supporting this work. The VIR instrument was funded and coordinated by the ASI and built by Selex ES, with the scientific leadership of the Institute for Space Astrophysics and Planetology, Italian National Institute for Astrophysics, Italy, and it is operated by the Institute for Space Astrophysics and Planetology, Rome, Italy. A portion of this work was carried out at the Jet Propulsion Laboratory, California Institute of Technology, USA, under contract to NASA. Dawn data are archived in NASA's Planetary Data System; VIR spectral data may be obtained at http://sbn.psi.edu/pds/resource/dwncvir.html.

5 February 2016; accepted 29 July 2016
10.1126/science.aaf4279

Downloaded from http://science.sciencemag.org/ on September 1, 2016

RESEARCH ARTICLE SUMMARY

PLANETARY SCIENCE

Detection of local H_2O exposed at the surface of Ceres

Jean-Philippe Combe,* Thomas B. McCord, Federico Tosi, Eleonora Ammannito, Filippo Giacomo Carrozzo, Maria Cristina De Sanctis, Andrea Raponi, Shane Byrne, Margaret E. Landis, Kynan H. G. Hughson, Carol A. Raymond, Christopher T. Russell

INTRODUCTION: Dwarf planet Ceres' low average-density (2162 ± 3 kg m^{-3}) indicates that it must contain considerable water. Water is likely a key component in the chemical evolution and internal activity of Ceres, possibly resulting in a layer of ice-rich material and perhaps liquid in the mantle. Mineral hydroxides (OH-bearing) and hydrates (H_2O-bearing), such as clays, carbonates, and various salts, would be created. These hypotheses were supported by the detection of hydroxyl (OH)–rich materials, OH-bearing molecule releases, H_2O vapor molecules, and haze. However, the presence of H_2O on the surface has not previously been confirmed. The detection and mapping of H_2O on Ceres is one objective of the Dawn spacecraft, in orbit around Ceres since March 2015.

ON OUR WEBSITE

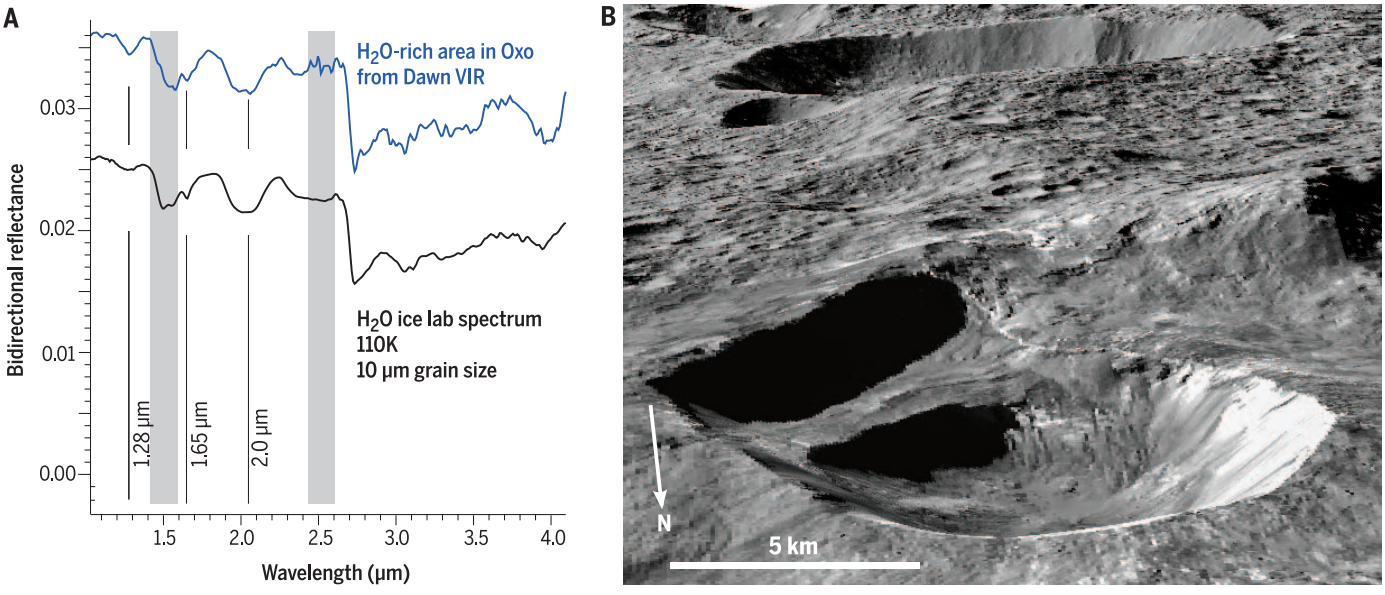
Read the full article at http://dx.doi.org/10.1126/science.aaf3010

RATIONALE: The purpose of the Dawn space mission at Ceres is to study the geology, geophysics, and composition remotely by means of high-resolution imagery and spectrometry. Dawn's Visible and InfraRed Mapping Spectrometer (VIR) measures the sunlight scattered by the surface of Ceres in a range of wavelengths between 0.25 and 5.1 μm. The position and shape of absorption features in VIR reflectance spectra are sensitive to the surface mineral and molecular composition. In spectroscopy, absorption bands at 2.0, 1.65, and 1.28 μm are characteristic of vibration overtones in the H_2O molecule.

RESULTS: Dawn has detected water-rich surface materials in a 10-km-diameter crater named Oxo, which exhibit all absorption bands that are diagnostic of the H_2O molecule (see the figure). These spectra are most similar to those of H_2O ice, but they could also be attributable to hydrated minerals. Oxo crater appears to be geologically very young (~1 million to 10 million years); it has sharp rims and its floor is almost devoid of impacts, suggesting a recent exposure of surface H_2O. The high latitude and morphology of the Oxo crater protects much of the surface area from direct solar illumination for most of the cerean day, presenting favorable conditions for the stability of water ice or heavily hydrated salts.

CONCLUSION: Four ways to create or transport H_2O on Ceres are considered: (i) Exposure of near-surface H_2O-rich materials by a recent impact or an active landslide seems most consistent with the presence of both mineral hydrates and water ice. (ii) Release of subsurface H_2O may occur on Ceres, similar to release on comet nuclei, but may never recondense on the surface. (iii) Infall of ice-bearing objects is not likely to deposit water on Ceres, because the H_2O molecule likely would dissociate upon impact. (iv) Implantation of protons from the solar wind on the surface is not a probable origin of OH on Ceres because of the low flux of solar wind charged particles. We therefore conclude that surface H_2O or hydrated minerals are the most plausible explanation. ■

The list of author affiliations is available in the full article online.
*Corresponding author. Email: jean-philippe_combe@bearfightinstitute.com
Cite this article as J.-Ph. Combe *et al.*, *Science* 353, aaf3010 (2016). DOI: 10.1126/science.aaf3010



Dawn VIR infrared observations of Oxo crater on Ceres demonstrate the detection of H_2O at the surface. (**A**) Reflectance spectrum collected where absorption bands of H_2O at 1.28, 1.65, and 2 μm are the strongest (in blue) compared with a laboratory spectrum of H_2O ice (black). The lab spectrum is scaled and vertically shifted for clarity. (**B**) Perspective view of Oxo crater observed by the Dawn Framing Camera (FC), where the two high-albedo areas right next to the scarps contain H_2O-rich materials.

Downloaded from http://science.sciencemag.org/ on September 1, 2016

RESEARCH ARTICLE

PLANETARY SCIENCE

Detection of local H_2O exposed at the surface of Ceres

Jean-Philippe Combe,[1]* Thomas B. McCord,[1] Federico Tosi,[2] Eleonora Ammannito,[2,3] Filippo Giacomo Carrozzo,[2] Maria Cristina De Sanctis,[2] Andrea Raponi,[2] Shane Byrne,[5] Margaret E. Landis,[5] Kynan H. G. Hughson,[3] Carol A. Raymond,[4] Christopher T. Russell[3]

The surface of dwarf planet Ceres contains hydroxyl-rich materials. Theories predict a water ice-rich mantle, and water vapor emissions have been observed, yet no water (H_2O) has been previously identified. The Visible and InfraRed (VIR) mapping spectrometer onboard the Dawn spacecraft has now detected water absorption features within a low-illumination, highly reflective zone in Oxo, a 10-kilometer, geologically fresh crater, on five occasions over a period of 1 month. Candidate materials are H_2O ice and mineral hydrates. Exposed H_2O ice would become optically undetectable within tens of years under current Ceres temperatures; consequently, only a relatively recent exposure or formation of H_2O would explain Dawn's findings. Some mineral hydrates are stable on geological time scales, but their formation would imply extended contact with ice or liquid H_2O.

The state and abundance of water on the dwarf planet Ceres have been major questions ever since hydroxyl (OH)–rich materials were proposed as surface components (*1*, *2*) and eventually observed (*3*–*8*). The prediction of ice and perhaps liquid in the mantle (*9*–*11*), observations of sporadic releases of OH-bearing molecules (*12*), the detection of water vapor molecules (*13*), and reports of haze (*14*) support the presence of water on Ceres. Water is a key component in the chemical evolution and internal activity of planetary bodies, and products of aqueous activity such as bright carbonates have been observed on Ceres (*15*). Reflectance spectroscopy is sensitive to surficial water and hydroxyl groups; measurement of OH and H_2O absorptions near 1.5, 2.0, and 3 μm thereby allows for remote detection of H_2O. The depth of photon penetration depends on the material: Photons may penetrate a few micrometers into absorbing components such as those found on Ceres or other low-albedo surfaces, whereas they may penetrate several centimeters in highly scattering materials such as pure ice and snow (*16*).

Because Ceres has a low bulk density of 2162 ± 3 kg m^{-3} (*17*), its composition is expected to contain a substantial proportion of water. Internal heat (mostly from decay of radionuclides) is expected to have differentiated Ceres at least partially into a rocky core and icy mantle (*9*–*11*). Contact between silicates and ice or liquid water would have resulted in aqueous alteration of minerals, producing hydroxylated (OH-bearing) phases such as clays and carbonates (*5*–*7*, *9*–*11*, *15*), or mineral hydrates (H_2O-bearing) such as salts.

The Dawn mission at Ceres (*18*) is dedicated to the characterization of the geology, geophysics, and composition of this dwarf planet. The first observational orbit (Rotation Characterization) occurred on 23 April 2015 at an altitude of 13,500 km. The orbit was subsequently lowered to 4400 km for the Survey phase of the mission, which operated from 5 to 22 June 2015. The Dawn Visible and InfraRed (VIR) mapping spectrometer (*19*) senses surface composition by reflectance spectroscopy. It covers wavelengths of 0.25 to 5.1 μm with two detectors that measure radiance, overlap around 1 μm, and have spectral sampling of 1.9 nm and 9.8 nm for the visible and infrared, respectively. Initial global VIR analyses of Ceres identified the ubiquitous presence of phyllosilicates, but no H_2O-bearing species (*7*, *8*).

Here, we present VIR detections of H_2O-rich surface materials on Ceres from five observations of the crater Oxo, which is 10 km in diameter and is centered at 359.7°E, 42.2°N (*20*) (Fig. 1). The data were collected on 1 and 4 May 2015, with a spatial resolution of about 3.4 km per pixel, and on 6 and 9 June 2015, with a spatial resolution of about 1.1 km per pixel. Absorptions near 2 μm at the surface of Ceres require H_2O molecules, as they are attributable to an O-H stretch overtone in this molecule (*21*, *22*) commonly seen in spectra of water ice and mineral hydrates (*23*). Other O-H vibration overtones at 1.65 μm and 1.28 μm produce narrower yet meaningful absorption bands (*24*) that are visible in the VIR spectra. The three absorption bands at 1.28 μm, 1.65 μm (Fig. 2, D to F), and 2.0 μm (Fig. 2, G to I) occur within the same areas in the Oxo crater, which makes a strong case for the detection of H_2O. Similar to the rest of Ceres' surface, a strong and broad absorption around 3 μm due to the fundamental vibration mode of O-H is also observed. However, this spectral feature alone is not unique to H_2O, as only the OH group is required. Spectral models show that H_2O-ice spectra fit VIR observations better than any spectrum of mineral hydrates (Fig. 3); thus, we consider it the most likely surface component observed in the Oxo crater.

H_2O-rich materials are found within a high reflectance area on the pole-facing wall of the Oxo crater (Fig. 2) and possibly on the southeastern scarp above the rim. The crater is about 50% brighter at 1.1 μm than surrounding surface materials (Fig. 2, A and B). The surface on the H_2O-rich spot is characterized by temperatures 10 to 20 K lower than the rest of the crater (Fig. 2, J to L); this would be expected of exposed water ice (*25*), which has a higher thermal inertia than the average Ceres surface regolith, and of high-albedo materials in general.

Geological description of Oxo crater

In Fig. 1E, high-resolution images from the Framing Camera (FC) indicate that Oxo has sharp rims and few superposed craters, which implies that it is geologically young. It is also characterized by a scarp in the southeastern part. This terrace feature likely resulted from block collapse and slumping of the southeastern rim toward the center of the crater, forming a depression outside the crater. Long, arcuate fractures subparallel to the terrace scarp, well-defined talus material, and an extensive boulder field within Oxo indicate that the terrace block has been actively collapsing in the recent geologic past and may be continuing to do so at the present time. Several kilometer- and subkilometer-scale lobate flow features related to mass wasting have been observed on the northeastern and southeastern rims of the terrace block. These flows, particularly the examples observed near the H_2O-rich region, display several morphologic similarities (i.e., sharply defined flow margins, large rounded blunt snouts, and apparent mass concentration near the flow termini) to numerous other features on Ceres that have been interpreted as ice-cemented flows (*26*). The location of the strongest H_2O detection in Oxo exhibits a sloped hummocky texture that is divided in several locations by linear and sinuous gully-like depressions.

Calibration of spectra and spectral processing

Reflectance defines the ratio of irradiance from the surface of Ceres to the solar radiance flux. In this study, VIR spectra have been further corrected for the photometric effects of variable incidence and emergence angle due to the local topography. This correction is based on the Akimov disk-function model (*27*) and is similar to the processing of VIR data at Vesta performed for global mapping (*28*). We standardize bidirectional reflectances to incidence angles of 0° and emission angles of 30°.

The spectral slope measures the slope of a straight line fitted to VIR spectra between 1.0 and 2.4 μm. Maps of the spectral slopes were calculated

[1]Bear Fight Institute, 22 Fiddler's Road, P.O. Box 667, Winthrop, WA 98862, USA. [2]Istituto di Astrofisica e Planetologia Spaziali–Istituto Nazionale di Astrofisica, Rome, Italy. [3]Institute of Geophysics and Planetary Physics, University of California, Los Angeles, CA, USA. [4]Jet Propulsion Laboratory, Pasadena, CA, USA. [5]Lunar and Planetary Laboratory, Tucson, AZ, USA.
*Corresponding author. Email: jean-philippe_combe@bearfightinstitute.com

Downloaded from http://science.sciencemag.org/ on September 1, 2016

after normalization with respect to the local average reflectance between 1.0 and 2.4 μm for each pixel, and after division to the average spectrum of Ceres. The result is a spectral slope of zero for the average of Ceres.

The spectral feature centered at 1.5 μm in Fig. 1, E to G, might also be due to O-H vibration overtone; however, it must be interpreted cautiously because of light scattering between two order-sorting filters of the instrument (*8*), and thus it is not considered in this study. Although the diagnostic absorption feature of H_2O at 1.65 μm falls near one of these junctions, it is considered safe for interpretation. Several pieces of observational evidence indicate that instrument light scattering does not contribute significantly to the signal at this wavelength: (i) Light scattering creates spectral oscillations that stop around 1.6 μm, even for the strongest artifacts. (ii) The absorption band depths at 1.28 μm, 1.65 μm, and 2.0 μm have very similar distributions, consistent with the hypothesis that H_2O absorption is the main contributor of the 1.65-μm feature. (iii) The band depth parameter at 1.5 μm is mostly sensitive to albedo-contrasted surface features, which is radically different from the distribution pattern of absorptions attributed to H_2O.

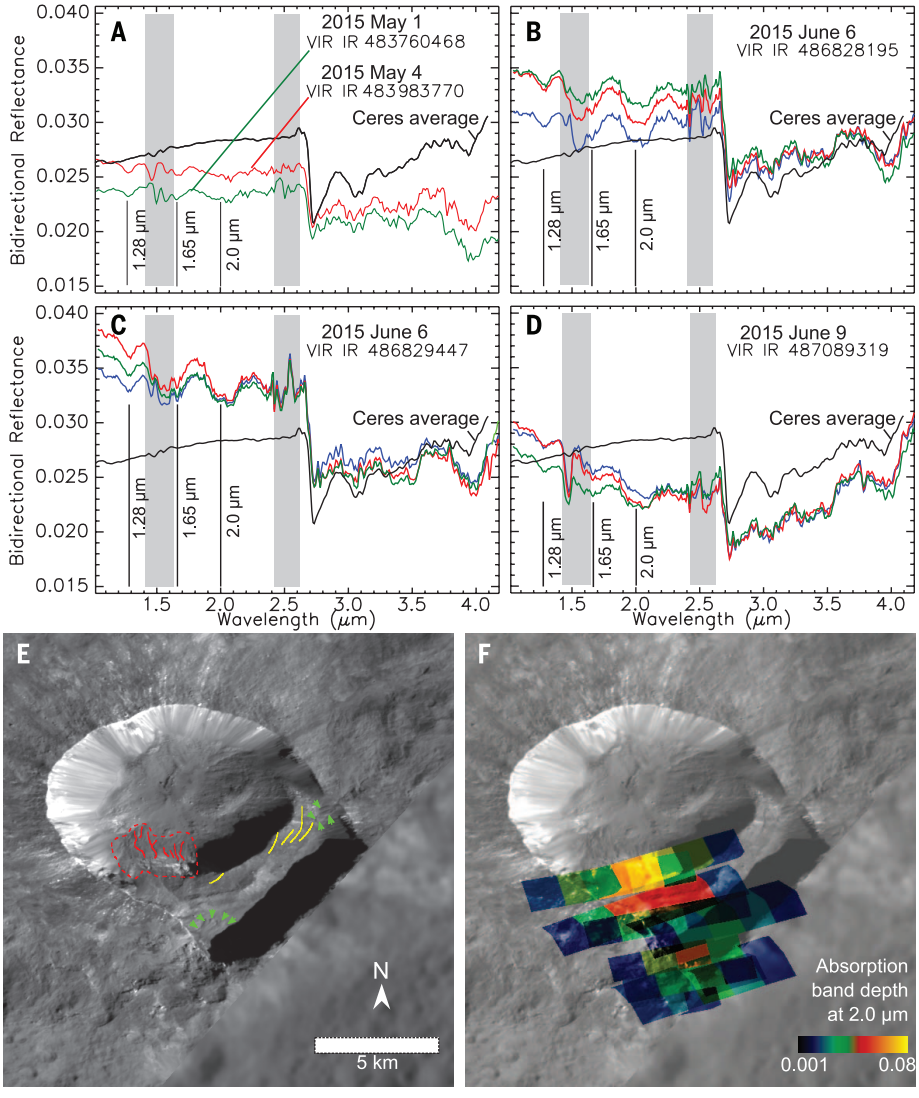


Fig. 1. Dawn VIR IR observations of Oxo crater on Ceres demonstrate the detection of H_2O at the surface. (**A** to **D**) Reflectance spectra collected where absorption bands of H_2O at 1.27, 1.65, and 2 μm are the strongest (in color) from distinct pixels within a VIR image. Each panel shows spectra from a different VIR image, except the average spectrum of Ceres (in black) displayed as a reference, showing no H_2O absorption bands. Gray rectangles define ranges of wavelengths where the spectra are the least reliable because they are at filter junctions [(*7*) and text]. (**E**) Oxo crater depicted by the Dawn Framing Camera in equirectangular projection. The red dashed line indicates the hummocky sloped material surrounding the region of strongest H_2O detection; solid red lines indicate linear and multiple juxtaposed (and partly overlapping) lobate mass wasting deposits. The yellow lines are superimposed upon arcuate fractures subparallel to the terrace scarp. The green arrows point toward the margins of lobate flow structures that are similar to other features on Ceres that have been interpreted as ice-cemented flows (*26*). (**F**) The same FC image mosaic as (A) is made brighter for clarity and overlain by the absorption band depth at 2 μm measured by the three VIR observations shown in (B) to (D). The area was more shaded during the acquisition of FC image than while VIR data were acquired.

Albedo and spectral characteristics of Oxo crater

Bright materials in the Oxo crater cover the northern and eastern rims, as well as a portion of the floor at the foot of the southern rim. The highly reflective unit has a negative spectral slope as a function of wavelength (bluer) in the near-infrared, whereas the rest of Ceres has a neutral or slightly positive spectral slope. VIR spectra with strong absorption bands at 1.28, 1.65, and 2 μm have a reflectance at 1.1 μm that is about 10% lower than the rest of the high-albedo unit and a moderately negative spectral slope (Fig. 2, M to O).

In Fig. 2F, VIR data from June 2015 overlain on FC images reveal that H_2O-rich materials correspond to high-albedo materials on the floor of the crater and possibly on the southeastern scarp above the rim. In all three observations, the illumination conditions (season and time of day) were similar, with a local incidence angle of 50° at noon local time. In an interval of 72.5 hours (nine cerean days), no variations of water absorption band depths could be measured, because instantaneous field of view of the observations did not overlap (Fig. 2F) and the H_2O-rich spot was likely smaller than a VIR pixel size (1.1 km). Only the two observations on 6 June 2015 sampled the high-albedo unit of the southern part of the crater floor, and both indicate an absorption band depth of about 8%. In the observation acquired on 9 June 2015, pixels were adjacent to only the bright spot—gaps exist between projected pixels because of the motion of the spacecraft—and the maximum absorption band depth measured was 3%.

Observations acquired in May 2015 (Fig. 1A) are consistent with an exposed H_2O-rich composition 1 month before the detection of the strongest absorption bands. The difference in spatial resolution between the Approach and Survey phases of the mission is sufficient to explain the differences in absorption band depth. These measurements suggest compositional stability within this time frame and a quantity of H_2O large enough to survive at the surface.

Spectral fitting by linear combination of spectra

Candidate materials (*9*, *11*) that exhibit absorption bands similar to VIR spectra of Oxo are free H_2O ice and H_2O-bearing minerals (mineral hydrates) such as chloride hydrates, magnesium sulfate hydrates ($MgSO_4$-nH_2O), ammonium sulfate hydrates (NH_4SO_4-nH_2O), sodium sulfate hydrates (Na_2SO_4-nH_2O), and sodium carbonate hydrates (Na_2CO_3-nH_2O), where n is the number of H_2O molecules per molecule of the mineral.

To interpret the composition of the H_2O-rich area in Oxo, we compared VIR spectra with laboratory spectra of several candidate materials by

Downloaded from http://science.sciencemag.org/ on September 1, 2016

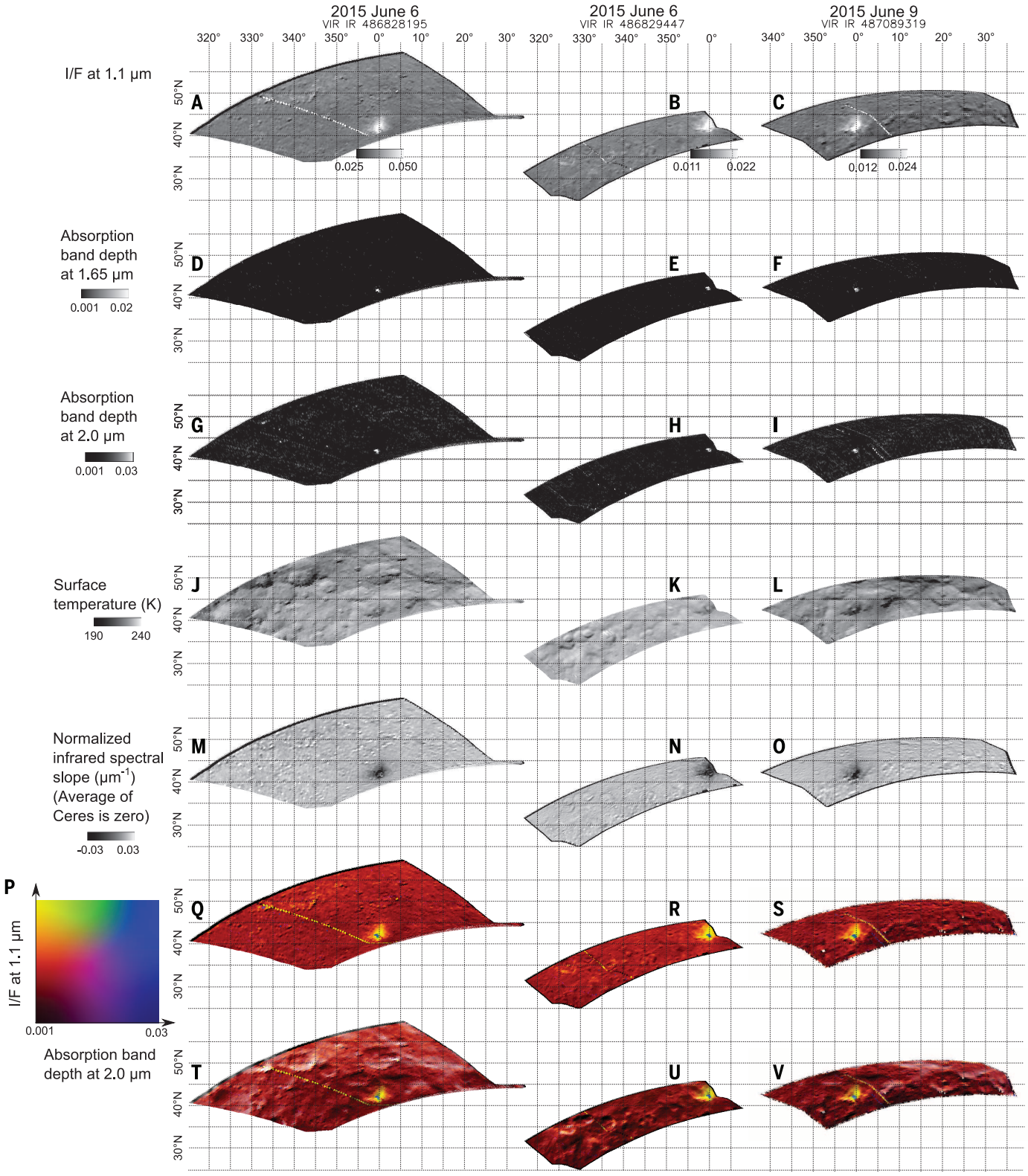


Fig. 2. Dawn VIR infrared observations of Oxo crater on Ceres obtained during the Survey phase of the mission demonstrate the detection of H_2O at the surface. (**A** to **C**) Reflectance at 1.1 μm, showing the location of a high-albedo surface unit. (**D** to **F**) Absorption band depth of H_2O at 1.65 μm. The brightest pixels correspond to the occurrence of the deepest absorption band. (**G** to **I**) Absorption band depth of H_2O at 2 μm. (**J** to **L**) Surface temperature retrieved from VIR data (*43*), which is also sensitive to terrain slopes. (**M** to **O**) Infrared spectral slope. (**P**) Two-dimensional color table that describes the meaning of the colors in (Q) to (V). (**Q** to **S**) Two spectral parameters (reflectance at 1.1 μm and absorption band depth at 2.0 μm) are represented in the same map, which illustrates the presence of H_2O-rich materials within the high-albedo unit. H_2O-rich materials (blue) exist within a high-albedo area (yellow) in the southern rim of the crater. (**T** to **V**) Same as (Q) to (S), except that the incidence angle with respect to the shape model of Ceres is overlain as a texture to better see the topography.

Downloaded from http://science.sciencemag.org/ on September 1, 2016

means of spectral modeling (29). An areal mixture is the simplest model, and it can be calculated by a linear combination of spectra. A linear spectral mixture does not necessarily represent light scattering in an ice-cemented regolith, which is an intimate mixture that results in nonlinear combinations of the spectra of each component. In addition, in the ranges of wavelengths of the H_2O absorption bands (where H_2O is mostly opaque), intimate mixing with a less absorbing material results in increased apparent overall reflectance and enhanced contrast of the absorption bands (23). This phenomenon of light scattering is also consistent with the fact that, in VIR spectra, the 2-μm absorption overtone of H_2O is almost as strong as the 3-μm fundamental absorption, which is never observed when H_2O ice is pure unless the 3-μm band is saturated. In Fig. 3 and Fig. 4, the spectra of pure components are multiplied by the coefficient of linear mixing; their sum added to the offset (dotted straight line) equals the modeled spectrum on top.

Figure 3 illustrates models (29) of spectral fitting of the same VIR spectrum with laboratory reflectance spectra of pure components between 1.02 and 2.5 μm at temperatures relevant to the asteroid belt and Jupiter satellites (30). Relative to VIR spectra, most chloride hydrates (31) have absorption bands of H_2O shifted toward shorter wavelengths (not represented here), except for frozen brines of the eutectic mixtures $MgCl_2$-12H_2O (Fig. 3F), KCl-H_2O, and NaCl-2H_2O. In all cases, laboratory spectra have a much higher reflectance than the surface of Ceres, which can be explained by mixtures on Ceres with low-albedo materials. The purpose of these comparisons is to visualize the position and shape of all the absorption bands associated with H_2O. Because the average spectrum of Ceres is relatively featureless between 1 and 2.5 μm (8), the models simulate these mixtures by scaling the reflectance spectra of pure components (gain) and by adding a spectrally neutral contribution (offset). The scaling factor is sensitive to the abundance of the H_2O-rich component, and the offset compensates empirically for some photometric effects and the absorption of neutral materials potentially present in the mixture. Achievement of a good quality of fit with this simple model indicates that several spectra of mineral hydrates can be considered in the interpretation and for future laboratory analyses, despite incomplete documentation of sample temperature and number of H_2O molecules in some mineral hydrates that are currently available.

Interpretation of linear combination of spectra

The spectral features of several H_2O-rich materials can fit VIR spectra for the small Oxo zone (Fig. 3). Among these candidates, H_2O ice provides the best fit of all (RMS = 0.00187%), hydrated sodium carbonates and hydrated magnesium sulfates are the next best (0.00262% < RMS < 0.00304%), and spectra of ammonium sulfates and sodium sulfates result in higher model residuals (RMS > 0.0032%). By definition, the RMS is proportional to the standard deviation of the residuals. For the best fit (Fig. 3A), the residuals from fitting an H_2O spectrum to the VIR spectrum of Oxo are on the same order of amplitude as the instrument calibration uncertainties, and their respective standard deviations are similar.

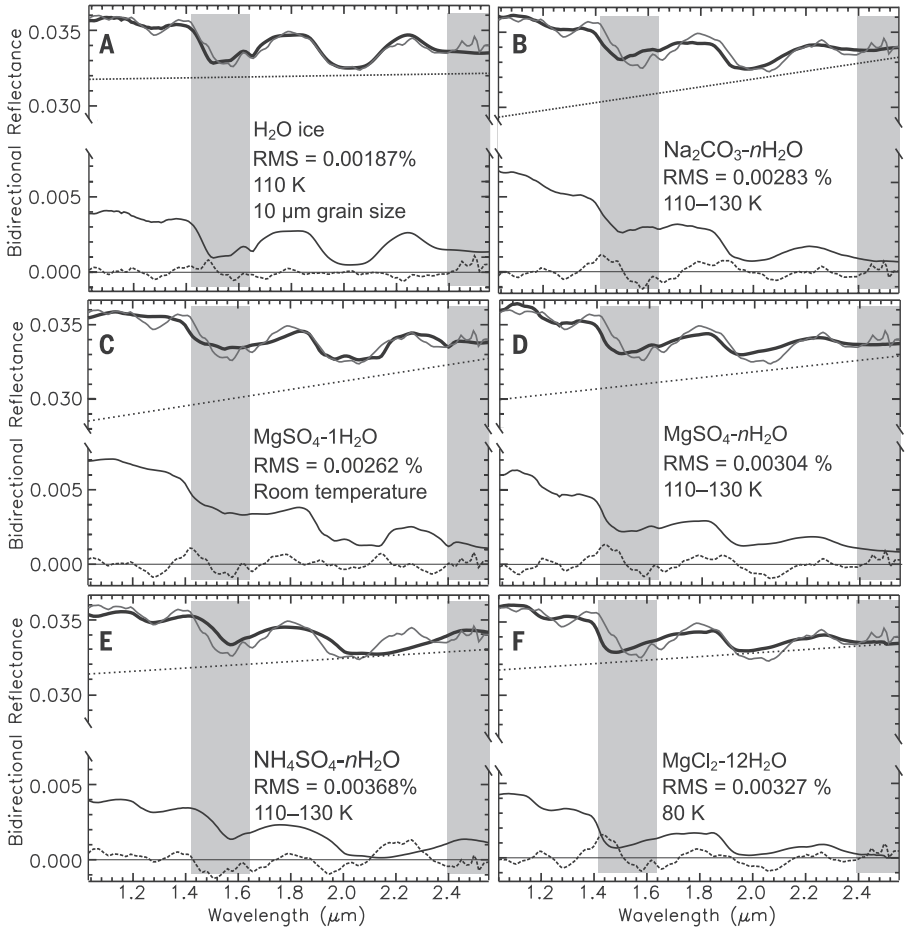


Fig. 3. Analysis and interpretation of the composition of H_2O-rich materials in Oxo. In each panel, one reflectance spectrum of the H_2O-rich zone in Oxo crater from Dawn VIR IR observation 486828195 (thin, black near top) is compared with a scaled reflectance spectrum of a pure hydrated component (thick, black). Gray rectangles define ranges of wavelengths where the spectra are the least reliable. Scaled laboratory spectra of several H_2O-rich samples (thin, black near bottom) and the offset (dotted line) used in each fit are shown. Near the bottom of each plot, model residuals (dashed curve) provide an indication of the quality of fit, along with the RMS value. (**A**) H_2O ice spectrum from the Johns Hopkins University Applied Physics Laboratory spectral library (22, 44). (**B**, **D**, and **E**) Spectra of mineral hydrates (30). (**C**) Monohydrated sulfate kieserite from the Reflectance Laboratory (RELAB) at Brown University (45). (**F**)The spectrum of frozen eutectic mixture $MgCl_2$-12H_2O is from (31).

Figure 4 presents the same VIR spectrum as in Fig. 1 from 1.02 to 4.2 μm, fitted with an H_2O ice spectrum linearly combined with the average spectrum of Ceres' surface and a spectral slope (straight line). The quality of fit over the extended range of wavelength, including the broad OH stretch fundamental absorption, demonstrates the presence of H_2O and confirms that water ice is the most likely component.

The scaling factor of 0.0057 in Fig. 4 only gives a lower limit for the proportion of H_2O ice in the surface covered by one pixel, because the H_2O-rich area in Oxo is not spatially resolved, and because low-albedo materials optically dominate when they are intimately mixed with a high-albedo material. Assuming, from Fig. 1, that the high-albedo area in Oxo crater floor is rich in H_2O ice, and that it corresponds to half of the surface covered by one pixel, then the proportion would be approximately 1% for the pixel that exhibits the strongest 2.0-μm absorption band. In the case of H_2O ice mixed with low-albedo material, over time, the sublimation of H_2O alone would leave a low-albedo lag deposit, forming a layer on top. Laboratory experiments of the effects of sprinkling charcoal grains on frost (22) indicate that reflectance decreases at a higher rate than the fractional areal coverage, and that a reflectance of 0.07 at 1 μm can be achieved with 30% areal coverage of ice. Our estimates from these calculations and assumptions is that the areal proportion of H_2O ice on the 1-km^2, high-albedo area is likely between 1 and 10%.

Downloaded from http://science.sciencemag.org/ on September 1, 2016

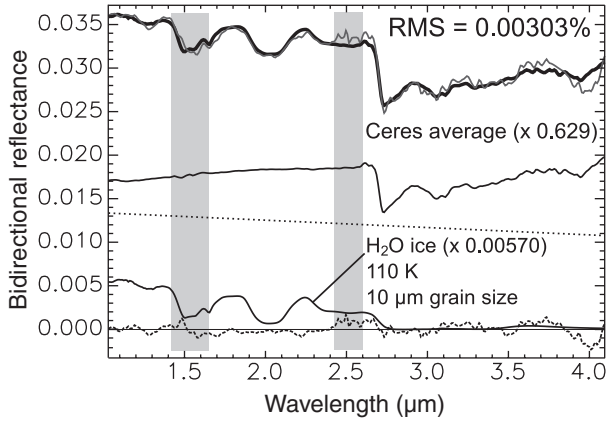


Fig. 4. Modeling of one reflectance spectrum of the H_2O-rich zone in the Oxo crater from Dawn VIR IR observation 486828195 with a linear combination (simulation of an areal mixture) of H_2O ice, the average spectrum of Ceres and a spectrally neutral, low-albedo spectral component (dotted straight line). This synthetic, spectrally neutral component also accounts for the relatively more negative spectral slope of the H_2O-rich area than the average spectrum of Ceres. The model residuals (dashed curve) and the RMS value document the quality of fit. Gray rectangles define ranges of wavelengths where the spectra are the least reliable.

Discussion

Among all VIR spectra acquired up to the Survey phase of the Dawn mission, Oxo is the only place on Ceres where we have found measurements of absorption band depth of 1% or more at 1.65 and 2.0 μm that correspond without ambiguity to the expected shape of H_2O absorption bands. These bands are most likely due to surface materials. Although cryovolcanic-like morphological features such as Ahuna Mons (*32*) suggest that H_2O ice might be present in the crust, hydrated salts were probably responsible for the liquid phase needed to form the mountain. However, H_2O-rich materials are not detected by spectroscopy at those places, because they are likely not exposed. There is no obvious connection with the finding of H_2O on the floor of the Oxo crater and previous reports of H_2O molecules above the surface of Ceres: (i) The location of Oxo differs from the reported H_2O molecule release on equatorial regions (*13*), and (ii) although haze was reported on Oxo and Occator (*14*), no surface H_2O has been identified by VIR within Occator (*15*).

The nature of the H_2O-rich surface of Oxo crater (H_2O ice or mineral hydrates) remains to be determined. VIR near-infrared spectra are better fitted by H_2O ice spectra than by hydrated minerals (Fig. 3); however, interpretation is still open. Thermodynamical properties can further constrain results provided by these initial observations. The small H_2O-rich area at Oxo may suggest a local origin. However, the finding of H_2O in a place that is likely protected from direct sunlight for most of the day (except around noon local time), even near summer solstice (solar longitude Ls was 81° on 6 to 9 June 2015), suggests the detected H_2O component could be more stable at this location because of limited direct solar illumination.

Pure surficial H_2O ice would sublime under current thermal conditions on Ceres (*25*, *33*, *34*), where daytime surface temperatures T span the range 180 to 240 K (*7*), with $T > 200$ K found in Oxo crater from 11 hours to 12 hours local solar time. This localized detection of exposed H_2O on the surface of Ceres could be consistent with predictions (*25*) of a near-surface ice table beginning at ~50° latitude, and of local surface ice deposits on a rough terrain; for example, at the latitude of Oxo, 1 m of pure, cohesive water ice would disappear within a few hundred years (*25*). Free water ice would require a relatively recent exposure of H_2O at the surface by landslides, by outgassing of water vapor followed by condensation, or by eruption of liquid water (cryovolcanism). According to some models, cometary-like activity or a landslide could expose H_2O ice mixed with dust. Depending on the amount of dust in the ice, it would become spectrally undetectable within 10 years (*33*, *35*) or tens of years because dust would become the dominant material within the optical thickness (a few micrometers at most). Even in the case of an ice-cemented regolith (more thermodynamically stable than pure water ice), the ablation rate would be significant over one cerean year.

We have estimated ice loss rates obtained by modeling surface and subsurface temperatures on Ceres by balancing surface insolation, thermal emission, and conduction to the subsurface (*33*) and incorporating a pole-vector determination from Dawn data. At 44°N, ablation is estimated to be 4 mm each cerean year, assuming horizontal ground, with an albedo of 13.5% and thermophysical parameters of ice-cemented regolith. At the solar longitude Ls = 81° when VIR observations were acquired, modeled water vapor production oscillated between 0.08 kg s^{-1} km^{-2} just before dawn to 0.22 kg s^{-1} km^{-2} in the afternoon. However, in the case of a pole-facing slope of 20°, ice loss is only ~50 μm of ice per cerean year, which makes the life span of a H_2O-ice rich layer about 80 times that of a flat surface.

Hydrated minerals could have formed very early in Ceres' evolution by contact with H_2O, either ice or liquid, before being exposed. Once at the surface, these species would dissociate at a slower rate than water ice, especially those with fewer H_2O molecule bonds (*30*, *36*). This is consistent with H_2O absorption bands of hydrated salts becoming asymmetric and shifted toward wavelengths shorter than 2 μm, sometimes by more than 0.1 μm, compared to water ice (Fig. 3), indicating higher energy and thus stronger bonds (*37*, *38*).

At least four ways to create or transport of H_2O on Ceres can be considered, listed here from the most likely to the least: (i) Exposure of endogenous near-surface H_2O-rich materials from an impact or local landslide could be consistent with both mineral hydrates and water ice. Other high-albedo units and young craters observed across Ceres may be preferential locations for searching for H_2O-rich materials. (ii) Release of subsurface H_2O occurs on comet nuclei and may exist on Ceres, although some models [e.g., (*35*)] predict that water vapor should not recondense. Long-lived radionuclide heat from the core (*9*–*11*) and potassium salts in the mantle or crust (*11*) may not be enough to drive endogenic activity that reaches the surface; however, collisions such as the one that created Oxo may have caused long-term activation (or reactivation) of regions with an ice-rich subsurface. (iii) Infall of hydrated meteorites or comets is a scenario that has brought OH-rich or H_2O-rich materials onto the surface of Vesta (*39*, *40*), and Oxo itself is a geologically recent impact (superposed crater counts suggest an age of less than 1 million to 10 million years); however, these H_2O molecules may well dissociate from the kinetic energy dissipated by the collision. (iv) The molecule of H_2O may form by implantation of protons from the solar wind as is the case on the Moon (*41*). Effects of the solar wind have not been observed on Vesta (*42*) despite a higher flux of solar wind particles [the distance from the Sun is shorter at Vesta (2.15 to 2.57 AU) than at Ceres (2.56 to 2.98 AU)]; therefore, this is not a probable origin of OH on Ceres.

REFERENCES AND NOTES

1. C. R. Chapman, J. W. Salisbury, Comparison of meteorite and asteroid spectral reflectivities. *Icarus* **19**, 507–522 (1973). doi: 10.1016/0019-1035(73)90078-X
2. T. B. McCord, M. J. Gaffey, Asteroids: Surface composition from reflection spectroscopy. *Science* **186**, 352–355 (1974). doi: 10.1126/science.186.4161.352; pmid: 17839866
3. L. A. Lebofsky, M. A. Feierberg, A. T. Tokunaga, H. P. Larson, J. R. Johnson, The 1.7- to 4.2-μm spectrum of asteroid 1 Ceres: Evidence for structural water in clay minerals. *Icarus* **48**, 453–459 (1981). doi: 10.1016/0019-1035(81)90055-5
4. P. Vernazza *et al*., Analysis of near-IR spectra of 1 Ceres and 4 Vesta, targets of the Dawn mission. *Astron. Astrophys.* **436**, 1113–1121 (2005). doi: 10.1051/0004-6361:20042506
5. A. S. Rivkin, E. L. Volquardsen, B. E. Clark, The surface composition of Ceres: Discovery of carbonates and iron-rich clays. *Icarus* **185**, 563–567 (2006). doi: 10.1016/j.icarus.2006.08.022
6. R. E. Milliken, A. S. Rivkin, Brucite and carbonate assemblages from altered olivine-rich materials on Ceres. *Nat. Geosci.* **2**, 258–261 (2009). doi: 10.1038/ngeo478
7. E. Ammannito *et al*., Distribution of phyllosilicates on Ceres. *Science* **353**, aaf4279 (2016).
8. M. C. De Sanctis *et al*., Ammoniated phyllosilicates with a likely outer Solar System origin on (1) Ceres. *Nature* **528**, 241–244 (2015). doi: 10.1038/nature16172; pmid: 26659184
9. T. B. McCord, C. Sotin, Ceres: Evolution and current state. *J. Geophys. Res.* **110**, E05009 (2005). doi: 10.1029/2004JE002244
10. P. C. Thomas *et al*., Differentiation of the asteroid Ceres as revealed by its shape. *Nature* **437**, 224–226 (2005). doi: 10.1038/nature03938; pmid: 16148926
11. J. Castillo-Rogez, T. B. McCord, Ceres' evolution and present state constrained by shape data. *Icarus* **205**, 443–459 (2010). doi: 10.1016/j.icarus.2009.04.008
12. M. F. A'Hearn, P. D. Feldman, Water vaporization on Ceres. *Icarus* **98**, 54–60 (1992). doi: 10.1016/0019-1035(92)90206-M
13. M. Küppers *et al*., Localized sources of water vapour on the dwarf planet (1) Ceres. *Nature* **505**, 525–527 (2014). doi: 10.1038/nature12918; pmid: 24451541

Downloaded from http://science.sciencemag.org/ on September 1, 2016

14. A. Nathues *et al*., Sublimation in bright spots on (1) Ceres. *Nature* **528**, 237–240 (2015). doi: 10.1038/nature15754; pmid: 26659183
15. M. C. De Sanctis *et al*., Bright carbonate deposits as evidence of aqueous alteration on (1) Ceres. *Nature* 10.1038/nature18290 (2016). doi: 10.1038/nature18290; pmid: 27362221
16. J. Dozier, R. O. Green, A. W. Nolin, T. H. Painter, Interpretation of snow properties from imaging spectrometry. *Remote Sens. Environ.* **113**, S25–S37 (2009). doi: 10.1016/j.rse.2007.07.029
17. C. T. Russell *et al*., Dawn arrives at Ceres: Exploration of a small, volatile-rich world. *Science* **353**, 1008 (2016).
18. C. T. Russell, C. A. Raymond, The Dawn mission to Vesta and Ceres. *Space Sci. Rev.* **163**, 3–23 (2011). doi: 10.1007/s11214-011-9836-2
19. M. C. De Sanctis *et al*., The VIR spectrometer. *Space Sci. Rev.* **163**, 329–369 (2011). doi: 10.1007/s11214-010-9668-5
20. Th. Roatsch *et al*., Ceres survey atlas derived from Dawn Framing Camera images. *Planet. Space Sci.* **121**, 115–120 (2016). doi: 10.1016/j.pss.2015.12.005
21. N. Ockman, thesis, University of Michigan (1957).
22. R. N. Clark, Water frost and ice: The near-infrared spectral reflectance 0.65-2.5 μm. *J. Geophys. Res.* **86**, 3087–3096 (1981). doi: 10.1029/JB086iB04p03087
23. R. N. Clark, P. G. Lucey, Spectral properties of ice-particulate mixtures and implications for remote sensing: I. Intimate mixtures. *J. Geophys. Res.* **89**, 6341–6348 (1984). doi: 10.1029/JB089iB07p06341
24. W. M. Grundy, B. Schmitt, The temperature-dependent near-infrared absorption spectrum of hexagonal H_2O ice. *J. Geophys. Res.* **103**, 25809–25822 (1998). doi: 10.1029/98JE00738
25. P. O. Hayne, O. Aharonson, Thermal stability of ice on Ceres with rough topography. *J. Geophys. Res.* **120**, 1567–1584 (2015). doi: 10.1002/2015JE004887
26. D. L. Buczkowski *et al*., The geomorphology of Ceres. *Science* **353**, aaf4332 (2016).
27. Yu. G. Shkuratov *et al*., Opposition effect from Clementine data and mechanisms of backscatter. *Icarus* **141**, 132–155 (1999). doi: 10.1006/icar.1999.6154
28. J.-Ph. Combe *et al*., Reflectance properties and hydrated material distribution on Vesta: Global investigation of variations and their relationship using improved calibration of Dawn VIR mapping spectrometer. *Icarus* **259**, 21–38 (2015). doi: 10.1016/j.icarus.2015.07.034
29. J.-Ph. Combe *et al*., Analysis of OMEGA/Mars Express data hyperspectral data using a Multiple-Endmember Linear Spectral Unmixing Model (MELSUM): Methodology and first results. *Planet. Space Sci.* **56**, 951–975 (2008). doi: 10.1016/j.pss.2007.12.007
30. T. B. McCord, G. Teeter, G. B. Hansen, M. T. Sieger, T. M. Orlando, Brines exposed to Europa surface conditions. *J. Geophys. Res.* **107**, 5004 (2002). doi: 10.1029/2000JE001453
31. J. Hanley, J. B. Dalton III, V. F. Chevrier, C. S. Jamieson, R. S. Barrows, Reflectance spectra of hydrated chlorine salts: The effect of temperature with implications for Europa. *J. Geophys. Res.* **119**, 2370–2377 (2014). doi: 10.1002/2013JE004565
32. O. Ruesch *et al*., Geologically recent cryo-volcanic activity on Ceres. *Science* **353**, aaf4286 (2016).
33. F. P. Fanale, J. R. Salvail, The water regime of asteroid (1) Ceres. *Icarus* **82**, 97–110 (1989). doi: 10.1016/0019-1035(89)90026-2
34. T. Titus, Ceres: Predictions for near-surface water ice stability and implications for plume generating processes. *Geophys. Res. Lett.* **42**, 2130–2136 (2015). doi: 10.1002/2015GL063240
35. M. Formisano, M. C. De Sanctis, G. Magni, C. Federico, M. T. Capria, Ceres water regime: Surface temperature, water sublimation and transient exo(atmo)sphere. *Mon. Not. R. Astron. Soc.* **455**, 1892–1904 (2016). doi: 10.1093/mnras/stv2344
36. M. Y. Zolotov, E. L. Shock, Composition and stability of salts on the surface of Europa and their oceanic origin. *J. Geophys. Res.* **106**, 32815–32827 (2001). doi: 10.1029/2000JE001413
37. A. Novak, Hydrogen bonding in solids, correlation of spectroscopic and crystallographic data. *Struct. Bonding* **18**, 177–212 (1974). doi: 10.1007/BFb0116438
38. T. B. McCord *et al*., Hydrated salt minerals on Europa's surface from the Galileo near-infrared mapping spectrometer (NIMS) investigation. *J. Geophys. Res.* **104**, 11827 (1999). doi: 10.1029/1999JE900005
39. M. C. De Sanctis *et al*., Detection of widespread hydrated materials on Vesta by the VIR Imaging Spectrometer on board the Dawn mission. *Astrophys. J.* **758**, L36 (2012). doi: 10.1088/2041-8205/758/2/L36
40. T. B. McCord *et al*., Dark material on Vesta from the infall of carbonaceous volatile-rich material. *Nature* **491**, 83–86 (2012). doi: 10.1038/nature11561; pmid: 23128228
41. T. B. McCord *et al*., Sources and physical processes responsible for OH/H_2O in the lunar soil as revealed by the Moon Mineralogy Mapper (M^3). *J. Geophys. Res.* **116**, E00G05 (2011). doi: 10.1029/2010JE003711
42. C. M. Pieters *et al*., Distinctive space weathering on Vesta from regolith mixing processes. *Nature* **491**, 79–82 (2012). doi: 10.1038/nature11534; pmid: 23128227
43. F. Tosi *et al*., Thermal measurements of dark and bright surface features on Vesta as derived from Dawn/VIR. *Icarus* **240**, 36–57 (2014). doi: 10.1016/j.icarus.2014.03.017
44. J. W. Salisbury, D. M. D'Aria, A. J. Wald, Measurements of thermal infrared spectral reflectance of frost, snow, and ice. *J. Geophys. Res.* **99**, 24235–24240 (1994). doi: 10.1029/94JB00579
45. J. F. Mustard, C. M. Pieters, Photometric phase functions of common geologic minerals and applications to quantitative analysis of mineral mixture reflectance spectra. *J. Geophys. Res.* **94**, 13619–13634 (1989). doi: 10.1029/JB094iB10p13619

ACKNOWLEDGMENTS

Support for this research was provided under the NASA Dawn mission through subcontract 2090-S-MB516 from the University of California, Los Angeles. The VIR instrument and VIR team are funded by ASI (Italian Space Agency) and INAF (Istituto Nazionale di Astrofisica). The involvement of S.B. and M.E.L. was made possible by award NNX15AI29G of the Dawn Guest Investigator Program. Dawn data for Ceres are archived in NASA's Planetary Data System Small Bodies Node (http://sbn.pds.nasa.gov/data_sb/target_asteroids.shtml#1_Ceres). We thank J. Castillo-Rogez, B. Ehlmann, H. Y. McSween, C. M. Pieters, P. Schenk, S. Schröder, and S. Uy for valuable discussions and critical reading of the manuscript.

5 February 2016; accepted 22 June 2016
10.1126/science.aaf3010

Downloaded from http://science.sciencemag.org/ on September 1, 2016

REPORTS

PLANETARY SCIENCE

Dawn arrives at Ceres: Exploration of a small, volatile-rich world

C. T. Russell,[1]* C. A. Raymond,[2] E. Ammannito,[1] D. L. Buczkowski,[3] M. C. De Sanctis,[4] H. Hiesinger,[5] R. Jaumann,[6] A. S. Konopliv,[2] H. Y. McSween,[7] A. Nathues,[8] R. S. Park,[2] C. M. Pieters,[9] T. H. Prettyman,[10] T. B. McCord,[11] L. A. McFadden,[12] S. Mottola,[6] M. T. Zuber,[13] S. P. Joy,[1] C. Polanskey,[2] M. D. Rayman,[2] J. C. Castillo-Rogez,[2] P. J. Chi,[1] J. P. Combe,[11] A. Ermakov,[13] R. R. Fu,[14] M. Hoffmann,[8] Y. D. Jia,[1] S. D. King,[15] D. J. Lawrence,[3] J.-Y. Li,[10] S. Marchi,[16] F. Preusker,[6] T. Roatsch,[6] O. Ruesch,[12] P. Schenk,[17] M. N. Villarreal,[1] N. Yamashita[10]

On 6 March 2015, Dawn arrived at Ceres to find a dark, desiccated surface punctuated by small, bright areas. Parts of Ceres' surface are heavily cratered, but the largest expected craters are absent. Ceres appears gravitationally relaxed at only the longest wavelengths, implying a mechanically strong lithosphere with a weaker deep interior. Ceres' dry exterior displays hydroxylated silicates, including ammoniated clays of endogenous origin. The possibility of abundant volatiles at depth is supported by geomorphologic features such as flat crater floors with pits, lobate flows of materials, and a singular mountain that appears to be an extrusive cryovolcanic dome. On one occasion, Ceres temporarily interacted with the solar wind, producing a bow shock accelerating electrons to energies of tens of kilovolts.

Ceres was discovered by G. Piazzi on 1 January 1801, between the orbits of Mars and Jupiter at the heliocentric distance expected for the missing planet predicted by the Titius-Bode law (*1*). The fourth asteroid to be discovered, Vesta, was explored by the Dawn spacecraft from June 2011 to August 2012 (*2*). Whereas Vesta is associated with a family of vestoids and the howardite-eucrite-diogenite (HED) achondrites, Ceres is not associated with a family of asteroids or known meteorites. Consequently, unlike at Vesta, there are few geochemical clues to its composition and few hypotheses to be tested. Remote sensing with telescopes at 1 astronomical unit (AU) and probing with Earth-based radar have revealed little about this low-albedo body, although they do indicate a clay-like surface (*3*, *4*). Hubble Space Telescope (HST) observations provided a size and shape (*5*) that suggested a geologically differentiated body. The size, combined with a mass estimate based on its gravitational interaction with Mars (*6*), indicated that Ceres' average density was about 2100 kg·m^{-3}. Thermodynamic models (*7*, *8*) predicted from this estimated bulk density that Ceres contained 17 to 27% free water by mass, and therefore it likely had fractionated into a silicate core and a water-rich mantle. These inferences of a "wet" dwarf planet were supported by a possible detection of OH with the International Ultraviolet Explorer (*9*), but could not be verified from ground-based telescopes. More recently, the Herschel Space Observatory confirmed the presence of water vapor molecules at Ceres with a source rate of about 6 kg·s^{-1} (*10*). The possible presence of ammonium-bearing minerals (*11*) and brucite mixed with carbonate (*12*) on Ceres' surface had been suggested from telescopic spectra. Global infrared spectra obtained on Dawn's approach to Ceres, without the interference of the Earth's atmospheric water and methane, confirmed a match to ammoniated phyllosilicates (*13*).

Dawn entered orbit about Ceres on 6 March 2015 and maneuvered into its rotational characterization orbit at a 14,000-km radius in which it operated from 23 April to 9 May. A 4900-km survey orbit followed from 6 to 30 June, and a 1950-km radius, high-altitude mapping orbit from 17 August to 23 October. Its final orbit, low-altitude mapping at a radius of 850 km, was entered on 16 December 2015. A refined Ceres coordinate system is anchored by a small crater at 0° longitude and 2°S, named Kait (*14*). Ceres longitudes increase eastward, in the direction of rotation (*15*). Using methods described in the supplementary materials, we find that Ceres rotates about an axis with a right ascension of 291.42° ± 0.01° and a declination of 66.76° ± 0.02° with a period of 9.074170 ± 0.000001 hours. The declination is a change of nearly 8° from that obtained earlier by HST (*5*). The angle between Ceres' orbital pole and rotational pole, its obliquity, is 4°. Ceres' mass, determined from Dawn's orbital parameters, is (9.384 ± 0.001) × 10^{20} kg, similar to earlier estimated values (*6*). Its triaxial elliptical dimensions are 483.1 by 481.0 by 445.9, all ± 0.2 km for a geometric mean radius of 469.7 km, similar to the recent value obtained at the Keck Observatory with adaptive optics (*16*). The resulting mean density is 2162 ± 3 kg m^{-3} (see methods section in supplementary materials).

Initial observations revealed Ceres to have a heavily cratered dark surface with a geometric albedo of ~0.09 (*17*), but punctuated with widely distributed small, bright deposits with one large complex of very bright areas on the floor of the 92-km Occator crater (*18*), near 239° longitude and 22°N latitude (Fig. 1). The location and distribution of the bright material in the crater floor suggest the presence of several subsurface conduits of bright material with differing fluences rather than emplacement due to multiple impacts, although mobilization could be associated with an impact. The material is in low-lying areas of the crater floor, albeit not in the lowest part of the crater floor. Visible colors of the bright material show a distinct spectral character (*18*). Infrared spectra of the bright material show the presence of abundant carbonates (*19*) and no detectable water-ice bands. These properties are consistent with cryovolcanism, delivering materials produced at depth to the surface, but not within the time frame of water-ice stability on the surface. The ubiquitous distribution of ammoniated phyllosilicates across Ceres requires a global mixing process (*20*).

A 4-km-high mountain, Ahuna Mons, is shown in Fig. 2, the faces of its flanks exhibiting bright streaks. The morphologically fresh appearance of the flanks, the general lack of debris at their base, and the scarcity of craters on the dome point to a geologically young feature. The overall morphometry and the morphologies on the mountain summit have been attributed to a formation through viscous extrusion. An accompanying paper (*21*) proposes that the extrusive event was enabled by the presence at depth of a cryomagma involving salts of low eutectic temperatures.

Although heavily cratered, as are other airless bodies in the solar system, the surface of Ceres differs from those of other bodies of similar size. Figure 3 compares similarly sized typical craters on Vesta, Ceres, and Rhea, an icy moon of Saturn. The vestan crater is excavated in deep regolith and is bowl-shaped with an almost circular

[1]Earth Planetary and Space Sciences, University of California, Los Angeles, 603 Charles Young Drive, Los Angeles, CA 90095-1567, USA. [2]Jet Propulsion Laboratory, California Institute of Technology, Pasadena, CA 91109-8099, USA. [3]Johns Hopkins University Applied Physics Laboratory, Laurel, MD 20723-6099, USA. [4]Istituto di Astrofisica e Planetologia Spaziali, Istituto Nazionale di Astrofisica, 00133 Roma, Italy. [5]Institut für Planetologie, 48149 Münster, Germany. [6]Deutsches Zentrum fur Luft-und Raumfahrt, Institute of Planetary Research, 12489 Berlin, Germany. [7]Department of Earth and Planetary Sciences, University of Tennessee, Knoxville, TN 37996-1410, USA. [8]Max-Planck-Institut für Sonnensystemforschung, Justus-von-Liebig-Weg 3, 37077 Göttingen, Germany. [9]Brown University, Department of Earth, Environmental, and Planetary Sciences, Providence, RI 02912, USA. [10]Planetary Science Institute, Tucson, AZ 85719, USA. [11]The Bear Fight Institute, Winthrop, WA 98862, USA. [12]NASA Goddard Space Flight Center, Greenbelt, MD 20771, USA. [13]Massachussetts Institute of Technology, Cambridge, MA 02139, USA. [14]Lamont-Doherty Earth Observatory, Columbia University, Palisades, NY 10968, USA. [15]Virginia Tech, Geosciences, Blacksburg, VA 24061, USA. [16]Southwest Research Institute, Boulder, CO 80302, USA. [17]Lunar and Planetary Institute, Houston, TX 77058, USA.
*Corresponding author. Email: ctrussell@igpp.ucla.edu

Downloaded from http://science.sciencemag.org/ on September 1, 2016

rim; the rhean crater is excavated in hard, cold ice and has an irregularly shaped rim and an irregular floor and steep walls. Although the cerean crater also has an irregularly shaped rim, an irregular floor, and steep walls, there is a large region of smooth floor, suggesting the production of impact melt. These craters illustrate that the surface of Ceres is intermediate in strength between that of rocky Vesta and icy Rhea. Impact melt was not observed at Vesta in appreciable amounts (*22*, *23*); thus, because of similar expected impact velocities, this observation is consistent with the presence of ice and other volatiles in the rocky crust of Ceres (*24*). However, if ice dominated the cerean crust, then craters would be expected to relax on short time scales (*25*). Because the crater size-frequency distribution (*26*) indicates that little relaxation occurs at the shorter wavelengths, the fractional content of ice in the crust must be limited. A mixture of ice and rock (or salt hydrates) could have the strength to retain these craters over billions of years (*27*). Ceres' crater distribution (*26*) and geomorphology (*24*) support the inference of a mechanically strong crust and upper mantle composed of rock, ice, and possibly salt hydrates that is periodically mobilized to produce extrusive features such as Ahuna Mons, as well as flow features and bright deposits. To date, only one area in the Oxo crater, centered at 359.7°E and 42.2° N, shows evidence of H_2O-rich surface materials (*28*). Exposed ice on Ceres at such mid-latitudes should become undetectable within hundreds of years, implying that Oxo has an active or recently exposed surface.

The gravity measurements described in the supplementary materials indicate that Ceres is close to hydrostatic equilibrium, with evidence for a denser core and low-density mantle and crust. The observed lack of large basins (*24*) and the subdued power at long wavelengths in Ceres' topographic spectrum indicate efficient relaxation of the topography at depth in the lower mantle, whereas the retention of small- to medium-sized craters points toward a strong upper mantle or lithosphere.

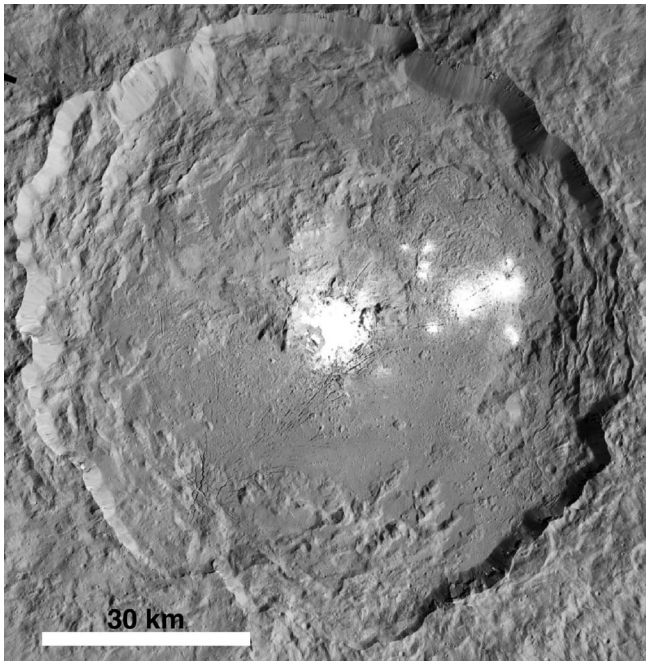


Fig. 1. Occator crater (239.3°E, 19.8°N) imaged from 1500-km altitude in a panchromatic filter. The brightest material has a normal visible albedo of about 0.5.

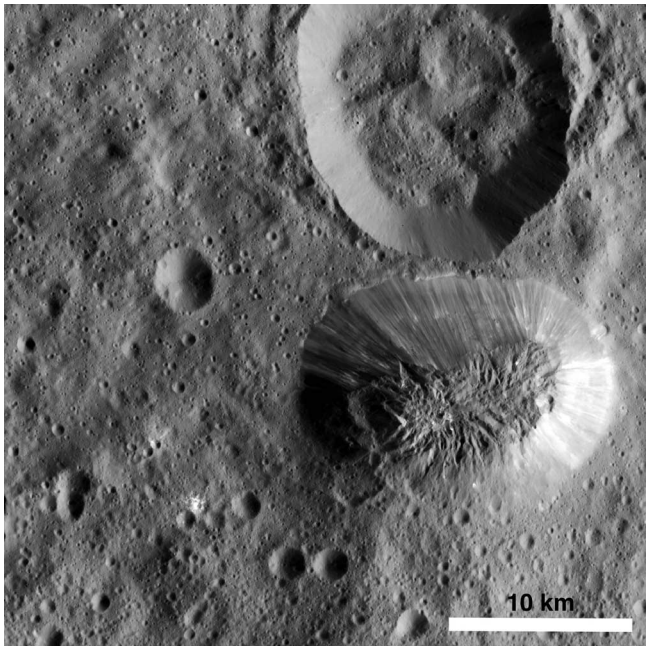


Fig. 2. Panchromatic image of Ahuna Mons (316.2°E, 10.5°S) from the low-altitude mapping orbit.

The Herschel Space Observatory detected water vapor around Ceres (*10*), but a search in forward-scattering conditions during the initial highest-altitude polar orbit in April and early May 2015 showed no scattered light due to possible ejected particles. A study of the bright regions on the Ceres surface, over the interval for which surface brightness has been measured with HST and then with Dawn, did not reveal any brightness changes during this period at 30-km scale (*17*). Dawn's instruments are not well suited to the type or level of water vapor reported by Herschel. A search for a detectable exosphere on Ceres using the Cosmic Origins Spectrometer on the HST was also unsuccessful (*29*).

An unexpected detection of energetic charged particles at Ceres may have an exospheric link. Figure 4 shows counts in the Dawn Gamma Ray and Neutron Detector (GRaND) (*30*) at an altitude of 4400 km. Results indicate detection of energetic electrons in the nadir-pointing detector, which has a field of view of close to 2π steradians. The broad peak on 18 to 21 June is a solar proton event. The unusual features are the rapid bursts seen on three successive orbits. These spikes in the counting rates are caused by the electromagnetic (bremsstrahlung) radiation produced by energetic electrons of many tens of kilo–electron volts impinging on the spacecraft. As shown in the supplementary materials, the locations of the observations on each of the three orbits over a 7-day period are plotted on a solar-oriented coordinate system. Alternatively, no ordering is seen if planetary longitude is used. Other energetic particle events have been detected during cruise, Vesta, and Ceres encounters; however, there were no accompanying electron bursts like those seen in Fig. 4. Similar electron bursts are seen by detectors on spacecraft in high-Earth orbit in the solar wind when the magnetic field at the spacecraft lies tangent to the surface of the bow shock. These signals are attributed to rapid acceleration of electrons to very high energies (*31*). When the interplanetary field lines are convected through the shock, the electrons orbiting that magnetic field line experience an increasing field strength that, near the point of tangency of the field line and the shock, rapidly accelerates electrons gyrating nearly perpendicular to the magnetic field up to very high energies. This mechanism is called fast Fermi acceleration (*32*, *33*) as it involves a magnetic mirror that moves very rapidly.

There are two ways for Ceres to produce a bow shock in a transient manner lasting ~6 days. First, a weak atmosphere at Ceres consistent with the Herschel observations could have been ionized by the energetic particles in the solar wind, mass loading the solar wind and producing a bow shock as the solar wind was deflected around the mass-loading obstacle. When the solar particle event terminated, the ionization stopped, and this exosphere would gradually disappear. The expected time scale for such a temporary exosphere to disappear is of the order of a week (*34*). A second means of possibly deflecting the solar wind is via the

Downloaded from http://science.sciencemag.org/ on September 1, 2016

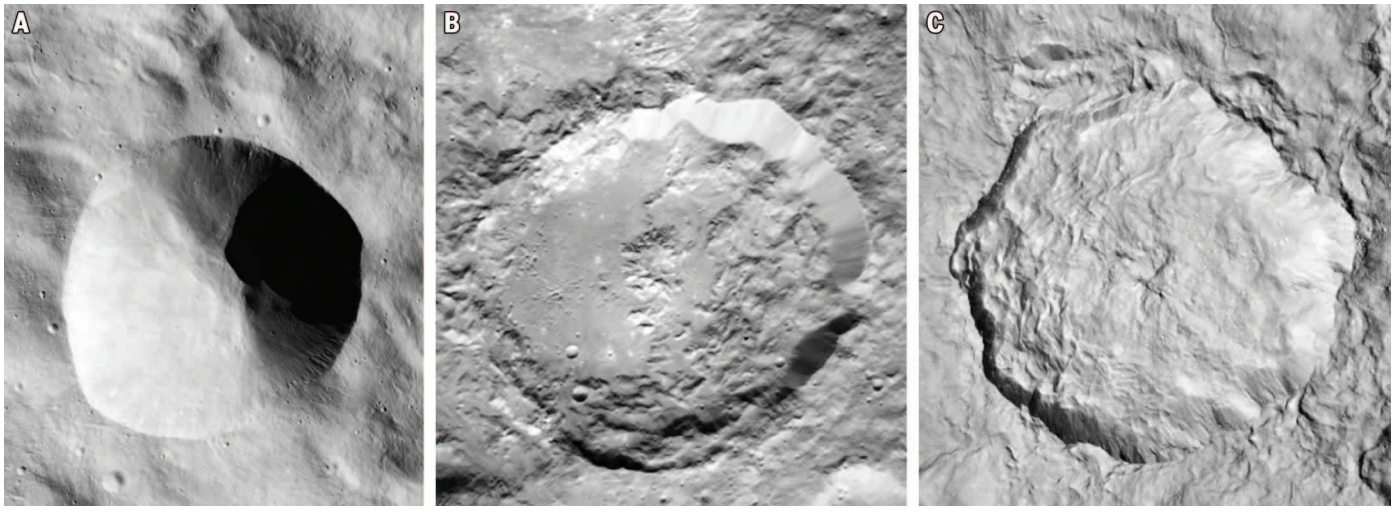


Fig. 3. Comparison of the morphologies of typical fresh craters of similar size. Torpeia crater on Vesta (**A**) is 40-km wide; Ikapati crater on Ceres (**B**) is 48-km wide; Inktomi crater on Saturn's icy moon Rhea (**C**) is 49-km wide.

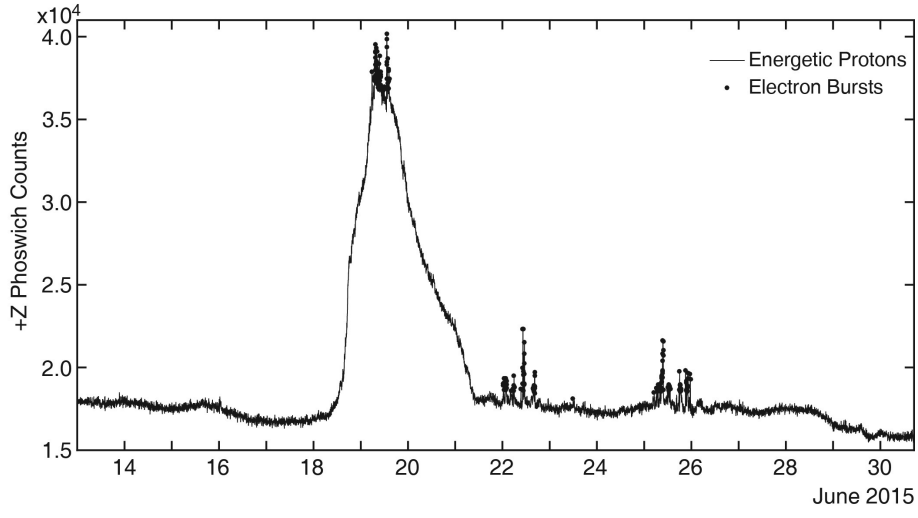


Fig. 4. Gross counts per 210 s measured by the +Z phoswich sensor within the gamma-ray and neutron detector. This sensor is sensitive to bremsstrahlung produced by the interaction of swift electrons with the instrument housing, and to solar energetic protons. The electron bursts were detected while GRaND was pointed toward the hemisphere that contained Ceres. The slowly varying solar proton event on 18 to 21 June and the energetic proton background are designated by the solid line. The electron burst contribution is indicated by the dotted peaks.

magnetic cloud that often accompanies such a solar energetic particle event. If, as has been hypothesized, Ceres is wet inside and the salty mix is electrically conductive, then the magnetic cloud would induce an electric current inside Ceres, creating a magnetic field that would deflect the solar wind. This magnetic barrier would exist until the currents inside Ceres decayed. Such models require electrical conductivities higher than we expect (see supplementary materials), as well as greater conducting shell thicknesses, to reproduce the observed time scales. Thus, we favor the temporary atmosphere explanation, because it reproduces the observed time scales with no assumptions about the conditions internal to Ceres.

REFERENCES AND NOTES

1. C. Peebles, *Asteroids: A History* (Smithsonian Institution Scholarly Press, 2000).
2. C. T. Russell, H. Y. McSween, R. Jaumann, C. A. Raymond, in *Asteroids IV*, P. Michel, F. E. DeMeo, W. F. Bottke, Eds. (Univ. of Arizona Press, 2015), pp. 419–432.
3. A. S. Rivkin *et al.*, *Space Sci. Rev.* **163**, 95–116 (2011).
4. W. J. Webster *et al.*, *Astrophys. J.* **95**, 1263–1268 (1988).
5. P. C. Thomas *et al.*, *Nature* **437**, 224–226 (2005).
6. A. S. Konopliv *et al.*, *Icarus* **211**, 401–428 (2011).
7. T. B. McCord, C. Sotin, *J. Geophys. Res.* **110**, E05009 (2005).
8. J. C. Castillo-Rogez, T. B. McCord, *Icarus* **205**, 443–459 (2010).
9. M. F. A'Hearn, P. D. Feldman, *Icarus* **98**, 54–60 (1992).
10. M. Küppers *et al.*, *Nature* **505**, 525–527 (2014).
11. T. V. V. King, R. N. Clark, W. M. Calvin, D. M. Sherman, R. H. Brown, *Science* **255**, 1551–1553 (1992).
12. R. E. Milliken, A. S. Rivkin, *Nat. Geosci.* **2**, 258–261 (2009).
13. M. C. De Sanctis *et al.*, *Nature* **528**, 241–244 (2015).
14. T. Roatsch *et al.*, *Planet. Space Sci.* **121**, 115–120 (2016).
15. M. A. Chamberlain, M. V. Sykes, G. A. Esquerdo, *Icarus* **188**, 451–456 (2007).
16. J. D. Drummond *et al.*, *Icarus* **236**, 28–37 (2014).
17. J.-Y. Li *et al.*, *Astrophys. J.* **817**, L22 (2016).
18. A. Nathues *et al.*, *Nature* **528**, 237–240 (2015).
19. M. C. De Sanctis *et al.*, *Nature* **536**, 54–57 (2016).
20. E. Ammannito *et al.*, *Science* **353**, aaf4279 (2016).
21. O. Ruesch *et al.*, *Science* **353**, aaf4286 (2016).
22. D. A. Williams *et al.*, *Planet. Space Sci.* **103**, 24–35 (2014).
23. P. Schenk *et al.*, *Science* **336**, 694–697 (2012).
24. D. L. Buczkowski *et al.*, *Science* **353**, aaf4332 (2016).
25. M. E. Bland, *Icarus* **226**, 510–521 (2013).
26. H. Hiesinger *et al.*, *Science* **353**, aaf4759 (2016).
27. W. B. Durham, S. H. Kirby, L. A. Stern, *J. Geophys. Res.* **97**, 20883–20897 (1992).
28. J.-P. Combe *et al.*, *Science* **353**, aaf3010 (2016).

ACKNOWLEDGMENTS

We thank the Dawn team for the development, cruise, orbital insertion, and operations of the Dawn spacecraft at Ceres. C.T.R. is supported by the Discovery Program through contract NNM05AA86C to the University of California, Los Angeles. R.R.F. thanks the Lamont-Doherty Earth Observatory Post-Doctoral Fellowship for support. A portion of this work was performed at the Jet Propulsion Laboratory, California Institute of Technology, under contract with NASA. Dawn's Gamma Ray and Neutron Detector is operated by the Planetary Science Institute under contract with the Jet Propulsion Laboratory, California Institute of Technology (JPL). Dawn data are archived with the NASA Planetary Data System. Framing camera data may be obtained at http://sbn.psi.edu/pds/resource/dwncfc2.html. Spectral data from Visible and Infrared Mapping Spectrometer may be obtained at http://sbn.psi.edu/pds/resource/dwncvir.html. GRaND data may be obtained at http://sbn.psi.edu/pds/resource/dwncgrd.html.

SUPPLEMENTARY MATERIALS

www.sciencemag.org/content/353/6303/1008/suppl/DC1
Supplementary Text
Materials and Methods
Figs. S1 to S6
Table S1
References (*29*–*43*)

4 February 2016; accepted 13 July 2016
10.1126/science.aaf4219

Downloaded from http://science.sciencemag.org/ on September 1, 2016

WATER SPLITTING

A highly active and stable $IrO_x/SrIrO_3$ catalyst for the oxygen evolution reaction

Linsey C. Seitz,[1] Colin F. Dickens,[1,2] Kazunori Nishio,[3,4] Yasuyuki Hikita,[3] Joseph Montoya,[2] Andrew Doyle,[2] Charlotte Kirk,[2] Aleksandra Vojvodic,[2] Harold Y. Hwang,[3,4] Jens K. Norskov,[1,2] Thomas F. Jaramillo[1,2]*

Oxygen electrochemistry plays a key role in renewable energy technologies such as fuel cells and electrolyzers, but the slow kinetics of the oxygen evolution reaction (OER) limit the performance and commercialization of such devices. Here we report an iridium oxide/strontium iridium oxide ($IrO_x/SrIrO_3$) catalyst formed during electrochemical testing by strontium leaching from surface layers of thin films of $SrIrO_3$. This catalyst has demonstrated specific activity at 10 milliamps per square centimeter of oxide catalyst (OER current normalized to catalyst surface area), with only 270 to 290 millivolts of overpotential for 30 hours of continuous testing in acidic electrolyte. Density functional theory calculations suggest the formation of highly active surface layers during strontium leaching with IrO_3 or anatase IrO_2 motifs. The $IrO_x/SrIrO_3$ catalyst outperforms known IrO_x and ruthenium oxide (RuO_x) systems, the only other OER catalysts that have reasonable activity in acidic electrolyte.

Advances in renewable energy largely rely on technologies for energy conversion and storage to mitigate intermittency issues associated with wind and sunlight. Electrochemical processes such as water splitting and CO_2 reduction have been widely studied for conversion of electrical energy into fuels and chemicals. Water oxidation, or the oxygen evolution reaction (OER), plays a key role by providing the protons and electrons needed for these processes; improving the efficiency and durability of OER catalysts has a direct impact on device efficiency and cost effectiveness. Here we report an OER catalyst that demonstrates activity and stability in acid electrolyte.

Decades of research investigating catalysts for the OER have led to substantial advancements in the field and the development of active catalysts. However, even the best currently known catalysts require >320 mV overpotential to reach 10 mA/cm^2_{oxide} (*1*–*8*), a measure of intrinsic activity acquired by normalizing the OER current to the catalyst surface area. To partially overcome the low intrinsic activity of known OER catalysts, the activity of an OER electrode can be improved on a geometric-area basis by increasing catalyst loadings or by improving catalyst morphologies to expose large surface areas. Such approaches, however, can ultimately become limited by mass transport and/or catalyst conductivity. Another major concern is the cost and scarcity of precious metal–based OER catalysts, particularly in acidic electrolyte.

Whereas there are a plethora of precious and nonprecious metal catalysts that exhibit activity and stability in alkaline electrolyte, IrO_x and RuO_x are currently the only known materials that can reach ~5 mA/cm^2_{oxide} with overpotentials less than 750 mV in acidic electrolyte (*1*, *9*). New OER catalysts for use in acidic environments could have a direct impact on improving polymer electrolyte membrane–based water electrolyzers, a recent technology that overcomes many of the disadvantages of conventional alkaline electrolyzers (*10*) but in which OER catalysts are primarily restricted to IrO_x.

The recent development of techniques for high-quality growth of epitaxial complex oxide thin films and heterostructures provides an intriguing opportunity for the conception and fundamental study of OER catalysts (*11*, *12*). Using such an approach, we developed a catalyst $IrO_x/SrIrO_3$, which is stable in acidic electrolyte and substantially outperforms known IrO_x catalysts. We applied density functional theory (DFT) calculations and several materials characterization techniques to understand the possible active sites contributing to the extremely high activity.

The bulk material of this catalyst consists of epitaxial $SrIrO_3$ thin films deposited on $SrTiO_3$ substrates by pulsed laser deposition (PLD; details are provided in the supplementary materials) (*12*). The catalyst activity and stability was assessed in 0.5 M H_2SO_4 by using alternating cyclic voltammetry and chronopotentiometric holds at 10 mA/cm^2_{geo} (current normalized to the geometric surface area of the electrode or the catalyst substrate) in a procedure similar to that which has been used in benchmarking studies for other electrochemical catalysts (*1*). Figure 1A shows the potential required to reach 10 mA/cm^2_{geo} during a 30-hour stability test, and fig. S1A shows example cyclic voltammograms (CVs) taken periodically during testing. Figure 1B shows a Tafel plot of the intrinsic, or specific, activities for both films over the course of the stability test, compared with the best reported catalysts in acidic electrolyte (*1*, *13*). Initially, the films require 340 mV of overpotential (measured by CV) to reach 10 mA/cm^2_{oxide} and improve to 320 mV of overpotential after 10 min of testing. The catalyst continues to increase in activity during the first 2-hour chronopotentiometric hold and requires only 270 to 290 mV of overpotential to reach 10 mA/cm^2_{oxide} for the remainder of the measurements. Figure 1B also presents specific activity for a flat 40-nm epitaxial rutile IrO_2 (110) film deposited on TiO_2 (110) by PLD as a direct comparison with our sample morphology. This rutile IrO_2 film has similar activity to rutile IrO_2 and RuO_2 nanoparticles (*13*) when normalized to the catalyst surface area, but the $IrO_x/SrIrO_3$ catalyst outperforms all of these by two orders of magnitude. Whereas Fig. 1B compares the $IrO_x/SrIrO_3$ catalyst with some of the best catalysts showing activity and reasonable stability in acidic electrolyte, for further comparison, another Tafel plot is shown in fig. S1B that includes the best reported catalysts in both acidic and alkaline electrolyte.

DFT calculations were performed to provide further understanding of the nature of the $SrIrO_3$ surface and its high activity. Consistent with previous studies (*14*, *15*), we assumed a four-step OER mechanism that proceeds through OH*, O*, and OOH* (where the asterisk indicates surface-bound species), and we evaluated OER activity on the basis of the theoretical overpotential, which is the overpotential required to make all elementary steps exergonic (further model details are included in the supplementary materials).

DFT simulations of the IrO_2 termination of $SrIrO_3$ (001) (Fig. 2B) yielded a theoretical overpotential of 0.59 V, which is well above the value that we calculated for rutile IrO_2 (110) (0.38 V). This suggests that surface sites at the (001) facet may not be responsible for the high activity of $SrIrO_3$ that we observed experimentally. It is well known that alkaline earth metals may leach from perovskites under aqueous conditions (*16*), and in the case of $SrIrO_3$, we calculated a thermodynamic driving force of 3.2 eV per Sr atom to form aqueous Sr^{2+} and rutile IrO_2 at the relevant experimental conditions. We investigated possible motifs of the Sr-deficient $IrO_x/SrIrO_3$ surface by examining a variety of overlayer structures that may arise during OER and contribute to catalytic activity.

The first overlayer structure that we considered was anatase IrO_2. Although rutile is known to be the most stable bulk polymorph of IrO_x, the anatase structure is much more commensurate with the $SrIrO_3$ perovskite lattice because their calculated lattice constants are within 2% of each other. The anatase and perovskite structures are also very similar when viewed down the *c* axis—both consist of IrO_6 octahedra that share corners

[1]SUNCAT Center for Interface Science and Catalysis, Department of Chemical Engineering, Stanford University, Shriram Center, 443 Via Ortega, Stanford, CA 94305, USA. [2]SUNCAT Center for Interface Science and Catalysis, SLAC National Accelerator Laboratory, 2575 Sand Hill Road, Menlo Park, CA 94025, USA. [3]Stanford Institute for Materials and Energy Sciences, SLAC National Accelerator Laboratory, 2575 Sand Hill Road, Menlo Park, CA 94025, USA. [4]Geballe Laboratory for Advanced Materials, Department of Applied Physics, Stanford University, 476 Lomita Mall, Stanford, CA 94305, USA.
*Corresponding author. Email: jaramillo@stanford.edu

Downloaded from http://science.sciencemag.org/ on September 1, 2016

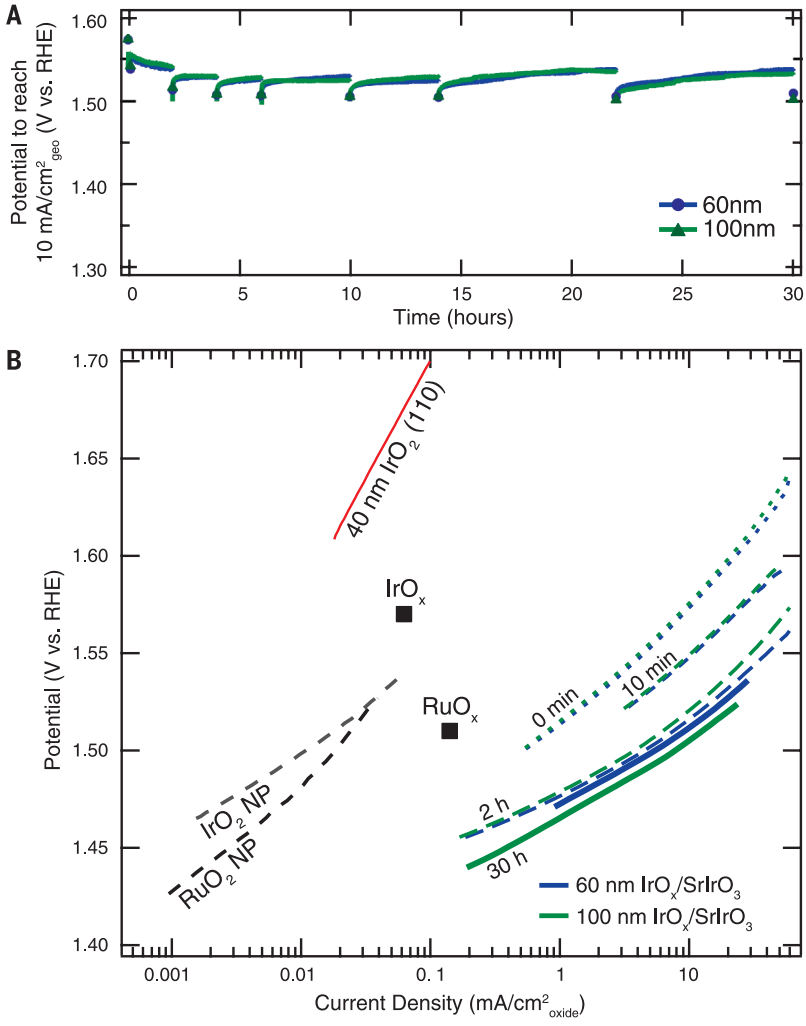


Fig. 1. Electrochemical activity. (**A**) Potential required to reach 10 mA/cm$^2_{geo}$ for IrO_x/$SrIrO_3$ films over 30 hours of electrochemical testing, measured using cyclic voltammetry (markers) and chronopotentiometric holds (lines). (**B**) Tafel plot comparing specific activity of IrO_x/$SrIrO_3$ with that of OER catalysts in acidic electrolyte. Green lines show 100-nm IrO_x/$SrIrO_3$ and blue lines show 60-nm IrO_x/$SrIrO_3$ specific activity at various points during electrochemical stability testing. The red line shows specific activity for a 40-nm rutile IrO_2 (110) film. Gray and black lines and squares are duplicated from literature (*1*, *13*). NP, nanoparticles. RHE, reversible hydrogen electrode.

in the (00*l*) planes—suggesting that a transformation between them may be kinetically accessible. Furthermore, the growth of micron-sized (001)-oriented TiO_2 anatase crystallites has been observed experimentally after soaking $SrTiO_3$ in water (*17*). On replacement of the top two layers of $SrIrO_3$ with anatase IrO_2 (001) (Fig. 2C), we calculated a stabilization of 2.2 eV per Sr atom and a theoretical overpotential of 0.30 V. For the limiting case of pure anatase IrO_2 (001) (Fig. 2D), which may occur in thicker overlayers where strain has been released, we calculated a similar theoretical overpotential of 0.28 V, which is very near the peak of the OER volcano (Fig. 2A). This is in agreement with a recent theoretical study of several metastable polymorphs of IrO_2 in the low coverage limit that found anatase to be the most active (*18*).

The second IrO_x overlayer structure that we considered was produced by simulated annealing using ab initio (DFT) molecular dynamics with the IrO_2-anatase/$SrIrO_3$ structure as an initial guess. This structure can be viewed as similar to ReO_3 with a "sheet" of oxygen removed in the (100) plane, which results in a series of square coordinated IrO_4 planes anchored by $SrIrO_3$ (001) (Fig. 2E). The stability of this structure is similar to that of the anatase overlayer starting point, but its calculated theoretical overpotential (0.78 V) was found to be much worse. Filling the vacant (100) planes with oxygen to form an IrO_3 film stabilizes the structure by −0.03 eV per O atom at OER equilibrium and improves the theoretical overpotential to 0.47 V (Fig. 2F). Removal of a third layer of Sr further reduces the overpotential value to 0.28 V (Fig. 2G). The observation of nominal Ir oxidation states greater than 4+ is unusual in solid oxides, but we predict their stability under the oxidizing experimental conditions.

Ultimately, our calculations suggest that the activity of $SrIrO_3$ is improved as Sr leaches into the electrolyte and that the formation of sites similar to IrO_3 or anatase IrO_2 may be responsible for the experimentally observed activity. Although we cannot exclude other, even more stable and active overlayer structures, these calculations illustrate that Sr deficiencies in the near-surface of $SrIrO_3$ can induce substantially improved OER activity on Ir sites. It is also worth noting that the surfaces considered in this study are concentrated at the more favorable, lower bound of the previously reported universal scaling relationship between OH and OOH (*10*) (Fig. 2J). This results in an elevated volcano peak in Fig. 2A and suggests that the most active surfaces considered here are at the limit of what is possible without breaking the scaling between OH and OOH.

After identifying active sites for this catalyst surface that may contribute to the observed activity, materials characterization provided further insight into the catalyst morphology and composition before and after electrochemical testing. Atomic force microscopy (AFM) was used to assess the surface morphology and roughness of these films. Figure 3A presents 2- by 2-μm maps and 2-μm line scans for a 100-nm $SrIrO_3$ film before and after 30 hours of testing. Although there was some surface rearrangement, the films were notably flat as prepared and exhibited uniform small features after stability testing. The root mean square roughness and surface roughness factors (film surface area normalized to geometric area) were quantified for both the $SrIrO_3$ and the IrO_2 PLD films and are presented in the table in Fig. 3B (AFM maps and line scans are shown in fig. S3). These measurements were used to normalize the electrochemical activity to the actual catalyst surface area, and the flat nature of the films allows for accurate quantification of specific activity.

The expected bulk crystal structure of $SrIrO_3$ was confirmed by x-ray diffraction (XRD). It has been previously reported that the perovskite-type $SrIrO_3$ with orthorhombic symmetry is stabilized on $SrTiO_3$ (100) (*12*, *19*, *20*); therefore, all XRD patterns are labeled using the pseudo-cubic notation for $SrIrO_3$. Figure 3C shows diffractograms of a 100-nm $SrIrO_3$ film before and after 30 hours of testing. Both display the characteristic sharp peaks of the $SrTiO_3$ substrate and the broader peaks of orthorhombic $SrIrO_3$. There is some observable decrease in $SrIrO_3$ peak intensities measured after OER testing, which is most visible in the $SrIrO_3$ (200) peaks (enlarged plot in fig. S4), but the bulk of the film appears to have remained crystalline. XRD results for the IrO_2 PLD film are shown in fig. S5.

The surface composition and chemical state of the IrO_x/$SrIrO_3$ catalysts were assessed by x-ray photoelectron spectroscopy (XPS). Sample Ir4f and Sr3d peaks are shown in Fig. 3D for a 100-nm IrO_x/$SrIrO_3$ sample before and after 30 min of electrochemical testing. The Ir4f peak can be fit with two doublets, as has been observed previously (*21*–*23*), which likely correspond to screened and unscreened components of an Ir^{4+} state. The Sr3d peak can be fit with two doublets before testing,

Downloaded from http://science.sciencemag.org/ on September 1, 2016

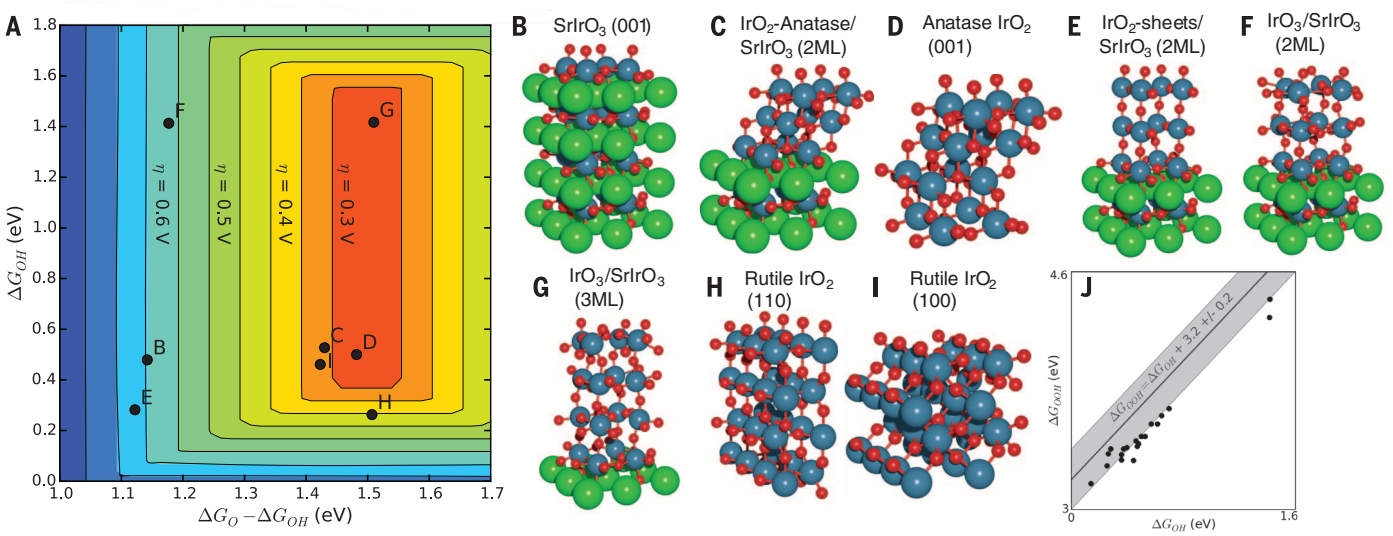
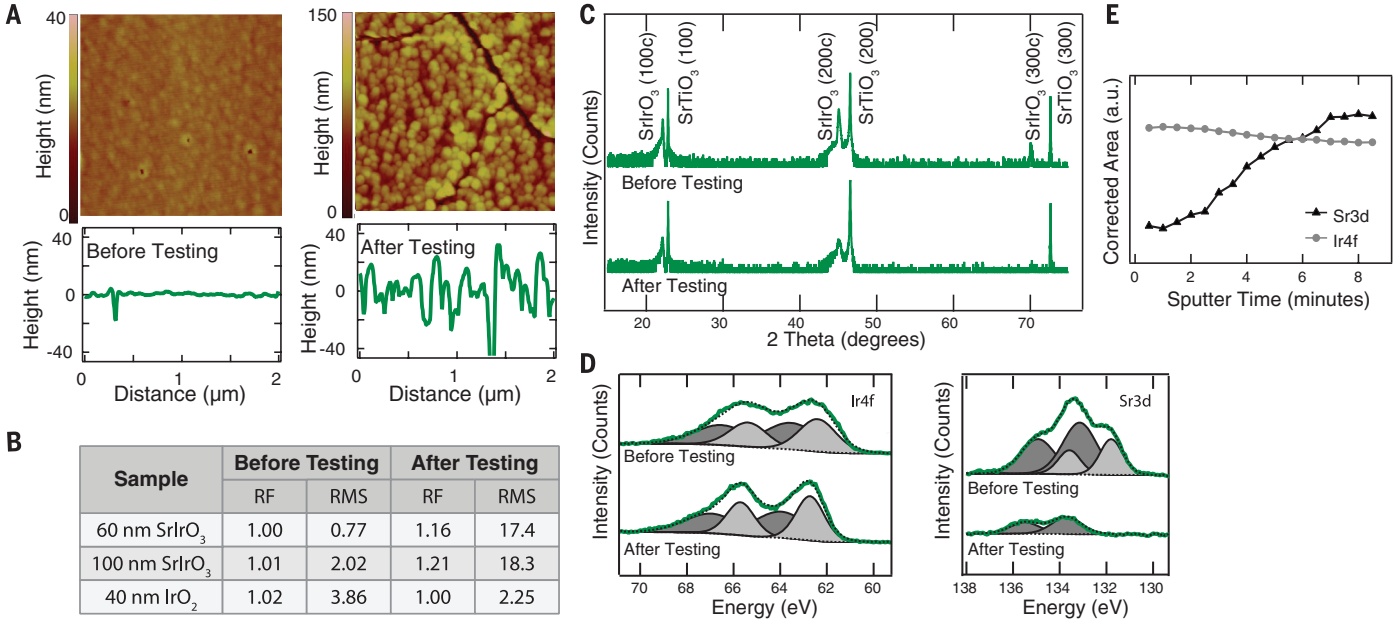


Fig. 2. OER theoretical analysis. (**A**) Theoretical overpotential (η) volcano plot with O* and OH* binding energies as descriptors, using the scaling relationship between OH and OOH shown in fig. S2B. (**B** to **I**) Visual representation of IrO_x and $SrIrO_3$ surfaces used for the DFT calculations, corresponding to the labeled points in (A) (strontium, green; iridium, blue; oxygen, red). (**J**) OH* and OOH* binding energies (black circles) overlaid on the universal scaling relationship (gray line with shaded uncertainty) that has been found for many transition metals and transition metal oxides (*10*). *G*, Gibbs free energy. ML, monolayers.



Sample	Before Testing		After Testing	
	RF	RMS	RF	RMS
60 nm $SrIrO_3$	1.00	0.77	1.16	17.4
100 nm $SrIrO_3$	1.01	2.02	1.21	18.3
40 nm IrO_2	1.02	3.86	1.00	2.25

Fig. 3. Material characterization. (**A**) AFM maps and line scans for a 100-nm $SrIrO_3$ film before and after 30 hours of OER testing. (**B**) Table summarizing the roughness factor (RF) and root mean square (RMS) roughness (in nanometers) for two $SrIrO_3$ samples and one IrO_2 sample before and after 30 hours of OER testing. (**C**) XRD of a 100-nm $SrIrO_3$ film before and after 30 hours of OER testing. (**D**) XPS on the Ir4f and Sr3d peaks for a 100-nm $SrIrO_3$ film before and after 30 min of OER testing. (**E**) Depth sputter profile indicating the relative quantities of each element near the surface after 30 min of OER testing. a.u., arbitrary units.

but as Sr is leached during the first 30 min of electrochemical testing, the signal decreases considerably and the spectral shape appears to change; the spectra are only fit with one doublet after testing. Additional XPS spectra are shown for Ir4f and Sr3d peaks in fig. S6, along with a more thorough peak-fitting analysis. A comparison of XPS spectra measured after varying periods of electrochemical testing on sister samples shows the Sr signal decreasing to 25 to 28% of its original value after 30 min and decreasing to about 20% of its original value after 24 hours, during which time the Ir signal remains constant. This indicates that Sr is leaching from the surface of the catalyst during electrochemical testing and suggests that the rate of Sr leaching is fastest during initial testing and slows or perhaps even stops with additional testing, likely because of kinetic barriers of Sr transport through the lattice. This is in agreement with previous measurements of Sr leaching from $SrTiO_3$ (*16*).

Furthermore, a decrease in the Sr XPS signal to 25% of its original value after 30 min of electrochemical testing would indicate that about seven monolayers of $SrIrO_3$ at the surface have been completely depleted of Sr. In reality, there is probably a distribution of Sr leaching from the topmost $SrIrO_3$ layers, as indicated by XPS results in Fig. 3E, which shows the Sr and Ir content as a function of depth from the catalyst surface. Inductively coupled plasma optical emission spectroscopy measurements of the electrolyte after testing provided complementary results, indicating that ~30 to 50% of the Sr is leached from the films in the first 30 min of testing (additional details are provided in the supplementary materials).

Downloaded from http://science.sciencemag.org/ on September 1, 2016

Evidence of Sr leaching and minor surface rearrangement of the resulting IrO_x films suggests that an $IrO_x/SrIrO_3$ catalyst is formed in situ and becomes increasingly active over the first 2 hours of electrochemical testing. Although the exact structure of the surface formed during reaction is still unknown, DFT calculations have identified possible structures that could be kinetically or epitaxially stabilized by the interface with $SrIrO_3$ and could contribute to the very high observed activity. The stability and high intrinsic activity of this catalyst show promise for its integration into renewable energy technologies, such as polymer electrolyte membrane electrolyzers, for the sustainable production of hydrogen or other fuels and chemicals.

REFERENCES AND NOTES

1. C. C. L. McCrory *et al.*, *JACS* **137**, 4347–4357 (2015).
2. J. Suntivich, K. J. May, H. A. Gasteiger, J. B. Goodenough, Y. Shao-Horn, *Science* **334**, 1383–1385 (2011).
3. A. Grimaud *et al.*, *Nat. Commun.* **4**, 2439 (2013).
4. E. A. Paoli *et al.*, *Chem. Sci.* **6**, 190–196 (2015).
5. L. Trotochaud, J. K. Ranney, K. N. Williams, S. W. Boettcher, *JACS* **134**, 17253–17261 (2012).
6. D. A. Corrigan, *J. Electrochem. Soc.* **134**, 377 (1987).
7. J. Bao *et al.*, *Angew. Chem. Int. Ed.* **54**, 7399–7404 (2015).
8. M. S. Burke, L. J. Enman, A. S. Batchellor, S. Zou, S. W. Boettcher, *Chem. Mater.* **27**, 7549–7558 (2015).
9. N. Danilovic *et al.*, *J. Phys. Chem. Lett.* **5**, 2474–2478 (2014).
10. M. Carmo, D. L. Fritz, J. Mergel, D. Stolten, *Int. J. Hydrogen Energy* **38**, 4901–4934 (2013).
11. R. Tang *et al.*, *J. Mater. Chem. A* **4**, 6831–6836 (2016).
12. K. Nishio, H. Y. Hwang, Y. Hikita, *APL Mater.* **4**, 036102 (2016).
13. Y. Lee, J. Suntivich, K. J. May, E. E. Perry, Y. Shao-Horn, *J. Phys. Chem. Lett.* **3**, 399–404 (2012).
14. I. C. Man *et al.*, *ChemCatChem* **3**, 1159–1165 (2011).
15. J. Rossmeisl, Z. W. Qu, H. Zhu, G. J. Kroes, J. K. Nørskov, *J. Electroanal. Chem.* **607**, 83–89 (2007).
16. H. W. Nesbitt *et al.*, *Nature* **289**, 358–362 (1981).
17. Z. Zhang, *J. Mater. Res.* **20**, 292–294 (2005).
18. Z. Xu, J. R. Kitchin, *Phys. Chem. Chem. Phys.* **17**, 28943–28949 (2015).
19. Y. K. Kim *et al.*, *Jpn. J. Appl. Phys.* **45**, L36–L38 (2006).
20. J. Matsuno *et al.*, *Phys. Rev. Lett.* **114**, 247209 (2015).
21. J. M. Kahk *et al.*, *Phys. Rev. Lett.* **112**, 117601 (2014).
22. T. Reier *et al.*, *J. Electrochem. Soc.* **161**, F876–F882 (2014).
23. H. G. Sanchez Casalongue *et al.*, *Angew. Chem. Int. Ed.* **53**, 7169–7172 (2014).

ACKNOWLEDGMENTS

This work was supported by the U.S. Department of Energy (DOE), Office of Science, Office of Basic Energy Sciences, under contract no. DE-SC0008685 and through the SUNCAT Center for Interface Science and Catalysis. Partial support was provided by the Center on Nanostructuring for Efficient Energy Conversion at Stanford University, an Energy Frontier Research Center funded by the DOE, Office of Science, under award no. DE-SC0001060. L.C.S. received fellowship support from the DARE (Diversifying Academia, Recruiting Excellence) Doctoral Fellowship supported by the Vice Provost for Graduate Education at Stanford University. Part of this work was performed at the Stanford Nano Shared Facilities. K.N., Y.H., and H.Y.H. acknowledge support from the DOE, Office of Science, Office of Basic Energy Sciences, Division of Materials Sciences and Engineering, under contract no. DE-AC02-76SF00515 (thin film synthesis), and from the Global Climate and Energy Project at Stanford University (modifications under ionic tuning). C.F.D. and C.K. acknowledge support from the NSF Graduate Research Fellowship program under grant no. DGE-114747. C.K. also acknowledges support from the Morgridge Family Stanford Graduate Fellowship.

SUPPLEMENTARY MATERIALS

www.sciencemag.org/content/353/6303/1011/suppl/DC1
Materials and Methods
Figs. S1 to S8
Tables S1 to S2
References (*24*–*52*)

22 February 2016; accepted 9 August 2016
10.1126/science.aaf5050

ORGANIC CHEMISTRY

Enantioselective cyanation of benzylic C–H bonds via copper-catalyzed radical relay

Wen Zhang,[1]* Fei Wang,[1]* Scott D. McCann,[2] Dinghai Wang,[1] Pinhong Chen,[1] Shannon S. Stahl,[2]† Guosheng Liu[1]†

Direct methods for stereoselective functionalization of sp^3-hybridized carbon–hydrogen [C(sp^3)–H] bonds in complex organic molecules could facilitate much more efficient preparation of therapeutics and agrochemicals. Here, we report a copper-catalyzed radical relay pathway for enantioselective conversion of benzylic C–H bonds into benzylic nitriles. Hydrogen-atom abstraction affords an achiral benzylic radical that undergoes asymmetric C(sp^3)–CN bond formation upon reaction with a chiral copper catalyst. The reactions proceed efficiently at room temperature with the benzylic substrate as limiting reagent, exhibit broad substrate scope with high enantioselectivity (typically 90 to 99% enantiomeric excess), and afford products that are key precursors to important bioactive molecules. Mechanistic studies provide evidence for diffusible organic radicals and highlight the difference between these reactions and C–H oxidations mediated by enzymes and other catalysts that operate via radical rebound pathways.

The clinical success of potential drug candidates has been shown to correlate with the fraction of sp^3-hybridized carbon atoms and the number of stereogenic centers in the molecule (*1*). Consequently, synthetic methods that enable stereoselective functionalization of C(sp^3)–H bonds could have a major effect on the discovery and development of new pharmaceuticals. Enzymatic oxygenases and halogenases, such as cytochrome P450 and nonheme iron enzymes (*2*–*4*), have inspired the discovery of synthetic methods for selective oxidation of C–H bonds [see, for example, (*5*–*8*)]. These enzymes and related small-molecule catalysts function via generation of a reactive metal-oxo species that abstracts an H atom from a C(sp^3)–H bond, followed by radical rebound (*9*) to the metal-bound hydroxide or halide group (Fig. 1A). Here, we report a complementary radical relay strategy for C(sp^3)–H oxidation whereby a reactive radical (**X**•) abstracts a hydrogen atom from an sp^3-hybridized carbon atom to produce a diffusible organic radical. This radical is then trapped by a second species that generates the functionalized sp^3 center (Fig. 1B). This concept is demonstrated in copper-catalyzed enantioselective cyanation of benzylic C–H bonds (Fig. 1C). Optically pure alkyl nitriles are featured in many bioactive natural products, pharmaceuticals, and agricultural chemicals (*10*). Moreover, benzylic nitriles are direct precursors to phenethylamine derivatives, which represent a broad class of hormones, neurotransmitters, and psychoactive drugs (*11*), as well as arylacetic acid derivatives, which are among the most widely used nonsteroidal anti-inflammatory drugs (NSAIDs) (*12*). The stereoselectivity is proposed to arise from reaction of an achiral carbon radical with a chiral copper(II) species (L*Cu^{II}–CN) (*13*), a pathway that contrasts with most enantioselective C–H functionalization reactions that involve selective, stereospecific activation of a prochiral C–H bond within an organic molecule (*14*, *15*).

In recent years, we have been investigating Cu-catalyzed methods for oxidation of styrenes and other alkenes [for example, (*16*, *17*)], as well as C–H bonds (*18*). The former reactions are proposed to proceed via reaction of a benzylic radical intermediate with copper(II), generating an organocopper(III) species that undergoes reductive elimination to afford a new C–C or C–heteroatom bond. This pathway, which resembles a number of recently reported nickel- and copper-catalyzed cross-coupling methods that involve the reaction of a carbon-centered radical with a transition-metal center [e.g., (*13*, *19*–*23*)], prompted us to consider how analogous concepts could be applied to C–H oxidation. Kharasch-Sosnovsky allylic oxidations and related reactions provide relevant precedent for this idea (*24*, *25*); however, these reactions face constraints that have greatly limited their synthetic utility over the nearly 60-year history of the reaction. For example, the alkene substrate is almost always used in large excess relative to the peroxide-based oxidant, a feature that severely restricts the net product yield and, in turn, the scope of suitable substrates. The majority of examples feature only simple cyclic alkene substrates, such

[1]State Key Laboratory of Organometallic Chemistry, Shanghai Institute of Organic Chemistry, University of Chinese Academy of Sciences, Chinese Academy of Sciences, 345 Lingling Road, Shanghai 200032, China. [2]Department of Chemistry, University of Wisconsin–Madison, 1101 University Avenue, Madison, WI 53706, USA.
*These authors contributed equally to this work. †Corresponding author. Email: stahl@chem.wisc.edu (S.S.S.); gliu@mail.sioc.ac.cn (G.S.L.)

Downloaded from http://science.sciencemag.org/ on September 1, 2016

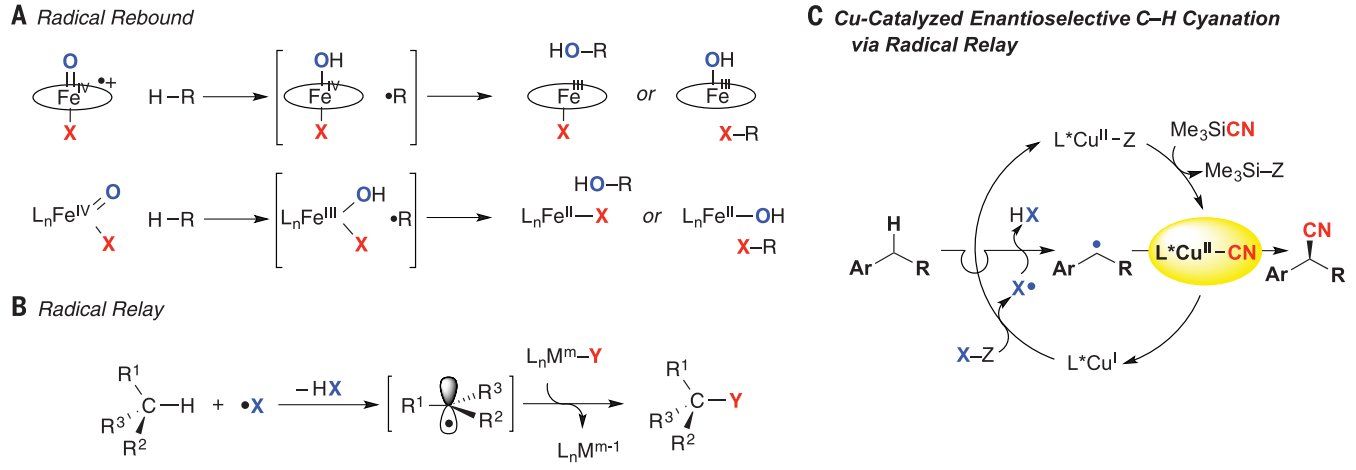


Fig. 1. Strategies for hydrogen-atom-transfer–mediated C–H oxidation. (**A**) Radical rebound mechanism for enzymatic and biomimetic C–H hydroxylation and halogenation (X = halide). (**B**) Radical relay pathway for C–H oxidation involving formation of a free radical that is trapped by a reactive metal center. (**C**) Proposed mechanism for Cu-catalyzed enantioselective cyanation of benzylic C–H bonds via radical relay.

as cyclopentene and cyclohexene. Reports of enantioselective reactivity retain this limited substrate scope and are characterized by poor catalytic efficiency that can result in multiday reaction times (*26*, *27*). A synthetically useful radical-relay C–H oxidation method would need to overcome these limitations.

The pharmaceutical interest in benzylic nitriles and products derived therefrom, together with the formation of benzylic nitriles in certain alkene difunctionalization reactions (*17*, *28*) [for broader context, see (*29*)], prompted us to target a method for enanatioselective cyanation of benzylic C–H bonds. Initial efforts focused on generation of benzylic radicals via hydrogen-atom abstraction in the presence of copper(II) and a cyanide source. We posited that reductive activation of peroxides and other diheteroatom-bonded oxidants (see X–Z, Fig. 1C) with a copper(I) source should afford a reactive radical species and copper(II). A series of oxidants, including $^{t}BuO_2H$, $(^{t}BuO)_2$, $PhCO_3{}^{t}Bu$, $(PhCO_2)_2$, oxone, *N*-fluorobenzenesulfonylimide (NFSI), and Selectfluor-BF_4, were tested in the cyanation of 1-ethylnaphthylene, **1a**, with trimethylsilyl cyanide (TMSCN) as cyanide source and $[Cu(MeCN)_4]PF_6$ as the copper(I) catalyst (see the supplementary materials for screening data). An achiral bis(oxazoline) ligand (**L1**) was included in the reactions, but virtually all of the reactions failed to give the desired cyanation product. NFSI was the only oxidant that afforded any amount of the benzylic nitrile (**2a**). The yield increased upon changing the solvent from acetonitrile to chlorobenzene and using CuOAc as the copper source (**L1**, 25% yield) (Fig. 2). Replacing the ligand **L1** with an enantiomerically pure, benzyl-substituted bisoxazoline (BOX) derivative **L2** and performing the reaction in benzene led to a significant improvement in the yield (up to 91%) and also afforded product **2a** in excellent (96%) enantiomeric excess (ee) (Fig. 2). In each of the reactions in Fig. 2, small quantities (trace to 12%) of benzylimide product derived from coupling with the bis(sulfonyl)imide of NFSI (*30*) were detected by proton nuclear magnetic resonance (^{1}H NMR) spectroscopy.

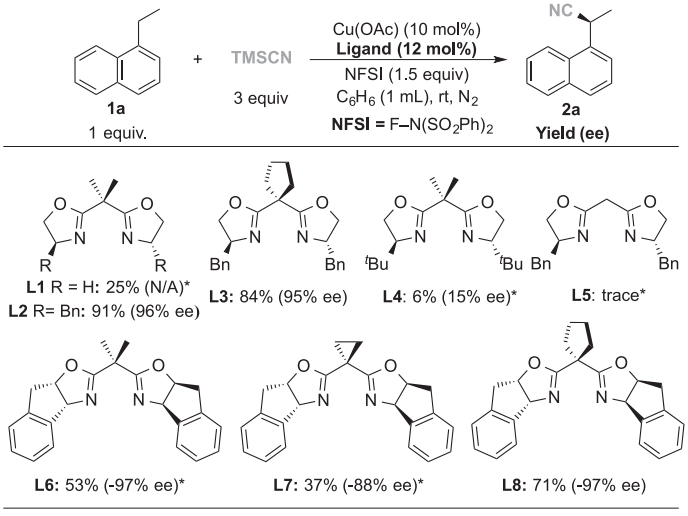


Fig. 2. Reaction optimization and representative ligand screening data. General reaction conditions: **1a** (0.2 mmol), trimethylsilyl cyanide (TMSCN) (0.6 mmol), NFSI (0.3 mmol), CuOAc (0.02 mmol), and ligand (0.024 mmol) in 1.0 mL of solvent at r.t. for 10 hours. Yield determined by ^{1}H NMR, CF_3CONMe_2 as internal standard. The ee value was determined by high-performance liquid chromatography (HPLC) with a chiral stationary phase. *Reaction conducted in chlorobenzene.

Assessment of various ligands showed that BOX ligands were the most effective ligand class, and testing of other BOX-ligand variants led to further insights and improvements (Fig. 2). Replacement of the *gem*-dimethyl substituents with a spirocyclic cyclopentyl group (**L3**) improved the enantioselectivity to 95% ee, whereas use of *tert*-butyl substituents on the oxazolines (**L4**), rather than benzyl groups, led to a significant dropoff in yield and enantioselectivity. Only trace product was observed with a ligand having an unsubstituted methylene linker between the two oxazolines (**L5**). Some of the best enantioselectivities were obtained with indane-derived BOX ligands, in particular, **L6** and **L8**.

In an effort to explore the scope of the benzylic cyanation reaction, three conditions identified in Fig. 2 were tested with a wide range of alkylarene substrates (Fig. 3). Simple 1-alkyl–substituted naphthylenes proved to be good substrates, providing the desired products **2a** to **2c** with excellent enantioselectivities (96 to 97% ee) in yields of 72 to 91%. Product **2d**, with a free primary alcohol, was obtained in excellent enantioselectivity (95% ee), but the reaction proceeded with only moderate conversion, resulting in a 42% product yield with 52% unreacted starting material. The analogous homobenzylic acetate derivative, however, exhibited very good reactivity (87% yield of **2e**), while retaining excellent enantioselectivity (99% ee). Versatile functional groups appended to the aliphatic chain, such as chloride, azide, phthalimide (Nphth), and carboxylic ester, were very well tolerated (**2f** to **2j**). A trifluoromethane sulfonate (OTf) group on the aromatic ring did not interfere with the reaction (products **2k** and **2m**) and provides a basis for subsequent derivatization of the product into more-complex molecules. The compatibility of these potentially sensitive functional groups included a primary alkyl bromide precursor to a CCR1 receptor antagonist of interest for treatment

Downloaded from http://science.sciencemag.org/ on September 1, 2016

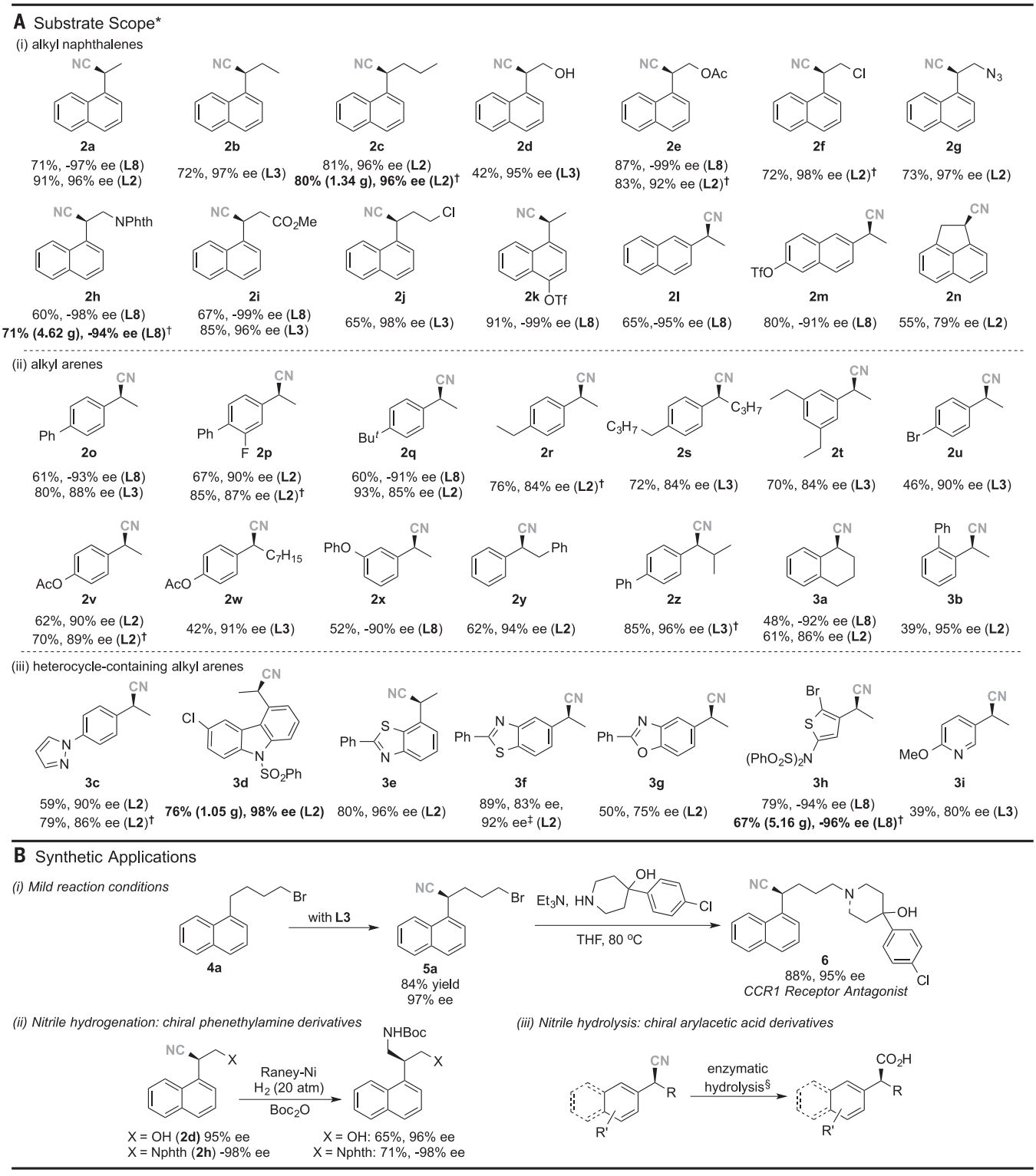


Fig. 3. Substrate scope and synthetic applications of Cu-catalyzed cyanation of benzylic C–H bonds. (**A**) Substrate scope. (**B**) Synthetic applications. *Reaction conditions: alkylarene as the limiting reagent (0.2 to 1 mmol scale), 10 mole % (mol %) $Cu^{I}(OAc)$, 12 mol % ligand; 1.5 equivalent (equiv) NFSI, 3 equiv TMSCN, C_6H_6 (0.2 M substrate); under N_2; isolated yields reported. Absolute stereochemical assignments are based on x-ray crystallographic characterization of (*R*)- and (*S*)-**2h**; see section 5 in the supplementary materials for details. Negative ee values reflect the opposite enantiomeric configuration relative to that depicted graphically. †Chlorobenzene used as the solvent. ‡ee value of product after recrystallization. §See (*34*).

Downloaded from http://science.sciencemag.org/ on September 1, 2016

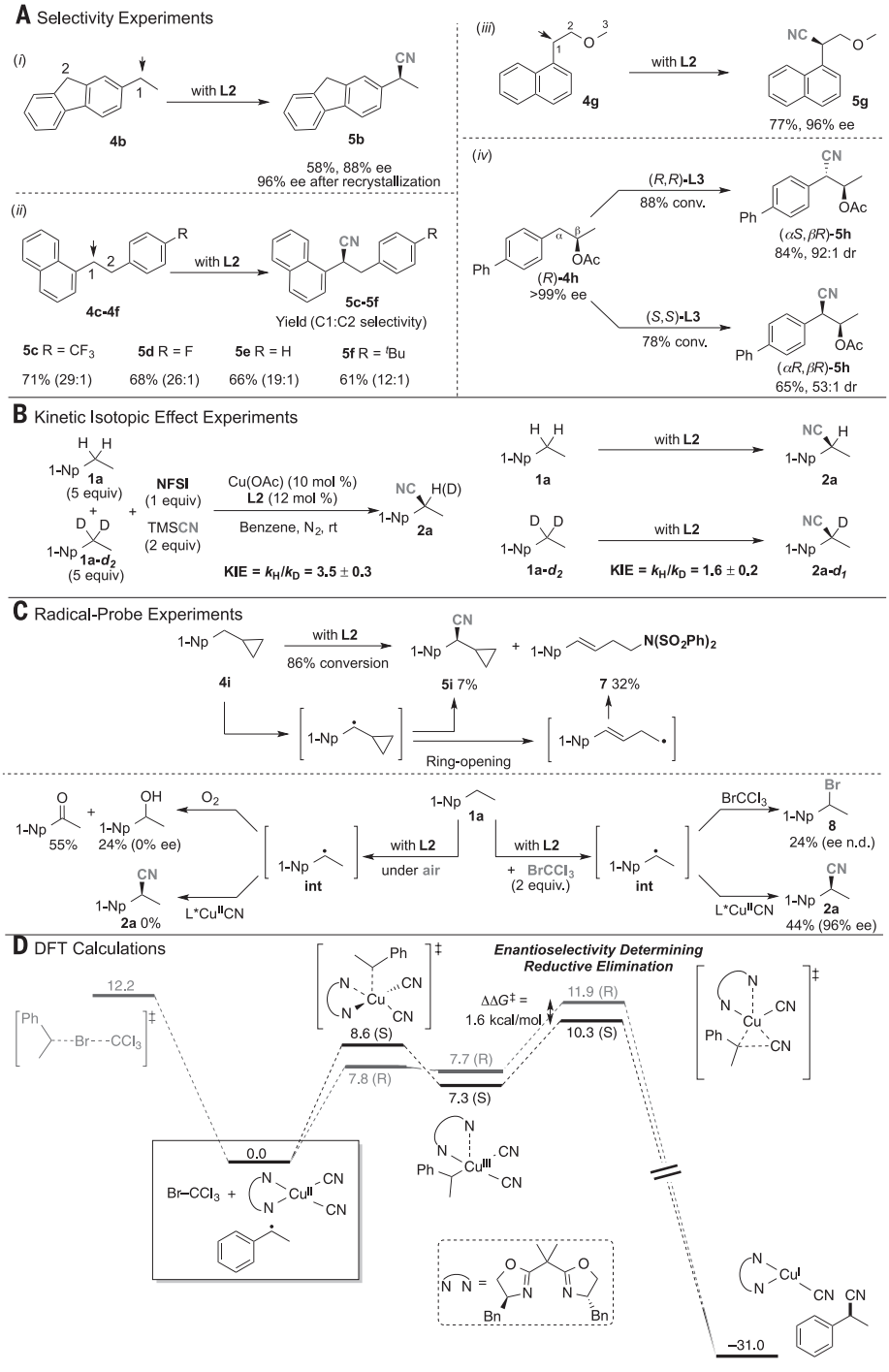


Fig. 4. Experimental and computational studies providing insight into the mechanism of the copper-catalyzed cyanation reaction. These include (**A**) reaction selectivity studies, (**B**) kinetic isotope effects, (**C**) radical trapping experiments, and (**D**) DFT computational studies.

of chronic inflammation (*31*), highlighting the mildness of reaction conditions (Fig. 3B, i). 2-Alkyl naphthylenes also proved to be good substrates for the enantioselective cyanation, affording products **2l** and **2m** in good yield and enantioselectivity. Desymmetrization of acenaphthene (**2n**) was achieved with good enantioselectivity (79% ee).

Ethyl- and related alkylbenzene derivatives were similarly effective for this transformation (products **2o** to **2z** and **3a** and **3b**). The cases with reduced yields (e.g., 40 to 60%) typically reflect poor conversion, which would allow for recovery of valuable unreacted starting material, if desired. The enantioselectivity typically remained excellent (>90%). With substrates featuring more than one benzylic C–H site (e.g., **2n**, **2r** to **2t**, **2y**, and **3a**), selectivity for the monocyanation product was observed, with consistently high ee. Good results were observed in the reaction of 4-isobutyl biphenyl (**2z**), demonstrating tolerance of branching in the homobenzylic position (see below for further discussion). Tertiary benzylic C–H bonds and substrates with larger substituents in the homobenzylic position were found to be unreactive with these catalyst systems, presumably because they present too much steric hindrance for effective hydrogen-atom abstraction. Numerous substrates containing pharmaceutically relevant heterocycles were tested, including those with a pyrazole, carbazole, benzothiazole, benzoxazole, thiophene, and pyridine (**3c** to **3i**). Yields ranged from moderate to excellent (up to 89%), whereas enantioselectivities were consistently good to excellent (up to 98% ee). Alkyl phenol and anilide substrates were found to be unreactive. In these cases, the presence of weak O–H and N–H bonds could serve as radical traps. Benzene was typically used as the solvent in these reactions, on the basis of the initial optimization results, but a number of substrates were also tested in chlorobenzene as an alternate less toxic solvent, and excellent results were obtained (see **2a**, **2c**, **2e**, **2f**, **2h**, **2p**, **2r**, **2v**, **3c**, and **3h**). In addition, four substrates were demonstrated on a 1- to 5-g scale to establish practical laboratory-scale utility (**2c**, **2h**, **3d**, and **3h**).

The results in Fig. 3 represent the most streamlined method to date for the preparation of enantiomerically enriched benzylic nitriles from readily available starting materials. Asymmetric hydrocyanation of vinylarenes is perhaps the most compelling alternative. Such methods have been known for some time (*32*) and are the subject of ongoing development (*33*), but the present methods exhibit advantages with respect to substrate accessibility (i.e., access to alkyl- versus vinyl-substituted arenes), functional-group compatibility and substrate scope, and enantioselectivity relative to asymmetric hydrocyanation of alkenes.

The enantiomerically enriched nitriles derived from these reactions are excellent precursors to phenethylamine and arylacetic acid derivatives. For example, benzylic nitriles **2d** and **2h** were subjected to hydrogenation over a Raney nickel catalyst, and the resulting primary amines were converted to a Boc (*tert*-butyloxycarbonyl) derivative before isolation. This sequence afforded the desired products in good yield with no loss in ee relative to the starting material (Fig. 3B, ii). Traditional methods for nitrile hydrolysis (e.g., in the presence of aqueous acid) erode the enantiomeric excess, but a number of biocatalytic processes are emerging for nitrile hydrolysis that proceed under very mild conditions (*34*). Although these enzymatic methods were not explored in the present study, they provide an excellent strategy for conversion of nitriles to arylacetic acids and could even provide a means to upgrade the enantioselectivity (Fig. 3B, iii).

Several observations suggest that site selectivity in these reactions is influenced by both steric and electronic effects (Fig. 4A). Subjection of 2-ethylfluorene **4b** to the Cu-catalyzed cyanation conditions results in selective cyanation of the benzylic site of the 2-ethyl group; no cyanation

Downloaded from http://science.sciencemag.org/ on September 1, 2016

of the highly activated, doubly benzylic methylene group of the fluorene is observed. We attribute this outcome to steric effects. The contribution of electronic effects is evident in the reactivity of the substituted phenethylnapthalene derivatives **4c** to **4f**. The site selectivity with these substrates is quite high, always favoring the benzylic position adjacent to the naphthalene, but the preference increases from 12:1 to 29:1 as the substituent at the para position changes from an electron-donating *tert*-butyl group to an electron-deficient $-CF_3$ group. Excellent enantioselectivity (97 to 98% ee) is observed in each case. The site selectivity is further evident from the reaction of the homobenzylic methyl ether substrate **4g**, which affords only the benzylic C–H cyanation product in good yield and excellent ee. Similarly, benzylic over tertiary C–H activation is observed in the formation of **2z** and suggests that the reactive imidyl radical shows exquisite selectivity in the hydrogen-atom-transfer (HAT) reaction. This observation contrasts with more potent HAT reagents, such as photoexcited benzophenone, which exhibit only modest selectivity toward different C–H bonds (*35*).

Stereoselectivity issues were probed in the reaction of enantiomerically pure homobenzylic acetate (*R*)-**4h**. Catalysts with each of the enantiomers of ligand **L3** were tested, and both led to products with excellent diastereoselectivity, reflecting high levels of catalyst- rather than substrate-controlled stereoselectivity. The differences in diastereomeric ratio and yield of the two products probably reflect a matched-mismatched effect between the ligand and substrate chirality.

A competition deuterium kinetic isotope effect (KIE) study, employing a mixture of **1a** and **1a-*d*$_2$**, revealed a KIE of 3.5 (Fig. 4B). On the other hand, independent measurement of the reaction rate of these two substrates revealed only a modest difference in rate (KIE = 1.6 ± 0.2). These values suggest that C–H cleavage is only partially turnover-limiting and that another mechanistic step also contributes to the catalytic turnover rate (e.g., generation of the reactive radical via activation of NFSI by Cu^{I}). Additional mechanistic studies are ongoing to secure further insights, but several observations provide clear evidence for formation of a diffusible carbon-centered radical in the reaction (Fig. 4C). Subjection of the cyclopropane-containing substrate **4i** to the reaction conditions results in a mixture of the benzylic cyanation product **5i** and a ring-opened product (**7**) in 7% and 32% yield, respectively, together with a mixture of other unidentified by-products. Additional evidence for a radical intermediate was obtained by performing the catalytic reactions of 1-ethylnaphthalene (**1a**) in the presence of O_2 or $BrCCl_3$. Under ambient air as a source of O_2, the reaction generated the racemic benzylic alcohol and ketone in 24% and 55% yields, respectively. This product mixture is consistent with trapping of the organic radical by O_2 and subsequent conversion of the organic peroxyl radical into the alcohol/ketone mixture. No cyanation product (**2a**) was observed under the aerobic conditions. When the reaction was performed in the presence of $BrCCl_3$ (2 equivalents), a mixture of the benzylic nitrile and bromide products was obtained (44 and 24% yields, respectively). This product ratio, together with precedent for efficient trapping of organic radicals by $BrCCl_3$ (*36*), implicates very rapid trapping of organic radicals by a chiral $L^*Cu^{II}(CN)$ species under the reaction conditions.

The proposed reaction of organic radicals with a $L^*Cu^{II}(CN)$ species is the subject of ongoing investigation, but the high enantioselectivity observed in the reactions suggests that the benzylic position is in close proximity to the chiral Cu center in the enantioselectivity-determining step. A plausible pathway involves reaction of the intermediate organic radical with Cu^{II}, an open-shell, d^9 metal center, to afford a benzyl–Cu^{III} species. Preliminary density functional theory (DFT) calculations support the viability of this pathway (Fig. 4D). An ethylbenzene-derived radical reacts at Cu^{II} in an (**L2**)$Cu^{II}(CN)_2$ species with a low barrier to afford a benzyl-Cu^{III} species. Subsequent $C(sp^3)$–CN reductive elimination generates the benzylic nitrile product. The calculations suggest that the transition state for the addition of the benzylic radical to Cu^{II} is lower in energy than reductive elimination, indicating that formation of the alkyl-Cu^{III} species is reversible and that enantioselectivity is determined by the reductive elimination step. An analogous conclusion was reached in a recent DFT study of Ni-catalyzed cross-coupling reactions, wherein reversible addition of an alkyl radical to a Ni^{II} catalyst precedes enantiodetermining reductive elimination (*37*). For the present system, the difference in the computed activation free energy ($\Delta\Delta G^{\ddagger}$) for reductive elimination of the two enantiomeric benzylic nitriles (1.6 kcal/mol) is very similar to the $\Delta\Delta G^{\ddagger}$ associated with the experimentally observed enantioselectivity (e.g., $\Delta\Delta G^{\ddagger}$ = 1.5 kcal/mol for **2q**) (Fig. 3). Moreover, the reductive elimination transition states for this pathway are calculated to be slightly lower than the calculated barrier for bromine transfer from $BrCCl_3$ to an ethylbenzene-derived radical ($\Delta G^{\ddagger}$ = 12.2 kcal/mol) (Fig. 4D), matching the slight preference for cyanation over bromination noted in Fig. 4C. Although the agreement between the computed pathways and several key experimental observations is quantitatively closer than can be justified by the uncertainties in the computational methods, the qualitative agreement is consistent with the proposed radical coupling pathway with $L^*Cu^{II}(CN)_2$.

The copper-catalyzed method for enantioselective cyanation of $C(sp^3)$–H bonds described herein represents a valuable demonstration of radical relay catalysis. The ability to use the $C(sp^3)$–H substrate as the limiting reagent, together with the mild reaction conditions, excellent enantioselectivity, and broad substrate scope, provide key foundations for the pursuit of other chemo-, regio-, and stereoselective C–H oxidation reactions.

REFERENCES AND NOTES

1. F. Lovering, J. Bikker, C. Humblet, *J. Med. Chem.* **52**, 6752–6756 (2009).
2. P. R. Ortiz de Montellano, *Chem. Rev.* **110**, 932–948 (2010).
3. B. Meunier, S. P. de Visser, S. Shaik, *Chem. Rev.* **104**, 3947–3980 (2004).
4. A. Butler, M. Sandy, *Nature* **460**, 848–854 (2009).
5. M. S. Chen, M. C. White, *Science* **318**, 783–787 (2007).
6. W. Liu, J. T. Groves, *Acc. Chem. Res.* **48**, 1727–1735 (2015).
7. A. Sharma, J. F. Hartwig, *Nature* **517**, 600–604 (2015).
8. J. C. Lewis, P. S. Coelho, F. H. Arnold, *Chem. Soc. Rev.* **40**, 2003–2021 (2011).
9. J. T. Groves, *J. Chem. Educ.* **62**, 928–931 (1985).
10. F. F. Fleming, L. Yao, P. C. Ravikumar, L. Funk, B. C. Shook, *J. Med. Chem.* **53**, 7902–7917 (2010).
11. K. W. Bentley, *Nat. Prod. Rep.* **18**, 148–170 (2001).
12. P. J. Harrington, E. Lodewijk, *Org. Process Res. Dev.* **1**, 72–76 (1997).
13. Q. M. Kainz *et al.*, *Science* **351**, 681–684 (2016).
14. F.-L. Zhang, K. Hong, T.-J. Li, H. Park, J.-Q. Yu, *Science* **351**, 252–256 (2016).
15. H. M. L. Davies, J. R. Manning, *Nature* **451**, 417–424 (2008).
16. F. Wang, D. Wang, X. Mu, P. Chen, G. Liu, *J. Am. Chem. Soc.* **136**, 10202–10205 (2014).
17. Z. Liang, F. Wang, P. Chen, G. Liu, *J. Fluor. Chem.* **167**, 55–60 (2014).
18. A. E. Wendlandt, A. M. Suess, S. S. Stahl, *Angew. Chem. Int. Ed.* **50**, 11062–11087 (2011).
19. J. C. Tellis, D. N. Primer, G. A. Molander, *Science* **345**, 433–436 (2014).
20. Z. Zuo *et al.*, *Science* **345**, 437–440 (2014).
21. D. J. Weix, *Acc. Chem. Res.* **48**, 1767–1775 (2015).
22. N. D. Schley, G. C. Fu, *J. Am. Chem. Soc.* **136**, 16588–16593 (2014).
23. T. S. Ratani, S. Bachman, G. C. Fu, J. C. Peters, *J. Am. Chem. Soc.* **137**, 13902–13907 (2015).
24. M. S. Kharasch, G. Sosnovsky, *J. Am. Chem. Soc.* **80**, 756 (1958).
25. R. T. Gephart III *et al.*, *J. Am. Chem. Soc.* **134**, 17350–17353 (2012).
26. M. B. Andrus, Z. Zhou, *J. Am. Chem. Soc.* **124**, 8806–8807 (2002).
27. J. Eames, M. Watkinson, *Angew. Chem. Int. Ed.* **40**, 3567–3571 (2001).
28. H. Zhang *et al.*, *Angew. Chem. Int. Ed.* **52**, 2529–2533 (2013).
29. B. Gaspar, E. M. Carreira, *Angew. Chem. Int. Ed.* **46**, 4519–4522 (2007).
30. Z. Ni *et al.*, *Angew. Chem. Int. Ed.* **51**, 1244–1247 (2012).
31. H. P. Ng *et al.*, *J. Med. Chem.* **42**, 4680–4694 (1999).
32. T. V. RajanBabu, A. L. Casalnuovo, *J. Am. Chem. Soc.* **118**, 6325–6326 (1996).
33. A. Falk, A. Cavalieri, G. S. Nichol, D. Vogt, H.-G. Schmalz, *Adv. Synth. Catal.* **357**, 3317–3320 (2015).
34. R. Kourist, P. Domínguez de María, K. Miyamoto, *Green Chem.* **13**, 2607–2618 (2011).
35. T. Hoshikawa, S. Yoshioka, S. Kamijo, M. Inoue, *Synthesis* **45**, 874–887 (2013).
36. L. Mathew, J. Warkentin, *Can. J. Chem.* **66**, 11–16 (1988).
37. O. Gutierrez, J. C. Tellis, D. N. Primer, G. A. Molander, M. C. Kozlowski, *J. Am. Chem. Soc.* **137**, 4896–4899 (2015).

ACKNOWLEDGMENTS

Financial support for this project was provided by the National Basic Research Program of China (973-2015CB856600), the National Natural Science Foundation of China (nos. 21225210, 21421091, 21532009, and 21472217) (G.S.L.), a National Institutes of Health predoctoral fellowship (F31-GM116443) (S.D.M.), and the Department of Energy (DE-FG02-05ER15690) (S.S.S.). The NSF provided partial support for the computational resources (CHE-0840494). G.S.L. thanks X. L. Wan at Shanghai Institute of Organic Chemistry for his assistance with HPLC analysis. Metrical parameters for the structures of (*R*)- and (*S*)-**2h** are available free of charge from the Cambridge Crystallographic Data Centre under accession numbers CCDC-1496364 and -1495535, respectively.

SUPPLEMENTARY MATERIALS

www.sciencemag.org/content/353/6303/1014/suppl/DC1
Materials and Methods
Figs. S1 to S3
Tables S1 to S3
References (*38*–*60*)

29 March 2016; accepted 1 August 2016
10.1126/science.aaf7783

Downloaded from http://science.sciencemag.org/ on September 1, 2016

TEXTILES

Radiative human body cooling by nanoporous polyethylene textile

Po-Chun Hsu,[1] Alex Y. Song,[2] Peter B. Catrysse,[2] Chong Liu,[1] Yucan Peng,[1] Jin Xie,[1] Shanhui Fan,[2] Yi Cui[1,3]*

Thermal management through personal heating and cooling is a strategy by which to expand indoor temperature setpoint range for large energy saving. We show that nanoporous polyethylene (nanoPE) is transparent to mid-infrared human body radiation but opaque to visible light because of the pore size distribution (50 to 1000 nanometers). We processed the material to develop a textile that promotes effective radiative cooling while still having sufficient air permeability, water-wicking rate, and mechanical strength for wearability. We developed a device to simulate skin temperature that shows temperatures 2.7° and 2.0°C lower when covered with nanoPE cloth and with processed nanoPE cloth, respectively, than when covered with cotton. Our processed nanoPE is an effective and scalable textile for personal thermal management.

Energy consumption and climate change are two major issues for humans in the 21st century. The high consumption of energy directly leads to excessive greenhouse gas emissions, which severely disturbs the climate balance and causes global warming and extreme weather (*1*, *2*). Consequently, numerous efforts are being made to develop renewable energy such as solar, wind, ocean, hydrogen, and carbon-neutral fuels (*3*–*9*). On the other hand, reducing current energy consumption and improving energy efficiency are equally important. In fact, improving energy efficiency, through the use of energy-efficient appliances or building designs, is the most cost-effective way to solve the energy issue, as compared with other energy sources in the United States (*10*).

Space heating and cooling are the dominant parts of residential and commercial energy consumption. They contribute to 12.3% of total U.S. energy consumption. Reducing the demand for indoor temperature regulation will have substantial impact on global energy use (*11*–*13*). Although conventional approaches have been focusing on improving building insulation and enabling smart temperature control (*14*–*16*), the concept of "personal thermal management" is emerging as a promising alternative. The objective of personal thermal management is to provide heating or cooling only to a human body and its local environment, without wasting excess power on heating and cooling an entire building. Because a human body has much smaller thermal mass as compared with that of an entire building, this approach should result in far higher energy efficiency (*17*). To achieve this objective, it is necessary to have better control over the heat dissipation process from the human body in an indoor environment. At the normal skin temperature of 34°C, the human body emits mid-infrared (IR) radiation in the wavelength range between 7 and 14 μm, with the peak emission at 9.5 μm wavelength. For a typical indoor scenario, IR radiative heat dissipation contributes to more than 50% of the total body heat loss (*18*, *19*). The objective of personal thermal management is to enhance radiative dissipation in the summer and suppress it in the winter. However, traditional textiles are not designed for infrared radiation control. We demonstrated promising results in achieving passive personal heating without energy input during cold weather by using a metallic nanowires–coated textile that reflects more than 40% of human body infrared radiation and warms up the human body (*20*). As for personal cooling in hot weather, we need to make textile IR-transparent in order to fully dissipate human body radiation (*21*). Because human skin is an excellent IR emitter (emissivity = 0.98) (*22*), an IR-transparent textile would allow for cooling setpoints to be higher while maintaining personal thermal comfort, with a 1° to 4°C increase in setpoint temperature translating to an energy savings of 7 to 45% (*23*). Unlike Peltier cooling or circulated water/air cooling, personal radiative cooling is passive and does not require integration with electronics and wiring (*24*, *25*). The IR-transparent textile should also possess wearability properties that are comparable with traditional human cloth, such as water-wicking and air permeability.

We numerically solved the steady-state heat transfer model of clothed human skin to estimate the impact of IR-transparency of textiles on an air conditioner setpoint (Fig. 1A). The model assumes constant human skin temperature and constant metabolic generation rate, so that the air conditioner setpoint will change according to different heat transfer coefficients of the textile. The setpoint rises because of the enhanced radiative cooling as the IR transmittance increases, approaching the limit of the bare skin case (26.6°C). Polyolefin films that have an IR-transmittance of 95% require a setpoint of 25.8°C, whereas IR-opaque materials such as cotton textile require a setpoint of 22.6°C, roughly 3°C lower.

The challenge for developing a material that is transparent to IR but opaque to visible light is that the radiation spectrum (7 to 14 μm) overlaps with most of the IR absorption wavelength of common textile materials—for example, C–O stretching (7.7 to 10 μm), C–N stretching (8.2 to 9.8 μm), aromatic C–H bending (7.8 to 14.5 μm), S=O stretching (9.4 to 9.8 μm), and others (*26*, *27*). As a result, most textile materials strongly absorb human body radiation and have very low IR transparency (fig. S1). Polyolefins such as polyethylene (PE) have only aliphatic C–C and C–H bonds and consequently have narrow absorption peaks centered at the wavelengths of 3.4, 3.5, 6.8, 7.3, and 13.7 μm (*28*), which are all far away from the peak of human body radiation. However, one cannot use a normal PE film as textile material because it is visibly transparent and does not have desired properties for textile, such as air permeability and water-wicking.

Here, we propose nanoporous PE (nanoPE) to be a good IR-transparent textile for human body cooling. NanoPE has interconnected pores that are 50 to 1000 nm in diameter (Fig. 1B). The pore sizes are in the size range comparable with the wavelength of visible light (400 to 700 nm), which scatter visible light strongly and make PE opaque to human eyes. The pore sizes are also much smaller than the IR wavelength, so the nanoPE film is still highly transparent to IR. The interconnected pores enable air permeability and can be water-wicking when the PE surface is chemically modified to be hydrophilic.

We modeled the visible and IR transmittance of nanoPE film using a rigorous coupled-wave analysis (RCWA) (Fig. 1C) (*29*). The nanoPE shows >90% total IR transmittance for wavelengths longer than 2 μm. The nanoPE has low visible-light specular transmittance, which better represents visible appearance, owing to strong nanopore scattering (Fig. 1C). As we increased the average pore size from 200 nm to 4.8 μm, the scattering-induced transmittance dip moved from visible to near-IR and then mid-IR (fig. S2A). All the features, including fibers and pores, are uniformly scaled, but the total thickness is fixed. The weighted-average IR transmittance based on human body radiation starts to decay at a pore size of 1.2 μm and reaches minimum at 2.4 μm. The transmittance dip moves to a longer wavelength at 4.8 μm, away from the human body radiation, which slightly increases the weighted average transmittance. For thicker nanoPE, the number of nanopores along the light path increases, so the transmittance variation is more profound (fig. S2, B and C). The dimensions of fibers also influence scattering property, so we fixed the pore dimensions and investigated the fiber size effect (fig. S3). The transmittance dips occur as well, but the magnitude becomes smaller because of lower air-pore filling ratio. We

[1]Department of Materials Science and Engineering, Stanford University, Stanford, CA 94305, USA. [2]E. L. Ginzton Laboratory, Department of Electrical Engineering, Stanford University, Stanford, CA 94305, USA. [3]Stanford Institute for Materials and Energy Sciences, SLAC National Accelerator Laboratory, 2575 Sand Hill Road, Menlo Park, CA 94025, USA.
*Corresponding author. Email: yicui@stanford.edu

Downloaded from http://science.sciencemag.org/ on September 2, 2016

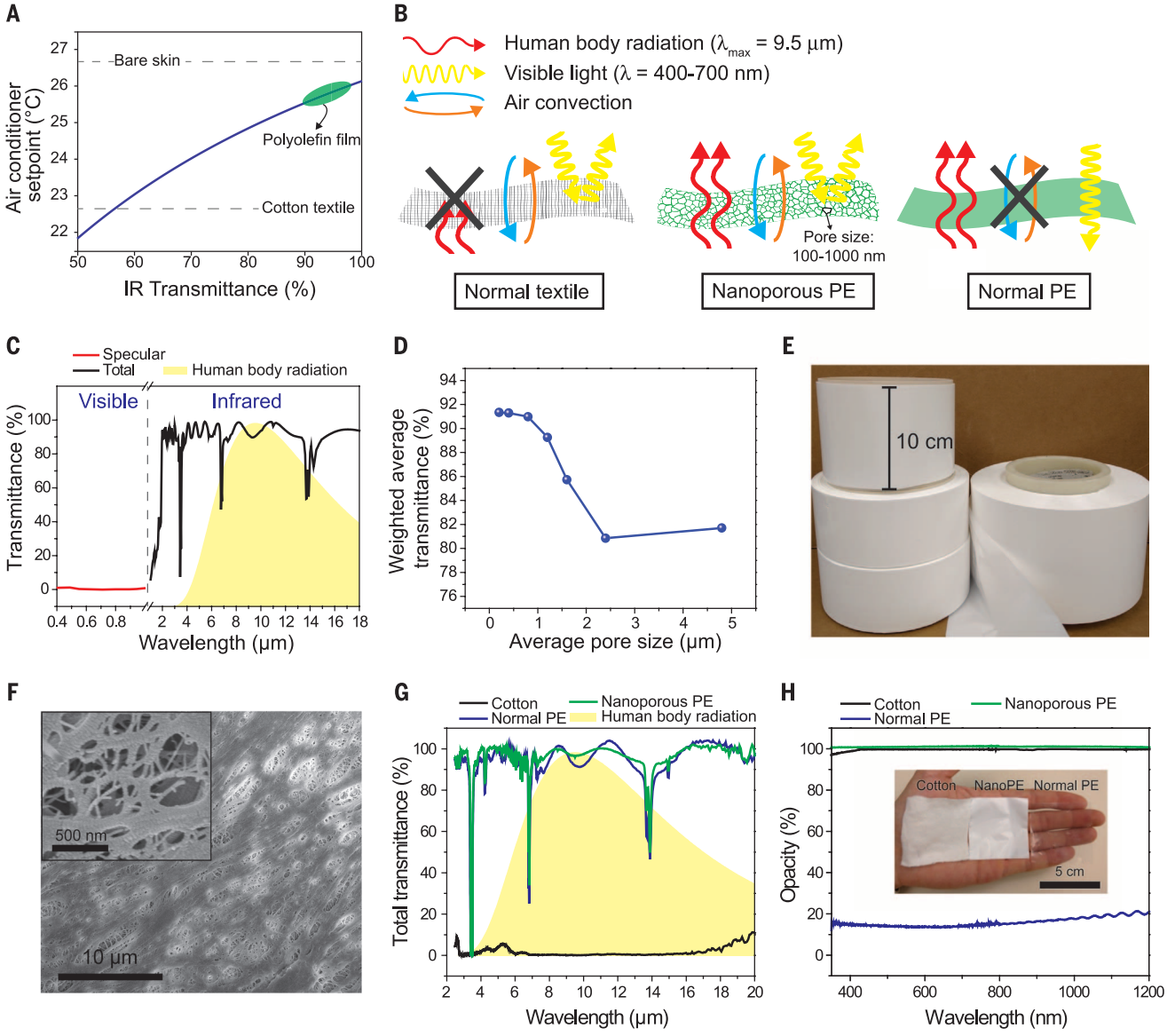


Fig. 1. Optical property and morphology of nanoPE. (**A**) Simulated air conditioner setpoint as the function of IR transmittance of textile at constant human skin temperature and metabolic generation rate. (**B**) Schematics of comparison between nanoPE, normal PE, and cotton. Only nanoPE satisfies IR transparency, visible light opacity, and air convection simultaneously. (**C**) Simulated total and specular transmittance of infrared and visible light for nanoPE, with average pore size of 400 nm. The thickness of nanoPE is 12 μm. Human body radiation is indicated by the yellow shaded region. (**D**) Simulated weighted average transmittance based on human body radiation for various pore sizes. The average transmittance drops from >90% to 80% as the pore size increases and begin to affect the transmission of human body radiation. (**E**) Photo of commercial nanoPE. (**F**) High-resolution SEM images of nanoPE. The nanopores are only 50 to 1000 nm in diameter, which is essential to ensure high IR transmittance. (**G**) Measured total FTIR transmittance of nanoPE, normal PE, and cotton. Because of the small pore size, nanoPE is as transparent as normal PE. Cotton, on the other hand, is completely opaque. (**H**) Visible opacity measurement quantitatively confirms that nanoPE is as opaque as cotton.

used the simulations as a guide for developing appropriate nanostructures for the material.

Remarkably, nanoPE is commercially available and widely used in lithium-ion batteries as a separator to prevent electrical shorting between anodes and cathodes. These PE separators (Fig. 1E) have interconnected nanopores, with ~50% pore volume for holding liquid electrolyte (*30*). The separators are white and have a comparable cost of ~$2/m^2 to normal textiles. The commercial nanoPE has pores of 50 to 1000 nm in size and some aligned fiber-like structure of a few micrometers wide (Fig. 1F). A zoomed-in scanning electron microscope (SEM) image (Fig. 1F, inset) clearly shows the nanopores that satisfy the size requirement of an ideal IR-transparent textile and form pathways for fluid permeation. We measured the total IR transmittance with a Fourier transform infrared (FTIR) spectrometer equipped with a diffuse gold integrating sphere (Fig. 1G). The nanopores do not affect the total IR transmittance, giving almost the same transmittance for nanoPE and normal PE. The weighted average transmittances based on human body radiation are 96.0% for nanoPE, 93.8% for normal PE, and only 1.5% for cotton. NanoPE and cotton both exhibit white color because of visible light scattering (*31*), whereas normal PE is visibly transparent (Fig. 1H, inset). Quantitatively, we define opacity as (1 – specular transmittance), representing the ability to prevent objects behind the textile to be recognized. We used an ultraviolet-visible (UV-Vis) spectrometer and found that both nanoPE and cotton have

Downloaded from http://science.sciencemag.org/ on September 2, 2016

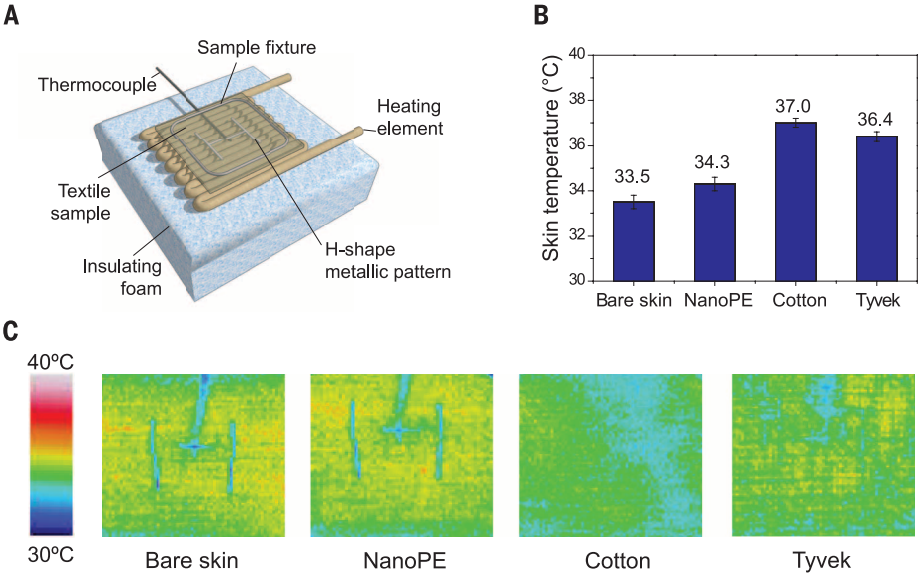


Fig. 2. Thermal measurement of nanoPE and various textile samples. (**A**) Experimental setup of textile thermal measurement. The heating element that generates constant heating power is used to simulate human skin, and the "skin temperature" is measured with the thermocouple. Lower skin temperature means a better cooling effect. (**B**) Thermal measurement of bare skin, nanoPE, cotton, and Tyvek. NanoPE has a much better cooling effect than that of cotton and Tyvek because of its high IR-transparency. (**C**) Thermal imaging of bare skin and the three samples. Only nanoPE can reveal the H-shape metallic pattern because of its IR-transparency.

opacity higher than 99% for the entire visible spectrum, whereas normal PE has only 20% opacity (Fig. 1H).

We experimentally demonstrated the cooling effect of nanoPE with a device that simulated the heat output of skin (Fig. 2A). NanoPE increases the simulated skin temperature by 0.8°C, compared with 3.5°C for cotton and 2.9°C for the fibrous PE textile Tyvek that DuPont manufactures (Fig. 2B). Because the difference between skin and ambient temperature (23.5°C) is small, this skin temperature difference can be approximated as the air conditioner setpoint difference. We used an H-shaped piece of metal to show the textile IR transmittance by use of thermal imaging (Fig. 2C). Whereas bare skin and nanoPE clearly show the H-pattern, cotton and Tyvek do not show the metallic pattern. Cotton and Tyvek also appear colder because IR radiation is blocked from transmission. Such difference in IR transmittance is because Tyvek has fiber and pore sizes that are tens of micrometers (fig. S4, A and B), which results in stronger scattering and makes it appealing for applications other than personal thermal management. At the same thickness, nanoPE is more IR-transparent than Tyvek by 9 to 14% (fig. S4C).

Besides high IR-transparency and high convective heat dissipation—which ensure superior cooling effect—wicking, mechanical strength, and

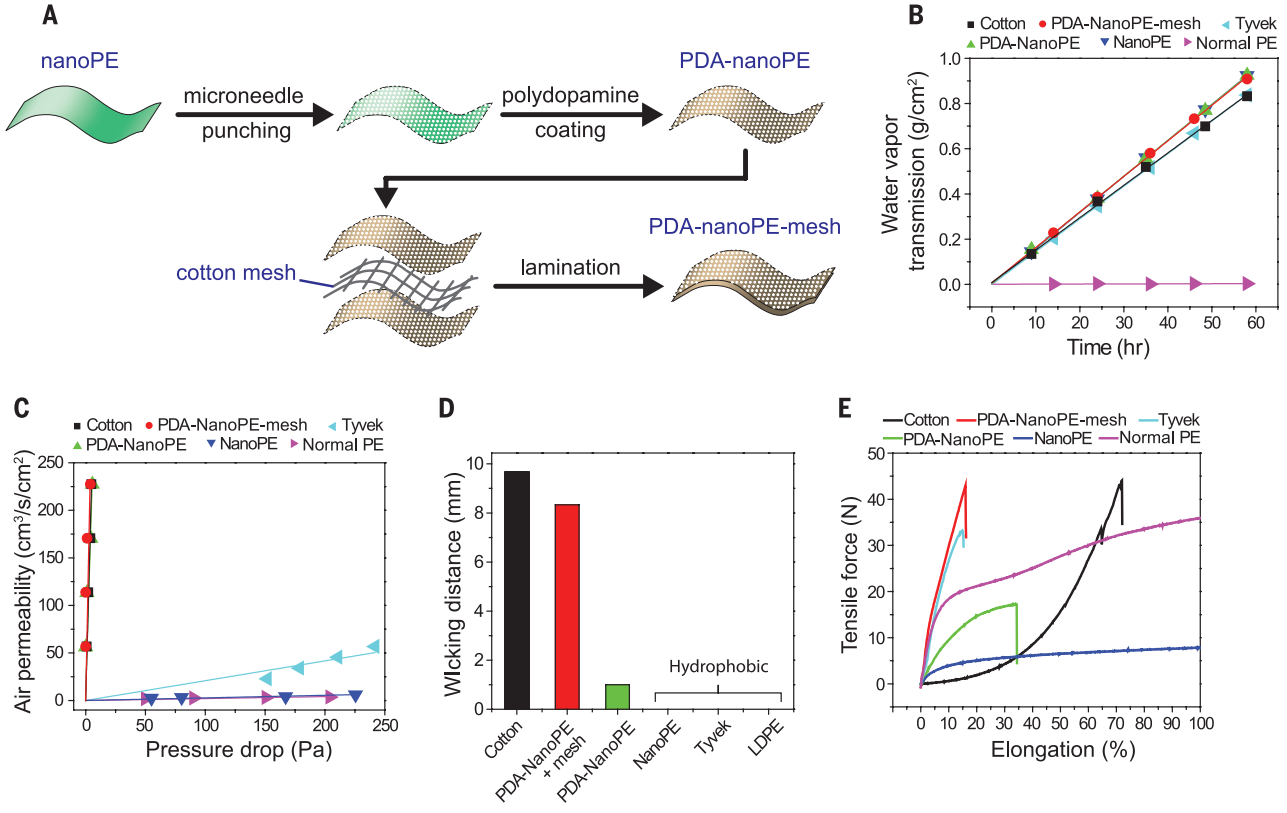


Fig. 3. The treatment of nanoPE for various wearability testing. (**A**) Schematic of the fabrication process of PDA-nanoPE-mesh. In all the textile tests, PDA-nanoPE-mesh shows performance comparable with that of cotton. (**B**) Water vapor transmission rate test shows how human perspiration can transmit through the textile. (**C**) Air permeability test examines the air flow rate through the textile at certain pressure drops. (**D**) Wicking distance shows the ability to transport perspiration for quick evaporation. (**E**) Tensile strength test demonstrates that PDA-nanoPE-mesh has the same ultimate tensile strength as that of cotton.

Downloaded from http://science.sciencemag.org/ on September 2, 2016

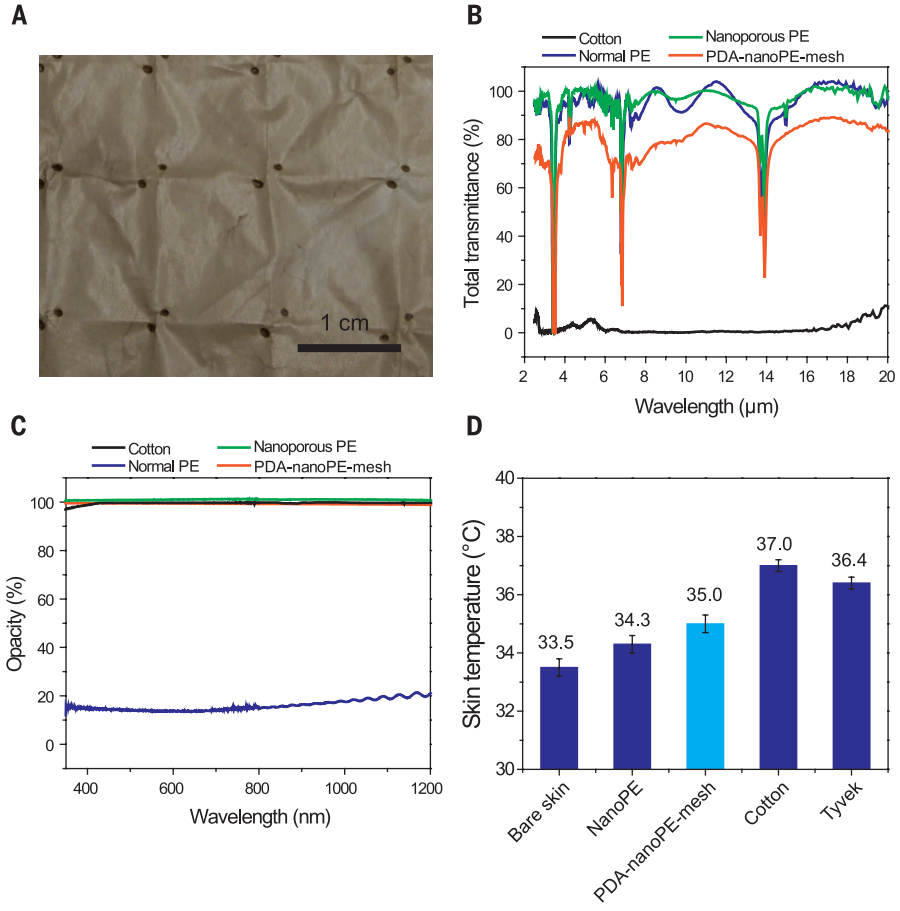


Fig. 4. Properties of PDA-nanoPE-mesh. (**A**) Photo of PDA-nanoPE-mesh. The spots that are 1 mm in diameter are the welding points. The microholes for improving air permeability are barely noticeable. (**B**) Total IR transmittance. (**C**) Visible opacity. (**D**) Thermal measurement.

air permeability are important for a textile to be wearable. We altered nanoPE with a number of processes in order to make it a suitable human cloth (Fig. 3A). We created 100-μm holes spaced 500 μm apart with commonly used microneedle punching (*32*). We coated the punched nanoPE with the benign hydrophilic agent polydopamine (PDA) (*33*–*35*) so as to enhance fluid wicking. We then sandwiched cotton mesh between two layers of PDA-nanoPE and bonded it with point welding in order to reinforce the mechanical strength. We performed several tests for common textile properties on PDA-nanoPE-mesh, PDA-nanoPE, nanoPE, Tyvek, cotton, and normal PE. All nanoPE samples (punched or not) have high water vapor transmission rate (WVTR) (~0.016 g/cm^2 hour), which is a proxy for transmitting water vapor from perspiration through natural diffusion and convection (Fig. 3B). This shows that the nanopores themselves are permeable enough for water vapor under the natural convection situation. Cotton and Tyvek have slightly lower WVTR (~0.014 g/cm^2 hour), and normal PE is completely nonpermeable. Air permeability is defined as the transmitted flow rate of air as a function of the applied pressure and represents the ability of the textile to let wind blow in and then carry the body heat away. Because of the microholes that resemble the spacing between the yarns in woven cotton textile, the air permeability of PDA-nanoPE-mesh, PDA-nanoPE, and cotton are similar, in the range of 40 to 60 cm^3/s cm^2 Pa (Fig. 3C). In contrast, Tyvek, nanoPE, and normal PE show inadequate air permeability (Fig. 3C). Because the microhole size is as small as human hair (100 μm), the visual opaqueness is not affected. Wicking rate shows how efficiently liquid water transports in the textile. Higher wicking rate means that perspiration can spread and evaporate quickly. Cotton is well known to have a high wicking rate due to the hydrophilic cellulose fibers, with a wicking distance of 9.7 mm (Fig. 3D). PDA-nanoPE-mesh has a comparable wicking distance of 8.3 mm because of the PDA coating and capillary effect from the dual-layer structure. PDA-nanoPE is hydrophilic, but the lack of horizontal spacing limits the capillary effect. Tyvek, nanoPE, and normal PE are hydrophobic and therefore do not have any wicking length. We measured the mechanical strength of a strip of 2-cm-wide PDA-nanoPE-mesh, which can endure 45 N of tensile force (Fig. 3E). The strength is comparable with cotton and is due to the cotton mesh integrated into our fabric.

By carefully choosing the PDA thickness, microhole size, and mesh-filling ratio, PDA-nanoPE-mesh can retain good optical and thermal property (Fig. 4). The weighted average IR transmittance is 77.8%, and the opacity remains >99%. The skin temperature increases by 0.7°C compared with wearing pristine nanoPE and is 2.0°C lower than when wearing cotton textile. We demonstrated nanoPE as a favorable material to realize IR-transparent human cloth for personal thermal management. It will be worthwhile to explore the potential wearability modification methods on the basis of nanoPE. Coloration, for example, can be done by mixing with masterbatches or flexography printing. The pigments need to have a low absorption coefficient in the wavelength range of 7 to 14 μm and be benign to the human body. Common pigments such as Prussian blue, ferric oxide, and ferrous oxide are all possible choices. PE and PDA coating are stable (*36*, *37*), but further study such as performance evolution with perspiration, wash cycles, abrasion cycles, or ultraviolet irradiance will be meaningful for practical use.

REFERENCES AND NOTES

1. N. Oreskes, *Science* **306**, 1686 (2004).
2. G. R. Walther *et al.*, *Nature* **416**, 389–395 (2002).
3. S. Chu, A. Majumdar, *Nature* **488**, 294–303 (2012).
4. International Energy Agency, *World Energy Outlook Special Report on Energy and Climate Change* (International Energy Agency, 2015).
5. P. Smith *et al.*, *Nat. Clim. Change* **6**, 42–50 (2015).
6. D. Kraemer *et al.*, *Nat. Mater.* **10**, 532–538 (2011).
7. N. S. Lewis *et al.*, *Basic Research Needs for Solar Energy Utilization* (U.S. Department of Energy Office of Science, 2005).
8. M. Chhowalla *et al.*, *Nat. Chem.* **5**, 263–275 (2013).
9. S. C. Roy, O. K. Varghese, M. Paulose, C. A. Grimes, *ACS Nano* **4**, 1259–1278 (2010).
10. M. Molina, *The Best Value for America's Energy Dollar: A National Review of the Cost of Utility Energy Efficiency Programs* (American Council for an Energy-Efficient Economy, 2014).
11. U.S. Energy Information Administration, *Annual Energy Outlook 2015 With Projections to 2040* (U.S. Energy Information Administration, 2015).
12. T. Bryant *et al.*, *Medium Term Energy Efficiency Market Report 2015* (International Energy Agency, 2015).
13. A. P. Raman, M. A. Anoma, L. Zhu, E. Rephaeli, S. Fan, *Nature* **515**, 540–544 (2014).
14. U.S. Department of Energy, *2011 Buildings Energy Data Book* (U.S. Department of Energy, 2012).
15. International Energy Agency Energy Conservation in Buildings and Community Systems Programme, *EBC Annual Report 2014* (International Energy Agency Energy Conservation in Buildings and Community Systems Programme, 2014).
16. L. Pérez-Lombard, J. Ortiz, C. Pout, *Energy Build.* **40**, 394–398 (2008).
17. T. Law, *The Future of Thermal Comfort in an Energy-Constrained World*. Springer Theses (Springer International Publishing, 2013).
18. J. D. Hardy, E. F. Dubois, *Proc. Natl. Acad. Sci. U.S.A.* **23**, 624–631 (1937).
19. C.-E. A. Winslow, L. P. Herrington, A. P. Gagge, *Am. J. Physiol.* **127**, 505 (1939).
20. P. C. Hsu *et al.*, *Nano Lett.* **15**, 365–371 (2015).
21. J. Tong *et al.*, *ACS Photonics* **2**, 769–778 (2015).
22. J. Steketee, *Phys. Med. Biol.* **18**, 686–694 (1973).
23. T. Hoyt, H. L. Kwang, H. Zhang, T. E. Arens, paper presented at the International Conference on Environmental Ergonomics, Boston, 2–7 August 2009.
24. D. M. Rowe, *CRC Handbook of Thermoelectrics* (CRC Press, 1995).

Downloaded from http://science.sciencemag.org/ on September 2, 2016

25. L. E. Bell, *Science* **321**, 1457–1461 (2008).
26. R. M. Silverstein, G. C. Bassler, T. C. Morrill, *Spectrometric Identification of Organic Compounds* (John Wiley and Sons, ed. 4, 1981).
27. B. H. Stuart, *Infrared Spectroscopy: Fundamentals and Applications* (John Wiley & Sons, 2005).
28. J. V. Gulmine, P. R. Janissek, H. M. Heise, L. Akcelrud, *Polym. Test.* **21**, 557–563 (2002).
29. V. Liu, S. Fan, *Comput. Phys. Commun.* **183**, 2233–2244 (2012).
30. X. Huang, *J. Solid State Electrochem.* **15**, 649–662 (2011).
31. H. L. Zhu, Z. Q. Fang, C. Preston, Y. Y. Li, L. B. Hu, *Energ. Environ. Sci.* **7**, 269–287 (2014).
32. V. Mrstina, F. Fejgl, *Needle Punching Textile Technology. Textile Science and Technology* (Elsevier, 1990).
33. H. Lee, S. M. Dellatore, W. M. Miller, P. B. Messersmith, *Science* **318**, 426–430 (2007).
34. M. H. Ryou, Y. M. Lee, J. K. Park, J. W. Choi, *Adv. Mater.* **23**, 3066–3070 (2011).
35. X. Liu *et al.*, *ACS Nano* **7**, 9384–9395 (2013).
36. J. Jiang *et al.*, *ACS Appl. Mater. Interfaces* **5**, 12895–12904 (2013).
37. Z.-Y. Xi, Y.-Y. Xu, L.-P. Zhu, Y. Wang, B.-K. Zhu, *J. Membr. Sci.* **327**, 244–253 (2009).

ACKNOWLEDGMENTS

This work was sponsored by the Advanced Research Projects Agency–Energy (ARPA-E), U.S. Department of Energy, under award DE-AR0000533. The authors thank H. Dai for lending the thermal camera. All data are available in the manuscript and the supplementary materials. Y.C., S.F., P.-C.H., A.Y.S., P.B.C., and Y.P. have a U.S. patent application (no. 62/296,549) related to this work. Y.C. and P.-C.H. conceived the idea. P.-C.H. and A.Y.S. conducted the FTIR spectrometry measurement. P.-C.H. conducted UV-Vis spectrometry measurement. P.-C.H. and C.L. designed and conducted the thermal measurement. P.-C.H., A.Y.S., and J.X. analyzed the FTIR data. A.Y.S. performed the RCWA simulation. P.-C.H. and P.B.C. constructed and simulated heat transport model. P.-C.H. conducted SEM and optical microscope characterization. P.-C.H. and Y.P. performed wearability tests. Y.C. and S.F. supervised the project. All authors contributed to the writing of the paper.

SUPPLEMENTARY MATERIALS

www.sciencemag.org/content/353/6303/1019/suppl/DC1
Materials and Methods
Supplementary Text
Figs. S1 to S8
Table S1
References (*38*–*42*)

25 February 2016; accepted 21 July 2016
10.1126/science.aaf5471

ASYMMETRIC CATALYSIS

Ligand-accelerated enantioselective methylene C(sp^3)–H bond activation

Gang Chen,[1]* Wei Gong,[1]* Zhe Zhuang,[1] Michal S. Andrä,[1] Yan-Qiao Chen,[1] Xin Hong,[2] Yun-Fang Yang,[2] Tao Liu,[1] K. N. Houk,[2]† Jin-Quan Yu[1]†

Effective differentiation of prochiral carbon–hydrogen (C–H) bonds on a single methylene carbon via asymmetric metal insertion remains a challenge. Here, we report the discovery of chiral acetyl-protected aminoethyl quinoline ligands that enable asymmetric palladium insertion into prochiral C–H bonds on a single methylene carbon center. We apply these palladium complexes to catalytic enantioselective functionalization of β-methylene C–H bonds in aliphatic amides. Using bidentate ligands to accelerate C–H activation of otherwise unreactive monodentate substrates is crucial for outcompeting the background reaction driven by substrate-directed cyclopalladation, thereby avoiding erosion of enantioselectivity. The potential of ligand acceleration in C–H activation is also demonstrated by enantioselective β-C–H arylation of simple carboxylic acids without installing directing groups.

Enantioselective functionalization of prochiral C–H bonds can potentially lead to a broad range of efficient routes to chiral compounds. Despite extensive efforts, the scope and efficiency of enantioselective C(sp^3)–H activation reactions are far from adequate for broad applications in asymmetric synthesis (*1*, *2*). Enantioselective carbene and nitrene insertions into C(sp^3)–H bonds have been demonstrated in both diastereoselective and enantioselective fashion (*3*–*7*). However, asymmetric C(sp^3)–H activation reactions via metal insertion are limited to the desymmetrization of two prochiral carbon centers (*8*–*15*) (Fig. 1A). For example, desymmetrizations of relatively reactive cyclopropyl and cyclobutyl C–H bonds have been achieved with Pd(II) catalysts and chiral monoprotected amino acid (MPAA) ligands (*8*–*11*). Desymmetrization of two carbon centers has also been achieved through a Pd(0)-catalyzed intramolecular C–H arylation, as demonstrated in a series of pioneering studies (*12*–*15*). Thus far, development of an efficient chiral metal catalyst that can differentiate prochiral C–H bonds residing on a single methylene carbon center via metal insertion remains a challenge. In terms of synthetic disconnection, such a process is also distinct from the desymmetrization, as the newly created chiral center of amide substrates resides at the β-methylene carbon instead of the α-carbon center. Recently, a transient chiral directing group has also been shown to perform enantioselective C–H arylation of benzylic C–H bonds (*16*). However, the transient amino acid directing group does not promote alkyl methylene C–H activation. Furthermore, the transient directing group is also incompatible with substrates derived from carboxylic acids.

The use of a bidentate 8-aminoquinoline directing group and a chiral phosphoric amide ligand has afforded moderate enantiomeric ratios (er), ranging from 74:26 to 91:9 with benzyl C–H bonds, though this method is much less successful with alkyl C–H bonds (63:37 er) (*17*). In general, such strongly coordinating directing groups promote ligandless C–H activation reactions, which could be detrimental for asymmetric catalysis, as these background reactions erode enantioselectivity. Bidentate coordination from substrates also prevents the exploitation of a wide range of potentially powerful chiral bidentate ligands in palladium catalysis due to a lack of vacant coordination sites. Practically, the requirement for bidentate coordination from substrates precludes the use of a variety of simple monodentate directing groups and native functional groups to direct C–H activation, an important goal of the field.

Despite the aforementioned challenges, enantioselective β-C–H functionalization has long been the focus of our research efforts due to the importance of constructing β-chiral centers in asymmetric synthesis. Current retrosynthetic disconnections for the asymmetric synthesis of β-functionalized chiral carboxylic acids or amides extensively use conjugate addition reactions of the corresponding olefins. Rh(I)-catalyzed asymmetric conjugate addition of α,β-unsaturated ketones with aryl boronic acids has afforded a useful method for the preparation of chiral β-arylated compounds (*18*, *19*). However, when a given substrate or synthetic intermediate contains a saturated aliphatic acid chain without double bonds, direct enantioselective arylation of the methylene C–H bonds at the β position of amides through palladium insertion provides a solution (Fig. 1B). In our early efforts, we adopted a chiral auxiliary approach to gain insight into stereoselective palladium insertion into β-C (sp^3)–H bonds (*20*). However, development of an enantioselective version of these diastereoselective β-C–H iodination and acetoxylation reactions has not been successful, owing to the lack of an appropriate ligand that can match the strongly coordinating oxazoline directing group (*21*). Employing a weakly coordinating amide directing group in combination with chiral MPAA ligands has led to desymmetrization of methyl, cyclopropyl, and cyclobutyl C–H bonds (Fig. 1A) at two different carbon centers (*9*, *10*). Unfortunately, MPAA ligands have proven ineffective in promoting palladium insertion into acyclic methylene C–H bonds.

Here we report the discovery of chiral acetyl-protected aminoethyl quinoline (APAQ) ligands that enable Pd(II)-catalyzed enantioselective arylation of β-methylene C–H bonds of aliphatic amides, with enantiomeric ratios reaching up to 96:4 and

[1]The Scripps Research Institute, 10550 North Torrey Pines Road, La Jolla, CA 92037, USA. [2]Department of Chemistry and Biochemistry, University of California, Los Angeles, CA 90095-1569, USA.
*These authors contributed equally to this work. †Corresponding author. Email: houk@chem.ucla.edu (K.N.H.); yu200@scripps.edu (J.-Q.Y.)

Downloaded from http://science.sciencemag.org/ on September 2, 2016

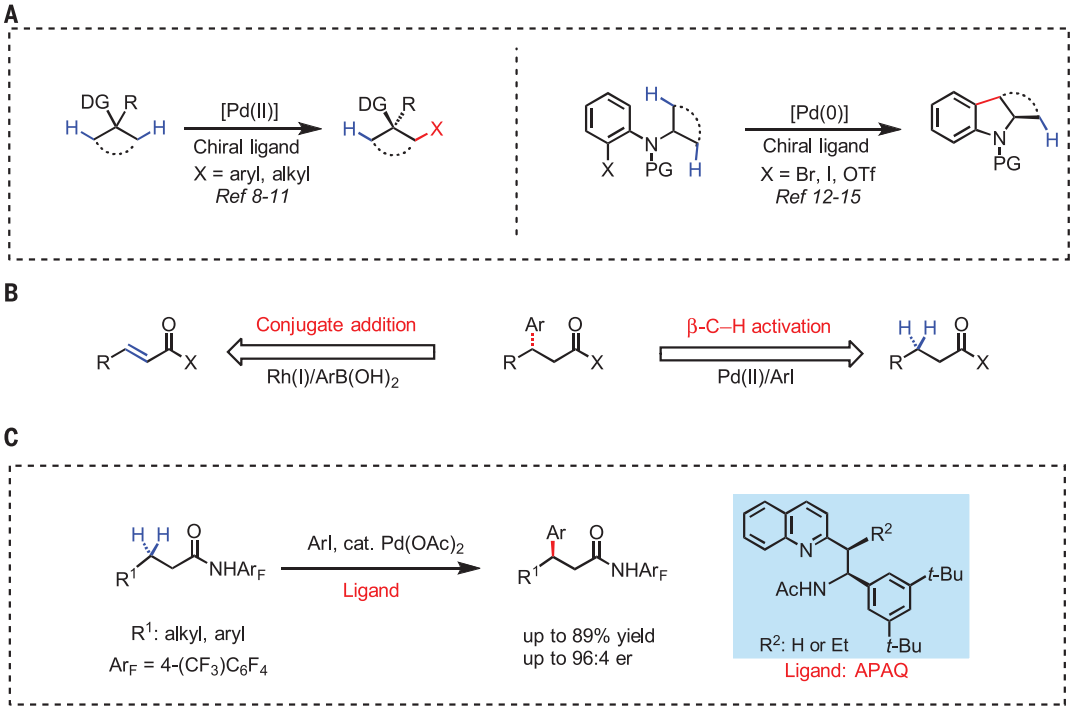


Fig. 1. Enantioselective methylene C–H activation reactions. (**A**) Enantioselective C–H activation via desymmetrization of two carbon centers. (**B**) Two synthetic disconnections. (**C**) Differentiating prochiral C–H bond on a single methylene carbon center. DG, directing group; PG, protecting group; OTf, trifluoromethanesulfonate; Ar, aryl group; Ac, acetyl group; Et, ethyl group; Bu, butyl group; R, alkyl or aryl group.

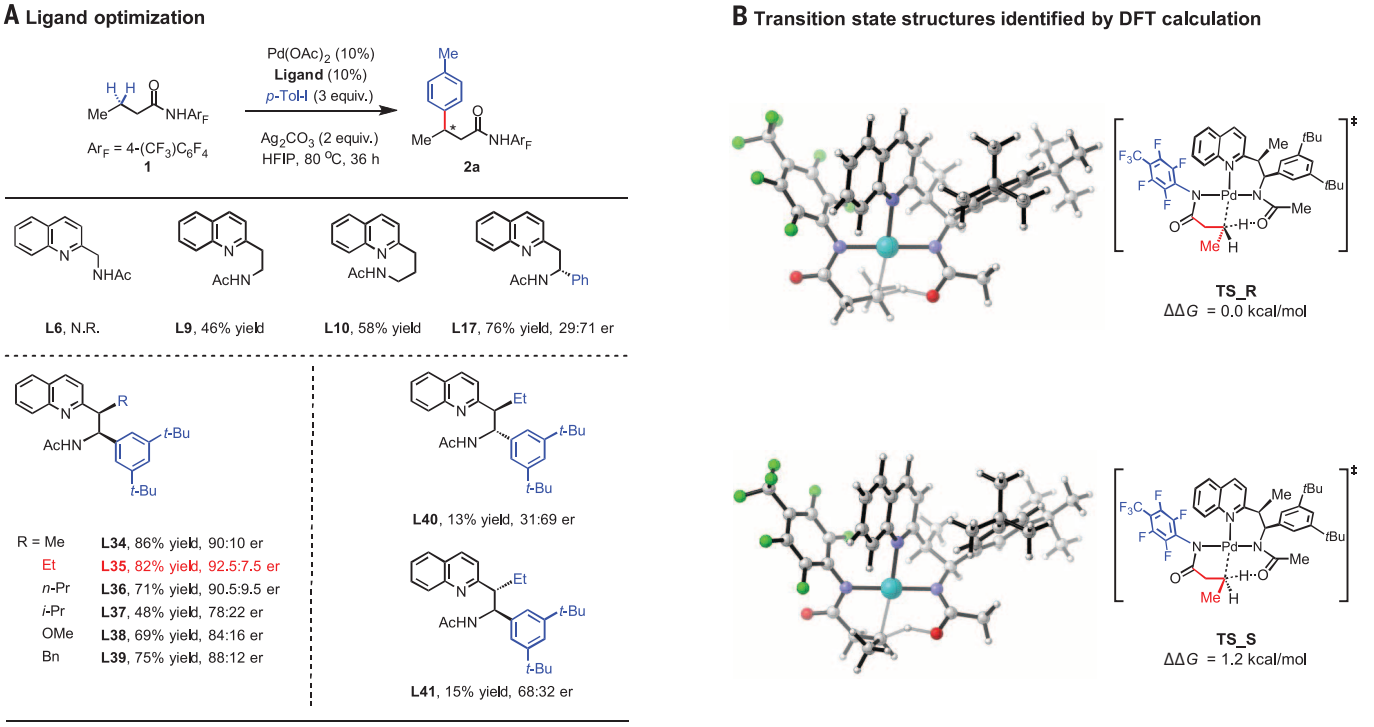


Fig. 2. Ligand optimization for enantioselective methylene C–H arylation. (**A**) Yields were determined by ^{1}H nuclear magnetic resonance analysis of the crude product, using CH_2Br_2 as an internal standard. Enantiomeric ratios were determined by chiral high-performance liquid chromatography. The absolute configuration of **L35** was determined by x-ray crystallography (fig. S4). *p*-Tol-I, *para*-tolyl iodide; equiv., equivalent; HFIP, hexafluoro-2-propanol; Me, methyl group; Ph, phenyl group; Pr, propyl group; Bn, benzyl group; N.R., no reaction. The asterisk indicates the presence of a chiral center at the atom. (**B**) DFT-optimized structures and relative free energies of the two enantiomeric C–H metalation-deprotonation transition states.

yields as high as 89% (Fig. 1C). These APAQ ligands containing quinoline and acetyl-protected amino coordinating moieties form six-membered bis-chelating rings with palladium, which drastically accelerates methylene C–H activation, thereby controlling the stereoselectivity. In contrast, the acetyl-protected aminomethyl quinoline coordinating with Pd(II) via five-membered bis-chelation is completely inactive in this reaction. Conceptually, the combination of weakly coordinating monodentate substrates and ligand acceleration opens the possibility for using a variety of simple

Downloaded from http://science.sciencemag.org/ on September 1, 2016

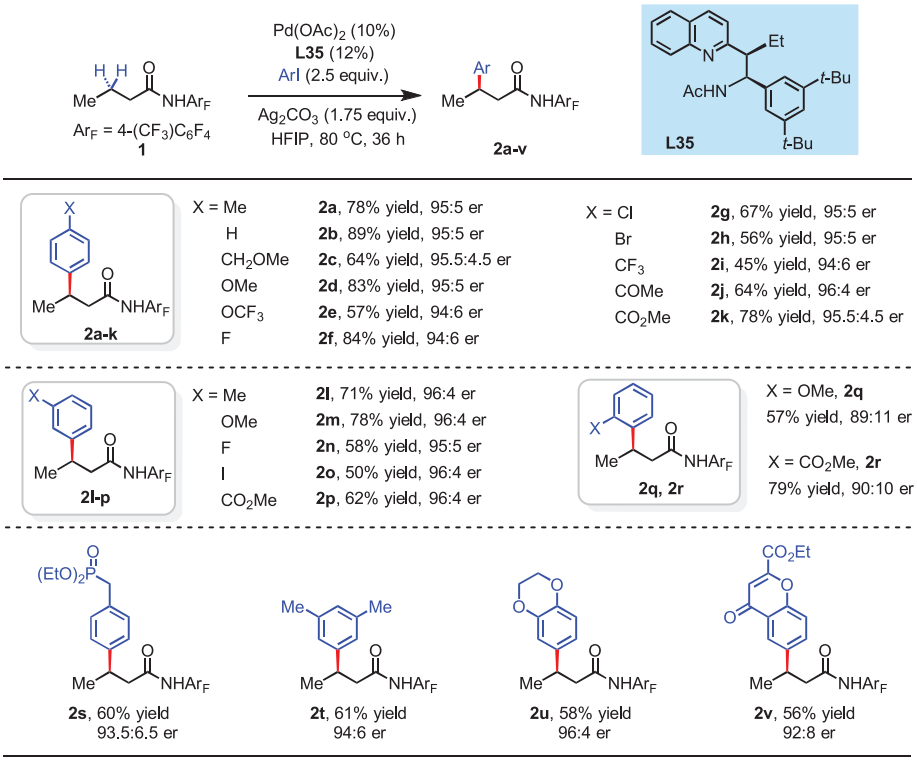


Fig. 3. Scope of aryl iodides in enantioselective methylene C–H arylation. Data are reported as isolated yield of purified compound. The absolute configurations of **2a**, **2e**, and **2k** were determined by x-ray crystallography (figs. S5 to S7).

coordinating groups, including native functional groups, to direct enantioselective C–H activation, as demonstrated with free carboxylic acid substrates.

Guided by our overarching goal of developing ligand-accelerated enantioselective C–H activation of weakly coordinating substrates, we set out to use the electron-deficient amide substrate **1** and evaluate the effects of chiral ligands on the extensively studied C–H arylation reaction (*22*–*24*). Following our previous finding that quinoline and pyridine ligands can accelerate C(sp^3)–H activation (*25*, *26*), we prepared a number of corresponding chiral ligands (including **L4** and **L5**) and examined their activity under standard reaction conditions (table S1). Unfortunately, these monodentate chiral ligands do not exert substantial influence on the stereochemistry of the palladium insertion step. Considering the effectiveness of bidentate MPAA ligands in controlling the stereochemistry of Pd-catalyzed desymmetrization of prochiral cyclopropyl and cyclobutyl C–H bonds on two carbon centers, we began to develop bidentate ligands incorporating structural motifs from both quinoline and MPAA ligands. The crucial role of the NHAc (Ac, acetyl) moiety of MPAA ligands in the C–H cleavage step, identified by experimental (*8*, *27*) and computational studies (*28*, *29*), prompted us to develop acetyl-protected aminomethyl quinoline ligands that incorporate this coordinating moiety. Disappointingly, such ligands (**L6** to **L8**) resulted in a complete loss of reactivity (Fig. 2A and table S1). We reasoned that the five-membered bidentate chelation with Pd(II) could result in the formation of a stable but inactive palladium complex tetra-coordinated with two ligands. As such, we prepared APAQ and aminopropyl quinoline ligands (**L9** and **L10**) that would coordinate with Pd(II) via six- and seven-membered chelate structures, respectively, both of which should have markedly reduced binding constants compared to the corresponding five-membered chelate (**L6**). Such subtle modification restored the reactivity with **L9** and **L10**, thus offering a bidentate ligand scaffold for further development.

Although aminopropyl quinoline **L10** is more reactive than aminoethyl quinoline **L9**, we chose to focus on the latter scaffold because of its synthetic accessibility. We used Ellman's highly efficient asymmetric imine addition reaction (*30*) to prepare a series of chiral APAQ ligands from 2-methylquinoline and optically pure sulfinyl imines . We initially found that ligand **L11** (table S1), containing an α-methyl group at the chiral center, enhanced the reactivity considerably (75% yield), albeit with poor enantioselectivity (47:53 er). The α-methyl group was then replaced with various alkyl groups: Only the sterically bulky isopropyl group was found to produce a substantially improved enantiomeric ratio (27:73), but it also led to diminished yield (**L16**, table S1). Although further tuning of the alkyl substitution proved less promising, the result obtained with the α-phenyl substitution in **L17** provided us with an encouraging lead for ligand optimization (76% yield, 29:71 er). With **L17** in hand, we examined the effect of the protecting groups on the amino group (table S2). Replacing the acetyl-protecting group by more sterically hindered analogous motifs decreased the yields considerably. Other types of protecting groups, such as carbamates and sulfonyls, proved completely inactive. We thus prepared a number of APAQ ligands [**L18** to **L33** (table S1)] with a range of steric and electronic variation on the α-phenyl ring. We found that the steric effect is predominant, as indicated by the markedly improved yield and enantioselectivity obtained with ligand **L32** bearing the sterically hindered 3,5-di-*tert*-butylphenyl group (85% yield, 19:81 er). At this point of optimization, we introduced a second chiral center at the benzylic position, hoping to further improve the enantioselectivity. Attributing the origin of the stereoselectivity to differentially hindered faces on the square planar palladium complex (*8*–*11*), we focused on the variations of syn-APAQ ligands in which both substituents would point up- or downward upon chelating with Pd(II). The introduction of a methyl group at the benzylic position (**L34**) afforded a substantial improvement in enantioselectivity (90:10 er) while maintaining the high yield. A slightly more bulky ethyl group (**L35**) further improved the enantioselectivity to 92.5:7.5 er. Further increasing steric hindrance at the benzylic position decreased both yield and enantioselectivity (**L36** to **L39**). To obtain insight into the stereochemical model of this enantioselective palladium-insertion process, we also tested the anti-APAQ ligands (**L40** and **L41**). Although both yield and enantioselectivity dropped considerably with these two anti-ligands, the reversal of chiral induction by altering the absolute configuration at the α position suggests that the chiral center adjacent to the amino group dictates enantioselection (table S3).

Building on results from previous computational studies (*28*, *29*), we explored the enantioselectivity in the C–H metalation-deprotonation step with density functional theory (DFT), using ligand **L34** and substrate **1**. The optimized structures and relative free energies of the most favorable transition states for the two enantiomers are shown in Fig. 2B. In both transition states, the palladium(II) center is coordinated with the quinoline nitrogen and the amide nitrogen of the deprotonated APAQ ligand, as well as one nitrogen from the amide substrate formed by deprotonation. The oxygen of the amide of the APAQ ligand acts as an intramolecular base to deprotonate the methylene C–H and facilitate the Pd–C bond formation. **TS_R** is more favorable than **TS_S** by 1.2 kcal/mol, in excellent agreement with the experimental selectivity (90:10 er). The distinct six-membered bis-chelate design and the bulky α-aryl substituent orient the amide in such a way that the β-C–H bond is activated. The terminal methyl group of the substrate is oriented differently in the R and S transition states, with more severe substrate distortion in **TS_S**, where the methyl group of the substrate methylene is on the same face as the bulky α-aryl substituent of the ligand and the peri-hydrogen of the quinoline. This discrepancy underlies the enantioselectivity (see supplementary materials).

Downloaded from http://science.sciencemag.org/ on September 1, 2016

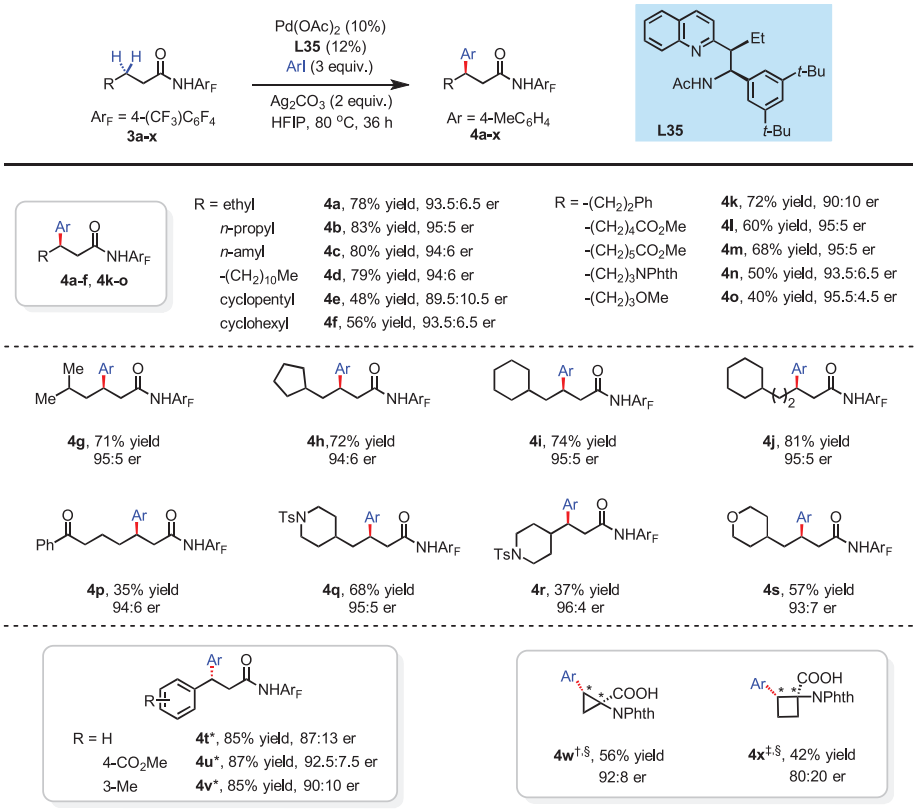


Fig. 4. Scope of amides and acids in enantioselective methylene C–H arylation. Data are reported as isolated yield of purified compound. Asterisks in the structures indicate the presence of a chiral center at the atom. The * symbol following a compound number indicates 1.5 equiv. of Ag_2CO_3, 2.5 equiv. aryl iodide, and 12 mole % (mol %) **L32**. The absolute configuration of **4u** was determined by x-ray crystallography (fig. S8). The † symbol indicates 1.0 equiv. K_2HPO_4 as additive, 20 mol % **L16**, and 100°C. The ‡ symbol indicates 1.0 equiv. $Na_2HPO_4{\cdot}7H_2O$ as additive, 2.0 equiv. AgOAc, 2.0 equiv. aryl iodide, and 12 mol % **L32**. The § symbol indicates that yields and er values were determined from corresponding methyl esters (see supplementary materials for experimental details). Phth, phthalimido group; Ts, tosyl group.

With the optimal ligand **L35** in hand, we further optimized the reaction conditions for the arylation of **1** and improved the enantioselectivity to 95:5 er (table S4, entry 21). We next surveyed the scope of aryl iodides for this enantioselective β-C–H arylation (Fig. 3). Arylation of **1** with simple iodobenzene afforded the desired product in 89% yield and 95:5 er (**2b**). A wide range of para-substituted aryl iodides was employed as coupling partners. Electron-donating groups afforded excellent enantioselectivity and good yields (**2a**, **2c**, and **2d**). Electron-deficient aryl iodides bearing trifluoromethoxy, fluoro, chloro, bromo, ketone, and ester substituents were also compatible, providing consistently high enantioselectivity (**2e** to **2h**, **2j**, **2k**), although the yield dropped to 45% with trifluoromethyl substitution (**2i**). Similar results were obtained with metasubstituted aryl iodides (**2l** to **2p**). Although slightly lower enantioselectivity was obtained with ortho-methoxylphenyl iodide (**2q**), the ortho-ester group was well tolerated (**2r**). An aryl iodide containing phosphonate moiety also afforded synthetically useful yield and enantioselectivity (**2s**). Disubstituted aryl iodides also proved to be suitable coupling partners (**2t** to **2v**).

This protocol for enantioselective arylation of methylene C–H bonds is also applicable to other aliphatic amides (Fig. 4). Aliphatic amides with various chain lengths were well tolerated, providing products **4a** to **4d** with excellent enantioselectivity and in high yields. The direct enantioselective β-C–H arylation of amides derived from naturally occurring caprylic acid and myristic acid demonstrates the utility of this method when a double bond is not available for conjugate addition (**4c** and **4d**). Substrates containing sterically hindered alkyl groups at the β position (cyclopentyl, cyclohexyl) provided good enantioselectivity but lower yields (**4e** and **4f**). Isopropyl, cyclopentyl, cyclohexyl, and cyclohexylmethyl moieties at the γ positions were well tolerated, affording satisfactory yields and enantioselectivity (**4g** to **4j**). Phenyl, ester, amino, ether, and ketone functionalities at the δ and ε positions consistently afforded high enantioselectivity (**4k** to **4p**). However, lower yields were obtained with the ether and ketone substrates (**4o** and **4p**). Piperidine at the γ position afforded good yield and high enantioselectivity (**4q**), whereas the presence of piperidine at the β position gave lower yield (**4r**). The presence of a tetrahydropyran motif at the γ position was also well tolerated, affording synthetically useful yield and enantioselectivity (**4s**). The enolate of the corresponding ester of product **4s** reacted with di-*tert*-butyl azodicarboxylate to give the chiral α-amino ester in >20:1 diastereoselectivity, providing a route for the preparation of complex chiral amino acids (see supplementary materials). Arylation of benzylic C–H with **3t** using ligand **L35** provided poor yield and enantioselectivity (38% yield, 68:32 er). Switching to ligand **L32** resulted in a marked improvement in both yield and enantioselectivity (**4t**). β-phenyl groups containing both electron-withdrawing and -donating groups were also compatible with this reaction (**4u** and **4v**). To demonstrate the advantage of using weakly coordinating monodentate substrates and chiral bidentate ligands, we applied the enantioselective β-C–H arylation protocol to two free carboxylic acids to provide **4w** and **4x** as cis-diastereomers exclusively. These products are not accessible by asymmetric conjugate addition.

In summary, a chiral bidentate APAQ ligand scaffold was found to enable Pd-catalyzed enantioselective arylation of prochiral β-C–H bonds on a single methylene carbon center. The feasibility of asymmetric palladium insertion into ubiquitous methylene C–H bonds with monodentate substrates opens a new avenue for developing a wide range of synthetically useful enantioselective C–H activation reactions.

REFERENCES AND NOTES

1. R. Giri, B.-F. Shi, K. M. Engle, N. Maugel, J.-Q. Yu, *Chem. Soc. Rev.* **38**, 3242–3272 (2009).
2. D. A. Colby, A. S. Tsai, R. G. Bergman, J. A. Ellman, *Acc. Chem. Res.* **45**, 814–825 (2012).
3. M. P. Doyle, R. Duffy, M. Ratnikov, L. Zhou, *Chem. Rev.* **110**, 704–724 (2010).
4. R. P. Reddy, H. M. L. Davies, *Org. Lett.* **8**, 5013–5016 (2006).
5. C. Liang *et al.*, *Angew. Chem. Int. Ed.* **45**, 4641–4644 (2006).
6. D. N. Zalatan, J. Du Bois, *J. Am. Chem. Soc.* **130**, 9220–9221 (2008).
7. E. Milczek, N. Boudet, S. Blakey, *Angew. Chem. Int. Ed.* **47**, 6825–6828 (2008).
8. B.-F. Shi, N. Maugel, Y.-H. Zhang, J.-Q. Yu, *Angew. Chem. Int. Ed.* **47**, 4882–4886 (2008).
9. M. Wasa, K. M. Engle, D. W. Lin, E. J. Yoo, J.-Q. Yu, *J. Am. Chem. Soc.* **133**, 19598–19601 (2011).
10. K.-J. Xiao *et al.*, *J. Am. Chem. Soc.* **136**, 8138–8142 (2014).
11. K. S. L. Chan, H.-Y. Fu, J.-Q. Yu, *J. Am. Chem. Soc.* **137**, 2042–2046 (2015).
12. M. Nakanishi, D. Katayev, C. Besnard, E. P. Kündig, *Angew. Chem. Int. Ed.* **50**, 7438–7441 (2011).
13. S. Anas, A. Cordi, H. B. Kagan, *Chem. Commun. (Camb.)* **47**, 11483–11485 (2011).
14. N. Martin, C. Pierre, M. Davi, R. Jazzar, O. Baudoin, *Chemistry* **18**, 4480–4484 (2012).
15. T. Saget, S. J. Lemouzy, N. Cramer, *Angew. Chem. Int. Ed.* **51**, 2238–2242 (2012).
16. F.-L. Zhang, K. Hong, T.-J. Li, H. Park, J.-Q. Yu, *Science* **351**, 252–256 (2016).
17. S.-B. Yan, S. Zhang, W.-L. Duan, *Org. Lett.* **17**, 2458–2461 (2015).
18. G. Berthon, T. Hayashi, in *Catalytic Asymmetric Conjugate Reactions*, A. Cordova, Ed. (Wiley, 2010), pp. 1–67.
19. J.-F. Paquin, C. Defieber, C. R. J. Stephenson, E. M. Carreira, *J. Am. Chem. Soc.* **127**, 10850–10851 (2005).
20. R. Giri, X. Chen, J.-Q. Yu, *Angew. Chem. Int. Ed.* **44**, 2112–2115 (2005).
21. K. M. Engle, J.-Q. Yu, *J. Org. Chem.* **78**, 8927–8955 (2013).
22. V. G. Zaitsev, D. Shabashov, O. Daugulis, *J. Am. Chem. Soc.* **127**, 13154–13155 (2005).

Downloaded from http://science.sciencemag.org/ on September 1, 2016

23. B. V. S. Reddy, L. R. Reddy, E. J. Corey, *Org. Lett.* **8**, 3391–3394 (2006).
24. Y. Feng, G. Chen, *Angew. Chem. Int. Ed.* **49**, 958–961 (2010).
25. M. Wasa *et al.*, *J. Am. Chem. Soc.* **134**, 18570–18572 (2012).
26. J. He *et al.*, *Angew. Chem. Int. Ed.* **55**, 785–789 (2016).
27. K. S. L. Chan *et al.*, *Nat. Chem.* **6**, 146–150 (2014).
28. D. G. Musaev, A. Kaledin, B.-F. Shi, J.-Q. Yu, *J. Am. Chem. Soc.* **134**, 1690–1698 (2012).
29. G.-J. Cheng *et al.*, *J. Am. Chem. Soc.* **136**, 894–897 (2014).
30. M. T. Robak, M. A. Herbage, J. A. Ellman, *Chem. Rev.* **110**, 3600–3740 (2010).

ACKNOWLEDGMENTS

We thank The Scripps Research Institute and the NIH (National Institute of General Medical Sciences grant 2R01GM084019) for financial support. We also thank the Shanghai Institute of Organic Chemistry, Zhejiang Medicine, and Pharmaron for a postdoctoral fellowship (G.C.) and the Deutsche Forschungsgemeinschaft for a research fellowship (M.S.A.). We acknowledge earlier computational studies that enhanced our understanding of catalyst development, conducted in collaboration with J. Musaev and K. Houk within the NSF Center for Chemical Innovation: Center for Selective C–H Functionalization (grant CHE-1205646). Author contributions: J.-Q.Y. conceived the concept. G.C. and W.G. developed the chiral ligands and optimized the reaction conditions. Z.Z., M.S.A., Y.-Q. C., and T.L. optimized the chiral ligands and surveyed the substrate scope. X.H., Y.-F.Y., and K.N.H. performed the DFT calculation. J.-Q.Y. directed the project. J.-Q.Y. and The Scripps Research Institute have filed a provisional patent application (62311039). Metrical parameters for the structures of **L13**, **L21**, **L40b**, **L35**, **2a**, **2e**, **2k**, and **4u** (see supplementary materials) are available free of charge from the Cambridge Crystallographic Data Centre under reference number CCDC-14522020, CCDC-14522021, CCDC-14522023, CCDC-14522022, CCDC-14522016, CCDC-14522017, CCDC-14522018, and CCDC-14522019, respectively.

SUPPLEMENTARY MATERIALS

www.sciencemag.org/content/353/6303/1023/suppl/DC1
Materials and Methods
Figs. S1 to S9
Tables S1 to S14
NMR Spectra
HPLC Traces
References (*31*–*55*)

9 February 2016; resubmitted 4 April 2016
accepted 9 August 2016
10.1126/science.aaf4434

PLANT SCIENCE

Plant development regulated by cytokinin sinks

Evelyne Zürcher,[1]* Jingchun Liu,[1]* Martin di Donato,[2] Markus Geisler,[2] Bruno Müller[1]†

Morphogenetic signals control the patterning of multicellular organisms. Cytokinins are mobile signals that are perceived by subsets of plant cells. We found that the responses to cytokinin signaling during *Arabidopsis* development are constrained by the transporter PURINE PERMEASE 14 (PUP14). In our experiments, the expression of *PUP14* was inversely correlated to the cytokinin signaling readout. Loss of *PUP14* function allowed ectopic cytokinin signaling accompanied by aberrant morphogenesis in embryos, roots, and the shoot apical meristem. PUP14 protein localized to the plasma membrane and imported bioactive cytokinins, thus depleting apoplastic cytokinin pools and inhibiting perception by plasma membrane–localized cytokinin sensors to create a sink for active ligands. We propose that the spatiotemporal cytokinin sink patterns established by PUP14 determine the cytokinin signaling landscape that shapes the morphogenesis of land plants.

Multicellular organisms depend on differential cell functions controlled by signaling systems. The precise determination of signal-perceiving cells is important to ensure normal development. Cytokinins are chemical plant signals that control morphogenesis, integrate environmental cues, and mediate biotic interactions (*1*–*3*). Cytokinins are perceived by largely redundantly acting hybrid kinases that activate a phosphorelay circuitry to stimulate the transcription of target genes. The spatiotemporal precision of the signaling patterns in different plant organs (*4*, *5*) raises the question of how control is established.

Each step involved in eliciting a signaling response, including ligand biosynthesis and expression of signaling components, could be differentially regulated and contribute to defining the signaling patterns to a greater or lesser degree. To identify limiting and regulated steps, we used *Arabidopsis* heart-stage embryos as a model in which the cytokinin response marks the provascular tissue (Fig. 1A). First, to evaluate whether bioactive cytokinins are limited, we incubated embryos for 16 hours with the degradation-insensitive cytokinin benzyladenine (BA) (*6*). This caused a stereotypic expansion of the synthetic cytokinin reporter *TCSn::GFP* (*Two Component signaling Sensor new::green fluorescent protein*) (*5*) (Fig. 1A), thereby confirming that cytokinin levels are controlled (*7*). However, excess cytokinins did not induce *TCSn::GFP* expression in the prospective cotyledons, despite the transcription of the cognate cytokinin receptor *ARABIDOPSIS HISTIDINE KINASE 4* (*AHK4*) in these domains (Fig. 1A); this finding suggests that failure to turn on signaling cannot be explained by missing receptors. To test whether signaling downstream of receptors is functional, we expressed *CYTOKININ INDEPENDENT 1* (*CKI1*). *CKI1* encodes a hybrid kinase with cytokinin-independent constitutive activity (*3*). Its short-term expression caused ubiquitous *TCSn::GFP* activation (Fig. 1A). Together, these results suggest that cells of the prospective cotyledons fail to activate cytokinin signaling despite a functional signaling system, and even upon addition of abundant active ligand.

We hypothesized that productive ligand-receptor interactions within organs could depend on cytokinin transporters that guide differential cellular localization of cytokinins. To test whether members of the *Arabidopsis* PURINE PERMEASE (PUP) family of transmembrane proteins implicated in cytokinin translocation (*8*) control the spatiotemporal landscape of cytokinin signaling, we first established a transcription profile of all family members, based on our own analysis and published transcriptome data (*9*–*11*) (fig. S1). *PUP14* expression was unique in that it prevailed in all organs and stages analyzed, including embryos. To determine the *PUP14* expression pattern, we analyzed *PUP14::PUP14-GFP* transgenic plants. In heart-stage embryos, PUP14-GFP localized to cells that failed to respond to cytokinins, including cells of the prospective cotyledons (Fig. 1B). We confirmed this pattern by mRNA in situ hybridization with a *PUP14* antisense probe (Fig. 1B and fig. S2A). The exclusive nature of *PUP14* expression and the cytokinin signaling pattern are compatible with an inhibitory function of PUP14 in the cytokinin response.

To eliminate *PUP14* function during defined time windows, thereby avoiding secondary effects and potential lethality issues, we constructed an ethanol-inducible artificial microRNA (*amiR*) (*12*) targeting *PUP14* (*35S>ALC>amiRPUP14*). Upon induction of the *amiRPUP14* transgene, *PUP14* mRNA and PUP14-GFP levels were reduced within 24 hours (Fig. 1D and fig. S2, B and C). Inducing *amiRPUP14* expression for 16 hours caused widespread ectopic cytokinin signaling in the embryo (Fig. 1B), even in cells of the prospective cotyledons that are nonresponsive to treatments with exogenous cytokinins (Fig. 1A); this result supports a role of PUP14 in confining the cytokinin response. The same treatment regime did not affect the auxin response (fig. S2D), indicating that PUP14 acts specifically on cytokinin signaling. After 2 days of *amiRPUP14* induction, morphological defects in the prospective cotyledons and the nascent root meristem became apparent (Fig. 1C), consistent with the ectopic cytokinin responses in these domains. The *amiRPUP14*-induced phenotypes were complemented by an *amiRPUP14*-resistant transgene (*PUP14**) encompassing the *PUP14* locus (fig. S2, E to G), which suggests that the inducible *amiRPUP14* acts specifically. In addition, an inducible *amiR* against nonexpressed *PUP19* and *PUP20* (fig. S1) did not cause obvious phenotypes (fig. S2, E to G). Finally, a T-DNA insertion to the *PUP14* promoter causing a reduction in *PUP14* mRNA levels showed qualitatively similar but weaker phenotypes in embryos, seedlings, and adult shoots relative to *amiRPUP14*-induced

[1]Zürich-Basel Plant Science Center, Department of Plant and Microbial Biology, University of Zürich, 8008 Zürich, Switzerland. [2]Plant Biology, Department of Biology, University of Fribourg, 1700 Fribourg, Switzerland.
*These authors contributed equally to this work. †**Corresponding author. Email: bruno.mueller@uzh.ch**

Downloaded from http://science.sciencemag.org/ on September 1, 2016

phenotypes (Fig. 1C and fig. S3, A to F), whereas a second T-DNA insertion downstream of the *PUP14* locus did not affect *PUP14* mRNA levels (fig. S3B) and produced no apparent phenotypes. Together, these results validate the use of the *amiRPUP14* line to study *PUP14* function.

Because loss of *PUP14* produces ectopic cytokinin responses, we expected the overexpression of *PUP14* to reduce cytokinin output. Although we were unable to recover plants transgenic for *35S::PUP14*, inducible *PUP14* expression in the embryo reduced the endogenous cytokinin response

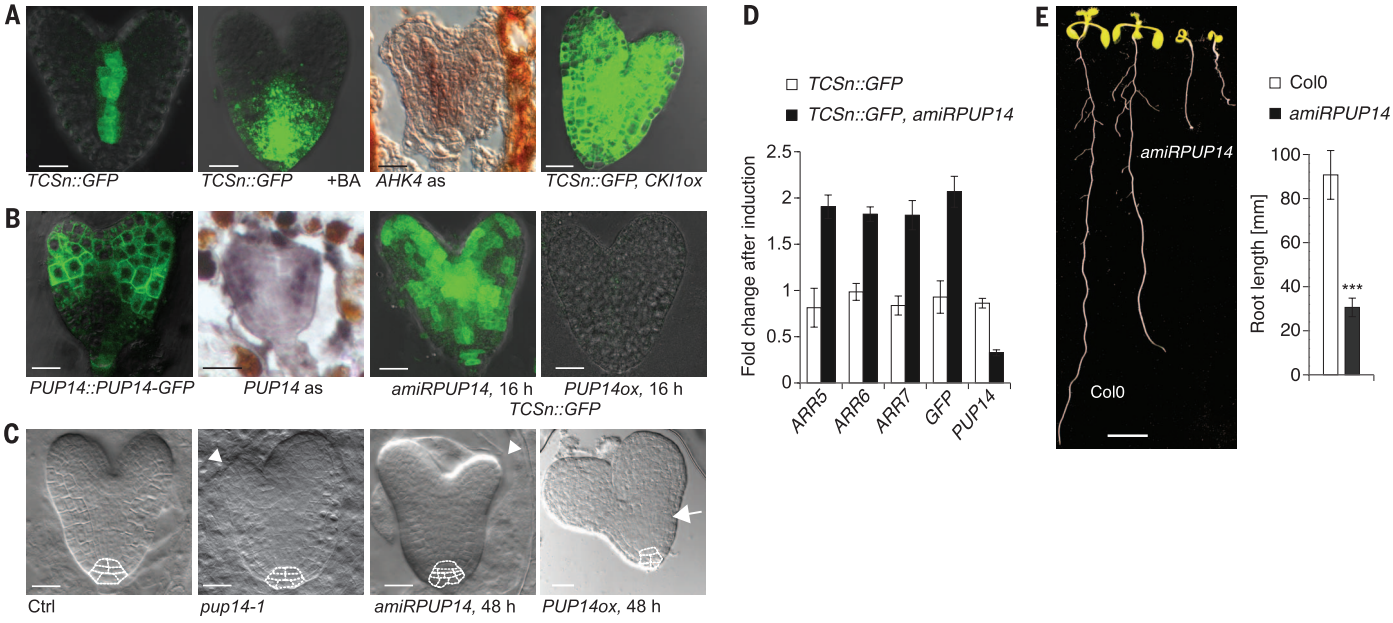


Fig. 1. PUP14 function in embryo and seedlings. (**A**) Heart-stage embryos subjected to 16 hours of mock treatment, 16 hours of treatment with 10 μM BA, 16 hours of hybridization with *AHK4* antisense (as) RNA, and 16 hours of *CKI1* expression from a *35S>ALC>CKI1* transgene (*5*) (*CKI1ox*). GFP reporter transgenes are indicated. (**B**) Left panels: *PUP14* expression detected by reporter gene and by *PUP14* as RNA probe. Right panels: *amiRPUP14* and *PUP14 35S>ALC>PUP14* transgene (*PUP14ox*) inductions. Ectopic *TCSn::GFP* in 85% of embryos, $n = 53$; loss of *TCSn::GFP* in 45% of embryos, $n = 11$. (**C**) Morphological defects 48 hours after transgene inductions and in *pup14-1*. For *amiRPUP14*, 47%, $n = 96$; for *pup14-1*, 37%, $n = 237$; for *PUP14* overexpression from *PUP14ox*, 50%, $n = 10$. Arrowheads point to affected cotyledons, arrow indicates shortened embryo root, and cell boundaries in root meristem are outlined with white dotted lines. (**D**) Relative changes of type-A *ARR5*, *ARR6*, and *ARR7* and *TCSn::GFP* [a group, significantly different: $P < 0.001$ (unpaired *t* test); *TCSn::GFP*, $n = 4$; *TCSn::GFP, amiRPUP14*, $n = 4$] and *PUP14* mRNA levels [significantly different: $P < 0.001$ (unpaired *t* test); *TCSn::GFP*, $n = 4$; *TCSn::GFP, amiRPUP14*, $n = 7$] after 16 hours of *amiRPUP14* induction in 7-day-old seedlings of indicated genotype, assessed by quantitative real-time polymerase chain reaction; error bars represent SEM. (**E**) *amiRPUP14* and *Col0* seedlings after 7 days on ethanol-containing medium; growth retardation of seedling roots, $n = 10$. Scale bars, 20 μm [(A) and (B)], 1 cm (E). ***$P < 0.001$ (unpaired *t* test).

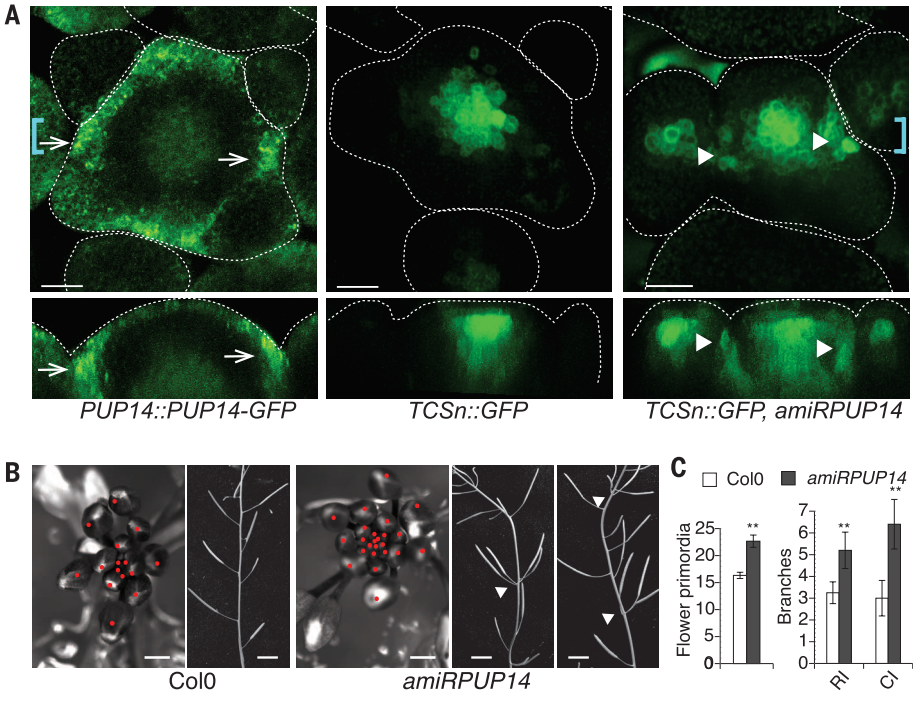


Fig. 2. PUP14 confines the cytokinin response in the SAM. (**A**) Floral SAM. Longitudinal optical sections (lower panels) are in cyan-colored brackets; dotted lines mark organ boundaries. Transgenes are indicated. Arrows indicate peak *PUP14-GFP* levels at organ-organ boundaries. Arrowheads indicate ectopic *TCSn::GFP* after *amiRPUP14* induction. (**B** and **C**) Comparisons of ethanol-treated *Col0* and *amiRPUP14* phenotypes. (B) Inflorescences and inflorescence stems. Red dots denote flower primordia; arrowheads indicate perturbations. (C) Numbers of flower primordia at stages 6 to 12 on the main apex (*30*), $n = 6$; numbers of primary rosette (RI) and primary cauline branching (CI), $n = 6$. Data are means ± SD. **$P < 0.01$ (unpaired *t* test). Scale bars, 20 μm (A), 1 mm [flower primordia in (B)], 1 cm [stems in (B)].

Downloaded from http://science.sciencemag.org/ on September 1, 2016

after 16 hours (Fig. 1B); after 48 hours of transgene induction, morphological defects in the embryo root were apparent (Fig. 1C). Similar to the embryo, we found *PUP14* expression in the meristematic region of the seedling's main root (fig. S4A), in the lateral root primordia (LRP) (fig. S4B), and in ovules and seeds (fig. S6, A and B), exhibiting patterns complementary to those of cytokinin signaling. As in the embryo, short-term *amiRPUP14* induction resulted in ectopic cytokinin signaling in the seedling root, particularly in the meristematic region of the root tip (fig. S4A) and in the LRP (fig. S4B). Accordingly, transcription of the immediate-early cytokinin target genes type-A *ARABIDOPSIS RESPONSE REGULATOR 5* (*ARR5*), *ARR6*, and *ARR7* (*13*) was induced in seedlings (Fig. 1D).

Continuous induction of *amiRPUP14* led to growth retardation of the seedling root and shoot, with suppression of lateral roots (*14*, *15*) (Fig. 1E); this finding suggests that the root and shoot meristem activities were both affected when cytokinin signaling patterns were perturbed by the inducible *amiRPUP14*. In contrast to the embryo (Fig. 1, B and C), *TCSn::GFP* expression remained unchanged after 24 hours of inducing ectopic *PUP14* in the seedling root (not shown). We visualized PUP14-GFP expressed from the inducible *35S>ALC>PUP14-GFP* transgene and found that, relative to *35S>ALC>GFP*, cells of the root apex and vasculature failed to express PUP14-GFP (fig. S5, A to C). This result suggests that ectopic PUP14 is not tolerated, which can explain the absent effects on *TCSn::GFP* in the seedling root apex and the lethality of the *35S::PUP14* transgene. In addition, relative to endogenous PUP14-GFP, the subcellular localization of ectopic PUP14-GFP was disturbed (fig. S5, B and C), which may impair its normal function.

In the shoot, cytokinin controls the homeostasis of the shoot apical meristem (SAM) (*16*), where increased cytokinin causes a more active meristem with more primordia (*17*). As observed in other developmental contexts (Fig. 1, A and B, fig. S4, and fig. S6, A and B), *PUP14* expression in the SAM was inversely correlated with cytokinin signaling output assayed by *TCSn::GFP* (Fig. 2A). Inducing *amiRPUP14* expression in adult plants that were allowed to complete embryogenesis and the early vegetative phase of development undisturbed caused ectopic cytokinin output in the SAM, which was accompanied by a 37% increase in number of primordia, a 94% increase in shoot branching relative to ethanol-treated wild-type plants, and disturbed phyllotaxis (Fig. 2, B and C). Similar phenotypes have been observed in plants mutant for *CYTOKININ OXIDASE 3* (*CKX3*) and *CKX5* (*17*), *ARABIDOPSIS HISTIDINE PHOSPHOTRANSFER PROTEIN 6* (*18*), and *ARR3* to *ARR9* (*19*), which also display ectopic cytokinin activities. Thus, PUP14 functions to limit the cytokinin response domains throughout development to support morphogenesis.

Next, we addressed the cellular function of PUP14. PUP14-GFP fusion proteins, supported by brefeldin A-sensitive vesicular transport, localized to the plasma membrane (fig. S6C). To test PUP14's cytokinin transport capacity, we conducted uptake experiments using labeled trans-zeatin (tZ), an abundant natural cytokinin (*20*). Transient expression of *PUP14* in mesophyll protoplasts or tobacco microsomes stimulated the uptake of labeled tZ (Fig. 3, A and B). Transport activity in PUP14 was higher than in PUP1 and was dependent on the presence of adenosine triphosphate (*8*) (Fig. 3B). Uptake was inhibited by unlabeled tZ, by the common natural cytokinin isopentenyl adenine (iP), by the aromatic cytokinin BA, and also by adenine, but not by tZ riboside, the major cytokinin transport form (*21*), nor by auxin (IAA) or allantoin, which is an unrelated substrate (Fig. 3, C and D). Energy-dependent cytokinin uptake into a microsomal cell-free system excludes the possibility that uptake is dependent on cytoplasmic metabolization. Conversely, relative to control seedlings, seedlings with decreased *PUP14* levels exhibited a reduced uptake rate for exogenously added tZ (Fig. 3E).

Our data show that plasma membrane–localized PUP14 imports bioactive cytokinins to the cytosol, implying that PUP14 activity depletes ligands from the apoplast, which leads to a suppression of the cytokinin response. In this scenario, extracellular cytokinins binding to the sensing domains of plasma membrane–localized receptors (*22*, *23*) are important to initiate the signaling response, whereas the cytoplasm represents a sink for bioactive ligands. To test this hypothesis, we devised experiments that compared the effects of differentially targeted cytokinin-degrading enzymes on the cytokinin signaling response. Mesophyll protoplast cells respond to as little as 100 pM exogenously added tZ by activating cytokinin signaling (*4*), which suggests that they depend on exogenous cytokinins and thus constitute a suitable model to study cytokinin perception independent of production. Transient transfection of PUP14 localizing to the plasma membrane (fig. S7A) caused a reduction of cytokinin-dependent *TCS::LUCIFERASE* (*LUC*) activity (Fig. 3F), recapitulating the phenotypes from *PUP14* overexpression in the embryo (Fig. 1B). Transient expression of wild-type CKX2 that is targeted for secretion to the apoplast (*20*) (fig. S7B) attenuated the cytokinin response triggered by tZ but not by the degradation-resistant BA. To target CKX2 to the exofacial side of the plasma membrane, we added a glycosylphosphatidylinositol (GPI) anchor (*24*), resulting in CKX2-GPI (fig. S7C), which also caused a reduction in the cytokinin response. In contrast, a variant of CKX2 that lacks the N-terminal signal

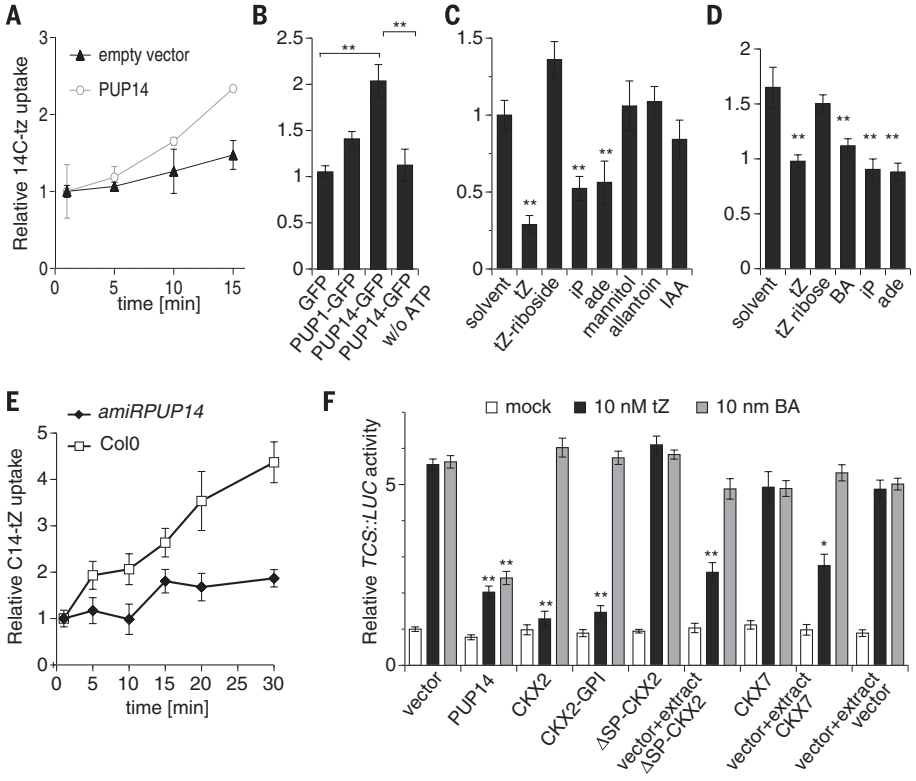


Fig. 3. PUP14 cellular function. (**A** to **E**) PUP14 transport assays, with relative ^{14}C-tZ uptake rates on *y* axis. (A) *PUP14*-transfected mesophyll protoplasts. (B) Microsomes derived from *GFP*-, *PUP1*-, or *PUP14*-transfected *Nicotiana benthamiana*. (C) Competition by indicated substances in *PUP14*-transfected protoplasts. (D) Competition in microsomes of *35S::PUP14*-transfected *N. benthamiana*. (E) *amiRPUP14* versus *Col0* seedlings. (**F**) Relative *TCSn::LUC* induction in protoplasts treated with 10 nM tZ or BA, cotransfected with effector genes, or with addition of cell extracts as indicated, normalized to empty vector control. Data are means ± SD [(A) and (E)] or means ± SEM [(B), (C), (D), and (F)]. $^{**}P < 0.01$, $^{*}P < 0.05$ (analysis of variance with Tukey HSD post hoc test).

Downloaded from http://science.sciencemag.org/ on September 1, 2016

peptide (ΔSP-CKX2) and colocalizes with a cytoplasmic marker (fig. S7D) did not affect the cytokinin response, and neither did CKX7, which also localizes to the cytoplasm (*25*) (fig. S7E). Crude cell extracts obtained from ΔSP-CKX2–transfected or CKX7-transfected cells added to the medium reduced the response triggered by tZ, indicating that these proteins are active. These data suggest that apoplastic cytokinins initiate signaling, whereas cytoplasmic cytokinins are inactive.

PUP14 imports cytokinins from the apoplast to the cytosol, away from sensing domains of plasma membrane–localized receptors, which causes a reduction in cytokinin signaling. Thus, PUP14 activity inversely correlates with the capacity of a cell to sense cytokinins (fig. S8), and PUP14 spatiotemporal activities cause region-specific depletion of cytokinins from the apoplast. In animals, the importance of such clearing activities is demonstrated by the powerful action of drugs that target dopamine influx transporters, thereby increasing dopamine's residence time in the synaptic cleft (*26*). Feeding experiments with radiolabeled bioactive cytokinin suggest that the bulk of imported cytokinins are inactivated by conversion to monophosphates by ADENINE PHOSPHORIBOSYL TRANSFERASE enzymes (*27*, *28*). Furthermore, N- or O-glycosylation, oxidative cleavage, or transport to other cells may contribute to clearance of intracellular cytokinins (*2*). PUP14 is the only family member to be linked to cytokinin signaling in all organs. In specific developmental contexts, additional PUP family members likely have overlapping functions with PUP14. The fact that *PUP* genes are specific to vascular plants (*29*) may suggest that *PUP* genes are needed to support more complex cytokinin signaling patterns associated with the bauplan of land plants. Because hormonal transporters are numerous and universal in plant and animal systems, transporters in other systems may also regulate patterning during morphogenesis.

REFERENCES AND NOTES

1. M. Miri, P. Janakirama, M. Held, L. Ross, K. Szczyglowski, *Trends Plant Sci.* **21**, 178–186 (2016).
2. J. J. Kieber, G. E. Schaller, *Arabidopsis Book* **12**, e0168 (2014).
3. I. Hwang, J. Sheen, B. Müller, *Annu. Rev. Plant Biol.* **63**, 353–380 (2012).
4. B. Müller, J. Sheen, *Nature* **453**, 1094–1097 (2008).
5. E. Zürcher *et al.*, *Plant Physiol.* **161**, 1066–1075 (2013).
6. P. Galuszka *et al.*, *J. Plant Growth Regul.* **26**, 255–267 (2007).
7. B. De Rybel *et al.*, *Science* **345**, 1255215 (2014).
8. B. Gillissen *et al.*, *Plant Cell* **12**, 291–300 (2000).
9. J. Adrian *et al.*, *Dev. Cell* **33**, 107–118 (2015).
10. M. F. Belmonte *et al.*, *Proc. Natl. Acad. Sci. U.S.A.* **110**, E435–E444 (2013).
11. R. K. Yadav, M. Tavakkoli, M. Xie, T. Girke, G. V. Reddy, *Development* **141**, 2735–2744 (2014).
12. R. Schwab, S. Ossowski, M. Riester, N. Warthmann, D. Weigel, *Plant Cell* **18**, 1121–1133 (2006).
13. I. B. D'Agostino, J. Deruère, J. J. Kieber, *Plant Physiol.* **124**, 1706–1717 (2000).
14. L. Laplaze *et al.*, *Plant Cell* **19**, 3889–3900 (2007).
15. J. P. To *et al.*, *Plant Cell* **16**, 658–671 (2004).
16. S. P. Gordon, V. S. Chickarmane, C. Ohno, E. M. Meyerowitz, *Proc. Natl. Acad. Sci. U.S.A.* **106**, 16529–16534 (2009).
17. I. Bartrina, E. Otto, M. Strnad, T. Werner, T. Schmülling, *Plant Cell* **23**, 69–80 (2011).
18. F. Besnard *et al.*, *Nature* **505**, 417–421 (2014).
19. A. Leibfried *et al.*, *Nature* **438**, 1172–1175 (2005).
20. T. Werner *et al.*, *Plant Cell* **15**, 2532–2550 (2003).
21. C. A. Beveridge *et al.*, *Plant J.* **11**, 339–345 (1997).
22. H. J. Kim *et al.*, *Proc. Natl. Acad. Sci. U.S.A.* **103**, 814–819 (2006).
23. K. Wulfetange *et al.*, *Plant Physiol.* **156**, 1808–1818 (2011).
24. A. Baral *et al.*, *Plant Cell* **27**, 1297–1315 (2015).
25. I. Köllmer, O. Novák, M. Strnad, T. Schmülling, T. Werner, *Plant J.* **78**, 359–371 (2014).
26. R. A. Vaughan, J. D. Foster, *Trends Pharmacol. Sci.* **34**, 489–496 (2013).
27. B. Moffatt, C. Pethe, M. Laloue, *Plant Physiol.* **95**, 900–908 (1991).
28. X. Zhang *et al.*, *Mol. Plant* **6**, 1661–1672 (2013).
29. S. B. Hildreth *et al.*, *Proc. Natl. Acad. Sci. U.S.A.* **108**, 18179–18184 (2011).
30. D. R. Smyth, J. L. Bowman, E. M. Meyerowitz, *Plant Cell* **2**, 755–767 (1990).

ACKNOWLEDGMENTS

We thank M. Philipp for technical assistance, I. Antoniadi and A. Schmidt for sharing unpublished results, E. Martinoia for help with transport assays, J. Sheen and K. Basler for critical discussions and comments on the manuscript, C. Baroux for comments on the manuscript, and U. Grossniklaus for support. Funding was provided by the Kanton of Zürich, Swiss National Science Foundation grant SNF31003A-149459, and a Syngenta Ph.D. fellowship from the Zürich-Basel Plant Science Center. The authors declare that they have no conflicts of interest. The supplementary materials contain additional data. Plasmid sequences were deposited to GenBank with accession numbers KX510271 to KX510275.

SUPPLEMENTARY MATERIALS

www.sciencemag.org/content/353/6303/1027/suppl/DC1
Materials and Methods
Figs. S1 to S8
Tables S1 and S2
References (*31*–*42*)

8 April 2016; accepted 4 August 2016
10.1126/science.aaf7254

SPEECH PROCESSING

Neural mechanisms for lexical processing in dogs

A. Andics,[1,2,3]* A. Gábor,[2] M. Gácsi,[1] T. Faragó,[1] D. Szabó,[1,2] Á. Miklósi[1,2]

During speech processing, human listeners can separately analyze lexical and intonational cues to arrive at a unified representation of communicative content. The evolution of this capacity can be best investigated by comparative studies. Using functional magnetic resonance imaging, we explored whether and how dog brains segregate and integrate lexical and intonational information. We found a left-hemisphere bias for processing meaningful words, independently of intonation; a right auditory brain region for distinguishing intonationally marked and unmarked words; and increased activity in primary reward regions only when both lexical and intonational information were consistent with praise. Neural mechanisms to separately analyze and integrate word meaning and intonation in dogs suggest that this capacity can evolve in the absence of language.

Various species rely on similar acoustic cues from vocalizations to infer inner states (*1*, *2*). Human vocal comprehension also uses association of arbitrary sound sequences with meaning. Lexical items (words) are the basic building blocks of human languages but are hardly ever found in nonhuman vocal communicative systems, even though several species are capable of learning and discriminating arbitrary sound sequences (*3*, *4*), associating vocalizations with specific meanings (*4*, *5*), or producing human-like lexical items after extensive training (*6*).

Lexical processing in humans is lateralized to the left hemisphere (LH) of the brain (*7*). According to acoustic theories, this is caused by LH bias for rapidly changing signals (*8*), which is not unique to humans (*9*). In contrast, functional theories assume LH bias for lexical representations of meaning, independent of acoustics (*10*). Nonhuman neural evidence for lexical processing is scarce. LH bias for broadly defined meaningfulness has been found for processing familiar, conspecific sounds (*11*–*13*). The comparison of human and nonhuman neural mechanisms for processing spoken words may reveal how speech-related hemispheric asymmetries and lexical representations emerged during evolution.

Dogs present an ideal model for such investigations. Domestication has increased dogs' abilities to engage in acoustic communication with humans (*14*), they are more receptive than wolves to human vocal signals (*15*), and their behavior is more easily brought under human vocal control (*16*, *17*). Dogs can recognize (up to ~1000) words as discriminative stimuli to retrieve different objects (*18*), and they process acoustic cues from human and dog vocalizations in overlapping auditory brain regions (*19*). A recent behavioral study found orienting asymmetries in dogs that listened to artificially manipulated spoken commands, providing indirect evidence of LH bias when the salience of meaningful phonemic cues increased and RH bias when the salience of intonational or speaker-related vocal cues increased (*20*).

We applied functional magnetic resonance imaging to disentangle lexical versus intonational processing in awake dogs (*19*) (fig. S1). Verbal praises were used as stimuli because (i) human languages signal praise both lexically ("Well done!") and intonationally [higher pitch and pitch range, specific pitch contour (*21*)]; (ii)

[1]MTA-ELTE Comparative Ethology Research Group, Eötvös Loránd University, H-1117 Budapest, Pázmány Péter sétány 1/C, Hungary. [2]Department of Ethology, Eötvös Loránd University, H-1117 Budapest, Pázmány Péter sétány 1/C, Hungary. [3]MR Research Centre, Semmelweis University, H-1083 Budapest, Balassa u. 6, Hungary.
*Corresponding author. Email: attila.andics@gmail.com

Downloaded from http://science.sciencemag.org/ on September 1, 2016

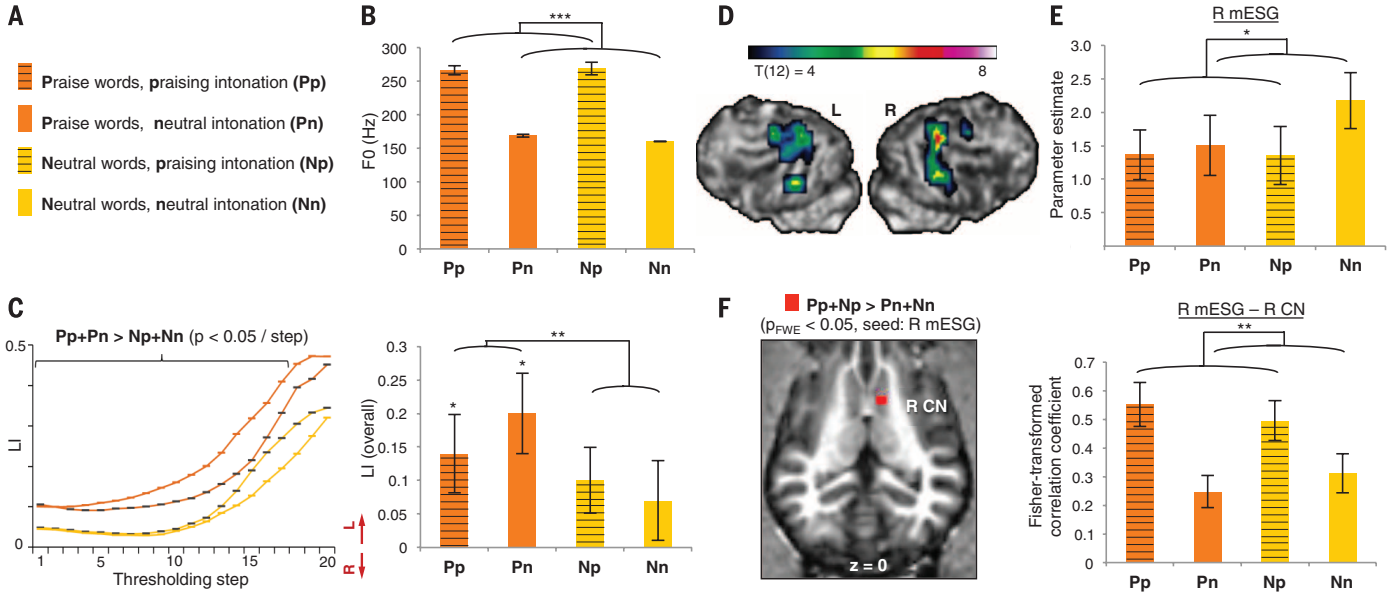


Fig. 1. Distinct neural patterns for lexical and intonation processing in dog brains. (**A**) Experimental conditions. (**B**) Acoustic variation of stimuli. (**C**) Hemispheric lateralization test. Lateralization indices (LI) are shown across thresholds (connecting lines) and overall (horizontal bars). Positive values, left hemisphere. (**D**) Dog auditory regions responsive to speech (table S2). The color bar shows the range for one-sample *t*-test scores (12 degrees of freedom) for the speech (Pp + Pn + Np + Nn) > silence contrast. (**E**) Random-effects tests in auditory regions. (**F**) Functional connectivity tests. Random-effects test results are superimposed on an axial (*z*) slice [whole-brain familywise error (FWE)–corrected $P < 0.05$]; table S4]. $N = 13$; ***$P < 0.001$; **$P < 0.01$; *$P < 0.05$; error bars, SEM.

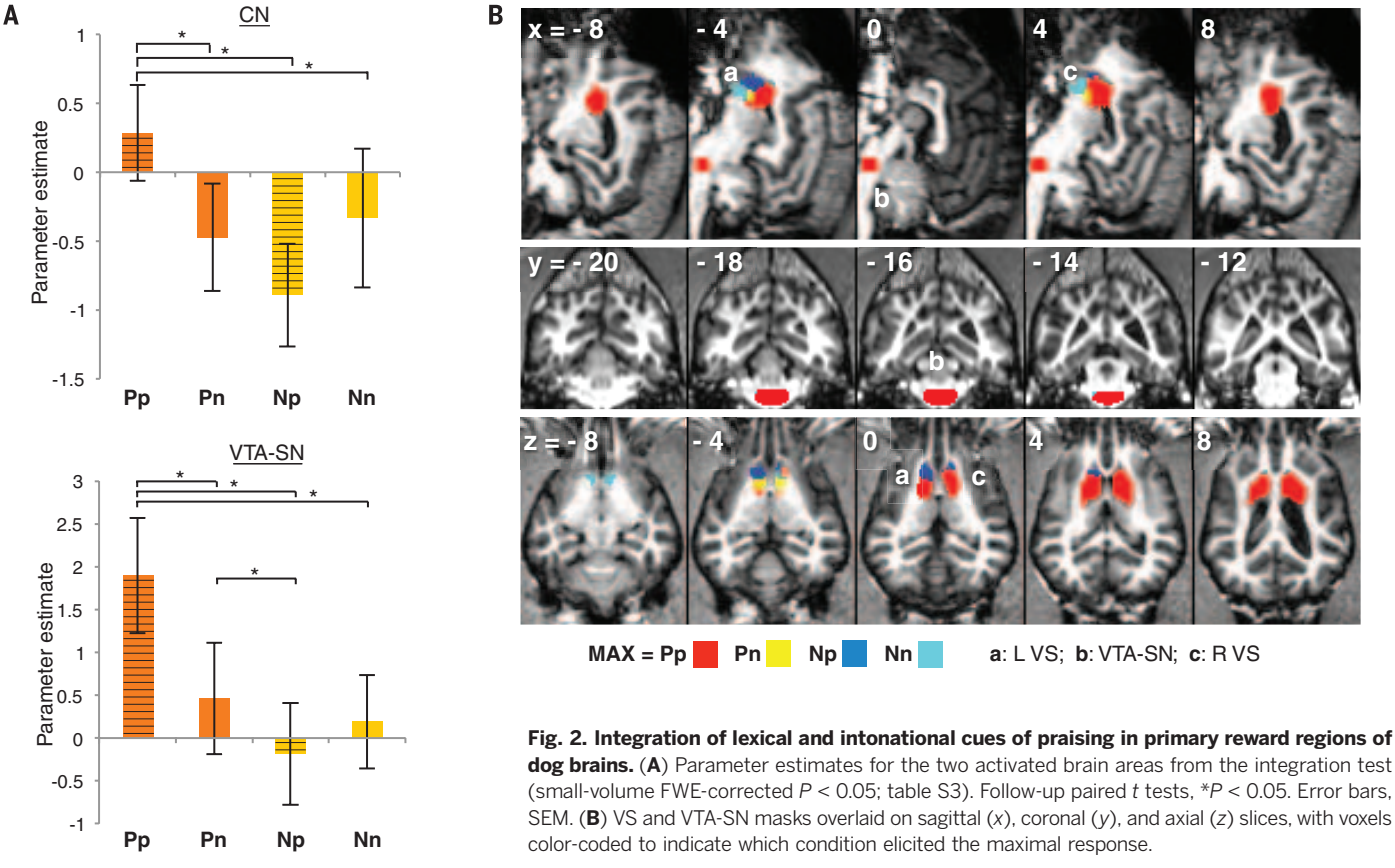


Fig. 2. Integration of lexical and intonational cues of praising in primary reward regions of dog brains. (**A**) Parameter estimates for the two activated brain areas from the integration test (small-volume FWE-corrected $P < 0.05$; table S3). Follow-up paired *t* tests, *$P < 0.05$. Error bars, SEM. (**B**) VS and VTA-SN masks overlaid on sagittal (*x*), coronal (*y*), and axial (*z*) slices, with voxels color-coded to indicate which condition elicited the maximal response.

verbal praises are often used in dog-directed speech as social rewards; and (iii) neural evidence on reward processing mechanisms is well established (*22*, *23*). Primary reward regions (the mesolimbic dopamine system), consisting of the ventral striatum (VS) and dopamine neurons of the ventral tegmental area and substantia nigra (VTA-SN) (*24*, *25*), consistently respond more strongly to reward than to nonreward signals in humans, and this is also the case in dogs (*26*).

We manipulated lexical information (marked, praise word; unmarked, neutral word) and intonation (marked, praising tone; unmarked, neutral tone) separately. Experimental conditions involved every combination of word type and

Downloaded from http://science.sciencemag.org/ on September 2, 2016

intonation (Fig. 1A): praise words in praising intonation (Pp), praise words in neutral intonation (Pn), neutral words in praising intonation (Np), and neutral words in neutral intonation (Nn). For praise words, we selected Hungarian expressions used by all test dog owners for praising. For neutral words, we used Hungarian conjunction words of similar frequency. Typically, praise but not neutral words are spoken with praising intonation, and only Pp is used to address dogs. We assumed that Pp is meaningful to dogs whereas Nn is not, and that praise words thus contain lexical cues but neutral words do not.

We hypothesized that if dogs maintain lexical representations, neural reward responses would depend on both lexical and intonational information. In contrast, if dogs do not segregate lexical information from intonation, neural reward responses would be modulated only by intonational cues. LH bias for lexical processing would be consistent with functional theories, no lateralization for lexical cues and RH bias for intonational cues would support the acoustic account, and LH bias for Pp (and perhaps Nn) relative to Pn and Np would argue for a role of familiarity.

Vocal stimuli from the dogs' female trainer were recorded. We used this single individual's voice, which was similarly well known to every dog, because speaker familiarity affects dogs' reactions to verbal utterances (*27*). Stimuli with praising intonation had a higher and more varying pitch, but no systematic acoustic differences were found between praise and neutral words (Fig. 1B). Non-Hungarian listeners scored intonationally but not lexically marked stimuli as more praising (*28*).

To assess overall lateralization, we used a bootstrapping approach with multiple cutoff thresholds (*29*) (Fig. 1C and table S1). Cortical responses for lexically marked (Pp and Pn) but not unmarked (Np and Nn) words were LH-lateralized. LH bias for lexically marked words was persistent across thresholds. There were no intonational or lexical-intonational effects. In a previous study (*19*), we found no lateralization bias for nonspeech human sounds. These findings support the functional account (*10*, *20*) and suggest that dog brains maintain intonation-independent lexical representations of meaning. Lateralization for Pp could also be related to its higher frequency in dog-directed speech, but Pn, though rare, elicits a similar LH bias, making a familiarity-based account improbable.

To investigate regional effects, we performed random-effects tests, focusing on two sets of brain areas: (i) auditory regions responsive to speech (Fig. 1D and table S2), localized functionally, and (ii) primary reward regions, VS and VTA-SN (*24*, *25*), defined anatomically (*30*). We tested for separate effects of lexical (Pp + Pn versus Np + Nn) and intonational (Pp + Np versus Pn + Nn) processing and for combined effects of lexical-intonational processing in three ways: an interaction test [(Pp versus Pn) versus (Np versus Nn)], a simple contrast or "integration" test (Pp versus Pn + Np + Nn), and a conjunction test [(Pp versus Pn)∩(Pp versus Np)].

Within auditory regions, we found intonation effects but no lexical or lexical-intonational effects. Intonation effects were only evident in the right middle ectosylvian gyrus (R mESG), with stronger responses for words with neutral intonation, independent of word meaning (Fig. 1E and table S3). We then modeled acoustic variation across stimuli, using parametric modulators. We found that R mESG activity negatively covaried with fundamental frequency (F0), paralleling findings of higher sensitivity to lower pitch in the near-primary auditory cortex in humans (*31*), macaques (*32*), and dogs (*19*). There was no intonation or F0 effect in the left homolog region (L mESG) but also no significant hemispheric bias (*2*, *28*). Unlike in human studies, we found no effect of F0 change (*33*) (table S3). In whole-brain condition-dependent functional connectivity analyses with auditory subregions as seeds, an intonation effect (stronger correlation for praising intonation) was only found between the R mESG (as the seed) and R caudate nucleus (CN; Fig. 1F and table S4). Connectivity results suggest a human-analog functional link between auditory and reward regions for processing praising intonation (*34*). The R mESG in dogs is thus involved in processing acoustic cues that are relevant for emotional intonation in both speech and nonspeech human and dog vocalizations (*19*). Analogously, emotional intonation processing in humans involves mechanisms that are not specific to speech (*35*–*37*).

In primary reward regions, we found combined lexical-intonational effects but no separate lexical or intonational effects. Pp elicited stronger neural responses than any other condition in the dopamine nuclei of the VTA-SN and in the CN (within the VS) (Fig. 2A and table S3). Dog reward regions thus respond most strongly to verbal praises when both lexical and intonational information fit. To further illustrate these findings, we calculated the maximal response for each voxel within the reward masks: Pp had the highest percentages in both the VS (Pp, Pn, Np, and Nn: 71.3, 6.2, 8.6, and 13.9%) and the VTA-SN (96.0, 0.0, 0.0, and 4.0%) (Fig. 2B). Similarly to humans, dogs appear to integrate lexical and intonational cues in speech to evaluate meaning in nonauditory brain regions (*38*).

We discovered three neural mechanisms of speech processing in dogs. First, there was a LH bias for processing meaningful words, independently of intonation. Second, acoustic cues of affective speech intonation were processed independently of word meaning in R mESG, and intonational markedness increased functional connectivity between auditory and caudate regions. Third, dogs relied on both word meaning and intonation when processing the reward value of verbal utterances. All three findings reveal functional analogies between dog and human brain mechanisms (*2*, *7*, *19*, *34*, *38*). We suggest that in a suitable ontogenetic environment, lexical representations can arise and be separated from acoustics, even in a nonprimate mammal. In dogs, specific selective forces during domestication could have also supported interspecific communicative and learning skills (*17*), but rapid evolution of speech-related hemispheric asymmetries is unlikely (*39*). Lateralized lexical processing does not appear to be a uniquely human capacity that follows from the emergence of language, but rather a more ancient function that can be exploited to link arbitrary sound sequences to meanings. What makes lexical items uniquely human is thus not the neural capacity to process them, but the invention of using them.

REFERENCES AND NOTES

1. E. F. Briefer, *J. Zool.* **288**, 1–20 (2012).
2. S. Frühholz, W. Trost, S. A. Kotz, *Neurosci. Biobehav. Rev.* **68**, 96–110 (2016).
3. M. J. Yip, *Trends Cogn. Sci.* **10**, 442–446 (2006).
4. K. Collier, B. Bickel, C. P. van Schaik, M. B. Manser, S. W. Townsend, *Proc. R. Soc. B Biol. Sci.* **281**, 20140263 (2014).
5. R. M. Seyfarth, D. L. Cheney, P. Marler, *Science* **210**, 801–803 (1980).
6. I. M. Pepperberg, H. R. Shive, *J. Comp. Psychol.* **115**, 376–384 (2001).
7. J. R. Binder, R. H. Desai, W. W. Graves, L. L. Conant, *Cereb. Cortex* **19**, 2767–2796 (2009).
8. D. Poeppel, *Speech Commun.* **41**, 245–255 (2003).
9. W. Wetzel, F. W. Ohl, H. Scheich, *Proc. Natl. Acad. Sci. U.S.A.* **105**, 6753–6758 (2008).
10. Y. Shtyrov, E. Pihko, F. Pulvermüller, *Neuroimage* **27**, 37–47 (2005).
11. A. Poremba *et al*., *Nature* **427**, 448–451 (2004).
12. G. Ehret, *Nature* **325**, 249–251 (1987).
13. H. U. Voss *et al*., *Proc. Natl. Acad. Sci. U.S.A.* **104**, 10667–10672 (2007).
14. P. Pongrácz, C. Molnár, A. Miklósi, *Vet. J.* **183**, 141–147 (2010).
15. J. M. Gibson, S. A. Scavelli, C. J. Udell, M. A. R. Udell, *Anim. Behav. Cogn.* **1**, 281–295 (2014).
16. Á. Miklósi, J. Topál, V. Csányi, *Anim. Behav.* **67**, 995–1004 (2004).
17. J. Topál, G. Gergely, A. Erdőhegyi, G. Csibra, A. Miklósi, *Science* **325**, 1269–1272 (2009).
18. J. Kaminski, J. Call, J. Fischer, *Science* **304**, 1682–1683 (2004).
19. A. Andics, M. Gácsi, T. Faragó, A. Kis, A. Miklósi, *Curr. Biol.* **24**, 574–578 (2014).
20. V. F. Ratcliffe, D. Reby, *Curr. Biol.* **24**, 2908–2912 (2014).
21. A. Fernald, *Child Dev.* **60**, 1497–1510 (1989).
22. W. Schultz, P. Dayan, P. R. Montague, *Science* **275**, 1593–1599 (1997).
23. J. P. O'Doherty, *Curr. Opin. Neurobiol.* **14**, 769–776 (2004).
24. S. N. Haber, B. Knutson, *Neuropsychopharmacology* **35**, 4–26 (2010).
25. S. J. Russo, E. J. Nestler, *Nat. Rev. Neurosci.* **14**, 609–625 (2013).
26. G. S. Berns, A. Brooks, M. Spivak, *PLOS ONE* **8**, e81698 (2013).
27. A. Kerepesi, A. Dóka, Á. Miklósi, *Behav. Processes* **110**, 27–36 (2015).
28. Materials and methods are available as supplementary materials on *Science* Online.
29. M. Wilke, V. J. Schmithorst, *Neuroimage* **33**, 522–530 (2006).
30. H. E. Evans, A. de Lahunta, *Miller's Anatomy of the Dog* (Saunders-Elsevier, ed. 4, 2013).
31. S. Norman-Haignere, N. Kanwisher, J. H. McDermott, *J. Neurosci.* **33**, 19451–19469 (2013).
32. D. Bendor, X. Wang, *Nature* **436**, 1161–1165 (2005).
33. D. Wildgruber, H. Ackermann, B. Kreifelts, T. Ethofer, *Prog. Brain Res.* **156**, 249–268 (2006).
34. V. N. Salimpoor *et al*., *Science* **340**, 216–219 (2013).
35. D. A. Sauter, F. Eisner, P. Ekman, S. K. Scott, *Proc. Natl. Acad. Sci. U.S.A.* **107**, 2408–2412 (2010).
36. T. Faragó *et al*., *Biol. Lett.* **10**, 20130926 (2014).
37. P. Belin *et al*., *Proc. R. Soc. B Biol. Sci.* **275**, 473–481 (2008).
38. S. A. Kotz, S. Paulmann, *Lang. Linguist. Compass* **5**, 108–125 (2011).
39. M. C. Corballis, *PLOS Biol.* **12**, e1001767 (2014).

ACKNOWLEDGMENTS

The study was supported by the Hungarian Academy of Sciences [Bolyai Scholarship to A.A. and a grant to the MTA-ELTE Comparative Ethology Research Group (F01/031)], the Hungarian Scientific Research Fund (OTKA; grants K100695, K115862, and PD116181), and the Stanton Foundation (Next Generation Canine Research Grant to T.F.). We thank F. Szalay for anatomy advice, and we thank all dog owners. Data are stored at Figshare (http://dx.doi.org/10.6084/m9.figshare.3436538).

SUPPLEMENTARY MATERIALS

www.sciencemag.org/content/353/6303/1030/suppl/DC1
Materials and Methods
Fig. S1
Tables S1 to S4
References (*40*–*43*)

1 February 2016; accepted 28 July 2016
Published online 30 August 2016
10.1126/science.aaf3777

Downloaded from http://science.sciencemag.org/ on September 2, 2016

DENGUE VACCINE

Benefits and risks of the Sanofi-Pasteur dengue vaccine: Modeling optimal deployment

Neil M. Ferguson,[1]*† Isabel Rodríguez-Barraquer,[2]* Ilaria Dorigatti,[1] Luis Mier-y-Teran-Romero,[2] Daniel J. Laydon, Derek A. T. Cummings[2,3]

The first approved dengue vaccine has now been licensed in six countries. We propose that this live attenuated vaccine acts like a silent natural infection in priming or boosting host immunity. A transmission dynamic model incorporating this hypothesis fits recent clinical trial data well and predicts that vaccine effectiveness depends strongly on the age group vaccinated and local transmission intensity. Vaccination in low-transmission settings may increase the incidence of more severe "secondary-like" infection and, thus, the numbers hospitalized for dengue. In moderate transmission settings, we predict positive impacts overall but increased risks of hospitalization with dengue disease for individuals who are vaccinated when seronegative. However, in high-transmission settings, vaccination benefits both the whole population and seronegative recipients. Our analysis can help inform policy-makers evaluating this and other candidate dengue vaccines.

The first dengue vaccine, the product of a 20-year development process by Sanofi Pasteur Ltd., has now been approved for use in six countries. Its development was considerably more challenging than for other flavivirus infections because of the immunological interactions between the four dengue virus (DENV) serotypes and the risk of immune-mediated enhancement of disease (*1*–*3*). Individuals experiencing their second natural DENV infection have a higher risk, by more than sixfold, of severe disease compared with those experiencing primary infection (*4*, *5*), which is hypothesized to be due to heterotypic antibody-dependent enhancement (*4*). If future trials are to avoid similar consequences, the ideal DENV vaccine should generate a balanced protective response against each of the four serotypes (*1*).

The Sanofi-Pasteur vaccine, Dengvaxia, a recombinant chimeric live attenuated DENV vaccine based on a yellow fever 17D vaccine backbone, was evaluated in two large multicenter phase 3 trials. One trial was conducted in Southeast Asia (*6*), among ~10,000 children aged 2 to 14 years, and the other in Latin America (*7*), among ~21,000 children aged 9 to 16 years. Both trials reported efficacy of ~60% against virologically confirmed symptomatic dengue disease (the primary outcome), as well as higher efficacy against severe dengue and variation in efficacy by serotype (*6*–*8*). The trials also revealed high efficacy in recipients who were seropositive to DENV at the time of vaccination, but much lower (and statistically insignificant) efficacy in those who were seronegative at the time of vaccination. Both trials also found lower vaccine efficacies in younger age groups—a pattern consistent with reduced efficacy in individuals who have not lived long enough to experience a natural infection.

Reduced efficacy in seronegative recipients initially indicates that it would be beneficial, but not essential, to optimize the target age group when developing vaccination programs. However, in July 2015, long-term follow-up results for the third year of the trial showed that vaccinees in the youngest age group (2- to 5-year-olds) of the Asian trial had a substantially and significantly higher risk of hospitalization for virologically confirmed dengue disease than controls had (*9*). In other age groups (in both trials), the vaccine was still protective against hospitalization, albeit efficacy was lower than that seen in the active phase of the trial [see supplementary materials (*10*)]. Immunogenicity data (*11*–*18*) have shown that seropositive vaccine recipients attain high and sustained antibody levels after the first dose of vaccine, whereas peak antibody levels in seronegative recipients are on average a factor of 10 lower and show rapid decay, apparent even between vaccine doses (*18*). Serological data were only collected from a subset of participants in each phase 3 trial, so it is not possible to determine whether the risk excess seen in the 2- to 5-year-old age group is driven by the effect of vaccine in the large proportion of seronegative recipients in this age group, but at present, this appears to be the most plausible explanation (*19*).

These trial results pose challenges in considering how best to use the vaccine. The heterogeneities in the efficacy profile—combined with the uncertainties regarding the vaccine's mechanism of action (*20*) and the underlying complexity of DENV epidemiology and transmission dynamics—make it far from simple to extrapolate from the trial results to predict the potential impact of wide-scale use of this vaccine.

We therefore developed mathematical models of DENV transmission (*10*) to explore hypotheses about vaccine action and to examine the potential consequences for the impact of routine use of this vaccine. Given the trial results (see table S1), any model needs to incorporate waning of efficacy over time. Hence, we fitted a "simple" model to the publicly available trial data (*6*–*8*), where efficacy was allowed to decay from an initial high value to some lower long-term value, with these efficacy values assumed to be different for seropositive and seronegative vaccine recipients. The resulting parameter estimates and poor overall fit (table S5 and fig. S5) led us to propose a more biologically motivated model, in which the immunological effect of vaccination is comparable to a silent natural infection (fig. S1). Seronegative recipients gain transient protective cross-reactive immunity akin to that observed for natural infection (*21*–*23*). After this protection decays, lower concentrations of heterotypic antibodies increase the risk of severe disease upon a breakthrough primary infection to the same level seen for secondary infections in nonvaccinees (*4*, *5*). Conversely, vaccination of recipients who have already had one DENV infection results in a boosting of immunity to levels comparable with someone who has had two natural infections, and their next infection will not have the higher severity associated with natural secondary infections, but rather, the much lower risk of severe disease associated with tertiary and quaternary (postsecondary) infections (*24*).

This model fitted well the patterns seen in both the active and long-term follow-up phases of the phase 3 clinical trial, including the variation in vaccine efficacy by age, serostatus at the time of vaccination, and time since vaccination (Fig. 1). The poorest aspect of model fit is to the sevenfold greater incidence of hospitalization with dengue seen in 2- to 5-year-old vaccine recipients compared with controls in the first year of the long-term follow-up in the Asian trial. However, model predictions lie within the confidence bounds of the data, and the model successfully reproduces a relative risk >1 for vaccine recipients compared with controls in that age group. Indeed, had the long-term follow-up data on the effects of vaccination in the 2- to 5-year-old age group not been included, our model would still have predicted a relative risk >1 in that age group, based on trends seen in the other age groups and the results of the active phase (table S4).

Consistent with prior knowledge (*5*), our parameter estimates indicated that secondary infections are about twice as likely to cause symptomatic infection as either primary or postsecondary infections (table S3). In addition, we estimated that the vaccine initially induces near-perfect heterologous protection in seronegative recipients but that this decays rapidly, with a mean duration of 7 months [95% credible interval (CI) of 4 to 11 months]. Our analysis did not resolve the extent to which such transient heterologous

[1]MRC Centre for Outbreak Analysis and Modelling, School of Public Health, Imperial College London, Norfolk Place, London W2 1PG, UK. [2]Department of Epidemiology, Johns Hopkins Bloomberg School of Public Health, 615 North Wolfe Street, Baltimore, MD 21205, USA. [3]Department of Biology and Emerging Pathogens Institute, University of Florida, Post Office Box 100009, Gainesville, FL 32610, USA.
*These authors contributed equally to this work. †Corresponding author. Email: neil.ferguson@imperial.ac.uk

Downloaded from http://science.sciencemag.org/ on September 2, 2016

protection is induced in seropositive recipients; the modal posterior estimate of the efficacy of such protection is 0 but the 95% CI spans 0 to 100%.

To predict the implications of our model of vaccine responses on the effectiveness of immunization policies, we simulated the effect of routine vaccination at 80% coverage, and explored the effect of varying the age at vaccination between 2 and 18 years of age. We deliberately examined ages below the 9-year minimum age approved by regulators to give greater insight into the interaction between age, transmission intensity, seroprevalence, and the impact of vaccination on dengue disease. Owing to the dependence of efficacy on serostatus at the time of vaccination, the impact of the vaccine critically depends on the proportion of the target age group who have experienced 0, 1, or more natural DENV infections before vaccination. Therefore, we quantify transmission intensity as the long-term average of the proportion of 9-year-olds who are seropositive. This metric maps monotonically onto the more commonly used metric of the basic reproduction number, R_0 (fig. S3), but has the advantages of being directly related to the key driver of vaccine efficacy (i.e., serostatus), which is readily measurable and interpretable and not dependent on specific model assumptions (*25*).

The predicted mean population impact of routine vaccination on symptomatic dengue disease and case incidence of hospitalization with dengue over 10- and 30-year periods is shown in Fig. 2. In high-transmission settings, vaccination is associated with modest (20 to 30%) reductions in both symptomatic disease and hospitalization. For a specific level of transmission, there is an optimal age of vaccination that decreases as transmission intensity increases. Although short-term (10-year) impacts are generally positive, over longer periods of time (30 years), vaccination may have positive or negative impacts on the incidence of symptomatic dengue disease and hospitalized dengue. This is particularly true in low-transmission settings. Vaccination is more likely to have a negative outcome for hospitalized dengue than symptomatic dengue as secondary or secondary-like infections (i.e., primary infections in vaccine recipients) have an approximately eightfold higher risk of hospitalization than primary infections but only a twofold higher risk of uncomplicated symptomatic disease (*10*, *26*).

The population-level impacts of vaccination hide enormous heterogeneity in benefits and risks at the level of the individual recipient (Fig. 3, A and B): Seropositive recipients always gain a substantial benefit from vaccination (>90% reduction in the risk of being hospitalized with dengue), whereas seronegative recipients experience an increased risk of being hospitalized with dengue. This is true both in the short-term (see supplementary materials) and in the long-term and raises fundamental issues about individual versus population benefits of vaccination. The increase in risk is greatest for low-transmission settings, where a substantial fraction of seronegative recipients would not normally experience a natural secondary infection. Conversely, in the highest-transmission settings, the main effect of vaccination on seronegative individuals is to bring forward in time the more severe secondary-like infection that they would have eventually naturally experienced. This, combined with a small indirect effect of vaccination on reducing transmission, leads to a small overall positive benefit to all recipients in high-transmission settings. Restricting the minimum licensed age of use of the vaccine to 9 years mitigates, but does not remove, the risk of negative population-level impacts in low-transmission settings where the majority of 9-year-olds are still seronegative. Conversely, in high-transmission settings, the optimal age to target for vaccination can be below 9 years.

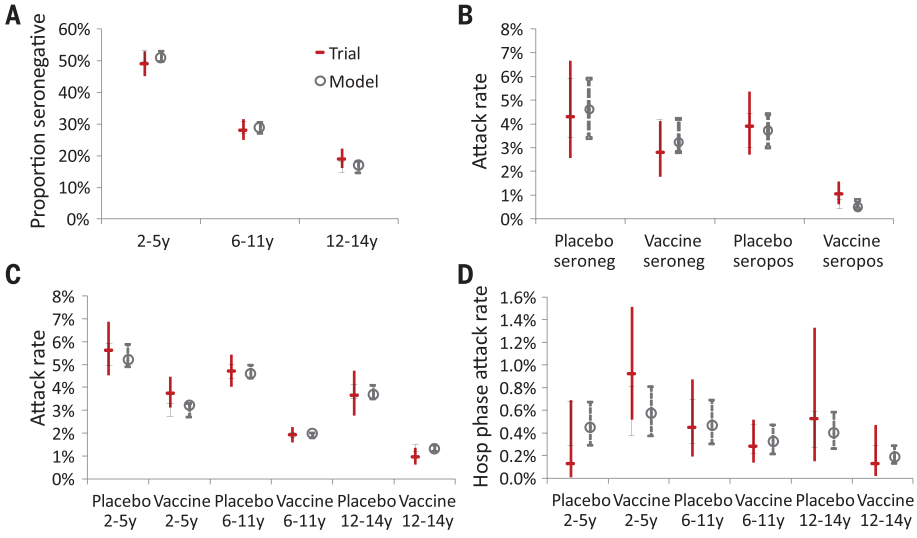


Fig. 1. Model fit to publicly available data from the Asian phase 3 clinical trial. See (*6*). Modal (best-fit) estimate and 95% credible intervals for four conditions. (**A**) Proportion of participants of the immunological subset of the trial who were seronegative at the time of receiving their first dose, by age. (**B**) Attack rate of virologically confirmed symptomatic dengue in immunological subset in first 2 years after dose 1 by trial arm and baseline serostatus. (**C**) Attack rate of virologically confirmed symptomatic dengue in all trial participants in first 2 years after dose 1 by trial arm and age group. (**D**) Attack rate of virologically confirmed hospitalization with dengue disease in all trial participants in third year after dose 1 (first year of long-term follow-up) by trial arm and age group. Fit to Latin American trial shown in the supplementary materials (*10*).

The vaccination policies that risk producing adverse outcomes can therefore be defined. The minimum average prevaccination seroprevalence required to avoid negative impacts is shown in Figure 3C from both the individual and population perspectives. An overall negative impact on the entire population can be avoided by choosing a target age for vaccination in which average seroprevalence exceeds ~35%. In contrast, it is harder to avoid an increased risk of hospitalization for individuals who are seronegative when vaccinated. Doing so requires that the indirect effects of vaccination in reducing overall dengue transmission exceed the increased risk of disease which vaccination causes in seronegative individuals via immune priming. Over a period of 30 years, this is only possible in high–transmission intensity settings when $R_0 > 3$ or seroprevalence in 9-year-olds exceeds ~70%. Only for the youngest age of vaccination considered (2 years, below the licensed minimum age) do population and individual thresholds converge. In part based on the modeling presented here, the World Health Organization's Strategic Group of Experts on Immunization has recently recommended population serological surveys be undertaken in populations where the vaccine is being considered for use and that vaccination is only recommended where seroprevalence in the targeted age group exceeds 50% (and preferably 70%) (*27*).

Serological testing of individuals offers an alternative solution to mitigate the potential risks and to maximize the benefits of dengue vaccination; rapid diagnostic tests could be used to screen potential vaccine recipients, with only seropositive individuals being vaccinated. Indeed, data from immunogenicity studies suggest that a single-dose vaccination schedule might be enough to achieve protective immunity in seropositive individuals. Such a policy could result in up to a 30% reduction in the incidence of hospitalization for dengue and a much-reduced risk of negative outcomes (Fig. 4A) after vaccinating only a fraction (those testing seropositive) of the target age group (Fig. 4B). Although such a policy would be logistically challenging in the context of mass vaccination campaigns, it should not be ruled out—if the cost of testing can be reduced to a level comparable with the cost of buying and delivering a single vaccine dose, such a strategy is likely to have substantially greater cost-effectiveness than the current three-dose strategy without testing. Using serological testing to inform vaccination decisions is not an entirely novel concept, as it has been recommended for pregnant women in relation to rubella and hepatitis B vaccination (*28*, *29*).

Because vaccination only transiently reduces the risk of infection and the main effect of vaccination

Downloaded from http://science.sciencemag.org/ on September 2, 2016

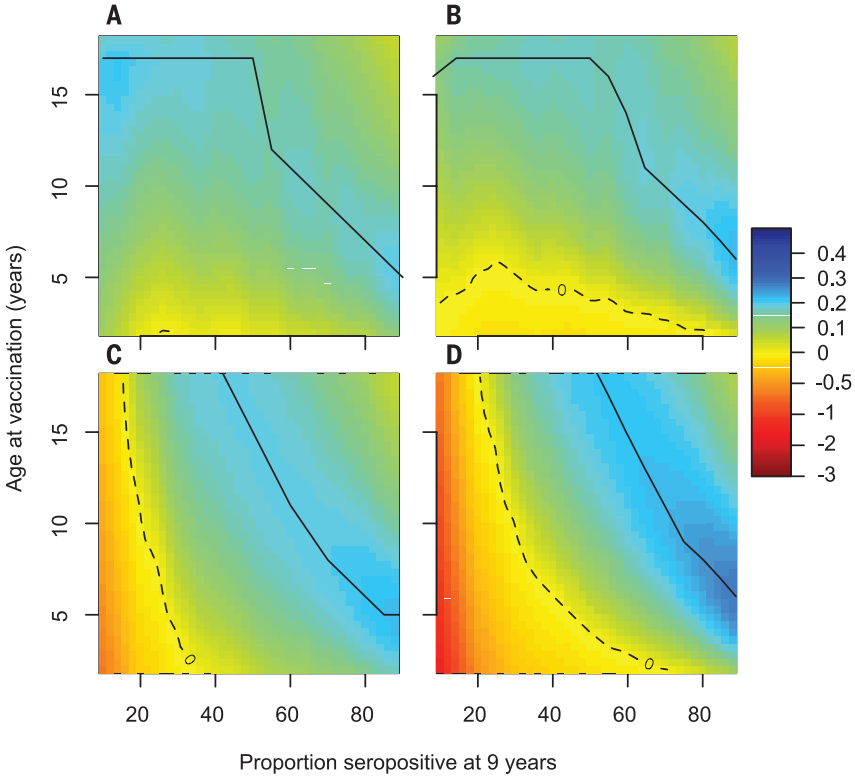


Fig. 2. Predicted population effects of vaccination on dengue disease for a range of transmission intensities (*x* axes) and ages of vaccination (*y* axes). Color scale indicates proportion of cases averted in the whole population (**A**) over 10 years, for all symptomatic dengue; (**B**) over 10 years, for participants hospitalized with dengue; (**C**) over 30 years, for all symptomatic dengue; and (**D**) over 30 years, for hospitalization with dengue. Negative proportions of cases averted indicate vaccination increases risk. Solid contours indicate the optimal age of vaccination for each transmission intensity. Dashed contours indicate the youngest age group that may be targeted to avoid negative effects at the population level.

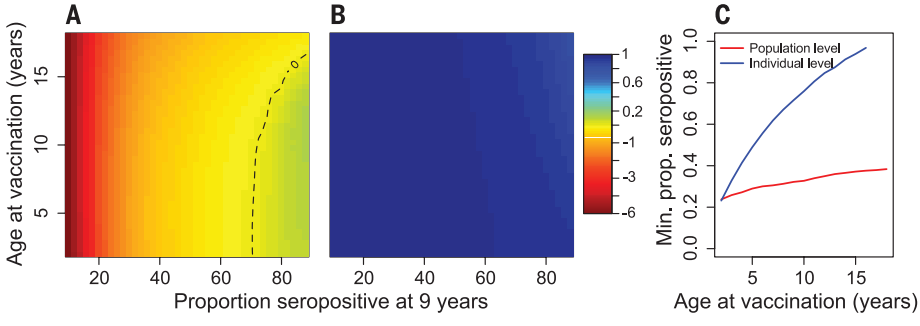


Fig. 3. Predicted individual effects of vaccination over 30 years. Proportion of hospitalized cases averted among individual vaccine recipients who are vaccinated: (**A**) when seronegative and (**B**) when seropositive. Dashed contour indicates the youngest age group that may be targeted to avoid negative effects at the individual level. (**C**) Minimum proportion of the age group (1-year age bands) targeted for routine vaccination that should be seropositive at the time of vaccine introduction to avert negative impacts (over a 30-year time frame) at the population (red) and individual (blue) level.

is to modify the risk of disease, our findings predict that the indirect effect of vaccination on DENV transmission will be limited. This explains why we found that the predicted impacts of routine vaccination (whether positive or negative) scale almost linearly with vaccine coverage. Our default assumption was that symptomatic infections are twice as infectious as asymptomatic infections, which leads to vaccination slightly reducing transmission in high–transmission intensity settings but slightly increasing transmission in low-transmission settings. Making the alternative assumption that all infections are equally infectious reduces the chance and magnitude of negative impacts of vaccine for low-transmission intensities but also reduces the positive impacts of vaccination when transmission intensity is high (figs. S9 and S10).

Our results also show that the effectiveness of vaccination would be expected to vary over time (figs. S6 to S8). In low-transmission settings, the introduction of vaccination could perturb transmission dynamics and lead to transient reductions in dengue disease incidence for 5 to 10 years. Only when the transmission dynamics reequilibrate are the long-term impacts seen. From the individual perspective, it is also important to consider the effect of vaccination on the cumulative lifetime risk of dengue disease and hospitalization. Among seronegative recipients, reductions in risk resulting from short-term vaccine-induced protection might exceed later increases in risk resulting from vaccine-induced immunological priming. This is particularly true in high-transmission settings where, in the absence of vaccination, nearly everyone experiences secondary infection with dengue at some point in their lives. Special consideration should be given to the policy and ethical considerations of shifting infections and/or symptomatic episodes among individuals to different times in their lives.

Our analysis has several limitations. We were not able to estimate serotype-specific efficacy parameters. Owing to cross-reactive immunity, in any one year, DENV incidence in single populations tends to be dominated by a single serotype, which is reproduced by our transmission model. However, the phase 3 trials showed substantial attack rates from all four serotypes, but underpinning this was much greater heterogeneity in serotype-specific attack rates between the countries contributing to the trial. To capture observed serotype-specific attack rates it is necessary to fit country- and serotype-specific trial data, which are not currently publicly available (*30*). However, in the supplementary materials (*10*), we show how the apparent serotype-specific efficacies seen may reflect differences between serotypes in the propensity to cause disease in primary, secondary, and postsecondary infection rather than actual differences in (serostatus-specific) efficacy (fig. S12). Including such asymmetry does not qualitatively affect model predictions (figs. S13 and S14). We also do not consider persistent variation in exposure to DENV at the individual or neighborhood level; if substantial proportions of the population consistently experience lower or higher levels of exposure than the average throughout their lives, then both the risks (to the low-exposure group) and benefits (to the high-exposure group) of vaccination may be larger than we estimate here. Although characterizing real-world levels of exposure heterogeneity is difficult, this issue should be a priority for future work.

All efficacy outcomes measured in the trial were based on clinically apparent disease, so we are currently unable to resolve whether the vaccine protects against infection or just against disease (*20*, *31*). Our baseline model assumes a combination of both—short-lived protection against infection, followed by a long-lived modification of future disease risk. We are also unable to assess the impact of breakthrough infections on vaccine-acquired immunity. If vaccination truly acts as a silent infection, then breakthrough infections in

Downloaded from http://science.sciencemag.org/ on September 2, 2016

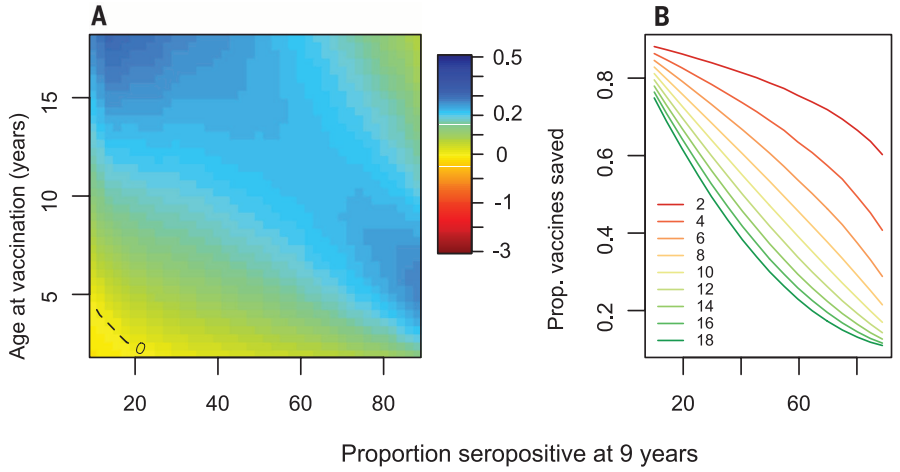


Fig. 4. Expected population effects of vaccination if vaccination is preceded by serological testing (with a rapid test assumed to have 90% sensitivity and specificity) and only individuals who test seropositive for dengue are vaccinated. For the population, 80% coverage is assumed. (**A**) Proportion of hospitalizations averted over a 30-year period for different transmission intensities and target age at vaccination. (**B**) Proportion of vaccine doses saved (*y* axis) if only seropositive individuals are targeted, for different transmission intensities (*x* axis) and target ages (different curves).

seronegative vaccinees should induce a broadly multitypic and protective immune response (akin to unvaccinated individuals who have experienced two natural infections)—our current model assumption. Understanding any differences between naturally and vaccine-acquired immunity will be critical in assessing the overall impact of vaccination on this group. In addition, although not required to reproduce the main trends seen in the trial, variation of efficacy with age cannot be ruled out. If vaccine efficacy were lower in younger age groups, independent of serostatus, the predicted outcomes of vaccination programs targeting older children would increase, particularly in lower-transmission settings. Last, in the modeling presented here, we assumed that vaccine-induced protection in seropositive individuals is long-lasting—future data may allow this optimistic assumption to be tested.

Successful licensing of the first vaccine against a major global pathogen is a significant achievement. However, the dependence of vaccine efficacy on prior immunity presents challenges to planning large-scale use. Other recent modeling efforts have predicted impacts of vaccination that are more beneficial than those presented here but used models that were not fit to the data from the clinical trial (*32*) or the long-term follow-up (*30*). Our analysis indicates that to maximize the population impact of vaccination and to prevent negative impacts, it will be necessary to carefully tailor vaccination strategies to local epidemiological conditions. Our results indicate that the vaccine should only be used in moderate- to high-transmission settings, at least until more data are available to clarify the extent to which the vaccine primes seronegative recipients for a higher risk of hospitalized disease. Careful selection of the age group to target for routine vaccination can maximize benefits, but our current estimates indicate that in all but the highest-transmission settings, use of this vaccine may lead to an increase in the risk of hospitalization for dengue in seronegative recipients even if the overall impact of vaccination is positive. We predict routine vaccination will cause, at most, moderate (10 to 20%) reductions in disease incidence, so it is important to set realistic expectations of impact for the policymakers and populations of countries likely to implement such policies. Population serosurveys can mitigate risks in planning routine vaccination, but individual serological testing, if feasible, might radically improve the benefit-risk trade-off.

The partial efficacy of this vaccine raises the question of how its use might be combined with more effective vector control measures [e.g., using new technologies, such as *Wolbachia* (*33*) to achieve greater overall public health impact]. Careful modeling of combined intervention strategies is a priority for future work, but a priori, the efficacy profile of this vaccine suggests the need for caution. If new vector control interventions substantially reduce (but do not eliminate) dengue transmission, population seroprevalence will decline over time. Unless vaccination strategies account for such effects, introduction of routine immunization against a background of recently substantially enhanced vector control may pose the same long-term risks of negative impacts of vaccination that we predict for vaccine use in other settings having low transmission intensity.

Efficacy data for the other DENV vaccine candidates under development are not yet available, but all candidates show similar differences in immunogenicity by prior serostatus to those seen for the Sanofi-Pasteur vaccine (*34*, *35*). Therefore, even though there are potentially relevant structural differences between the candidates, it is feasible that they may share similar efficacy profiles. Therefore, our analysis may have application beyond the Sanofi vaccine. More generally, our work and that undertaken for the RTS,S malaria vaccine (*36*) reinforce the value of modeling in interpreting trial results and planning how best to use partially effective vaccines with complex efficacy profiles.

REFERENCES AND NOTES

1. J. R. Stephenson, *Bull. World Health Organ.* **83**, 308–314 (2005).
2. R. Edelman, J. Hombach, *Vaccine* **26**, 4113–4119 (2008).
3. B. R. Murphy, S. S. Whitehead, *Annu. Rev. Immunol.* **29**, 587–619 (2011).
4. S. B. Halstead, *Prog. Allergy* **31**, 301–364 (1982).
5. D. S. Burke, A. Nisalak, D. E. Johnson, R. M. Scott, *Am. J. Trop. Med. Hyg.* **38**, 172–180 (1988).
6. M. R. Capeding *et al.*, *Lancet* **384**, 1358–1365 (2014).
7. L. Villar *et al.*, *N. Engl. J. Med.* **372**, 113–123 (2015).
8. A. Sabchareon *et al.*, *Lancet* **380**, 1559–1567 (2012).
9. S. R. Hadinegoro *et al.*, *N. Engl. J. Med.* **373**, 1195–1206 (2015).
10. Supplementary materials are available on *Science* Online.
11. L. Á. Villar *et al.*, *Pediatr. Infect. Dis. J.* **32**, 1102–1109 (2013).
12. G. H. Dayan *et al.*, *Am. J. Trop. Med. Hyg.* **89**, 1058–1065 (2013).
13. Y. Sin Leo *et al.*, *Hum. Vaccin. Immunother.* **8**, 1259–1271 (2012).
14. C. F. Lanata *et al.*, *Vaccine* **30**, 5935–5941 (2012).
15. R. Z. Capeding *et al.*, *Vaccine* **29**, 3863–3872 (2011).
16. D. Morrison *et al.*, *J. Infect. Dis.* **201**, 370–377 (2010).
17. I. Dorigatti *et al.*, *Vaccine* **33**, 3746–3751 (2015).
18. M. R. Capeding, T. M. Laot, M. Boaz, T. A. Wartel, D. Crevat, *Trials Vaccinol.* **4**, 19–23 (2015).
19. B. Guy, N. Jackson, *Nat. Rev. Microbiol.* **14**, 45–54 (2016).
20. I. Rodríguez-Barraquer, L. Mier-y-Teran-Romero, D. S. Burke, D. A. T. Cummings, *PLOS Negl. Trop. Dis.* **7**, e2126 (2013).
21. T. J. Kochel *et al.*, *J. Infect. Dis.* **191**, 1000–1004 (2005).
22. A. B. Sabin, *Am. J. Trop. Med. Hyg.* **1**, 30–50 (1952).
23. A. B. Sabin, *Bacteriol. Rev.* **14**, 225–232 (1950).
24. S. Olkowski *et al.*, *J. Infect. Dis.* **208**, 1026–1033 (2013).
25. P. S. Wikramaratna, C. P. Simmons, S. Gupta, M. Recker, *PLOS ONE* **5**, e12347 (2010).
26. A. Nisalak *et al.*, *Am. J. Trop. Med. Hyg.* **68**, 191–202 (2003).
27. Strategic Advisory Group of Experts on Immunization, "Summary of the April 2016 meeting of the Strategic Advisory Group of Experts on Immunization (SAGE)," Geneva, Switzerland, 12 to 14 April 2016 (SAGE, WHO, Geneva, 2016); http://www.who.int/immunization/sage/meetings/2016/april/SAGE_April_2016_Meeting_Web_summary.pdf?ua=1.
28. H. Q. McLean, A. P. Fiebelkorn, J. L. Temte, G. S. Wallace, *MMWR Recomm. Rep.* **62** (RR-04), 1–34 (2013).
29. Centers for Disease Control and Prevention, *Morb. Mortal. Wkly. Rep.* **37**, 341–346 (1988)
30. L. Coudeville, N. Baurin, E. Vergu, *Vaccine* 10.1016/j.vaccine.2015.11.023 (2015).
31. I. Rodríguez-Barraquer, L. Mier-y-Teran-Romero, N. Ferguson, D. S. Burke, D. A. T. Cummings, *Lancet* **385**, 1726 (2015).
32. T. J. Hladish *et al.*, *PLOS Negl. Trop. Dis.* **10**, e0004661 (2016).
33. N. M. Ferguson *et al.*, *Sci. Transl. Med.* **7**, 279ra37 (2015).
34. C. Sirivichayakul *et al.*, *J. Infect. Dis.* **213**, 1562–1572 (2016).
35. B. D. Kirkpatrick *et al.*, *J. Infect. Dis.* **212**, 702–710 (2015).
36. M. A. Penny *et al.*, *Lancet* **387**, 367–375 (2016).

ACKNOWLEDGMENTS

The authors acknowledge research funding from the UK Medical Research Council, the UK National Institute of Health Research under the Health Protection Research Unit initiative, National Institute of Allergy and Infectious Diseases and National Institute of General Medical Sciences (NIH) under the MIDAS initiative, and the Bill and Melinda Gates Foundation. Views expressed do not necessarily represent those of the funders. N.M.F., I.R.-B., and D.A.T.C. have advised Sanofi Pasteur Ltd., without payment, on the implications that this work has on the use of their vaccine. We thank N. Grassly for comments on the manuscript and N. Jackson and L. Coudeville at Sanofi Pasteur for useful discussions. All clinical trial data used for these models are publicly available in the original publications (cited), and model code is available from the authors.

SUPPLEMENTARY MATERIALS

www.sciencemag.org/content/353/6303/1033/suppl/DC1
Materials and Methods
Supplementary Text
Figs. S1 to S14
Tables S1 to S5
References (*37*–*54*)

25 April 2016; accepted 29 July 2016
10.1126/science.aaf9590

Downloaded from http://science.sciencemag.org/ on September 2, 2016

NEURODEVELOPMENT

De novo synaptogenesis induced by GABA in the developing mouse cortex

Won Chan Oh,[1] Stefano Lutzu,[2] Pablo E. Castillo,[2] Hyung-Bae Kwon[1,3]*

Dendrites of cortical pyramidal neurons contain intermingled excitatory and inhibitory synapses. We studied the local mechanisms that regulate the formation and distribution of synapses. We found that local γ-aminobutyric acid (GABA) release on dendrites of mouse cortical layer 2/3 pyramidal neurons could induce gephyrin puncta and dendritic spine formation via GABA type A receptor activation and voltage-gated calcium channels during early postnatal development. Furthermore, the newly formed inhibitory and excitatory synaptic structures rapidly gained functions. Bidirectional manipulation of GABA release from somatostatin-positive interneurons increased and decreased the number of gephyrin puncta and dendritic spines, respectively. These results highlight a noncanonical function of GABA as a local synaptogenic element shaping the early establishment of neuronal circuitry in mouse cortex.

The spatial arrangement of synapses determines the functional consequences of excitation and inhibition for synaptic integration, action potential generation, and repetitive activity (*1*–*5*). The initial processes of synapse formation are regulated by genetically programmed intrinsic mechanisms; later, synapses are further shaped by neuronal activity (*6*). Recently, a fine-scale optical approach using two-photon laser scanning microscopy and two-photon laser photoactivation revealed the processes of individual excitatory synapse formation in real time and the underlying signaling pathways in various brain regions such as the neocortex, hippocampus, and basal ganglia (*7*–*9*). However, the spatiotemporal mechanisms that govern activity-dependent de novo inhibitory synapse formation in a developing circuit remain poorly understood. Here, we used two-photon GABA photolysis to deliver spatiotemporally controlled patterns of GABA release in mouse dendrites and monitored how GABA release influences synapse formation. These activity-induced processes were visualized as gephyrin puncta and dendritic spines, which are inhibitory and excitatory synapse markers, respectively (fig. S1) (*10*, *11*).

We first examined the total number of gephyrin puncta along the apical and basal dendrites in organotypic slice cultures during normal development. Both gephyrin puncta and dendritic spines rapidly increased between EP6–8 and EP10–12 [EP (equivalent postnatal) day = postnatal day at slice culturing + days in vitro] (fig. S2), and these changes were not affected by Teal fluorescent protein fused to gephyrin (Teal-gephyrin) expression (fig. S3). A similar timeline of gephyrin puncta and dendritic spine formation was observed in vivo (fig. S4). These data indicate that the synapse-forming machinery operates efficiently in our experimental system. On the basis of these results, we focused on oblique dendrites localized >70 μm away from the soma at ages EP6 to EP8 for the following synaptogenesis experiments.

Because the timing and location of GABA release can be controlled with high spatial and temporal resolution (fig. S5) (*12*), we examined how local GABA release influences synaptogenesis. Repetitive GABA release [high-frequency uncaging (HFU); 60 times at 10 Hz, duration 2 ms] effectively induced the formation of gephyrin clusters, with a success rate of ~48% (Fig. 1, A and B). This finding suggests that GABA is sufficient to drive inhibitory synapse formation, analogous to glutamate-induced spinogenesis (*9*). In addition, we found that GABA HFU triggered dendritic spine formation (Fig. 1, A and B). To resolve whether both GABA and glutamate trigger common signaling mechanisms to generate gephyrin clusters and dendritic spines, we next performed glutamate uncaging. Unlike GABA uncaging, glutamate HFU led to spine formation but not to gephyrin clustering (Fig. 1, A and B). These results demonstrate that there is a segregated downstream mechanism that is selectively activated by GABA but not by glutamate for gephyrin clustering, suggesting the input specificity of de novo inhibitory synapse formation. To determine whether the same phenomenon could occur in vivo, we performed GABA uncaging on layer 2/3 pyramidal neurons in vivo (*13*). Similar to slice cultures, both gephyrin puncta and dendritic spines were induced by in vivo GABA uncaging (Fig. 1, A and C). Neither mock stimulation nor uncaging of a similar caged compound, NPEC-caged-D-AP5 (fig. S6), led to successful induction (fig. S7). When we performed the same experiments in older slices (EP14 to EP18), success rates of both gephyrin clustering and spinogenesis were reduced, but not in younger slices (EP3 or EP4) (Fig. 1B). The induction was spatially precise (Fig. 1D). However, expression mechanisms differed (Fig. 1E). Most gephyrin puncta and spines formed during the initial 5-min period after GABA HFU were stable and likely to become fully mature (Fig. 1, F and G).

To investigate whether GABA acts as an excitatory signal and triggers Ca^{2+} influx during early development (*9*, *14*), we examined the chloride reversal potential (E_{Cl}) at P6 to P7, P11 to P14, and P18 to P24 by means of perforated patch-clamp recording. E_{Cl} was –46 mV in young neurons and –66 mV in mature neurons (Fig. 2, A and B). We found a similar E_{Cl} by single-channel recording (fig. S8). Furthermore, layer 2/3 neurons were depolarized by GABA uncaging in cell-attached current clamp mode, and this depolarization was prevented by the chloride cotransporter (NKCC1) inhibitor bumetanide (fig. S9). GABA uncaging was sufficient to trigger Ca^{2+} influx in young neurons in a GABAzine-sensitive manner (Fig. 2, C and D). Thus, GABA, which normally acts as an inhibitory neurotransmitter in the mature brain, can initiate excitatory signaling cascades for synaptogenesis in the developing cortex.

GABA signals via ionotropic and metabotropic receptors (*15*). We tested the involvement of these two receptor types. GABA type A receptor (GABAAR) blockade by GABAzine significantly reduced gephyrin clustering (Fig. 2E), whereas GABA type B receptor blockade did not alter gephyrin puncta formation (Fig. 2E), although CGP55845 reversed the baclofen-mediated reduction of cell firing (fig. S10). Given that GABA depolarizes young neurons and triggers formation of gephyrin puncta, we examined the involvement of voltage-dependent calcium channels (VDCCs). L-type VDCCs promote gephyrin and glycine receptor clustering (*16*) and can be activated through the Cav1.3 subunit at a hyperpolarized potential (~ –55 mV) (*17*). Blockade of L-type VDCCs by nifedipine did not affect gephyrin clustering but did cause dispersal of gephyrin puncta (Fig. 2E). Blockade of T-type VDCCs (low voltage–activated Ca^{2+} channels) by mibefradil, which is also a partial antagonist of L-type VDCCs, reduced GABA-induced gephyrin clustering (Fig. 2E). Spine formation by GABA uncaging was inhibited by GABAzine, nifedipine, and mibefradil (Fig. 2F). Blockade of the depolarizing action of GABA by bumetanide reduced the success rate of both gephyrin clustering and spinogenesis. Lower-frequency GABA uncaging (LFU; 1 Hz) also reduced the success rate (Fig. 2, E and F). Thus, gephyrin puncta and dendritic spine formation induced by GABA are triggered by GABAAR activation followed by Ca^{2+} influx through L- and T-type VDCCs. Neither gephyrin clustering nor spine formation were induced by GABA uncaging in a Ca^{2+}-free artificial cerebrospinal fluid (Fig. 2, E and F).

Structural changes of newly formed spines are associated with adaptive functional changes in cortical circuits (*9*, *18*–*20*), but whether gephyrin clusters can lead to functional inhibitory synapse formation is unknown. To address this question, we measured uncaging-evoked inhibitory postsynaptic currents (uIPSCs) from newly formed gephyrin puncta. When GABA HFU was delivered at the target spot in whole-cell clamp mode (fig. S11), new gephyrin puncta formed rapidly and the amplitudes of uIPSCs subsequently increased

[1]Max Planck Florida Institute for Neuroscience (MPFI), Jupiter, FL 33458, USA. [2]Dominick P. Purpura Department of Neuroscience, Albert Einstein College of Medicine, Bronx, NY 10461, USA. [3]Max Planck Institute of Neurobiology, Martinsried 82152, Germany.
*Corresponding author. Email: hyungbae.kwon@mpfi.org

Downloaded from http://science.sciencemag.org/ on September 2, 2016

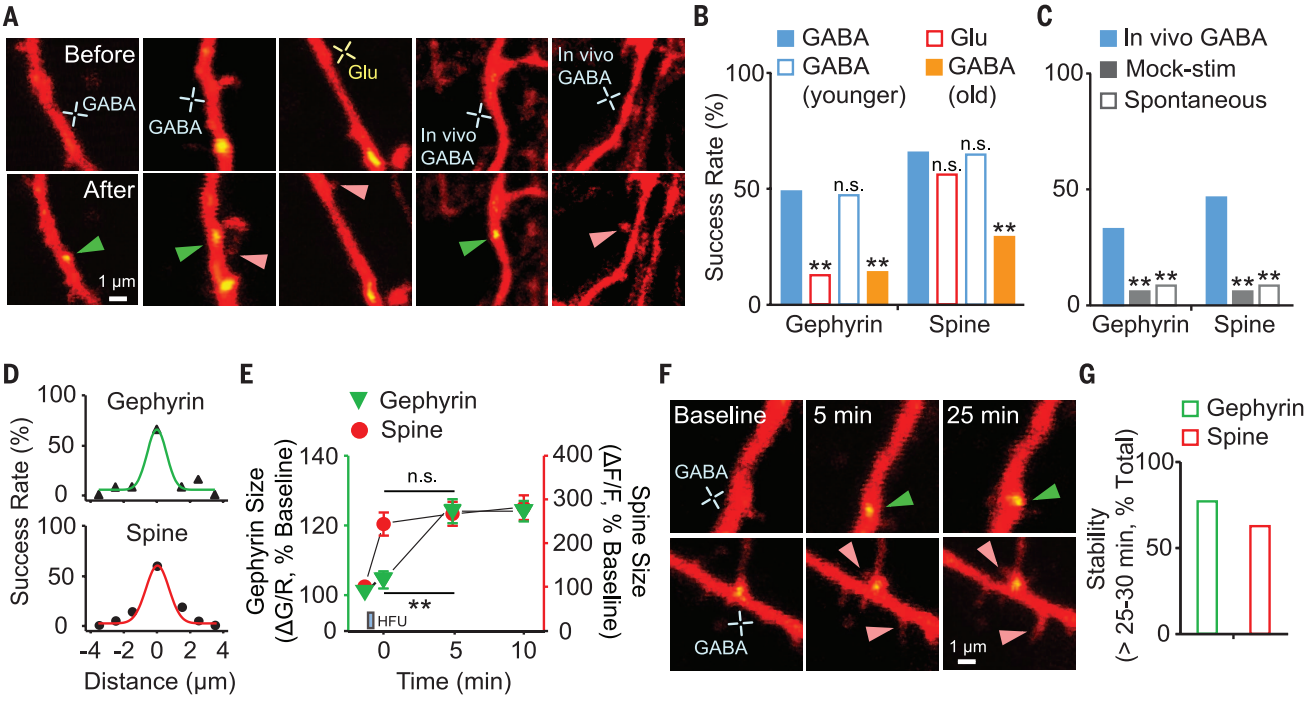


Fig. 1. GABA induces de novo formation of gephyrin puncta and dendritic spines during early development. (**A**) Images of newly formed gephyrin puncta (green arrowheads) and dendritic spines (pink arrowheads) in vitro and in vivo. (**B** and **C**) Success rate of de novo gephyrin and spine formation by GABA and glutamate HFU in vitro [(B); GABA, n = 29 trials, 16 cells; glutamate, n = 24 trials, 12 cells; GABA in younger, n = 17 trials, 7 cells; GABA in old, n = 36 trials, 16 cells] and in vivo [(C); GABA, n = 61 trials, 55 cells, 5 mice; mock stimulation, n = 52 trials, 45 cells, 5 mice; spontaneous, n = 71 trials, 52 cells, 6 mice]. (**D**) Summary plots of distance-dependent de novo gephyrin and spine formation. (**E**) Time course for size changes of new gephyrin puncta (n = 18) and spines (n = 24). (**F**) Time-lapse images of GABA HFU–induced gephyrin puncta and spines. (**G**) Stability of newly formed gephyrin puncta (12 of 15) and dendritic spines (15 of 24). $^{**}P < 0.01$; n.s., not significant. Error bars in (E) denote SEM.

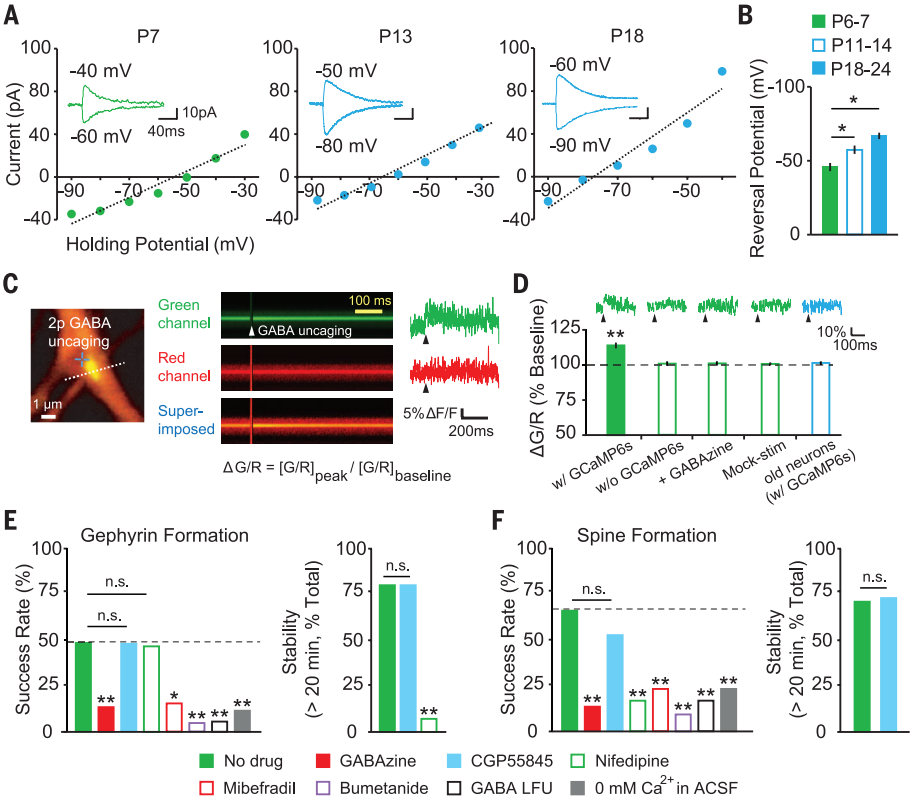


Fig. 2. Molecular mechanisms of GABA-induced de novo gephyrin puncta and dendritic spine formation. (**A**) Current-voltage curves measured by perforated patch-clamp recordings. (**B**) Summary graph of E_{Cl} at P6 to P7 (−45.9 ± 2.7 mV, n = 5), P11 to P14 (−57.2 ± 2.8 mV, n = 7), and P18 to P24 (−66.3 ± 2.1 mV, n = 6). (**C**) Image of a dendrite coexpressing GCaMP6s, tdTomato, and Teal-gephyrin. Dashed line indicates line-scan path. Green and red fluorescences were measured by line scanning before and after GABA uncaging. (**D**) Averaged traces and summary ΔG/R [$(G/R)_{peak}/(G/R)_{baseline}$, where G (green) is GCaMP6s fluorescence and R (red) is tdTomato fluorescence] in young (EP6 to EP8) and old (EP16 to EP18) neurons (with GCaMP6s, n = 13 cells; without GCaMP6s, n = 8; GABAzine, n = 9; mock stimulation, n = 9; old neurons, n = 8). (**E** and **F**) Success rate and stability of de novo gephyrin puncta and spine formation (no drug, n = 29 trials, 16 cells; 10 μM GABAzine, n = 30 trials, 17 cells; 3 μM CGP55845, n = 21 trials, 12 cells; 10 μM nifedipine, n = 30 trials, 14 cells; 10 μM mibefradil, n = 26 trials, 13 cells; 10 μM bumetanide, n = 21 trials, 9 cells; GABA LFU, n = 18 trials, 8 cells, 1 Hz; 0 mM Ca^{2+}, n = 26 trials, 14 cells). $^{*}P < 0.05$, $^{**}P < 0.01$; error bars represent SEM.

Downloaded from http://science.sciencemag.org/ on September 2, 2016

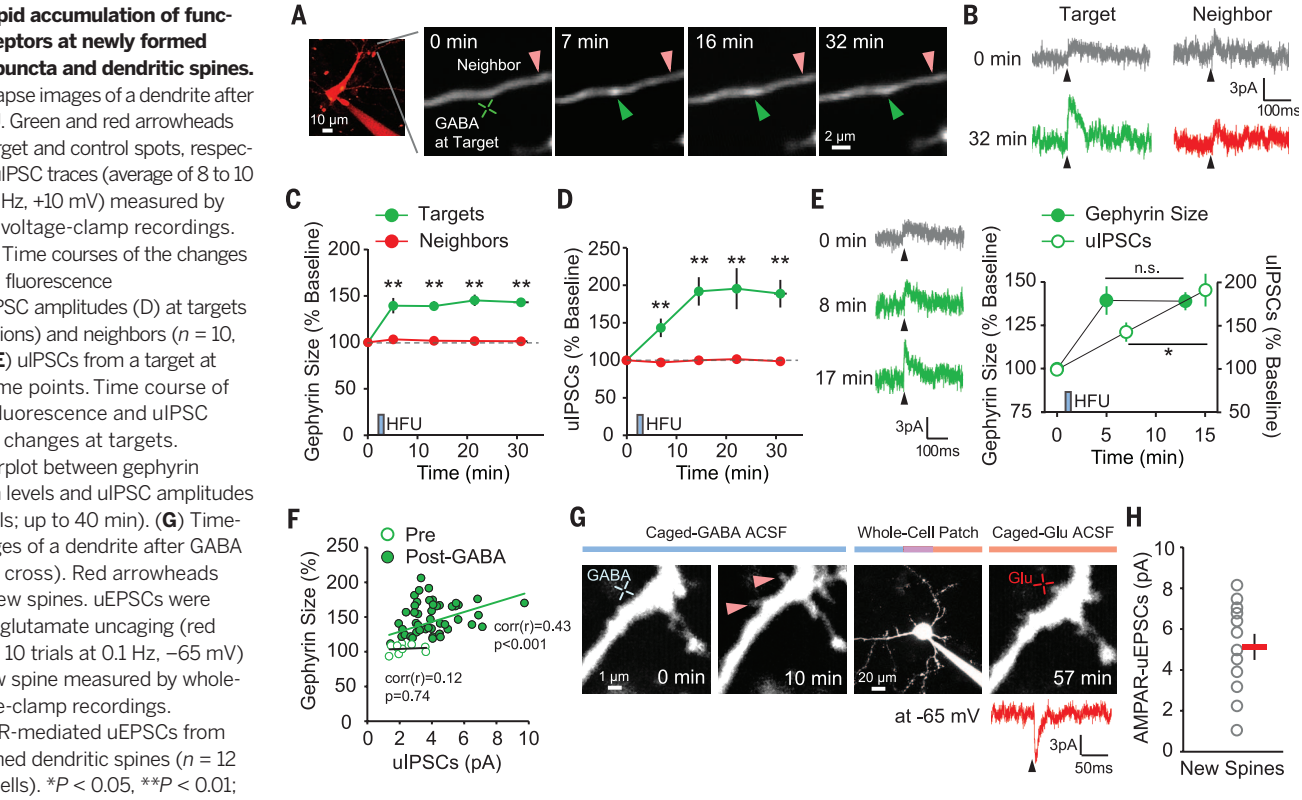


Fig. 3. Rapid accumulation of functional receptors at newly formed gephyrin puncta and dendritic spines. (**A**) Time-lapse images of a dendrite after GABA HFU. Green and red arrowheads indicate target and control spots, respectively. (**B**) uIPSC traces (average of 8 to 10 trials at 0.1 Hz, +10 mV) measured by whole-cell voltage-clamp recordings. (**C** and **D**) Time courses of the changes in gephyrin fluorescence (C) and uIPSC amplitudes (D) at targets (n = 10 regions) and neighbors (n = 10, 10 cells). (**E**) uIPSCs from a target at different time points. Time course of gephyrin fluorescence and uIPSC amplitude changes at targets. (**F**) Scatterplot between gephyrin expression levels and uIPSC amplitudes (n = 10 cells; up to 40 min). (**G**) Time-lapse images of a dendrite after GABA HFU (blue cross). Red arrowheads indicate new spines. uEPSCs were evoked by glutamate uncaging (red cross, 8 to 10 trials at 0.1 Hz, −65 mV) from a new spine measured by whole-cell voltage-clamp recordings. (**H**) AMPAR-mediated uEPSCs from newly formed dendritic spines (n = 12 spines, 5 cells). *P < 0.05, **P < 0.01; error bars represent SEM.

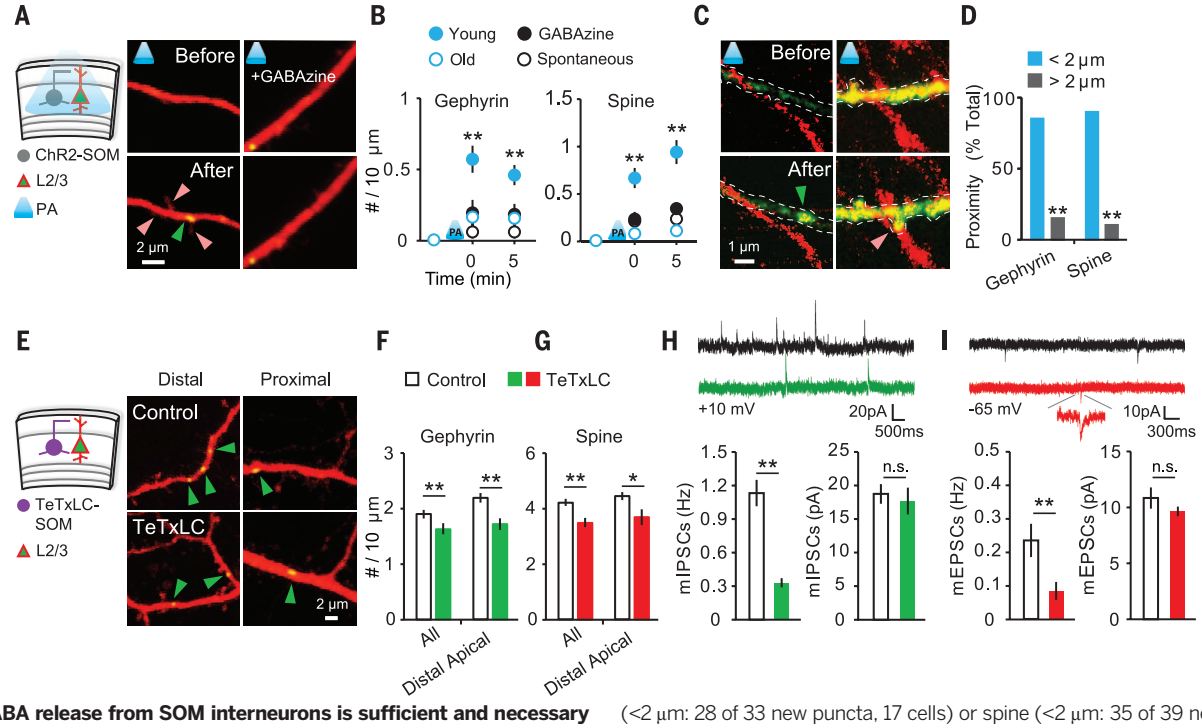


Fig. 4. GABA release from SOM interneurons is sufficient and necessary for inhibitory and excitatory synaptogenesis during early development. (**A**) Experimental schematic and images of newly formed gephyrin cluster (green arrowhead) and spines (red arrowheads). (**B**) Summary data of photoactivation-induced de novo synaptogenesis (young, n = 23 dendrites, 13 cells; GABAzine, n = 22 dendrites, 13 cells; old at EP16 to EP18, n = 19 dendrites, 11 cells; spontaneous, n = 13 dendrites, 11 cells). (**C**) Axons of SOM and de novo gephyrin punctum (green arrowhead) and dendritic spine (red arrowhead) imaged at 1045 nm. (**D**) Proximity between an axon of SOM and a new gephyrin cluster (<2 µm: 28 of 33 new puncta, 17 cells) or spine (<2 µm: 35 of 39 new spines). (**E**) Experimental schematic and images of dendrites in noninfected and TeTxLC-infected slices at EP12. (**F** and **G**) Quantitative analysis of gephyrin puncta density at EP11 and EP12 (control, n = 13 cells; TeTxLC, n = 15 cells) and spine density at EP7 (control, n = 8 cells; TeTxLC, n = 10 cells). (**H** and **I**) Traces of mIPSCs (H) and mEPSCs (I) measured by whole-cell patch-clamp recordings. Quantitative analyses of mIPSCs (control, n = 11 cells; TeTxLC, n = 11 cells) and mEPSCs (control, n = 7 cells; TeTxLC, n = 11 cells) are shown. *P < 0.05, **P < 0.01; error bars represent SEM.

Downloaded from http://science.sciencemag.org/ on September 2, 2016

at the target location but not at a neighboring control location (Fig. 3, A to D, and fig. S12). These data imply that functional GABAARs are rapidly recruited to newly formed gephyrin clusters (Fig. 3, E and F). We also found that newly formed dendritic spines became functional, as indicated by glutamate uncaging–evoked AMPA receptor (AMPAR)–mediated excitatory postsynaptic currents (uEPSCs) (Fig. 3, G and H). Thus, newly formed gephyrin clusters and dendritic spines gain functions by recruiting functional receptors.

To determine whether endogenous GABAergic synaptic activity also promotes both inhibitory and excitatory synaptogenesis, we used optogenetics to activate cortical interneurons. We first verified the efficacy of viral infection during early development (fig. S13 and movies S1 and S2) (*21*). We infected adeno-associated virus (AAV)–dflox. hChR2 (H134R)–mCherry into cortical slices from somatostatin (SOM)–Cre mice (fig. S14); 3 to 5 days after viral infection, we delivered three rounds of blue light illumination (fig. S14). Photostimulation of ChR2-transfected SOM interneurons caused rapid formation of new gephyrin puncta and dendritic spines in young neurons, which was blocked by GABAzine; the same stimulation did not make induction in old slices (Fig. 4, A and B). To examine the proximity between presynaptic boutons and new gephyrin clusters or dendritic spines, we visualized both presynaptic SOM and postsynaptic pyramidal neurons (Fig. 4C) and found that the majority of gephyrin puncta and dendritic spines were formed close (<2 μm) to the axonal boutons of SOM interneurons (Fig. 4D). Thus, GABA uncaging–induced synaptogenesis is triggered by the same mechanisms as synaptic GABA release under physiological conditions.

We next abolished GABA release by injecting AAV-containing tetanus toxin light chain (TeTxLC) inverted in a flip-excision (FLEX) cassette into EP3 culture from SOM-Cre mice (*22*). We confirmed that TeTxLC on its own prevented vesicle release (fig. S15) and did not affect synapse development (fig. S16). In TeTxLC-expressing SOM-Cre slices at EP11 and EP12, we found that the gephyrin puncta density in distal apical dendrites of layer 2/3 pyramidal neurons was reduced (Fig. 4, E and F, and fig. S17); this result implies that SOM-positive interneurons target distal apical dendrites of pyramidal neurons (*23*, *24*). Spine density at apical dendrites was also reduced at EP7 (Fig. 4G), making spine numbers closer to those at EP3 or EP4 (fig. S18). Consistent with structural changes, TeTxLC expression reduced the frequency of both miniature IPSCs (mIPSCs) and miniature EPSCs (mEPSCs) in slices (Fig. 4, H and I) and in vivo (fig. S19). Thus, we suggest that early-developing GABAergic inputs from cortical interneurons control both inhibitory and excitatory circuitry during cortical development.

Our findings suggest that GABA sets the balance between inhibitory and excitatory synapses in early postnatal stages, laying the foundation for later circuit development (*6*, *25*–*27*). Because the developing dendrites in our study did not have predetermined spots for inhibitory or excitatory synapses, localization of axonal boutons may be an early step in the precise formation of inhibitory and excitatory circuits (*9*, *28*, *29*). Thus, early-depolarizing GABA action appears to promote local synaptogenesis and shapes cortical circuitry during brain development.

REFERENCES AND NOTES

1. T. Branco, B. A. Clark, M. Häusser, *Science* **329**, 1671–1675 (2010).
2. C. Q. Chiu *et al.*, *Science* **340**, 759–762 (2013).
3. T. Hayama *et al.*, *Nat. Neurosci.* **16**, 1409–1416 (2013).
4. A. Losonczy, J. C. Magee, *Neuron* **50**, 291–307 (2006).
5. N. Spruston, *Nat. Rev. Neurosci.* **9**, 206–221 (2008).
6. P. Caroni, F. Donato, D. Muller, *Nat. Rev. Neurosci.* **13**, 478–490 (2012).
7. A. M. Hamilton *et al.*, *Neuron* **74**, 1023–1030 (2012).
8. Y. Kozorovitskiy, A. Saunders, C. A. Johnson, B. B. Lowell, B. L. Sabatini, *Nature* **485**, 646–650 (2012).
9. H. B. Kwon, B. L. Sabatini, *Nature* **474**, 100–104 (2011).
10. J. L. Chen *et al.*, *Neuron* **74**, 361–373 (2012).
11. D. van Versendaal *et al.*, *Neuron* **74**, 374–383 (2012).
12. M. Matsuzaki, T. Hayama, H. Kasai, G. C. Ellis-Davies, *Nat. Chem. Biol.* **6**, 255–257 (2010).
13. T. Kim, W. C. Oh, J. H. Choi, H. B. Kwon, *Proc. Natl. Acad. Sci. U.S.A.* **113**, E1372–E1381 (2016).
14. Y. Ben-Ari, *Neuroscience* **279**, 187–219 (2014).
15. C. Lüscher, L. Y. Jan, M. Stoffel, R. C. Malenka, R. A. Nicoll, *Neuron* **19**, 687–695 (1997).
16. J. Kirsch, H. Betz, *Nature* **392**, 717–720 (1998).
17. T. A. Hage, Z. M. Khaliq, *J. Neurosci.* **35**, 5823–5836 (2015).
18. G. W. Knott, A. Holtmaat, L. Wilbrecht, E. Welker, K. Svoboda, *Nat. Neurosci.* **9**, 1117–1124 (2006).
19. U. V. Nägerl, G. Köstinger, J. C. Anderson, K. A. Martin, T. Bonhoeffer, *J. Neurosci.* **27**, 8149–8156 (2007).
20. K. Zito, V. Scheuss, G. Knott, T. Hill, K. Svoboda, *Neuron* **61**, 247–258 (2009).
21. R. Batista-Brito, R. Machold, C. Klein, G. Fishell, *Cereb. Cortex* **18**, 2306–2317 (2008).
22. A. J. Murray *et al.*, *Nat. Neurosci.* **14**, 297–299 (2011).
23. S. X. Chen, A. N. Kim, A. J. Peters, T. Komiyama, *Nat. Neurosci.* **18**, 1109–1115 (2015).
24. J. Cichon, W. B. Gan, *Nature* **520**, 180–185 (2015).
25. M. Cane, B. Maco, G. Knott, A. Holtmaat, *J. Neurosci.* **34**, 2075–2086 (2014).
26. B. Dejanovic *et al.*, *PLOS Biol.* **12**, e1001908 (2014).
27. C. E. Flores *et al.*, *Proc. Natl. Acad. Sci. U.S.A.* **112**, E65–E72 (2015).
28. Z. J. Huang, *J. Physiol.* **587**, 1881–1888 (2009).
29. M. Miller, A. Peters, *J. Comp. Neurol.* **203**, 555–573 (1981).

ACKNOWLEDGMENTS

We thank members of the Kwon laboratory for discussion, E. Nedivi for Teal-gephyrin, and H. Taniguchi for Flex-TeTxLC. Supported by the MPFI, a NARSAD Young Investigator grant, and NIH grants MH107460 (H.-B.K.) and MH081935 and DA017392 (P.E.C.). Supplementary materials contain additional data. Author contributions: W.C.O. and H.-B.K. conceived and designed the study; W.C.O. performed and analyzed all experiments except perforated patch-clamp recordings, which were performed and analyzed by S.L. and P.E.C.; W.C.O. prepared the figures; W.C.O. and H.-B.K. wrote the manuscript; and all authors revised the manuscript.

SUPPLEMENTARY MATERIALS

www.sciencemag.org/content/353/6303/1037/suppl/DC1
Materials and Methods
Figs. S1 to S19
Movies S1 and S2
References (*30*–*36*)

22 February 2016; accepted 3 August 2016
Published online 11 August 2016
10.1126/science.aaf5206

ION CHANNELS

Instantaneous ion configurations in the K^+ ion channel selectivity filter revealed by 2D IR spectroscopy

Huong T. Kratochvil,[1] Joshua K. Carr,[1] Kimberly Matulef,[2] Alvin W. Annen,[2] Hui Li,[3] Michał Maj,[1] Jared Ostmeyer,[3] Arnaldo L. Serrano,[1] H. Raghuraman,[3]* Sean D. Moran,[1]† J. L. Skinner,[1] Eduardo Perozo,[3]‡ Benoît Roux,[3]‡ Francis I. Valiyaveetil,[2]‡ Martin T. Zanni[1]‡

Potassium channels are responsible for the selective permeation of K^+ ions across cell membranes. K^+ ions permeate in single file through the selectivity filter, a narrow pore lined by backbone carbonyls that compose four K^+ binding sites. Here, we report on the two-dimensional infrared (2D IR) spectra of a semisynthetic KcsA channel with site-specific heavy ($^{13}C^{18}O$) isotope labels in the selectivity filter. The ultrafast time resolution of 2D IR spectroscopy provides an instantaneous snapshot of the multi-ion configurations and structural distributions that occur spontaneously in the filter. Two elongated features are resolved, revealing the statistical weighting of two structural conformations. The spectra are reproduced by molecular dynamics simulations of structures with water separating two K^+ ions in the binding sites, ruling out configurations with ions occupying adjacent sites.

Ion channels that mediate the flux of K^+ are responsible for determining the resting membrane potential and for the repolarization phase of action potentials of excitable cells (*1*). Ion permeation through all K^+ channels is characterized by high selectivity and throughput approaching the diffusion limit. These permeation properties are defined by the selectivity filter, a highly conserved structural element consisting of four K^+ binding sites (S1 to S4, labeled

Downloaded from http://science.sciencemag.org/ on September 1, 2016

extracellular to intracellular) (Fig. 1B). During translocation, K^+ coordination is carried out by main-chain carbonyl oxygens (plus a threonine side chain in S4) (*2*, *3*).

The mechanism of ion permeation through the selectivity filter has been investigated using diverse experimental techniques such as radiotracer flux assays, single-channel electrophysiological measurements, x-ray crystallography, and computational studies (*3*–*11*). These experiments are broadly supportive of a mechanism commonly referred to as "knock–on" permeation (*4*). This mechanism posits that the narrow selectivity filter is simultaneously occupied by two K^+ ions in single file, either at sites S1 and S3 or at sites S2 and S4, with intervening water molecules (Fig. 1, C and D) (*9*–*13*). The approach of a third K^+ ion from the intracellular side of the channel would advance the single file of alternating ions and water to the extracellular side, resulting in the net translocation of one K^+ ion and one water molecule across the membrane. However, the experimental data are not sufficiently conclusive to rule out alternative models for the permeation mechanism (*14*–*16*). Of these, a recently proposed "hard-knock" permeation model suggests a very different mechanism. It postulates that the conductance of K^+ channels arises from direct, short-range ion-ion collisions inside the filter, so that a pair of adjacent K^+ ions occupy the selectivity filter at adjacent sites S2 and S3 with no intervening water molecules [0, S2, S3, 0] (*17*). In this model, permeation would take place when a third K^+ ion enters the S4 binding site [0, S2, S3, S4], colliding directly with the S2/S3 ion pair to create the ion configuration [S1, S2, 0, S4]. Eventually, S1 would leave the filter and the K^+ at S4 transitions to S3, starting over again (*17*). Here, we have used two-dimensional infrared (2D IR) spectroscopy and protein semisynthesis to test these permeation models, providing new experimental data on the ion and water configurations in the selectivity filter of the KcsA channel.

Atomic bond vibrations are sensitive to their electrostatic environment, so the frequencies are dictated by nearby ions and water as well as the structure and dynamics of the protein itself (*18*). The inherent time resolution of 2D IR spectroscopy is a few picoseconds, which implies that a 2D IR spectrum provides a nearly instantaneous snapshot of the dynamic channel and the content of the pore (*19*). In essence, it is a weighted average of the ion configurations and protein structural distributions (*20*). For the 2D IR experiments, we used protein semisynthesis to selectively isotope-label the ion-binding sites in the selectivity filter. Using the native chemical ligation reaction, we assembled the KcsA protein from a synthetic peptide (residues 70 to 81) that encompasses the selectivity filter and two recombinant peptides corresponding to the rest of the protein. (*21*, *22*). We introduced $^{13}C^{18}O$ labels on the backbone carbonyls of Val^{76}, Gly^{77}, and Gly^{79} by using the appropriately labeled residues during synthesis of the peptide fragment (Fig. 1B). The $^{13}C^{18}O$ labels cause a 65 cm^{-1} shift of the carbonyl frequency (amide I vibrations) (*23*), enabling us to spectroscopically isolate and probe the selectivity filter. Gly^{77} and Val^{76} probe the S1, S2, and S3 binding sites. These are good sites for labeling because these sites have different ion occupancies according to the two models. Labeling Gly^{77} and Val^{76} together makes the spectra particularly sensitive to ion configurations because of vibrational coupling between these two residues (*24*).

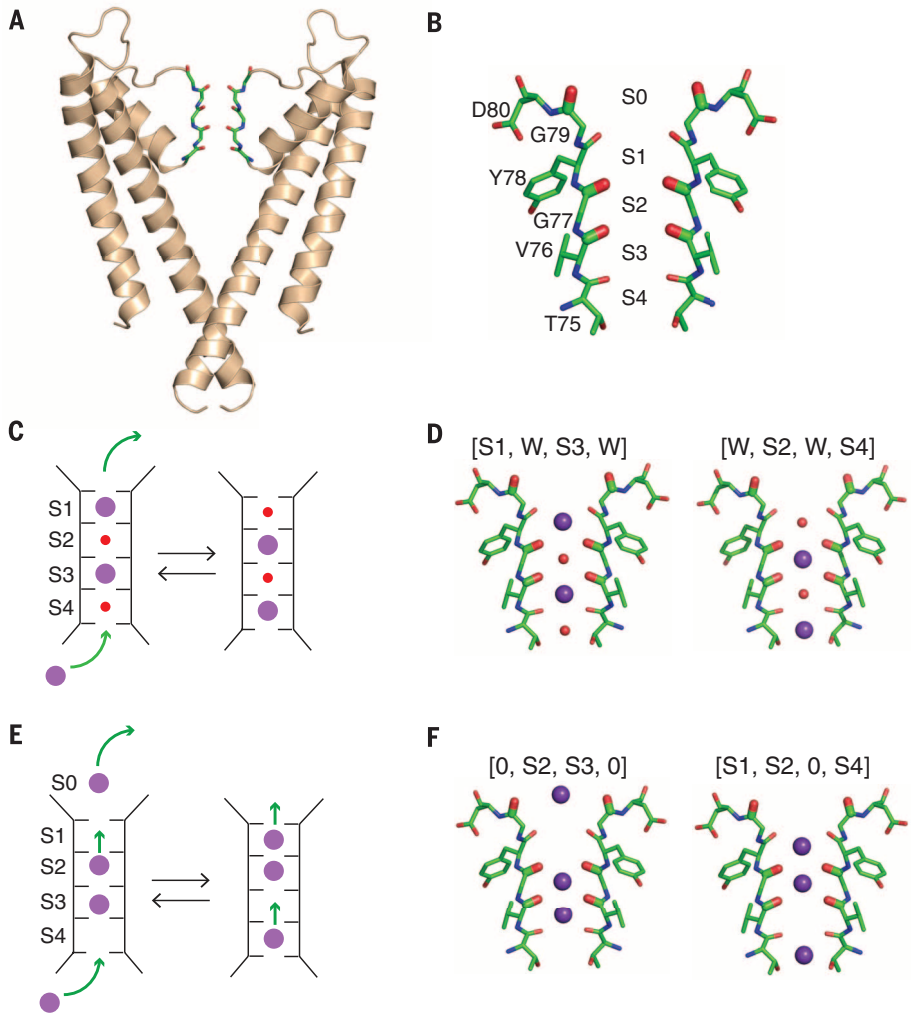


Fig. 1. Overview of ion permeation mechanisms of KcsA. (**A**) X-ray crystal structure of KcsA (PDB ID 1K4C), with two of the four protein subunits shown. (**B**) The selectivity filter of KcsA is lined with the carbonyl groups (oxygen in red) of four amino acids (Thr^{75}, Val^{76}, Gly^{77}, and Tyr^{78}). Amino acids that were $^{13}C^{18}O$ isotope labeled for the experiment are shown bolded (Val^{76}, Gly^{77}, and Gly^{79}). The binding sites (S1 to S4) span the selectivity filter. (**C**) Knock-on mechanism for potassium ion permeation through the channel. In this mechanism, K^+ ions (purple) alternate with water molecules (red) and collectively move through the filter when a new K^+ enters the filter. (**D**) The two most prominent ion-binding configurations for the knock-on mechanism used to simulate the 2D IR spectra: (left) [S1, W, S3, W] and (right) [W, S2, W, S4]. (**E**) The hard-knock model for ion conduction. When a K^+ ion enters the S4 binding site, strong electrostatic repulsions simultaneously translocate two ions upward. No water is involved in this mechanism. (**F**) The two ion configurations used to simulate the 2D IR spectra: (left) [0, S2, S3, 0] and (right) [S1, S2, 0, S4]. Simulations for 97% of the ion configurations proposed by the hard-knock mechanism are shown in fig. S7. Single-letter abbreviations for the amino acid residues are as follows: A, Ala; C, Cys; D, Asp; E, Glu; F, Phe; G, Gly; H, His; I, Ile; K, Lys; L, Leu; M, Met; N, Asn; P, Pro; Q, Gln; R, Arg; S, Ser; T, Thr; V, Val; W, Trp; and Y, Tyr.

[1]Department of Chemistry, University of Wisconsin-Madison, Madison, WI 53706, USA. [2]Program in Chemical Biology, Department of Physiology and Pharmacology, Oregon Health and Science University, Portland, OR 97239, USA. [3]Department of Biochemistry and Molecular Biology, The University of Chicago, Chicago, IL 60637, USA.
*Present address: Crystallography and Molecular Biology Division, Saha Institute of Nuclear Physics (SINP), Kolkata 700 064, India.
†Present address: Department of Chemistry and Biochemistry, Southern Illinois University Carbondale, Carbondale, IL 62901, USA.
‡Corresponding author. Email: eperozo@uchicago.edu (E.P.); roux@uchicago.edu (B.R.); valiyave@ohsu.edu (F.I.V.); zanni@chem.wisc.edu (M.T.Z.)

Downloaded from http://science.sciencemag.org/ on September 1, 2016

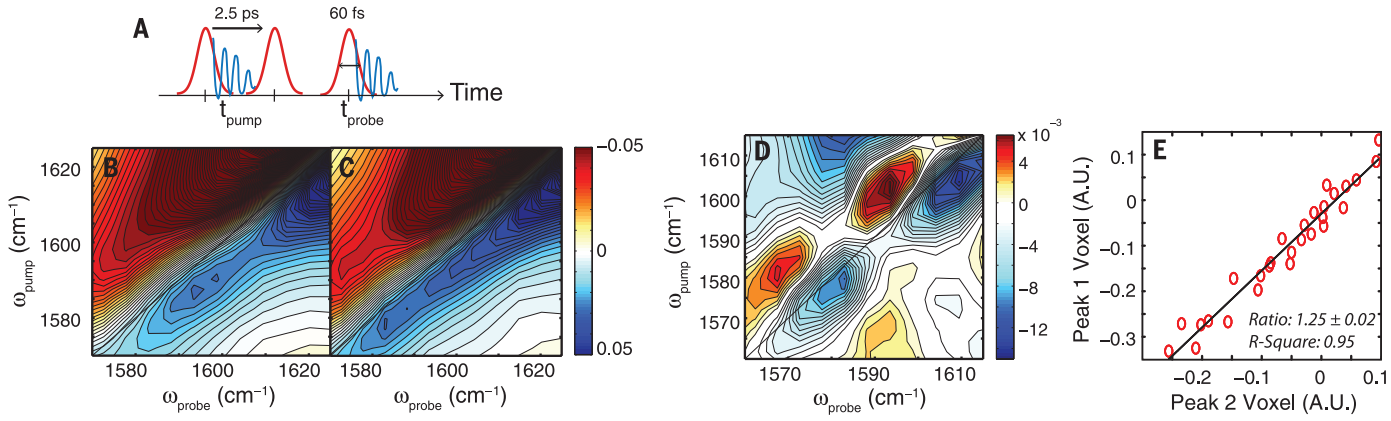


Fig. 2. Experimental 2D IR spectra of unlabeled and $^{13}C^{18}O$-labeled KcsA at high potassium concentrations. (**A**) Pulse sequence for 2D IR spectrum with illustrated vibrational coherences (blue). Fourier transform of the coherence during t_{probe} to give the ω_{probe} axis, while the time between the pump pulses, t_{pump}, is computationally Fourier transformed to give the ω_{pump} axis. (**B**) 2D IR spectrum of unlabeled KcsA showing the absorption of side chains in the region where the isotope-labeled features are expected to appear. (**C**) 2D IR spectrum of labeled KcsA shows a 50% increase in intensity in this region, consistent with absorption by the $^{13}C^{18}O$ labeled residues. (**D**) Subtraction of the unlabeled spectrum from the labeled spectrum yields two pairs of peaks. The bleaches (blue) appear at (ω_{pump}, ω_{probe}) = (1603 cm^{-1}, 1609 cm^{-1}) and (1580 cm^{-1}, 1582 cm^{-1}), respectively. (**E**) For every unique combination of difference spectra, the intensities of the 3 by 3 pixel array centered at the pixels for (ω_{pump}, ω_{probe}) = (1603 cm^{-1}, 1609 cm^{-1}) (peak 1) and (1580 cm^{-1}, 1582 cm^{-1}) (peak 2) were integrated, respectively. The slope of the fit yielded an intensity ratio of 1.25 ± 0.02, with an *R*-square of 0.95.

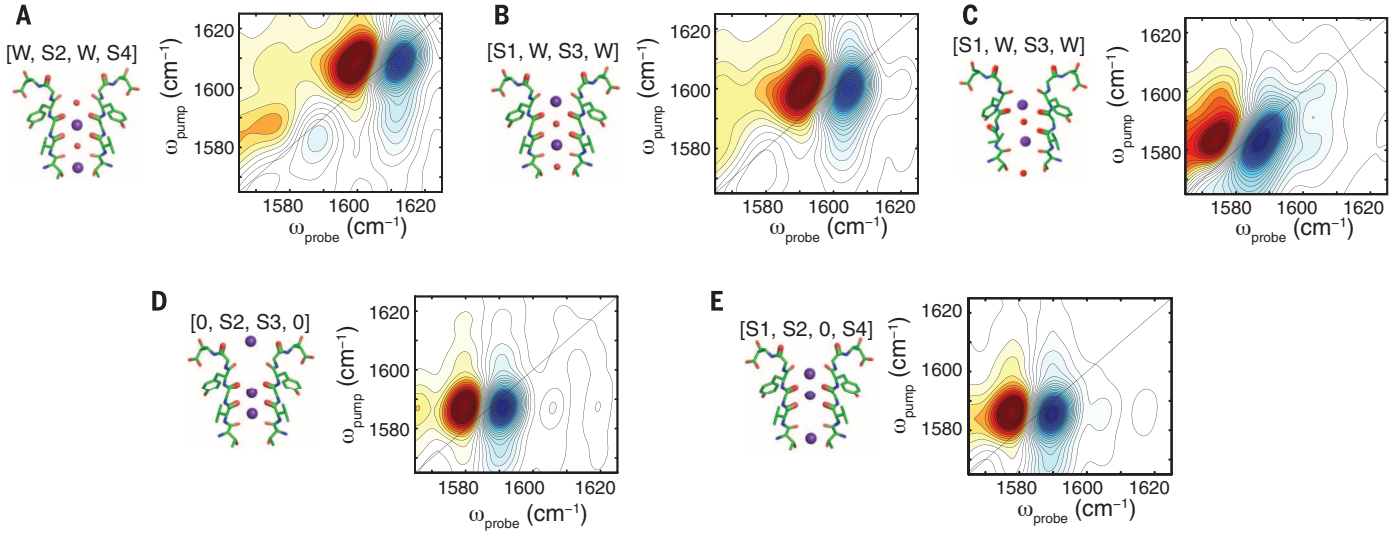


Fig. 3. Calculated 2D IR spectra to test proposed ion configurations of the KcsA selectivity filter. The calculated 2D IR spectra for the (**A**) [W, S2, W, S4], (**B**) [S1, W, S3, W], (**C**) [S1, W, S3, W] with a single Val^{76} flip, (**D**) [0, S2, S3, 0], and (**E**) [S1, S2, 0, S4] K^+ binding configurations of the labeled KcsA filter from MD simulations using a K^+ charge profile described in (*35*). In (A), we have the spectrum for the [W, S2, W, S4] ion-binding configuration in which all of the Val^{76} residues point into the filter. In this case, we observe peaks at (ω_{pump}, ω_{probe}) = (1608 cm^{-1}, 1612 cm^{-1}). (B) For the [S1, W, S3, W] configuration, we see a similar spectrum with (ω_{pump}, ω_{probe}) = (1600 cm^{-1}, 1604 cm^{-1}). (C) For the [S1, W, S3, W] ion configuration of the Val^{76}-flipped state, we get a pair of inhomogeneous peaks at (ω_{pump}, ω_{probe}) = (1583 cm^{-1}, 1587 cm^{-1}). (D) and (E) are the calculated 2D IR spectra of the [0, S2, S3, 0] and [S1, S2, 0, S4] binding configurations, respectively. In (E), we observe a single homogeneous peak at (ω_{pump}, ω_{probe}) = (1587 cm^{-1}, 1591 cm^{-1}), which is similar to the homogeneous peak we observe in (F) at (ω_{pump}, ω_{probe}) = (1585 cm^{-1}, 1589 cm^{-1}). The spectra have been normalized for visualization purposes.

Shown in Fig. 2C is the 2D IR spectrum of labeled KcsA. This spectrum was collected using the pulse sequence shown in Fig. 2A. This approach is analogous to that used in 2D nuclear magnetic resonance spectroscopy, but probing vibrational modes. This pulse sequence produces an infrared signal that oscillates as a function of the time delay between the pump pulses and after the probe pulse, respectively. The signal is Fourier transformed along these two time axes to give a 2D IR spectrum that correlates the two frequency axes. The spectrum in Fig. 2C is shown in the region that the $^{13}C^{18}O$-labeled carbonyls absorb [full spectra are shown in the supplementary materials (SM)]. Acidic side chains also absorb in this region, creating a background (*25*, *26*). To remove the background, we also measured a KcsA sample without isotope labels under identical conditions. The intensity of the unlabeled KcsA spectrum is about 50% lower in this region, which is approximately what we would expect based on the ratio of labels to acidic side chains.

Figure 2D shows the difference spectrum generated by subtracting Fig. 2, B and C. It contains two pairs of oppositely signed peaks, with blue, negative peaks corresponding to the

Downloaded from http://science.sciencemag.org/ on September 1, 2016

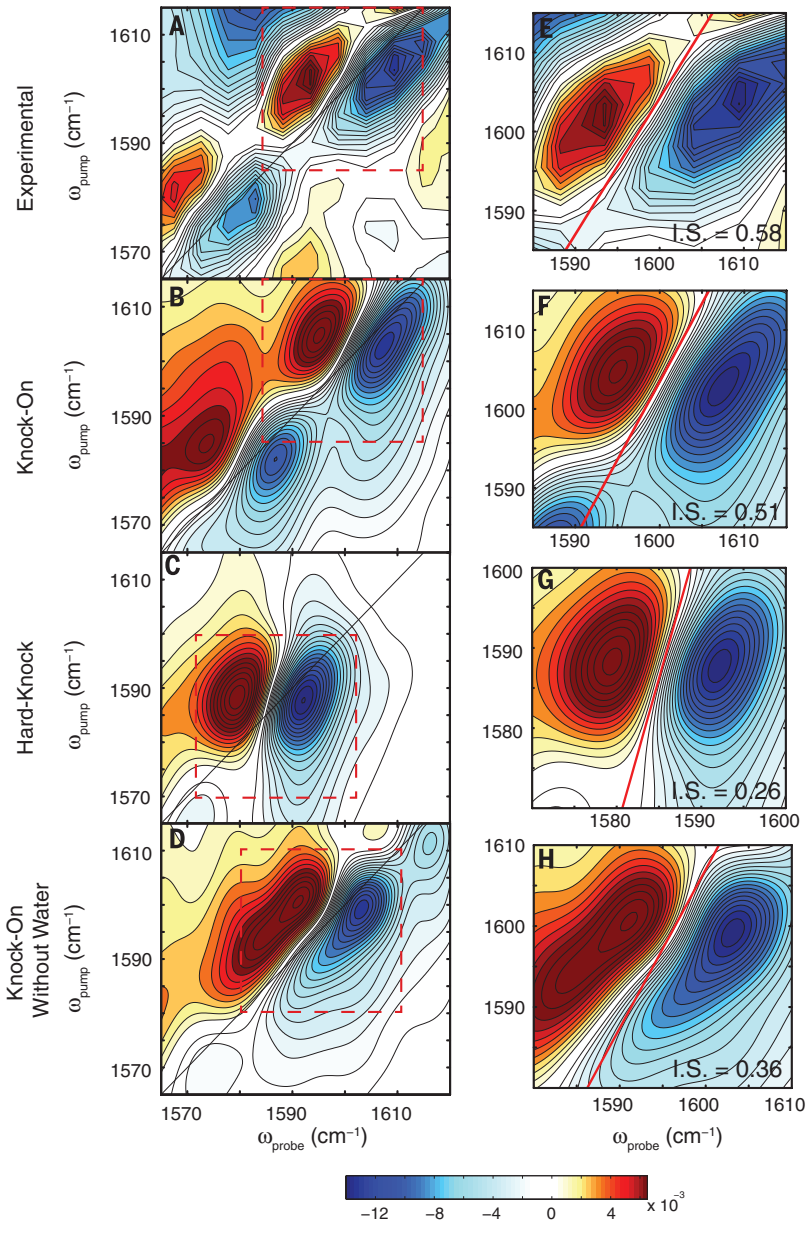


Fig. 4. Comparison of 2D IR experimental spectrum to the simulated spectra of the knock-on models (with and without water) and the hard-knock model. (**A**) Experimental difference spectrum shown in Fig. 2C. (**B**) Simulated 2D IR spectrum for the knock-on model with water generated by a weighted average of the [W, S2, W, S4], [S1, W, S3, W], and Val^{76} flipped [S1, W, S3, W] ion configurations in a ratio of 0.3:0.3:0.4, respectively. The simulated spectrum agrees well with peak positions, 2D lineshapes, and intensity ratio. (**C**) Simulated 2D IR spectrum for the hard-knock model from a weighted average of [0, S2, S3, 0] and [S1, S2, 0, S4], along with other hard-knock states (see SM). (**D**) Simulated 2D IR spectrum of the knock-on model with water removed with the same ratios of states used to match experiment (Fig. 4B). No linear combination of these states without water (see fig. S14) reproduces the experimental spectrum. Therefore, water must be present within the filter. (**E** to **H**) Zoom-ins of the high-frequency peak of each spectra. The nodal line slopes are illustrated by red lines with values of the inverse slope (I.S.).

0→1 vibrational transition and red, positive peaks corresponding to the 1→2 vibrational transition. For each isotope label, our pulse sequence will create a pair of oppositely signed peaks, with the negative peak on the diagonal. Thus, the difference spectrum resolves two vibrational features, which we refer to by their frequencies along the y axis, ω_{pump} = 1603 cm^{-1} and 1580 cm^{-1}. The frequencies reflect the magnitude of the electric fields inside the filter as well as the coupling between residues set by the backbone structure (*27*, *28*). The two pairs of peaks have very different frequencies, with a peak separation of 23 cm^{-1} along ω_{pump}, indicating that there is either a single protein structure or ion configuration that has distinct electrostatics at the separate binding sites or a weighted average of two conformations with very different electrostatics. A statistical analysis is presented in the SM that addresses reproducibility and statistical significance. A portion of this analysis is shown in Fig. 2E, which plots the intensity of the 1603 and 1580 cm^{-1} peaks for every combination of foreground and background spectra that we collected. If the experimental peaks were not reproducible, then this plot would be uncorrelated. Instead, a strong correlation is observed with a slope of 1.25 ± 0.02, which equals the relative intensities of the two peaks. As we show below, the relative intensity gives the statistical weighting of ion channel structures.

To determine whether these experimental features can be explained by either of the two permeation models described above, we conducted molecular dynamics (MD) simulations and computed 2D IR spectra for all relevant ion configurations (see SM for methods). Shown in Fig. 3, A and B, are 2D IR spectra calculated for each of the two multi-ion configurations predicted to occur during ion conduction according to the knock-on model, [W, S2, W, S4] and [S1, W, S3, W]. The spectrum of the [W, S2, W, S4] ion configuration has an intense pair of peaks at 1608 cm^{-1}. A similar spectrum is predicted for the [S1, W, S3, W] ion-binding configuration, albeit centered at 1600 cm^{-1}. Simulations of the individual residues reveal that Val^{76}, which is coordinating the S2 K$^+$ ion, is mostly responsible for the frequency and the spectral intensity that we observe in this ion-binding configuration (see SM). MD simulations also predict that the Val^{76} carbonyl is often flipped outward (*16*, *29*), away from the pore (see Fig. 3C) when the ions are in the [S1, W, S3, W] configuration. Simulations of that structure predict a pair of peaks that are much lower in frequency, absorbing at 1583 cm^{-1}. The flipped state is not predicted to exist for the [W, S2, W, S4] ion configuration (*29*).

Shown in Fig. 3, C and D, are the calculated 2D IR spectra for two of the ion configurations of the new hard-knock model, [0, S2, S3, 0] and [S1, S2, 0, S4]. Both ion configurations predict nearly the same 2D IR spectrum, with frequencies of 1587 and 1585 cm^{-1}. Ions in the channel tend to shift carbonyls to lower frequencies because of their charge, which is why this model predicts low frequencies for both ion configurations. The hard-knock model also contains other ion configurations in its mechanism, whose computed spectra are given in the SM (fig. S7). The predicted spectra for the ion configuration corresponding to the knock-on and the hard-knock models are very different from one another in both peak frequency and 2D lineshape.

For comparison to experiment, the simulated spectra of the structures in the knock-on model ([W, S2, W, S4]:[S1, W, S3, W]:flipped[S1, W, S3, W]) were added at a ratio of 0.3:0.3:0.4 to match the relative intensities in the experimental spectra

Downloaded from http://science.sciencemag.org/ on September 1, 2016

(the experimental peaks have a ratio of 1.25 ± 0.02, from Fig. 2E). The agreement between the knock-on model and experiment is good (Fig. 4B versus 4A), especially considering that the only adjustable parameters in these calculations are the relative ratios. We also added together the 2D spectra for 97% of the ion configurations predicted from the hard-knock model (Fig. 3, D and E, and fig. S7), which gives the spectrum in Fig. 4C (*17*). The agreement to experiment is poor; the simulations only predict one set of peaks instead of two. There is no linear combination of hard-knock ion configurations or structures that can match the experiment. We have also explored whether the ion configurations of the hard-knock model occur, albeit less frequently, along with the configurations for the knock-on states. To do so, we added the spectra of the hard-knock configurations to the knock-on states (fig. S12). We estimate that there cannot be more than 15% of the states in the hard-knock configuration, because increasing the population beyond this limitation decreases the frequency separation and changes the 2D lineshapes of the peaks. Therefore, our data are consistent with ion distributions in the filter predicted by the classic knock-on model but not the hard-knock model proposed more recently.

An analysis of the 2D lineshapes corroborates our conclusions and provides additional insights. The calculated 2D lineshapes are elongated for the knock-on model and rounder for the hard-knock model (Fig. 4, B and D, respectively). Two-dimensional lineshapes are elongated along the diagonal when there is a heterogeneous subset of frequencies—and, accordingly, structures—each with its own set of electric fields. In essence, the 2D lineshapes measure the structural distribution of the selectivity filter for each ion configuration (*30*). Shown in Fig. 4, E to H (red lines), are nodal line slopes that quantify the inhomogeneity of the 2D lineshapes. The experiment and simulations of the knock-on model both have inverse slopes of about 0.6, whereas the hard-knock model has an inverse slope of about 0.3 (see table S3). To test the effect of water on the knock-on spectra, we reran the molecular dynamics simulations without water in the selectivity filter (Fig. 4D). The simulations predict that the high-frequency peak bifurcates because the [0, S2, 0, S4] ion-binding configuration blueshifts 4 cm^{-1} (see fig. S13), and the inverse slope is too small. There are no linear combinations of the knock-on states without water that can reproduce the experimental spectrum in Fig. 4B. Thus, water must be present in the channel to reproduce the experimental 2D lineshape. It follows that during ion conduction, one water molecule is transported for each K^+ ion, in accord with streaming potential (*9*, *12*, *13*).

Analyzing the angles of the isotope-labeled carbonyls inside the selectivity filter, we found that removing the water from the knock-on model reduces the angular distribution by as much as 36% (see fig. S11). The hard-knock model, which also lacks water, has a similarly narrow angular distribution. Without the water, the high positive charge inside the filter causes a more rigid protein conformation and less dynamic K^+ ions, similar to experiments on K^+ binding to model peptides (*24*).

Because the temporal resolution of 2D IR spectroscopy is orders of magnitude shorter than the time scales for ion permeation, we can determine from the 2D IR spectra the relative populations of each of these ion-binding states. The experimental peaks have a ratio of 1.25 ± 0.02 from Fig. 2E. It follows that the relative equilibrium population of the [W, S2, W, S4], [S1, W, S3, W], and Val^{76}-flipped [S1, W, S3, W] ion configurations required to account for differences in lineshape and transition dipole strengths can be determined to be 30%, 30%, and 40%, respectively. The [W, S2, W, S4] and [S1, W, S3, W] ion configurations are equally populated, to within 5% of each other, which is in agreement with the ratio of states found in x-ray diffraction studies (*6*, *9*). Thus, the Val^{76}-flipped [S1, W, S3, W] ion configuration accounts for roughly 40% of the states at equilibrium. This flipped state has been reported in MD simulations (*29*) but has not been observed with x-ray crystallography.

The ultrafast time resolution of 2D IR spectroscopy provides an opportunity to test short-lived configurations extracted from MD simulations. Because the 2D IR time resolution of 1 to 2 ps is faster than almost all protein dynamics, the spectrum reports on the instantaneous distribution of ions, water, and protein structures. As a result, 2D IR spectroscopy provides a means to test protein conformations observed in crystal structures and to empirically refine simulations to effectively reweight configurations. Energy differences on the order of k_BT (k_BT = 0.593 kcal mol^{-1} at 298 K) are below the accuracy of current force fields (*31*), so simulations generated from different force fields could lead to different conclusions (*31*). Rather than test individual hypotheses, one might also simulate 2D IR spectra generated from Markov state models to analyze entire trajectories (*32*, *33*). Essential for this study was the ability to selectively introduce $^{13}C^{18}O$ isotope labels into the ion-binding sites in the filter. Advances in the semisynthesis methodology or, alternatively, the use of nonsense suppression approaches have widely expanded the range of membrane proteins that can be selectively labeled and therefore investigated using 2D IR spectroscopy (*34*). We anticipate that the combination of these new labeling methods, molecular dynamics, and 2D IR spectroscopy will be an important addition to the tool kit presently used to investigate the functional mechanisms that operate in membrane proteins.

REFERENCES AND NOTES

1. B. Hille, *Ion Channels of Excitable Membranes* (Sinauer, Sunderland, MA, 2001).
2. L. Heginbotham, T. Abramson, R. MacKinnon, *Science* **258**, 1152–1155 (1992).
3. D. A. Doyle *et al.*, *Science* **280**, 69–77 (1998).
4. A. L. Hodgkin, R. D. Keynes, *J. Physiol.* **128**, 61–88 (1955).
5. S. Uysal *et al.*, *Proc. Natl. Acad. Sci. U.S.A.* **106**, 6644–6649 (2009).
6. J. H. Morais-Cabral, Y. Zhou, R. MacKinnon, *Nature* **414**, 37–42 (2001).
7. A. N. Thompson *et al.*, *Nat. Struct. Mol. Biol.* **16**, 1317–1324 (2009).
8. S. Y. Noskov, S. Bernèche, B. Roux, *Nature* **431**, 830–834 (2004).
9. Y. Zhou, R. MacKinnon, *J. Mol. Biol.* **333**, 965–975 (2003).
10. S. Bernèche, B. Roux, *Nature* **414**, 73–77 (2001).
11. S. Bernèche, B. Roux, *Proc. Natl. Acad. Sci. U.S.A.* **100**, 8644–8648 (2003).
12. C. Alcayaga, X. Cecchi, O. Alvarez, R. Latorre, *Biophys. J.* **55**, 367–371 (1989).
13. M. Iwamoto, S. Oiki, *J. Neurosci.* **31**, 12180–12188 (2011).
14. J. Åqvist, V. Luzhkov, *Nature* **404**, 881–884 (2000).
15. S. Furini, C. Domene, *Proc. Natl. Acad. Sci. U.S.A.* **106**, 16074–16077 (2009).
16. P. W. Fowler, E. Abad, O. Beckstein, M. S. Sansom, *J. Chem. Theory Comput.* **9**, 5176–5189 (2013).
17. D. A. Köpfer *et al.*, *Science* **346**, 352–355 (2014).
18. S. D. Fried, S. Bagchi, S. G. Boxer, *J. Am. Chem. Soc.* **135**, 11181–11192 (2013).
19. A. Ghosh, J. Qiu, W. F. DeGrado, R. M. Hochstrasser, *Proc. Natl. Acad. Sci. U.S.A.* **108**, 6115–6120 (2011).
20. P. Stevenson *et al.*, *J. Phys. Chem. B* **119**, 5824–5831 (2015).
21. F. I. Valiyaveetil, R. MacKinnon, T. W. Muir, *J. Am. Chem. Soc.* **124**, 9113–9120 (2002).
22. A. G. Komarov, K. M. Linn, J. J. Devereaux, F. I. Valiyaveetil, *ACS Chem. Biol.* **4**, 1029–1038 (2009).
23. J. Torres, A. Kukol, J. M. Goodman, I. T. Arkin, *Biopolymers* **59**, 396–401 (2001).
24. Z. Ganim, A. Tokmakoff, A. Vaziri, *New J. Phys.* **13**, 113030 (2011).
25. A. Barth, *Prog. Biophys. Mol. Biol.* **74**, 141–173 (2000).
26. A. Barth, C. Zscherp, *Q. Rev. Biophys.* **35**, 369–430 (2002).
27. H. Kim, M. Cho, *Chem. Rev.* **113**, 5817–5847 (2013).
28. Y. S. Kim, R. M. Hochstrasser, *J. Phys. Chem. B* **113**, 8231–8251 (2009).
29. S. Bernèche, B. Roux, *Structure* **13**, 591–600 (2005).
30. P. Hamm, M. T. Zanni, *Concepts and Methods of 2D Infrared Spectroscopy* (Cambridge University Press, New York, 2011).
31. H. Li *et al.*, *J. Phys. Chem. B* **119**, 9401–9416 (2015).
32. C. R. Baiz *et al.*, *Biophys. J.* **106**, 1359–1370 (2014).
33. C. R. Schwantes, V. S. Pande, *J. Chem. Theory Comput.* **9**, 2000–2009 (2013).
34. L. Leisle, F. Valiyaveetil, R. A. Mehl, C. A. Ahern, in *Novel Chemical Tools to Study Ion Channel Biology*, C. Ahern, S. Pless, Eds. (Springer, New York, 2015), vol. 869, chap. 7, pp. 119–151.
35. S. Kraszewski, C. Boiteux, C. Ramseyer, C. Girardet, *Phys. Chem. Chem. Phys.* **11**, 8606–8613 (2009).

ACKNOWLEDGMENTS

This research was supported by U.S. National Institutes of Health grant NIH DK79895 (H.T.K., A.L.S., S.D.M., M.M., and M.T.Z), the University of Wisconsin Foundation (J.K.C. and J.L.S.), NIH R01-GM062342 (H.L. and B.R.), NIH GM087546 (K.M., A.W.A., and F.I.V.), NIH R01-GM057846 (E.P. and H.R), and the Membrane Protein Structural Dynamics Consortium U54 GM087519. F.I.V. and A.W.A. thank members of the Xiao group for advice on chemical synthesis. M.T.Z. is an owner of PhaseTech Spectroscopy, Inc. Additional materials, methods, and supplementary text detailing the data reported in this paper can be found in the supplementary materials.

SUPPLEMENTARY MATERIALS

www.sciencemag.org/content/353/6303/1040/suppl/DC1
Materials and Methods
Supplementary Text
Figs. S1 to S13
Tables S1 to S3
References (*36*–*59*)

14 May 2016; accepted 3 August 2016
10.1126/science.aag1447

Downloaded from http://science.sciencemag.org/ on September 1, 2016

HIV-1 ANTIBODIES

Antibody-mediated protection against SHIV challenge includes systemic clearance of distal virus

Jinyan Liu,[1] Khader Ghneim,[2] Devin Sok,[3] William J. Bosche,[4] Yuan Li,[4] Elizabeth Chipriano,[4] Brian Berkemeier,[4] Kelli Oswald,[4] Erica Borducchi,[1] Crystal Cabral,[1] Lauren Peter,[1] Amanda Brinkman,[1] Mayuri Shetty,[1] Jessica Jimenez,[1] Jade Mondesir,[1] Benjamin Lee,[1] Patricia Giglio,[1] Abishek Chandrashekar,[1] Peter Abbink,[1] Arnaud Colantonio,[5] Courtney Gittens,[6] Chantelle Baker,[6] Wendeline Wagner,[6] Mark G. Lewis,[6] Wenjun Li,[7] Rafick-Pierre Sekaly,[2]* Jeffrey D. Lifson,[4]* Dennis R. Burton,[3,8]* Dan H. Barouch[1,8]*†

HIV-1–specific broadly neutralizing antibodies (bNAbs) can protect rhesus monkeys against simian-human immunodeficiency virus (SHIV) challenge. However, the site of antibody interception of virus and the mechanism of antibody-mediated protection remain unclear. We administered a fully protective dose of the bNAb PGT121 to rhesus monkeys and challenged them intravaginally with SHIV-SF162P3. In PGT121-treated animals, we detected low levels of viral RNA and viral DNA in distal tissues for seven days following challenge. Viral RNA–positive tissues showed transcriptomic changes indicative of innate immune activation, and cells from these tissues initiated infection after adoptive transfer into naïve hosts. These data demonstrate that bNAb-mediated protection against a mucosal virus challenge can involve clearance of infectious virus in distal tissues.

Multiple broadly neutralizing antibodies (bNAbs) targeting HIV-1 envelope (Env) have demonstrated complete protection against simian-human immunodeficiency virus (SHIV) challenges in rhesus monkeys (*1*–*6*) and are currently being evaluated as a strategy to prevent HIV-1 acquisition in humans. However, the anatomic sites and mechanisms of antibody-mediated protection have not been fully elucidated. In particular, it remains unclear whether bNAbs completely block virus at the local portal of entry after mucosal virus challenge. To address this question, we performed comprehensive necropsies following intravaginal SHIV-SF162P3 challenge of rhesus monkeys that received a fully protective dose of the potent V3 glycan–dependent bNAb, PGT121 (*7*).

We verified the protective efficacy of PGT121 against intravaginal challenge with SHIV-SF162P3 (*8*–*10*) in a preliminary study in 12 female rhesus monkeys (*Macaca mulatta*). Consistent with previously published data (*1*), an intravenous infusion of 2 mg PGT121 per kilogram of body weight (mg/kg) afforded complete protection against intravaginal challenge with 5×10^4 median tissue culture infectious dose ($TCID_{50}$) SHIV-SF162P3, as evidenced by no detectable plasma viral RNA for more than 6 months following challenge (fig. S1). To evaluate the mechanism of this observed protection, 24 female rhesus monkeys received 2 mg/kg PGT121 ($N = 12$) or an isotype-matched sham control antibody ($N = 12$) by the intravenous route on day −1 and were challenged intravaginally with 5×10^4 $TCID_{50}$ SHIV-SF162P3 on day 0. Serum PGT121 levels were 20 to 50 μg/ml on the day of challenge in all animals. We performed serial necropsies on day 1 ($N = 4$), day 3 ($N = 4$), day 7 ($N = 10$), and day 10 ($N = 6$) following challenge for comprehensive assessments of virologic, immunologic, and transcriptomic profiles in multiple tissues in each animal (*11*).

Tissue viral RNA levels were quantified by an ultrasensitive nested reverse transcription polymerase chain reaction assay (*12*), which assessed 30 independent tissues from each animal from the female reproductive tract, draining lymph nodes, gastrointestinal tract, distal lymph nodes, tonsil, spleen, bone marrow, thymus, lung, liver, and central nervous system. In 75% (three out of four) of PGT121-treated animals on day 1 and day 3 following SHIV challenge, we observed low levels of viral RNA in at least one tissue distal to the female reproductive tract, primarily in draining lymph nodes and gastrointestinal tissue (Fig. 1A). Viral RNA was observed more frequently in PGT121-treated animals than in sham controls at these time points ($P = 0.02$, two-sided Fisher's exact test) (Fig. 1A); this observation suggested that the antibody may have facilitated translocation of virus across the mucosal barrier. On day 7, viral RNA distal to the female reproductive tract was still detected sporadically in 75% (three out of four) of PGT121-treated animals but was not detected in plasma. Viral RNA was detected far more extensively in sham controls than in PGT121-treated animals on day 7 ($P = 0.01$) (Fig. 1B). On day 10, viral RNA was not detected in any PGT121-treated animals at distal sites but was present at high levels in all tissues in the sham controls ($P = 0.01$), as expected (*13*–*15*) (Fig. 1C).

Viral DNA was also observed sporadically and at a declining frequency in PGT121-treated animals on days 1, 3, and 7 after challenge (Fig. 2, A to C). In contrast, viral DNA was detected at increasing magnitude and frequency over time in the sham controls, as expected. Taken together, these data show that low but declining levels of viral RNA and viral DNA were detectable in distal tissues in PGT121-treated animals for ~7 days following SHIV-SF162P3 challenge but were undetectable by day 10 (Figs. 1 and 2 and fig. S2).

In our SHIV-SF162P3 challenge stock, the level of viral *gag* RNA (7.5×10^8 copies/ml) was ~3 logs as great as the corresponding level of viral *gag* DNA (7.9×10^5 copies/ml) (Fig. 2D). In the four animals that exhibited viral DNA in distal tissues on days 1 to 7 (BD66, CP20, E41, and 6345), the median level of viral RNA (6.9×10^3 copies/10^8 cell equivalents) was similarly ~3 logs as high as the median level of viral DNA (<10 copies/10^8 cell equivalents) at the site of inoculation in the female reproductive tract, consistent with the notion that this virus largely represented the input challenge stock. In contrast, in distal tissues, the median level of viral RNA (4.0×10^1 copies/10^8 cell equivalents) was slightly lower than the median level of viral DNA (2.2×10^2 copies/10^8 cell equivalents) (Fig. 2D). Moreover, in the day 1 genital-pelvic lymph node from monkey BD66, viral RNA and viral DNA were detected in purified (>99%) $CD4^+$ T lymphocytes (Fig. 2E). These data suggest that the viral DNA detected in distal tissues reflected a limited degree of new virus replication at the distal sites.

We next assessed Gag-specific $CD8^+$ and $CD4^+$ T lymphocyte responses in multiple tissues from each animal by multiparameter intracellular cytokine staining assays (*16*, *17*). $CD8^+$ T lymphocyte responses were not detected in any tissue at any time point in the PGT121-treated animals, but these responses were observed in the female genital tract in all sham controls on day 7 and day 10 (figs. S3 to S5). The lack of detectable T lymphocyte responses in the PGT121-treated animals indicates insufficient antigen exposure to induce measurable cellular immune responses and suggests that virus-specific T cell responses were likely not responsible for the clearance of virus in distal tissues at these early time points.

We next evaluated gene expression profiles in multiple tissues in each animal at necropsy (*11*, *18*). A multidimensional scaling plot revealed differences between PGT121-treated animals and controls for all tissues analyzed (fig. S6). We compared transcriptomic profiles in viral RNA–positive compared with viral RNA–negative tissues in the PGT121-treated animals. Inflammasome-related genes [$P = 0.00013$; the NLR domain, pyrin domain containing 3 (NLRP3), Toll-like receptor genes],

[1]Center for Virology and Vaccine Research, Beth Israel Deaconess Medical Center, Boston, MA 02215, USA. [2]Case Western Reserve University, Cleveland, OH 44106, USA. [3]The Scripps Research Institute, La Jolla, CA 92037, USA. [4]AIDS and Cancer Virus Program, Leidos Biomedical Research, Frederick National Laboratory, Frederick, MD 21702, USA. [5]Harvard Medical School, Boston, MA 02115, USA. [6]Bioqual, Rockville, MD 20852, USA. [7]University of Massachusetts Medical School, Worcester, MA 01655, USA. [8]Ragon Institute of Massachusetts General Hospital, Massachusetts Institute of Technology, and Harvard, Cambridge, MA 02139, USA.
*These authors contributed equally to this work. †Corresponding author. Email: dbarouch@bidmc.harvard.edu

Downloaded from http://science.sciencemag.org/ on September 2, 2016

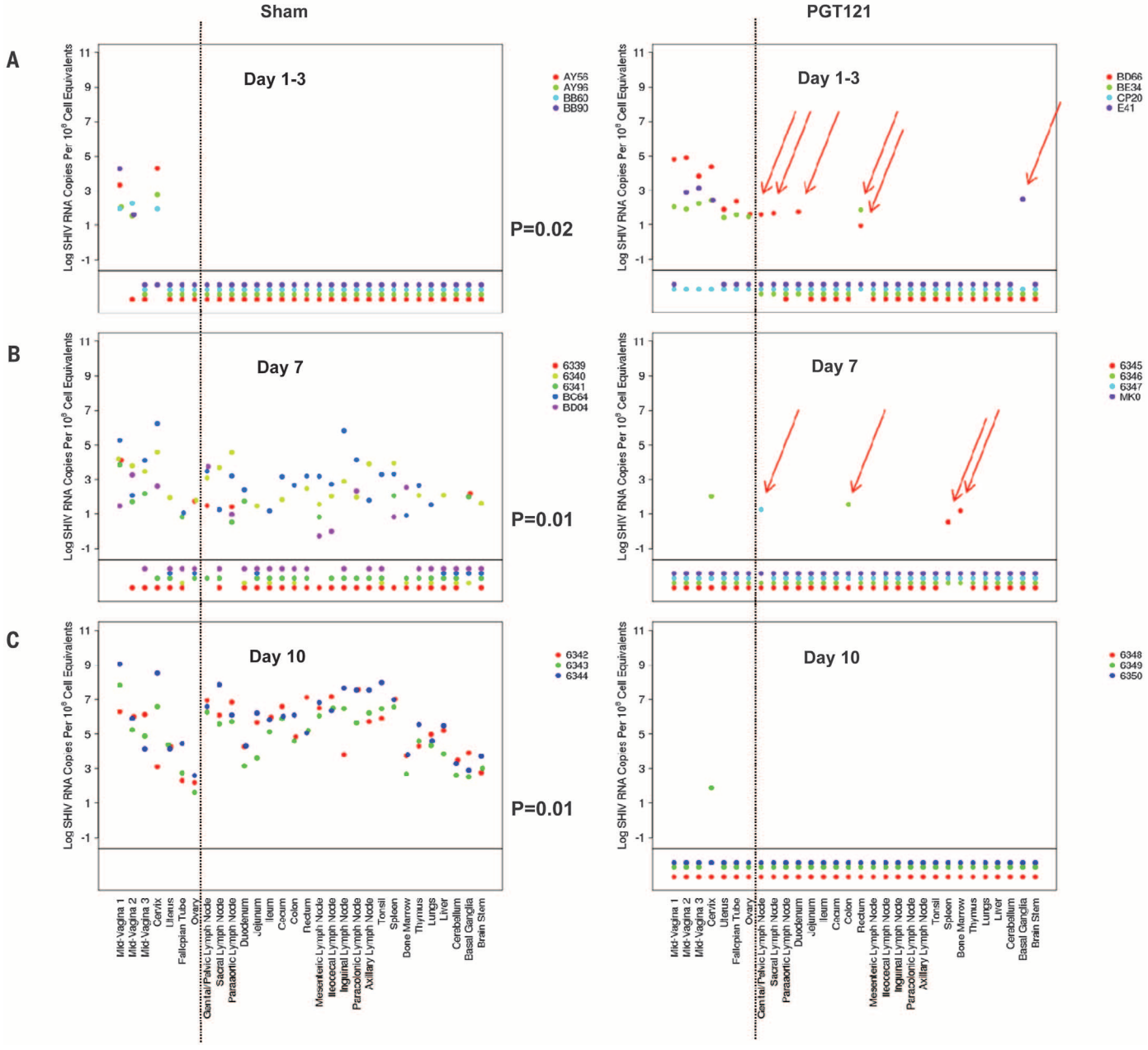


Fig. 1. Viral RNA in tissues following SHIV-SF162P3 challenge. Tissue viral RNA (log RNA copies/10^8 cell equivalents) across multiple tissues at necropsy in PGT121-treated animals and sham controls on (**A**) day 1 (AY56, AY96, BD66, and BE34) and day 3 (BB60, BB90, CP20, and E41), (**B**) day 7, and (**C**) day 10 following SHIV-SF162P3 challenge. Colors on each plot reflect individual animals (see keys). Values plotted below the horizontal line indicate samples for which viral RNA was not measured above the threshold of detection. Values to the right of the vertical line reflect samples distal to the female reproductive tract. Red arrows highlight viral RNA–positive distal tissues in the PGT121-treated animals. *P* values reflect Fisher's exact tests. Data are presented based on calculations normalized as log viral RNA copies/10^8 diploid genome equivalents of DNA; for this study, the majority of the specimens analyzed contained 10^6 to 10^7 cell equivalents.

and interferon-stimulated genes [P = 0.000046; *IFITM2*, *interleukin 8* (*IL8*), *S100A8*] were up-regulated specifically in viral RNA–positive local and distal tissues from animals that received PGT121 (Fig. 3A and fig. S7). Pathway analysis (*19*) confirmed up-regulation of several pathways associated with host response to viruses (interferon-α and interferon-β) and cellular activation (hypoxia, tumor necrosis factor signaling via nuclear factor κB, and Janus kinase signal transducers and activators of transcription signaling) in these tissues (fig. S8). Moreover, a linear regression analysis revealed a transcriptomic signature that correlated with viral RNA levels in PGT121-treated animals necropsied on days 1, 3, and 7 (P = 0.00029) (Fig. 3B). Network inference analysis (*20*, *21*) revealed that this signature involved activation of innate immunity and antiviral pathways, including type 1 interferon signaling [false discovery rate (FDR) =1.64×10^{-46}], host response to viral infection (FDR = 2.85×10^{-29}), regulation of viral replication (FDR = 2.49×10^{-17}), and response to interferon-γ (FDR = 1.91×10^{-16}) (Fig. 3C and fig. S9).

We also observed an increase in the number of differentially expressed total and interferon-stimulated genes over the first 7 days in viral RNA–positive tissues from PGT121-treated animals (fig. S10). By day 7, up-regulation of classic antiviral restriction factors such as IRF7, TRIM5,

Downloaded from http://science.sciencemag.org/ on September 2, 2016

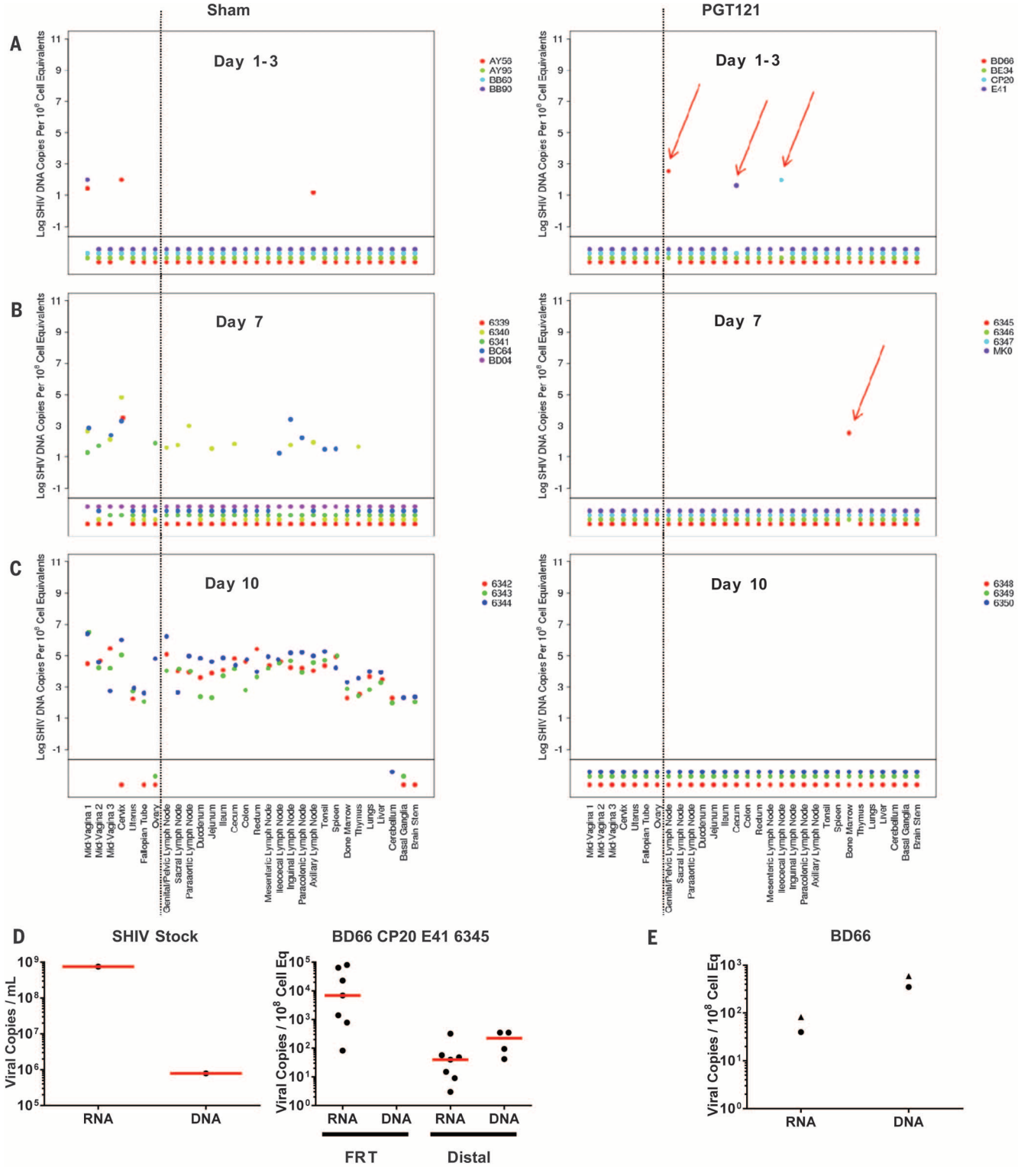


Fig. 2. Viral DNA in tissues following SHIV-SF162P3 challenge. Tissue viral DNA (log DNA copies/10^8 cell equivalents) across multiple tissues at necropsy in PGT121-treated animals and sham controls on (**A**) days 1 and 3, (**B**) day 7, and (**C**) day 10 following SHIV-SF162P3 challenge. Colors on each plot refer to individual animals (see keys). Values plotted below the horizontal line indicate samples for which viral DNA was not measured above the threshold of detection. Values to the right of the vertical line indicate samples distal to the female reproductive tract. Red arrows highlight viral DNA–positive distal tissues in the PGT121-treated animals. Data are presented based on calculations normalized as log viral DNA copies/10^8 diploid genome equivalents of DNA; for this study, the majority of the specimens analyzed contained 10^6 to 10^7 cell equivalents. (**D**) Viral RNA and viral DNA in the SHIV-SF162P3 stock (left) and in female reproductive tract (FRT) and distal tissues in the four animals that were viral DNA–positive on days 1 to 7 (BD66, CP20, E41, and 6345) (right). Median, red line. (**E**) Viral RNA and viral DNA in total cells (circles) and in purified $CD4^+$ T lymphocytes (triangles) from BD66 genital-pelvic lymph node on day 1. Data are based on analysis of 2.7×10^6 purified $CD4^+$ T lymphocytes.

Downloaded from http://science.sciencemag.org/ on September 2, 2016

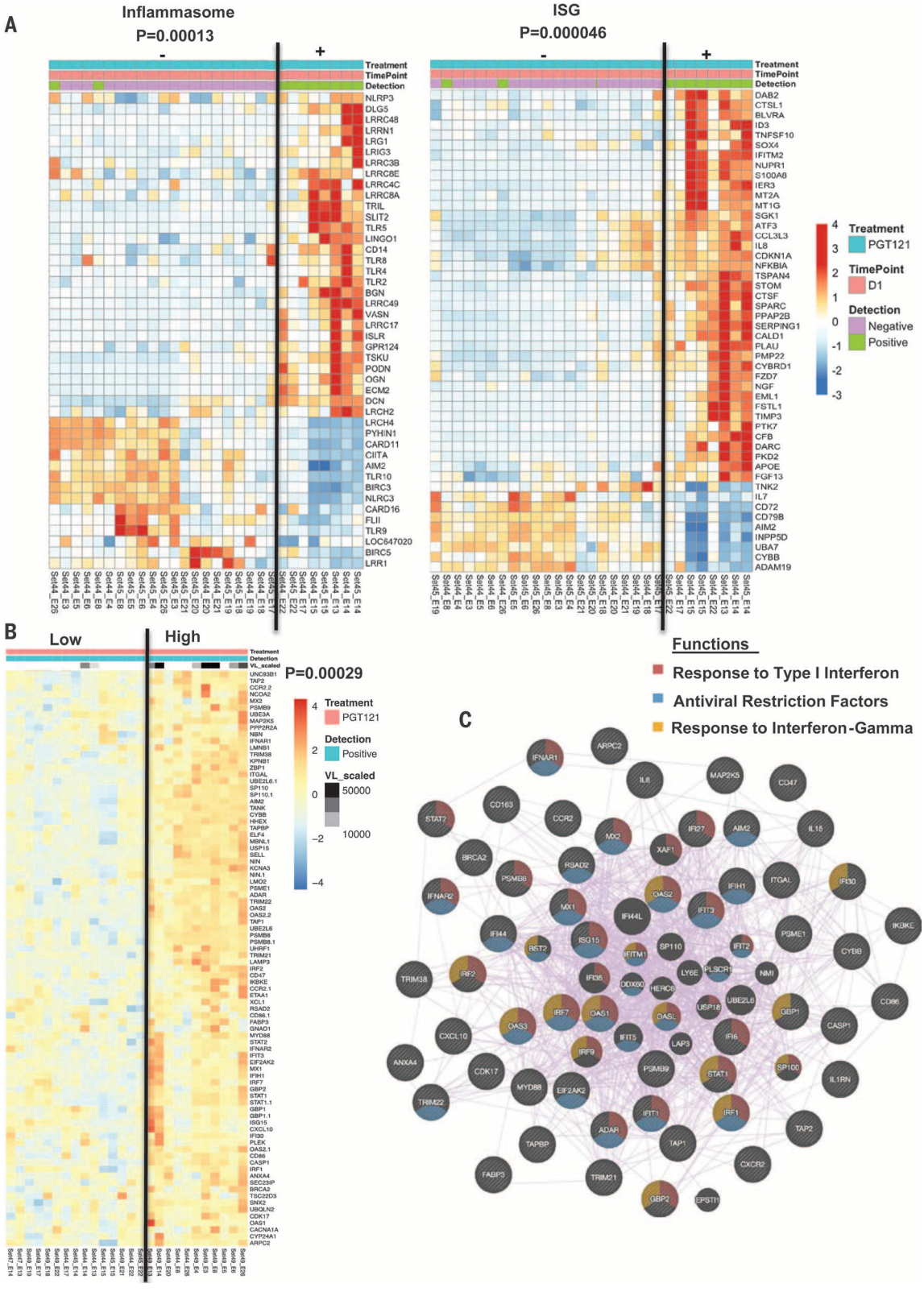


Fig. 3. Transcriptomic signature in viral RNA–positive tissues from PGT121-treated animals. (**A**) Heat maps reveal inflammasome and interferon-stimulated gene (ISG) signatures in viral RNA–positive compared with viral RNA–negative local and distal tissues from PGT121-treated animals on day 1 following SHIV-SF162P3 challenge. Gene expression is represented by standardized expression (*Z*-score) with $P < 0.05$. Red and blue correspond to up-regulated and down-regulated genes, respectively. *P* values represent the significance of the two clusters using Fisher's exact tests. From two monkeys (BD66 and BE34), 29 samples are represented; they reflect 10 viral RNA–positive samples and 19 viral RNA–negative samples. (**B**) Linear regression analysis of viral RNA as a continuous variable and gene expression (Linear Models for Microarray Data *t* test with $P < 0.05$) in viral RNA–positive tissues from PGT121-treated animals reveals a transcriptomic signature that correlates with levels of viral RNA. Heat map represents the top positively correlated genes that were part of the full regression signature. From four monkeys, 26 samples were included in this analysis, reflecting 10 samples from day 1, 2 samples from day 3, and 14 samples from day 7. (**C**) Network of genes that positively correlated with levels of viral RNA in tissues from PGT121-treated animals. Nodes represent genes and purple lines represent coexpression between genes.

APOBEC, and IFITM was evident in these tissues, suggesting an evolving antiviral innate response. The late expression of these antiviral restriction factors is consistent with our previous findings in simian immunodeficiency virus SIVmac251 infection (*11*). The up-regulated genes in viral RNA–positive tissues from PGT121-treated animals also partially overlapped with a previously defined transcriptomic signature for viral replication (*22*) (fig. S11).

To investigate whether the low levels of detectable virus in distal tissues in PGT121-treated

Downloaded from http://science.sciencemag.org/ on September 2, 2016

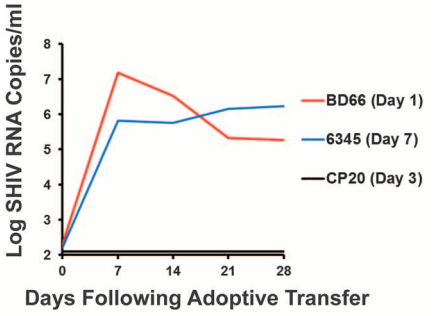


Fig. 4. Adoptive transfer studies. Adoptive transfer of 30 million cells into naïve hosts by the intravenous route from tissues from BD66 (genital-pelvic lymph node from day 1), CP20 (ileocecal lymph node from day 3), and 6345 (spleen from day 7). Plasma viral RNA copies/ml are shown following adoptive transfer.

animals were infectious, we adoptively transferred 30 million cells from the following animals and tissues into naïve hosts by the intravenous route: BD66 (genital-pelvic lymph node; day 1), CP20 (ileocecal lymph node; day 3), and 6345 (spleen; day 7). Tissues from BD66 and 6345 were positive for both viral RNA and viral DNA, whereas tissues from CP20 were negative for viral RNA but positive for viral DNA. Adoptive transfer of cells from BD66 and 6345 into naïve hosts efficiently transferred infection, resulting in 5.8 to 7.1 log RNA copies/ml of replicating virus by day 7 after adoptive transfer (Fig. 4) and demonstrating that the viral RNA and viral DNA detected in these samples included replication-competent infectious virus when removed from the host milieu of antibody and innate factors. Cells from CP20 did not detectably transfer infection; this suggests that the amount of virus in this sample was too low or that the viral DNA in this sample was defective and noninfectious.

In summary, we detected low levels of viral RNA and/or viral DNA in at least one tissue distal to the female reproductive tract in 87.5% (seven of eight) of monkeys on days 1, 3, and 7 following intravaginal SHIV-SF162P3 challenge, despite receiving a fully protective dose of PGT121 (fig. S12). Virus in distal tissues triggered transcriptomic responses involving activation of innate immunity and antiviral pathways, and a subset of these samples proved infectious after adoptive transfer into naïve hosts. These data demonstrate that PGT121 did not completely block the challenge virus at the mucosal portal of entry. Instead, some virions appeared to transit to distal tissues, where they were progressively cleared over a period of ~7 days and potentially involved Fc effector mechanisms, such as antibody-dependent cellular cytotoxicity. The viral RNA to viral DNA ratio at distal sites (Fig. 2D), the presence of viral RNA and viral DNA in purified $CD4^+$ T lymphocytes (Fig. 2E), and the transcriptomics signatures (fig. S11) suggested a limited degree of new virus replication at distal sites.

Although our studies were limited to PGT121, it is likely that other bNAbs, as well as vaccine-elicited antibodies (*9*), also involve viral clearance in distal tissues rather than complete blockade of virus at the mucosal surface. These data emphasize the potential importance of antibodies to clear virally infected cells in tissues to block the establishment of chronic infection (*9*, *23*–*25*). These data are also consistent with previous findings from our laboratory and others that the virus can disseminate rapidly and trigger inflammatory responses in host tissues following mucosal challenge (*11*, *26*–*28*). Moreover, our findings are consistent with the observation that bNAbs may be able to abort initial infection in infant rhesus monkeys when administered therapeutically after SHIV challenge (*29*). The possibility that PGT121 may have actually facilitated virus translocation across the mucosal barrier, potentially via immune complexes captured on Fc receptor–bearing cells, warrants further investigation.

Our findings have important implications for the development of vaccines, passively transferred antibodies, and other interventions to block HIV-1 infection. In particular, our data suggest that a systemic component of an antiviral intervention may be necessary for optimal efficacy to clear early foci of disseminated virus in distal tissues. It is noteworthy that high concentrations of topically applied bNAbs are required to protect against mucosal SHIV challenge, whereas much lower serum concentrations of intravenously administered bNAbs are required for protection (*30*, *31*). Our data also show that the initial virus that is seeded in distal tissues may still be vulnerable to immune-mediated elimination before the establishment of a permanent viral reservoir. Further exploitation of this vulnerability may lead to improved HIV-1 eradication strategies, as well as improved HIV-1 prevention strategies.

REFERENCES AND NOTES

1. B. Moldt *et al.*, *Proc. Natl. Acad. Sci. U.S.A.* **109**, 18921–18925 (2012).
2. M. Shingai *et al.*, *J. Exp. Med.* **211**, 2061–2074 (2014).
3. J. R. Mascola *et al.*, *J. Virol.* **73**, 4009–4018 (1999).
4. J. R. Mascola *et al.*, *Nat. Med.* **6**, 207–210 (2000).
5. T. W. Baba *et al.*, *Nat. Med.* **6**, 200–206 (2000).
6. A. J. Hessell *et al.*, *Nat. Med.* **15**, 951–954 (2009).
7. L. M. Walker *et al.*, *Nature* **477**, 466–470 (2011).
8. D. H. Barouch *et al.*, *Cell* **155**, 531–539 (2013).
9. D. H. Barouch *et al.*, *Science* **349**, 320–324 (2015).
10. D. H. Barouch *et al.*, *Nature* **503**, 224–228 (2013).
11. D. H. Barouch *et al.*, *Cell* **165**, 656–667 (2016).
12. S. G. Hansen *et al.*, *Nature* **502**, 100–104 (2013).
13. Q. Li *et al.*, *Nature* **434**, 1148–1152 (2005).
14. J. J. Mattapallil *et al.*, *Nature* **434**, 1093–1097 (2005).
15. J. M. Brenchley *et al.*, *J. Exp. Med.* **200**, 749–759 (2004).
16. D. H. Barouch *et al.*, *Nature* **482**, 89–93 (2012).
17. H. Li *et al.*, *J. Virol.* **85**, 11007–11015 (2011).
18. Y. Fukazawa *et al.*, *Nat. Med.* **18**, 1673–1681 (2012).
19. A. Subramanian *et al.*, *Proc. Natl. Acad. Sci. U.S.A.* **102**, 15545–15550 (2005).
20. S. Mostafavi, Q. Morris, *Bioinformatics* **26**, 1759–1765 (2010).
21. S. Mostafavi, D. Ray, D. Warde-Farley, C. Grouios, Q. Morris, *Genome Biol.* **9** (suppl. 1), S4 (2008).
22. J. W. Schoggins *et al.*, *Nature* **472**, 481–485 (2011).
23. A. J. Hessell *et al.*, *Nature* **449**, 101–104 (2007).
24. S. Bournazos *et al.*, *Cell* **158**, 1243–1253 (2014).
25. A. W. Chung *et al.*, *Cell* **163**, 988–998 (2015).
26. C. J. Miller *et al.*, *J. Virol.* **79**, 9217–9227 (2005).
27. P. Ribeiro dos Santos *et al.*, *PLOS ONE* **6**, e19493 (2011).
28. J. Hu, M. B. Gardner, C. J. Miller, *J. Virol.* **74**, 6087–6095 (2000).
29. A. J. Hessell *et al.*, *Nat. Med.* **22**, 362–368 (2016).
30. D. R. Burton *et al.*, *Proc. Natl. Acad. Sci. U.S.A.* **108**, 11181–11186 (2011).
31. R. S. Veazey *et al.*, *Nat. Med.* **9**, 343–346 (2003).

ACKNOWLEDGMENTS

We thank A. Schultz, Q. Dang, M. Pensiero, M. Ferguson, F. Stephens, J. Nkolola, K. Smith, J. Smith, S. Blackmore, L. Parenteau, S. Mathew, S. Levin, C. Shaver, and Z. Pippin for generous advice, assistance, and reagents. The SIVmac239 peptides were obtained from the NIH AIDS Research and Reference Reagent Program. The data presented in this paper are tabulated in the main paper and in the supplementary materials. The authors declare no competing financial interests. Correspondence and requests for materials should be addressed to D.H.B. (dbarouch@bidmc.harvard.edu). We acknowledge support from the National Institutes of Health (AI060354, AI095985, AI096040, AI100645, AI100663, AI124377, HHSN261200800001E) and the Ragon Institute of Massachusetts General Hospital, Massachusetts Institute of Technology, and Harvard. Transcriptomics data can be accessed at GEO (GSE83702) and the National Center for Biotechnology Information, NIH (17948367).

SUPPLEMENTARY MATERIALS

www.sciencemag.org/content/353/6303/1045/suppl/DC1
Materials and Methods
Supplementary Text
Figs. S1 to S12
References

4 May 2016; accepted 10 August 2016
Published online 18 August 2016
10.1126/science.aag0491

Downloaded from http://science.sciencemag.org/ on September 2, 2016



PHOTO: CRG

BEN LEHNER MAKES TAILOR-MADE MEDICINE A REALITY

- From worms to databases of human DNA, he explores factors that turn genomes into individuals who respond uniquely to mutations, diseases and treatments.
- The Genetics Systems group he leads is based at the Center for Genomic Regulation in Barcelona, Spain.
- He is the 2016 laureate of the Liliane Bettencourt Prize for Life Sciences awarded each year to an exceptional scientist under 45 by the Bettencourt Schueller Foundation.

BETTENCOURT
SCHUELLER
FOUNDATION

The Liliane Bettencourt Prize for Life Sciences rewards a European researcher under the age of 45.

It has been awarded every year since 1997 to scientists recognized within the community for the quality of their international publications, the promising prospects of their projects and the leadership demonstrated in mobilising an entire team.

Created by a family, the Foundation trusts in people and their capacities, emphasizing inititative, creativity, quality and openness.

Its convictions define its spirit and ways of working – in the common interest, not for profit, and with social responsibility in mind.

27-29 rue des Poissonniers • 92200 Neuilly-sur-Seine • France
sciences@fondationbs.org

Find out more about Ben Lehner, the Bettencourt Schueller Foundation's purpose and this year's awards at ***www.fondationbs.org***

AMERICAN ASSOCIATION FOR THE ADVANCEMENT OF SCIENCE

BE THE CORE MIND SPIRIT FACE HEART REACH CENTER VOICE OF SCIENCE.

AAAS members harness the power of scientific thinking to help tackle complex, global challenges.

Join the community of scientists, engineers, and educators whose work impacts millions.

How will YOU make your mark in science?

Join AAAS today.
www.aaas.org/join

AAAS

Foshan



Dare to be the pioneer , and lead the future development

After the baptism of history and the reform and opening-up policy, Foshan citizens have built the urban spirit of " pioneering, pragmatic and harmonious", which given play to the urban construction and innovative development.













Foshan is known as a marvelous place with outstanding people which has a unique charm through the ages

The history of Foshan could trace back to 5000 years ago. The ancestors of the Bai Yue nationality had lived here for generations and created the primitive civilization by their wisdom and diligence. As early as the Tang and Song Dynasties, Foshan had become the first commercial port in Lingnan area and one of the "Top Four Famous Towns" in China. In the Ming and Qing dynasties, it became the largest commodity distribution center in the south, and was known as the "Top Four Gather" with Beijing, Wuhan and Suzhou. In addition, Foshan is not only the origin of Lingnan culture, but also the representative of Cantonese culture. In the meanwhile, it has some high reputations like "Ceramic Capital of the South" and the "Hometown of Cantonese Opera" for a long time because of its shining intangible cultural heritage, such as, Cantonese operas, Cantonese tunes, art potteries of Shiwan, folk art papercuts, wood engraving pictures, autumn scenery, martial arts, southern lion and dragon dancing, and so on.

There are three international masters of martial arts that come from this miraculous land, who are Wong Feihung, Yip Man, and Bruce Lee, as well as the wealthy businessmen and tycoons like Jane's brothers, Chen Qiyuan and Huang Danian. In the contemporary era, eleven national masters of pottery art have emerged successively here.

About **Foshan**

Located in the Pearl River Delta region, which is the most dynamic economic region in China, Foshan has jurisdiction over the districts of Chancheng, Nanhai, Shunde, Gaoming and Sanshui. With a total area of 3797.72 km², it has 7.43 million residents including registered population of 3.89 million. Foshan and Guangzhou form the "Guangzhou-Foshan Metropolitan Area", which is a significant part of the "Guangzhou-Foshan-Zhaoqing Economic Zone" and the "Pearl River-Xi River Economic Zone".It leads the way in the economic and social development of Guangdong province.

Foshan borders on Hong Kong and Macao. It takes about two hours from Foshan to Hong Kong or Macao by car. With the Guangzhou-Shenzhen high-speed railway and the Guangzhou-Zhuhai Inter-city railway commencing operations, Foshan, Hong Kong and Macao form a "one hour traffic circle."













With optimized and upgraded industrial structure
the integrated competitiveness of Foshan is becoming forceful >>>>>>>

Foshan has continued promoting adjustment, transformation and upgrading of industrial structure, and become a comprehensive reform pilot of national manufacturing industry transformation and upgrading in 2015.

It has a lot of advantaged industries, such as mechanical equipment, household electric appliance, ceramic building materials, metal materials processing and products, textile and garment, electronic information, food and beverage, fine chemical and pharmaceutical industries and so on. Meanwhile some other industries are emerging rapidly, such as, photoelectricity, new materials, new energy, energy conservation and environmental protection, new medicine. In addition,modern industrial system is established preliminary with gradually impeccable supporting capacity.

According to 2015 Blue Book of Chinese City Competitiveness, which was recently released by the Chinese Academy of Social Sciences, the overall economic competitiveness of Foshan has ranked No.11 among 294 cities in the cross-strait four places of China.

In 2015, the regional GDP of Foshan has reached 800.392 billion yuan, with an increase of 8.5%, which ranked the No.3 in Guangdong and No.16 in China. Moreover, Foshan has achieved above-scale total industrial output value of 1.977493 trillion yuan, with an increase of 7.9%.The ratio of the three industries is 1.7: 60.5: 37.8, which shows the obvious predominance of second industry.

NEW ENGLAND BioLabs® Inc.

Migrate to Monarch®.

Environmentally-friendly Nucleic Acid Purification Kits from New England Biolabs

Want to feel good about your choice in DNA purification? With our fast and reliable Monarch Nucleic Acid Purification Kits, you can achieve optimal purification while creating less waste. Available for plasmid minipreps, DNA gel extraction and enzymatic cleanup (including PCR), our products use up to 44% less plastic and are packaged using responsibly-sourced, recyclable materials. Make the change and migrate to Monarch today.



> *These kits might be the best I have used for the price. The best part is that it uses less plastic for production!! Thank you for caring about our environmental impacts, NEB!!!*
>
> – NEB customer

Request your free sample at **www.NEBMonarch.com**

NEW ENGLAND BIOLABS®, NEB® and MONARCH® are registered trademarks of New England Biolabs, Inc.

invitrogen



One conductor, a symphony of enzymes

Finally, a complete, one-buffer system–for beautifully simple cloning

Introducing the Invitrogen™ Anza™ Restriction Enzyme Cloning System:

- One buffer for all restriction enzymes
- One digestion protocol for all DNA types
- Complete digestion in 15 minutes
- Overnight digestion without star activity

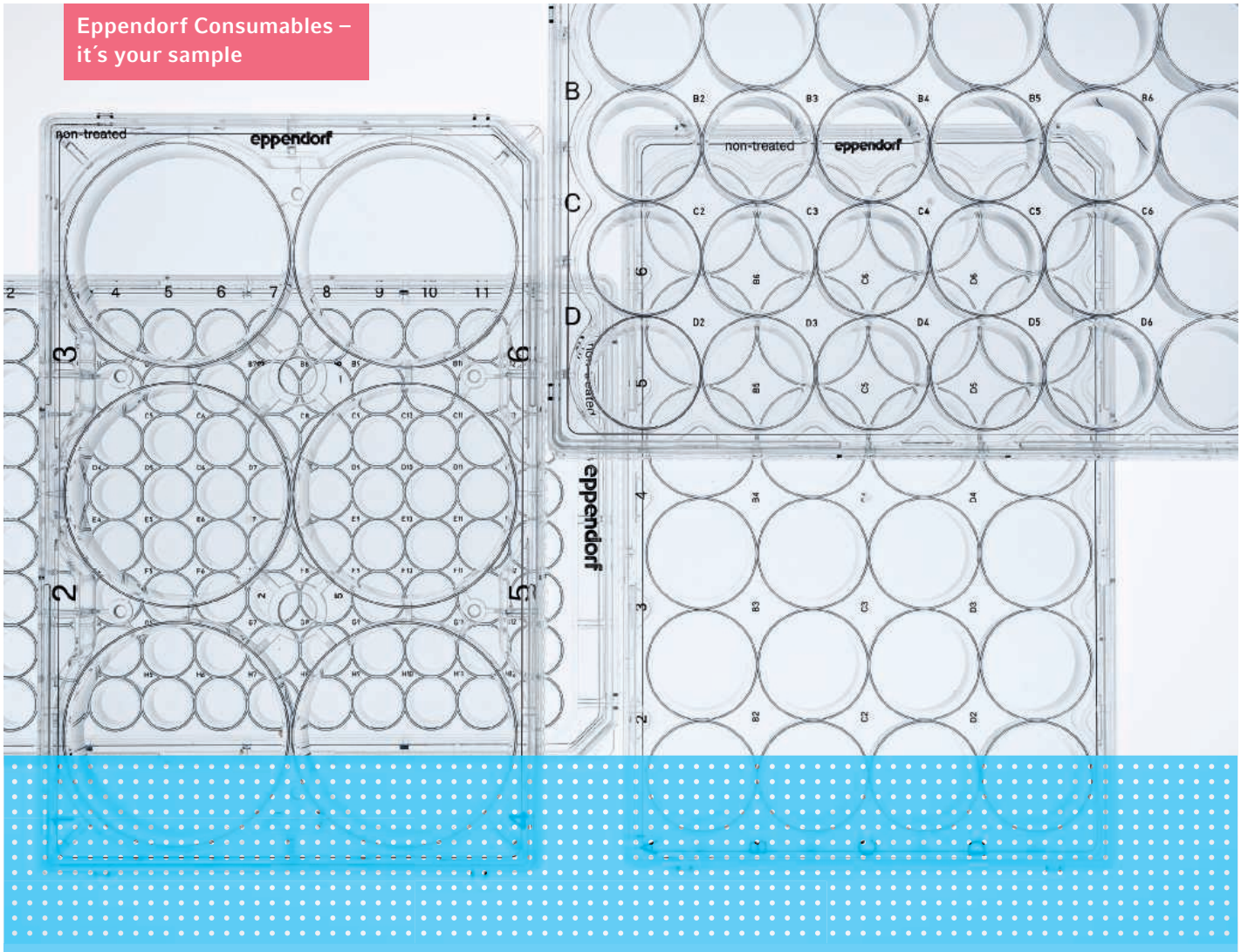
Choose simplicity at **thermofisher.com/Anza**

ThermoFisher SCIENTIFIC

For Research Use Only. Not for use in diagnostic procedures. © 2015 Thermo Fisher Scientific Inc. All rights reserved. All trademarks are the property of Thermo Fisher Scientific and its subsidiaries unless otherwise specified. **CO126010 0815**

eppendorf

Eppendorf Consumables –
it´s your sample



Impress Yourself

Eppendorf Cell Culture Consumables
Proven Eppendorf quality brought to a new level. Premium in all aspects: Product, Performance and Packaging according to highest Eppendorf standards.

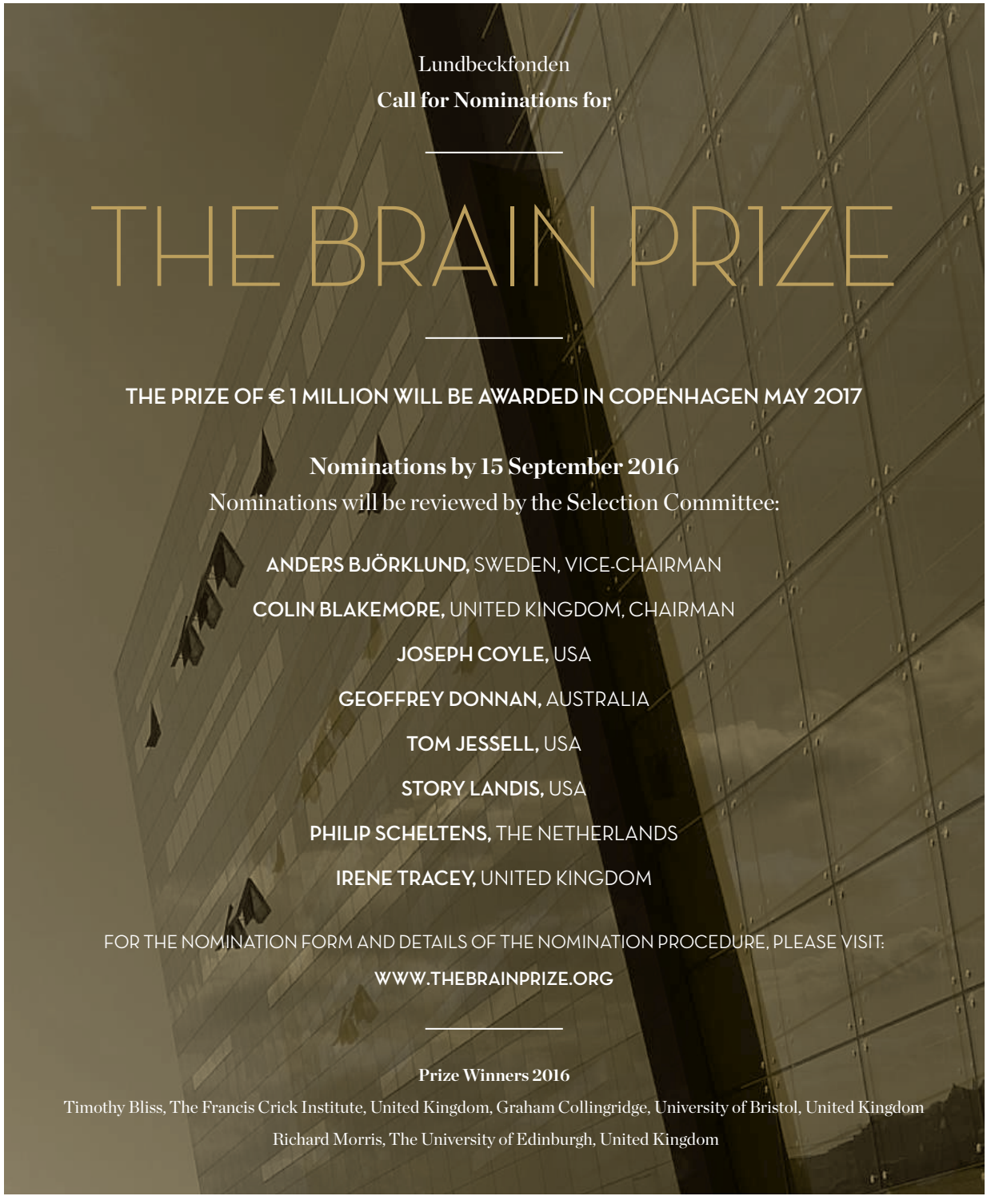
Find more information about our outstanding quality as a result of experience and constant development on www.eppendorf.com/ccc



www.eppendorf.com/consumables

Watch Video!

Eppendorf® and the Eppendorf logo are registered trademarks of Eppendorf AG, Germany.
All rights reserved, including graphics and images. Copyright © 2016 by Eppendorf AG.



Lundbeckfonden

Call for Nominations for

THE BRAIN PRIZE

THE PRIZE OF € 1 MILLION WILL BE AWARDED IN COPENHAGEN MAY 2017

Nominations by 15 September 2016

Nominations will be reviewed by the Selection Committee:

ANDERS BJÖRKLUND, SWEDEN, VICE-CHAIRMAN

COLIN BLAKEMORE, UNITED KINGDOM, CHAIRMAN

JOSEPH COYLE, USA

GEOFFREY DONNAN, AUSTRALIA

TOM JESSELL, USA

STORY LANDIS, USA

PHILIP SCHELTENS, THE NETHERLANDS

IRENE TRACEY, UNITED KINGDOM

FOR THE NOMINATION FORM AND DETAILS OF THE NOMINATION PROCEDURE, PLEASE VISIT:

WWW.THEBRAINPRIZE.ORG

Prize Winners 2016

Timothy Bliss, The Francis Crick Institute, United Kingdom, Graham Collingridge, University of Bristol, United Kingdom

Richard Morris, The University of Edinburgh, United Kingdom

THE BRAIN PRIZE

The Brain Prize recognizes and rewards outstanding contributions to European neuroscience, from basic to clinical

DEPArray™ NxT

choose 100% purity



BREAKING THE BARRIER OF TUMOR HETEROGENEITY

Get conclusive data by selecting, sorting and collecting pure tumor and stromal cells to clearly assign genetic variant frequency. Achieving the unlimitate level of purity is a necessary step to unambiguously resolve sample heterogeneity.

NEW FEATURES

High-resolution Imaging • 96 Recoveries • High-level Automation • Benchtop Instrument

D 2.23 ft x W 2.62 ft x H 2.02 ft

www.siliconbiosystems.com

MENARINI silicon biosystems

FISH Assay

The MicroFISH Assay System is a clinically validated method combining microvolume, multiwell slides with SciGene slide processing instruments to economically perform routine cellular fluorescence in situ hybridization (FISH) in cytogenetic laboratories. The system uses a 1-µL probe for each 1-µL sample on specially coated 8-well MicroFISH slides. No coverslip sealant is needed. Coverslip removal and slide washing is automated. The lower volume conserves precious samples while reducing probe costs by 75% and labor costs by 50%.

SciGene
For info: 408-733-7337
www.scigene.com

Rotary Evaporator

The rotary evaporator Rotavapor R-300 evaporates liquids for separation. The modular concept offers many options for upgrades and customization (e.g., hand lift/electrical, touchscreen controllers, 2-L and 5-L bath, protection shield, various vessel types, etc.). Several vacuum pumps and recirculation coolers complete the product family. The I-300 and I-300 Pro are interfaces for the BUCHI Rotavapor R-300. Both are fully automated process controllers of all system components—attached on the rotary evaporator. The I-300 Pro offers the additional option of navigating the menu by using either the function buttons/pushwheel or the touchscreen display, or both combined. The different modes (operating or processing) are visually separated by reversing the display colors. The equipment suits a wide range of industries such as pharmaceuticals, chemicals, food and beverage, feed, environmental analysis, and academia.

Büchi Labortechnik AG
For info: +41-(0)-71-394-63-63
www.buchi.com



Motorized Z-Axis Microscope Focus Blocks

The FB series of Z-axis motorized focus blocks from Prior Scientific offer precise and repeatable positioning of loads with a weight of up to 14 kg. When creating an imaging system, it is often necessary to move components and samples, such as an XY microscope stage, vertically. Achieving precise movement in the Z-Axis is essential for high-quality imaging but can be difficult, especially with heavier components. Designed and manufactured to the highest standards, Prior Scientific Z-axis motorized focus blocks deliver the repeatability (± 0.7 µm) and precision (± 20 nm) required for almost any imaging application. Even with a full load, these motorized focus blocks may be driven between 1 mm/sec and 14 mm/sec over a travel range of 38 mm, making them a versatile choice for integration with a wide range of imaging systems. Standard and custom FB series motorized focus blocks are available to suit most applications.

Prior Scientific
For info: +44-(0)-1223-881711
www.prior.com

Manual Pipettes

Unlike traditional pipettes, which utilize a single rotating plunger to set volumes, the EVOLVE features three adjustable dials for setting each individual volume digit. Simply depress and twist the plunger to unlock the volume dials. Once unlocked, freely adjust the three dials to rapidly set the desired volume. This approach allows users to set volumes more than 10 times faster than is possible with traditional pipettes. Available in single-, 8-, and 12-channel formats, covering a volume range of 0.2 µL–5,000 µL, the ultra-lightweight, well-balanced design of the EVOLVE enhances productivity and comfort. EVOLVE manual pipettes are optimized for use with INTEGRA's wide range of GripTips pipette tips. GripTips snap into place with minimal tip-loading effort, providing a secure connection and superior accuracy and precision. The new INTEGRA linear stand holds up to 13 EVOLVE pipettes. Users can add up to four charging/communication stations to convert the linear stand into a charging stand.

Integra Biosciences
For info: 603-578-5800
www.integra-biosciences.com

Portable Infrared Spectrometer

The Delta IRIS with URI Connect is a new solution that extends the continuous measurement of isotope ratios and concentrations of CO_2 in air to discrete samples, such as headspace analysis or direct injection of small amounts of CO_2. By simultaneously detecting ^{13}C and ^{18}O, the system allows scientists to measure both isotopologues and concentration in one step, without destroying the sample. The universal reference interface (URI) Connect system lets the user interface with samples containing as little as 80 µg of CO_2, such as in vials, syringes, or bags, which can then be analyzed with the Delta Ray isotope ratio infrared spectrometer (IRIS) analyzer. The instrument was designed with field portability and operational simplicity in mind, so that scientists can place it right at the point of their research interest. The URI Connect interface balances the concentration of reference gases against that of the sample, targeting accuracy with minimum effort from the user.

Thermo Fisher Scientific
For info: 800-955-6288
www.thermofisher.com

DNA Ladder

The Vivantis VC DNA Ladders offer numerous choices to give you an accurate determination of size and quantity of DNA or DNA fragments to complete your electrophoresis work. They are suitable for the sizing of PCR products or double-stranded DNA (dsDNA) fragments. Each DNA ladder comes complete with loading buffer. Choices include VC 1kb (kilobase) DNA ladder, VC 1kb-ex (extended) DNA ladder, VC 100bp (base pair) DNA ladder, VC 100bp Plus DNA ladder, and VC DNA ladder mix. A DNA ladder is a marker that consists of DNA fragments of specific base-pair lengths. It has a set of molecular weight standards that are used in identifying the estimated size of a molecule run on gel during electrophoresis, such as the size and quantity of DNA fragments of genomic, plasmid, and PCR DNA. It can be run either in agarose or polyacrylamide gels.

Vivantis Technologies
For info: 603-8025-1603
www.vivantechnologies.com

Electronically submit your new product description or product literature information! Go to www.sciencemag.org/about/new-products-section for more information.

Newly offered instrumentation, apparatus, and laboratory materials of interest to researchers in all disciplines in academic, industrial, and governmental organizations are featured in this space. Emphasis is given to purpose, chief characteristics, and availability of products and materials. Endorsement by *Science* or AAAS of any products or materials mentioned is not implied. Additional information may be obtained from the manufacturer or supplier.

WILL YOUR RESEARCH LEAD TO BETTER LIVES FOR PATIENTS?



Gopinath Sutendra and Evangelos D. Michelakis, "Pulmonary Arterial Hypertension: Challenges in Translational. Research and a Vision for Change", *Sci. Transl. Med.* 5, 208sr5 (2013) Credit: *Science* Source

Science Translational Medicine | AAAS
INTEGRATING SCIENCE, ENGINEERING, AND MEDICINE

Find out more about the scope of the journal and submit your research today. **ScienceTranslationalMedicine.org**

ELECTROPHYSIOLOGY SYSTEMS

Bundled Configurations

NEW



Sutter Instrument is now offering several systems or "Big Kits" that include dual manipulators and either manipulator stands and scope translator or a large moving stage.

FEATURES

- Discounted pricing offers savings and value
- Classic electrophysiology design – single system configuration
- 2 manipulators with each bundled system
- Easy toggle selection of active component
- Single ROE controls manipulators and components
- Manipulator, stage and translator features retained
- Compatible with a wide range of imaging software platforms

SUTTER INSTRUMENT

PHONE: 415.883.0128 | FAX: 415.883.0572
EMAIL: INFO@SUTTER.COM | WWW.SUTTER.COM



Image: jim / AdobeStock

Be Among the First to Publish in *Science Robotics*

NOW ACCEPTING MANUSCRIPTS

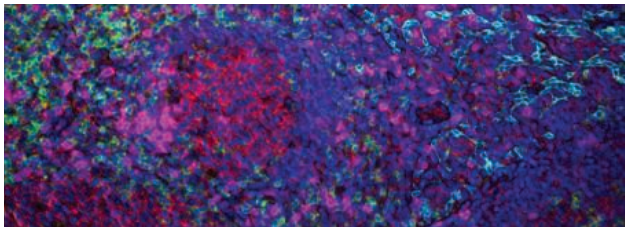
ScienceRobotics.org

Science Robotics is a unique journal created to help advance the research and development of robotics for all environments. *Science Robotics* will provide a much-needed central forum to share the latest technological discoveries and to discuss the field's critical issues.

Join in the excitement for the Fall 2016 debut!

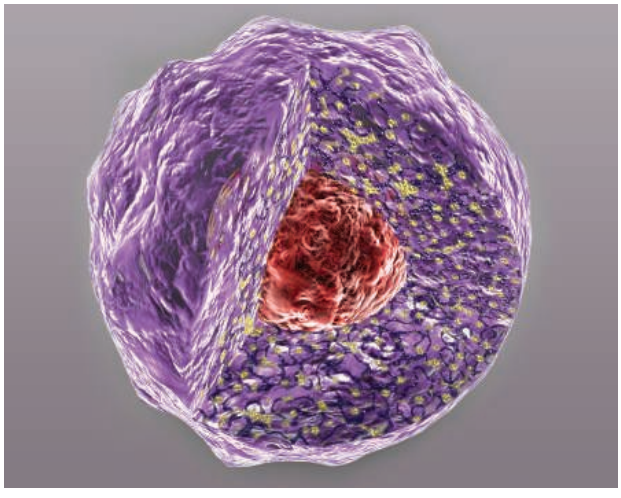
Science Robotics
AAAS

want new technologies?





antibodies
apoptosis
biomarkers
cancer
cytometry
data
diseases
DNA
epigenetics
genomics
immunotherapies
medicine
microbiomics
microfluidics
microscopy
neuroscience
proteomics
sequencing
toxicology
transcriptomics





watch our webinars

Learn about the latest break-throughs, new technologies, and ground-breaking research in a variety of fields. Our expert speakers explain their quality research to you and answer questions submitted by live viewers.

VIEW NOW!
webinar.sciencemag.org

Science
AAAS

Brought to you by the *Science*/AAAS Custom Publishing Office

@SciMagWebinars

CELL SIGNALING TECHNOLOGY

Rooted In Science



As a company rooted in science we are committed to producing and rigorously validating our products in house. This ensures they will work in your experiments and be worthy of the important research eff orts they support.

We are proud to be recognized by scientists for our eff orts to be leaders in key validation areas.*

*#1 Rank: *2015 Biocompare Antibody Market Report* • www.cellsignal.com/**rooted**

16PADSCORP0090ENG

For Research Use Only. Not For Use In Diagnostic Procedures.

© 2016 Cell Signaling Technology, Inc. Cell Signaling Technology, and CST are trademarks of Cell Signaling Technology, Inc.

Cell Signaling TECHNOLOGY®



There's only one Science

Science Careers Advertising

For full advertising details, go to ScienceCareers.org and click For Employers, or call one of our representatives.

Tracy Holmes
Worldwide Associate Director
Science Careers
Phone: +44 (0) 1223 326525

THE AMERICAS

E-mail: advertise@sciencecareers.org
Fax: +1 (202) 289 6742

Tina Burks
Phone: +1 (202) 326 6577

Nancy Toema
Phone: +1 (202) 326 6578

Online Job Posting Questions
Phone: +1 (202) 312 6375

EUROPE / INDIA / AUSTRALIA / NEW ZEALAND / REST OF WORLD

E-mail: ads@science-int.co.uk
Fax: +44 (0) 1223 326532

Sarah Lelarge
Phone: +44 (0) 1223 326527

Kelly Grace
Phone: +44 (0) 1223 326528

Online Job Posting Questions
Phone: +44 (0) 1223 326528

JAPAN

Katsuyoshi Fukamizu (Tokyo)
E-mail: kfukamizu@aaas.org
Phone: +81 3 3219 5777

Hiroyuki Mashiki (Kyoto)
E-mail: hmashiki@aaas.org
Phone: +81 75 823 1109

CHINA / KOREA / SINGAPORE / TAIWAN / THAILAND

Ruolei Wu
E-mail: rwu@aaas.org
Phone: +86 186 0082 9345

Danny Zhao
E-mail: dzhao@aaas.org
Phone: +86 131 4114 0012

All ads submitted for publication must comply with applicable U.S. and non-U.S. laws. *Science* reserves the right to refuse any advertisement at its sole discretion for any reason, including without limitation for offensive language or inappropriate content, and all advertising is subject to publisher approval. *Science* encourages our readers to alert us to any ads that they feel may be discriminatory or offensive.

ScienceCareers
FROM THE JOURNAL SCIENCE AAAS

ScienceCareers.org



There's only one *Science*.

Faculty Careers

Issue date: September 16
Book ad by August 30
Ads accepted until Sept 9 if space allows

Issue date: October 7
Book ad by September 20
Ads accepted until Sept 30 if space allows

Hiring Faculty? Whatever your timing, we've got two special features for your faculty ads this fall! The Sept 16 feature offers advice on how to develop skills for reviewing grants and papers. The Oct 7 feature covers business principles for researchers. Reach *Science* readers and share opportunities at your university.

What makes *Science* the best choice for recruiting?

- Read and respected by 400,000 readers around the globe
- 62% of our weekly readers work in academia and 65% are Ph.D.s. *Science* connects you with more scientists in academia
- Your ad dollars support AAAS and its programs, which strengthens the global scientific community.

Why choose these Faculty Features for your advertisement?

- Relevant ads lead off these career sections with a special Faculty banner
- October 7 issue will be distributed at the American Society of Human Genetics meeting, 18–22 October, Vancouver.

Expand your exposure by posting your print ad online:

- Link on the job board homepage directly to Faculty jobs
- Dedicated landing page for faculty positions.

*Ads accepted until Sept 9 and Sept 30 if space allows.

Produced by the until *Science*/AAAS Custom Publishing Office.



SCIENCECAREERS.ORG

Science Careers
AAAS

To book your ad: **advertise@sciencecareers.org**

The Americas
202 326 6582

Europe/RoW
+44(0)1223 326500

Japan
+81 3 3219 5777

China/Korea/Singapore/Taiwan
+86 186 0082 9345

ÖAW AUSTRIAN ACADEMY OF SCIENCES

IMBA – INSTITUTE OF MOLECULAR BIOTECHNOLOGY

GROUP LEADER POSITIONS IN MOLECULAR, CELLULAR AND ORGANISMAL BIOLOGY

We invite applications for fully funded group leader positions at the Institute of Molecular Biotechnology of the Austrian Academy of Sciences (IMBA), Vienna.

The recruitment package includes positions for 2 PhD students, 1 postdoctoral researcher and 1 technician with consumables and investment budgets. Research groups enjoy free access to scientific core services including a Mouse House, Microscopy & Cytometry, Mass Spectrometry, Bioinformatics, and Stem Cell and Genome Engineering Facilities.

IMBA is one of the world's leading biomedical research institutes. Together with the IMP, GMI and MFPL, IMBA is part of the Vienna Biocenter (VBC) with one of the most competitive international PhD programs. The VBC is home to 1400 scientists and 700 students from over 40 different countries.

Vienna is a multicultural capital city, consistently ranking amongst the top 3 cities worldwide for the quality of living. Child care facilities are available at the VBC.

For further information, see: ***www.imba.oeaw.ac.at***.

Applications should include a CV, a summary of research achievements and future research plans, and the contact details for 3 referees. In your publication list please explain in a few sentences the relevance of your most important work.

Applications should be submitted electronically to
Sandra Prassel (*sandra.prassel@imba.oeaw.ac.at*) by **October 15, 2016**.

WWW.IMBA.OEAW.AC.AT

DR. BOHR-GASSE 3 | 1030 VIENNA, AUSTRIA
T: +43 1 79044 | F: +43 1 79044-110

IMBA Institute of Molecular Biotechnology of the Austrian Academy of Sciences

ÖAW AUSTRIAN ACADEMY OF SCIENCES

IMBA – INSTITUTE OF MOLECULAR BIOTECHNOLOGY

GROUP LEADER POSITIONS IN STEM CELL & DEVELOPMENTAL BIOLOGY AND MOLECULAR MEDICINE

We invite applications for fully funded group leader positions at the Institute of Molecular Biotechnology of the Austrian Academy of Sciences (IMBA), Vienna.

The recruitment package includes positions for 2 PhD students, 1 postdoctoral researcher and 1 technician with consumables and investment budgets. Research groups enjoy free access to scientific core services including a Mouse House, Microscopy & Cytometry, Mass Spectrometry, Bioinformatics, and Stem Cell and Genome Engineering Facilities.

IMBA is one of the world's leading biomedical research institutes. Together with the IMP, GMI and MFPL, IMBA is part of the Vienna Biocenter (VBC) with one of the most competitive international PhD programs. The VBC is home to 1400 scientists and 700 students from over 40 different countries.

Vienna is a multicultural capital city, consistently ranking amongst the top 3 cities worldwide for the quality of living. Child care facilities are available at the VBC.

For further information, see: ***www.imba.oeaw.ac.at***.

Applications should include a CV, a summary of research achievements and future research plans, and the contact details for 3 referees. In your publication list please explain in a few sentences the relevance of your most important work.

Applications should be submitted electronically to
Sonja Paulick (*Sonja.Paulick@imba.oeaw.ac.at*) by **October 15, 2016**.

WWW.IMBA.OEAW.AC.AT

DR. BOHR-GASSE 3 | 1030 VIENNA, AUSTRIA
T: +43 1 79044 | F: +43 1 79044-110

IMBA Institute of Molecular Biotechnology of the Austrian Academy of Sciences

Science Careers online @sciencecareers.org

ETH zürich

Professor or Assistant Professor (Tenure Track) of Observational Galactic Astrophysics

→ The Department of Physics (www.phys.ethz.ch) at ETH Zurich invites applications for this position.

→ Applicants should have already demonstrated leadership of research programs on major international observing facilities and must present a compelling vision for the future scientific exploitation of facilities such as ALMA, JWST and the E-ELT. We are particularly interested in the general research field of star and planet formation, but candidates in other related areas of Galactic astrophysics are also encouraged to apply. The primary consideration in the appointment will be demonstrated excellence of achievements and outstanding scientific potential for the future. Switzerland is a full member of both ESO and ESA and has access to all of their facilities. The professorship will be provided with sufficient resources in order to establish a significant research group. The new professor will be expected to teach undergraduate level courses in e.g. introductory physics (in either German or English) as well as graduate level courses in astrophysics (in English).

→ Depending on the experience, the position will be filled at assistant professor (tenure track) or full professor level. Assistant professorships have been established to promote the careers of younger scientists. ETH Zurich implements a tenure track system equivalent to other international top universities.

→ **Please apply online at www.facultyaffairs.ethz.ch**

→ Applications should include a curriculum vitae, a list of publications, a statement of future research and teaching interests, and three of your most important achievements. The letter of application should be addressed **to the President of ETH Zurich, Prof. Dr. Lino Guzzella. The closing date for applications is 31 October 2016**.
ETH Zurich is an equal opportunity and family friendly employer and is further responsive to the needs of dual career couples. Women are specifically encouraged to apply.

UT Southwestern Medical Center

TENURE-TRACK POSITIONS

The Department of Physiology invites outstanding scientists with Ph.D., M.D., or equivalent degrees to apply for tenure-track faculty positions at the level of Assistant or Associate Professor. Candidates who use innovative optical, mechanical, electrical, molecular biological or computational methods with important applications to physiological systems, ranging from individual genes and proteins to cells and organs are encouraged to apply. The scientific excellence of the candidates is more important than the specific area of research.

These positions are part of the continuing growth of the Department at one of the country's leading academic medical centers. They will be supported by significant laboratory space, competitive salaries, state-of-the-art core facilities and exceptional start up packages. The University of Texas Southwestern Medical Center is the scientific home to six Nobel Prize laureates and many members of the National Academy of Sciences and Institute of Medicine. UT Southwestern conducts more than 3,500 research projects annually totaling more than $417 million. Additional information about the Department of Physiology can be found at **http://www.utsouthwestern.edu/education/medical-school/departments/physiology/index.html**.

Applicants should submit a CV, a brief statement of current and proposed research, and summary of your two most significant publications describing the importance of the work (100-150 words each). Please arrange to have three letters of recommendation sent on his/her behalf. All items should be submitted to **http://academicjobsonline.org/ajo/jobs/7612**. Completed applications will be reviewed starting **November 1, 2016**. You may email questions to **ron.doris@utsouthwestern.edu**.

UT Southwestern Medical Center is an Equal Opportunity/Affirmative Action Employer. Women, minorities, veterans and individuals with disabilities are encouraged to apply.

Penn

Assistant Professor in the Energy Cluster at the University of Pennsylvania

As part of a larger investment to create the new Vagelos Institute for Energy Science and Technology, the School of Arts and Sciences at the University of Pennsylvania seeks to add faculty to our newly formed Energy Cluster spanning the natural sciences. We invite applications for a tenure-track assistant professor position in one of the following departments: Biology, Chemistry, Earth and Environmental Science, or Physics and Astronomy. Exceptional senior candidates will also be given consideration. The successful candidate will mount an innovative program of fundamental scientific research that impacts our societal energy challenges, broadly defined, and in doing so will forge collaborative links with other Penn scientists and engineers involved in energy research.

Applicants must apply online at **http://facultysearches.provost.upenn.edu/postings/937**. Required application materials include: curriculum vitae with a list of publications, a research statement that includes the candidate's perspective on how she or he fits into one of the four departments and identifies potential collaborative links with other natural science departments, and a teaching statement. Applicants should also submit the names and contact information for three individuals who will provide letters of recommendation. Review of applications will start on **October 15, 2016** and will continue until the position is filled. The School of Arts and Sciences is strongly committed to Penn's Action Plan for Faculty Diversity and Excellence and to establishing a more diverse faculty (for more information see: http://www.upenn.edu/almanac/volumes/v58/n02/diversityplan.html).

The University of Pennsylvania is an Equal Opportunity Employer. Minorities/Women/Individuals with disabilities/Protected Veterans are encouraged to apply.

ÉCOLE POLYTECHNIQUE
FÉDÉRALE DE LAUSANNE

Faculty Position in Advanced Micro-manufacturing

at the Ecole polytechnique fédérale de Lausanne (EPFL)

The Institute of Microengineering (IMT) within the School of Engineering at EPFL invites applications for a full-time faculty position in the area of **advanced micro-manufacturing**. Appointments will be considered at the level of tenure-track assistant professor or tenured professor, depending on the qualifications of the applicant.

This new position is part of the recently launched EPFL Micro-manufacturing Science and Engineering Center (EMC). It is aimed at reinforcing the leading position of the Swiss microengineering industry by providing the means to further strengthen its competitiveness through continuous innovation.

Specific areas include, but are not limited to:

- Additive and hybrid manufacturing processes of miniaturized components with micro-level precision;
- New approaches for the manufacturing of complex three-dimensional microsystems using a combination of digital manufacturing technologies.

Experience in successful collaborative research programs with industry is highly desirable. The IMT-EPFL offers a particularly advantageous position thanks to its historically very strong links to the diverse and well-established local high-technology industry.

As a faculty member of the School of Engineering, the successful candidate will be expected to initiate an independent and creative research program, participate in undergraduate and graduate teaching, and establish strong links with industrial partners within the framework of the new EMC.

Internationally competitive salaries, start-up resources and benefits are offered.

EPFL is a dynamically growing and well-funded institution fostering excellence and diversity. It has a highly international campus at an exceptionally attractive location boasting first-class infrastructure. As a technical university covering essentially the entire palette of engineering and science, EPFL offers a fertile environment for research cooperation between different disciplines. The EPFL environment is multi-lingual and multi-cultural, with English often serving as a common interface.

Applications should include a cover letter with a statement of motivation, curriculum vitae, list of publications and patents, concise statement of research and teaching interests, and the names and addresses of at least five referees. Applications must be uploaded in PDF format to the recruitment web site:

go.epfl.ch/imt-search

Formal evaluation of candidates will begin on **December 1st, 2016** and continue until the position is filled.

Enquiries may be addressed to:

Prof. Christian Enz
Search Committee Chair
Email: **imt-search@epfl.ch**

For additional information on EPFL, please consult the web sites:
www.epfl.ch, sti.epfl.ch and **imt.epfl.ch**.

EPFL is committed to increasing the diversity of its faculty, and strongly encourages women to apply.

ÉCOLE POLYTECHNIQUE
FÉDÉRALE DE LAUSANNE

Faculty Position in Bioengineering

at the Ecole polytechnique fédérale de Lausanne (EPFL)

The Institute of Bioengineering at EPFL is soliciting applications for a tenure-track assistant professor conducting cutting-edge research at the *interface of bioengineering and cancer biology*. Appointments at other ranks will be exceptionally considered as well. Areas of interest include, but are not limited to: synthetic biology, biomolecular engineering, organoid and organ/tumor-on-a-chip technology, immune-engineering as well as innovative approaches to detecting, monitoring and treating cancer.

Bioengineering at EPFL is well integrated between the School of Engineering and the School of Life Sciences. Close interactions with the Ludwig Institute for Cancer Research, the University of Lausanne, the Canton of Vaud University Hospital (CHUV), and the Wyss Center in Geneva are possible, and encouraged.

The EPFL is a dynamic science and engineering university fostering excellence and diversity. It is consistently ranked among the top research institutions in Europe, and offers a rich international environment with English as the common language. Research is supported by numerous outstanding core facilities including imaging, proteomics, bioinformatics, transgenomics, flow cytometry, microfabrication, and biomolecular screening.

Successful candidates are expected to initiate independent, creative research programs and participate in undergraduate and graduate-level teaching. Internationally competitive salaries, start-up resources and benefits are offered.

Applications should include a cover letter, a curriculum vitae with a list of publications, a concise statement of research and teaching interests, and the names and addresses (including e-mail) of at least three referees. Applications should be uploaded (as PDF files) to the recruitment web site:

go.epfl.ch/ibi-search

Formal evaluation of candidates will begin on **December 1st, 2016** and continue until the position is filled.

Enquiries may be sent to:

Prof. Matthias P. Lütolf
Search Committee Chair
Email: **ibi-search@epfl.ch**

For additional information on the EPFL and the Institute of Bioengineering, please consult: **www.epfl.ch, sti.epfl.ch, sv.epfl.ch** and **bioengineering.epfl.ch**.

EPFL is committed to increasing the diversity of its faculty, and strongly encourages women to apply.

ScienceCareers online @sciencecareers.org

ScienceCareers online @sciencecareers.org

MEDICAL SCHOOL
UNIVERSITY OF MICHIGAN

Bioinformatics Lecturer Position

The Department of Computational Medicine and Bioinformatics at the University of Michigan Medical School seeks outstanding applicants for a full-time Lecturer position.

Major duties include:

1. Redesign and teach an introductory graduate-level programming course with a focus on bioinformatics data analysis and applications. This course should be accessible to non-bioinformatics students with little or no prior programming experience.
 - Integrate lectures and hands-on laboratory sessions.
 - Prepare course objectives, lessons, exercises/projects, exams, and hands-on problem sets; make efficient use of existing online teaching infrastructure.
 - Develop didactic material for real-life applications.
 - Annually update as the field evolves, with student questionnaires to evaluate effectiveness of the curriculum.
 - Supervise the Graduate Student Instructor for the course.
2. Teach in DCMB's existing introductory graduate bioinformatics course.
 - Work with the Course Director on course design.
 - Prepare, update, and present lectures on bioinformatics topics, with adequate biological background.
 - Develop and present bioinformatics laboratory sessions to complement the lectures.
 - Supervise the activities of the Graduate Student Instructors for the course
3. Depending on the candidate's background in biological sciences, he/she may participate in teaching the two-week intensive Introduction to Biology course in the summer, Bioinformatics Basic Biology Lab, also known as the "Biology Boot Camp" or in the currently 1 week intensive Introduction to Biocomputing camp.
4. Participate in the review, recruitment, and admissions of the Master's in Bioinformatics Program. Assist in advising master's students in the program about research options and external internship opportunities.
5. Organize the weekly DCMB graduate student research presentations. This includes scheduling the talks, preparing announcements, and attending and moderating the student presentations.

There are opportunities for a partial research-track faculty appointment in a related department. This position is covered under the collective bargaining agreement between the U-M and the Lecturers Employee Organization, AFL-CIO, which contains and settles all matters with respect to wages, benefits, hours and other terms and conditions of employment.

Qualifications: Candidates for this position should have a PhD in Bioinformatics, Biology or a related field with experience in bioinformatics, and ability to program comfortably in multiple languages. Ability to teach an introductory programming course, preferably in Python, is required. Preferred candidates will have sufficient background in biology to teach introductory course to students lacking a background in college-level biology. Also desired are 2+ years of teaching at college or graduate level and evidence of expertise in course development and evaluation. Must have outstanding verbal and written communication skills. Favorable attention will be given to demonstrated interest and ability in developing additional course(s) that closely follow the emerging topics in bioinformatics, including but not limited to cloud computing, cybersecurity, mobile apps, e-notebooks, and high-performance computing.

Applicants should send a letter of interest with Curriculum Vitae, Statement of teaching philosophy and interests, and a list of three or more references with current contact information to:

Search Committee,
Department of Computational Medicine and Bioinformatics
Job Code 400
The University of Michigan
2017 Palmer Commons
100 Washtenaw Ave
Ann Arbor, MI. 48109-2218
email: ccmbrecruit@umich.edu

http://www.ccmb.med.umich.edu

UNIVERSITÄT DUISBURG ESSEN

CRC 1242

Several PhD Positions Open at Universität Duisburg-Essen to Study Time-Evolution of Non-Equilibrium Situations in Condensed Matter

We are seeking several highly motivated PhD students to work in the Collaborative Research Centre 1242 "Non-Equilibrium Dynamics of Condensed Matter in the Time Domain" newly granted by the German Science Foundation for initially 4 years. The centre is formed by 21 principal investigators that are specialists in areas such as ultra-fast laser and/or electron spectroscopy, ion scattering, surface microscopy or theoretical condensed matter physics. By combining sophisticated experiments with high-level theory development and modelling, we aim to develop a fundamental understanding of the mechanisms governing the time-evolution of strongly excited condensed matter systems.

You will be a key player in one of the scientific projects which will provide you with research experience in an excellent scientific environment and ensure that you develop scientific independence and the skills to work successfully in a team. In addition, an Internal Research Training Group (IRTG) will help you to develop the skills necessary for a future career in academics or industry. Moreover, the IRTG supports a one-month exchange visit to a partner laboratory abroad during the course of your PhD work.

Since the CRC 1242 is devoted to promoting the equitable participation of women in chemistry and physics, we especially encourage young women to apply to our programme to pursue a career in science. Women can take advantage of special supportive offerings to help them excel throughout the entire programme.

Aside from excellent performance in your studies, we anticipate that you have a great enthusiasm for science and a keen interest in attaining research goals. Furthermore, we expect your participation in the joint organisation of the IRTG and its activities, such as workshops, training courses and presentations.

- **For further information and application details please visit: https://www.uni-due.de/sfb1242/open_positions.php**
- **Applications should preferably be received by Oct 15st, 2016**
- **The PhD positions are for three years**



Keep your job search out of the cheap seats.

- Search thousands of job postings
- Create job alerts based on your criteria
- Get career advice from our Career Forum experts
- Download career advice articles and webinars
- Complete an individual development plan at "myIDP"

Target your job search using relevant resources on **ScienceCareers.org**.

ScienceCareers
FROM THE JOURNAL SCIENCE AAAS

ÉCOLE POLYTECHNIQUE
FÉDÉRALE DE LAUSANNE

Faculty Position in Inorganic Materials

at the Ecole polytechnique fédérale de Lausanne (EPFL)

The School of Engineering (STI) of EPFL invites applications for a tenure-track assistant position in **inorganic materials** within the Institute of Materials. We seek exceptional individuals who will develop and drive a research program at the forefront of the discipline, who have a strong dedication to teaching at the undergraduate and graduate levels, and who will be proactive members of a vibrant Materials community.

Top-level applications are invited in all areas related to the design, synthesis, processing and characterization of functional inorganic materials including, but not limited to: materials for energy harvesting, conversion or storage; novel semiconductors; electronic, catalysis or photonic materials as well as materials for information technology or devices.

As a faculty member of the School of Engineering, the successful candidate will be expected to initiate an independent and creative research program and participate in undergraduate and graduate teaching. Internationally competitive salaries, start-up resources and benefits are offered.

EPFL, with its main campus located in Lausanne, Switzerland, is a dynamically growing and well-funded institution fostering excellence and diversity. It has a highly international campus at an exceptionally attractive location boasting first-class infrastructure. As a technical university covering essentially the entire palette of engineering and science, EPFL offers a fertile environment for research cooperation between different disciplines. The EPFL environment is multi-lingual and multi-cultural, with English often serving as a common interface.

Applications should include a cover letter with a statement of motivation, curriculum vitae, list of publications and patents, concise statement of research and teaching interests, and the names and addresses of at least five referees. Applications must be uploaded in PDF format to the recruitment web site:

go.epfl.ch/imx-search

Formal evaluation of candidates will begin on **December 1st, 2016** and continue until the position is filled.

Enquiries may be addressed to:

Prof. Harm-Anton Klok
Search Committee Chair
Email: **imx-search@epfl.ch**

For additional information on EPFL, please consult the web sites: **www.epfl.ch, sti.epfl.ch** and **imx.epfl.ch**.

EPFL is committed to increasing the diversity of its faculty, and strongly encourages women to apply.



FRIEDRICH-ALEXANDER
UNIVERSITÄT
ERLANGEN-NÜRNBERG

NATURWISSENSCHAFTLICHE
FAKULTÄT

The Faculty of Sciences invites applications for a permanent

W3 Professorship in Mathematics in Life Sciences

at the Department of Biology to be filled by the earliest possible starting date.

Applicants should be recognized internationally for their expertise in spatial and temporal mathematical modelling of phenomena in cell physiology, modelling of integrative processes in system biology, or self-organisation in molecular and cellular processes. The successful candidate is expected to teach mathematics in the Integrated Life Sciences degree programme.

The professorship is part of a dynamic and interdisciplinary environment linking mathematics, physics, biology, and medicine. The appointed professor will have the opportunity to become a member of the new Centre for Physics and Medicine, which is currently being established by FAU in collaboration with the Max Planck Institute for the Science of Light. Collaborations with Collaborative Research Centres and other research initiatives are desirable.

Prerequisites for the position are a university degree, university level teaching experience, a doctoral degree, and additional academic qualifications. These should be in the form of a Habilitation or equivalent research achievements. The necessary qualifications may also have been acquired in a non-university context or through a junior faculty position (e.g. W1 Professor or Assistant Professor).

FAU expects applicants to become actively involved in the administration of academic affairs, managing research projects and raising third-party funding.

The University of Erlangen-Nürnberg pursues a policy of intense student mentoring and therefore expects its teaching staff to be present during lecture periods.

FAU is a family-friendly employer and is also responsive to the needs of dual career couples. In its pursuit of academic excellence, FAU is committed to equality of opportunity and to a proactive and inclusive approach, which supports and encourages all under-represented groups, promotes an inclusive culture and values diversity.

Please submit your complete application documents (CV, list of publications, list of lectures and courses taught, copies of certificates and degrees, list of third-party funding) to the Dean of the Faculty of Sciences, FAU Erlangen-Nürnberg, Universitätsstraße 40, 91054 Erlangen, by **17.10.2016**. Please also send an electronic version to dekanat-nat@fau.de.

Grundzertifikat 2008 audit familiengerechte hochschule

www.fau.de

ScienceCareers online @sciencecareers.org

10 ways that *Science* Careers can help advance your career

1. Register for a free online account on **ScienceCareers.org**.
2. Search thousands of job postings and find your perfect job.
3. Sign up to receive e-mail alerts about job postings that match your criteria.
4. Upload your resume into our database and connect with employers.
5. Watch one of our many webinars on different career topics such as job searching, networking, and more.
6. Download our career booklets, including Career Basics, Careers Beyond the Bench, and Developing Your Skills.
7. Complete an interactive, personalized career plan at "my IDP."
8. Visit our Career Forum and get advice from career experts and your peers.
9. Research graduate program information and find a program right for you.
10. Read relevant career advice articles from our library of thousands.



Visit **ScienceCareers.org** today — all resources are free

ScienceCareers

FROM THE JOURNAL SCIENCE AAAS

SCIENCECAREERS.ORG

2016 Annual
Top Employers in Biotech & Pharma

Special Career Feature:
October 28, 2016

Reserve your ad by October 11 to guarantee space.

Ads accepted until October 21 if space is still available.



For recruitment in science, there's only one Science

WHO IS NO. 1 THIS YEAR?

Science publishes the results of its 15th annual Top Employers Survey on October 28. *Science* has a long history of providing a forum for scientists to express their opinions about the biotech and pharma industry.

Recruit or brand your organization and reach both ACTIVE and PASSIVE job seekers.

Start building your pipeline today with *Science*.



SCIENCECAREERS.ORG

ScienceCareers
FROM THE JOURNAL SCIENCE AAAS

To book your ad:
advertise@sciencecareers.org

The Americas
202-326-6582

Japan
+81-3-3219-5777

Europe/RoW
+44(0)1223-326500

China/Korea/Singapore/Taiwan
+86-186-0082-9345

University of Zurich[UZH]

Faculty of Science

The Faculty of Science at the University of Zurich invites applications for a

Professorship in Pure Mathematics

in order to complement our team of experts in mathematics.

Candidates are expected to be internationally recognized mathematicians. Candidates with outstanding records in algebra, analysis, geometry or topology are particularly encouraged to apply. Applicants with a background in other relevant fields of pure mathematics are also encouraged to apply.

The successful candidate is expected to develop an independent research group in pure mathematics. Contributing to the existing undergraduate and graduate teaching efforts in mathematics (in English or German) will form an integral part of the position. The successful candidate should further contribute to the development of the institute and is expected to acquire external funding. The position will be preferentially filled at the level of full professor, but offers the possibility of open rank hiring as well. The position may be occupied as a part-time or shared professorship.

The University of Zurich provides generous research support, including dedicated funds for personnel and running expenses, and competitive start-up packages. Zurich's scientific environment includes a rich spectrum of research activities in mathematics, and provides extensive opportunities for collaborations within the University and with the ETH Zurich. Switzerland provides excellent opportunities for external funding of research. The University and the city of Zurich also offer a stimulating cultural and family-friendly environment.

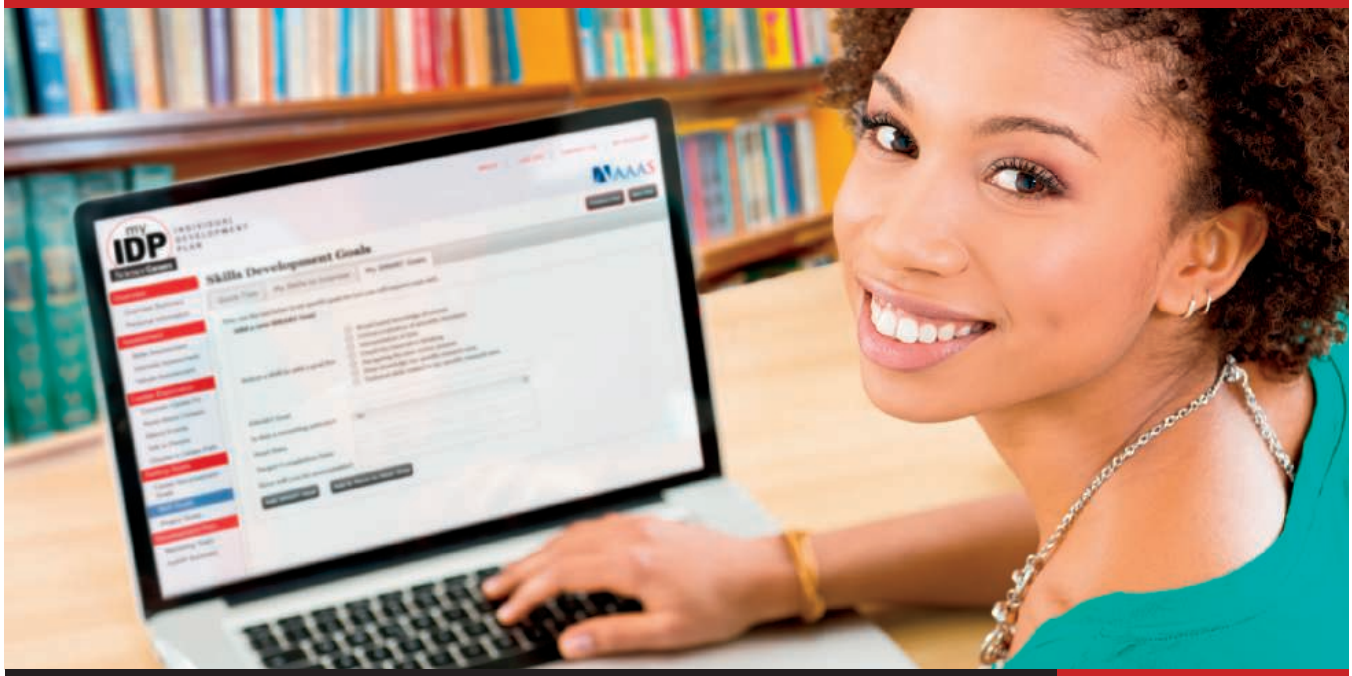
Application packages should include a one-page summary; motivation letter; a full curriculum vitae; a vision statement of research and teaching interests. Applicants may provide names and addresses of up to three potential referees (see http://jobs.mnf.uzh.ch/mat for guidelines). Documents should be addressed to Prof. Dr. Michael Schaepman, Dean of the Faculty of Science, University of Zurich, and uploaded **as a single PDF file** to http://jobs.mnf.uzh.ch/mat by October 23, 2016. For further information, please contact Prof. Dr. Alberto Cattaneo at alberto.cattaneo@math.uzh.ch, or visit the homepage at www.math.uzh.ch.

The University of Zurich is an equal opportunity employer.

ScienceCareers online @sciencecareers.org

ScienceCareers online @sciencecareers.org

myIDP: A career plan customized for you, by you.



For your career in science, there's only one Science

my IDP
ScienceCareers

Recommended by leading professional societies and the NIH

Features in myIDP include:

- Exercises to help you examine your skills, interests, and values.
- A list of 20 scientific career paths with a prediction of which ones best fit your skills and interests.
- A tool for setting strategic goals for the coming year, with optional reminders to keep you on track.
- Articles and resources to guide you through the process.
- Options to save materials online and print them for further review and discussion.
- Ability to select which portion of your IDP you wish to share with advisors, mentors, or others.
- A certificate of completion for users that finish myIDP.

Visit the website and start planning today!
myIDP.sciencecareers.org

ScienceCareers In partnership with:

advancing the life sciences 1912-2012 FASEB Federation of American Societies for Experimental Biology

UCSF University of California San Francisco

Medical College of Wisconsin

Burroughs Wellcome Fund

DEPARTMENT HEAD OF ECOLOGY
Montana State University

The Ecology Department seeks an excellent scientist/experienced leader with strong academic credentials and a commitment to excellence in teaching and research to provide vision, leadership, direction, and expert administration for a dynamic, productive department. The department includes thirteen tenured or tenure-track faculty and two USGS Cooperative Fishery Research Unit faculty with research programs that are recognized regionally, nationally and internationally, a rapidly growing undergraduate program with more than 400 majors, and successful M.S. and Ph.D. programs that include more than 50 graduate students. The department offers B.S. degrees with emphases in Fish and Wildlife Ecology and Management, Conservation Biology and Ecology, Organismal Biology, and Biology Teaching and graduate degrees in Ecology and Environmental Science, Fish and Wildlife Biology and Management, and Biological Science. We seek a head to facilitate and promote the continued progress in this outstanding department. For more information and application instructions see website: **https://jobs.montana.edu/postings/5631**. Screening of applications will begin on or before **October 3, 2016**; however, applications will continue to be accepted until the position is filled. *Montana State University is an Equal Opportunity Employer, Veterans/Disabled*

Post your jobs
Fast and Easy



ScienceCareers
employers.sciencecareers.org

Post Your Jobs
1.4 million candidates*
235,000 job applications*

Reach Scientists.
Fill Positions.

*Jan–Dec 2015

ScienceCareers
employers.sciencecareers.org

Williams

Molecular Geneticist
Tenure -Track Faculty Position
Biology Department

The Biology Department at Williams College, a premier liberal arts college with a long-standing tradition of excellence in the sciences, invites applications for a tenure-track position at the rank of Assistant Professor, to begin July 2017. We are especially interested in candidates who can contribute to the intellectual vibrancy and diversity of the academic community through their research, teaching, and service, and who are committed to working effectively with a diverse student population.

We seek a broadly trained molecular geneticist whose research should incorporate state-of-the-art methods and address questions of broad biological significance. The successful candidate will teach an introductory core course in genetics as well as upper level courses in his or her area of specialty. This individual will advise undergraduates in research and participate in interdisciplinary programs in Biochemistry and Molecular Biology, and/or Bioinformatics, Genomics & Proteomics. Normally, faculty members teach one course and two associated laboratory sections (or the equivalent) each semester.

A dynamic research program that is attractive to extramural funding agencies and involves talented undergraduates is expected. Start-up funds and internal funding for research are available. A Ph.D., postdoctoral experience, and a strong research record are required. We anticipate the appointment at the beginning assistant professor level, although a more senior appointment may be possible under special circumstances.

Application deadline is **October 24, 2016** and all applications should be submitted through Interfolio at **https://apply.interfolio.com/36614**. Email, fax, and paper applications will not be accepted. The application should include a cover letter addressed to Professor Joan Edwards (Chair, Biology Department), a curriculum vitae, concise statements of teaching and research plans, and three current letters of recommendation. All offers of employment are contingent upon completion of a background check. Further information is available here: http://faculty.williams.edu/prospective-faculty/background-check-policy/.

Williams College is a coeducational liberal arts institution located in the Berkshire Hills of western Massachusetts. The College has built its reputation on outstanding teaching and scholarship and on the academic excellence of its approximately 2,000 students. Please visit the Williams College website (**http://www.williams.edu**). Beyond meeting fully its legal obligations for non-discrimination, Williams College is committed to building a diverse and inclusive community where members from all backgrounds can live, learn, and thrive.

Williams

Evolutionary Ecologist
Tenure -Track Faculty Position
Biology Department

The Biology Department at Williams College, a premier liberal arts college with a long-standing tradition of excellence in the sciences, invites applications for a tenure-track position at the rank of Assistant Professor, to begin July 2017. We are especially interested in candidates who can contribute to the intellectual vibrancy and diversity of the academic community through their research, teaching, and service, and who are committed to working effectively with a diverse student population.

We seek a broadly trained evolutionary ecologist whose research incorporates state-of-the-art methods and a strong field component to address questions of broad ecological significance. The successful candidate will teach the organismal course in our introductory sequence as well as upper-level courses in ecology and evolutionary biology. This individual will advise undergraduates in research and potentially participate in interdisciplinary programs such as Environmental Studies and/or Bioinformatics, Genomics and Proteomics. Normally, faculty members teach one course and two associated laboratory sections (or the equivalent) each semester.

A dynamic research program that is attractive to extramural funding agencies and involves talented undergraduates is expected. Start-up funds and internal funding for research are available. A Ph.D., postdoctoral experience, and a strong research record are required. We anticipate the appointment at the beginning assistant professor level, although a more senior appointment may be possible under special circumstances.

Application deadline is **October 24, 2016** and all applications should be submitted through Interfolio at **https://apply.interfolio.com/36611**. Email, fax, and paper applications will not be accepted. The application should include a cover letter addressed to Professor Joan Edwards (Chair, Biology Department), a curriculum vitae, concise statements of teaching and research plans, and three current letters of recommendation. All offers of employment are contingent upon completion of a background check. Further information is available here: http://faculty.williams.edu/prospective-faculty/background-check-policy/.

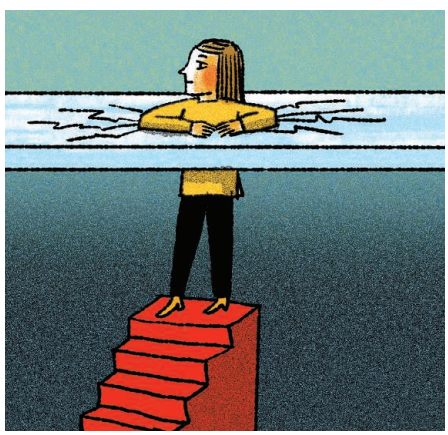
Williams College is a coeducational liberal arts institution located in the Berkshire Hills of western Massachusetts. The College has built its reputation on outstanding teaching and scholarship and on the academic excellence of its approximately 2,000 students. Please visit the Williams College website (**http://www.williams.edu**). Beyond meeting fully its legal obligations for non-discrimination, Williams College is committed to building a diverse and inclusive community where members from all backgrounds can live, learn, and thrive.

By **Yarrow Axford**

Thanks to the glass ceiling breakers

The night that Hillary Clinton was nominated as a candidate for president, my Facebook feed lit up with cries of historic triumph. But my own celebration was bittersweet. I was thrilled to see Hillary crack that glass ceiling, but I couldn't stop thinking about the spine of steel it took for her to reach that milestone. Sexism has stalked her relentlessly on her climb up the ladder, taking forms including mocking references to "cankles" and cackling, a "Bern the Witch" debate viewing party, and "Trump that Bitch" buttons. For me, she has long personified both the progress that women have made and the challenges we still face as we climb the rungs of our professions.

As a high school student in 1992, when Bill Clinton ran for president, I was delighted to see a prospective first lady (a law partner!) use her maiden name and get political. That same year, I silently fumed when my geometry teacher repeatedly told my class that girls were doomed to struggle with math because their brains are washed with corrosive chemicals in the womb. The next year, though, a different math teacher suggested that I consider a career in science. Things seemed to be moving in a positive direction—and indeed they were.



"Every woman ... at the head of a table helps, although they remain too rare."

Today, I'm living my dream of a tenure-track job at a great university with progressive family leave policies and supportive, inspiring co-workers. I am a grateful beneficiary of decades of hard work by others to make science more inclusive. The prevalent "no girls allowed" attitudes that female scientists encountered in decades past have dwindled. Science even has its own recent breakers of glass ceilings, such as geophysicist Marcia McNutt, who this year became the first female president of the National Academy of Sciences (NAS).

And yet, despite how far science has come, I still hear frequent echoes of those comments from my geometry teacher. I have an androgynous name, and have lost track of how many times I've met a colleague for the first time and been told, "I've read your papers. I thought you were a man!" While conducting fieldwork, my much younger male student has repeatedly been mistaken for the professor. (And me for what? His graying apprentice? His mom?)

I try to laugh off such encounters to hide how they make me cringe. They generally reveal unconscious biases held by well-meaning people. Such incidents seem trivial compared with, say, the sexual harassment that 70% of women reported experiencing during fieldwork in a 2014 survey of anthropologists. But all experiences of bias or sexism, from the almost comical to the clearly criminal, combine to form a discouraging drumbeat that only the affected can hear: You still don't belong. Well-documented biases in metrics such as supervisors' evaluations and students' course ratings amplify that drumbeat.

Some of the remaining challenges for women in science are either so personal (as with sexual harassment) or superficially innocuous (as with "I thought you'd be a man") that we don't often share them beyond close friends. Examples of sexism occasionally reach the public spotlight, as when a Nobel laureate opined last year about his "trouble with girls" in the lab, but more often they are a quiet part of day-to-day working life. My own stories are unremarkable, but that in itself is a reason to share them.

Two decades into my scientific career, the drumbeat continues but is easier to disregard. I have been fortunate to work with a long list of supportive mentors and colleagues. Every line that I add to my CV reminds me that I belong at the table. Every woman scientist I see at the head of a table helps, although they remain too rare. (NAS and *Science* have each had just one woman at the helm, and they are the same woman.) My parents always insisted that I could grow up to be anything, and thanks to breakers of glass ceilings that is increasingly true. But true equality won't be achieved until our daughters can march through their careers to the same drumbeat their brothers hear. ■

Yarrow Axford is an assistant professor of earth and planetary sciences at Northwestern University in Evanston, Illinois. Send your story to SciCareerEditor@aaas.org.

ILLUSTRATION: ROBERT NEUBECKER

Downloaded from http://science.sciencemag.org/ on September 2, 2016

Published by AAAS